GEOSPACE OBSERVATION OF NATURAL HAZARDS

EDITED BY: Dimitar Ouzounov, Jann-Yenq Liu, Patrick Timothy Taylor and Katsumi Hattori

PUBLISHED IN: Frontiers in Earth Science

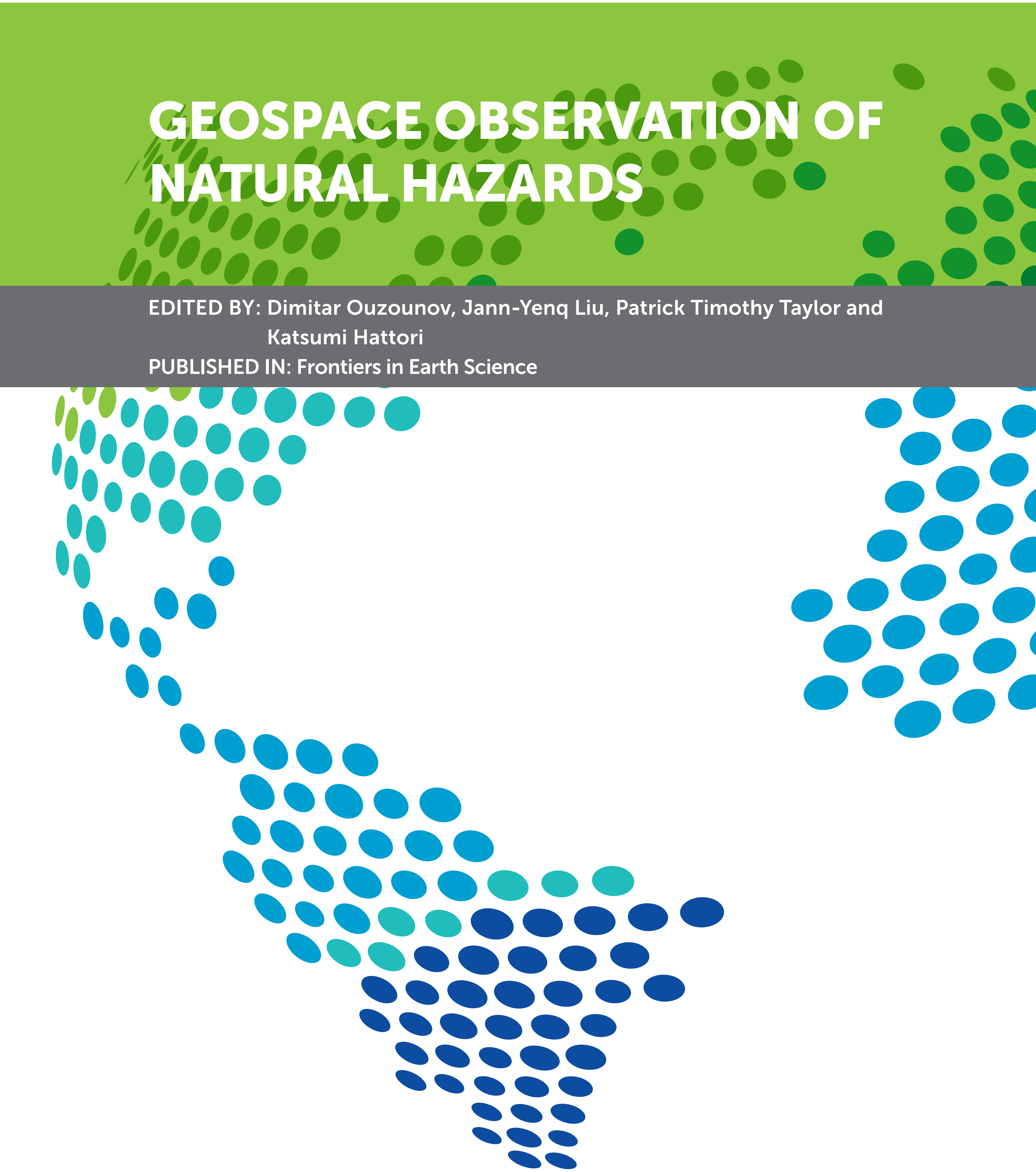

frontiers Research Topics

ISSN 1664-8714
ISBN 978-2-88974-525-8
DOI 10.3389/978-2-88974-525-8

About Frontiers

Frontiers is more than just an open-access publisher of scholarly articles: it is a pioneering approach to the world of academia, radically improving the way scholarly research is managed. The grand vision of Frontiers is a world where all people have an equal opportunity to seek, share and generate knowledge. Frontiers provides immediate and permanent online open access to all its publications, but this alone is not enough to realize our grand goals.

Frontiers Journal Series

The Frontiers Journal Series is a multi-tier and interdisciplinary set of open-access, online journals, promising a paradigm shift from the current review, selection and dissemination processes in academic publishing. All Frontiers journals are driven by researchers for researchers; therefore, they constitute a service to the scholarly community. At the same time, the Frontiers Journal Series operates on a revolutionary invention, the tiered publishing system, initially addressing specific communities of scholars, and gradually climbing up to broader public understanding, thus serving the interests of the lay society, too.

Dedication to Quality

Each Frontiers article is a landmark of the highest quality, thanks to genuinely collaborative interactions between authors and review editors, who include some of the world's best academicians. Research must be certified by peers before entering a stream of knowledge that may eventually reach the public - and shape society; therefore, Frontiers only applies the most rigorous and unbiased reviews.
Frontiers revolutionizes research publishing by freely delivering the most outstanding research, evaluated with no bias from both the academic and social point of view. By applying the most advanced information technologies, Frontiers is catapulting scholarly publishing into a new generation.

What are Frontiers Research Topics?

Frontiers Research Topics are very popular trademarks of the Frontiers Journals Series: they are collections of at least ten articles, all centered on a particular subject. With their unique mix of varied contributions from Original Research to Review Articles, Frontiers Research Topics unify the most influential researchers, the latest key findings and historical advances in a hot research area! Find out more on how to host your own Frontiers Research Topic or contribute to one as an author by contacting the Frontiers Editorial Office: frontiersin.org/about/contact

GEOSPACE OBSERVATION OF NATURAL HAZARDS

Topic Editors:
Dimitar Ouzounov, Chapman University, United States
Jann-Yenq Liu, National Central University, Taiwan
Patrick Timothy Taylor, Goddard Space Flight Center, National Aeronautics and Space Administration, United States
Katsumi Hattori, Chiba University, Japan

Citation: Ouzounov, D., Liu, J.-Y., Taylor, P. T., Hattori, K., eds. (2022). Geospace Observation of Natural Hazards. Lausanne: Frontiers Media SA.
doi: 10.3389/978-2-88974-525-8

Table of Contents

frontiers
in Earth Science

EDITORIAL
published: 24 January 2022
doi: 10.3389/feart.2022.836629

Editorial: Geospace Observation of Natural Hazards

Dimitar Ouzounov[1], Jann-Yenq Liu[2], Patrick T. Taylor[3] and Katsumi Hattori[4]*

[1]Center of Excellence for Earth Systems Science and Observations, Chapman University, Orange, CA, United States, [2]Center for Astronautical Physics and Engineering, National Central University, Jungli City, Taiwan, [3]Goddard Space Flight Center, National Aeronautics and Space Administration, Greenbelt, MD, United States, [4]Department of Earth Sciences, Chiba University, Chiba, Japan

Keywords: geospace, natural hazards, satellite, earthquakes, flood, LEO, GPS/TEC, LAIC

Editorial on the Research Topic

Geospace Observation of Natural Hazards

This collection of technical papers aims to bring recent data from many sources into the study of natural hazards. They represent a multi-instrumental approach using both ground observations: Global Navigation Satellite System (GNSS); and Low Earth Orbiting Electromagnetic (LEO EM) satellites missions together with Earth Observations (EO), which could reveal new information. Results from latest satellite missions, [(NPP/NASA/NOAA(US), CENTINEL, Swarm/ESA (EU), HIMAWARI (JMA, Japan), FORMOSAT-5 (Taiwan, August 2017), CSES1 (China/Italy, Feb 2018), and FORMOSAT-7/COSMIC-2 (Taiwan/United States, May 2019)], are represented in this volume.

In addition, these results expand the analysis of assessing natural hazards using the latest geospace observations and by presenting the latest results with cross-disciplinary studies of earthquakes, volcanoes, tsunamis, and hurricanes/typhoons. These significant results advance existing interdisciplinary studies of several processes: for example, the lithosphere-atmosphere-ionosphere coupling processes.

Data from LEO satellites provide a comprehensive, global view of the variability of near-Earth space and complement ground-based observations that lack local coverage. These observations follow the earlier DEMETER (CNES, 2004–2010) satellite mission, specifically designed to make measurements in the thermosphere-ionosphere to investigate ionospheric anomalies and relate them to geohazards and space weather. We are taking advantage of the broad scope of observable electromagnetic activities by integrating ground-based observations and LEO satellites, helping to clarify the missing scientific knowledge in studying the genesis and evolution of the significant natural hazard events from space. All the studies presented are covered within the scope of Research Topics represented by two reviews, one brief research report, and nine original research papers and carried out by the community of international experts from 15 countries working in Geospace and natural hazards studies and reviewed by 28 peers, to whom we are graciously thankful.

Since the late seventies, many space observations have recorded signals associated with earthquakes. The DEMETER mission has constituted a milestone for space-based investigations of seismo-associated phenomena. A critical review of space-based observations covering a wide range of observations from electromagnetic field components (in a large band of frequencies) to plasmas parameters and from particles detection to thermal anomalies were summarized by (Picozza et al.). Along with a historical review, there is an assessment of the latest developments of the most recent mission investigating the near-Earth electromagnetic environment–CSES-01 satellite—developed within a Sino-Italian and Austrian collaboration. The second review paper (Conti et al.) provided a detailed summary of the observations carried out on the ground to identify pre-earthquake activity by distinguishing them from the background characterized by natural electromagnetic and artificial

Edited and reviewed by:
Alexander Kokhanovsky,
Telespazio Belgium, Germany

****Correspondence:***
Dimitar Ouzounov
ouzounov@chapman.edu

Specialty section:
This article was submitted to Environmental Informatics and Remote Sensing,
a section of the journal
Frontiers in Earth Science

Received: *15 December 2021*
Accepted: *05 January 2022*
Published: *24 January 2022*

Citation:
Ouzounov D, Liu J-Y, Taylor PT and Hattori K (2022) Editorial: Geospace Observation of Natural Hazards.
Front. Earth Sci. 10:836629.
doi: 10.3389/feart.2022.836629

sources. This study focuses only on case studies and statistical analyses and the main hypotheses and models proposed in the literature to explain these observed phenomena.

The data from Seismic Electromagnetic Emissions associated with large earthquakes and the satellites DEMETER (Zhima et al.), Swarm (Zhu et al.), and NOAA Electron Bursts (Fidani) satellites provide new information about the seismic-ionospheric disturbance coupling mechanism. Spatial-temporal microwave brightness variations recorded from the Aqua satellite AMSR-2 show temperature (MBT) anomalies associated with the Mw 7.3 earthquake near the Iran-Iraq border on November 12, 2017 (Ding et al.). Transient variations in the atmosphere/ionosphere were recorded from data during Nepal's M7.8 and M7.3 earthquakes. They have also been studied with data from the NOAA Longwave radiation sensors and simultaneously with GPS/TEC and VLF/LF (Ouzounov et al.). These data followed a general temporal-spatial evolutionary pattern within a large area (but inside the preparation region estimated by Dobrovolsky-Bowman); this feature has also been seen in other large earthquakes worldwide.

A complex model describing the ionosphere Sounding for Identification of Pre-seismic Anomalies was given by (Pulinets et al.). A physical mechanism explaining the ionospheric pre-seismic anomalies generated from the ground to the ionosphere were formulated within the framework of the Lithosphere-Atmosphere-Ionosphere Coupling (LAIC) model. The detailed classification of these anomalies was presented for different ionosphere regions, and the signatures of these pre-seismic anomalies were detected from the ground. Satellite-based instruments were described and classified, defining the methodology of the precursor's identification from ionospheric multi-instrumental measurements.

A new analysis of sub-ULF (<1 msec) magnetic field measurements made during the time of the Chi-Chi earthquake, Taiwan, September 20, 1999, by a joint investigation of satellite measurements in interplanetary space (ACE satellite) and on-ground measurements were made (Anagnostopoulos). Four groups of sub-ULF waves in the Taiwan data coincided, in time, with the quasi-periodic detection of two solar wind streams by the ACE satellite with approximately the solar rotation period (~28 days). This observational evidence shows that sub-ULF electromagnetic radiation on the Earth was probably part of geotectonic processes formulating for the Taiwan 1999 earthquake.

The propagation of sub ionospheric VLF/LF (15–50 kHz) frequencies from navigation or time service transmitters over distances of thousands of kilometers (with low attenuation ~2–3 dB per Mm) enables remote sensing over large regions of the upper atmosphere in which ionospheric modifications lead to changes in the received amplitude and phase of the signals. Such results were included in the Research volume reported for the inland earthquake in Japan (Nagao et al.) and before and during the 2015 M7.8 and M7.3 Gorkha–Nepal earthquakes (Ouzounov et al.). Nagao et al. introduced an electromagnetic-wave arrival discrimination algorithm that combines the autoregressive model and the Akaike information criterion to obtain accurate data on the time of arrival (TOA) of electromagnetic waves.

The seismo-ionospheric perturbations prior to large earthquakes are based on total electron content (TEC) in the global ionosphere map is quite challenging since it is due to the dynamic complexity of the ionosphere and the identification of precursory ionospheric changes. This study analyzed the total electron content (TEC) in the global ionosphere map, with a singular Spectrum Analysis of the TEC. Chen et al. investigate the GPS/TEC changes prior to $M \geq 6.0$ earthquakes in China from 1998 to 2013 to identify possible seismo-ionospheric precursors. They confirmed that the negative anomalies are dominant 1–5 days before the earthquake at the fixed point (35°N, 90°E) during 0600–1000 LT.

The Flood susceptibility modeling of central India's sub-tropical Middle Ganga Plain (MGP) has been presented with a machine learning ensemble approach (Pandey et al.) This study compares two machine learning ensemble models, one first time built and the other used in other natural hazards but not for floods, in mapping the flood susceptible zones in the subtropical fluvial basin of the MGP. The result indicates that both ensembles delineate flood susceptible zones in low-latitude, subtropical monsoonal regions like MGP with reasonably good accuracy and precision.

In conclusion, the availability of new global satellite data and models on the thermosphere/ionosphere interactions demonstrate that satellites that have not been specifically designed for natural hazard studies can provide valuable contributions to this field. Such multi-instrumental observations could expand our knowledge of the geosphere's interaction associated with natural hazards.

AUTHOR CONTRIBUTIONS

DO organized and wrote the manuscript. PT, J-YL, and KH provided critical feedback. All authors contributed to the submitted version of the article.

frontiers
in Earth Science

ORIGINAL RESEARCH
published: 22 October 2020
doi: 10.3389/feart.2020.572393

The Seismic Electromagnetic Emissions During the 2010 Mw 7.8 Northern Sumatra Earthquake Revealed by DEMETER Satellite

Zeren Zhima[1]*, Yunpeng Hu[2], Mirko Piersanti[3], Xuhui Shen[1], Angelo De Santis[4], Rui Yan[1], YanYan Yang[1], Shufan Zhao[1], Zhenxia Zhang[1], Qiao Wang[1], Jianping Huang[1] and Feng Guo[1]

[1]Space Observation Research Center, National Institute of Natural Hazards, Ministry of Emergency Management of China, Beijing, China, [2]Department of Space Science, School of Space and Environment, Beihang University, Beijing, China, [3]National Institute of Nuclear Physics, University of Rome "Tor Vergata," Rome, Italy, [4]Environment Department of Istituto Nazionale di Geofisica e Vulcanologia, Rome, Italy

The abnormal electromagnetic emissions recorded by DEMETER (the Detection of Electro-Magnetic Emissions Transmitted from Earthquake Regions) satellite associated with the April 6, 2010 Mw 7.8 northern Sumatra earthquake are examined in this study. The variations of wave intensities recorded through revisiting orbits from August 2009 to May 2010 indicate that some abnormal enhancements at Extremely Low Frequency range of 300–800 Hz occurred from 10 to 3 days before the main shock, while they remained a relatively smooth trend during the quiet seismic activity times. The perturbation amplitudes relative to the background map which were built by using the same-time seasonal window (February 1 to April 30) data from 2008 to 2010 further suggest strong enhancements of wave intensities during the period prior to the earthquake. We further computed the wave propagation parameters for the electromagnetic field waveform data by using the Singular Value Decomposition method, and results show that there are certain portions of the Extremely Low Frequency emissions obliquely propagating upward from the Earth toward outer space direction at 10 and 6 days before the main shock. The potential energy variation of acoustic-gravity wave suggests the possible existence of acoustic-gravity wave stability with wavelengths roughly varying from 5.5 to 9.5 km in the atmosphere at the time of the main shock. In this study, we comprehensively investigated the link between the electromagnetic emissions and the earthquake activity through a convincing observational analysis, and preliminarily explored the seismic-ionospheric disturbance coupling mechanism, which is still not fully understood at present by the scientific community.

Keywords: the seismic electromagnetic emissions, 2010 Mw 7.8 Sumatra earthquake, revisiting orbit analysis, wave vector analysis, acoustic-gravity wave stability, DEMETER satellite

Edited by:
Jann-Yenq Liu,
National Central University, Taiwan

Reviewed by:
Michel Parrot,
UMR7328 Laboratoire de physique et chimie de l'environnement et de l'Espace (LPC2E), France
Mukesh Gupta,
Catholic University of Louvain, Belgium

***Correspondence:**
Zeren Zhima
zerenzhima@qq.com

Specialty section:
This article was submitted to Environmental Informatics and Remote Sensing, a section of the journal Frontiers in Earth Science

Received: *14 June 2020*
Accepted: *18 September 2020*
Published: *22 October 2020*

Citation:
Zhima Z, Hu Y, Piersanti M, Shen X, De Santis A, Yan R, Yang Y, Zhao S, Zhang Z, Wang Q, Huang J and Guo F (2020) The Seismic Electromagnetic Emissions During the 2010 Mw 7.8 Northern Sumatra Earthquake Revealed by DEMETER Satellite. Front. Earth Sci. 8:572393. doi: 10.3389/feart.2020.572393

INTRODUCTION

The abnormal electromagnetic emissions associated with earthquake (EQ) activities, during either its preparation phase or its occurrence, have been widely documented since the last century. Both ground-based observations and lab experiments on rock-rupture-processing confirm that the electromagnetic emissions induced by EQ activities can appear over a broad frequency range from Direct Current (DC) to Ultra Low Frequency (ULF), Extremely Low Frequency (ELF), Very Low Frequency (VLF), and even up to High Frequency range (e.g., Gokhberg et al., 1982; Huang and Ikeya, 1998; Sorokin et al., 2001; Pulinets et al., 2018). With the development of space technology, by the early 1980s some satellites recorded the abnormal electromagnetic emissions, plasma parameter irregularities, as well as energetic particle precipitations over seismic fault zones (e.g., Gokhberg et al., 1982; Larkina et al., 1989; Parrot, 1989; Serebryakova et al., 1992), indicating that the possible seismic-ionospheric perturbations are likely propagating upward from lithosphere to the atmosphere and ionosphere, and in particular circumstances, even up to the inner magnetosphere. For example, Larkina et al. (1989) revealed abnormal ELF/VLF emissions at 0.1–16 kHz frequency range before strong EQs according to the observations of Intercomos-19 and Aureol-3 satellites; Serebryakova et al. (1992) presented strong ELF emissions below 450 Hz over seismic regions based on Cosmos-1809 and Aureol-3 satellites. Parrot (1994) statistically studied 325 EQs with magnitude larger than 5 based on Aureol-3 satellite, and found that the seismic ELF/VLF emissions can be observed all along the magnetic meridian passing over the epicenter. Admittedly, these ideas were not universally accepted: for example, Henderson et al. (1993) stated no clear ELF/VLF signatures related to earthquakes based on a statistical analysis on DE 2 satellite; Rodger et al. (1996) reported no significant precursory, co-seismic or post-seismic effects associated with ELF/VLF electromagnetic activities recorded by ISIS (International Satellites for Ionospheric Studies) 2 satellite.

In the early 21st century, France launched the Detection of Electro-Magnetic Emissions Transmitted from Earthquake Regions (DEMETER) satellite mission (Lagoutte et al., 2006) which successfully operated from 2004 to 2010 and is regarded as the world's first space platform mainly devoted to study ionospheric perturbations caused by earthquakes, volcanic eruptions and human activities (Parrot et al., 2006a). Since then, a growing number of studies have been devoted to the scientific field of seismic-ionospheric disturbances. For examples, Parrot et al. (2006b) examined the abnormal ELF waves as well as the simultaneous variations of the ionospheric plasma parameters and energetic particle precipitations occurring over several seismic zones. Bhattacharya et al. (2007) reported strong ULF/ELF emissions occurring 4 days before the 2006 Gujarat EQ with a magnitude of 5.5. Nemec et al. (2009) investigated the statistical variations of ELF/VLF wave intensity values for shallow earthquakes with magnitude over 4.8 (depth less than 40 km) occurred all over the world in the same period of DEMETER observations, and confirmed the existence of a very small but statistically significant decrease of wave intensity at 1.7 kHz about 0–4 h before the main shocks. Błęcki et al. (2010) found some abnormal ELF emissions from 11 days before the 2008 Mw 7.9 Wenchuan EQ, with the most intensive emissions from a few tens of hertz up to 350 Hz that appeared 6 days before the Wenchuan main shock. Zeng et al. (2009) further analyzed the wave propagation parameters and reported a portion of emissions at ELF 300 Hz obliquely propagating upward to the satellite's position over the Wenchuan epicenter zone with right-handed polarization. More recently Bertello et al. (2018), using DEMETER electromagnetic data, found the appearance of anomalous electromagnetic waves at 333 Hz one day before the April 6, 2009 L'Aquila EQ. However, at present, the physical mechanism about how those abnormal signals from the seismic fault zone couple into ionosphere and how excite electromagnetic emissions or disturb the plasma parameters is still poorly understood, and the present proposed mechanism is still questionable. It is still a challenge to extract the real seismic anomaly or so called "earthquake precursor" from either ground-based or space-based observations.

This study searches for possible ionospheric electromagnetic disturbances from DEMETER satellite observations, and reports another interesting case study that is the 2010 moment magnitude 7.8 (Mw 7.8) northern Sumatra EQ, which occurred at 22:15 UT on April 6, 2010, with an epicenter at 2.38°N, 97.05°E and depth of 31 km. This Mw 7.8 EQ is the result of the Indo-Australian plates moving north-northeast relative to the Sunda plate at a velocity of about 60–65 mm/year (https://earthquake.usgs.gov/). The Sumatra region in Indonesia is located at the boundary between Indo-Australian and Sunda plates with very active fault movements, so that this area is naturally prone to strong EQs, eventually producing great disasters. In recent decades, the strong seismic activity in Sumatra region has becoming more and more frequent, the most devastating one was the December 26, 2004 Mw 9.1 EQ which resulted in the largest tsunami event in recorded history.

Previous studies on EQ activities of the Sumatra region found some clear seismic-ionospheric disturbance phenomena (e.g., Molchanov et al., 2006; Liu et al., 2010; Kumar et al., 2013; Liu et al. 2016). Kumar et al. (2013) analyzed ground-based VLF transmitter receiver network data and found that VLF radio wave amplitude decreased by about 5 dB at nighttime and 3 dB at daytime during a magnitude 5.8 shock on December 18, 2006. Molchanov et al. (2006) reported a decrease of signal to noise ratio values of VLF radio wave amplitude before the 2004 Mw 9.0 EQ based on DEMETER's observations Heki et al. (2006) presented various waveforms and relative amplitudes changes of the shortly pre- and co-seismic-ionospheric-disturbances during the 2004 Mw 9.0 EQ by GPS-TEC (Global Positioning System, Total Electron Content) data. Liu et al. (2016) reported GPS-TEC perturbations appearing at the east part of epicenter 2 days before the 2005 Ms 7.2 Sumatra EQ, with electron density simultaneously enhanced at the altitude of 710 km over the west of the GPS-TEC perturbations due to the E × B drift effects. Marchetti et al. (2020) combined the multi-source observations from skin temperature, total column water vapor aerosol optical thickness of atmosphere, magnetic field, and electron density of ionosphere, revealed the evidence of Lithosphere-Atmosphere-Ionosphere coupling (LAIC) phenomena during the September 28, 2018 Mw 7.5 EQ in the same region.

In the present work, we report the abnormal ELF electromagnetic emissions appeared at frequencies 300–800 Hz under quiet ionosphere environment conditions preceding the April 6, 2010 northern Sumatra earthquake. This paper is organized in the following way. A brief introduction to DEMETER satellite and its associated payloads are provided in *Dataset*, the variations of ELF wave intensity investigated by the revisiting orbits and the background map methods are presented in *Wave Intensity Analysis*. *Wave Vector Analysis* presents wave vector analysis by using the Singular Value Decomposition method. *Discussions* are devoted to the possible mechanism of the abnormal seismic emissions by acoustic-gravity wave (AGW) instability evaluations, and *Conclusions* briefly summarizes the main results.

DATASET

In this study, we mainly utilized the ELF/VLF electromagnetic field observations from the low earth orbit satellite DEMETER. This satellite was launched on June 29, 2004 to a sun-synchronous circular orbit with an initial altitude of 710 km (before December 2005) then lowered to 660 km (after December 2005), and ended operation on December 10, 2010 (Lagoutte et al., 2006; Parrot et al., 2006a). DEMETER had a full orbit period of ~1.6 h, i.e., it performed ~15 orbits per day, and its measurements were operated in the region with magnetic latitudes below 65° (Parrot et al., 2006a). DEMETER is the first electromagnetic satellite aimed to detect and study the electromagnetic signals likely associated with earthquakes, volcanic eruptions, or anthropogenic activities. The scientific payloads of DEMETER included five sensors which allowed it to measure the electromagnetic fields and waves, plasma parameters (both electrons and ions), and energetic particles. In the present study, we mainly used the observations provided by the electric field experiment (ICE, Instrument Champ Electrique) (Berthelier et al., 2006) and the search coil magnetometer (IMSC, Instrument Magnetic Search Coil) (Parrot et al., 2006a). ICE consisted of four spherical electrodes with embedded preamplifiers separately installed at the end of four booms (4-m long), measuring the electric field over a wide frequency range from DC to 3.175 MHz, that is subdivided into four frequency channels, i.e., DC/ULF, ELF, VLF, and High Frequency (Berthelier et al., 2006). IMSC was a three-orthogonal magnetic antennae linked to a pre-amplifier unit with a shielded cable of 80 cm, including a permalloy core on which a main coil with several thousand turns (12,000) of copper wire, and a secondary coil with a few turns were wound (Parrot et al., 2006a).

DEMETER had two observations modes: survey and burst mode. For the ELF/VLF electromagnetic field detection, the survey mode provided the power spectral density (PSD) data for one component of the electric field and the magnetic field in frequency range from 19.5 to 20 kHz with a frequency resolution of 19.5 Hz, respectively. The burst-mode provided six components of the electromagnetic waveform data in frequency below 1.25 kHz, with a sampling rate of 2.5 kHz over the prone earthquake area or the ground-based experiments. The burst-mode waveform data is not available for the whole orbit trajectory, being very limited compared to the survey mode observations. In this study, we collected DEMETER's survey mode observations of the variant magnetic field from 2008 to 2010, and burst-mode electromagnetic field waveform data recorded from March 20 to April 10, 2010 in the earthquake's epicenter ±8° area (5.6°S–10.4°N, 89°E–105°E).

We used the vertical temperature profile of atmosphere, which is retrieved from the ERA-5 climate reanalysis dataset (https://confluence.ecmwf.int/) to compute the AGW instability at the moment of earthquake. ERA-5 is an assimilated climate reanalysis dataset released by European Center for Medium-Range Weather Forecasts (ECMWF). ERA-5 provides global and hourly temperature profiles with high resolution at 137 different pressure levels from near surface to 0.01 hPa (~80-km altitude). The horizontal resolution is about 0.28° in both longitude and latitude. In this study, gridded data with a resolution of 0.3° were produced and downloaded from the ECMWF Web Applications Server (http://apps.ecmwf.int/data-catalogues/era5/).

WAVE INTENSITY ANALYSIS

Revisiting Orbits

First, we examined the wave intensity values of the variant magnetic field at different frequency ranges (200 Hz–20 kHz) from March 20 to April 10, 2010 over the Mw 7.8 northern Sumatra epicentral area by using PSD values provided by survey-mode observations of DEMETER. These results reveal that those orbits passing over the epicentral area show certain enhancement of wave intensity at ELF frequency (300–800 Hz) (**Figure 1**). **Figure 1** displays the average PSD values of the magnetic field at frequency 300–800 Hz from March 20 to April 10, 2010 with the red star marking the epicenter (2.4°N, 97.1°E). It can be seen that the enhancement phenomena at ELF frequency band (300–800 Hz) over the seismic zone is evident. In order to exclude external origins for this enhancement (such as solar flare events, geomagnetic storms, etc.), which directly disturb the upper ionosphere, we removed all the orbits recorded under disturbed space weather conditions (Dst ≤ −30 nT; Kp ≥ 3). The Dst and Kp index are used to characterize the disturbance condition of space, Dst is derived from the equatorial geomagnetic stations, while Kp is computed by geomagnetic stations located at middle-high latitudes. The Geomagnetic Data Service (http://wdc.kugi.kyoto-u.ac.jp/index.html) provides the real time data of Dst and Kp index. The space weather conditions from March to April 2010 are presented in **Figure 2**. It can be seen that the 2010 Mw 7.8 northern Sumatra EQ occurred during the recovery phase of a moderate geomagnetic storm (Dst index reached a minimum of - 80 nT on April 6, 2010). For this reason, those orbits recorded during the main phase and recovery phase (mostly from April 3–8) are

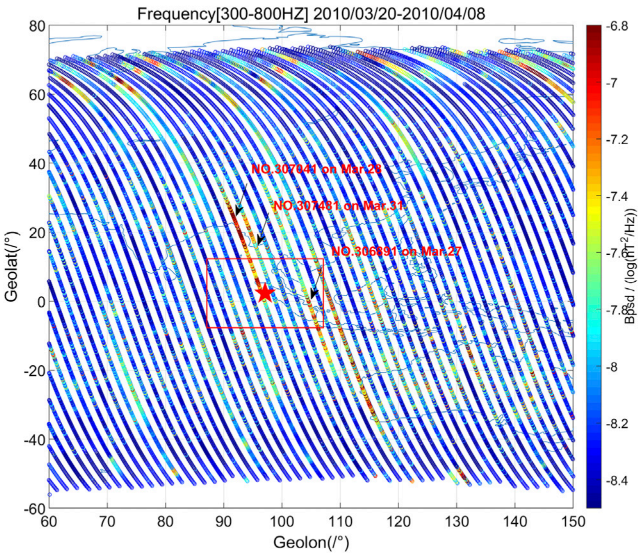

FIGURE 1 | The variation of extremely low frequency magnetic field wave intensity during the 2010 April 6, Mw 7.8 Sumatra earthquake from March 20 to April 8, 2010, represented by power spectral density (PSD) values at frequency range (300–800 Hz). The red star denotes the epicenter, the red rectangle indicates the area of study. The horizontal and vertical axis represent the geo-longitude and latitude, respectively; the PSD values are color coded along the orbit trajectories.

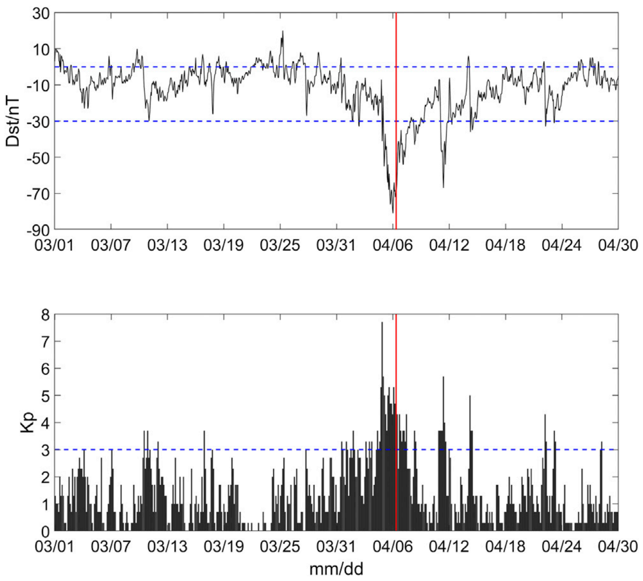

FIGURE 2 | The geomagnetic field disturbance index from March to April 2010 (top: Dst, bottom: Kp). The vertical red lines represent the occurrence of the main shock. The horizontal dashed blue lines represent the thresholds for data selection applied in the study (for more details, see the main text).

not illustrated in **Figure 1**, and data from these times were not considered in our later analysis. It can be seen that around the epicenter area +8° (denoted by the red square in **Figure 1**), the enhancement of wave intensity mainly occurred at those orbits passing near the epicenter area, especially at orbits No. 306891 on March 27, No. 307041 on March 28, No. 307481 on March 31, 2010, and on these days the fluctuation amplitude of Dst index varied over −30 to ~0 nT, and Kp index remained below 3, it can be said that no significant geomagnetic external activity was present.

It is not convincing to simply relate the enhancements of those orbits to the seismic activity just according to a short space and time window including the earthquake location and occurrence. We further selected previous observations along the same orbit trajectories (i.e., revisiting orbits) to investigate the long-term variation pattern. The sun-synchronous circular orbit feature of DEMETER allows the satellite to return to the same orbit trajectory at the same local time approximately every ~13 days in 2010 (the recursive period changes due to the slight shift of satellite position). By using this feature of revisiting orbits, we can examine a longer time window to determine the normal electromagnetic environment background trend along the same orbital trace at the same local time.

According to **Figure 1**, we selected five orbits showing certain enhancements before the main shock which are: No. 306891 on March 27, No. 307041 on March 28, No. 307191 on March 29, No. 307921 on April 3, and No. 308071 on April 4, 2010, respectively. Then, we selected their corresponding revisiting orbits from August 2009 to May 2010 under quiet space weather conditions (Dst ≥ −30 nT and Kp ≤ 3). We also checked the solar activity during this half year period which kept a weak and stable level revealed by the sunspot numbers and there were no strong solar proton events occurring during this time period (not shown). We finally got 25 revisiting orbits for each of those above five orbits. The trajectories of those five orbits (colored) and their revisiting orbits (gray) are shown in **Figure 3**. Interestingly, in this time-window (August 2009 to May 2010), there was another earthquake occurred on March 5, 2010 with a magnitude of 6.8 in the vicinity of the 2010 Mw 7.8 northern Sumatra epicenter area (https://earthquake.usgs.gov/earthquakes/map), indicating that the fault movement in Sumatra area is very active. In **Figure 3**, the red star represents the April 6, 2010 Mw 7.8 EQ, and the orange one denotes the March 5, 2010 Mw 6.8 EQ.

According to the empirical equation of the earthquake preparation zone put forward by Dobrovolsky et al. (1979), the influential zone of a 7.8 magnitude earthquake in the lithosphere is a circle with a radius of 2,260 km. For convenience, considering the projection feature of satellite orbit on the ground, we chose a square area of around 1,800 km at satellite's altitude, that is the epicenter (2.4°N, 97.1°E) ± 8° area, or (5.6°S–10.4°N, 89°E–105°E). We then extracted the PSD values at frequency (300–800 Hz) over the studied area from each revisiting orbit of the above five orbits, and re-sorted them as five sets of time-series data, and then we applied a running quartile method (Zhima et al., 2012b; Liu et al., 2013; Shen et al., 2017) to examine the long-term trend, as shown in **Figure 4**. The running medians, along with the inter-quartile ranges (IQR, being equal to the difference between the third and first quartiles) were computed by using the three previous and three successive orbits of the current orbit (7 orbits in total). We

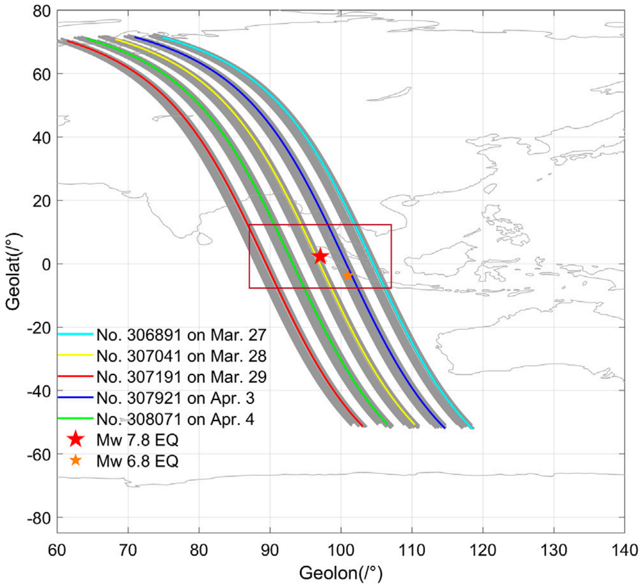

FIGURE 3 | The trajectories of five orbits (No. 306891, 307041, 307191, 307921, and 308071, differently colored) with their revisiting orbits (gray lines) from August 2009 to May 2010. The red star represents the 2010 April 6, Mw 7.8 EQ, and the orange one denotes the 2010 March 5, Mw 6.8 EQ. The red rectangle represents the area of study.

defined the running median PSD values as the background trend (denoted by blue lines in **Figure 4**), while the median PSD values of the current orbit as the current variation level (represented by red lines). The upper and lower bound were computed by the running median PSD values ± IQR values, denoted by the black and green lines, respectively. It can be seen in **Figure 4** that three orbit trajectories, No. 306891, No. 307041, and No. 307921, show enhancements over the background trend before the two EQs. The recorded PSD values at frequency (300–800 Hz) along these three orbit trajectories are comparatively stable from August 2009 to February 2010, then start to fluctuate near the time of the two major shocks. However, the other two orbit traces at the west side of the epicenter (No. 307191, No. 308071, the last two panels in **Figure 4**) show no obvious difference between earthquake and non-earthquake time, it is difficult to identify any earthquake related abnormal signals from the variation pattern of the last two orbits, so we do not further discuss their relationship to earthquake any further.

Specifically, for the orbit No. 306891 (see the first panel in **Figure 4**), which recorded on the east side of epicenter on March 27, 2010, the PSD values reach to ~$10^{-6.7}$ nT^2/Hz before the Mw 7.8 EQ, far exceeding the background threshold (see the black and green lines). In addition, it shows a relatively smaller enhancement (~$10^{-7.5}$ nT^2/Hz) within one month before the Mw 6.8 EQ. The orbit No. 307041, which is located right above the Mw 7.8 epicenter (see **Figure 3**) on March 28, 2010, presents a low and stable trend until the time very near to the two major shocks, then it becomes strongly disturbed (see the second panel in **Figure 4**), reaching maximum values of ~$10^{-7.8}$ nT^2/Hz during the Mw 6.8 EQ, and ~10^{-6} nT^2/Hz before the Mw 7.8 EQ. Along the orbit No. 307921, which closely passed over the Mw 6.8 epicenter area (see **Figure 3**) on April 3, 2010, the variation keeps a relative normal background trend far before the main shock time too, mainly gets disturbed on February 23, 2010 before the Mw 6.8 EQ, and after the Mw 6.8 EQ on March 8, and become

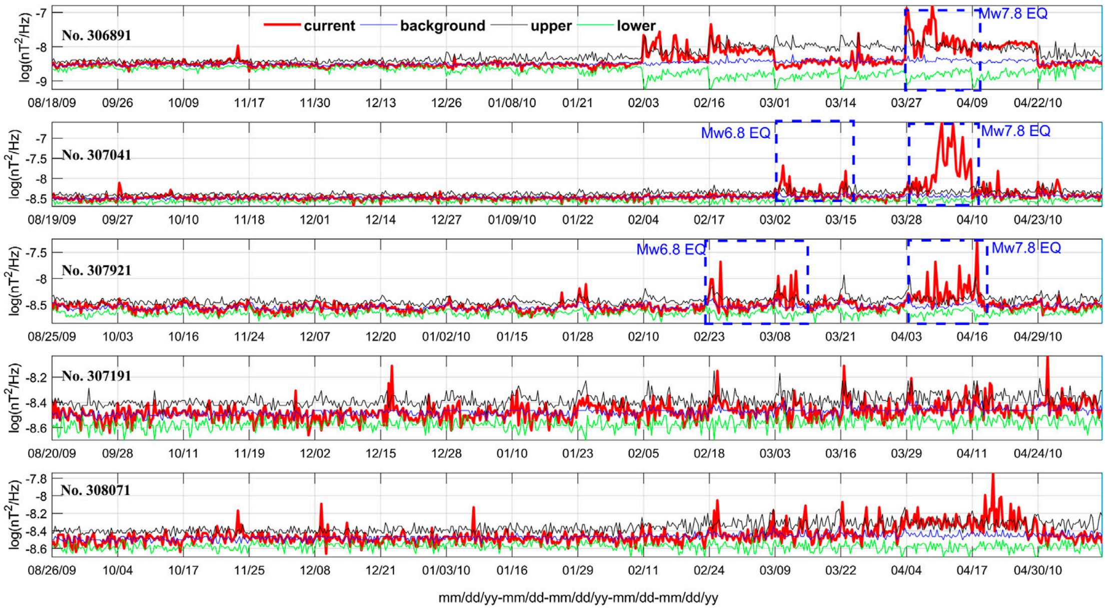

FIGURE 4 | The long-term variation of wave intensities at extremely low frequency (300–800 Hz) revealed by the five orbits (No. 306891, 307041, 307191, 307921, and 308071) and their revisiting orbits recorded from August 2009 to May 2010. The red lines represent the current observation values, the blue ones denote the median values computed by data from 2009 to 2010, and the black and green lines are the upper/lower bounds (median values ± IQR values) also computed by data from 2009 to 2010.

highly enhanced from $10^{-8.4}$ nT^2/Hz to $10^{-6.3}$ nT^2/Hz during the Mw 7.8 EQ (see the third panel in **Figure 4**).

In all, the variation patterns of the above three orbits indicate that the wave intensity at frequency (300–800 Hz) indeed show enhancements with the location of during the Mw 7.8 EQ, compared to other quiet seismic activity times. Specifically, on March 27, 2010, 10 days before the Mw 7.8 EQ, the wave intensities started to increase with peak value around $10^{-6.7}$ nT^2/Hz on the orbit trace of No. 306891; and 3 days before the main shock, the wave intensities varied from $10^{-8.4}$ to $10^{-7.6}$ nT^2/Hz along the orbit trace of No. 307921 (April 3). The strongest enhancement, of about $10^{-6.0}$ nT^2/Hz, was recorded along the orbit trace closest to the epicenter (No. 307041 on March 28) of the Mw 7.8 main shock.

Background Map

To obtain more convincing evidence of these abnormal ELF emissions, the longer term observations under quiet space weather condition ($Dst \geq -30$nT and $Kp \leq 3$) from 2008 to 2010 were selected to build a background map over the Mw 7.8 Sumatra EQ area. We extracted the data in a same-time-window from Feb. 1 to April 30 for each year from 2008 to 2010. Through this way, the variations related to the seasonal conditions can be eliminated.

In this study, we adopted the method put forward by Zhima et al. (2012a, 2012b) to build a background map based on longer-term satellite observations over the epicenter area. First, we extracted the observations over the area ±8° about the epicenter (5.6°S–10.4°N, 89°E–105°E) from February 1 to April 30 for each year, then computed the average PSD values of wave intensity. The average PSD values were binned as a function of latitude (5.6°S–10.4°N) and longitude (89°E–105°E) in steps of 2°. With these three-year data, we computed the median value of PSD values and the standard deviation value in each 2° × 2° bin and defined these data matrixes as $\beta_{2008-2010}$ and $\sigma_{2008-2010}$, respectively.

For 2010, the year of Mw 7.8 EQ, we built four data sets with four time intervals T_i (i = February 1 to February 28, March 1 to March 20, March 21 to April 6, April 7 to April 30, 2010, respectively). The median PSD values in each 2° × 2° bin for these four time-intervals were computed and defined as matrixes $\alpha_{Ti,2010}$, respectively. Then we define the perturbation amplitude $\Delta\rho$ by **Eq. 1** below:

$$\Delta\rho = \left(\alpha_{Ti,2010} - \beta_{2008-2010}\right)/\sigma_{2008-2010} \qquad (1)$$

where $\Delta\rho$ is regarded as the perturbation amplitude during earthquake time T_i compared to the background map $\beta_{2008-2010}$. The difference between the magnetic field wave intensity at earthquake time ($\alpha_{Ti,2010}$) and the long-term background map ($\beta_{2008-2010}$) is normalized by the standard deviation ($\sigma_{2008-2010}$) in each 2° × 2° data bin. We computed the $\Delta\rho$ for different frequency ranges from 300 to 800 Hz, and found that at the frequency range (468–566 Hz) there exists strong enhancements during the earthquake impending time [March 21–April 6, 2010] as shown in **Figure 5**.

Figure 5 shows the variation pattern of the perturbation amplitude $\Delta\rho$ during time intervals from February 1 to April 30, 2010. It can be seen that during the February 1 to March 20 time period (**Figures 5A,B**), the $\Delta\rho$ values in the epicenter area remain at a relatively low level, mostly varying around 0 and the maximum value peaking about 1.2. However, during the earthquake impending time interval from March 21 to April 6 (see **Figure 5C**), the $\Delta\rho$ gets enhanced (~over 3), with the strongest enhancement mainly spread along the latitudinal direction of the near northwest side of the epicenter area (almost right above the epicenter). The eastern part of the epicenter gets a wide scope enhancement both along the longitudinal and latitudinal direction marked by the dashed square in **Figure 5**. After the main shock (**Figure 5D**), the $\Delta\rho$ returns back to a relatively low disturbance amplitude level, mostly around 0, and maximum value 1.2, similar to the levels in **Figures 5A,B**. Due to the disturbed space weather conditions, the observations during the earthquake impending days from April 3 to 6, 2010 (see **Figure 2**) were not included in this computation, so the enhancement showed in **Figure 5C** is very likely attributed to the seismic activity.

WAVE VECTOR ANALYSIS

We further checked the burst-mode observations which were automatically triggered when DEMETER flies above known seismic fault zones (Parrot et al., 2006a). The electromagnetic payloads ICE and IMSC in burst-mode provide six-components of waveform data at frequency range below 1.25 kHz with sampling rate of 2.5 kHz. However, the waveform data are not available at any time of interest during this earthquake. Fortunately, the orbit No. 306891 on March 27 (10 days before the main shock), and No. 307481 on March 31, 2010 (6 days before the main shock), coincidentally triggered burst-mode observations over the epicenter zone, allowing us to compute the wave propagation parameters by wave vector analysis method. **Figure 6** shows the exact burst-mode operation locations of these two orbits.

Figures 7A,B show the detailed electromagnetic spectral values computed by the waveform data of orbit No. 306891. It can be seen that near the epicenter area (2.38° N, 97.05°E), at the latitudes from ~ 8° to 3.8°S, longitude from 107°E to ~105°E, there exists electromagnetic wave activities (denoted by white arrows) mainly from 14:43 to 14:45 UT at L shells roughly from 1.4 to 1.09 where the satellite is quite near to the Mw 7.8 epicenter area.

To compute the wave propagation parameters of these emissions over the epicenter zone, we built a Field Aligned Coordinate (FAC) system in the orbit space of DEMETER satellite. Under this FAC coordinate system, the Z-axis is along direction of the background magnetic field B_0, the Y-axis is horizontally perpendicular to the Z-axis cross the position vector of the satellite (so that the positive Y-axis is nominally eastward at the equator), and the X-axis completes the right-handed system. The background magnetic field B_0 is obtained by IGRF 2000 model (Olsen et al., 2000) according to DEMETER's position. The angles θ and ϕ are defined as the wave normal angle (polar angle) and the azimuthal angle between the B_0 and the wave vector k. A value of 180° in azimuthal angle ϕ indicates that k propagates toward decreasing L shell direction, i.e., downward to the Earth direction, while 0° means that k

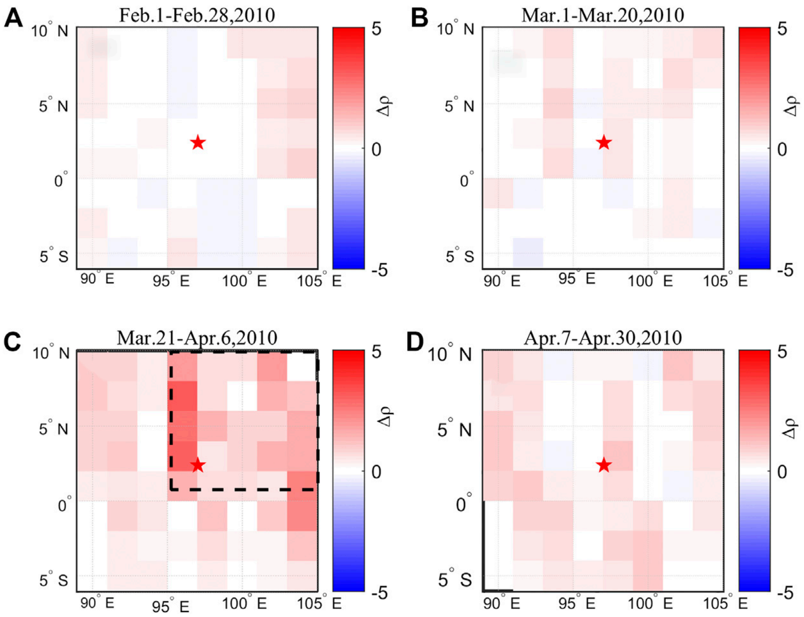

FIGURE 5 | The $\Delta\rho$ distribution over the epicenter area computed by power spectral density values of magnetic field at frequency (468–566 Hz) during the 2010 Mw 7.8 Sumatra earthquake; **(A)** February 2 to February 28, 2010; **(B)** March 1 to March 20, 2010; **(C)** March 21 to April 6, 2010; **(D)** from April 7 to April 30, 2010. The star represents the 2010 Mw 7.8 Sumatra epicenter, the $\Delta\rho$ means the perturbation amplitude of current time intervals (a, b, c, d) relative to the background map built by observations from 2008 to 2010 (see text for explanation). The black dashed rectangle denotes the a wide scope area of power spectral density values' enhancement.

propagates toward the increasing *L* shell direction in the meridian plane (i.e., from the Earth direction upward to the outer space direction). Then, the Singular Value Decomposition method put forward by Santolik et al. (2003) to compute wave propagation parameters, which has been widely used in the analysis of ELF/VLF space electromagnetic waves (Parrot et al., 2006b; Wei et al., 2007; Zhima et al., 2015a; Zhima et al., 2015b), was adopted to compute the wave normal angles, ellipticity, polarization, and planarity.

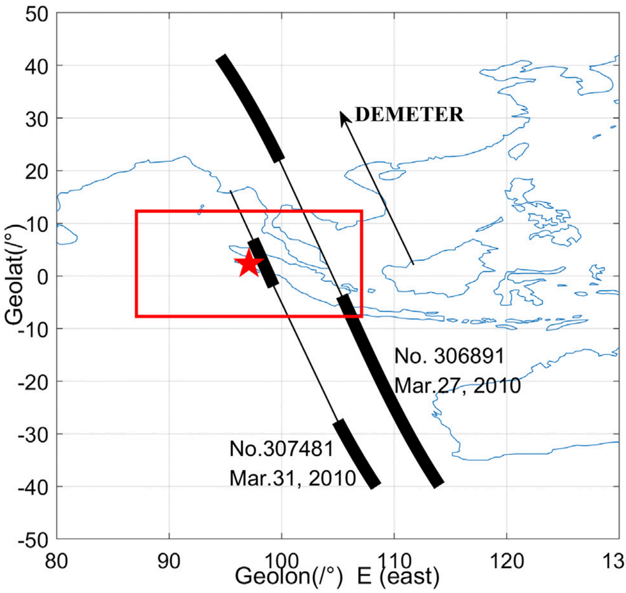

FIGURE 6 | The available waveform data (thick lines) recorded by burst-mode observations near the seismic zone. The red rectangle is the area of study.

The computed wave propagation parameters from No. 306891 are shown in **Figures 7C–F**. The parameters computed by the low intensity waveform data (lower than $10^{-7.8}$ nT^2/Hz) are not shown for a better visual inspection. The wave normal angles θ of wave vector *k* are displayed in **Figure 7C**, which varies roughly from 40° to 80°, indicating these emissions are obliquely propagating. **Figure 7D** shows the azimuthal angles ϕ with a wide varying range from 0° to 180°. However, it can be clearly identified that there are some portions of emissions showing azimuthal angles $\phi \sim 0°$ (see the black squares) mainly at frequency from 300 to 800 Hz (even up to ~1,100 Hz) at ~14:43:44 to 14:44:58 UT. According to the FAC coordinate system defined above, the propagation direction of these portions of emissions points upward from the Earth direction to the outer space direction (increasing *L* shell), indicating that these waves come from lower altitudes than the satellite.

It is noted that the strong emissions around 400–450 Hz with wave normal angles $\theta \sim 90°$ (**Figure 7C**), azimuthal angles $\phi \sim 180°$ (**Figure 7D**), the right handed ellipticity values of 1, are obliquely propagating downward from the higher altitudes (or decreasing *L* shell direction) than satellite position to the Earth direction, and they are identified as ionospheric hiss waves which might originate from the plasmasphere or the inner

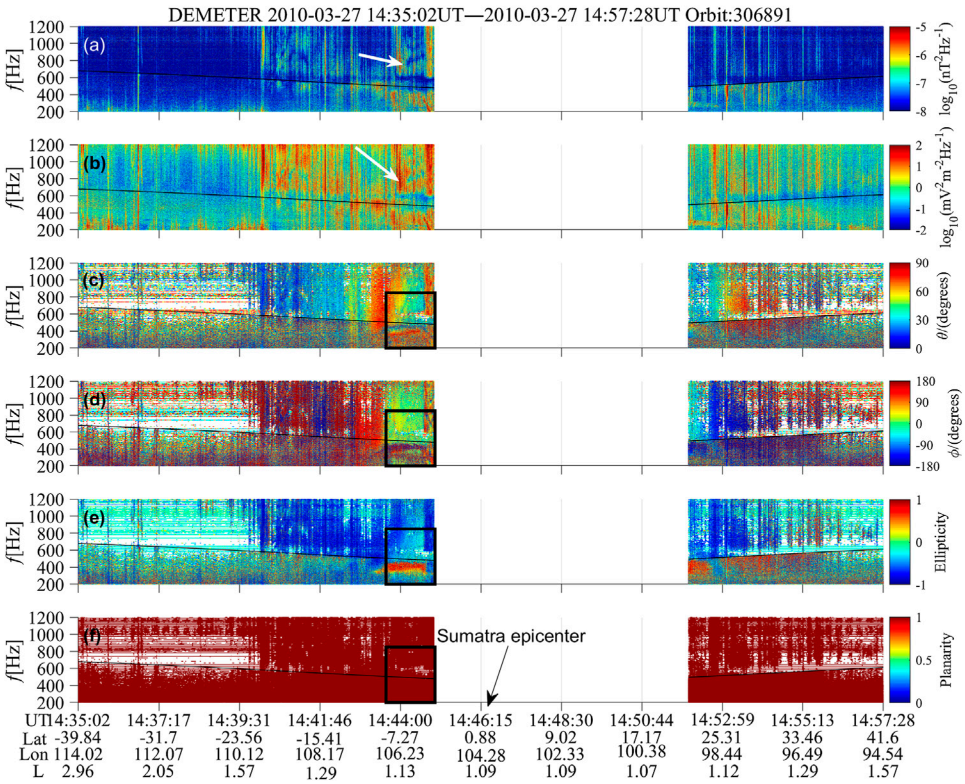

FIGURE 7 | The wave propagation parameters of extremely low frequency waveform recorded by orbit No. 306891. The black lines represent the local proton cyclotron frequency. From top to bottom: **(A,B)** the power spectral values of magnetic field and electric field, **(C)** the wave normal angle θ; **(D)** the azimuthal angles ϕ; **(E)** the ellipticity, **(F)** the planarity. The arrow indicates the time of the orbit crosses the EQ epicenter. The black rectangular box denotes the abnormal waves near the epicenter area, which wave propagation parameters are statistically analyzed in **Figure 8**.

magnetosphere (Chen et al., 2017; Zhima et al., 2017; Xia et al., 2019), these emissions are not related to the earthquake activity.

The ellipticity values are given in **Figure 7E**, which represent the ratio of the axes of the polarization ellipse. The value +1 of ellipticity means that the wave is right-hand polarized, while −1 indicates that the wave is left-hand polarized, while 0 is the linearly polarized. For these portions of upward propagation waves (azimuthal angles ϕ ~ 0°) the ellipticity mainly varies around 0 at frequencies 300–400 Hz, meaning that they are linearly polarized, while at frequencies below 300 Hz or above 450–800 Hz, even up to 1,100 Hz, the waves change to the left hand polarized (ellipticity varying from 0 to −1). The planarity of waves, which represents wave propagating in a single plane (+1) or in spherical direction (0), is presented in **Figure 7F**, with a value mostly being +1, implying that the observed waves are coming toward the spacecraft as plane wave propagation.

We also statistically analyzed the distributions of wave propagation parameters for the waves at frequency range (300–800 Hz) marked by the black square area in **Figure 7** (including the downward right-handed hiss at frequency 400–450 Hz), as shown in **Figure 8**. The overlapped red curves represent the fitted curves computed by the kernel density distribution function. The majority of wave normal angles θ varies below 80°. The azimuthal angles ϕ mainly peaked at 0°. The ϕ values of ±180° are mostly attributed to the downward hiss waves at 400–450 Hz. For the ellipticity, the values of -0.5 to −1 are mostly related to the upward direction waves, and +1 to the downward hiss waves. The planarity predominates at values of 1.

As with orbit No. 306891, the wave propagation parameters of waveform data for orbit No. 307481 at 15:08–15:10 UT on March 31, 2010 are shown in **Figure 9**. As can be seen from **Figure 9** that the waveforms recorded at latitudes from 1.95°S to 6.8°N, longitudes from 99.29°E to 97.44°E are exactly over the epicenter zone (see **Figure 5**). The strong electromagnetic emissions along this orbit mainly appeared at frequencies below 500 Hz. The wave propagation parameters also show basically similar features as the waves recorded by No. 306891, although they are not as significant as the ones of No. 306891. However, it can be clearly identified that there are waves with azimuthal angles ϕ of 0°. **Figure 10** shows the statistical features of the waves recorded from (1.95°S–6.89°N, 99.29°–97.44°E). For these waves, the wave normal angles θ vary at a broad range from 0° to 90°, indicating waves are obliquely propagating. The azimuthal angles ϕ have three peaks: ±180° and 0°, meaning there are waves mixed both from the Earth direction (ϕ = 0) and the outer space direction (ϕ = ±180°). The ellipticity mainly peaks around ±0.5, and the planarity is 1.

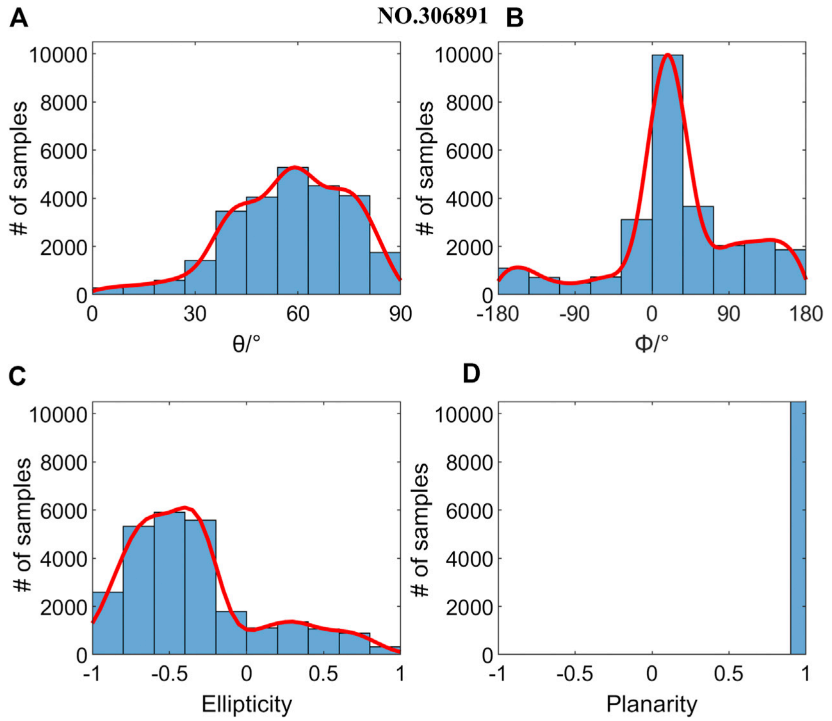

FIGURE 8 | Distribution of wave propagation parameters for the waves in extremely low frequency (300–800 Hz) in the area (7.4°–3.8°S, 106.1°–105.6°E) recorded by No. 306891 at ~14:44 to 14:45 UT, marked by the black square in **Figure 7**. The overlapped red lines represent fitted curves computed by a probability density function; **(A)** wave normal angle θ; **(B)** and azimuth angle ϕ of the wave vector; **(C)**the ellipticity; **(D)** planarity.

DISCUSSIONS

The 2010 Mw 7.8 northern Sumatra EQ occurring at the equatorial area over where the equatorial ionosphere has less energetic particle precipitations compared to the high-latitude ionosphere, we do not need to consider the possibility of energetic particle precipitation induced wave activity in this study. Considering that the upper ionosphere environment space weather conditions are quiet during the studied time-window, there are two major generation sources for electromagnetic emissions we must consider: the atmosphere lightning activities and ground-based VLF transmitters.

The lightning activities from the atmosphere also serve as an embryonic source for strong ELF/VLF emissions in the upper ionosphere (Santolík et al., 2009; Shklyar et al., 2012; Zhima et al., 2017). The azimuthal angles of wave vector of lightning induced ELF/VLF emissions usually predominate around 0° (Zhima et al., 2017) in the above defined FAC coordinate system, which means that this kind of wave propagation direction points away from the Earth direction to outer space (in the increasing *L* shell direction). The lightning induced wave also presents either right or left handed polarization (Santolík et al., 2009), but most importantly, the lightning induced ELF/VLF emissions usually appear as a series of intensive burst spectra with vertical lines or whistler-mode falling/rising tones along the whole frequency range from a few hertz up to over 3 kHz or even 10 kHz (Zhima et al., 2017). In this study, the strong ELF emissions over the Sumatra epicenter zone appeared in a much lower frequency range (below 1,100 Hz), mainly at 300–800 Hz. Additionally, the variations of revisiting orbits also confirm that these emissions mainly get enhanced near earthquake time, while keeping a relatively smooth trend during the quiet-seismic activity time. Further, the perturbation amplitude relative to the background map also indicates that the enhancement of wave intensity at 300–800 Hz mainly occurs during the earthquake impending time intervals (see **Figure 5C**) but not in other time windows. So we exclude the possibility of lightning activity as the generation source for these abnormal ELF emissions.

Another kind of known electromagnetic emissions which can propagate from lithosphere to ionosphere are the artificial VLF radio waves emitted by the powerful ground-based VLF transmitters. VLF radio waves are mainly used as long-distance communication and navigation in the lithosphere-ionosphere waveguide, however, some portions of VLF radio wave energies leak into the ionosphere, propagating upward and reaching to satellite altitudes. The satellite recorded VLF radio waves usually appear at frequencies over 10 kHz to even to 30 kHz (Zhao et al., 2019), the spectra of VLF radio waves recorded by satellite usually exhibit a narrow transversal spectrum peak at the central frequency of the emitted radio waves (Shen et al., 2017; Zhang et al., 2018). Additionally, no VLF transmitter is reported near Sumatra area. So the association with VLF radio waves is excluded as a possible explanation of the observations presented here.

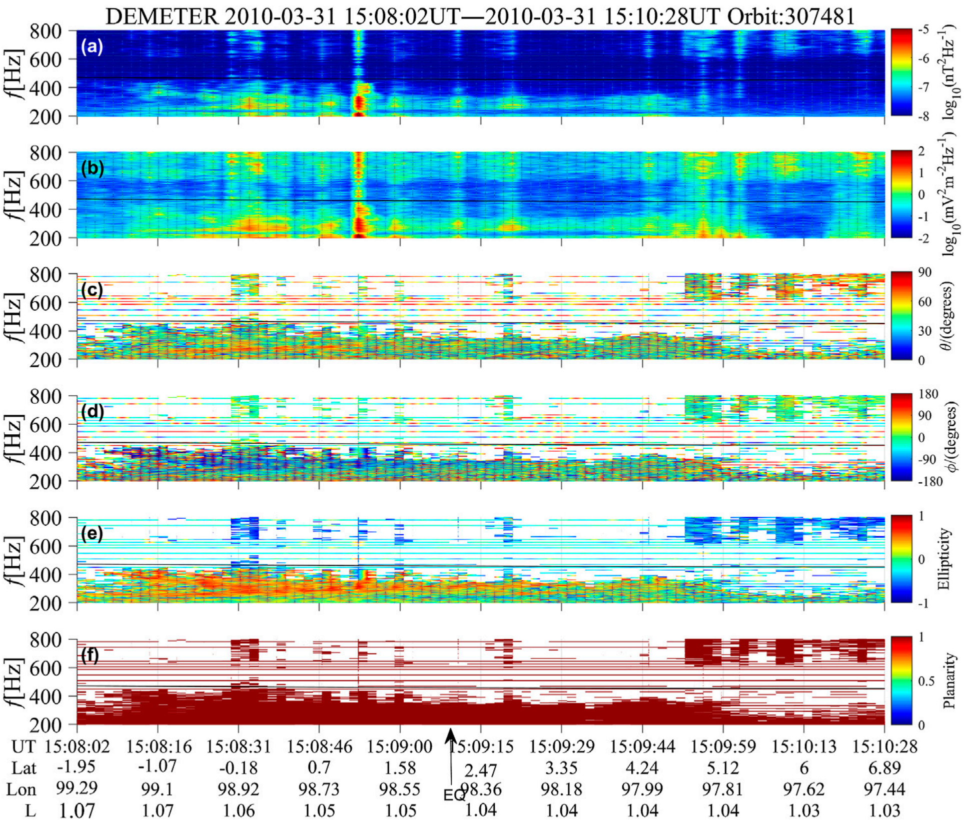

FIGURE 9 | The wave propagation parameters of extremely low frequency waves recorded by orbit No. 307481 at 15:08 to 15:10 UT on March 31, 2010. From top to bottom: **(A,B)** the power spectral values of magnetic field and electric field, **(C)** the wave normal angle θ; **(D)** the azimuthal angles ϕ; **(E)** the ellipticity, **(F)** planarity.

Previous studies (Sorokin et al., 2001; Sorokin et al., 2003; Molchanov et al., 2004; Pulinets and Ouzounov, 2011; Pulinets et al., 2018) have been undertaken to interpret the mechanism of the electromagnetic disturbances induced by earthquakes. Pulinets and Ouzounov (2011) presented the LAIC mechanism based on a complex multidisciplinary approach, trying to interpret the physical processes involved in generation of anomalous atmospheric and ionospheric phenomena associated with strong earthquakes.

First, the lithospheric rock due to tectonics plate movement, are stressed and release radon or other different kinds of gases into air (e.g., methane, helium, hydrogen, and carbon dioxide); subsequently, the radon radiation in the atmosphere changes the air conductivity resulting in a vertical electric current (see Figure 10 in Pulinets and Ouzounov (2011) and Figure 6 in Sorokin et al. (2001)). Correspondingly, the local growth of electric currents in the atmosphere develops AGW instabilities as well as a horizontal inhomogeneity of ionospheric conductivity (Sorokin et al., 2001), finally generating the magnetic field aligned currents, plasma irregularity or the ULF/ELF emissions (Sorokin et al., 2001). For example, during the 2004 Mw 9.0 Sumatra-Andaman EQ, a clear co-seismic AGW instability appeared in the atmosphere at VLF from 1.4 to 2.8 mHz with a group velocity around 300–314 m/s and amplitudes varying from ~1 to 12 Pa (Mikumo et al., 2008).

AGW can be evaluated by the wind field and temperature data and the total wave energy (E_0) of AGW can be described by the sum of kinetic (E_K) and potential energies (E_P) which correspond to the fluctuations in the wind field and temperature of atmosphere (Yang et al., 2019), respectively. E_0 and E_P energies are proportional to each other (VanZandt, 1985; de la Torre et al., 1999), so that we can examine AGW instability through E_P, which is defined as (VanZandt, 1985; Yang et al., 2019):

$$E_P = \frac{1}{2}\left(\frac{g}{N}\right)^2 \overline{\left(\frac{T'}{\overline{T}}\right)^2} \tag{2}$$

where g is the gravitational acceleration constant (9.8 ms^{-2}), T' is the perturbation atmosphere temperature deviated from the background temperature $\overline{T}$. N is the Brünt-Vaisala frequency defined as (Fritts and Alexander, 2003):

$$N = \sqrt{\frac{g}{\theta}\frac{d\theta}{dz}} \tag{3}$$

where N is a function of altitude and potential temperature, where $\theta = T\left(\frac{P_0}{P}\right)^{\frac{R}{c_p}}$ is the potential temperature, z is the altitude, P_0 is the standard reference pressure (1 hPa), P is air pressure, R is the gas

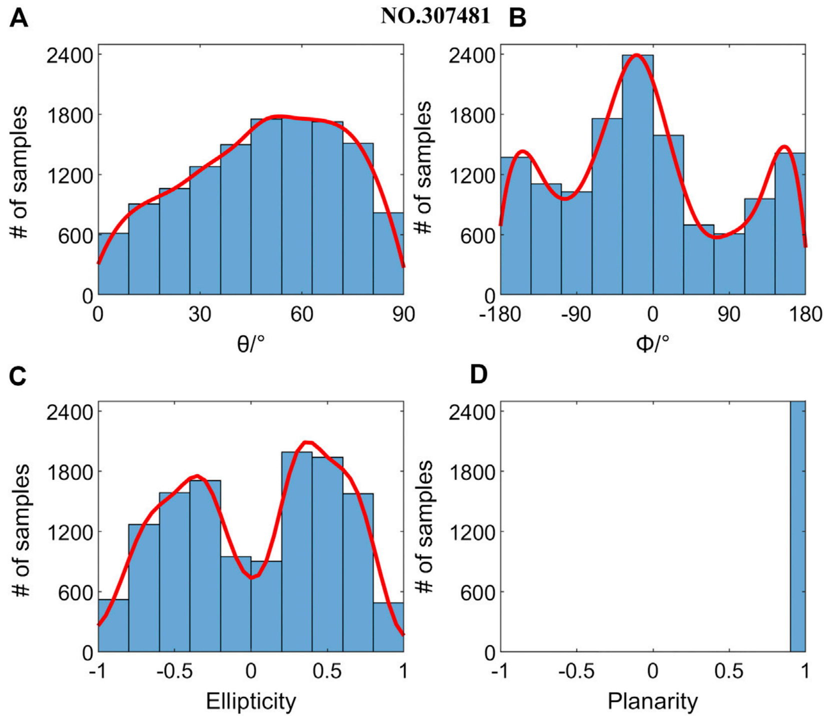

FIGURE 10 | Distribution of wave propagation parameters for the waves at extremely low frequency (300–800 Hz) in the area (1.95°S–6.89°N, 99.29°–97.44°E) at 15:08 to 15:10 UT recorded by No. 307481 on March 31, 2010. The overlapped red lines represent fitted curves computed by a probability density function; **(A)** wave normal angle θ; **(B)** and azimuth angle ϕ of the wave vector; **(C)** the ellipticity; **(D)** planarity.

constant of air and c_p is the specific heat capacity at a constant pressure, $R/c_p = 0.286$ for air.

The variance term $\overline{\left(\frac{T'}{\overline{T}}\right)^2}$ is calculated within a layer of 2 km thickness as:

$$\overline{\left(\frac{T'}{\overline{T}}\right)^2} = \frac{1}{z^{max} - z^{min}} \int_{z^{min}}^{z^{max}} \left(\frac{T'}{\overline{T}}\right)^2 dz \qquad (4)$$

where $z_{\max}$ and $z_{\min}$ are the top and bottom altitudes of the layer.

Here we computed the E_P variation over the 2010 Sumatra epicenter area by using the technique developed by Yang et al. (2019) with some procedures modified to fit in the ERA-5 data, as shown in **Figure 11**. **Figure 11A** shows the vertical temperature profile retrieved from ERA-5 dataset over the Sumatra EQ epicenter, and **Figure 11B** is the background temperature from **Figure 11A** filtered by a moving average of every 2 km; **Figure 11C** displays the temperature deviation computed by removing the background from the original temperature profile; **Figure 11D** represents the squared term of the Brunt-Väisälä frequency computed by **Eq. 3** with the temperature profile; **Figure 11E** is the potential energy as calculated by **Eq. 2**.

It can be seen from **Figure 11E** that the E_P value peaks around the altitude of 17 km (the tropopause), which is a common phenomenon (Yang et al., 2019). Four wave crests can be identified in the temperature deviation profile at the altitudes of 18.23, 27.71, 36.36, and 41.82 km (denoted by arrows in **Figure 11C**). We computed the wavelength of a full sinusoidal period of these four wave crests in the temperature deviation but not in the E_P profile. The corresponding vertical wavelengths are 9.5, 8.7, and 5.5 km for the four wave crests, which are consistent with previous understanding that the vertical wavelength of stratospheric AGW is about 2–10 km (Tsuda et al., 1994). Therefore, we suggest the possible existence of AGW wave in the atmosphere at the moment of the 2010 Sumatra EQ occurrence.

It must be admitted that through this computation, we only found the possibility of AGW generation during main shock. Because of the complicated LAIC coupling mechanism, it is impossible to build a coupling model at every key altitude (or layer) from the lithosphere to the satellite's location, and to evaluate how the coupling processing is developing. Anyway, we can tentatively interpret the link between the AGW propagation and the electric field observations in terms of a mechanical interaction between the atmospheric pressure gradient induced by the AGW and the ionosphere which causes a local instability in the plasma distribution. Such plasma variation gives rise, in the E-layer, to a local non-stationary electric current which, successively, generates an electromagnetic (EM) wave (Yang 2019; Piersanti et al., 2020, submitted).

The interpretation of LAIC mechanism needs a multidisciplinary synergy (Pulinets and Ouzounov, 2011) with the simultaneous observational data at different altitudes in lithosphere-atmosphere-ionosphere system which are sensitive to various kinds of disturbances. The

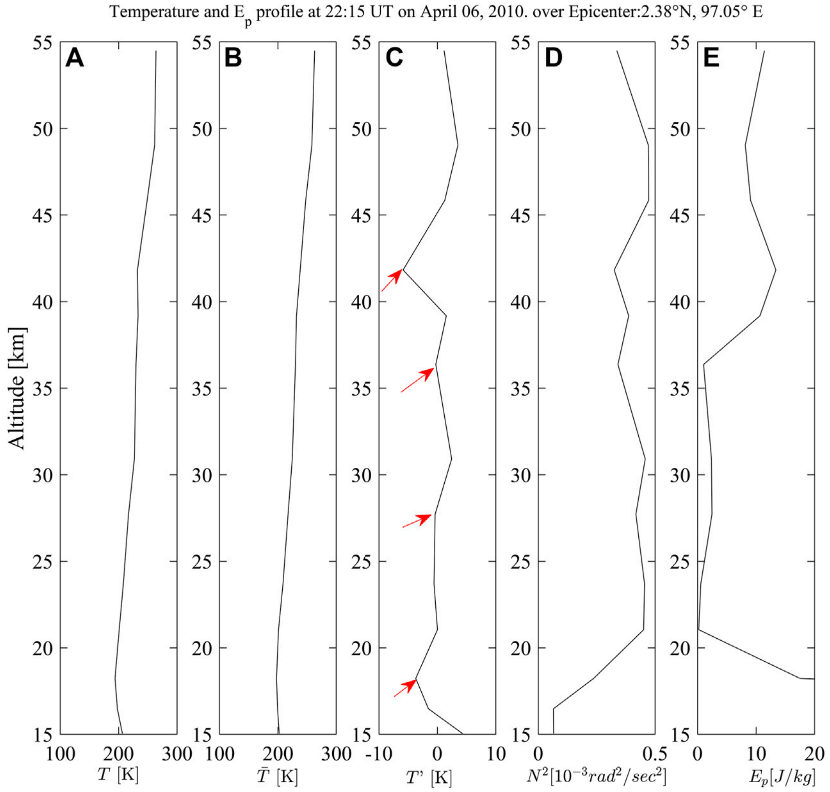

FIGURE 11 | The simulation of Acoustic Gravity Waves propagation over the 2010 Mw 7.8 Sumatra epicenter. From left to right: **(A)** the vertical temperature profile retrieved from ERA-5 dataset; **(B)** the background temperature profile filtered by an every 2 km moving average of **Figure 11A**; **(C)** the temperature deviation between **Figures 11A,B**; **(D)** the squared term N^2 of the Brunt-Väisälä frequency; **(E)** the potential energies (E_P) computed over epicenter area.

relatively very weak precursors of earthquakes can be submerged by other stronger perturbations even during quiet space weather conditions. At present, the LAIC mechanism still lacks reliable experimental evidence with direct and simultaneous observations at different layers or altitudes. It involves geophysical, chemical and even biological knowledge to interpret the mystery of seismic-ionospheric coupling. Many of the reported seismic-ionospheric case studies still require the further experimental confirmation and objective statistical studies.

CONCLUSIONS

This paper investigated the abnormal electromagnetic emissions during the 2010 April 6 Mw 7.8 Sumatra earthquake based on DEMETER satellite observations. The PSD values show that there are certain enhancements of wave intensity at frequency range (300–800 Hz) on 10–3 days before the main shock. The variation patterns along the same orbit trajectories which were computed from the revisiting orbits (August 2009 to May 2010) further indicate that the wave intensity indeed got enhanced during seismic activity time compared to the relatively stable variation patterns during quiet seismic activity time. Specifically, on March 28, 2010 (9 days before main shock), the wave intensity started to increase with peak value around $10^{-6.7}$ nT^2/Hz on the orbit trace of No. 306891 (3 days before the main shock), the wave intensity varied from $10^{-8.4}$ to $10^{-6.3}$ nT^2/Hz along the orbit trace of No. 307921. The strongest enhancement of $10^{-6.0}$ nT^2/Hz was recorded along the orbit trace nearest to the epicenter (No. 307041).

We further investigated the perturbation amplitude relative to the background map which is built by four years' of quiet space weather time data using the same time window (each year from February 1 to April 30), and found that the perturbation amplitude of wave intensities at frequency range (468–566 Hz) were indeed enhanced during the earthquake impending time interval (from March 21 to April 6).

We further computed the wave propagation parameters for the electromagnetic field waveform data by using Singular Value Decomposition method. Results show that there does exist some portions of ELF emissions mainly at 300–800 Hz, propagating upward from some altitudes lower than the satellite over the seismic zone. We excluded other generation sources for ELF/VLF emissions under quiet space weather conditions, such as the lightning activity and ground-based VLF transmitters. Considering the wave propagation features and their locations, we suggest that these portions of upward propagating ELF waves are very likely excited during the earthquake preparation processing.

According to the previous studies (e.g., Gokhberg et al., 1982; Larkina et al., 1989; Bhattacharya et al., 2007; Błęcki et al., 2010; Zhima et al., 2012a; Zhima et al., 2012b; Pulinets et al., 2018) and the reference therein, it is sure that the ELF electromagnetic emission is a promising tool for earthquake precursor detection. It usually appears a few days or weeks over the earthquake preparation zone, especially during the impend moment of a shock rupture in which the variation of stress on the rocks excite electromagnetic emissions at a broad band.

In this study we mainly took an approach of extraction the anomaly information before the strong earthquake by a case study. We didn't involve the aftershock effects in this study. We will leave it for future deep research after we accumulated enough evidence for the abnormal seismic emissions from satellite observations.

For the possible mechanism, we computed the potential energy of AGW at the moment of earthquakes and results confirm the possible existence of AGW with wavelength roughly varying from 5.5 to 9.5 km in the atmosphere at the moment of the main shock. It must be admitted that in this study, we just suggest the possibility of AGW generation over the epicenter area, due to the very complicated LAIC coupling mechanism and the impossibility of building a coupling model at every key altitude (or layer) from lithosphere to ionosphere space with the present day's science and technology levels. The comprehensive interpretation on the LAIC is beyond the scope of the present study, but we hope to explore this topic in the future.

DATA AVAILABILITY STATEMENT

The datasets presented in this study can be found in online repositories. The names of the repository/repositories and accession number(s) can be found below: DEMETER: http://demeter.cnrs-orleans.fr/. The geomagnetic index: https://cdaweb.sci.gsfc.nasa.gov/index.html/. ECMWF ERA5: https://www.ecmwf.int/en/forecasts/datasets/reanalysis-datasets/era5.

AUTHOR CONTRIBUTIONS

ZZ: scientific analysis and manuscript writing. YH: data collection and data processing. MP: AGW wave simulation and its scientific analysis. XS and AS: scientific analysis. RY, YY, SZ, ZZ, QW, JH, and FG: data collection and scientific analysis

FUNDING

This work was supported by NSFC Grant 41874174, 41574139, National Key R&D Program of China (Grant No. 2018YFC1503501), the NSFC Grant 41904149, the APSCO Earthquake Research Project Phase II and ISSI-BJ project. MP and ADS thank Italian Space Agency (ASI) for the financial support under the contract ASI "LIMADOU scienza" no. 2016-16-H0. ADS received partial funds by SAFE Project funded by ESA (European Space Agency).

ACKNOWLEDGMENTS

We acknowledge DEMETER scientific mission center for providing observations of electromagnetic field (http://demeter.cnrs-orleans.fr/). The geomagnetic index Kp and Dst index is provided by (https://cdaweb.sci.gsfc.nasa.gov/index.html/); the vertical temperature profile data of atmosphere are available through the ECMWF Web Applications Server (https://www.ecmwf.int/en/forecasts/datasets/reanalysis-datasets/era5). The authors sincerely thank Marc Hairston of the University of Texas at Dallas for assistance in copyediting this paper.

REFERENCES

Bertello, I., Piersanti, M., Candidi, M., Diego, P., and Ubertini, P. (2018). Electromagnetic field observations by the DEMETER satellite in connection with the 2009 L'Aquila earthquake. *Ann. Geophys.* 36, 1483–1493. doi:10.5194/angeo-36-1483-2018

Berthelier, J. J., Godefroy, M., Leblanc, F., Malingre, M., Menvielle, M., Lagoutte, D., et al. (2006). ICE, the electric field experiment on DEMETER. *Planet. Space Sci.* 54 (5), 456–471. doi:10.1016/j.pss.2005.10.016

Bhattacharya, S., Sarkar, S., Gwal, A., and Parrot, M. (2007). Satellite and ground-based ULF/ELF emissions observed before Gujarat earthquake in March 2006. *Curr. Sci.* 93 (1), 41–46. http://www.jstor.org/stable/24099425

Błęcki, J., Parrot, M., and Wronowski, R. (2010). Studies of the electromagnetic field variations in ELF frequency range registered by DEMETER over the Sichuan region prior to the 12 May 2008 earthquake. *Int. J. Remote Sens.* 31 (13), 3615–3629. doi:10.1080/01431161003727754

Chen, L., Santolík, O., Hajoš, M., Zheng, L., Zhima, Z., Heelis, R., et al. (2017). Source of the low-altitude hiss in the ionosphere. *Geophys. Res. Lett.* 44, 2060. doi:10.1002/2016GL072181

de la Torre, A., Alexander, A. P., and Giraldez, A. (1999). The kinetic to potential energy ratio and spectral separability from high-resolution balloon soundings near the Andes Mountains. *Geophys. Res. Lett.* 26 (10), 1413–1416. doi:10.1029/1999gl900265

Dobrovolsky, I. P., Zubkov, S. I., and Miachkin, V. I. (1979). Estimation of the size of earthquake preparation zones. *Pure. Appl. Geophys.* 117, 1025–1044. doi:10.1007/bf00876083

Fritts, D. C., and Alexander, M. J. (2003). Gravity wave dynamics and effects in the middle atmosphere. *Rev. Geophys.* 41, 1–68. doi:10.1029/2001rg000106

Gokhberg, M. B., Morgounov, V. A., Yoshino, T., and Tomizawa, I. (1982). Experimental measurement of electromagnetic emissions possibly related to earthquakes in Japan. *J. Geophys. Res.* 87 (B9), 7824. doi:10.1029/JB087iB09p07824

Heki, K., Otsuka, Y., Choosakul, N., Hemmakorn, N., Komolmis, T., and Maruyama, T. (2006). Detection of ruptures of Andaman fault segments in the 2004 great Sumatra earthquake with coseismic-ionospheric disturbances. *J. Geophys. Res.* 111 (B9), B09313–B09311. doi:10.1029/2005jb004202

Henderson, T. R., Sonwalkar, V. S., Helliwell, R. A., Inan, U. S., and Fraser-Smith, A. C. (1993). A search for ELF/VLF emissions induced by earthquakes as observed in the ionosphere by the DE 2 satellite. *J. Geophys. Res.* 98, 9503–9514. doi:10.1029/92ja01533

Huang, Q., and Ikeya, M. (1998). Seismic electromagnetic signals (SEMS) explained by a simulation experiment using electromagnetic waves. *Phys. Earth Planet. Inter.* 109 (3), 107–114. doi:10.1016/s0031-9201(98)00135-6

Kumar, A., Kumar, S., Hayakawa, M., and Menk, F. (2013). Subionospheric VLF perturbations observed at low latitude associated with earthquake from Indonesia region. *J. Atmos. Sol. Terr. Phys.* 102, 71–80. doi:10.1016/j.jastp.2013.04.011

Lagoutte, D., Brochot, J. Y., De Carvalho, D., Elie, F., Harivelo, F., Hobara, Y., et al. (2006). The DEMETER science mission centre. *Planet. Space Sci.* 54 (5), 428–440. doi:10.1016/j.pss.2005.10.014

Larkina, V. I., Migulin, V. V., Molchanov, O. A., Kharkov, I. P., Inchin, A. S., and Schvetcova, V. B. (1989). Some statistical results on very low frequency radiowave emissions in the upper ionosphere over earthquake zones. *Phys. Earth Planet. Inter.* 57 (1), 100–109. doi:10.1016/0031-9201(89)90219-7

Liu, J., Zhang, X., Novikov, V., and Shen, X. (2016). Variations of ionospheric plasma at different altitudes before the 2005 Sumatra Indonesia M s 7.2 earthquake. *J. Geophys. Res. Space Phys.* 121 (9), 9179–9187. doi:10.1002/2016ja022758

Liu, J. Y., Chen, Y. I., Chen, C. H., and Hattori, K. (2010). Temporal and spatial precursors in the ionospheric global positioning system (GPS) total electron content observed before the 26 December 2004 M9.3 Sumatra–Andaman Earthquake. *J. Geophy. Res.* 115 (A9), A09312–A09313. doi:10.1029/2010ja015313

Liu, J. Y., Wang, K., Chen, C. H., Yang, W. H., Yen, Y. H., Chen, Y. I., et al. (2013). A statistical study on ELF-whistlers/emissions and M ≥ 5.0 earthquakes in Taiwan. *J. Geophys. Res. Space Phys.* 118 (6), 3760–3768. doi:10.1002/jgra.50356

Marchetti, D., De Santis, A., Shen, X., Campuzano, S. A., Perrone, L., Piscini, A., et al. (2020). Possible lithosphere-atmosphere-ionosphere coupling effects prior to the 2018 Mw = 7.5 Indonesia earthquake from seismic, atmospheric and ionospheric data. *J. Asian Earth Sci.* 188, 104097. doi:10.1016/j.jseaes.2019.104097

Mikumo, T., Shibutani, T., Le Pichon, A., Garces, M., Fee, D., Tsuyuki, T., et al. (2008). Low-frequency acoustic-gravity waves from coseismic vertical deformation associated with the 2004 Sumatra-Andaman earthquake (Mw = 9.2). *J. Geophys. Res.* 113 (B12), B12402–B12411. doi:10.1029/2008jb005710

Molchanov, O., Fedorov, E., Schekotov, A., Gordeev, E., Chebrov, V., Surkov, V., et al. (2004). Lithosphere-atmosphere-ionosphere coupling as governing mechanism for preseismic short-term events in atmosphere and ionosphere. *Nat. Hazards Earth Syst. Sci.* 4, 757–767. doi:10.5194/nhess-4-757-2004

Molchanov, O., Rozhnoi, A., Solovieva, M., Akentieva, O., Berthelier, J. J., Parrot, M., et al. (2006). Global diagnostics of the ionospheric perturbations related to the seismic activity using the VLF radio signals collected on the DEMETER satellite. *Nat. Hazards Earth Syst. Sci.* 6, 745–753. doi:10.5194/nhess-6-745-2006

Nemec, F., Santolik, O., and Parrot, M. (2009). Decrease of intensity of ELF/VLF waves observed in the upper ionosphere close to earthquakes: a statistical study. *J. Geophys. Res.* 114 (A04303), 1–10. doi:10.1029/2008JA013972

Olsen, N., Sabaka, T. J., and Tøffner-Clausen, L. (2000). Determination of the IGRF 2000 model. *Earth Planets Space.* 52, 1175–1182. doi:10.1186/bf03352349

Parrot, M. (1989). VLF emissions associated with earthquakes and observed in the ionosphere and the magnetosphere. *Phys. Earth Planet. Inter.* 57 (1–2), 86–99. doi:10.1016/0031-9201(89)90218-5

Parrot, M. (1994). Statistical study of ELF/VLF emissions recorded by a low-altitude satellite during seismic events. *J. Geophys. Res.* 99 (A12), 23339. doi:10.1029/94ja02072

Parrot, M., Benoist, D., Berthelier, J. J., Błęcki, J., Chapuis, Y., Colin, F., et al. (2006a). The magnetic field experiment IMSC and its data processing onboard DEMETER: scientific objectives, description and first results. *Planet. Space Sci.* 54 (5), 441–455. doi:10.1016/j.pss.2005.10.015

Parrot, M., Berthelier, J., Lebreton, J., Sauvaud, J., Santolik, O., and Blecki, J. (2006b). Examples of unusual ionospheric observations made by the DEMETER satellite over seismic regions. *Phys Chem Earth Parts A/B/C* 31 (4–9), 486–495. doi:10.1016/j.pce.2006.02.011

Pulinets, S., Ouzounov, D., and Davidenko, D. (2018). *The possibility of earthquake forecasting: learning from nature*. Bristol, UK: IOP Publishing. doi:10.1088/978-0-7503-1248-6ch2

Pulinets, S., and Ouzounov, D. (2011). Lithosphere-atmosphere-ionosphere coupling (LAIC) model - an unified concept for earthquake precursors validation. *J. Asian Earth Sci.* 41 (4), 371–382. doi:10.1016/j.jseaes.2010.03.005

Rodger, C. J., Thomson, N. R., and Dowden, R. L. (1996). A search for ELF/VLF activity associated with earthquakes using ISIS satellite data. *J. Geophys. Res.* 101 (A6), 13369–13378. doi:10.1029/96ja00078

Santolík, O., Parrot, M., Inan, U. S., Burešová, D., Gurnett, D. A., and Chum, J. (2009). Propagation of unducted whistlers from their source lightning: a case study. *J. Geophys. Res.* 114 (A3), A03212. doi:10.1029/2008ja013776

Santolik, M., Parrot, M., and Lefeuvre, F. (2003). Singular value decomposition methods for wave propagation analysis. *Radio Sci.* 38 (1), 1010. doi:10.1029/2000RS002523

Serebryakova, O. N., Bilichenko, S. V., Chmyrev, V. M., Parrot, M., Rauch, J. L., Lefeuvre, F., et al. (1992). Electromagnetic ELF radiation from earthquake regions as observed by low-altitude satellites. *Geophys. Res. Lett.* 19 (2), 91–94. doi:10.1029/91gl02775

Shen, X., Zhima, Z., Zhao, S., Qian, G., Ye, Q., and Ruzhin, Y. (2017). VLF radio wave anomalies associated with the 2010 Ms 7.1 Yushu earthquake. *Adv. Space Res.* 59 (10), 2636–2644. doi:10.1016/j.asr.2017.02.040

Shklyar, D. R., Storey, L. R. O., Chum, J., Jiříček, F., Němec, F., Parrot, M., et al. (2012). Spectral features of lightning-induced ion cyclotron waves at low latitudes: DEMETER observations and simulation. *J. Geophys. Res.* 117 (A12), 16. doi:10.1029/2012ja018016

Sorokin, V. M., Chmyrev, V. M., and Yaschenko, A. K. (2001). Electrodynamic model of the lower atmosphere and the ionosphere coupling. *J. Atmos. Sol. Terr. Phys.* 63 (16), 1681–1691. doi:10.1016/s1364-6826(01)00047-5

Sorokin, V. M., Chmyrev, V. M., and Yaschenko, A. K. (2003). Ionospheric generation mechanism of geomagnetic pulsations observed on the Earth's surface before earthquake. *J. Atmos. Sol. Terr. Phys.* 65 (1), 21–29. doi:10.1016/s1364-6826(02)00082-2

Tsuda, T., Murayama, Y., Nakamura, T., Vincent, R. A., Manson, A. H., Meek, C. E., et al. (1994). Variations of the gravity wave characteristics with height, season and latitude revealed by comparative observations. *J. Atmos. Terr. Phys.* 56 (5), 555–568. doi:10.1016/0021-9169(94)90097-3

VanZandt, T. E. (1985). A model for gravity wave spectra observed by Doppler sounding systems. *Radio Sci.* 20 (6), 1323–1330. doi:10.1029/RS020i006p01323

Wei, X. H., Cao, J. B., Zhou, G. C., Santolík, O., Rème, H., Dandouras, I., et al. (2007). Cluster observations of waves in the whistler frequency range associated with magnetic reconnection in the Earth's magnetotail. *J. Geophys. Res.* 112 (A10), A10225. doi:10.1029/2006ja011771

Xia, Z., Chen, L., Zhima, Z., Santolík, O., Horne, R. B., and Parrot, M. (2019). Statistical characteristics of ionospheric hiss waves. *Geophys. Res. Lett.* 46 (13), 7147–7156. doi:10.1029/2019GL083275

Yang, S. S., Asano, T., and Hayakawa, M. (2019). Abnormal gravity wave activity in the stratosphere prior to the 2016 Kumamoto earthquakes. *J. Geophys. Res. Space Phys.* 124 (2), 1410–1425. doi:10.1029/2018ja026002

Zhang, Z., Chen, L., Li, X., Xia, Z., Heelis, R. A., and Horne, R. B. (2018). Observed propagation route of VLF transmitter signals in the magnetosphere. *J. Geophys. Res. Space Phys.* 123 (7), 5528–5537. doi:10.1029/2018ja025637

Zhao, S., Zhou, C., Shen, X., and Zhima, Z. (2019). Investigation of VLF transmitter signals in the ionosphere by ZH-1 observations and full-wave simulation. *J. Geophys. Res. Space Phys.* 124 (6), 4697–4709. doi:10.1029/2019ja026593

Zhima, Z., Cao, J., Fu, H., Liu, W., Chen, L., Dunlop, M., et al. (2015a). Whistler mode wave generation at the edges of a magnetic dip. *J. Geophys. Res. Space Phys.* 120 (4), 2469–2476. doi:10.1002/2014JA020786

Zhima, Z., Chen, L., Fu, H., Cao, J., Horne, R. B., and Reeves, G. (2015b). Observations of discrete magnetosonic waves off the magnetic equator. *Geophys. Res. Lett.* 42 (22), 9694–9701. doi:10.1002/2015GL066255

Zhima, Z., Chen, L., Xiong, Y., Cao, J., and Fu, H. (2017). On the origin of ionospheric hiss: a conjugate observation. *J. Geophys. Res.* 122 (11), 11784–11793. doi:10.1002/2017JA024803

Zhima, Z., Xu-Hui, S., Jin-Bin, C., Zhang, X., Huang, J., Jing, L., et al. (2012a). Statistical analysis of ELF/VLF magnetic field disturbances before major earthquakes. *Chinese J Geophys.* 55, 3699–3708. doi:10.6038/j.issn.0001-5733.2012.11.017

Zhima, Z., Xuhui, S., Xuemin, Z., Jinbin, C., Jianping, H., Xinyan, O., et al. (2012b). Possible ionospheric electromagnetic perturbations induced by the Ms7. 1 Yushu earthquake. *Earth Moon Planets.* 108 (3–4), 231–241. doi:10.1007/s11038-012-9393-z

Conflict of Interest: The authors declare that the research was conducted in the absence of any commercial or financial relationships that could be construed as a potential conflict of interest.

The reviewer (MP) declared a past co-authorship with some of the authors (ZZ, RY) to the handling editor.

frontiers in Earth Science

ORIGINAL RESEARCH
published: 08 April 2021
doi: 10.3389/feart.2021.610193

Ionosphere Sounding for Pre-seismic Anomalies Identification (INSPIRE): Results of the Project and Perspectives for the Short-Term Earthquake Forecast

Sergey Pulinets[1,2]*, Andrzej Krankowski[1], Manuel Hernandez-Pajares[3], Sergio Marra[4], Iurii Cherniak[1], Irina Zakharenkova[1], Hanna Rothkaehl[4], Kacper Kotulak[1], Dmitry Davidenko[2], Leszek Blaszkiewicz[1], Adam Fron[1], Pawel Flisek[1], Alberto Garcia Rigo[3] and Pavel Budnikov[6]

[1]University of Warmia and Mazury in Olsztyn, (UWM), Space Radio-Diagnostics Research Centre, Olsztyn, Poland, [2]Space Research Institute of Russian Academy of Sciences, (IKI), Moscow, Russia, [3]Polytechnic University of Catalonia (UPC), Barcelona, Spain, [4]European Space Research and Technology Centre ESA/ESTEC, Noordwijk, Netherlands, [5]Space Research Centre, Polish Academy of Sciences (CBK PAN), Warsaw, Poland, [6]Fedorov Institute of Applied Geophysics, IPG, Moscow, Russia

OPEN ACCESS

Edited by:
Jann-Yenq Liu,
National Central University, Taiwan

Reviewed by:
Kwangsun Ryu,
Korea Advanced Institute of Science and Technology, South Korea
Xuemin Zhang,
China Earthquake Administration, China

***Correspondence:**
Sergey Pulinets
pulse1549@gmail.com

Specialty section:
This article was submitted to Environmental Informatics and Remote Sensing, a section of the journal Frontiers in Earth Science

Received: *25 September 2020*
Accepted: *15 February 2021*
Published: *08 April 2021*

Citation:
Pulinets S, Krankowski A, Hernandez-Pajares M, Marra S, Cherniak I, Zakharenkova I, Rothkaehl H, Kotulak K, Davidenko D, Blaszkiewicz L, Fron A, Flisek P, Rigo AG and Budnikov P (2021) Ionosphere Sounding for Pre-seismic Anomalies Identification (INSPIRE): Results of the Project and Perspectives for the Short-Term Earthquake Forecast. Front. Earth Sci. 9:610193. doi: 10.3389/feart.2021.610193

The INSPIRE project was dedicated to the study of physical processes and their effects in ionosphere which could be determined as earthquake precursors together with detailed description of the methodology of ionospheric pre-seismic anomalies definition. It was initiated by ESA and carried out by an international consortium. The full set of key parameters of the ionospheric plasma was selected based on the retrospective analysis of the ground-based and satellite measurements of pre-seismic anomalies. Using this classification the multi-instrumental database of worldwide relevant ionospheric measurements (ionosonde and GNSS networks, LEO-satellites with *in situ* probes including DEMETER and FORMOSAT/COSMIC ROC missions) was developed for the time intervals related to selected test cases. As statistical processing shows, the main ionospheric precursors appear approximately 5 days before the earthquake within the time interval of 30 days before and 15 days after an earthquake event. The physical mechanisms of the ionospheric pre-seismic anomalies generation from ground to the ionosphere altitudes were formulated within framework of the Lithosphere-Atmosphere-Ionosphere Coupling (LAIC) model. The processes of precursor's development were analyzed starting from the crustal movements, radon emission and air ionization, thermal and atmospheric anomalies, electric field and electromagnetic emissions generation, variations of the ionospheric plasma parameters, in particular vertical TEC and vertical profiles of the electron concentration. The assessment of the LAIC model performance with definition of performance criteria for earthquake forecasting probability has been done in statistical and numerical simulation domains of the Global Electric Circuit. The numerical simulations of the earthquake preparation process as an open complex system from start of the final stage of earthquake preparation up to the final point–main shock confirms that in the temporal domain the ionospheric precursors are one of the most late in the sequence of precursors. The general algorithm for the identification of the ionospheric precursors was formalized which also takes into account the external Space Weather factors able to generate the false alarms. The importance of the special stable pattern called the “precursor mask” was highlighted which is based on self-similarity of pre-seismic ionospheric variations. The role of expert decision in pre-seismic anomalies interpretation for generation of seismic warning is important as well. The algorithm performance of the LAIC seismo-ionospheric effect detection module has been demonstrated using the L’Aquila 2009 earthquake as a case study. The results of INSPIRE project have demonstrated that the ionospheric anomalies registered before the strong earthquakes could be used as reliable precursors. The detailed classification of the pre-seismic anomalies was presented in different regions of the ionosphere and signatures of the pre-seismic anomalies as detected by ground and satellite based instruments were described what clarified methodology of the precursor’s identification from ionospheric multi-instrumental measurements. Configuration for the dedicated multi-observation experiment and satellite payload was proposed for the future implementation of the INSPIRE project results. In this regard the multi-instrument set can be divided into two groups: space equipment and ground-based support, which could be used for real-time monitoring. Together with scientific and technical tasks the set of political, logistic and administrative problems (including certification of approaches by seismological community, juridical procedures by the governmental authorities) should be resolved for the real earthquake forecast effectuation.

Keywords: earthquake precursors, LAIC model, ionosphere, TEC, GNSS, LEO-satellites

INTRODUCTION

The end of the first decade of the third millennium passed under impression from the French satellite DEMETER results. DEMETER was dedicated to the monitoring of ionospheric anomalies appearing around the time of strong earthquakes, in the ionosphere over the areas where earthquake happened (Li and Parrot, 2013; Parrot and Li, 2018). Majority of signals have been registered by satellite several days before the seismic shock, what delivers enough evidence for the existence of the ionospheric precursors of earthquakes. Because of high altitude of DEMETER satellite orbit (in comparison with the altitude of the peak height of the ionosphere), the ionospheric precursor’s proofs were obtained mainly statistically while the GNSS TEC technology, with higher spatial and temporal resolution, provided more and more solid results demonstrating that ionospheric precursors have real practical merit for resolving the problem of the short-term earthquake forecast (Liu et al., 2009; Pulinets et al., 2010; Pulinets et al., 2015; Liu et al., 2018).

Year 2004, when DEMETER satellite was launched, has been marked by one more event–the publication of the monograph where for the first time general problems of ionospheric precursor’s generation mechanism, morphology of this phenomena and technology of their monitoring were thoroughly considered (Pulinets and Boyarchuk, 2004). It was demonstrated in monograph that anomalous variations registered in the ionosphere before earthquakes were reported as early as in 1960s after the Alaska “Good Friday” earthquake (Davies and Baker, 1965). The purposeful studies of ionospheric precursors with the use of ground-based ionosondes started in 1970s (Datchenko et al., 1972) and most convincing results using the satellite technology were obtained using the topside sounding technique (Pulinets, 1998; Pulinets and Legen’ka, 2003). Together with rapidly developing GNSS TEC technology, it is used for the earthquake precursors detection (Liu et al., 2004; Krankowski et al., 2006). Just then word “detection” became the key concept in scientific discussions on how to identify the ionospheric precursors of earthquakes (Dautermann et al., 2007; Thomas et al., 2012).

From the very beginning, the publications on seismo-ionospheric anomalies split into two directions. The first one used the simplest approach associating the observed anomalies with the epicenter position and time of earthquakes (Liu et al., 2004; Kon et al., 2011; Li and Parrot, 2013). However, nobody can guarantee that coincidence with place and time of earthquake confirms that this means the cause-effect relationship. The second approach uses the uniqueness of the physical mechanism generating the seismo-ionospheric anomalies. This uniqueness is a reliable marker for the observed anomaly as related to the earthquake preparation (Pulinets et al., 2003; 2004a; 2007a; Pulinets and Davidenko, 2014; Pulinets and Davidenko, 2018; Davidenko and Pulinets, 2019).

The growing snowball of the publications devoted to the seismo-ionospheric effects initiated the series of international projects aimed to the effect validation. Among them, the European projects should be mentioned. Two simultaneously ongoing FP7 projects: PRE-EARTHQUAKES (Processing Russian and European Earth observations for earthquakes precursors Studies) [http://www.pre-earthquakes.org] and SEMEP (Search for Electro-Magnetic Earthquake Precursors combining satellite and ground-based facilities) with duration through 2013–2015 (http://www.ssg.group.shef.ac.uk/semep/). More representative international project including, except European, the scientists from United States, Japan, Taiwan were organized by the International Space Science Institute (ISSI) in Bern. The project "Multi-instrument Space-Borne Observations and Validation of the Physical Model of the Lithosphere-Atmosphere-Ionosphere-Magnetosphere Coupling" (https://www.issibern.ch/teams/spaceborneobserve/) lasted in 2013–2015 confirmed the validity of the Lithosphere-Atmosphere-Ionosphere Coupling model based on the expertize of the leading scientists working in the area of space physics. As a result of this project the extended AGU Monograph 234 from the Geophysical Monograph Series was published (Ouzounov et al., 2018), including, among others (Pulinets et al., 2018).

Taking into account the success of the DEMETER mission and solid scientific basis of the physical substantiation of the seismo-ionospheric effects, the European Space Agency in 2013 opened the call ESA ITT AO/1–7,548/13/NL/MV for ionospheric sounding for pre-seismic activity identification. One can see that here we encounter the word "identification" what means the main intention of the project to use its results for practical application. This competition was won by the Consortium created by three European institutions: University of Warmia and Mazury in Olsztyn (UWM) as a Prime Contractor, Space Research Center of the Polish Academy of Sciences, and Polytechnic University of Catalonia (UPC), Spain. This project was called INSPIRE (ionosphere Sounding for Pre-seismic anomalies Identification REsearch) and the present paper will be devoted the description of the project results.

MATERIALS AND METHODS

The effectiveness of the technologies of ionosphere monitoring in ionospheric precursors detection was demonstrated in many researches worldwide. Among them we should mention the vertical ionospheric sounding by ground-based ionosondes (Pulinets et al., 2004b; Liu et al., 2006), by vertical topside sounding from satellites (Pulinets and Legen'ka, 2003), by GNSS TEC monitoring (Liu et al., 2004; 2018), by applying GNSS GIM technique (Liu et al., 2009; Pulinets et al., 2010), by *in-situ* satellite measurements of the local ionospheric plasma parameters (Parrot and Li, 2018), by low orbit ionospheric tomography (Pulinets et al., 2009; Hirooka et al., 2011), by GNSS occultation technique (Chang et al., 2015), subionospheric VLF waves propagation anomalies (Rozhnoi et al., 2009), oblique ground-based ionospheric sounding (Blaunstein and Hayakawa, 2009), and probably some exotic techniques more. The problem of this diversity is in fact that majority of scientists are working in their own domain and do not imply other techniques. Therefore, the main purpose of the project was the integration of this diversity having in mind searching the most optimal algorithms for the ionospheric precursor's identification. This means to find the advantages and disadvantages of every technique mentioned above, and to find the most optimal combinations of their application. The second purpose is to demonstrate their common Physical Mechanism, to use the monitoring data not blindly calculating their amplitude outliers and interpreting them as precursor anomalies but finding variations corresponding the dynamical development of the physical processes affecting the ionosphere before earthquakes. And finally, provide recommendations for creating the complex system for Application in the short-term earthquake forecast activity. We consider that the present state of our knowledge and technology is sufficiently advanced for creating of such a system and becomes the matter of political and administrative decisions.

According to the main tasks within the project framework, we provided the analysis of different techniques of the ionosphere monitoring to reveal the limitations of different diagnostic techniques with the purpose of their integration using their advantages. As a test for the physical mechanism validation, we selected the case of L'Aquila M6.3 earthquake on April 6, 2009 in Italy where the extended collected database made it possible to combine different techniques to develop the optimal configuration of the monitoring system. The last part of the project was devoted to the road map definition to create the complex system of the ionosphere monitoring for the task of the short-term earthquake forecast.

One of the crucial points for building the coherent services is validation and unification of different databases in order to mitigate the bias and measurement techniques errors. The currently existing space- and ground-based diagnostics still have a number of gaps in time and space domains. Unfortunately, very often we have to incorporate different type of interpolation and extrapolation methods, which in consequence distort or loose part of the relevant information.

Limitations

Ground based ionosonde stations are distributed essentially sparsely on the globe (in comparison with permanent GNSS stations–few hundreds up to few thousands in each regional network). Absence of the ionosonde stations in the essential seismoactive regions can dramatically limit the proper forecast and we can only study time series of data to reveal anomalous changes in diurnal variability. Sensitivity of the ionosonde to the earthquake precursors is limited by the size of earthquake preparation zone determined by the expression R (km) = $10^{0.43\ M}$ where M–is the earthquake magnitude (Dobrovolsky et al., 1979). Therefore, it does not allow to study the spatial features and sizes of the anomalies. Due to these reasons, not for all the earthquakes cases the ionosonde data are available.

The range of the oblique sounding ionosondes is essentially larger than vertical ones, but the number of such instruments is even less than the vertical ones. In additions, the functioning of the oblique sounding ionosondes depends on the availability of transmitters providing the proper signal passes over the seismically active regions.

It could sound strange but similar limitation is also characteristic to the network of stationary GNSS receivers for GNSS TEC measurements due to the lack of receivers in ocean regions where many earthquakes take place and in several countries with limited number of receivers. In addition, GNSS TEC data do no permit to observe variations of vertical profiles of electron concentration shape which is an important characteristic of the precursory ionospheric variations.

Topside sounding limitation is common for all techniques of low orbiting satellite monitoring: very limiting time over the monitored regions, and (in case of solar synchronized orbit) inability to monitor precursor's dynamics in local time.

The *in-situ* space plasma diagnostics located on board of low orbiting satellite are affected by the same limitations as for the topside sounding satellites. In addition, it is impossible to get the satellite orbit altitude close to the main maximum of the ionosphere (250–350 km). Usually, the satellite orbit is near 600 km and higher (DEMETER satellite), and it is able to observe very tiny variations which could be properly estimated mainly statistically.

For the LEO satellites, using the radio occultation method, the problem is the limitation of observations over a specific region. In general, single satellite passes over specific regions happen only two times per day, with exception of FORMOSAT-3/COSMIC constellation mission providing about 1500 RO daily soundings.

Regardless of the large number of IGS receivers providing GNSS TEC data for GIM technology we still have areas both on the land (for example, Russia, African regions) and over the ocean where we do not have enough receivers to produce accurate maps of electron content. In these regions the real data are either replaced by models or interpolated and we should have some reservation using the GNSS TEC data for ionospheric precursor's analysis by GIM technology, with a limited space and time resolution.

The VLF subionospheric propagation anomaly diagnostics of signals associated with earthquakes have the same problems as oblique ionospheric sounding and depends on the proper transmitters availability. It could be used only as a proxy detecting the preparation of the earthquake without the determination of the epicenter position.

Low orbiting tomography needs the proper networks of receiving stations whose number is very limited (Romanov et al., 2013), so this technique is still could be regarded as perspective for future years. The tomography based on neural network analysis (Hirooka et al., 2011) needs the dense network of GPS receivers and can be applied only in a limited number of developed countries.

Also incorporation of newly available real-time and near-real time GNSS receivers is sometimes difficult, due to its dependence on many different organizations and infrastructure maintenance cost.

Advantages

Regardless the abovementioned limitations, the vertical sounding probably is the most informative technique of the ionospheric precursors monitoring. The ground-based sounding permits to provide the round the clock state of the ionosphere including the local time dependence of the ionospheric precursors (Pulinets and Davidenko, 2018; Davidenko and Pulinets, 2019). Additional information could be obtained from the vertical profiles modification before earthquakes formation of sporadic E layers and formation of specific traces on vertical ionograms, interpreted as particle precipitation and indicator of earthquake approaching (Bogdanov et al., 2017).

In comparison with GNSS TEC mapping with uneven distribution of GPS receivers and their absence in some areas, the topside sounding provides the evenly spaced grid of measurements causing greater confidence in the received maps. Additional information increasing the confidence of ionospheric precursor's identification is obtained from vertical profiles shape variations before earthquakes (Pulinets et al., 2003).

In comparison with vertical sounding data the oblique sounding provides very important information giving almost imminent alert for earthquake approaching: 8 h in advance(Blaunstein and Hayakawa, 2009).

Main advantage of GNSS TEC data is that they are most affordable and widespread. In addition, similarly as vertical sounding, we get information round the clock, what permits also to obtain the local time dependence of ionospheric variations before earthquakes, what is one of the main precursor footprints for earthquake time determination.

In situ diagnostics of the ionospheric plasma gives information on several parameters such as electron and ion concentration and temperature, composition and particle precipitation, what provides the complex depiction of precursory situation (Pulinets et al., 2003).

With the further development of vertical profiles reconstruction by LEO occultation technology, it is possible to provide the information on the electron concentration profiles variation before earthquakes with wider coverage in the local time. It is still necessary to develop technique to select the profiles with the same track of occultation direction over selected regions to exclude the variations connected with longitudinal differences due to different track direction and to get the pure ionosphere variations connected with the earthquake preparation process.

The neural network based tomography can provide the vertical profiles variation before earthquakes similarly to the vertical sounding. Its advantage that it is able to reconstruct the complete profile without the separation on topside and bottomside parts (Hirooka et al., 2011).

RESULTS

Identification of the ionospheric precursors based on their physical mechanism is similar to recognition of a person by signs characteristics belonging only to him, so we call this process as cognitive recognition (Pulinets et al., 2021). We propose a completely different approach based on the physical mechanism of generation of disturbances created by the interaction of the ionosphere with the lithosphere and atmosphere. At the same time, this interaction gives the observed variations unique properties characteristic only to earthquake precursors, on the basis of which the precursors are identified using an intelligent algorithm. Another advantage of this approach is that the method we call cognitive identification does not need large deviations

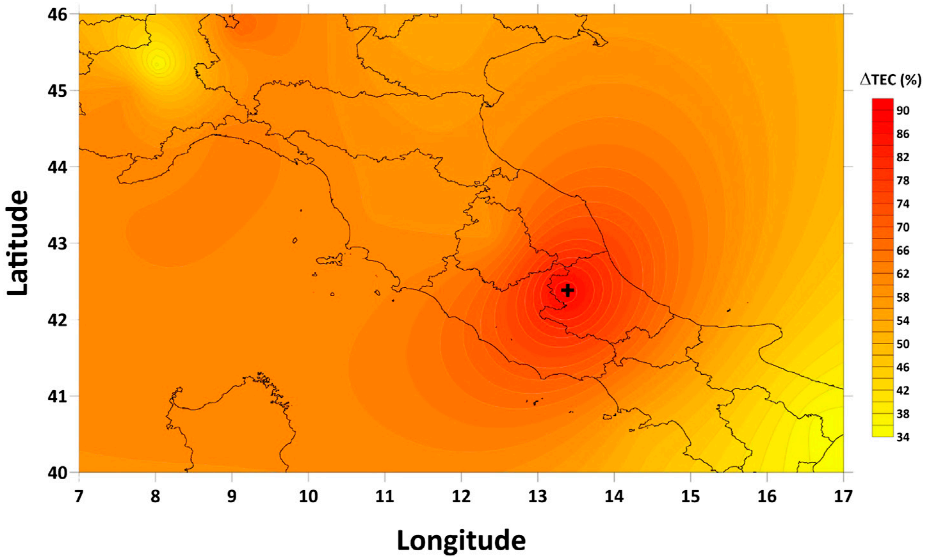

FIGURE 1 | Differential map of GPS TEC registered at 22:10 UT on April 4, 2009, 27.3 h before the L'Aquila earthquake.

from unperturbed values, since it is based on the recognition of the "portrait" of the precursor, which is formed by its morphological features, and can be effectively used even at low values of the signal/noise ratio.

We will demonstrate this using the database collected by our group for the L'Aquila earthquake.

Physical mechanism of seismo-ionospheric coupling and phenomenology of ionospheric precursors of earthquakes.

The most recent research demonstrates that the information from underground pre-earthquake transformation of the Earth's crust before earthquake is transmitted to the ionosphere by electromagnetic coupling through the Global Electric Circuit (Pulinets and Davidenko, 2014). Large-scale modification of the boundary layer conductivity leads to the changes of the ionosphere electric potential what causes the generation of anomalous electric field in the ionosphere. These fields were detected recently by Advanced ionospheric Probe (AIP) installed onboard FORMOSAT5 (Liu and Chao, 2017). As demonstrated our research (Pulinets and Davidenko, 2018) the most favorable conditions for seismo-ionospheric coupling in Europe are created during nighttime. In majority of cases they are positive, but under specific conditions (just in Italy) the negative nighttime anomalies could be observed before earthquakes (Davidenko and Pulinets, 2019). The unique local time behavior of the ionospheric precursors together with their other established morphological features (Pulinets et al., 2003) create conditions when they could be uniquely identified. Let us check this conception taking the case of the L'Aquila earthquake as an example. The main shock with magnitude Mw6.3 occurred at 03:32 CEST (01:32 UTC) on April 6, 2009 at the point with coordinates 42.35 N, 13.38 E in the Italian region Abruzzo near L'Aquila city.

First and main property of the ionospheric precursor is its locality. The ionospheric anomaly appears over the earthquake preparation zone, and this cannot be mixed up with the effect of geomagnetic storm that is essentially global. The local TEC differential map is presented in **Figure 1**. We used the data of the local network of GNSS receivers. The maximum deviation was registered by the receiver *aqui* situated directly in L'Aquila. To construct difference maps of the total electron content of the ionosphere, we used the data from GNSS (Global Navigation Satellite Systems) receivers in the RINEX (Receiver Independent Exchange) format (for example, for the Aquila earthquake, we used the data ftp://geodaf.mt.asi.it/GEOD/GPSD/RINEX/). For each receiver, the vertical total electron content was calculated. After that we calculated and constructed differential maps of regional vertical TEC, which represent the deviation of the current values of vertical TEC from the background, in the MATLAB environment. We calculated the difference maps according to the formula $\Delta TEC = 100\ (TEC–TECa)/TECa$, where the TECa -average TEC values calculated from 15 previous numerical values for the same moment of time were used as the background values. The deviation from the background values was expressed in percentages.

One can see from the Figure that the deviation is still positive even outside the Italy borders, so it is worth to try the TEC map technology to see how large the positive anomaly is in space. The differential GIM map is presented in **Figure 2**.

According to (Pulinets et al., 2004a) the locality of the seismo-ionospheric anomaly could be checked by correlation analysis between different stations in the area situated at different distances from the epicenter. This could be applied to both, the ground based ionosondes and the GNSS receivers. In addition, the variations of the cross-correlation coefficient gives an idea on the time of earthquake because the drop of cross correlation coefficient takes place from 1 to 5 days before the main shock. The cross-correlation coefficient is calculated for the daily arrays of vertical TEC measurements at the selected pairs of receivers for the GPS TEC data and daily arrays of the

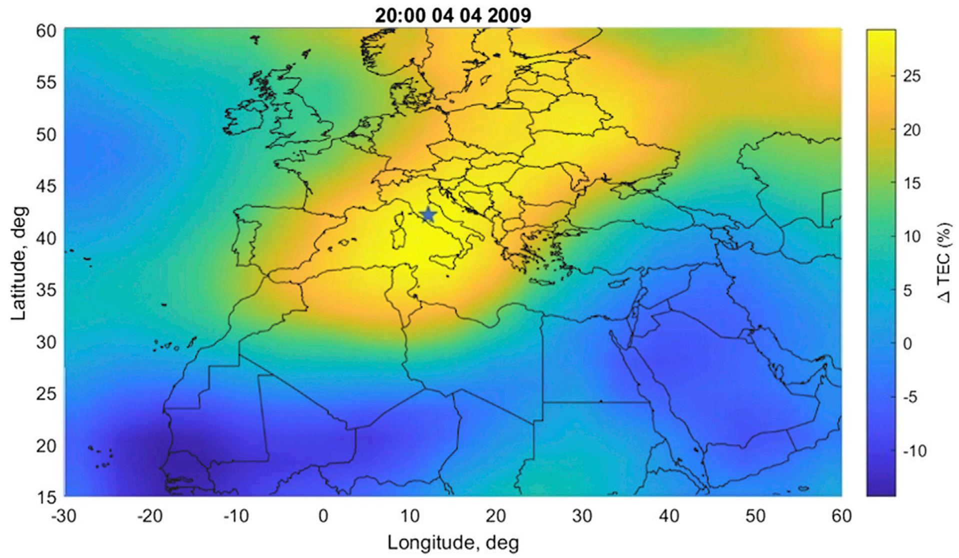

FIGURE 2 | Differential GIM map registered at 20:00 UT 03.04.2009, 2 days and 5.5 h before the L'Aquila earthquake.

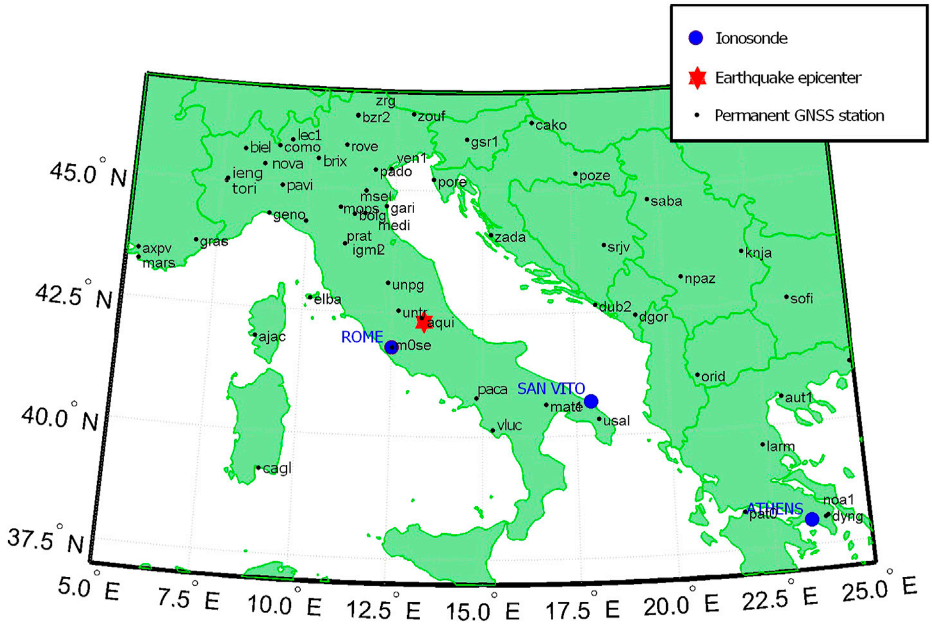

FIGURE 3 | Map of the L'Aquila earthquake case area with locations of ionosondes and all used permanent GNSS stations (in a single-station VTEC studies as well as differential TEC map generation).

critical frequency foF2 for selected pairs of ionosondes. Ionosondes selected for the L'Aquila earthquake case study as well as all used GNSS permanent stations are presented on **Figure 3**.

One more proof that the observed effect is connected with the earthquake preparation is the fact, that for two pairs (Rome-Athens and Rome-San Vito) when the connecting line passes over the earthquake preparation zone, we observe the drop of the cross-correlation coefficient, while for the pair San Vito-Athens, where connecting line is outside the earthquake preparation zone, the drop of cross-correlation coefficient is absent (Tsolis and Xenos, 2010), (**Figure 4**).

The similar picture we obtain for the cross-correlation coefficient calculated for the three pairs of the GNSS receivers' records (**Figure 5**) (Pulinets and Ouzounov, 2018). The calculation was carried out using data from the aqui (Aquila;

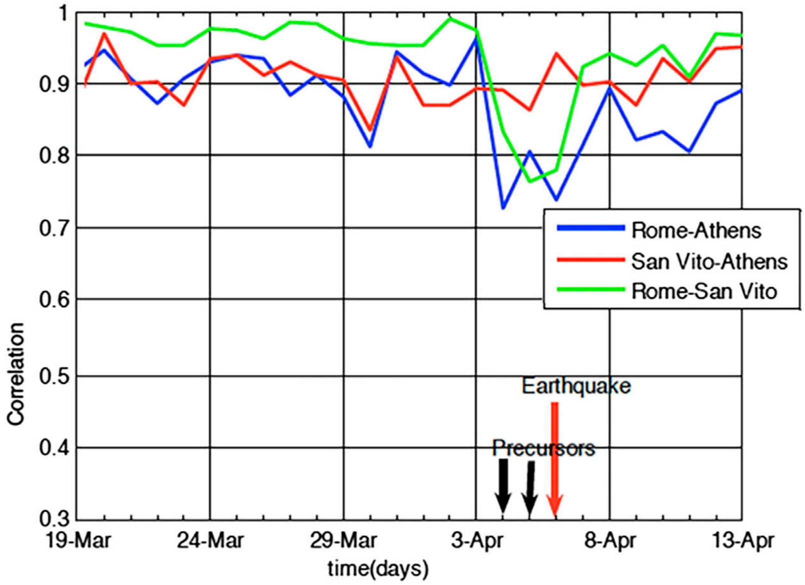

FIGURE 4 | Cross-correlation coefficient for three pairs of ionosondes, March-April 2009 (Tsolis and Xenos, 2010), modified.

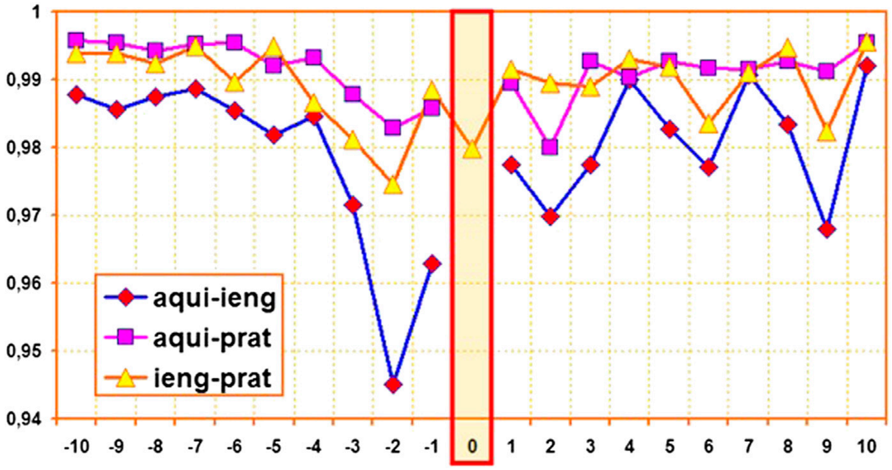

FIGURE 5 | Cross-correlation coefficient for three pairs of GPS receivers around the time of L'Aquila earthquake. Time in days around the time of L'Aquila earthquake.

aqui (42.368 N, 13.35 E)), ieng (Turin; ieng (45.015 N, 7.639 E)) and prat (Prato; prat (43.886 N, 11.099 E)) receivers. All these receivers were located inside the earthquake preparation zone, the ieng receiver being the farthest from the epicenter. Nevertheless, the reaction of the ionosphere to the earthquake preparation process is seen quite clearly—two days before the earthquake, a significant decrease in the cross-correlation coefficient occurs. The most significant drop in the coefficient is observed between the daily values of the receiver closest to the epicenter and the one farthest from it.

It should be noted that the magnitude of the cross-correlation coefficient drop for GNSS receivers is smaller than for ionosondes what means that the ground based vertical sounding is more sensitive for the correlation analysis.

If the cross-correlation coefficient gives idea on the difference of the seismo-ionospheric effect connected with the distance from epicenter, local spatial scintillation index (LSSI) reflects the variability of the ionosphere within the earthquake preparation zone (Pulinets et al., 2007a).

LSSI demonstrates the scatter of the readings of the GNSS receivers due to mosaic character of gas sources emanating from the system of active faults, its intensity increases as the earthquake approaches (Mareev et al., 2002). The sporadically distributed over the earthquake preparation zone patches of gas emission

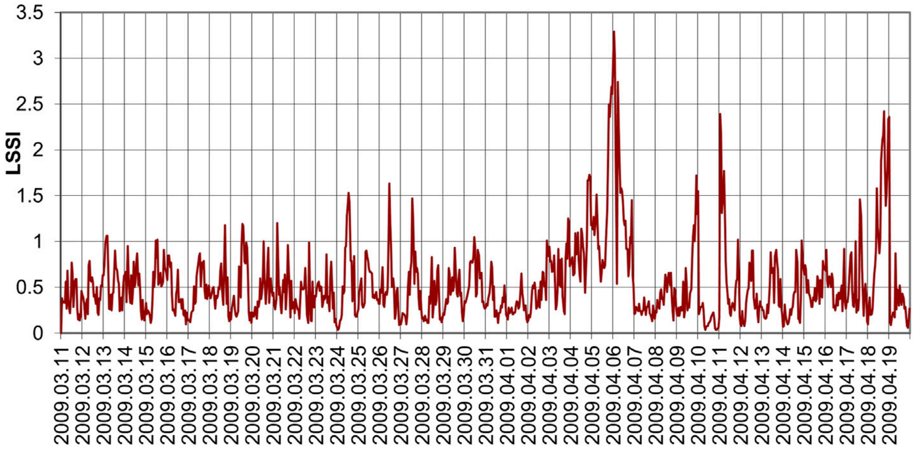

FIGURE 6 | Hourly averaged LSSI around the time of L'Aquila earthquake.

concentrated mainly around the active parts of tectonic faults provide the local ionization of the near ground layer of atmosphere changing its electric conductivity. These variations are transported by the Global Electric Circuit to the ionosphere and create the effect of spatial scintillation of TEC over the area. Its distribution before the Hector Mine earthquake is shown in (Pulinets and Ouzounov, 2018; **Figure 4**). The local spatial scintillation index of variability was introduced as the difference between the maximal and minimum values of TEC for every given moment for all the stations under study within the area of interest. The hourly averaged variation of the LSSI index around the time of L'Aquila earthquake is shown in **Figure 6**.

Nevertheless, still somebody may demonstrate the doubts, why some variations we associate with the earthquake preparation, and other–with geomagnetic disturbances. In this moment we again should turn to the physical mechanism, which implies that the pre-seismic variations are generated during the nighttime (behind the solar terminator) while the anomalies associated with geomagnetic disturbances are present round the clock and their appearance is connected with the time of geomagnetic disturbance onset (Pulinets and Davidenko, 2018). To notice this difference, we use the special presentation of ionospheric variations called "precursor mask". Let us look at **Figure 7** where from top to bottom are presented the variations of GNSS TEC in percentage for GNSS receiver installed at L'Aquila, variations of the critical frequency foF2 from the Rome ionosonde (also in percentage), and variations of the Global equatorial geomagnetic index Dst also in the 2D colored format similarly to the precursors mask, and then as usual time series graph. The variations of GNSS TEC and Dst presented in the form of mask where the horizontal axis is the day of the year (DOY), vertical axis is the universal Time (UT), and by color scale we demonstrate variations of the parameter under consideration.

The periods of small geomagnetic disturbances (first one -31 nT, and other two near -25 nT) are marked at all four plots as black rectangles. Looking at the plots within these rectangles we can mark some effects both in GPS TEC variations and in variations of the critical frequency. They are manifested as vertical blue and red columns (negative and positive deviations). Their appearance depends on the time of geomagnetic disturbance onset, so they are generated both during the day and nighttime. Simultaneously we observe in the first two plots the positive variations which appear only during nighttime, especially few days before the L'Aquila earthquake and one day after (90–97 DOY). Their duration (in local time) is larger for GPS TEC, but the period of their appearance in days before the mainshock is larger in the plot of foF2. Actually, we do not see the emphasized period in post-sunset variations in the ionosonde data, what implies that we possibly observe the pre-reversed enhancement effect (PRE). The only reservation remains that the PRE is essentially the low latitude effect while L'Aquila belongs to the middle latitudes (Eccles et al., 2015).

The most interesting phenomenon, which is obvious at the ΔfoF2 plot is that the pre-sunrize and post sunset anomalies are exactly following the solar terminator. We are in period of equinox when the day length is fast increasing and in the beginning of period of observation (DOY 65–six of March) the time of sunrise is 6:33, and sunset 18:02, and at the end of observation period 17 April the time of sunrise is 6:21, and sunset 19:50. The anomaly in the morning stops earlier than terminator time and in the evening starts earlier than terminator time because of the fact that at altitude of the ionosphere terminator appears earlier than at the ground surface for which we have data for sunrise and sunset time. Lines of terminator time are shown at the ΔfoF2 plot by dashed blue lines. Summarizing: the presented results follow the physical mechanism (Pulinets and Davidenko, 2014; 2018), and ionospheric precursors could be registered by different techniques of the ionosphere monitoring. Using the techniques of data processing (local and GIM mapping, cross-correlation analysis, LSSI index and precursors mask), we were able to uniquely identify the precursors, to find the position of the epicenter of impended earthquakes, and to estimate the time.

To estimate the magnitude, we should have the good estimation of the ionospheric anomaly size which is the same order of magnitude as the size of earthquake preparation zone

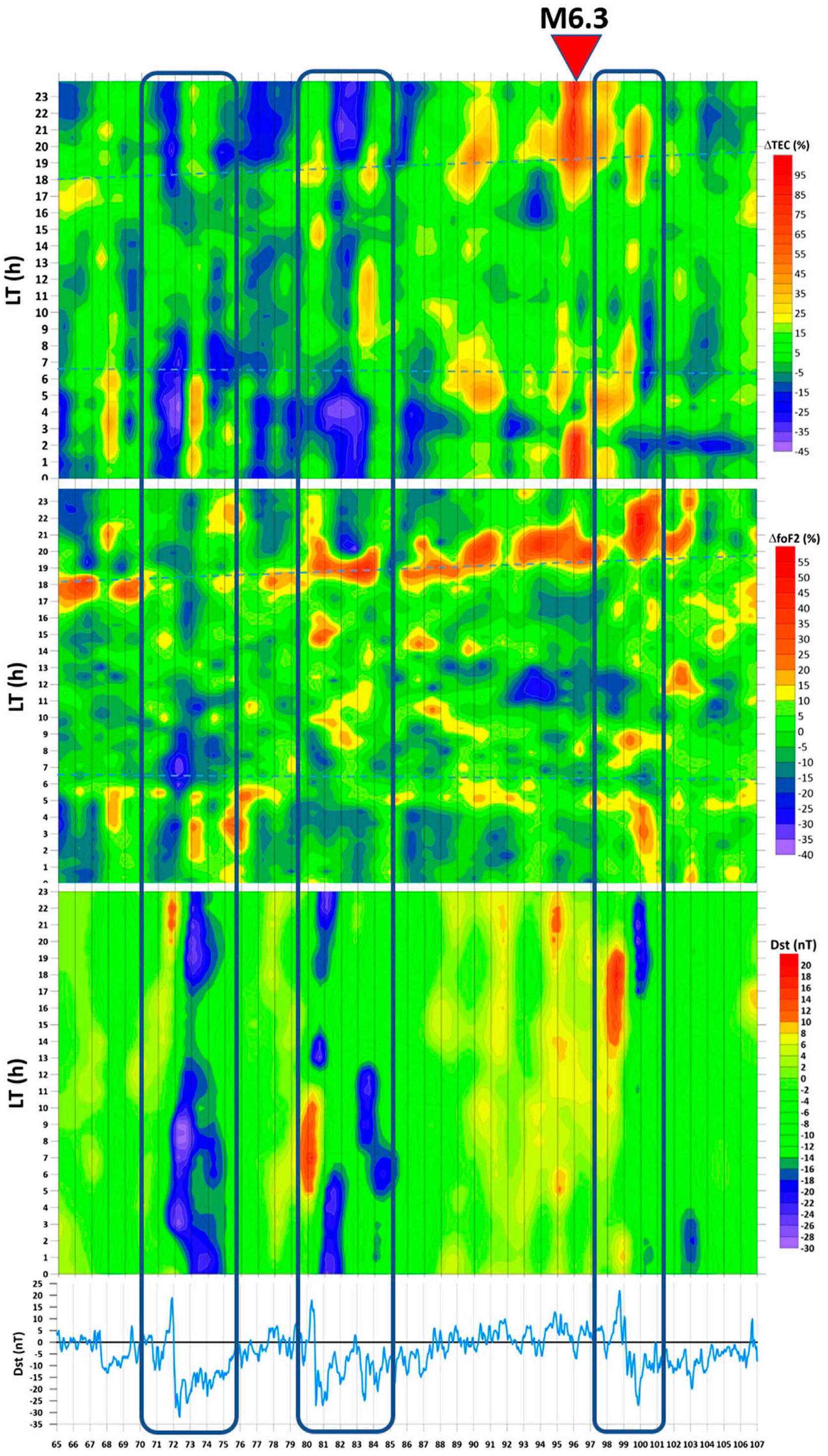

FIGURE 7 | From top to bottom: ΔTEC, ΔfoF2, Dst (mask), Dst (time series). In the upper three panels the vertical axis is the Local time, For all panels the horizontal axis is day of the year (DOY). The deviation of the TEC and foF2 in upper two panels is coded by colors and expressed in percentage deviation from the running 15 days median. Dst in the color panel is expressed by colors in nT, In the bottom picture the dst values are shown in the vertical axis.

(Dobrovolsky et al., 1979). Unfortunately, the maps presented in **Figures 1**, **2** strongly depend on the positions of GPS receivers, quality of interpolation and modeling of GNSS GIM, as well as from the network density and configuration. Additional difficulties for mapping appear if earthquake epicenter is in the ocean. In these circumstances, we should have the direct

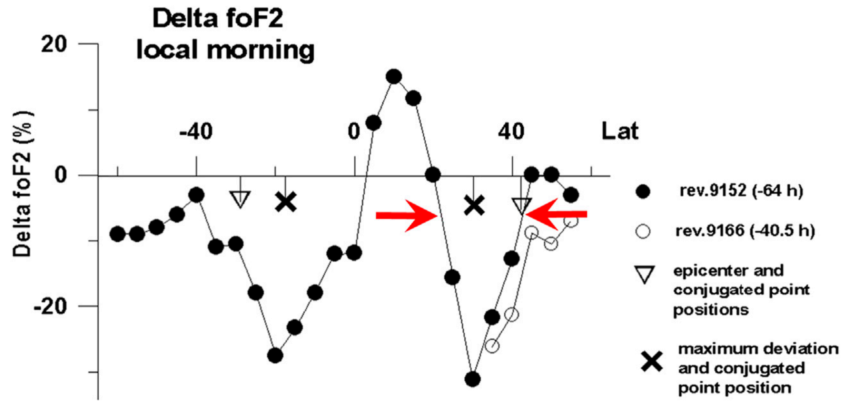

FIGURE 8 | Deviation of the critical frequency foF2 along the orbit of Intercosmos-19 satellite.

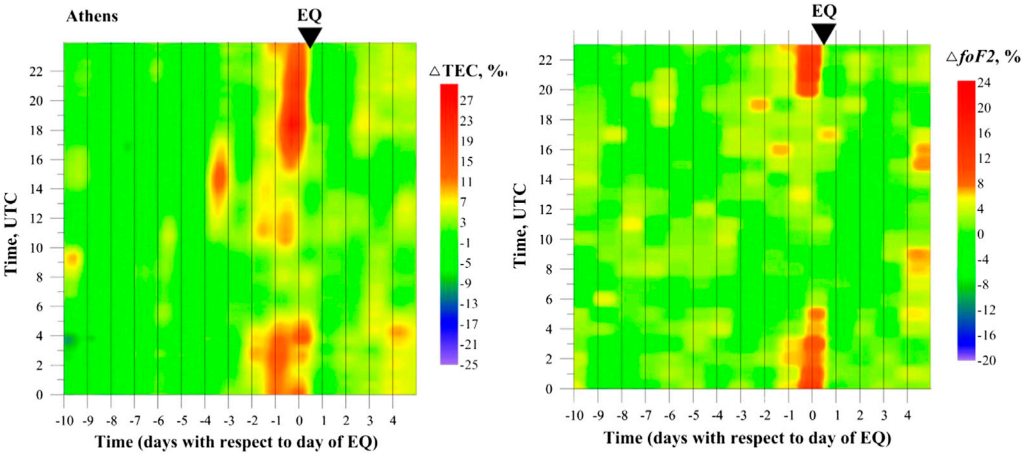

FIGURE 9 | Left panel–the precursor mask derived from the data of GPS TEC receiver in Rome; right panel–the precursors mask for critical frequency foF2 deviations derived from the data of the Rome ionospheric station of vertical sounding (Davidenko and Pulinets, 2019).

measurements of the ionospheric anomaly dimensions that could be provided only by topside sounding as it was done for Irpinia M6.9 earthquake on November 23, 1980 in Italy (Pulinets et al., 2007b). This technology is demonstrated in **Figure 8** presenting the variations of critical frequency foF2 deviation from undisturbed state while satellite passing over the seismo-ionospheric anomaly. Estimating anomaly radius as 900 km, the magnitude M would be M = [log (900)]/0.43 = 6.9.

DISCUSSION

The presented examples reveal the variety of techniques for the reliable identification of the ionospheric precursors, only for one event–the L'Aquila earthquake. Then a natural question arise: how stable these characteristic features of the ionospheric precursors are. Whether we will observe similar results worldwide, and not only in quiet geomagnetic conditions, but also in the disturbed cases?

The statistical study of the precursor mask stability was provided for Greece and Italy areas (Davidenko and Pulinets, 2019). The left panel of **Figure 9** shows an averaged mask for earthquakes with M ≥ 6 in Greece for period 2006–2018, and the right panel–the mask for the critical frequency variation for the same interval of time. GNSS TEC data were collected from receiver located in Athens, while vertical sounding data from two ionosondes situated in Athens and Sofia.

As we observed in **Figure 7** the GNSS TEC anomalies last longer (within the day) than the critical frequency ones.

The situation in Italy is more complex and probably due to the difference in geological structure of the Apennines peninsula (Meletti et al., 2000). We observe a similar precursor mask structure for the northern and central Italy, and opposite sign of the pre-seismic anomaly (negative deviations) for the southern Italy except Sicily. This issue is the subject of future research. For a clarity and consistence of the discussion we demonstrate here in **Figure 10** the GNSS TEC (left panel) and critical frequency (right panel) masks for the northern part of Italy. Taking into account

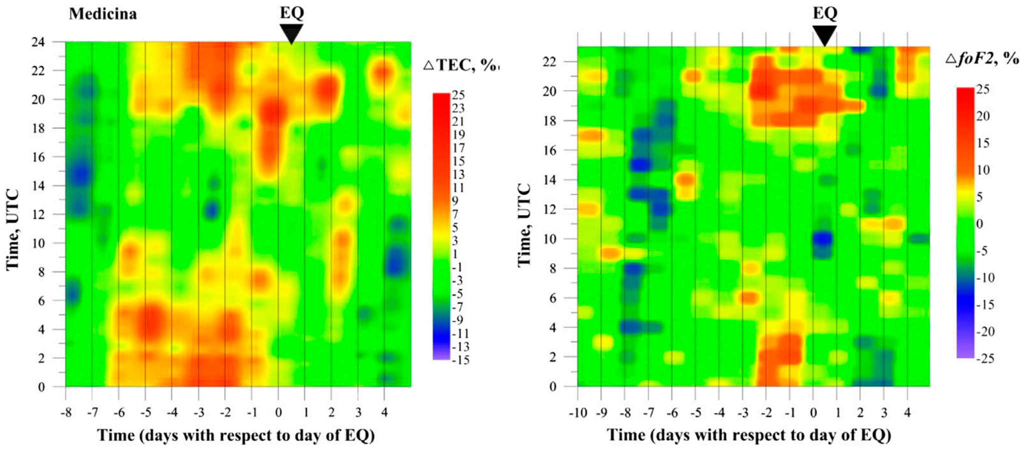

FIGURE 10 | Left panel–the precursor mask derived from the data of GPS TEC receiver in Medicine; right panel–the precursors mask for critical frequency foF2 deviations derived from the data of the Rome ionospheric station of vertical sounding (Davidenko and Pulinets, 2019).

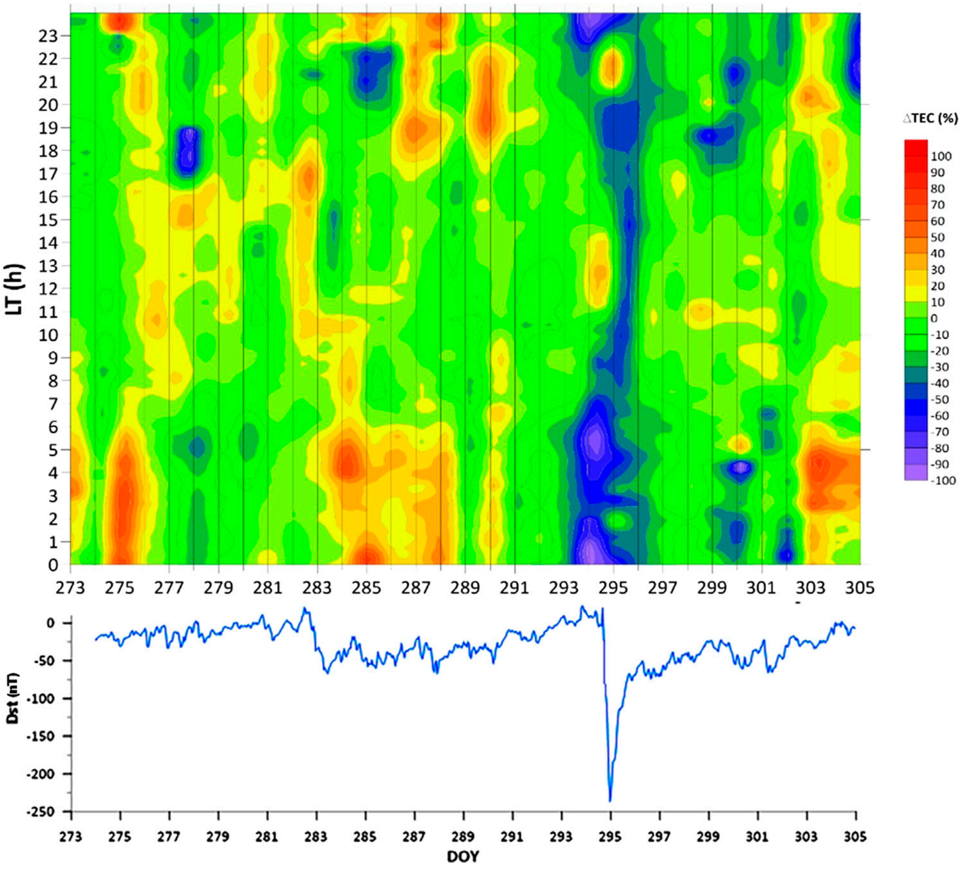

FIGURE 11 | Upper panel GPS TEC mask for *gol2* GPS receiver (35.4 N; 243.1 W), Hector Mine earthquake 289 DOY, lower panel global equatorial geomagnetic index Dst.

that the seismic activity in Italy is generally lower than in Greece, we set the lower magnitude threshold –5.4. On the other hand, the period of ionosphere data availability is even longer than in Greece: 1962–2017 for the Rome ionosonde (used for earthquakes in the range of 300 km in northern direction from Rome) and 1997–2017 for Medicine GNSS receiver (used for

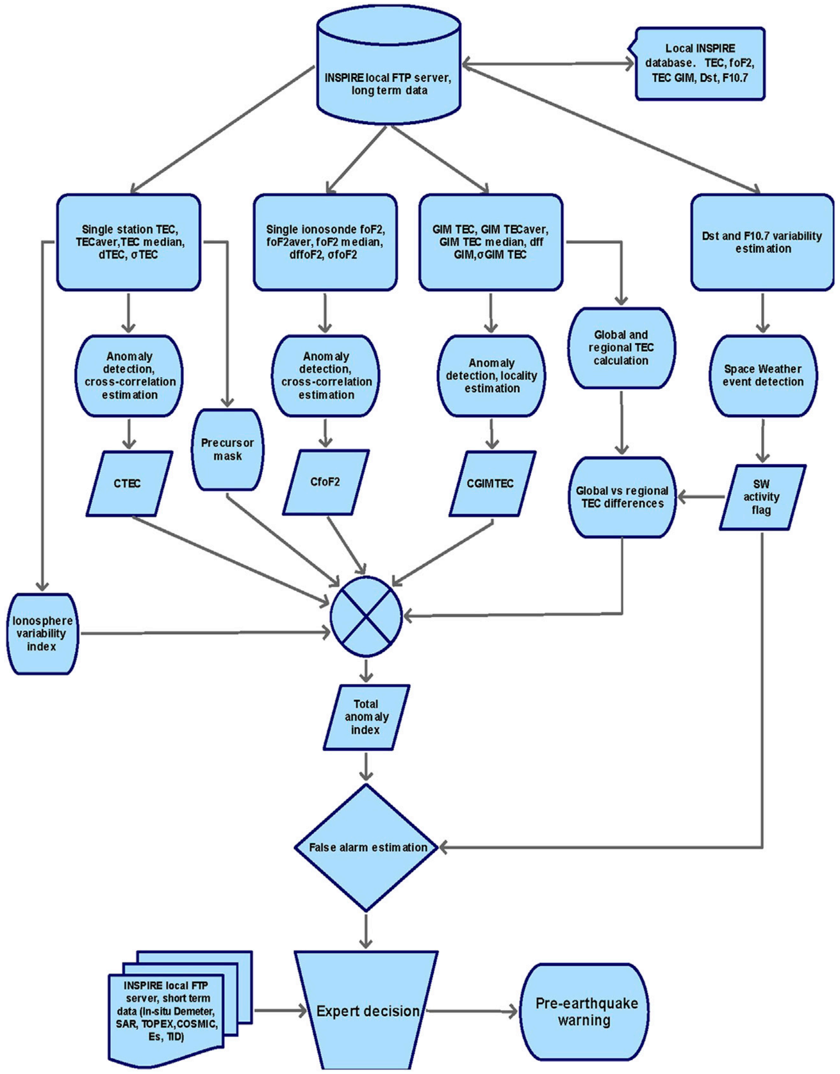

FIGURE 12 | The algorithm based on the sequence of operations in the corresponded branches of the data processing.

earthquakes with M ≥ 6 in northern Italy). One can clearly see the high similarity the GNSS TEC and critical frequency foF2 masks regardless the different intervals of integration what confirms the high stability of the observed effect for multi-year observations.

In Italy–similarly to the L'Aquila case–precursory structure is observed during several consecutive days whereas in Greece precursor is observed only during one day.

It is interesting to note that precursors identification using the mask technology is possible not only in quiet geomagnetic conditions with small disturbances but also during strong geomagnetic storms and high geomagnetic activity. In **Figure 11** one can see the precursor mask for the case of Hector Mine M7.1 earthquake on October 16, 1999 in California.

The nighttime positive anomalies are clearly visible from one to four days before the Hector mine earthquake, as well as a thick blue negative bar during strong geomagnetic storm with −250 nT peak value.

Having the technology of ionospheric precursor identification, we propose the system for automatic data processing, interpretation, precursors identification and possible earthquake forecast.

Implementation

The developed algorithm presented in **Figure 12** shows the sequence of operations in the corresponded branches of the data processing. The implementation of these operations leads to detection of the anomaly which corresponds with seismo-ionospheric coupling mechanism triggered during an earthquake's preparation period.

In order to give comprehensive prediction, specifications the multi-parameter and systematic approach of different databases described above can be established.

The databases involve a range of ionospheric, Space Weather and some additional observations and products. The ionospheric parameters database includes ionosonde measurements of the critical frequency foF2, Global VTEC maps (GIMs) and local VTEC values calculated for each station. The Space Weather part includes series of solar and geomagnetic activity parameters–F10.7 solar flux and Dst indices. The additional database include short-time observations performed with a range of different instruments (RO electron density profiles from COSMIC observations, *in-situ* observations from Demeter mission, altimeter VTEC observations, InSAR co-seismic displacement data).

The further processing is divided in separate branches: the local TEC anomaly processing, the local foF2 anomaly processing, the global TEC processing, and Space Weather processing.

The local TEC processor calculates the TEC anomaly and TEC variability index based on the VTED values observed with the selected stations. This branch incorporates also building the TEC precursor mask. The mask is a matrix A_{ij}, where i is the TEC sample in a day and j corresponds with subsequent days preceding the earthquake. The precursor pattern matrix created using statistical data processing and image recognizing techniques (on the base of a-priori geological information/maps) in the given region is compared with the current measurements.

The foF2 processor branch, similarly to the local TEC branch, calculates the foF2 anomaly and variation index, by calculating the running average of the parameter, differential foF2 and cross-correlation between two sets of the diurnal variation (same as) of the critical frequency values from two spaced ionosondes.

The global TEC processing branch calculates the 2D TEC anomaly as well as the TEC anomaly location together with the Global Electron Content (GEC) and Regional Electron Content (REC).

The Space Weather branch processes the F10.7 and Dst indices series to obtain disturbances flags, by a proper leveling and generating flags, when index exceeds the threshold.

In the next step, the synergic analyzer collects previously obtained parameters together with other, non-ionospheric seismic information. The synergic analyzer checks the temporal sequence and spatio-temporal synchronization of the detected anomalies and compares to the model pattern. Also very important is the step of false alarm detection, where the false alarm flag against the total anomaly index is provided.

The final step involves the experts' decision, during which the seismologists and geophysicists examines the detected anomalies of ionospheric and non-ionospheric origin, their spatial and temporal characteristics. Also the role of an expert is to make a decision about the pre-seismic warning.

Earthquake preparation process is a complex open system including inter-geosphere interactions; therefore, we should control all the system at different levels, starting from underground through atmosphere up to the ionosphere and magnetosphere. One of the main important topics is the adequate real time data acquisition with time delay no more than 1 h including also validation, authorization and unification data derived from different instruments and databases. In addition, the detailed calibration procedure for determination of set of meridian environmental condition for selected territories of seismoactive zone can be established.

Indication of New Experimental Investigations and Observations

The global and local networks of ground-based GNSS-receivers give an unique chance for monitoring of the near Earth's environment conditions in a global scale. Nowadays more than 5,000 permanent ground-based GNSS stations provide measurements to the community. Further evolution relates with increasement of the number of GNSS stations and modernization of receivers with ability to track signals from various systems. The development of the European Galileo system, the Russian GLONASS and the Chinese BeiDou/COMPASS system will improve the monitoring and diagnostics of the seismic origin TEC perturbations. Furthermore, microwave and HF radars diagnostics scatterometers, altimeters for topography, GNSS satellite receivers for reflectometry, and imaging radars SAR together with space plasma diagnostics *in situ* can be an excellent set for such new diagnostics campaign.

The recently launched Jason-3 mission continues the core satellite altimetry measurements. Its payload consists of the same core instruments as Jason-2: a Poseidon class Ku/C-band radar altimeter to provide the primary ranging measurement, a nadir-looking three frequency (18.7, 23.8, and 34.0 GHz) microwave radiometer (as flown on Jason-2), along with a POD (Precise Orbit Determination) package consisting of a GPS (Global Positioning System) receiver, DORIS (Doppler Orbitography and Radiopositioning Integrated by Satellite), and a LRA (Laser Retroreflector Array), as flown on prior Jason series missions. The satellite is placed on a circular non Sun synchronous orbit with altitude of 1,336 km and inclination 66.038°.

To support the ionospheric precursors monitoring the additional parameters provided by satellite systems could be useful, namely, the mechanical deformations and thermal pre-earthquake anomalies. The fast developing SENTINEL program gives the perfect opportunities for these additions. The SENTINEL-1 Satellite Constellation consist of two satellites: SENTINEL-1A and SENTINEL-1B launched in 2014 and 2016 respectively. Both of them have a single C-band synthetic-aperture radar (C-SAR) which is able to provide the high resolution SAR interferometry to detect land deformation before and after earthquakes. The SENTINEL-3 satellite constellation: SENTINEL-3A and SENTINAL-3B were launched in 2006 and 2018 respectively have SLSTR (Sea and Land Surface Temperature Radiometer) to measure the surface ocean and land temperature what will permit to detect the thermal anomalies before earthquakes, and SRAL (Synthetic Aperture Radar Altimeter) also could be used for SAR interferometry. The new ESA's Swarm mission was launched on November 2013. The mission is a constellation of the three identical satellites Alpha, Bravo and Charlie. Two of them fly in a tandem with one degree separation at the altitude of 460 km, the third one is placed higher, at 510 km. The latter allows comparison of measurements from identical instruments at different altitudes and in the different longitudinal sectors. The satellite payload has Langmuir Probe instrument for the *in situ* plasma density measurements and GPS receiver for POD measurements. Near polar orbits are required to provide a global coverage—multi-point measurements at global and regional scales, as required for spatial and temporal sampling of the fields, imply the deployment of a constellation. The main Swarm instrument is the Vector Field Magnetometer. It performs high-precision measurements of the magnitude and direction of the magnetic field. Together with the Absolute Scalar Magnetometer it is a very sensitive instrument to study tiny magnetic signatures from ground. Also the ESA-funded project SAFE (SwArm For Earthquake study) devoted to the pre-seismic effects and based on the Swarm magnetometric measurement data is worth mentioning. This project is coordinated by the INGV (Italy). The investigations are based on the data collected from satellites and from ground-based instruments, the phase preceding the great earthquakes with the aim to identify any electromagnetic signal from space.

The topside ionosphere sounding based on LEO nano satellite cluster located in different local time sectors, as well as ground based ionosonde network, can give an opportunity for detailed diagnostics of morphology and dynamic of large and small scales ionosphere structures. New 3D measurements of the electric and magnetic fields particles diagnostics located on LEO nano satellites should bring the additional improvement of the atmosphere-ionosphere-magnetosphere coupling processes monitoring.

Finally, the radio-occultation inversion techniques for ionospheric tomography, already improved in the last years, are able to provide worldwide distributed electron density profiles over the land and seas in a very efficient way. The coverage is still increasing with the launch of COSMIC constellation, and with the already launched COSMIC-2 constellation and Chinese Feng Yun 3C satellite constellations.

The new follow-on mission to the FORMOSAT-3/COSMIC is the FORMOSAT-7/COSMIC-2. It is a constellation of six remote sensing microsatellites able to provide new data for ionosphere research. The goal is to collect a large amount of atmospheric and ionospheric data. The new constellation provides improved performance and a significant increase in number of measurements. Formosat-7 established operational Mission of near real-numerical weather prediction that collects few thousands of the electron density profiles per day. The satellite RO receivers have GPS, GALILEO and GLONASS tracking capability. COSMIC-2 also has RF Beacon transmitters and Velocity, Ion Density, and Irregularities (VIDI) instruments—plasma probes. The launch of six satellites of the low inclination constellation took place on June 25, 2019. The constellation of six satellites is planned to reach their operational orbits at 24° inclination, which will enhance observations in the equatorial region, on first quarter of 2021.

So, it is possible to conclude that a unique opportunity to study the seismo-ionospheric effects with an unprecedentable number of ground and space base measurements, will exist in the near future.

Obviously, we are living now in the epoch when the amount of the multi-instrumental ground- and space-based measurements is extremely high and it increases progressively. But only specific earthquake-oriented satellite mission can bring a clue on how to match all these new and wide datasets to a consitent interpretation of the Lithosphere-Atmosphere-Ionosphere Coupled System.

Indication of the Possible New Services Based on the Proposed

The technology of ionosphere monitoring described in the previous chapters, combined with the ground support and other (not ionospheric) precursors monitoring, are able to provide the reliable information on the main parameters necessary for the short-term earthquake forecast: i.e., epicenter position, magnitude and time of the impending seismic event. The service of the short-term forecast could be proposed in conditions that the corresponding infrastructure will be created for the continuous real monitoring of indicated parameters of ionosphere and magnetosphere and described in terms of atmospheric parameters.

As a limited option for some areas with extended network of ground-based GNSS receivers such as Japan, California, Europe such service can be proposed now, but again this service should be organized through a proper infrastructure of data-centers and analysis centers with corresponding connection with decision makers in governmental municipal institutions.

Special service of the short-term warning can be created for the users of mobile devices in the earthquake-prone areas.

Taking into account that the model has a worldwide scope in terms of the atmosphere-ionosphere coupling, the other natural and anthropogenic hazards could be monitored using the same technology–like the dust and sand storms, hurricanes, volcano eruptions and the ash clouds tracking, radioactive pollution (for example, emergencies at the atomic power plants, such as Three-Mile Island, Chernobyl or Fukushima). Also the nuclear weapon tests could be monitored. The both tests in the Northern Korea were registered in the ionosphere using the GIM maps.

The specialized space mission should be initiated to make the proposed project live, real, and working in real time.

DATA AVAILABILITY STATEMENT

The datasets presented in this article are not readily available because The dataset is based of LAIC model by Sergey Pulinets. Requests to access the datasets should be directed to pulse1549@gmail.com.

AUTHOR CONTRIBUTIONS

SP, AK, IZ, and IC contributed the methodology of the study; SP, AK, MH-P, IC, IZ, DD, HR, KK, PF, AF, AR, and PB contributed in the data acquisition and dataset building; IC, IZ, DD, KK, PF, LB. AF, AR, and PB contributed in the data analysis; SP, AK, MH-P, IC, IZ, and KK contributed in the manuscript preparation, AK and SM were responsible for the project supervising.

FUNDING

In years 2014–2016 works were supported by the ESA Project “INSPIRE, ionosphere Sounding for Pre-seismic anomalies Identification Research (INSPIRE)” nr 4000,111,456/14/NL/MV. The work is supported by the National Center for Research and Development, Poland, through Grant ARTEMIS (decision no. DWM/PL-CHN/97/2019, WPC1/ARTEMIS/2019); The authors thank also the Ministry of Science and Higher Education (MSHE), Poland for granting funds for the Polish contribution to the International LOFAR Telescope “(MSHE decision no. DIR/WK/2016/2017/05–1)” and for maintenance of the LOFAR PL-612 Baldy (MSHE decisions: no. 59/E-383/SPUB/SP/2019.1). This work is supported by the National Science Centre, Poland, through Grants 2017/25/B/ST10/00479 and 2017/27/B/ST10/02190.

ACKNOWLEDGMENTS

The work was based on the data provided by the IGS, EPN, UNAVCO, GIRO, DEMETER, FORMOSAT-3/COMIC-7 and SWARM services.

REFERENCES

Blaunstein, N., and Hayakawa, M. (2009). Short-term ionospheric precursors of earthquakes using vertical and oblique ionosondes. *Phys. Chem. Earth, Parts A/B/C* 34, 496–507. doi:10.1016/j.pce.2008.07.002

Bogdanov, V. V., Kaisin, A. V., Pavlov, A. V., Polyukhova, A. L., and Meister, C.-V. (2017). Anomalous behavior of ionospheric parameters above the kamchatka peninsula before and during seismic activity. *Phys. Chem. Earth, Parts A/B/C* 98, 154–160. doi:10.1016/j.pce.2016.04.002

Chang, F. Y., Liu, J. Y., Chang, L. C., Lin, C.-H., and Chen, C.-H. (2015). Three-dimensional electron density along the WSA and MSNA latitudes probed by FORMOSAT-3/COSMIC coupling of the high and mid latitude ionosphere and its relation to geospace dynamics space science. *Earth, Planets and Space* 67 (1). doi:10.1186/s40623-015-0326-8

Datchenko, E. A., Ulomov, V. I., and Chernyakova, C. P. (1972). Electron density anomalies as the possible precursor of tashkent earthquake. *Dokl. Uzbek. Acad. Sci.* 12, 30–32.

Dautermann, T., Calais, E., Haase, J., and Garrison, J. (2007). Investigation of ionospheric electron content variations before earthquakes in southern California, 2003-2004. *J. Geophys. Res.* 112, B02106. doi:10.1029/2006JB00444710.1029/2006jb004447

Davidenko, D. V., and Pulinets, S. A. (2019). Deterministic variability of the ionosphere on the eve of strong (M ≥ 6) earthquakes in the regions of Greece and Italy according to long-term measurements data. *Geomagn. Aeron.* 59 (4), 493–508. doi:10.1134/S001679321904008X

Davies, K., and Baker, D. M. (1965). Ionospheric effects observed around the time of the Alaskan earthquake of March 28, 1964. *J. Geophys. Res.* 70, 2251–2253. doi:10.1029/jz070i009p02251

Dobrovolsky, I. P., Zubkov, S. I., and Miachkin, V. I. (1979). Estimation of the size of earthquake preparation zones. *Pageoph* 117, 1025–1044. doi:10.1007/bf00876083

Eccles, J. V., St. Maurice, J. P., and Schunk, R. W. (2015). Mechanisms underlying the prereversal enhancement of the vertical plasma drift in the low-latitude ionosphere. *J. Geophys. Res. Space Phys.* 120, 4950–4970. doi:10.1002/2014JA020664

Hirooka, S., Hattori, K., Nishihashi, M., and Takeda, T. (2011). Neural network based tomographic approach to detect earthquake-related ionospheric anomalies. *Nat. Hazards Earth Syst. Sci.* 11, 2341–2353. doi:10.5194/nhess-11-2341-2011

Kon, S., Nishihashi, M., and Hattori, K. (2011). Ionospheric anomalies possibly associated with M⩾6.0 earthquakes in the Japan area during 1998-2010: case studies and statistical study. *J. Asian Earth Sci.* 41 (4), 410–420. doi:10.1016/j.jseaes.2010.10.005

Krankowski, A., Zakharenkova, I. E., and Shagimuratov, I. I. (2006). Response of the ionosphere to the baltic sea earthquake of 21 september 2004. *Acta Geophys.* 54, 90–101. doi:10.2478/s11600-006-0008-9

Li, M., and Parrot, M. (2013). Statistical analysis of an ionospheric parameter as a base for earthquake prediction. *J. Geophys. Res. Space Phys.* 118 (A6), 3731–3739. doi:10.1002/jgra.50313

Liu, J.-Y., and Chao, C.-K. (2017). An observing system simulation experiment for FORMOSAT-5/AIP detecting seismo-ionospheric precursors. *Terr. Atmos. Ocean. Sci.* 28, 117–127. doi:10.3319/TAO.2016.07.18.01(EOF5)

Liu, J. Y., Chen, Y. I., Chen, C. H., Liu, C. Y., Chen, C. Y., Nishihashi, M., et al. (2009). Seismoionospheric GPS total electron content anomalies observed before the 12 May 2008Mw7.9 Wenchuan earthquake. *J. Geophys. Res.* 114 (A04320). doi:10.1029/2008JA013698

Liu, J. Y., Chen, Y. I., Chuo, Y. J., and Chen, C. S. (2006). A statistical investigation of preearthquake ionospheric anomaly. *J. Geophys. Res.* 111 (A05304). doi:10.1029/2005JA011333

Liu, J. Y., Chuo, Y. J., Shan, S. J., Tsai, Y. B., Chen, Y. I., Pulinets, S. A., et al. (2004). Pre-earthquake ionospheric anomalies registered by continuous GPS TEC measurements. *Ann. Geophys.* 22 (5), 1585–1593. doi:10.5194/angeo-22-1585-2004

Liu, J.-Y., Hattori, K., and Chen, Y. (2018). “Application of total electron content derived from the Global Navigation Satellite System for detecting earthquake precursors,” in *In pre-earthquake processes: a multidisciplinary approach to earthquake prediction studies (geophysical monograph 234)*. Editors D. Ouzounov, S. Pulinets, K. Hattori, and P. Taylor (Washington, DC: American Geophysical UnionJohn Wiley and Sons, Inc.), 305–318.

Mareev, E. A., Iudin, D. I., and Molchanov, O. A. (2002). “Mosaic source of internal gravity waves associated with seismic activity,” in *In seismo-electromagnetics: lithosphere-atmosphere-ionosphere coupling*. Editors M. Hayakawa and O. A. Molchanov (Tokyo, Japan: TERRAPUB), 335–342.

Meletti, C., Patacca, E., and Scandone, P. (2000). Construction of a seismotectonic model: the case of Italy. *Pure Appl. Geophys.* 157, 11–35. doi:10.1007/pl00001089

Ouzounov, D., Pulinets, S., Hattori, K., and Taylor, P. (2018). *Pre-earthquake processes: a multidisciplinary approach to earthquake prediction studies*. in *Geophysical monograph series, No 234*. Hoboken, NJ: American Geophysical UnionAGU/Wiley. doi:10.1002/9781119156949

Parrot, M., and Li, M. (2018). “Statistical analysis of the ionospheric density recorded by DEMETER during seismic activity,” in *In pre-earthquake processes: a multidisciplinary approach to earthquake prediction studies (geophysical monograph 234)*. Editors D. Ouzounov, S. Pulinets, K. Hattori, and P. Taylor (Washington, DC: American Geophysical UnionJohn Wiley and Sons, Inc.), 319–330.

Pulinets, S. A., Biagi, P., Tramutoli, V., Legen’ka, A. D., and Depuev, V. K. (2007). Irpinia earthquake 23 November 1980 – lesson from Nature revealed by joint data analysis. *Ann. Geophys.* 50 (1), 61–78. doi:10.4401/ag-3087

Pulinets, S. A., Bondur, V. G., Tsidilina, M. N., and Gaponova, M. V. (2010). Verification of the concept of seismoionospheric coupling under quiet heliogeomagnetic conditions, using the Wenchuan (China) earthquake of May 12, 2008, as an example. *Geomagn. Aeron.* 50, 231–242. doi:10.1134/s0016793210020118

Pulinets, S. A., Davidenko, D. V., and Budnikov, P. A. (2021). Cognitive recognition of the ionospheric precursors of earthquakes. *Geomagnetism and Aeronomy* 61, 39–50. doi:10.4401/ag-3087

Pulinets, S. A., and Davidenko, D. V. (2018). The nocturnal positive ionospheric anomaly of electron density as a short-term earthquake precursor and the possible physical mechanism of its formation. *Geomagn. Aeron.* 58, 559–570. doi:10.1134/s0016793218040126

Pulinets, S. A., Gaivoronska, T. B., Leyva Contreras, A., and Ciraolo, L. (2004a). Correlation analysis technique revealing ionospheric precursors of earthquakes. *Nat. Hazards Earth Syst. Sci.* 4, 697–702. doi:10.5194/nhess-4-697-2004

Pulinets, S. A., Kotsarenko, A. N., Ciraolo, L., and Pulinets, I. A. (2007a). Special case of ionospheric day-to-day variability associated with earthquake preparation. *Adv. Space Res.* 39 (5), 970–977. doi:10.1016/j.asr.2006.04.032

Pulinets, S. A., Legen'ka, A. D., Gaivoronskaya, T. V., and Depuev, V. K. (2003). Main phenomenological features of ionospheric precursors of strong earthquakes. *J. Atmos. Solar-Terrestrial Phys.* 65, 1337–1347. doi:10.1016/j.jastp.2003.07.011

Pulinets, S. A., and Legen'ka, A. D. (2003). Spatial-temporal characteristics of large scale distributions of electron density observed in the ionospheric F-region before strong earthquakes. *Cosmic Res.* 41 (3), 221–230. doi:10.1023/a:1024046814173

Pulinets, S. A., Liu, J. Y., and Safronova, I. A. (2004). Interpretation of a statistical analysis of variations in the foF2 critical frequency before earthquakes based on data from Chung-Li ionospheric station (Taiwan). *Geomagnetism and Aeronomy* 44 (1), 102–106.

Pulinets, S. A., Ouzounov, D. P., Karelin, A. V., and Davidenko, D. V. (2015). Physical bases of the generation of short-term earthquake precursors: a complex model of ionization-induced geophysical processes in the lithosphere–atmosphere–ionosphere–magnetosphere system. *Geomagnetism and Aeronomy* 55 (4), 540–558. doi:10.1134/s0016793215040131

Pulinets, S. A., Romanov, A. A., Urlichich, Y. M., Romanov, A. A., Doda, L. N., and Ouzounov, D. (2009). The first results of the pilot project on complex diagnosing earthquake precursors on sakhalin. *Geomagn. Aeron.* 49 (1), 115–123. doi:10.1134/s0016793209010162

Pulinets, S. A. (1998). Strong earthquake prediction possibility with the help of topside sounding from satellites. *Adv. Space Res.* 21 (3), 455–458. doi:10.1016/s0273-1177(97)00880-6

Pulinets, S., and Boyarchuk, K. (2004). *Ionospheric precursors of earthquakes*. Mexico, Springer.

Pulinets, S., and Davidenko, D. (2014). Ionospheric precursors of earthquakes and global electric circuit. *Adv. Space Res.* 53, 709–723. doi:10.1016/j.asr.2013.12.035

Pulinets, S., Ouzounov, D., Karelin, A., and Davidenko, D. (2018). ""Lithosphere–Atmosphere–Ionosphere–Magnetosphere coupling – a concept for pre-earthquake signals generation," in *In pre-earthquake processes: a multidisciplinary approach to earthquake prediction studies (geophysical monograph 234).* Editors D. Ouzounov, S. Pulinets, K. Hattori, and P. Taylor (Washington, DCHoboken, NJ: American Geophysical UnionJohn Wiley and Sons, Inc.), 79–98.

Pulinets, S., and Ouzounov, D. (2018). The possibility of earthquake forecasting. *Learning from nature*. Bristol: IOP Publishing. doi:10.1088/978-0-7503-1248-6

Romanov, A. A., Romanov, A. A., Trusov, S. V., and Urlichich, Y. M. (2013). *Satellite tomography of the ionosphere*. Moscow: Fizmatlit publ

Rozhnoi, A., Solovieva, M., Molchanov, O., Schwingenschuh, K., Boudjada, M., Biagi, P. F., et al. (2009). Anomalies in VLF radio signals prior the Abruzzo earthquake (M=6.3) on 6 April 2009. *Nat. Hazards Earth Syst. Sci.* 9, 1727–1732. doi:10.5194/nhess-9-1727-2009

Thomas, J. N., Love, J. J., Komjathy, A., Verkhoglyadova, O. P., Butala, M., and Rivera, N. (2012). On the reported ionospheric precursor of the 1999 hector mine, California earthquake. *Geophys. Res. Lett.* 39, L06302. doi:10.1029/2012GL051022

Tsolis, G. S., and Xenos, T. D. (2010). A qualitative study of the seismo-ionospheric precursors prior to the 6 April 2009 earthquake in L'Aquila, Italy. *Nat. Hazards Earth Syst. Sci.* 10, 133–137. doi:10.5194/nhess-10-133-2010

Conflict of Interest: The authors declare that the research was conducted in the absence of any commercial or financial relationships that could be construed as a potential conflict of interest.

frontiers in Earth Science

ORIGINAL RESEARCH
published: 15 April 2021
doi: 10.3389/feart.2021.621976

Analysis of Swarm Satellite Magnetic Field Data Before the 2016 Ecuador (Mw = 7.8) Earthquake Based on Non-negative Matrix Factorization

Kaiguang Zhu[1,2], **Mengxuan Fan**[1,2], **Xiaodan He**[1,2], **Dedalo Marchetti**[1,2,3], **Kaiyan Li**[1,2], **Zining Yu**[1,2], **Chengquan Chi**[1,2], **Huihui Sun**[1,2] **and Yuqi Cheng**[1,2]*

[1] College of Instrumentation and Electrical Engineering, Jilin University, Changchun, China, [2] Key Laboratory of Geo-Exploration Instrumentation, Ministry of Education of China, Changchun, China, [3] Environment Department of Istituto Nazionale di Geofisica e Vulcanologia, Rome, Italy

OPEN ACCESS

Edited by:
Patrick Timothy Taylor,
Goddard Space Flight Center,
United States

Reviewed by:
Luis Gomez,
University of Las Palmas de Gran Canaria, Spain
Livio Conti,
Università Telematica Internazionale Uninettuno, Italy

***Correspondence:**
Yuqi Cheng
547670158@qq.com

Specialty section:
This article was submitted to Environmental Informatics and Remote Sensing, a section of the journal Frontiers in Earth Science

Received: *27 October 2020*
Accepted: *15 March 2021*
Published: *15 April 2021*

Citation:
Zhu K, Fan M, He X, Marchetti D, Li K, Yu Z, Chi C, Sun H and Cheng Y (2021) Analysis of Swarm Satellite Magnetic Field Data Before the 2016 Ecuador (Mw = 7.8) Earthquake Based on Non-negative Matrix Factorization. Front. Earth Sci. 9:621976. doi: 10.3389/feart.2021.621976

In this paper, based on non-negative matrix factorization (NMF), we analyzed the ionosphere magnetic field data of the Swarm Alpha satellite before the 2016 (Mw = 7.8) Ecuador earthquake (April 16, 0.35°N, 79.93°W), including the whole data collected under quiet and disturbed geomagnetic conditions. The data from each track were decomposed into basis features and their corresponding weights. We found that the energy and entropy of one of the weight components were more concentrated inside the earthquake-sensitive area, which meant that this weight component was more likely to reflect the activity inside the earthquake-sensitive area. We focused on this weight component and used five times the root mean square (RMS) to extract the anomalies. We found that for this weight component, the cumulative number of tracks, which had anomalies inside the earthquake-sensitive area, showed accelerated growth before the Ecuador earthquake and recovered to linear growth after the earthquake. To verify that the accelerated cumulative anomaly was possibly associated with the earthquake, we excluded the influence of the geomagnetic activity and plasma bubble. Through the random earthquake study and low-seismicity period study, we found that the accelerated cumulative anomaly was not obtained by chance. Moreover, we observed that the cumulative Benioff strain S, which reflected the lithosphere activity, had acceleration behavior similar to the accelerated cumulative anomaly of the ionosphere magnetic field, which suggested that the anomaly that we obtained was possibly associated with the Ecuador earthquake and could be described by one of the Lithosphere–Atmosphere–Ionosphere Coupling (LAIC) models.

Keywords: Ecuador earthquake, Swarm satellites magnetic field, non-negative matrix factorization, decomposition, cumulative number of anomalous tracks

INTRODUCTION

Earthquakes are the most energetic phenomena in the lithosphere and on the Earth (Bolt, 1999). During the long-term earthquake preparation processing and at the largest energy release moment of earthquakes, some seismic-linked anomalies could occur in the lithosphere, atmosphere, and ionosphere (Parrot, 1995; Freund, 2000; Liu et al., 2015; Hattori and Han, 2018; Piscini et al., 2019).

With the development of the Lithosphere–Atmosphere–Ionosphere Coupling (LAIC) model, the study of seismo-ionospheric anomalies has attracted more and more attention (Hayakawa and Molchanov, 2002; Pulinets and Ouzounov, 2011; De Santis et al., 2015, 2019a; Shen et al., 2018; Li et al., 2019; Fu et al., 2020; Zhima et al., 2020). Recently, a substantial amount of satellite observation data are used to study the ionosphere anomalies before large earthquakes (Pulinets and Boyarchuk, 2005; Ho et al., 2018; Natarajan and Philipoff, 2018; Marchetti et al., 2019c; Zhang et al., 2019).

Swarm is a satellite mission of the European Space Agency (ESA). The mission consists of three satellites (Alpha, Bravo, and Charlie) that are devoted to studying the geomagnetic field and its dynamics (Olsen et al., 2006; Bouffard et al., 2019). The magnetic field data of Swarm satellites are widely used in fields, such as studying the ionospheric current systems (Alken, 2016) and the magnetic storms (Wang et al., 2019), and constructing the magnetic field models (Finlay et al., 2015, 2016). Beyond this, the high-precision magnetic field data are also applied to study the ionosphere anomalies, which are possibly related to earthquakes (De Santis et al., 2019b; Marchetti et al., 2019a). After the launch of the Swarm satellites at the end of 2013, some large earthquakes occurred. We focused on the 7.8 Mw earthquake that occurred in Ecuador (0.35°N, 79.93°W) on April 16, 2016.

Since satellite magnetic field data are affected by geomagnetic activity (Zhima et al., 2014; Perrone et al., 2018), in the routine analysis of the anomalies of earthquakes, the data under strong geomagnetic conditions are usually deleted. Zhang et al. (2009) studied the 2007 Chile M7.9 earthquake using the DEMETER satellite magnetic field data with $Kp < 3$ and $Dst > -20\ nT$ and found that the low frequency electromagnetic disturbances increased 1 week before the earthquake. Akhoondzadeh et al. (2019) used the magnetic field data collected under quiet geomagnetic conditions to study the 2017 Sarpole Zahab (Mw = 7.3) earthquake and observed ionospheric magnetic anomalies between 8 and 11 days prior to the occurrence of the event. De Santis et al. (2019c) used the Swarm satellite magnetic field data with $|Dst| \leq 20\ nT$ and $a_p \leq 10\ nT$ to study 12 earthquakes with magnitudes from 6.1 to 8.3, and they observed some ionospheric magnetic field anomalies before most of the events (Yan et al., 2013; Marchetti and Akhoondzadeh, 2018; De Santis et al., 2019b; Marchetti et al., 2019a,b).

Hattori et al. (2004) applied the principal component analysis to decompose the magnetic field data of three ground-based stations (including the data under strong geomagnetic activity). The first and the second principal components were found to be associated with the geomagnetic variation and man-made activity, respectively, and the residual third component contained the earthquake precursory signature. Then, in 2019, the principal component analysis was applied to the satellite magnetic field data by Zhu et al. (2019); they removed the component, which has a high correlation coefficient with the a_p index, and extracted earthquake-related anomalies using the residual component.

Non-negative matrix factorization (Lee and Seung, 1999) is a parts-based matrix decomposition method that has the advantage of obtaining local features from the whole data, which differs from the principal component analysis. NMF has been successfully applied in various fields. Lee and Seung (1999) proposed NMF and applied the method to decompose face images into basis images, such as the mouth, the nose, and other facial parts. Smaragdis and Brown (2003) applied NMF to decompose complex piano music and obtained the spectral bases of each note and its weight in time. Mouri et al. (2009) applied NMF to decompose electromagnetic data with extremely low-frequency bands from multiple ground stations and obtained local signals (which are emitted by regional electromagnetic radiation sources) from the extremely low-frequency data. Since the impact of earthquakes occurs only near the epicenters. Based on the advantage of NMF that could obtain local features from the overall data, in this paper, we used the NMF to analyze the ionosphere magnetic field data of Swarm Alpha satellite, including the data collected under quiet geomagnetic conditions and those under strong geomagnetic conditions, to explore the 2016 Ecuador earthquake (April 16, 0.35°N, 79.93°W).

First, we briefly described the Swarm satellite magnetic field data and the NMF method. Next, we performed NMF to decompose the short-time Fourier transform (STFT) magnitude spectra of each track and obtained three basis features and their corresponding weights. We calculated the energy-entropy ratio of the three weight components. For the weight component with the highest energy-entropy ratio, we computed the cumulative number of tracks, which had anomalies inside the earthquake-sensitive area. In addition, we analyzed the influence of geomagnetic activity and plasma bubbles on the cumulative anomaly. From the random earthquake study and low-seismicity period study, we explored whether the cumulative anomaly was obtained by chance. Finally, we studied the correlation between the ionosphere magnetic anomaly and the lithosphere activity.

DATA AND METHOD

Swarm Satellite Magnetic Field Data

The Swarm mission consisted of three identical satellites (Alpha, Bravo, and Charlie), which had been launched into near-polar orbits on November 22, 2013 (Bouffard et al., 2019). The satellites, Alpha and Charlie, flew almost side-by-side (longitudinal separation of 1.4° at the equator) at an altitude near 462 km (initial altitude) and the Bravo flew higher, near 511 km (initial altitude). The three satellites completed one track in about 90 min, accomplished nearly 15 day-and-night passes every 24 h, and drifted about 1 h in local time (LT), every 10 days. The objective of the mission was to provide the best survey and the temporal evolution of the geomagnetic field, obtain a space-time characterization of the internal field sources in the Earth, while improving the understanding of the interior of the Earth and the Geospace environment (Friis-Christensen et al., 2006, 2008; Olsen et al., 2006).

Each satellite of the Swarm mission was equipped with seven instruments. The main sensors included two magnetometers, an Absolute Scalar Magnetometer that provided measurements of the field intensity, and a Vector Field Magnetometer that measured the magnetic field from three different directions. These sensors made high-precision and high-resolution measurements of the strength, direction, and variation of the magnetic field. The observations are provided as Level-1b data, which are then calibrated and formatted time series (Olsen et al., 2013).

The observation data of vector magnetic field in L1b products are shown in two reference systems: (1) the instrument frame and (2) the North (X) East (Y) Center (Vertical, Z) frame. The magnetic field of the Y-East component could be affected by lithospheric activity and is less influenced by external magnetic disturbances (Pinheiro et al., 2011). In this study, we analyzed the Y-East component magnetic field data (Level-1b 1 Hz data) of the Swarm Alpha satellite to study the 2016 Ecuador earthquake.

Non-negative Matrix Factorization

The non-negative matrix factorization (Paatero and Tapper, 1994; Lee and Seung, 2000; Smaragdis, 2004; Cichocki et al., 2006) is a matrix factorization algorithm that approximates a given non-negative matrix as a product of two other non-negative matrices. The two decomposed non-negative matrices consist of a few basis vectors which contain the potential structures of the given non-negative matrix. This algorithm can obtain parts-based representations of non-negative data and make no further assumptions about their statistical dependencies. Thus, NMF could obtain local features from the overall data.

The goal of NMF is to approximate the non-negative matrix V as a product of two non-negative matrices, W and H. The approximate factorization can be written as in Equation (1).

$$\begin{aligned} V &\approx WH \\ &\approx [W_{*1} \ \cdots \ W_{*r}] \begin{bmatrix} H_{1*} \\ \vdots \\ H_{r*} \end{bmatrix} \end{aligned} \tag{1}$$

where, $V \in \mathbb{R}^{\geq 0,\, m\times n}$ is the original matrix, $W \in \mathbb{R}^{\geq 0, m\times r}$ is the basis matrix, and $H \in \mathbb{R}^{\geq 0, r\times n}$ is the weight matrix. $W_{*1}, \ldots, W_{*r}$ are the columns of matrix W and can be interpreted as basis vectors of matrix V. $H_{1*}, \ldots, H_{r*}$ are the rows of matrix H, which have a one-to-one correspondence with the columns of W and can be interpreted as the weights of these basis vectors. The rank r corresponds to the number of basis vectors, and is generally selected, such that $(n+m)r < nm$.

To minimize the error of reconstruction of V by WH, we use the cost function based on the generalized Kullback–Leibler divergence. We constrained the solutions of NMF problems by the minimum determinant constraint (Schachtner et al., 2009), which could achieve unique and optimal solutions in a general setting. The cost function is shown in Equation (2).

$$\begin{aligned} D_{detKL}(V|W,H) = \sum_{i=1}^{m}\sum_{j=1}^{n}\left(V_{ij}\ln\frac{V_{ij}}{[WH]_{ij}} - V_{ij} + [WH]_{ij}\right) \\ + \alpha \ \det\left(HH^T\right) \end{aligned} \tag{2}$$

where, α is the balance parameter. When α remains small enough, the reconstruction error does not increase during an iteration step, and very satisfactory results are obtained.

To optimize this function, we used an efficient multiplicative update algorithm introduced by Lee and Seung (2000); the iterative updated rules of basis matrix, W and weight matrix, H are shown in Equations (3) and (4).

$$W \leftarrow W \frac{\frac{V}{[WH]} H^T}{IH^T} \tag{3}$$

$$H \leftarrow H \left(\frac{W^T \frac{V}{[WH]}}{W^T I} - \alpha det\left(HH^T\right) \frac{\left[\left(HH^T\right)^{-1} H\right]}{W^T I} \right) \tag{4}$$

We stopped the iteration when the $D_{detKL}(V|W,H)$is was smaller than the threshold Th or the number of iterations reached the upper limit, N_{iter}. The formula for calculating Th is shown in Equation (5).

$$Th = \varepsilon \sum_{i=1}^{m}\sum_{j=1}^{n} V_{ij} \tag{5}$$

where, ε is the error factor. This parameter should be a small value and set according to the actual needs.

Overall, the NMF algorithm can be summarized as follows:

1. Initialize matrix W and matrix H to non-negative values.
2. Update matrix W and H using Equations (3) and (4).
3. Calculate $D_{detKL}(V|W,H)$ using Equation (2). If $D_{detKL}(V|W,H)$ is smaller than Th or the number of iterations reaches the upper limit, $N_{iter,}$ stop updating; otherwise return to Step 2.

For the initialization (Step 1), we used the Gauss random.

According to NMF, each element in matrix V can be described by the corresponding row of basis matrix W and the column of weight matrix H, as shown in Equation (6).

$$V_{ij} = \sum_{nr=1}^{r} W_{i,nr} H_{nr,j} \tag{6}$$

where, *Vij* is the element in *i* row and *j* column of matrix V.

From this formula, we can see that the element *Vij* in matrix V can be calculated by the corresponding *i* row of W and *j* column of H. Since NMF uses a small amount of data to represent the original data, matrix W contains the main vertical features of matrix V and matrix H contains the horizontal information of these features. When there exists a local feature in the original matrix V, which has a special vertical feature and concentrates in a certain local position in the horizontal direction, this feature can be represented by one of the basis vectors of W and its corresponding weight of H. We expect that the anomalies possibly produced by earthquakes are special, in terms of frequency and/or pattern, and occur not so far from the epicenters. Thus, some of these anomalies could have local features, and through NMF, we can potentially obtain the components which represent the anomalies possibly related to the earthquake.

DATA PROCESSING AND RESULTS

Ecuador Earthquake and Data Selection

On April 16, 2016, at 23:58:36 Coordinated Universal Time (UTC), a strong earthquake with a magnitude of Mw = 7.8, occurred ∼27 km south-southeast of Muisne, in the province of Esmeraldas, offshore of the west coast of northern Ecuador. The Ecuador earthquake was "the result of shallow thrust faulting on or near the plate boundary between the Nazca and South American plates. At the location of the earthquake, the Nazca plate subducted eastward, beneath the South American plate at a velocity of 61 mm/year" [from the United States Geological Survey (USGS)]. The location of the Ecuador earthquake is marked as a red star (0.35°N, 79.93°W, depth 21.0 km) in **Figure 1A**.

We studied the tracks that crossed the rectangular region, with $R = 2259.4$ km (half the side length), which is shown as a black rectangle in **Figure 1A**. The distance, R is the Dobrovolsky radius strain (Dobrovolsky et al., 1979); $R = 10^{0.43M}$(M is the magnitude of the earthquakes) estimates the size of the effective precursor manifestation zone of an earthquake. We assumed that the rectangular region was affected by the Ecuador earthquake, and referred to it as the "earthquake-sensitive area," while the outside area was not influenced by the earthquake. Moreover, the geomagnetic latitudes of the tracks that we investigated ranged *from* $-50°$to $+ 50°$ (we avoided aurora and polar interferences). Taking April 13–15, 2016, as an example, the tracks of the Swarm A satellites flying over the earthquake-sensitive area are shown in **Figure 1B**.

Since we expected the influence of earthquakes to occur only near the epicenters, and due to the advantage of NMF to obtain local features from the overall data, we applied NMF to all the observed satellite magnetic field data, and did not delete the data under strong geomagnetic activity. We analyzed 302 effective tracks from February 16 to May 16, 2016.

Swarm Alpha Satellite Magnetic Field Data Decomposition

In this part, we applied NMF to decompose the Y-East component magnetic field data of the Swarm Alpha satellite. First, we preprocessed the magnetic field data. For each track, the predicted value from the CHAOS-6 geomagnetic field model was subtracted from the magnetic field measurement to remove the core and the static crustal magnetic fields (Finlay et al., 2016). Then, we calculated the first difference of the residuals, along the tracks. The preprocessed magnetic field data for one track data is represented by the vector X as reported in Equation (7).

$$X = \left[x_1, x_2, \ldots, x_{L-1}\right] \tag{7}$$

where, L is the number of samples along the track.

After preprocessing, we performed STFT to X, setting the window length to be equal to 64 and the step length to be equal to 16 (with 1 Hz sampling rate of the data, the spatial resolution would be about 122 km). Then the STFT magnitude spectrum V was decomposed by NMF to three basis vectors, namely W_{*1}, $W_{*2,}$ and W_{*3}, and their corresponding weights , H_{1*}, $H_{2*,}$ and H_{3*}, as shown in Equation 8, with the number of basis vector, $r = 3$. For convenience, we refer below the three basis vectors as W1, W2, and W3, and the three corresponding weights as H1, H2, and H3. In addition, we set the times of the iterative update threshold, $N_{iter} = 1000$, the balance parameter $\alpha = 0.001$ in Equations (2) and (4), and the error factor, $\varepsilon = 0.0001$ in Equation (5).

$$V \approx \left[W_{*1} \;\; W_{*2} \;\; W_{*3}\right] \begin{bmatrix} H_{1*} \\ H_{2*} \\ H_{3*} \end{bmatrix} \tag{8}$$

The magnitude spectrum, V describes the amplitude–frequency characteristics at different locations along the track. The W1, W2, and W3 describe the basis features (vertical structure) of V. H1, H2, and H3 describe the weight coefficients of the three basis features over location and could show where the features W1, W2, and W3 appeared along the track. If there exists a basis feature, Wx (x = 1, 2, or 3), the high value of the corresponding weight Hx concentrates inside the earthquake-sensitive area; this feature reflects the local feature of the area and it is possibly associated with the Ecuador earthquake. We regarded it as a kind of anomaly inside the earthquake-sensitive area.

Taking one track on April 9, 2016 as an example, the NMF decomposition results of the Y-East component magnetic field data for this track is shown in **Figure 2**. The preprocessed magnetic field data of the track is shown in **Figure 2A**. The STFT magnitude spectrum V of the data is shown in **Figure 2B**. The three basis vectors, W1, W2, and W3 are shown in **Figure 2C**. The three weight components, H1, H2, and H3 are shown in **Figure 2D**.

As shown in **Figures 2A,B**, before applying NMF, the features of the preprocessed data occurred inside and outside the earthquake-sensitive area. After decomposition, in **Figures 2C,D**, for feature W1, the corresponding weight, H1 has high values inside the earthquake-sensitive area at ∼5° N latitude [with the highest value of 0.5560 which is over 5**RMS* (Root Mean Square) of H1], and it has low values outside the area. For feature W2, the corresponding weight, H2 has slightly high values outside the earthquake-sensitive area (with the highest value of 0.4015, which is 0.78 of 5**RMS* of H2). For feature W3, the corresponding weight, H3 has a very high value at approximately 22° S latitude outside the earthquake-sensitive area (with the highest value of 0.6831, which is over the 5**RMS* of H3) and slightly higher weights inside the area (with the highest value of 0.28244, which exceeds the 5**RMS* of H3 by half of the same value). From these decomposition results, for the example track, the high values of weight, H1 is concentrated inside the earthquake-sensitive area. Thus, the basis feature of W1 reflects the local feature of this area and is possibly associated with the Ecuador earthquake. The high value of H1 is an anomaly inside the earthquake-sensitive area.

The basis vectors describe features and their corresponding weights describe where these features are located along the track. We utilized the weight H components to detect whether anomalies existed inside the earthquake-sensitive area, which are possibly related to earthquakes. The higher the concentration of

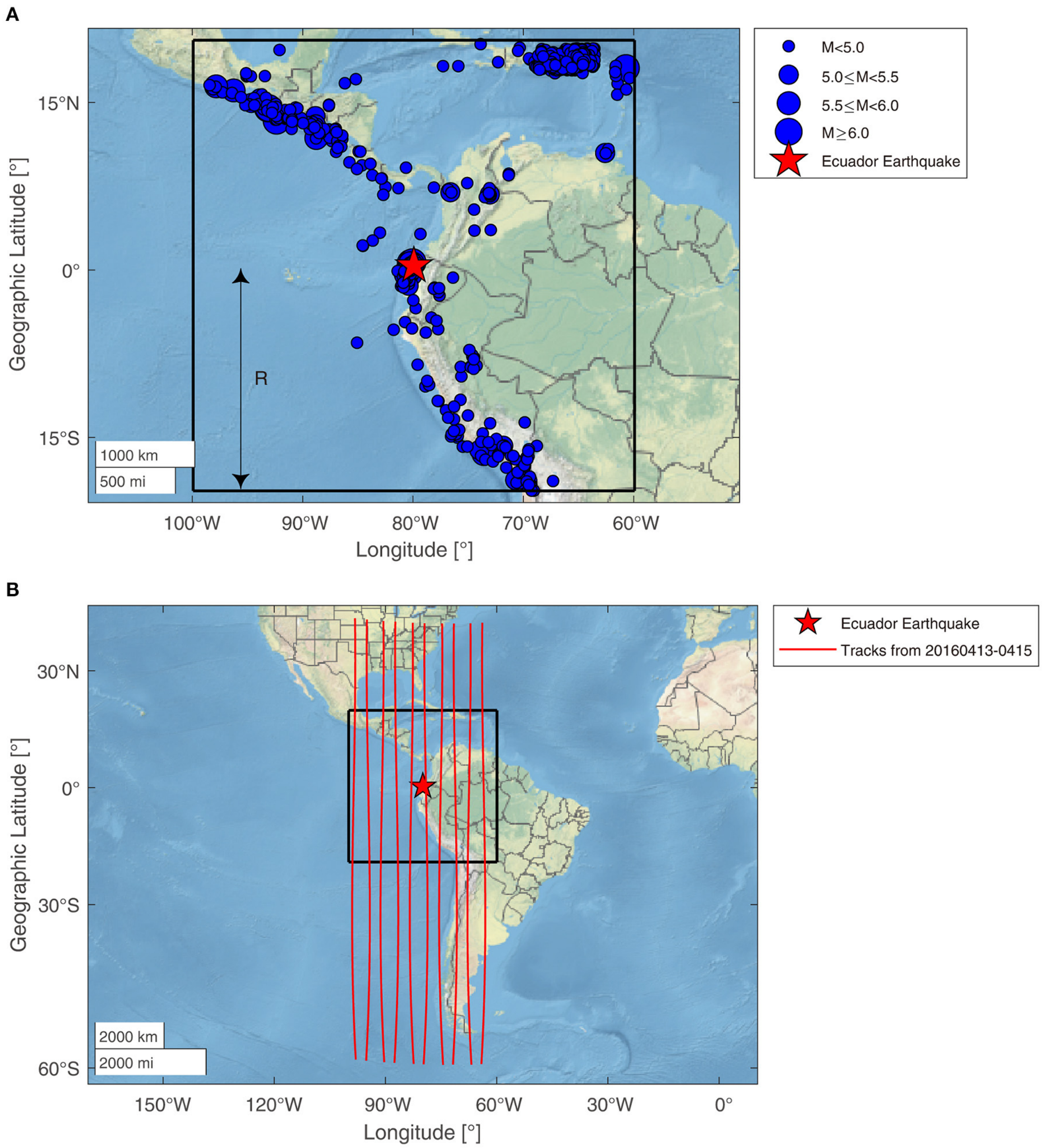

FIGURE 1 | Geographical location and earthquake-sensitive area selected for the Ecuador earthquake. The geographical distribution of the investigated tracks from April 13 to 15, 2016. **(A)** The epicenter and the earthquake-sensitive area of 2016 Ecuador earthquake. The red star and the black rectangle are the epicenter and the earthquake-sensitive area of the Ecuador earthquake, respectively. The blue dots with black edges mark the earthquakes occurred inside the earthquake-sensitive area from February 16 to May 16, 2016. The half of side length *R* is the Dobrovolsky's radius strain. **(B)** The geographical distribution of the investigated tracks from April 13 to 15, 2016. The red lines are investigated tracks.

the H components concentrated inside the earthquake-sensitive area, the more likely this component would have anomalies inside the earthquake-sensitive area. We evaluated the concentration of energy and entropy inside the earthquake-sensitive area for three H components of all the studied tracks, by the energy-entropy ratio. The energy-entropy ratio shows the energy and entropy of the earthquake-sensitive area over those of the whole track, as shown in Equation (9).

$$\gamma_n = \frac{\frac{\sum_{j=P_s}^{Pe} Hn_j^2}{\sum_{j=1}^{N} Hn_j^2} + \frac{Z_{inXsn}}{Z_{sXsn}}}{2}, \quad (n = 1,\ 2,\ 3) \tag{9}$$

where, the points between P_s and $P_e$are located inside the earthquake-sensitive area, as shown in **Figure 2D**. *Xsn* is the

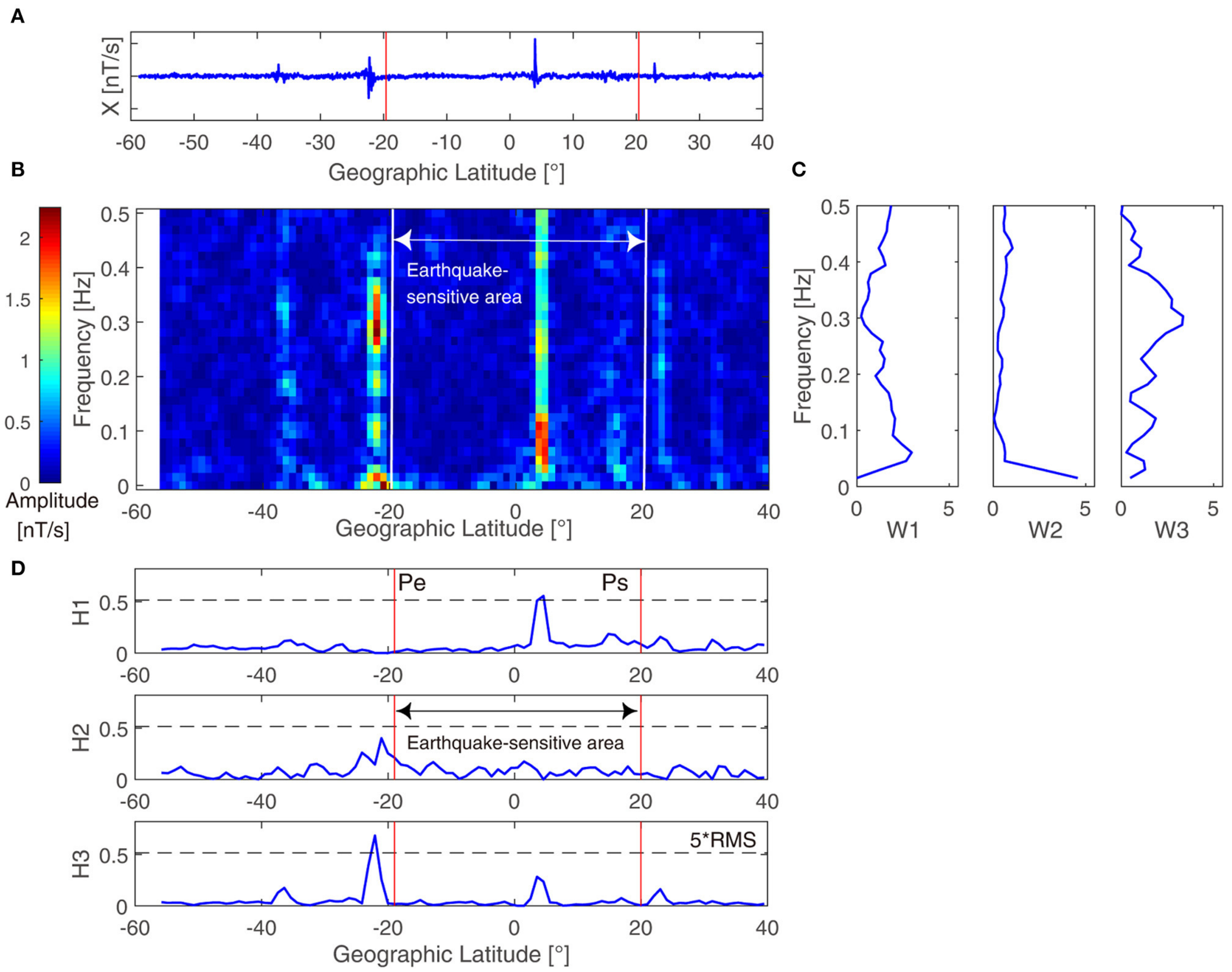

FIGURE 2 | The NMF decomposition results of the Y-East component magnetic field data of a track on April 9, 2016. **(A)** The preprocessed Y-East component magnetic field data of this track. The red lines show the edges of the earthquake-sensitive area. **(B)** The STFT magnitude spectrum V of this track. The white lines show the edges of the earthquake-sensitive area. **(C)** The three basis vectors W1, W2, and W3 of magnitude spectrum V decomposed by NMF. **(D)** The three weight components H1, H2, and H3 corresponding to the basis vectors. The points between P_s and P_e are inside the earthquake-sensitive area. The red lines show the edges of the earthquake-sensitive area. The black horizontal dotted lines show the 5 times RMS of the components, H1, H2, and H3, respectively.

time-domain reconstruction signal for the Hn component. Z_{sXsn} is the Shannon entropy (Shannon, 2001) of the whole track for Xsn, and Z_{inXsn} is the entropy inside the earthquake-sensitive area for Xsn.

The average and standard deviation of the largest energy-entropy ratio, the second largest energy-entropy ratio, and the smallest energy-entropy ratio for the three decomposed H components of all the studied tracks are 0.571 ± 0.106, 0.456 ± 0.114, and 0.340 ±0.103, respectively. The largest average value is 25.22% higher than the second largest average value, and 67.94% higher than the smallest average value. From this statistical result, we could see that there existed an H component among the three decomposed H components, whose energy and entropy is much more concentrated inside the earthquake-sensitive area than in the other two H components. Therefore, this H component is more likely to have anomalies inside the earthquake-sensitive area, which is possibly related to the Ecuador earthquake. We refer to this component as Hs1 (the H component with the largest energy-entropy ratio), and the remaining two H components as Hs2 and Hs3, by the descending order of their energy-entropy ratio.

Definition of Anomalous Tracks

Here, we defined the anomalous tracks for the H components. We calculated the RMS of the Hsn ($_{n} = 1, 2$, or 3) component and set the threshold, $K^{*}RMS$ ($K = 5$). The values that exceeded the threshold are the anomalies of this Hsn component, and a track with one or more anomalies is an anomalous track for this Hsn component. The track is an inside anomalous track for this Hsn component, if one or more anomalies occurred inside

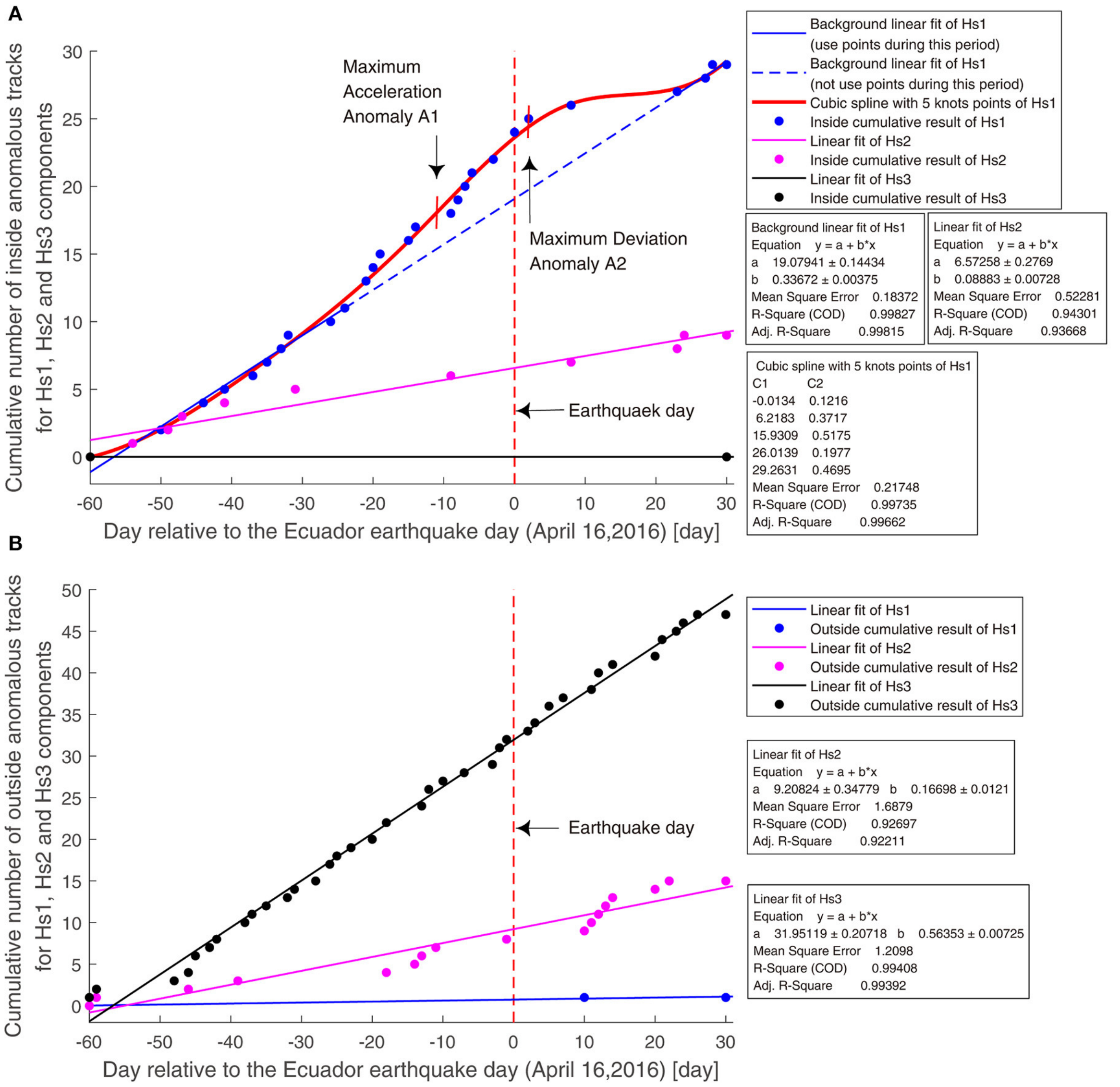

FIGURE 3 | The cumulative number of inside anomalous tracks and those of outside anomalous tracks for components Hs1, Hs2, and Hs3, from 60 days before to 30 days after the earthquake. **(A)** The cumulative number of inside anomalous tracks for components Hs1, Hs2 and Hs3. The red curve is the cubic spline with 5-knots points using all points. The solid line indicates that we use the points during this period to do the linear fit. The dashed line indicates that we do not use the points during this period to do the linear fit. The day of the earthquake is represented as a red vertical dotted line. **(B)** The cumulative number of outside anomalous tracks for components, Hs1, Hs2, and Hs3. The day of the earthquake is represented as a red vertical dotted line.

the earthquake-sensitive area. The track is an outside anomalous track for this Hsn component, if one or more anomalies occurred outside the earthquake-sensitive area. For example, the track in **Figure 2** is an inside anomalous track for Hs1 component, but an outside anomalous track for Hs3 component.

Results

In this part, we calculated the cumulative number of inside anomalous tracks for Hs1 component, from 60 days before the earthquake to 30 days after the earthquake, to study the Ecuador earthquake. In addition, the cumulative number of inside anomalous tracks for Hs2 and Hs3 components and that of the outside anomalous tracks for the three H components were also computed for comparison. Finally, we obtained six cumulative results over time, which are presented in **Figure 3**. The three inside cumulative results are shown in **Figure 3A**, and the three outside cumulative results are shown in **Figure 3B**.

Moreover, if there are nx anomalous tracks on the t^{th} day, the cumulative sequence $Nx(t)$ is increased by nx on the previous day. For the cumulative results without any value on the first day (day -60), we made 0 as the value of the first day (day -60). For the cumulative results without any value on the last day of the cumulative (day $+30$), we made the last value of the result as the value of this day (day $+30$). Thus, all the cumulative results

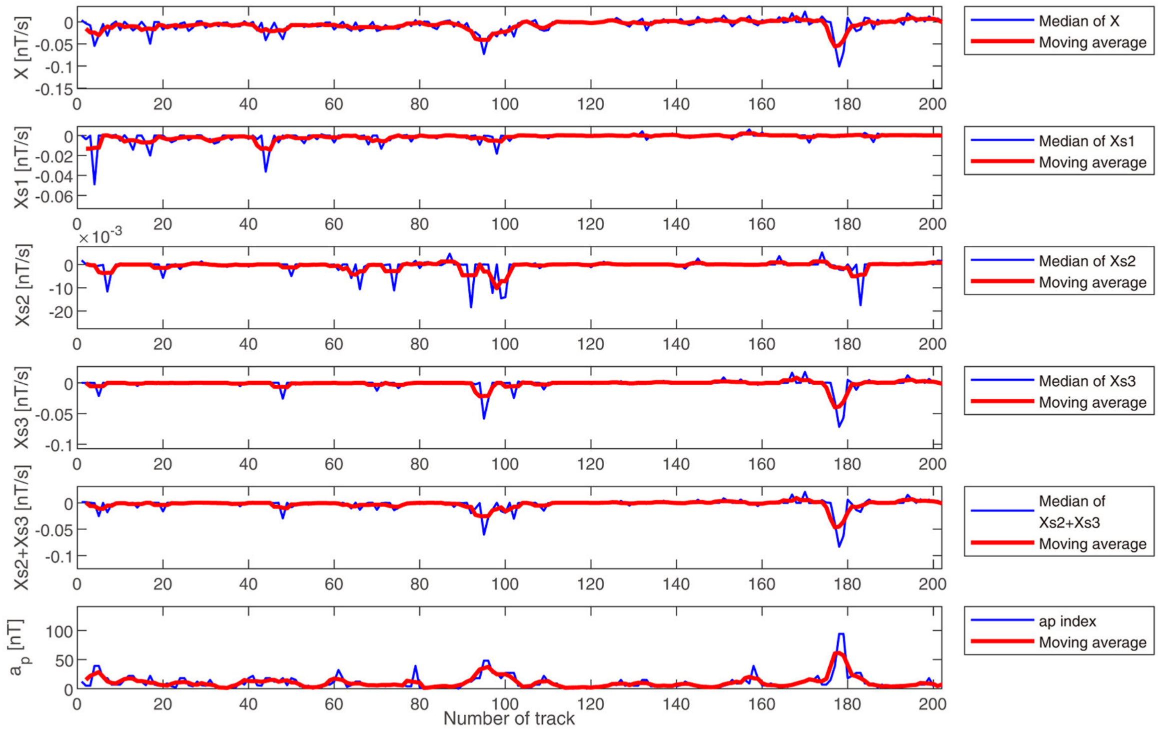

FIGURE 4 | The median value of the X, Xs1, Xs2, Xs3, and Xs2 + Xs3 from 30 days before to 30 days after the earthquake, and their corresponding $a_p$index. The X is the time domain signal before the NMF decomposition. The Xs1, Xs2, Xs3, and Xs2 +Xs3 are the time-domain reconstruction signal of H components. The red curves are the moving averages of the signals.

had values on the first day and last day during the cumulative range. In this way, all the cumulative results had exactly the same time range, and all the results show the variation of the entire investigated time range.

For the inside cumulative result of Hs1 component, we performed sigmoid fit, 3-degree polynomial fit, 6-degree polynomial fit, cubic spline with 2-knot points, and cubic spline with 5- knot points (D'Errico, 2021), using all of the blue points. The two cubic spline fits are constrained to be monotonical. We compared the mean squared error, adjusted the coefficient of determination and akaike information criterion, and found that the cubic spline with 5-knot points has the best fitting effect. Thus, for the inside cumulative result of Hs1 component, we performed a cubic spline with 5-knot points using all of the points, as shown in the red curve in **Figure 3A**. Based on this fit, we selected the points from day −60 to day −24 and from day +23 to day +30, and performed a linear fit to show the anomaly part of the cumulative result and we referred to it as background linear fit of the Hs1 component.

In **Figure 3A**, the inside cumulative result of Hs1 component shows a clear acceleration before the earthquake, deviating from the previous linear growth, and then recovers after the event. Compared to this result, the inside cumulative result of Hs2 exhibits approximately linear growth, and the Hs3 component does not have an inside anomalous track, as shown in **Figure 3A**.

As shown in **Figure 3B**, Hs1 component has only one outside anomalous track. The outside cumulative result of the Hs2 component presents roughly a linear growth. There are two clear increase groups in the cumulative result. We checked the Dst, a_p, and AE indices of the anomalous tracks for these two groups. The group from-14 days to −11 days has three anomalous tracks, two of them with $|Dst| > 20\ nT$ and $a_p > 10\ nT$. The group from +10 days to +14 days has five anomalous tracks; the tracks in day +11, day +12, and day +14 present values of the AE index higher than 100 nT, 80 nT, and 300 nT, respectively. Moreover, the AE index is 299 nT 2 h before the anomalous track in day +11 and 3 h before the anomalous track in day +12. From these results, we infer that the anomalous tracks of these two groups are likely to be affected by the geomagnetic activity. The outside cumulative result of Hs3 component shows a quasi-linear trend.

Moreover, on comparing the cumulative number of inside cumulative results with those outside for the three H components, we found that almost all anomalies of Hs1 component occur inside the earthquake-sensitive area. However, for the Hs2 component, some anomalies are located inside the earthquake-sensitive area, some anomalies are located outside this area, and all anomalies of Hs3 component are outside the earthquake-sensitive area. From these results, we found that the inside cumulative result of Hs1 component is more likely to reflect the anomalies of the Ecuador earthquake.

Then, we further analyzed the inside result of the Hs1 component. From **Figure 3A**, until 20 days before the main shock, the cumulative number of Hs1 has exhibited linear growth and then begins to show accelerated growth. The increased speed reaches its maximum 11 days before the main shock, which is shown as the maximum acceleration anomaly, A1 in **Figure 3A**. Meanwhile, the cumulative number deviates from the previous linear growth, and the deviation extent reaches its highest in 2 days after the Ecuador earthquake, which is shown as the maximum deviation anomaly, A2 in **Figure 3A**. Eight days after the main shock, the cumulative number stops increasing temporarily, which is consistent with the deceleration time of the aftershock cumulative seismicity for the northern and southern patches (Agurto-Detzel et al., 2019). Thus, we speculated that the gap between +8 days to +22 days is possibly affected by the decrease of the seismic activity. Then, 23 days after the main shock, the cumulative number recovers to its linear growth. The abnormal phenomenon of the inside cumulative result for Hs1 component that the cumulative number accelerated before the earthquake and recovered after it is consistent with the studies of De Santis et al. (2017, 2019c). These studies indicated that the cumulative number of anomalies for a critical system would accelerate when approaching its critical time and recover after a large event (De Santis et al., 2017, 2019c), that is, the 7.8 Mw earthquake.

We also found that the accelerated cumulative anomaly of Hs1 component is similar to the results of the other two studies on the Ecuador earthquake, which also used the magnetic field data of the Swarm satellites but excluded the influences of the geomagnetic activity. The maximum acceleration anomaly, A1 in **Figure 3A** corresponds to a study by Akhoondzadeh et al. (2018). Their study shows that the cumulative number of anomalous tracks accelerates ∼9 days before the Ecuador earthquake, when the magnetic field data collected under quiet geomagnetic conditions are considered. The maximum deviation anomaly, A2 in **Figure 3A** is consistent with the study of Zhu et al. (2019). Their study indicated that the increased speed of the cumulative number of anomalous tracks reaches its maximum around the time of the Ecuador earthquake, after using principal component analysis to remove the component affected by geomagnetic activity.

In addition, we performed some confutation analysis to prove that the accelerated cumulative anomaly is possibly related to the Ecuador earthquake rather than caused by other disturbances.

CONFUTATION ANALYSIS

Geomagnetic Activity Influence Study

To study whether the accelerated cumulative anomaly of Hs1 component is affected by geomagnetic activity, we performed two types of research. First, we analyzed the correlation between the time-domain reconstruction signal of Hs1 component and the geomagnetic index and compared the results with those of the original time domain signal and the other two H components.

For each investigated track (from 30 days before the earthquake to 30 days after the earthquake), we computed the median value of the time-domain signal X before the NMF decomposition and those of the time-domain reconstruction signal for the H components, Xs1, Xs2, Xs3 and Xs2 + Xs3. We compared the variation of the median value for the signals with their corresponding a_p index [from the International Service of Geomagnetic Indices (ISGI)], as shown in **Figure 4**.

In **Figure 4**, Xs1 is not significantly correlated to the a_p index, but the X, Xs3 and Xs2 + Xs3 seem to be adequately correlated with the geomagnetic a_p index. Then, we calculated the correlation coefficient between the a_p index and X, Xs1, Xs2, Xs3, and Xs2 + Xs3, where the results *show the values*, a −0.76, −0.20, −0.40, −0.82, and −0.84, respectively. These results reflect that the time-domain signals, X, Xs3, and Xs2, + Xs3 have strong correlations with the a_p index; the absolute values of these correlation coefficients are over 0.8. In contrast, the correlation coefficient between Xs1 and the a_p index is very low; the absolute value of the correlation coefficient is 0.20. Thus, after the NMF decomposition, the signal influenced by the geomagnetic activity seems to be included in the Xs2 and Xs3 components. However, the Xs1 component is not likely to relate to the geomagnetic activity.

Second, we examined the influence of the geomagnetic activity on the anomalous tracks of Hs1 component, and compared the results with those of the other two components. We set the *Dst* index (from ISGI) classification standard and divided the spatial conditions into four levels, from *L*0 to*L*3. Then, we calculated the numbers and percentages of anomalous tracks for Hs1, Hs2, and Hs3 components, before the earthquake, at different *Dst* levels, as shown in **Table 1**.

From **Table 1**, with the increase of the *Dst* level, the percentage of anomalous tracks for the Hs1 component shows a slight fluctuation; it first decreases by 20% and then increases by 35%. The percentage of anomalous tracks for the Hs2 and Hs3 components continuously increase with stronger geomagnetic activity. The percentage of anomalous tracks for Hs2 increases by 85% and then increases by 103%. At the *L*0 level, the percentage of anomalous tracks for the Hs3 is similar to Hs1, but at the L_2 and L_1 levels, the results of Hs3 are approximately twice as large as those of Hs1. Therefore, the anomalous tracks of Hs2 and Hs3 components are likely to be influenced by the geomagnetic activity. However, the anomalous tracks of Hs1 component are almost not affected by the geomagnetic activity.

From these two studies, we come to know that the accelerated cumulative anomaly of Hs1 component is hardly influenced by the geomagnetic activity.

We also assess the solar activity index, namely the F10.7 index within the study time range. Although the solar activity index near the earthquake is high [max: 107 solar flux unit (sfu)], no sudden change is evident. In addition, a previous study showed that the solar radio flux parameter probably did not affect the seismo-ionospheric anomalies detected around the date of Ecuador earthquake (Akhoondzadeh et al., 2018). Therefore, we did not consider the influence of the solar activity index, F10.7 on the ionosphere magnetic anomalies.

Plasma Bubbles Influence Study

The ionospheric magnetic field data might be affected by small-scale ionospheric irregularities, namely plasma bubbles. To

TABLE 1 | The numbers and percentages of anomalous tracks for Hs1, Hs2, and Hs3 components at different *Dst* levels before the Ecuador earthquake.

Component	Level	Dst index range [nT]	Total number of tracks	Number of anomalous tracks	Percentage
Hs1	L0	$\|Dst\| \leq 20$	147	21	14.29%
	L1	$20 < \|Dst\| \leq 40$	44	5	11.36%
	L2	$40 < \|Dst\| \leq 60$	13	2	15.38%
	L3	$\|Dst\| > 60$	1	0	0
Hs2	L0	$\|Dst\| \leq 20$	147	9	6.12%
	L1	$20 < \|Dst\| \leq 40$	44	5	11.36%
	L2	$40 < \|Dst\| \leq 60$	13	3	23.08%
	L3	$\|Dst\| > 60$	1	0	0
Hs3	L0	$\|Dst\| \leq 20$	147	20	13.61%
	L1	$20 < \|Dst\| \leq 40$	44	11	25.00%
	L2	$40 < \|Dst\| \leq 60$	13	4	30.77%
	L3	$\|Dst\| > 60$	1	0	0

TABLE 2 | The locations, earthquake-sensitive areas, and study time ranges of Ecuador earthquake, four random pseudo earthquakes, and two low-seismicity period cases.

Case	Epicenter	Latitude range	Longitude range	Time range
Ecuador earthquake	(0.35°N, 79.93°W)	19.65°S–20.35°N	99.93°W–59.93°W	February 16 to May 16, 2016
Random 1	(0.98°S, 139.31°W)	19.02°S–20.98°N	159.31°W–119.31°W	February 16 to May 16, 2016
Random 2	(0.35°N, 30°E)	19.65°S–20.35°N	10°E–50°E	February 16 to May 16, 2016
Random 3	(20.59°N, 174.17°W)	0.59°N–40.59°N	165.83°E–154.17°W	February 16 to May 16, 2016
Random 4	(30.60°S, 24.86°W)	50.60°S–10.60°S	44.86°W–4.86°W	February 16 to May 16, 2016
Low 1	(0.35°N, 79.93°W)	19.65°S–20.35°N	99.93°W–59.93°W	May 11 to August 9, 2015
Low 2	(0.35°N, 79.93°W)	19.65°S–20.35°N	99.93°W–59.93°W	April 1 to June 30, 2018

explore whether the accelerated cumulative anomaly of Hs1 component is affected by plasma bubbles, we checked the Bubble index and the Bubble probability of the anomalous tracks (Park et al., 2013).

Both the Bubble index and the Bubble probability of the points inside the earthquake-sensitive area of the inside anomalous tracks for Hs1 component, from day−14 to day +2, at the critical accelerated phase are 0, which means that the data are not affected by the plasma bubbles. So, we can speculate that the accelerated cumulative anomaly of Hs1 component is not probably caused by the plasma bubble.

Random Earthquake Study and Low-Seismicity Period Study

In this section, we performed a random earthquake study proposed by Parrot (2011) and low-seismicity period study to analyze the relationship between the Ecuador earthquake and the accelerated cumulative anomaly of the magnetic field data.

We randomly selected four pseudo earthquake epicenters around the world, which cover different latitude positions (excluding high latitudes), and studied them with the same time duration and the same size of earthquake-sensitive area as those of the Ecuador earthquake, without earthquakes over 5.5, as shown in **Table 2** and **Figure 5**. In particular, we noted that the latitude of the Random 1 epicenter is similar to that of the Ecuador earthquake epicenter and the Random 2 epicenter is in a region that sometime has active ionospheric irregularities (Yizengaw and Groves, 2018). The LT of the four random pseudo earthquakes is almost the same as that of the Ecuador earthquake.

We also studied two low-seismicity periods with the same location and earthquake-sensitive area as those of the Ecuador earthquake; no earthquake with a magnitude over 5.8 occurred in these two periods, as shown in **Table 2**. Although the LT of the data for the two cases are not exactly same with those for the Ecuador earthquake, they cover the LT (sweeps from 21 to 20 LT for nighttime tracks and from 9 to 8 LT for daytime tracks) at the increased phase of the cumulative results.

Likewise, we calculated the cumulative number of the inside anomalous tracks of Hs1 component for the four random pseudo earthquakes and two low-seismicity periods, and then compared them with the cumulative results of the Ecuador earthquake, as shown in **Figures 6**, **7**.

In **Figures 6**, **7**, the cumulative number of the inside anomalous tracks for four random pseudo earthquakes and two low-seismicity period cases show approximately linear growth. To avoid the influence of LT, we checked the cumulative results of Low 1 and Low 2 from 21 (9) to 20 (8) LT, as shown by the green curves in **Figure 7**, and we found that they did not show accelerated increase. Thus, in non-earthquake regions or during non-earthquake periods, the cumulative results exhibited linear increase trend. The results are consistent with the "typical random process," proposed by De Santis

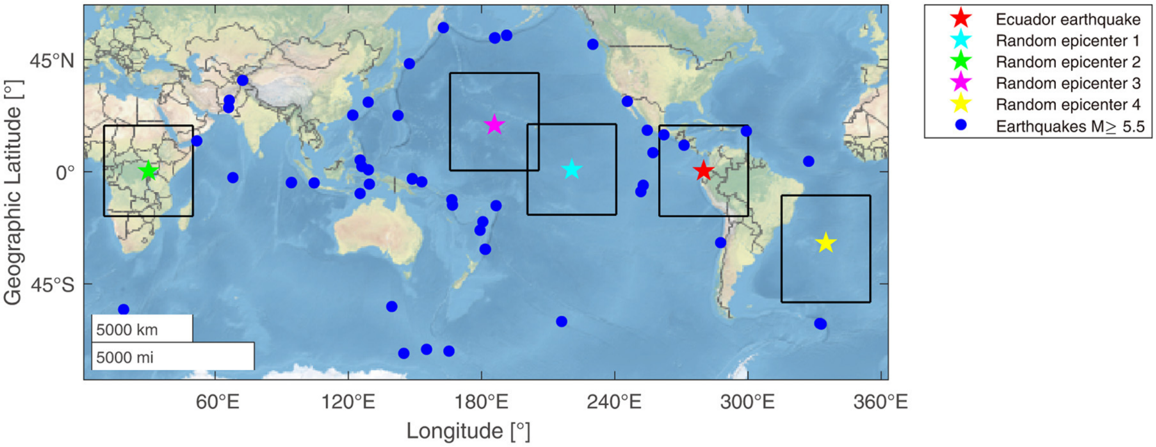

FIGURE 5 | The geographical locations and earthquake-sensitive areas of the Ecuador earthquake and four random pseudo earthquakes. The black rectangles show the earthquake-sensitive areas of the Ecuador earthquake and four random pseudo earthquakes. The blue dots show the earthquakes with magnitude ≥5.5 worldwide from February 16 to May 16, 2016.

et al. (2017); for a random process, the accumulated value is expected to show a statistically linear increase. However, for the actual Ecuador earthquake, as the earthquake approaches, the cumulative number of anomalous tracks accelerates growth and then recovers after the event, confirming that this trend seems to be related to the seismic event.

Moreover, from **Figure 6** before the day of the earthquake, the average number of anomalous tracks for the four random earthquakes is ∼10, while the number of anomalous tracks of the real Ecuador earthquake is ∼25. This result shows that the number of anomalies for non-earthquake region cases is less than that of the real earthquake, which possibly supports the earthquake source of at least a subset of the anomalies (15 during the 2 months before the Ecuador earthquake), which is also consistent with the study of Parrot (2011).

These results further verify that the accelerated cumulative anomaly of Hs1 component of the ionosphere magnetic field is not obtained by simple chance or influenced by the study time period, geographical location, and LT, and it is possibly associated with the Ecuador earthquake.

Cumulative Benioff Strain S Study

In this section, we studied the correlation between the accelerated cumulative anomaly of the ionosphere magnetic field data and the lithosphere activities. Considering the cumulative effect of a series of N earthquakes before a large earthquake, we calculated the cumulative Benioff strain S (Benioff, 1949; De Santis et al., 2019a), which could estimate the strain-rebound increment by the earthquake energy, to study the lithosphere activity before the Ecuador earthquake, and compared it with the cumulative result of Hs1 component for the ionosphere magnetic field data.

Because of the limitations in the detection capability of the seismograph network, some weak earthquakes are not recorded. We used the maximum curvature technique (Xie et al., 2019) to estimate the smallest magnitude Mc that could be completely detected in the seismic-relevant area (with half large size of the earthquake-sensitive area of the Ecuador earthquake). The estimated complete magnitude is $Mc = 4.3$ by the seismic events (from USGS) in 2016. Then we selected the seismic events with magnitudes ≥4.3 and hypocentral depths ≤50 km, from February 16, 2016 until the moment of the Ecuador earthquake, in the seismic-relevant area to calculate the cumulative Benioff strain S.

For each selected seismic event, we calculated the released energy as explained in Equation (10) (Han et al., 2014).

$$E_i = 10^{4.8+1.5M_i} \tag{10}$$

where, Mi is the magnitude of the ith earthquake. Then we computed the cumulative Benioff strain S as explained in Equation (11) (Marchetti et al., 2019c).

$$S = \sum_{i=1}^{nc} \sqrt{E_i} \tag{11}$$

where, nc is the total number of the earthquakes.

The cumulative Benioff strain S around the epicenter of the Ecuador earthquake and the cumulative number of the inside anomalous tracks of Hs1 component for ionospheric magnetic field data are shown in **Figure 8**.

In **Figure 8**, until 8 days before the main shock, the cumulative Benioff strain S shows an approximate linear increase. After this day, the cumulative result shows a trend of accelerated growth and it continues until the moment of occurrence before the Ecuador earthquake. The clustering of earthquakes before a large earthquake might be a result of several physical mechanisms operating in the seismogenic crust (Shcherbakov et al., 2019). Therefore, this acceleration phenomenon may correspond to the energy release before the Ecuador earthquake and may be connected to the lithosphere activities before the earthquake, that is, the seismic activation of the fault system (Marchetti et al., 2019c).

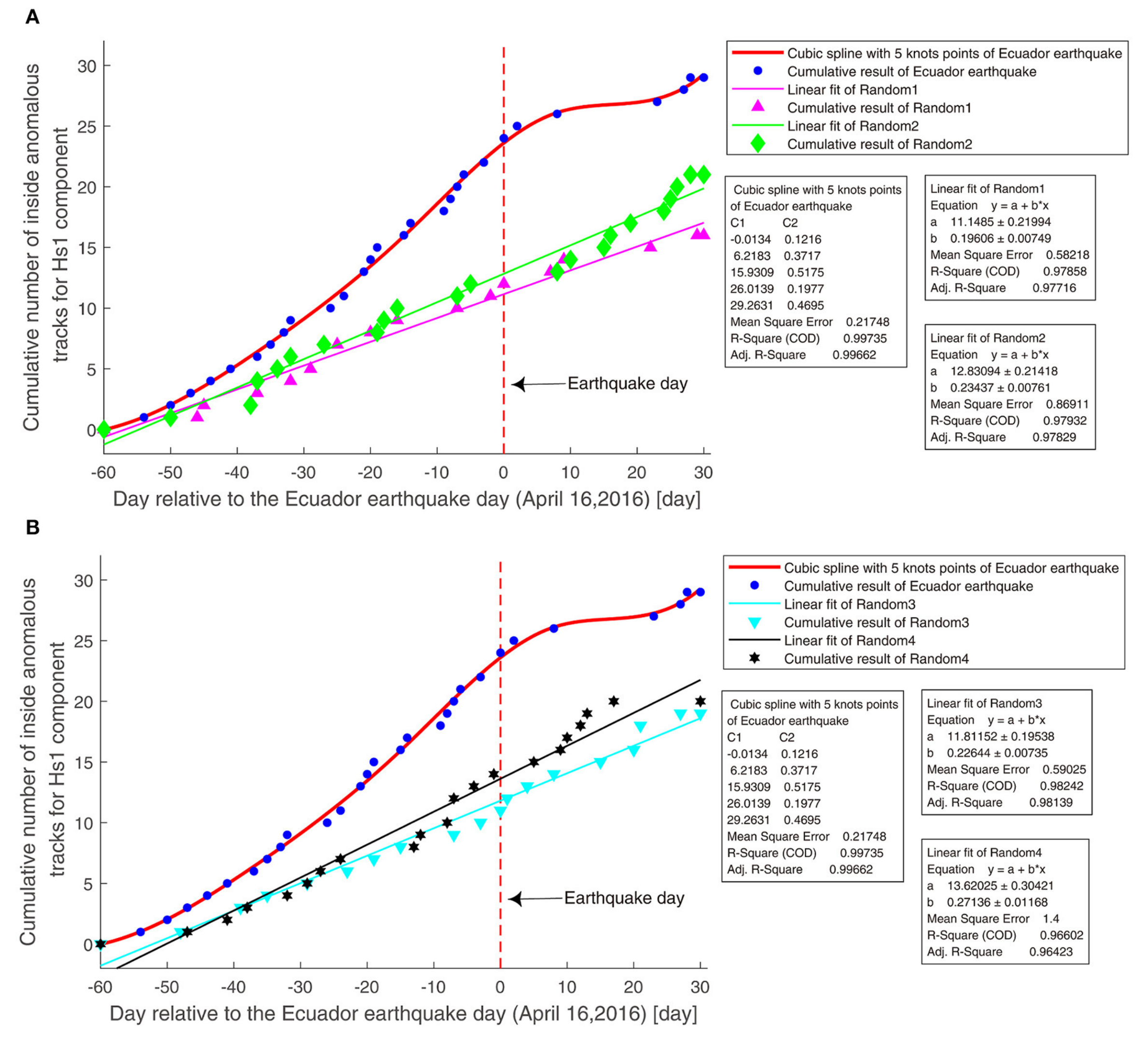

FIGURE 6 | The cumulative number of inside anomalous tracks of Hs1 component for the Ecuador earthquake and the four random pseudo earthquakes. **(A)** The cumulative results for two low latitude random pseudo earthquakes, Random 1, Random 2, and the Ecuador earthquake. The day of the earthquake is represented as a red vertical dotted line. **(B)** The cumulative results for two middle latitude random pseudo earthquakes, Random 3, Random 4, and the Ecuador earthquake. The day of the earthquake is represented as a red vertical dotted line.

Comparing the cumulative Benioff strain S and the cumulative results of Hs1 component of the ionosphere magnetic field data, we found that they have similar accelerate growth trend before the earthquake. And, as the earthquake approached, the anomaly phenomena in both the ionosphere and lithosphere became more and more obvious. Meanwhile, the acceleration day (8 days before the earthquake) of the cumulative Benioff strain S is near the day (11 days before the earthquake) when the increased speed of the cumulative number of the magnetic field data reached its maximum. This consistency indicates that the accelerated cumulative anomaly of Hs1 component for the ionosphere magnetic field data are possibly associated with the lithosphere activities, which are related to the Ecuador earthquake.

The correspondence between the accelerated cumulative anomaly of the ionosphere magnetic field data and the lithosphere activities is consistent with the study on the Nepal earthquake by De Santis et al. (2017). This study indicates that the cumulative number of ionosphere magnetic anomalies and those of M4+ earthquakes have similar trends before and after the earthquake. By *De* Santis, this similar behavior between them supports the LAIC and the hypothesis that "the noticed magnetic anomalies in Swarm data are mostly of internal origin, due to a LAI coupling."

According to LAIC models, the anomalies, which occurred in different layers before strong earthquakes, could be explained as a synergy between the lithosphere, atmosphere (included the Earth's surface), and ionosphere processes

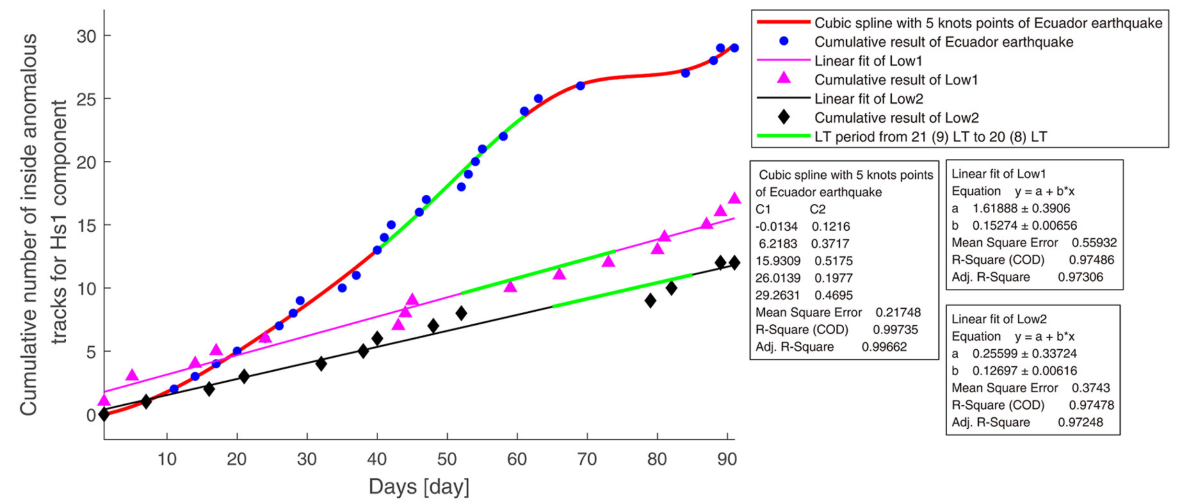

FIGURE 7 | The cumulative number of inside anomalous tracks of Hs1 component for the Ecuador earthquake and two low-seismicity period cases. The green curves show the LT period from 21 (9) to 20 (8) LT for the three cumulative results.

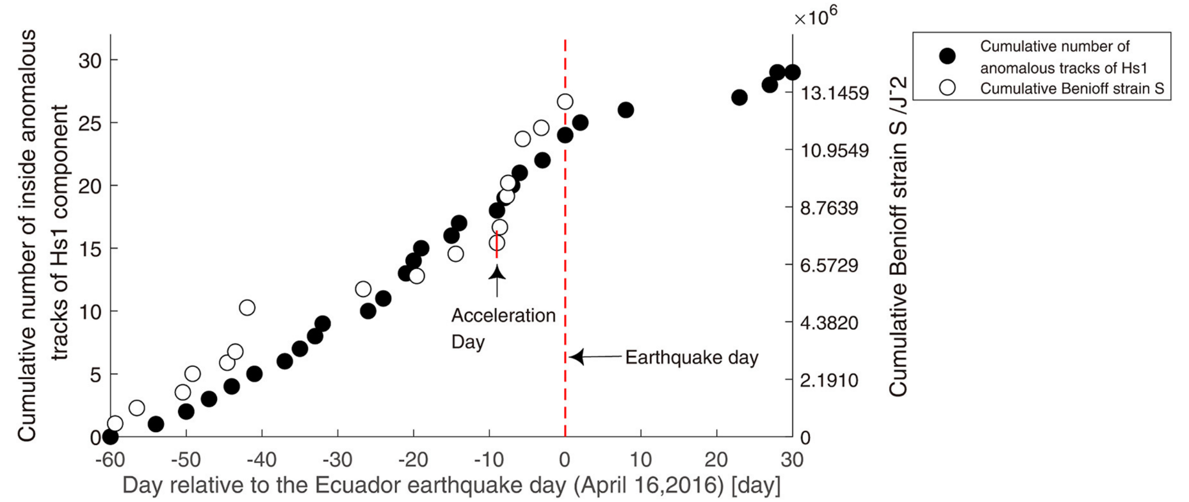

FIGURE 8 | The cumulative Benioff strain S around the Ecuador earthquake epicenter and the cumulative number of inside anomalous tracks of Hs1 component for the magnetic field data, from February 16, 2016, to May 16, 2016. The day of the earthquake is represented as a red vertical dotted line.

and anomalous variations which are usually named as medium/short-term earthquake precursors. From the LAIC model, before the earthquake, fault activation releases some positive charged holes (Freund, 2011) or leads to gas migration including radon emanation (Pulinets and Ouzounov, 2011). Then the release of radon induces the ionization of the atmosphere. Formation of large ion clusters led to variations in the atmospheric electricity which is the main source of ionospheric anomalies over seismically active areas including the electromagnetic anomaly before the earthquake. Other coupling mechanisms have also been hypnotized; for example, a complete electric coupling induced by a change in the ground resistivity due to the variation of the strain on the fault (Kuo et al., 2014), or even a surface warming could produce an acoustic gravity wave before the occurrence of the earthquake (Hayakawa, 2011).

This correspondence between the anomalous behavior in the ionosphere and that in the lithosphere is consistent with the synergy among the processes of the different layers, and their anomalies are explained by one of the LAIC models. Therefore, our result supports the LAIC effects and we suggest that the Ecuador earthquake possibly involved a physical coupling between the lithosphere and the ionosphere in its preparation phase, and the accelerated cumulative anomaly of Hs1 component for the ionosphere magnetic field data is likely to originate in the lithosphere.

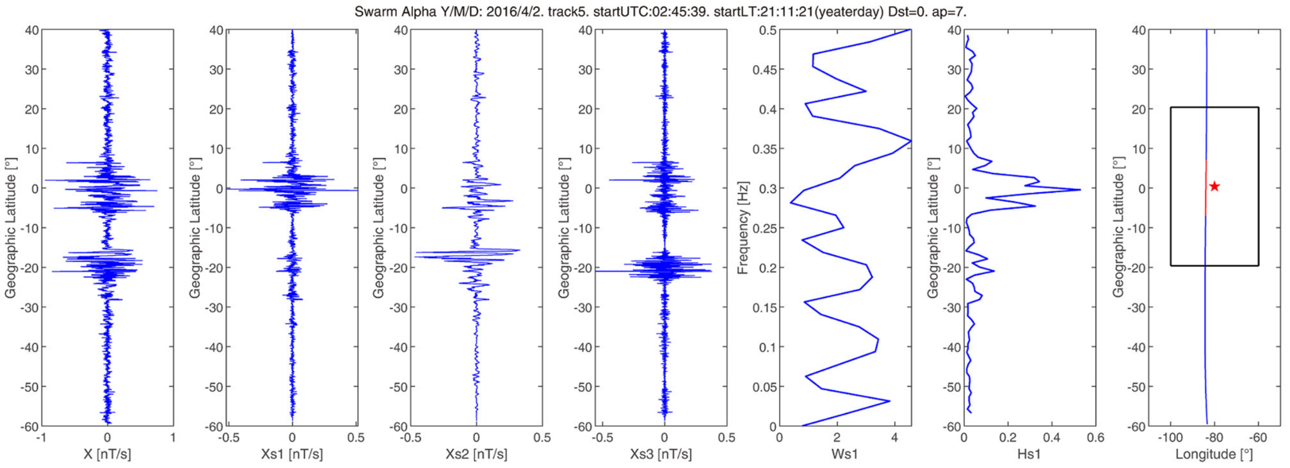

FIGURE 9 | Analysis of the anomaly closer to the epicenter of the Ecuador earthquake which occurred in the anomalous track on April 2, 2016. X represents the preprocessed East component of magnetic field data for this track. Xs1, Xs2, and Xs3 are the time-domain reconstruction signals of three decomposition component of this track. The Ws1 and Hs1 are, respectively, the feature and weight of this anomaly. The red star represents the epicenter of the Ecuador earthquake and the black square represents the earthquake-sensitive area of the earthquake. The blue line represents the flight path of this track. The short red line shows the location of this anomaly.

Investigation of Anomalies During the Accelerated Increase Phase

We investigated the anomalies extracted during the accelerated increase phase, from 26 days before the earthquake to the day of the earthquake (the anomalies in these days are more possibly related to the earthquake).

We checked the extracted anomalies one by one and found that the anomaly at track 5 on April 2, 2016, 14 days before the earthquake, is the closest anomaly to the epicenter of the Ecuador earthquake (<500 km away from the epicenter). The preprocessed East component of magnetic field data X for this anomalous track, the time-domain reconstruction signals, Xs1, Xs2, and Xs3 of the three decomposition components of this track, the feature Ws1, the weight, Hs1 and the location of this anomaly are shown in **Figure 9**. From **Figure 9**, it is clear that in Xs1, the anomaly lasted from −7° latitude to +7° latitude and the maximum value of this anomaly is almost at the same latitude of the epicenter. According to Ws1, the frequency with the highest amplitude of this anomaly is around 0.36 Hz. According to Hs1, the weight of this anomaly is surely concentrated inside the earthquake-sensitive area. Compared with Xs1, the original data X has two obvious anomalies. The northern one centered about at 0° latitude is found also in Xs1, while a double pattern is found in Xs2 and Xs3. Although these two anomalies in X are nearer and symmetrical to the geomagnetic equator (around −10° geographic latitude), the LT is 21 o'clock, they are not directly to be affected by the sunset. Moreover, the NFM technique underlines that the northern anomaly is different from the standard double pattern, which could be a residual of the daily interaction between the Sun and the ionosphere. From these results, the anomaly of Xs1 is more likely related to the earthquake.

In addition, we analyzed the relationship between the amplitude of anomalies and their distance from the epicenters, from 26 days before the earthquake to the day of the earthquake. The smallest distance from the epicenter is 465 km and the largest distance from the epicenter is 2,792 km. We divided the anomalies into three groups, according to their distance from the epicenter. For each group, we calculated the average energy of the anomalies. The relationship between the average energy of the anomalies and their distances from the epicenter is shown in **Figure 10A**. From **Figure 10A**, we can see that as the location of the anomaly is farther from the epicenter of the earthquake, the average energy of the anomaly decreased. This result is consistent with one of the standards for excellent earthquake precursors proposed by the International Association of Seismology and Physics of Earth's Interior (IASPEI) in 1991 and 1997 (Wyss, 1991, 1997; Wyss and Booth, 1997). This standard observes that "the amplitude of the observed anomaly should bear a relation to the distance from the eventual mainshock," and it is also affirmed by Rikitake and Yamazaki (1985).

The relationship between the amplitude and the time of occurrence of the anomalies was also investigated. The anomalies were divided into three groups, according to their time of occurrence. The average energy of the anomalies for each group was computed. The relationship between the average energy of the anomalies and their occurrence time is shown in **Figure 10B**. According to **Figure 10B**, at the advent of earthquake, the average energy of the anomalies increased. This result is reasonable, since generally with the advent of the earthquake, the anomalies should be stronger.

These two analyses further prove that the anomalies we extracted at the accelerated increase phase before the earthquake are likely to be related to the earthquake.

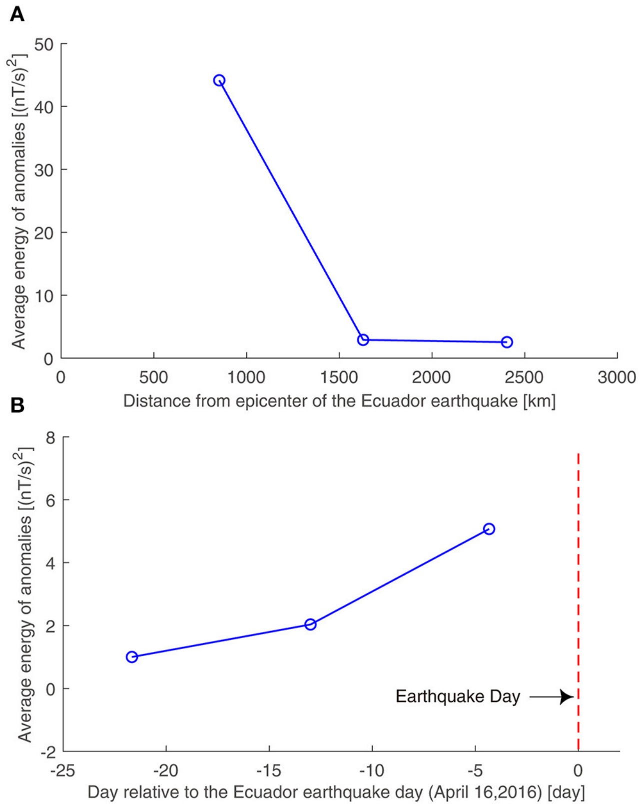

FIGURE 10 | The investigations of the average energy of the anomalies**. (A)**The relationship between the average energy of the anomalies and the distance from the epicenter of the anomalies. **(B)** The relationship between the average energy of the anomalies and the occurrence time of anomalies. The anomalies were extracted from 26 days before the earthquake to the day of the earthquake.

CONCLUSIONS

In this paper, we used the NMF to analyze the magnetic field data of Swarm Alpha satellite and explored the 2016 Mw 7.8 Ecuador earthquake, including all the observation data, regardless of the strength of the geomagnetic activity. After decomposition, we obtained three H components, and found that almost all the anomalies of one of the H components, that is the Hs1 component, occurred inside the earthquake-sensitive area, and the inside cumulative result of this component showed a clear acceleration before the Ecuador earthquake and recovered after it, which obeys the power-law behavior of a critical system (De Santis et al., 2017). By different analyses, we excluded the influence of the geomagnetic activity and the plasma bubbles on the accelerated cumulative anomaly, and proved that this anomaly was not obtained by simple chance. Moreover, we found that the accelerated cumulative anomaly for the ionosphere magnetic field data was possibly associated with the lithosphere activities before the Ecuador earthquake, which also corresponds to the LAIC effect. By investigating the anomalies, we further found that as the location of the anomaly is farther from the epicenter of the earthquake, the average energy of the anomaly decreased, and with the advent of the earthquake, the average energy of the anomalies increased. Thus, the anomalies that we extracted are possibly related to the Ecuador earthquake.

These abovementioned results show that the NMF method has the capacity to detect the local feature of the earthquake-sensitive area. For the Ecuador earthquake, based on NMF decomposition, by using all the observed magnetic field data without considering the geomagnetic activity, we obtained a weight component, whose cumulative result has an accelerated anomaly that is possibly related to the earthquake and not affected by the geomagnetic activity. This type of method could introduce a new perspective and analyze as much observation data as possible to study the earthquakes.

We suggest that our paper promotes the development from the search of anomalies that are likely to be related to earthquakes at the quiet geomagnetic conditions (which is still a difficult task) to the search of the anomalies that are likely to be related to earthquakes without considering the geomagnetic activity. We propose to address this problem with the use of NMF, but we do not exclude other methods that can more efficiently achieve the same goal.

We remind that the objective of these present analyses is not a retrospective prediction of an earthquake, but to emphasize that by NMF, we can use more data to analyze earthquakes. We would expect that using the satellite magnetic field data without considering the geomagnetic condition might be a better and more comprehensive method to understand earthquakes than using the data at quiet geomagnetic conditions alone.

In addition, further study should analyze the regular patterns among the local feature of the earthquake-sensitive area for different tracks. More case studies should be undertaken especially the investigation of other large earthquakes will be an important matter for future work.

DATA AVAILABILITY STATEMENT

Publicly available datasets were analyzed in this study. This data can be found here: Swarm data: https://swarm-diss.eo.esa.int/. The geomagnetic index: http://isgi.unistra.fr/data_download.php. The F10.7: ftp://ftp.ngdc.noaa.gov/STP/swpc_products/daily_reports/space_weather_indices. The seismic data: https://earthquake.usgs.gov/earthquakes/search/.

AUTHOR CONTRIBUTIONS

KZ conceived and designed the project, guided the writing of the manuscript, and revised the manuscript. MF worked on the data analysis, the interpretation of the data, and wrote the manuscript. XH and KL contributed to data acquisition and revised the manuscript. DM contributed to data interpretation, gave some guiding opinions, and revised the manuscript. ZY, CC, HS, and YC contributed to the data interpretation and revised the manuscript. All authors contributed to the revision of the manuscript, read, and approved the submitted version.

FUNDING

This research was supported by the National Natural Science Foundation of China under Grant No. 41974084 and the International Cooperation Project of Department of Science and Technology of Jilin Province No. 20200801036GH.

ACKNOWLEDGMENTS

The authors would like to acknowledge the European Space Agency for the Swarm data, the International Service of Geomagnetic Indices for the *Dst* index data and a_p index data, the National Oceanic Atmospheric Administration for the F10.7 data, and the United States Geological Survey for the seismic events list data. We are grateful to the College of Instrumentation and Electrical Engineering of Jilin University, the Key Laboratory of Geo-Exploration Instrumentation of the Ministry of Education in Jilin University of China, and the National Institute of Geophysics and Volcanology. We are grateful to Prof. Xuhui Shen (from the Institute of Crustal Dynamics, China Earthquake Administration), Prof. Xiuying Wang (from the Institute of Crustal Dynamics, China Earthquake Administration), and Prof. Angelo De Santis (from the Environment Department of Istituto Nazionale di Geofisica e Vulcanologia, Rome, Italy) for their contribution to this article.

REFERENCES

Agurto-Detzel, H., Font, Y., Charvis, P., Régnier, M.,Rietbrock, A., Ambrois, D., et al. (2019). Ridgesubduction and afterslip control aftershock distribution of the 2016 Mw 7.8 Ecuador earthquake. *Earthand Planet. Sci. Lett.* 520, 63–76. doi: 10.1016/j.epsl.2019.05.029

Akhoondzadeh, M., De Santis, A., Marchetti, D., Piscini, A., and Cianchini, G. (2018). Multi precursorsanalysis associated with the powerful Ecuador (Mw= 7.8) earthquake of 16 April 2016 using Swarmsatellites data in conjunction with other multi-platform satellite and ground data. *Adv. Space Res.* 61, 248–263. doi: 10.1016/j.asr.2017.07.014

Akhoondzadeh, M., De Santis, A., Marchetti, D., Piscini, A., and Jin, S. (2019). Anomalous seismo-laivariations potentially associated with the 2017 Mw=7.3 Sarpol-e Zahab (Iran) earthquake from Swarmsatellites, GPS-TEC and climatological data. *Adv. Space Res.* 64, 143–158. doi: 10.1016/j.asr.2019.03.020

Alken, P. (2016). Observations and modeling of the ionospheric gravity and diamagnetic current systemsfrom CHAMP and Swarm measurements. *J. Geophys. Res. Space Phys.* 121, 589–601. doi: 10.1002/2015ja022163

Benioff, H. (1949). Seismic evidence for the fault origin of oceanic deeps. *Bull. Geol. Soc. Am.* 60, 1837–1856. doi: 10.1130/0016-7606(1949)60[1837:SEFTFO]2.0.CO;2

Bolt, B. A. (1999). *Earthquake.* NewYork, NY: W. H. Freeman.

Bouffard, J., Floberghagen, R., and Olsen, N. (2019). *The Swarm Satellite Trio Studies Earth and* Its *Environment*. EOS.

Cichocki, A., Zdunek, R., and Amari, S. (2006). "New algorithm for non-negative matrix factorization inapplication to blind source separation," in *Proceedings of ICASSP'06* (Toulouse: IEEE Press), 621–624.

De Santis, A., Abbattista, C., Alfonsi, L., Amoruso, L., Campuzano, S. A., Carbone, M., et al. (2019a). Geosystemics view of earthquakes. *Entropy* 21:412. doi: 10.3390/e21040412

De Santis, A., Balasis, G., Pavón-Carrasco, F. J., Cianchini, G., and Mandea, M. (2017). Potential earthquake precursory pattern from space: the 2015 Nepal event as seen by magnetic Swarm satellites. *Earth Planet. Sci. Lett.* 461, 119–126. doi: 10.1016/j.epsl.2016.12.037

De Santis, A., De, F., G., Spogli, L., Perrone, L., Alfonsi, L., Qamili, E., et al. (2015). Geospaceperturbations induced by the earth: the state of the art and future trends. *Phys. Chem. Earth* 85–86, 17–33. doi: 10.1016/j.pce.2015.05.004

De Santis, A., Marchetti, D., Pavon-Carrasco, F. J., Cianchini, G., Perrone, L., Abbattista, C., et al. (2019b). Precursory worldwide signatures of earthquake occurrences on Swarm satellite data. *Sci. Rep.* 9:20287. doi: 10.1038/s41598-019-56599-1

De Santis, A., Marchetti, D., Spogli, L., Cianchini, G., Pavón-Carrasco, F. J., Franceschi, G. D., et al. (2019c). Magnetic field and electron density data analysis from Swarm satellites searching for ionosphericeffects by great earthquakes: 12 case studies from 2014 to 2016. *Atmosphere* 10:371. doi: 10.3390/atmos10070371

D'Errico, J. (2021). *SLM - Shape Language Modeling, MATLAB Central File Exchange.* Available online at: https://www.mathworks.com/matlabcentral/fileexchange/24443-slm-shape-language-modeling (accessed February 23, 2021).

Dobrovolsky, I. R., Zubkov, S. I., and Myachkin, V. I. (1979). Estimation of the size of earthquakepreparation zones. *Pure Appl. Geophys.* 117, 1025–1044. doi: 10.1007/BF00876083

Finlay, C. C., Olsen, N., Kotsiaros, S., Gillet, N., and Tøffner-Clausen, L. (2016). Recent geomagneticsecular variation from Swarm and ground observatories as estimated in the CHAOS-6 geomagnetic fieldmodel. *Earth Planets Space* 68:112. doi: 10.1186/s40623-016-0486-1

Finlay, C. C., Olsen, N., and Tøffner-Clausen, L. (2015). DTU candidate field models for IGRF-12 and theCHAOS-5 geomagnetic field model. *Earth Planets Space* 67:114. doi: 10.1186/s40623-015-0274-3

Freund, F. (2000). Time-resolved study of charge generation and propagation in igneous rocks. *J. Geophys. Res. Solid Earth* 105, 11001–11019. doi: 10.1029/1999JB900423

Freund, F. (2011). Pre-earthquake signals: underlying physical processes. *J. Asian Earth Sci.* 41, 383–400. doi: 10.1016/j.jseaes.2010.03.009

Friis-Christensen, E., Lühr, H., and Hulot, G. (2006). Swarm: a constellation to study the Earth's magneticfield. *Earth Planets Space* 58, 351–358. doi: 10.1186/BF03351933

Friis-Christensen, E., Lühr, H., Knudsen, D., and Haagmans, R. (2008). Swarm - an earth observationmissioninvestigatinggeospace. *Adv. Space Res.* 41, 210–216. doi: 10.1016/j.asr.2006.10.008

Fu, C., Lee, L., Ouzounov, D., and Jan, J. (2020). Earth's outgoing longwave radiation variability prior to $M \geq 6.0$earthquakes in the Taiwan area during 2009-2019. *Front. Earth Sci.* 8:364. doi: 10.3389/feart.2020.00364

Han, P., Hattori, K., Hirokawa, M., Zhuang, J., Chen, C., Febriani, F., et al. (2014). Statistical analysis ofULF seismomagnetic phenomena at Kakioka, Japan, during 2001-2010. *J. Geophys. Res. Space Phys.* 119, 4998–5011. doi: 10.1002/2014JA019789

Hattori, K., and Han, P. (2018). "Statistical analysis and assessment of ultralow frequency magnetic signals inJapan as potential earthquake precursors," in *Pre-earthquake Processes: A Multidisciplinary Approach toEarthquake Prediction Studies*, eds D. Ouzounov, S. Pulinets, K. Hattori, and P. Taylor (Hoboken, NJ: John Wiley & Sons), 229–240.

Hattori, K., Serita, A., Gotoh, K., Yoshino, C., Harada, M., Isezaki, N., et al. (2004). ULF geomagneticanomaly associated with 2000 Izu Islands earthquake swarm, Japan. *Phys. Chem. Earth Parts A B C* 29, 425–435. doi: 10.1016/j.pce.2003.11.014

Hayakawa, M. (2011). On the fluctuation spectra of seismo-electromagnetic phenomena. *Nat. Hazards Earth Syst. Sci.* 11, 301–308. doi: 10.5194/nhess-11-301-2011

Hayakawa, M., and Molchanov, O. A. (2002). *Seismo Electromagnetics Lithosphere-Atmosphere-Ionosphere Coupling.* Tokyo: TERRA-PUB.

Ho, Y., Jhuang, H., Lee, L., and Liu, J. (2018). Ionospheric density and velocity anomalies before $M \geq 6.5$ earthquakes observed by DEMETER satellite. *J. Asian Earth Sci.* 166, 210–222. doi: 10.1016/j.jseaes.2018.07.022

Kuo, C. L., Lee, L. C., and Huba, J. D. (2014). An improved coupling model for the lithosphere-atmosphere-ionosphere system. *J. Geophys. Res.:Space Phys.* 119, 3189–3205, doi: 10.1002/2013JA019392

Lee, D. D., and Seung, H. S. (1999). Learning the parts of objects by non-negative matrix factorization. *Nature* 401, 788–791.

Lee, D. D., and Seung, H. S. (2000). “Algorithms for non-negative matrix Factorization,” in *International Conference on Neural Information Processing Systems*, NIPS (Denver, CO: MIT Press), 556–562.

Li, M., Lu, J., Zhang, X., and Shen, X. (2019). Indications of ground-based electromagnetic observationsto a possible lithosphere-atmosphere-ionosphere electromagnetic coupling before the 12 May 2008 Wenchuan Ms 8.0 earthquake. *Atmosphere* 10:355. doi: 10.3390/atmos10070355

Liu, J. Y., Chen, Y. I., Huang, C. C., Parrot, M., Shen, X. H., Pulinets, S. A., et al. (2015). A spatial analysison seismo-ionospheric anomalies observed by DEMETER during the 2008 M8.0 Wenchuan earthquake. *J. Asian Earth Sci.* 114, 414–419. doi: 10.1016/j.jseaes.2015.06.012

Marchetti, D., and Akhoondzadeh, M. (2018). Analysis of Swarm satellites data showing seismo-ionosphericanomalies around the time of the strong Mexico (mw=8.2) earthquake of 08 September 2017. *Adv. Space Res.* 62, 614–623. doi: 10.1016/j.asr.2018.04.043

Marchetti, D., De Santis, A., D’Arcangelo, S., Poggio, F., Jin, S., Piscini, A., et al. (2019a). Magneticfield and electron density anomalies from Swarm satellites preceding the major earthquakes of the2016-2017 Amatrice-Norcia (central italy) seismic sequence. *Pure Appl. Geophys.* 177, 305–319. doi: 10.1007/s00024-019-02138-y

Marchetti, D., De Santis, A., D’Arcangelo, S., Poggio, F., Piscini, A., A., et al. (2019b). Pre-earthquake chain processes detected from ground to satellite altitude in preparation of the 2016-2017seismic sequence in central Italy. *Remote Sens. Environ.* 229, 93–99. doi: 10.1016/j.rse.2019.04.033

Marchetti, D., De Santis, A., Shen, X., Campuzano, S. A., Perrone, L., Piscini, A., et al. (2019c). Possiblelithosphere-atmosphere-ionosphere coupling effects prior to the 2018 Mw=7.5 Indonesia earthquakefrom seismic, atmospheric and ionospheric data. *J. Asian Earth Sci.* 188:104097. doi: 10.1016/j.jseaes.2019.104097

Mouri, M., Funase, A., Cichocki, A., Takumi, I., Yasukawa, H., and Hata, M. (2009). “Implementation of matrix factorization based onminimizing quasi-absolute distance for electromagnetic global signal elimination,” in *17th Europe SignalProcessing Conference* (Glasgow: EUSIPCO), 24–28.

Natarajan, V., and Philipoff, P. (2018). Observation of surface and atmospheric parameters using “NOAA 18”satellite: a study on earthquakes of Sumatra and Nicobar Is regions for the year 2014 ($M \geq 6.0$). *Nat. Hazards* 92, 1097–1112. doi: 10.1007/s11069-018-3242-y

Olsen, N., Friis-Christensen, E., Floberghagen, R., Alken, P., Beggan, C. D., Chulliat, A., et al. (2013). The Swarm Satellite Constellation Application and Research Facility (SCARF) and Swarm data products. *Earth Planets Space* 65, 1189–1200. doi: 10.5047/eps.2013.07.001

Olsen, N., Haagmans, R., Sabaka, T. J., Kuvshinov, A., Maus, S., Purucker, M. E., et al. (2006). The SwarmEnd-to-End mission simulator study: a demonstration of separating the various contributions to Earth’smagnetic field using synthetic data. *Earth Planets Space* 60, 359–370. doi: 10.1186/BF03351934

Paatero, P., and Tapper, U. (1994). Positive matrix factorization: a non-negative factor model with optimalutilization of error estimates of data values. *Environmetrics* 5, 111–126. doi: 10.1002/env.3170050203

Park, J., Noja, M., Stolle, C., and Lühr, H. (2013). The ionospheric Bubble Index deduced from magnetic field and plasma observations onboard Swarm. *Earth Planets Space* 65, 1333–1344. doi: 10.5047/eps.2013.08.005

Parrot, M. (1995). Use of satellites to detect seismo-electromagnetic effects. *Adv. Space Res.* 15, 27–35. doi: 10.1016/0273-1177(95)00072-M

Parrot, M. (2011). Statistical analysis of the ion density measured by the satellite DEMETER in relation withthe seismic activity. *Earthquake Sci.* 24, 513–521. doi: 10.1007/s11589-011-0813-3

Perrone, L., De Santis, A., Abbattista, C., Alfonsi, L., Amoruso, L., Carbone, M., et al. (2018). Ionosphericanomalies detected by ionosonde and possibly related to crustal earthquakes in Greece. *Ann. Geophys.* 36, 361–371. doi: 10.5194/angeo-36-361-2018

Pinheiro, K. J., Jackson, A., and Finlay, C. C. (2011). Measurements and uncertainties of the occurrencetime of the 1969, 1978, 1991, and 1999 geomagnetic jerks. *Geochem. Geophys. Geosyst.* 12:Q10015. doi: 10.1029/2011GC003706

Piscini, A., Marchetti, D., and De Santis, A. (2019). Multi-parametric climatological analysis associatedwith global significant volcanic eruptions during 2002-2017. *Pure Appl. Geophys.* 176, 3629–3647. doi: 10.1007/s00024-019-02147-x

Pulinets, S., and Boyarchuk, K. (2005). *Ionospheric Precursors of Earthquakes.* New York, NY: Springer-Verlag Berlin Heidelberg.

Pulinets, S., and Ouzounov, D. (2011). Lithosphere-Atmosphere-Ionosphere Coupling (LAIC) model –anunified concept for earthquake precursors validation. *J. Asian Earth Sci.* 41, 371–382. doi: 10.1016/j.jseaes.2010.03.005

Rikitake, T., and Yamazaki, Y. (1985). “The nature of resistivity precursor,” in *Practical Approaches to Earthquake Prediction and Warning*, eds C. Kisslinger and T. Rikitake (Dordrecht: Springer), 559–570.

Schachtner, R., Pöppel, G., Tomé, A. M., and Lang, E. W. (2009). “Minimum determinant constraint for non-negative matrix factorization,” in *Independent Component Analysis and Signal Separation*, ICA (Paraty), 106–113.

Shannon, C. (2001). A mathematical theory of communication. *ACM SIGMOBILE Mobile Comput. Commun. Rev.* 5, 3–55. doi: 10.1145/584091.584093

Shcherbakov, R., Zhuang, J., Zöller, G., and Ogata, Y. (2019). Forecasting the magnitude of the largestexpected earthquake. *Nat. Commun.* 10:4051. doi: 10.1038/s41467-019-11958-4

Shen, X., Zhang, X., Yuan, S., Wang, L., Cao, J., Huang, J., et al. (2018). The state-of-the-art of theChina Seismo-Electromagnetic Satellite mission. *Scie. China Technol. Sci.* 61, 634–642. doi: 10.1007/s11431-018-9242-0

Smaragdis, P. (2004). “Non-negative matrix factor deconvolution; extraction of multiple sound sourcesfrom monophonic inputs,” in *International Conference on Independent Component Analysis and Signal Separation* (Granada), 494–499.

Smaragdis, P., and Brown, J. (2003). “Non-negative matrix factorization for polyphonic music transcription,” in *IEEE Workshop on Applications of Signal Processing to Audio and Acoustics* (New Paltz).

Wang, H., He, Y., Lühr, H., Kistler, L., Saikin, A., Lund, E., et al. (2019). Storm time EMIC waves observedby Swarm and Van Allen Probe satellites. *J. Geophys. Res. Space Phys.* 124, 293–312. doi: 10.1029/2018JA026299

Wyss, M. (1991). Evaluation of proposed earthquake precursors. *Eos Transac. Am. Geophys. Union* 72:411. doi: 10.1029/90EO10300

Wyss, M. (1997). Second round of earthquake of proposed earthquake precursors. *Pure Appl. Geophys.* 149, 3–16. doi: 10.1007/BF00945158

Wyss, M., and Booth, D. C. (1997). The IASPEI procedure for the evaluation of earthquake precursors. *Geophys. J. Int.* 131, 423–424. doi: 10.1111/j.1365-246X.1997.tb06587.x

Xie, W., Hattori, K., and Han, P. (2019). Temporal variation and statistical assessment of the b value offthe pacific coast of Tokachi, Hokkaido, Japan. *Entropy* 21:249. doi: 10.3390/e21030249

Yan, R., Wang, L., Hu, Z., Liu, D., Zhang, X., and Zhang, Y. (2013). Ionospheric disturbances before and afterstrong earthquakes based on DEMETER data. *Acta Seismol. Sin.* 35, 498–511. doi: 10.1155/2013/530865

Yizengaw, E., and Groves, K. M. (2018). Longitudinal and seasonal variability of equatorial ionosphericirregularities and electrodynamics. *Space Weather* 16, 946–968. doi: 10.1029/2018SW001980

Zhang, X., Qian, J., Ouyang, X., Shen, X., Cai, J., and Zhao, S. (2009). Ionospheric electromagneticperturbations observed on DEMETER satellite before Chile M7.9 earthquake. *Earthquake Sci.* 22, 251–255. doi: 10.1007/s11589-009-0251-7

Zhang, X., Zhao, S., Song, R., and Zhai, D. (2019). The propagation features of LF radio waves at topsideionosphere and their variations possibly related to Wenchuan earthquake in 2008. *Adv. Space Res.* 63, 3536–3544. doi: 10.1016/j.asr.2019.02.008

Zhima, Z., Cao, J., Liu, W., Fu, H., Wang, T., Zhang, X., et al. (2014). Storm time evolution of ELF/VLFwaves observed by DEMETER satellite. *J. Geophys. Res. Space Phys.* 119, 2612–2622. doi: 10.1002/2013JA019237

Zhima, Z., Hu, Y., Piersanti, M., Shen, X., De Santis, A., Yan, R., et al. (2020). The seismic electromagnetic emissions during the 2010 Mw 7.8 Northern Sumatra earthquake revealed by DEMETER satellite. *Front. Earth Sci.* 8. doi: 10.3389/feart.2020.572393

Zhu, K., Li, K., Fan, M., Chi, C., and Yu, Z. (2019). Precursor analysis associated with the Ecuadorearthquake using swarm a and c satellite magnetic data based on PCA. *IEEE Access* 7, 93927–93936. doi: 10.1109/ACCESS.2019.2928015

Conflict of Interest: The authors declare that the research was conducted in the absence of any commercial or financial relationships that could be construed as a potential conflict of interest.

frontiers in Earth Science

BRIEF RESEARCH REPORT
published: 14 May 2021
doi: 10.3389/feart.2021.658825

Development and Preliminary Analysis of a VLF-Band Electromagnetic-Wave Observation System for Short-Term Earthquake Precursory Monitoring

Toshiyasu Nagao[1]*, *Masashi Kamogawa*[2], *Jun Izutsu*[3], *Tomoyuki Suzuki*[2], *Airi Saito*[4], *Shigeki Sugiura*[5] and *Hitoshi Kondo*[5]

[1]*Institute of Oceanic Research and Development, Tokai University, Shizuoka, Japan,* [2]*Global Center for Asian and Regional Research, University of Shizuoka, Shizuoka, Japan,* [3]*International Digital Earth Applied Science Research Center, Chubu University, Kasugai, Japan,* [4]*School of Marine Science and Technology, Tokai University, Shizuoka, Japan,* [5]*Genesis Research Institute, Inc., Nagoya, Japan*

OPEN ACCESS

Edited by:
Dimitar Ouzounov,
Chapman University, United States

Reviewed by:
Pier Francesco Biagi,
University of Bari Aldo Moro, Italy
Zeren Zhima,
Ministry of Emergency Management (China), China
Michel Parrot,
UMR7328 Laboratoire de physique et chimie de l'environnement et de l'Espace (LPC2E), France

***Correspondence:**
Toshiyasu Nagao
nagao@scc.u-tokai.ac.jp

Specialty section:
This article was submitted to Geo hazards and Georisks, a section of the journal Frontiers in Earth Science

Received: *27 January 2021*
Accepted: *29 April 2021*
Published: *14 May 2021*

Citation:
Nagao T, Kamogawa M, Izutsu J, Suzuki T, Saito A, Sugiura S and Kondo H (2021) Development and Preliminary Analysis of a VLF-Band Electromagnetic-Wave Observation System for Short-Term Earthquake Precursory Monitoring.
Front. Earth Sci. 9:658825.
doi: 10.3389/feart.2021.658825

Preseismic VLF electromagnetic pulses occasionally increase a few days before large earthquakes, especially inland earthquakes. More than two decades ago, the Tokai University group developed a digital recording system for collecting the preseismic electromagnetic pulse data and showed remarkable results. However, due to the limitations of personal computers' data storage and CPU power during that time, they discontinued the observation. We relaunched this research using current technology. This paper shows the development of the new observation system and presents preliminary results. In addition, we introduce an electromagnetic-wave arrival discrimination algorithm that combines the autoregressive model and the Akaike information criterion, which are commonly used for automatic waveform reading in seismology, to obtain accurate data on the time of arrival (TOA) of electromagnetic waves. Then, source positioning was performed using TOA of electromagnetic waves. Seven electromagnetic pulses near the epicenter were observed 2 days before the largest inland earthquake (M = 5.6) that occurred near the observation network during the observation period (2016–2020). These VLF pulses may be a seismic precursory phenomenon because they were not electromagnetic pulses originating from lightning. These results encourage future observations.

Keywords: earthquake prediction, precursor, VLF, AIC, lightning

INTRODUCTION

Many Japanese seismologists, having experienced the Tohoku Earthquake in 2011 and the Kobe Earthquake in 1995, are extremely pessimistic about realizing the earthquake prediction. The authors highlight the problem that research on short-term prediction, such as that involving one day or one week, which is the most useful, is rarely conducted at the national level.

Various electromagnetic-precursory phenomena of earthquakes have been reported (e.g., Gokhberg et al., 1982; Warwick et al., 1982; Fraser-Smith et al., 1990; Nagao et al., 2019); in Japan, an increase in electromagnetic noise is claimed to occur just before an earthquake. When the Mikawa Earthquake occurred in 1945 (M = 6.8), the radio was always broadcast to allow people to listen to air-raid warnings during World War II. A rumor has circulated that one can recognize an impending earthquake by listening to radio noise that occurs before an aftershock. A pioneering study was conducted by Professor Kazuo Oike of Kyoto University (Oike and Ogawa, 1986; Oike and Yamada, 1994).

Oike and his group reported the results of inland earthquakes with a magnitude of six or greater. An LF band noise was observed for a few days (in particular, two days) before the earthquakes. Although most LF band noises have been interpreted to originate from lightning, Oike mentioned that the peak of noises before an earthquake may include earthquake-precursory electromagnetic signals. Intense LF-VLF pulses were observed just before the 1995 Kobe Earthquake (Yamada and Oike, 1996; Nagao et al., 2002; Izutsu and Oike, 2003; Izutsu, 2007).

More than two decades ago, the Tokai University group developed a digital waveform recording system and showed remarkable results (Asada et al., 2001). However, given the limitations of personal computers' data storage and CPU power during the time, they discontinued the observation. We relaunched the research using current technology. This paper is a follow-up of the research led by Asada et al. (2001), which had been suspended for 2 decades. The observation was conducted as a part of the national earthquake prediction research project by using the most advanced digital technology in the 21st century.

OBSERVATION AND ANALYSIS

We faithfully reproduced the coil sensor used by Asada et al. (2001) because promising results were obtained. The research should be relaunched using coil sensors with the same frequency characteristics, given that the electromagnetic waves preceding an earthquake is unknown. The sensor wounds a 0.6 ΦPEW wire (polyester enameled wire) around the ferrite core 600 times. The inductance of the coil is 25 mH. An antenna having almost the same frequency characteristics as the antenna produced by Asada et al. (2001) was reproduced. A detailed technical description is presented by Nagao et al. (2016). The A/D converter used by Asada et al. (2001) was 12 bits and two channels at 1 MHz sampling. In this observation, we used a 12-bit, six-channel, 100 MHz sampling A/D converter. This A/D converter was originally developed for the measurement of gamma rays, X-rays, muons, etc.

Asada and his group analyzed only the linearly polarized magnetic components of electromagnetic waves to conduct direction findings via the Goniometer method. However, in our system, the source can be determined based on the time of arrival (TOA) of electromagnetic waves. The theoretical spatial resolution (1 least significant bit [LSB] = 10^{-8} Hz) at a 100 MHz sampling is 3 m. Therefore, a time synchronization system using GPS was adopted to maintain the accuracy of the clock, and a time accuracy of 10 ns at the maximum and 2–3 ns in most cases could be obtained (Nagao et al., 2016).

In this project, two prototypes were developed in 2014. The routine observation started in November 2015 at three stations. The five-station operation (**Figure 1**) has been conducted since May 2017. The stations are located at Tokyo Gakugei University in Koganei city (kgn: 35.7052°N, 139.4906°E), Tokai University in Shimizu city (smz: 34.9900°N, 138.5140°E), Kanazawa University in Kanazawa city (knz: 36.5440°N, 136.7042°E), Shinshu

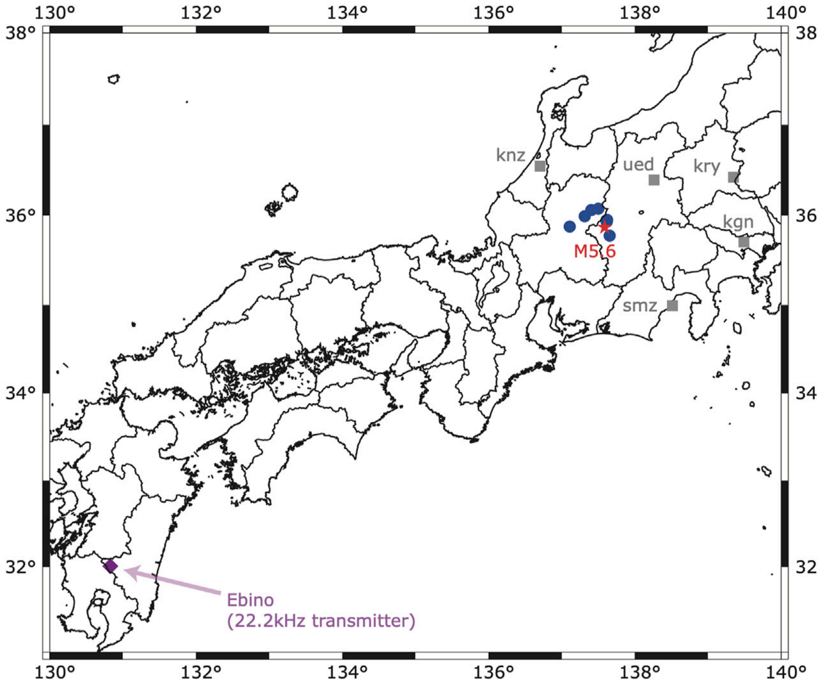

FIGURE 1 | Locations of the five observation stations (gray square) and the epicenter of the earthquake (red star) on June 25, 2017 (M5.6, focal depth = 7 km). The blue solid circles are the source locations of possible precursory electromagnetic waves. The purple rhombus denotes the VLF transmitter at Ebino.

University in Ueda city (ued: 36.3913°N, 138.2635°E), and Gunma University in Kiryu city (kry: 36.4241°N, 139.3490°E).

In this observation, the acquisition of triggering data was designed at 1 and 9 ms before and after the trigger time, respectively. Given the test observation results (**Figure 2**), we confirmed that the radio wave of 22.2 kHz transmitted from the Ebino (**Figure 1**) for the Self-Defense Forces communication for submarines was also accurately observed.

As mentioned above, the sampling rate of 100 MHz indicates that the spatial resolution of the theoretical 1 LSB is 3 m. The TOA method allows the determination of the position of an electromagnetic wave source by using the trigger time as the TOA. However, the expected TOA was earlier than the recorded trigger time when the signal intensity was close to the background noise. Note that the trigger time was recorded when the signal intensity exceeded a certain threshold.

RESULTS AND DISCUSSION

Asada et al. (2001) only selected the linearly polarized horizontal magnetic component of electromagnetic waves for analysis when the correlation coefficient between two horizontal magnetic components was more than 0.9 (H. Baba, personal communication) and then estimated the source position by using a goniometer method. However, given that this observation was a test observation, we decided to conduct the observation on the rooftop of the university where our research collaborators were located. We found that the electromagnetic wave of elliptical polarization was observed much more than the electromagnetic wave of linear polarization. The electromagnetic field was possibly distorted because other antennas and outdoor units of air conditioners were installed on the roof. We do not know the exact reason so far.

For electromagnetic waves with a large intensity, such as lightning activity, the source location can be accurately determined via the simple TOA method, even when the trigger time is used as the TOA of the electromagnetic wave. However, when the intensity of the electromagnetic wave was small, we observed cases where the source could not be determined well when the trigger time was used as the TOA of the electromagnetic wave.

To solve this problem, we developed a system that uses the autoregressive model and Akaike's information criterion (AIC),

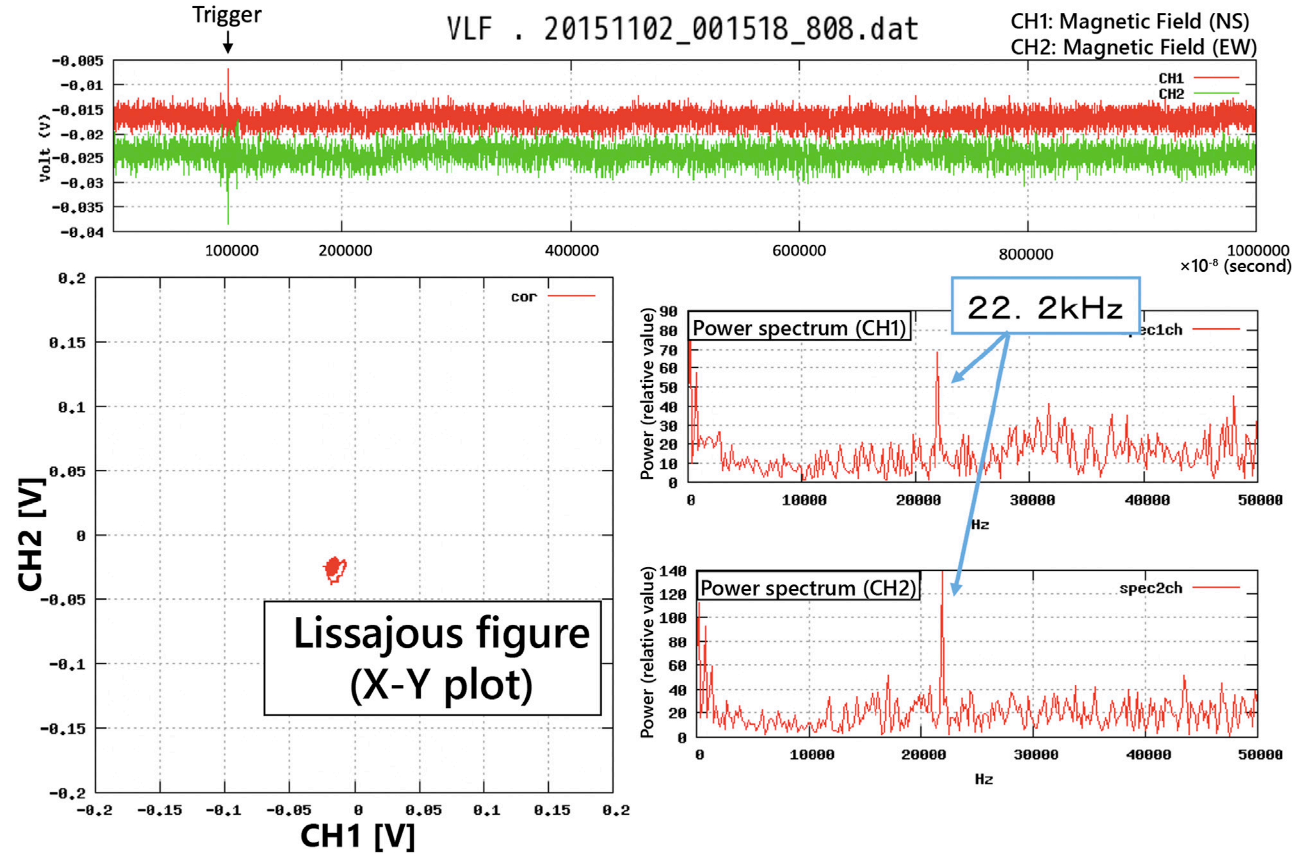

FIGURE 2 | Output image of the observed electromagnetic waveforms and power spectrums (Top) Observed waveforms. CH1 (red line) shows the north-south (NS) component of the observed magnetic field, and CH2 (green line) shows the east-west (EW) component. Waveforms were recorded 1 ms before and 9 ms after triggering during this test period (Lower left) A Lissajous figure (X–Y plot) of the observed electromagnetic wave (Lower right) Power spectrums of CH1 and CH2. A peak at 22.2 kHz was caused by the electromagnetic waves transmitted from Ebino, as shown in **Figure 1**.

which are commonly used in seismology (Akaike, 1974), to automatically determine the TOAs of electromagnetic waves (Takanami and Kitagawa, 1988; Takanami and Kitagawa, 1991). AIC is described as follows:

$$\text{AIC}\ (\text{M}) = -2\text{MLL}\ (\text{M}) + 2k$$

Where MLL (M) is the maximum log-likelihood for the data M, and k is a term of the number of parameters, which corresponds to a penalty when the model is complicated. It is considered the most probable model for data when the value of AIC takes a minimum value. In this study, we calculated the AIC by generating 1 MHz data for the combined output of two horizontal components of the magnetic field (**Figure 3**).

An M5.6 earthquake occurred at 07:02 JST on June 25, 2017, with a focal depth of 7 km. This is the largest earthquake that occurred in the vicinity of the observation network during the observation period. We applied AIC analyses for the data from 0 to 5 days before the earthquake, which empirically demonstrated the most probable period by Asada et al. (2001), Oike and Ogawa (1986), and Oike and Yamada (1994). We identified seven pulses within 30 km of the epicenter only two days before the earthquake on June 23 (**Figure 1**). These results agreed with those of Oike and Ogawa (1986), Oike and Yamada (1994), and Asada et al. (2001).

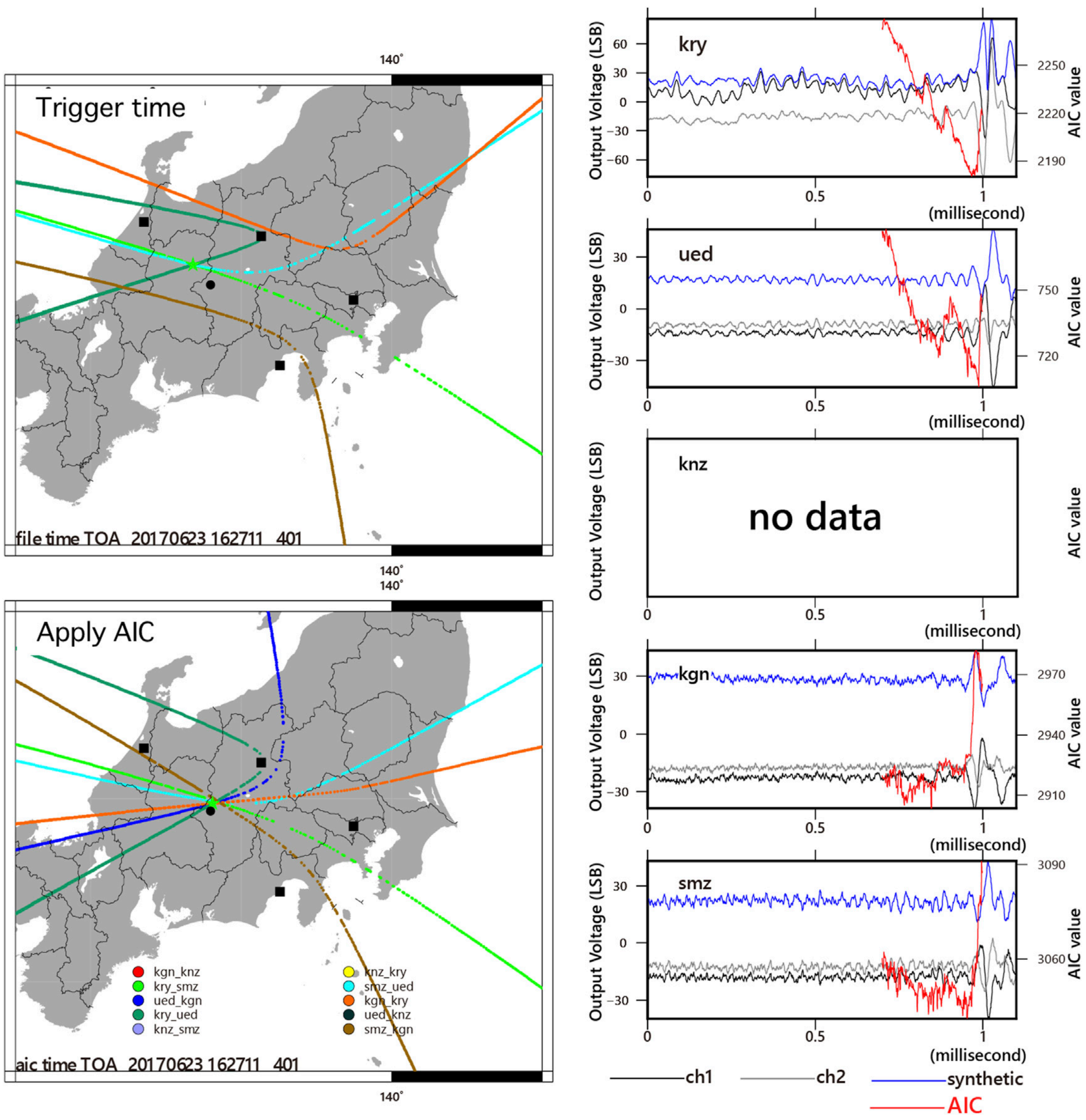

FIGURE 3 | Example of source location identification via the time of arrival (TOA) method. The trigger time is assumed to be equal to the TOA of an electromagnetic wave (upper left panel). In this case, three hyperbolas intersect at one point, but other hyperbolas do not contribute to the intersection. The electromagnetic wave TOA is the time at which the AIC is minimized. All six hyperbolas intersect at one point (lower left panel). It is an equivalent method to estimate the hypocenter based on the initial motion of the seismic wave in seismology. The right panels show the waveform data of kry, ued, knz (no data), kgn, and smz from the top. These waveforms were triggered at the point of 1 ms. The calculated AIC is displayed as a red line. The time when AIC becomes minimum is defined as the TOA of an electromagnetic wave.

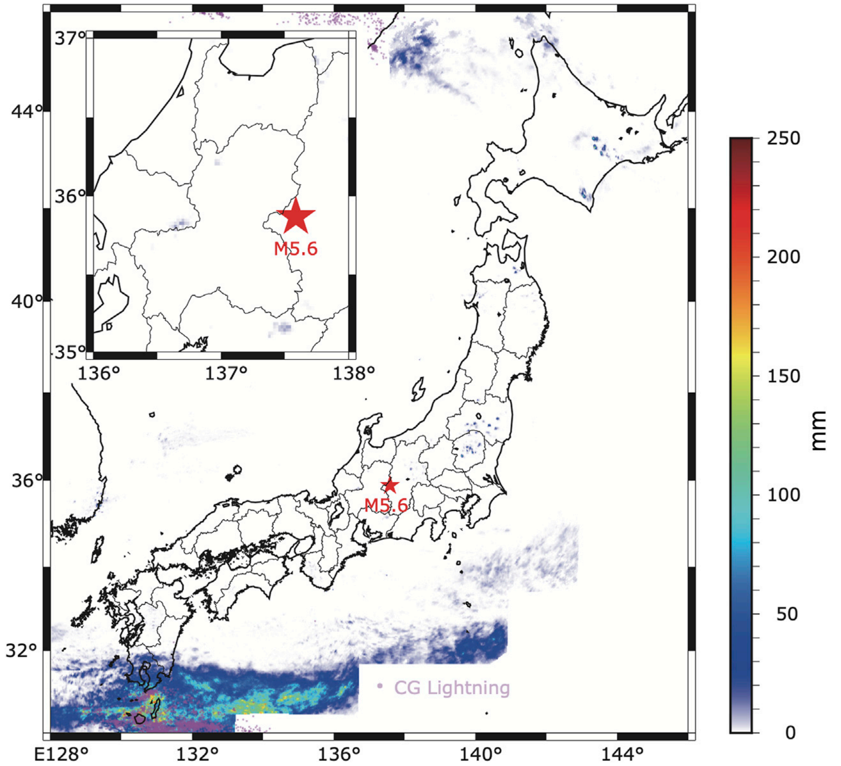

FIGURE 4 | Composite radar echo and lightning map from 03:00 to 21:00 June 23, 2017 (JST). This time period includes the occurrence time of seven pulses. The composite radar echo provided by JMA corresponds to the total rainfall at the 2 km altitude during the period. Note that the radar echo away from the inland of Japan was not provided. The CG lightning was provided by the WWLLN. A star denotes the epicenter of the earthquake on June 25, 2017. The magnified figure near the epicenter is shown in the upper left panel. No lightning was detected around the epicenter.

No pulse was identified within 30 km of the epicenter on any other day.

Clearly, the largest source of electromagnetic waves observed in the VLF-band was lightning. The purple dots in **Figure 4** indicate the cloud-to-ground (CG) lightning from 3:00 JST to 21:00 JST on June 23, 2017, measured at the World Wide Lightning Location Network (Dowden et al., 2002; Holzworth et al., 2019). The composite radar echo corresponding to the rainfall at 2 km altitude was provided by the Japan Meteorological Agency to confirm the thunderstorm, as shown in **Figure 4**. Therefore, we concluded that no lightning activity occurred near the epicenter.

We also confirmed that the observed record as linear polarization was little. A vertical electric field observation for the derivation of the Poynting vector for determining the electromagnetic wave arrival direction was also carried out at some observation stations. The analysis of elliptically polarized electromagnetic waves will also be carried out in the future. The trigger level could not be lowered further in the environment of the current university rooftop, and the measurement system will be transferred to an observation station with less noise in the future. Furthermore, the very small pulse numbers were due to the tightened intersections of hyperbolas.

CONCLUSION

In this paper, the performance of our observation system was investigated using data on lightning location, radar, and artificial radio waves. On June 23, 2017, two days before the occurrence of an M5.6 earthquake, electromagnetic pulses originating from the vicinity of the epicenter were observed, although the pulse number was at most seven. Given that the pulses did not originate from lightning, we concluded that the seven pulses were highly possibly earthquake precursors.

DATA AVAILABILITY STATEMENT

The VLF electromagnetic data was stored by Tokai University (TS). The lightning data was provided by the the World Wide Lightning Location Network (WWLLN; http://wwlln.net), a collaboration among over 50 universities and institutions, for providing the lightning location data used in this paper. The composite radar echo was provided by Japan Meteorological Agency.

AUTHOR CONTRIBUTIONS

The VLF electromagnetic observation network for the earthquake precursor study was operated by TN, MK, and JI. The analysis was conducted by TN, MK, JI, TS, and AS. The interpretation and discussion were conducted by TN, MK, JI, TS, AS, SS, and HK. All authors contributed in writing the text.

FUNDING

The equipment was developed with full support from the Ministry of Education, Culture, Sports, Science and Technology (MEXT) of Japan under its “The Second Earthquake and Volcano Hazards Observation and Research Program” (Earthquake and Volcano Hazard Reduction Research), which started in 2015, and Genesis Research Institute, Inc. The lightning analysis was supported partly by JSPS KAKENHI (Grant Number 20H02419).

ACKNOWLEDGMENTS

The AIC software was provided by T. Takanami. The authors thank E. Arakawa (Tokyo Gakugei University), K. Motojima (Gunma University), M. Ozaki (Kanazawa University), T. Yamabe and Y. Enomoto (Shinshu University) for maintaining the observation. The authors' thanks are extended to H. Baba for his useful advice through the research.

SUPPLEMENTARY MATERIAL

The Supplementary Material for this article can be found online at: https://www.frontiersin.org/articles/10.3389/feart.2021.658825/full#supplementary-material

REFERENCES

Akaike, H. (1974). A New Look at the Statistical Model Identification. *IEEE Trans. Automat. Contr.* 19, 716–723. doi:10.1109/tac.1974.1100705

Asada, T., Baba, H., Kawazoe, M., and Sugiura, M. (2001). An Attempt to Delineate Very Low Frequency Electromagnetic Signals Associated with Earthquakes. *Earth Planet. Sp.* 53, 55–62. doi:10.1186/bf03352362

Dowden, R. L., Brundell, J. B., and Rodger, C. J. (2002). VLF Lightning Location by Time of Group Arrival (TOGA) at Multiple Sites. *J. Atmos. Solar-Terrestrial Phys.* 64 (7), 817–830. doi:10.1016/s1364-6826(02)00085-8

Fraser-Smith, A. C., Bernardi, A., McGill, P. R., Ladd, M. E., Helliwell, R. A., and Villard, O. G., Jr. (1990). Low-frequency Magnetic Field Measurements Near the Epicenter of the Ms7.1 Loma Prieta Earthquake. *Geophys. Res. Lett.* 17, 1465–1468. doi:10.1029/gl017i009p01465

Gokhberg, M. B., Morgounov, V. A., Yoshino, T., and Tomizawa, I. (1982). Experimental Measurement of Electromagnetic Emissions Possibly Related to Earthquakes in Japan. *J. Geophys. Res.* 87 (B9), 7824–7828. doi:10.1029/jb087ib09p07824

Holzworth, R. H., McCarthy, M. P., Brundell, J. B., Jacobson, A. R., and Rodger, C. J. (2019). Global Distribution of Superbolts. *J. Geophys. Res. Atmos.* 124, 9996–10005. doi:10.1029/2019jd030975

Izutsu, J. (2007). Influence of Lightning on the Observation of Seismic Electromagnetic Wave Anomalies. *Terr. Atmos. Ocean. Sci.* 18 (5), 923–950. doi:10.3319/tao.2007.18.5.923(t)

Izutsu, J., and Oike, K. (2003). The Waveforms of VLF Electromagnetic Waves Recorded at the Time of the 1995 Hyogo-Ken Nanbu Earthquake. *Proc. Jpn. Acad. Ser. B.* 79B, 125–130. doi:10.2183/pjab.79b.125

Nagao, T., Enomoto, Y., Fujinawa, Y., Hata, M., Hayakawa, M., Huang, Q., et al. (2002). Electromagnetic Anomalies Associated with 1995 KOBE Earthquake. *J. Geodynamics*. 33, 401–411. doi:10.1016/s0264-3707(02)00004-2

Nagao, T., Kamogawa, M., Izutsu, J., Baba, H., Narushima, T., Takamura, N., et al. (2016). First Report of the Electromagnetic Wave Detection System in VLF Range, Tokai University-Proven for the Existence of Preseismic Phenomena-. *Bull. Inst. Oceanic Res. Develop.* 37, 29–36.

Nagao, T., Kamogawa, M., and Uyeda, S. (2019). “Earthquake Precursors and Prediction,” in *Encyclopedia of Solid Earth Geophysics. Encyclopedia of Earth Sciences Series*. Editor H. Gupta (Berlin, Germany: Springer).

Oike, K., and Ogawa, T. (1986). Electromagnetic Radiations from Shallow Earthquakes Observed in the LF Range. *J. Geomagn. Geoelec.* 38, 1031–1040. doi:10.5636/jgg.38.1031

Oike, K., and Yamada, T. (1994). “Relationship between Shallow Earthquakes and Electromagnetic Noises in the LF and VLF Ranges,” in *Electromagnetic Phenomena Related to Earthquake Prediction*. Editors M. Hayakawa and Y. Fujinawa (Tokyo, Japan: Terrapub), 115–130.

Takanami, T., and Kitagawa, G. (1991). Estimation of the Arrival Times of Seismic Waves by Multivariate Time Series Model. *Ann. Inst. Statist. Math.* 43 (3), 407–433. doi:10.1007/bf00053364

Takanami, T., and Kitagawa, G. (1988). A New Efficient Procedure for the Estimation of Onset Times of Seismic Waves. *J. Phys. Earth*. 36, 267–290. doi:10.4294/jpe1952.36.267

Warwick, J. W., Stoker, C., and Meyer, T. R. (1982). Radio Emission Associated with Rock Fracture: Possible Application to the Great Chilean Earthquake of May 22, 1960. *J. Geophys. Res.* 87, 2851–2859. doi:10.1029/JB087iB04p02851

Yamada, T., and Oike, K. (1996). Electromagnetic Radiation Phenomena before and after the 1995 Hyogo-Ken Nanbu Earthquake. *J. Phys. Earth*. 44, 405–412. doi:10.4294/jpe1952.44.405

Conflict of Interest: SS and HK were employed by the company Genesis Research Institute, Inc.

The remaining authors declare that the research was conducted in the absence of any commercial or financial relationships that could be construed as a potential conflict of interest.

frontiers in Earth Science

ORIGINAL RESEARCH
published: 28 May 2021
doi: 10.3389/feart.2021.677163

Singular Spectrum Analysis of the Total Electron Content Changes Prior to M ≥ 6.0 Earthquakes in the Chinese Mainland During 1998–2013

Hongyan Chen[1], *Miao Miao*[1], *Ying Chang*[2], *Qiao Wang*[3], *Xuhui Shen*[3], *Katsumi Hattori*[4,5] and *Peng Han*[1]*

[1]Department of Earth and Space Sciences, Southern University of Science and Technology, Shenzhen, China, [2]Institute of Mining Engineering, BGRIMM Technology Group, Beijing, China, [3]National Institute of Natural Hazards, Ministry of Emergency Management of China, Beijing, China, [4]Graduate School of Science, Chiba University, Chiba, Japan, [5]Center for Environmental Remote Sensing, Chiba University, Chiba, Japan

Early studies have shown evidence of the seismo-ionospheric perturbations prior to large earthquakes. Due to dynamic complexity in the ionosphere, the identification of precursory ionospheric changes is quite challenging. In this study, we analyze the total electron content (TEC) in the global ionosphere map and investigate the TEC changes prior to M ≥ 6.0 earthquakes in the Chinese Mainland during 1998–2013 to identify possible seismo-ionospheric precursors. Singular spectrum analysis is applied to extract the trend and periodic variations including diurnal and semi-diurnal components, which are dominated by solar activities. The residual ΔTEC which is mainly composed of errors and possible perturbations induced by earthquakes and geomagnetic activities is further investigated, and the root-mean-square error is employed to detect anomalous changes. The $F_{10.7}$ and Dst index is also used as criterion to rule out the anomalies when intense solar or geomagnetic activities occur. Our results are consistent with those of previous studies. It is confirmed that the negative anomalies are dominant 1–5 days before the earthquakes at the fixed point (35°N, 90°E) during 0600–1000 LT. The anomalies are more obvious near the epicenter area. The singular spectrum analysis method help to establish a more reliable variation background of TEC and thus may improve the identification of precursory ionospheric changes.

Keywords: total electronic content, earthquake, singular spectrum analysis, ionospheric anomaly, statistical analysis

Edited by:
Juergen Pilz,
University of Klagenfurt, Austria

Reviewed by:
Xin Liu,
Shandong University of Science and Technology, China

Correspondence:
Peng Han
hanp@sustech.edu.cn

Specialty section:
This article was submitted to Environmental Informatics and Remote Sensing,
a section of the journal
Frontiers in Earth Science

Received: *07 March 2021*
Accepted: *14 May 2021*
Published: *28 May 2021*

Citation:
Chen H, Miao M, Chang Y, Wang Q, Shen X, Hattori K and Han P (2021) Singular Spectrum Analysis of the Total Electron Content Changes Prior to M ≥ 6.0 Earthquakes in the Chinese Mainland During 1998–2013.
Front. Earth Sci. 9:677163.
doi: 10.3389/feart.2021.677163

INTRODUCTION

Earthquake is one of the most dangerous disasters that can cause significant threats to human life and property. Many scholars have devoted themselves to studying the complex process of earthquakes and some people tried to predict them (e.g., Lazaridou-Varotsos, 2013; Sarlis et al., 2013; Han et al., 2017; Ouzounov et al., 2018a; Ouzounov et al., 2018b; Hattori and Han, 2018; Xie et al., 2019; Han et al., 2020; Sarlis et al., 2020). The pre-earthquake ionospheric perturbation is one of the most important phenomena of earthquakes precursor studies (Liu et al., 2001; Pulinets et al., 2003; Liu et al., 2006; He et al., 2011; Le et al., 2011; Sarkar et al., 2011; Parrot, 2012; Li and Parrot, 2013; Pisa et al., 2013; Guo et al., 2015; Rozhnoi et al., 2015). The total electron content (TEC) changes of the ionosphere associated with earthquakes have been reported by many researchers worldwide (e.g., Liu et al., 2001; Liu et al., 2004; Saroso et al., 2008; Heki, 2011; Heki and Enomoto, 2015; Iwata and Umeno, 2016; Liu et al., 2018; Tariq et al., 2019; Shah et al., 2020; Zhang et al., 2020). For instance, some studies displayed TEC anomalies prior to devastating earthquakes including the Wenchuan earthquake (Lin et al., 2009; Zhang et al., 2019), the Tohoku earthquake (Heki, 2011; Yao et al., 2012; Hirooka et al., 2016; Iwata and Umeno, 2016), and so on. Most studies showed the TEC in the ionosphere is abnormally disturbed in the few days prior to the earthquake. However, there are still debates about anomalous perturbations in the ionosphere prior to large earthquakes. Some studies analyzed the Global ionosphere maps (GIM) of TEC data and found no significant changes in GIM-TEC prior to earthquakes (Thomas et al., 2017). The relationship between TEC changes and earthquakes has been challenged (Dautermann et al., 2007; Afraimovich and Astafyeva, 2008; Astafyeva and Heki, 2011).

Due to the trend, long period and short period terms, such as annual, seasonal, and diurnal variations in the ionosphere, which might be much stronger than the seismo-ionospheric perturbations, the identification of precursory ionospheric changes is quite difficult. There are several methods to detect the ionospheric anomalies, including the median-interquartile range (IQR) method (Liu et al., 2006; Chen et al., 2015) and the average-standard deviation (STD) method (Kon et al., 2011). Both methods usually take previous some days as the reference background and compute the dynamic ranges of TEC variation. Recently, Guo et al. (2019) analyzed the TEC of two earthquake cases by singular spectrum analysis (SSA) and indicated the presence of obvious anomalous characteristics of the seismic-ionospheric coupling effect. The implementation of SSA could help to eliminate the influence of various periodical changes and might improve the detection of TEC anomalies.

Chen et al. (2015) found the electron density decreased 1–5 days before $M \geq 6.0$ earthquakes in China by using the previous 15-day as the reference background. To test possible relationship between ionospheric disturbances and earthquakes, we conduct similar analysis as Chen et al. (2015) and examine the changes in GIM-TEC for $M \geq 6.0$ earthquakes in the Chinese mainland during 1998–2013. In this study, the SSA method is used to remove the trend and periodical components, particularly the 27-day (Pancheva and Lastovicka, 1989; Pancheva et al., 1991) and diurnal variations in TEC. The possible effect of solar and geomagnetic activity is further discussed, as the ionosphere is sensitive to solar and geomagnetic activities (Carter et al., 2013).

DATA

TEC and Earthquake Data

GIM-TEC data are derived from GPS signals. There are seven ionosphere analysis centers (IAACs) all over the world, and each IAAC can calculate the global ionosphere map (GIM) with different computing strategies and the final GIM products can be obtained by weighting the GIM from each IAAC (Li et al., 2017). In this paper, we obtain TEC data which are generated on a daily basis from the Center for Orbit Determination in Europe (CODE), University of Berne, Switzerland. GIM-TEC covers ± 180° (longitude) and ± 87.5° (latitude) with a spatial resolution of 5.0° and 2.5°, respectively. The GIM-TEC data are released once a day with a 2-h resolution. We apply interpolation using a cubic spline function (de Boor, 1978) to obtain TEC data every 1 h. A list of 56 $M \geq 6.0$ earthquakes in the Chinese Mainland during 1998–2013 are used in this study, the same as the earthquake catalog used by Chen et al. (2015), so that we can compare the results with previous studies. **Figure 1** shows the locations of these earthquakes and the GIM-TEC used. Because it is not possible to know the GIM TEC over the "epicenter" before the earthquake occurs, therefore, for the practical application, we should examine GIM-TEC at a fixed location to analyze whether there are anomalies before the surrounding earthquake occurrence.

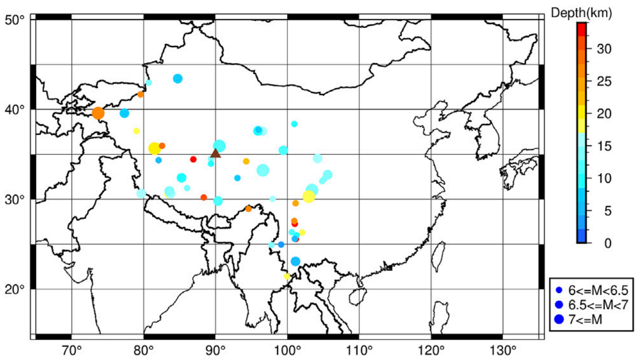

FIGURE 1 | Spatial distribution of 56 $M \geq 6.0$ earthquakes in the Chinese Mainland during 1998–2013. The triangle indicates the fixed location (35°N, 90°E) of GIM-TEC used in this paper.

Geomagnetic Dst and Solar Activity $F_{10.7}$ Index

Previous study suggested that the ionosphere was sensitive to solar and geomagnetic activities. Thus, it is necessary to analyze the geomagnetic indices and solar activity when identifying the earthquake-related TEC anomalies. The Dst index with a time resolution of 1-h provided by the World Data Center for Geomagnetism, Kyoto are used in this study. The geomagnetic storms can be classified into weak ($-50\,nT < Dst \leq -30\,nT$), moderate ($-100\,nT < Dst \leq -50\,nT$), and intense ($Dst \leq -100\,nT$) storms (Gonzalez et al., 1994). The solar radiation flux $F_{10.7}$ index provided by Space Physics Data Facility (SPDF) of NASA are used and $F_{10.7}$ is usually <100 SFU when solar activity is quiet (Guo et al., 2019).

METHODS

We apply the SSA method to study and decompose the TEC time series and use Correlation value to analyze main components. SSA is a model-free approach to analyze the periodic oscillation of time series, which can be used to extract information from the original signal containing different periodic components (Keppenne and Ghil, 1992; Robert and Pascal, 1992). First, we obtain the TEC dataset for each earthquake 31 days before and after its occurrence day. The timespan of each dataset is 63 days and centers on the earthquake day. The SSA results will be different if using different data length. We use the length of 63 days to do SSA and use 60 days to analyze so that it is consistent with the previous results. Some researcher used the different data length to do analyze, depending on their own demand (Shi et al., 2020; Zhang et al., 2021). Next, we create a trajectory matrix with a window length of 20 days for each dataset. We choose 20 days because that the window length (L) of SSA should be $2 < L < N/2$ (Golyandina et al., 2001) and we use $N/3$, where N is the length of the time series. Then we obtain the reconstructed time series after embedding, SVD, grouping, and diagonal averaging. For two reconstructed series $X^{(1)}$ and $X^{(2)}$, the inner product is defined by (Golyandina et al., 2001).

$$\left(X^{(1)}, X^{(2)}\right)_w = \sum_{i=1}^{N} w_i X_i^{(1)} X_i^{(2)} \tag{1}$$

where

$$w_i = \begin{cases} i & for\ \ 1 \le i < L \\ L & for\ \ L \le i < K\,(K = N - L + 1) \\ N - i + 1 & \text{for}\ K \le i \le N \end{cases} \tag{2}$$

To measure the degree of approximate separability between two series $X^{(1)}$ and $X^{(2)}$, the Correlation value is defined as

$$\rho^{(w)}\left(X^{(1)}, X^{(2)}\right) = \frac{\left(X^{(1)}, X^{(2)}\right)_w}{\sqrt{\left(X^{(1)}, X^{(1)}\right)_w \left(X^{(2)}, X^{(2)}\right)_w}} \tag{3}$$

The reconstructed components with large correlation values reflect that they are correlated from each other and usually composed of trend and periodic components, and the reconstructed components with small correlation values reflect that they are well separated from each other and contain different period components (Elsner, 2002). When extracting the reconstructed components, we select the first few principal components according to their energy, sorted by the corresponding eigenvalues λ^i. When the energy $\left(\frac{\lambda_i}{\sum_{i=1}^{L} \lambda_i}\right)$ of the i'th components is lower than 0.12%, we stop and take the rest components as the noises part. We select 0.12% as cut-off energy because this threshold value can ensure the TEC data of 56 earthquakes to exclude diurnal and semi-diurnal variations. Finally, we remove the semi-diurnal, diurnal, and long-term variations and obtain the residual denoted by ΔTEC. ΔTEC is mainly composed of computing errors and possible perturbations induced by earthquakes and geomagnetic activities. Note that here we use the TEC principal components for each earthquake 30 days before and after its occurrence day to avoid the boundary effects.

RESULTS

Extraction of Main Components by SSA

We start by looking at an example of TEC data before and after the 2008 Wenchuan earthquake (Ms8.0) to show the extraction of main components by SSA. **Figure 2** is an example of the Wenchuan earthquake from April 12, 2008 to June 11, 2008. We extract the first seven components based on the cut-off energy. **Figure 2A** is the correlation result of the first 20 reconstruction components by using SSA. It can be found the first seven components are separable and the eighth to later components are mixed with each other. **Figure 2B** shows the first seven reconstructed components. The first component is the trend component. The second to the fifth components are the diurnal variation and semi-diurnal variation, respectively. The sixth to the seventh components are approximately the 27-day variation and its half cycle.

The ionosphere is an integrated product of the interaction between the Sun and the Earth's environment. The TEC changes are mainly controlled by the intensities of solar electromagnetic radiation (He et al., 2012). Analyzing the correlation between the TEC component derived from SSA including trend and periodical components and geophysical indices including $F_{10.7}$ and Dst may help us to know the ionospheric effect from solar activity. The comparison of reconstructed components and $F_{10.7}$/Dst are as shown in **Figure 3**, and their Pearson correlation analysis are calculated. Because the $F_{10.7}$ data are of the 1-day resolution, the mean GIM-TEC of each day are used. The daily geomagnetic disturbance is measured by the minimum of the Dst indices on the day. As shown in **Figure 3A**, it is evident that the variation of the reconstructed components (RCs) 1–7 is similar to that of the $F_{10.7}$, and the RC 1 shows similar trend with $F_{10.7}$, suggesting a high correlation. The Pearson correlation analysis is demonstrated in **Figure 3B**, the correlation coefficient between RCs 1–7 and $F_{10.7}$ reaches 0.8, and the correlation coefficient between RC 1 and $F_{10.7}$ is 0.63. By the correlation analysis, it could be found that the influence from solar radiation at the daily timescale and above can be efficiently removed through the SSA method. In contrast, in **Figure 3C**, the correlation coefficient between RCs 1–7 and Dst is −0.22, between RC 1 and Dst is −0.26, showing a weak negative correlation.

After using SSA to extract the trend and periodic components which are mainly from the effects of solar activities, we subtract them from TEC data and obtain the residual ΔTEC. To give a more panoramic view, **Figure 4A** shows the original and reconstructed TEC results of the Wenchuan earthquake. **Figure 4B** shows the ΔTEC of the Wenchuan earthquake and its upper/lower bounds with ±RMS. The RMS is the root-mean-square error provided by the CODE on each grid point, which reflects the precision of the TEC data. Similar to (Guo et al., 2019), we use the RMS as the criterion for TEC anomaly detection. The ΔTEC value exceeding the upper/lower bounds implies that the ionosphere might be affected by solar activities or earthquakes. The ΔTEC at the fixed point (35°N, 90°E) for Wenchuan earthquake agrees with the results of (Chen et al., 2015). The ΔTEC decreased 1–4 days (from May 8 to May 12, 2008) before the earthquake and increased from May 3 to 5 May, as shown in **Figure 4B**.

Statistical Results

We select the most significant time 0600–1000 LT and calculate the percentages of the earthquakes with negative and positive anomalies that appear 30 days before and after the 56 earthquakes

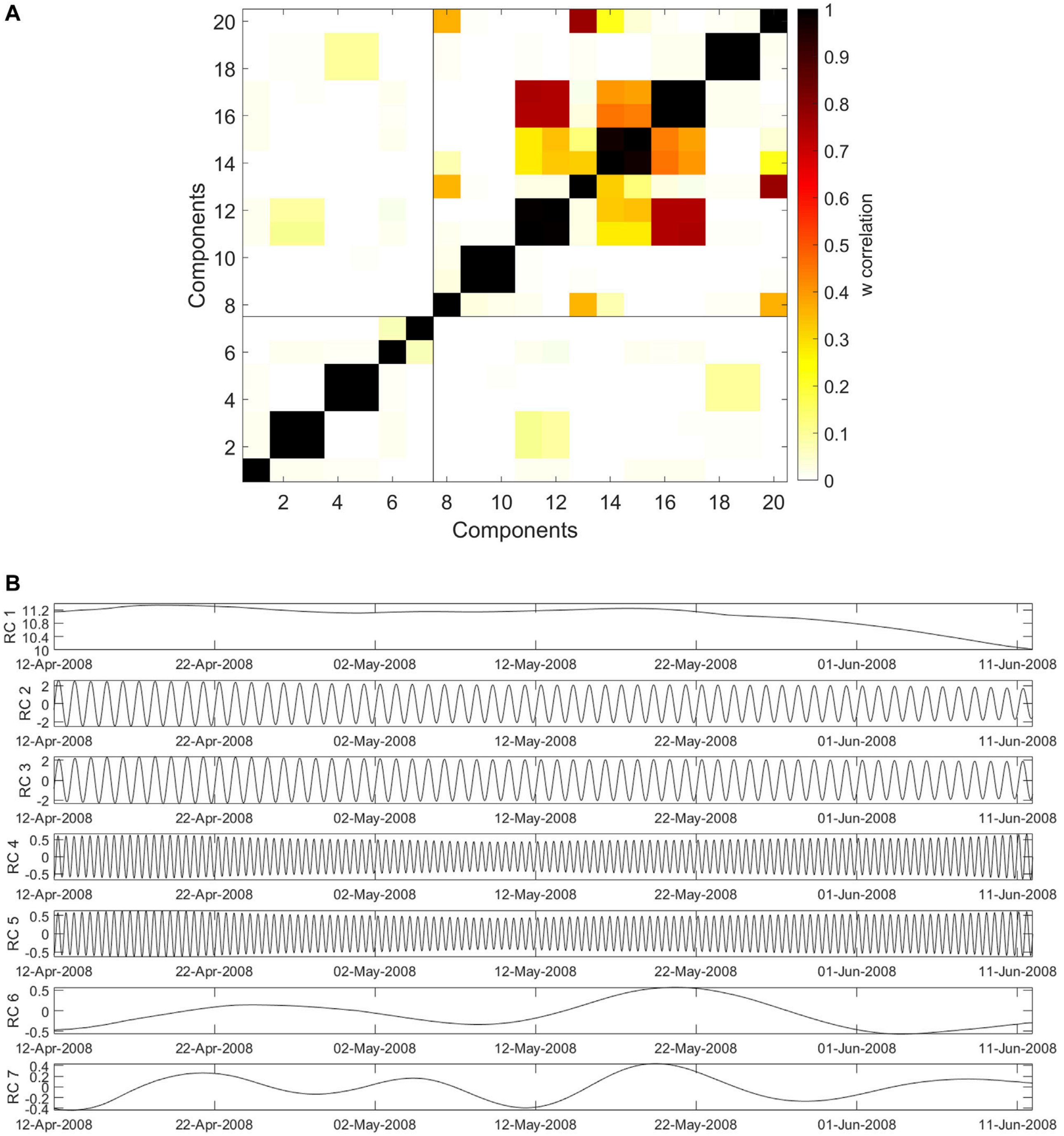

FIGURE 2 | An example of GIM-TEC reconstructed data at fixed point (35°N, 90°E) 30 days before and after Wenchuan earthquake based on SSA **(A)** Correlation for the first 20 reconstructed components, and **(B)** the first seven reconstructed time series.

(following Chen et al., 2015). If one-third of the time in the 0600–1000 LT time span (3 h or more) occurred negative or positive anomalies, we count it a negative or positive anomaly day (following Chen et al., 2015). **Figure 5** displays the percentages of the earthquakes with negative and positive precursory days and gives which kind of precursor is dominated. There are obvious negative anomalies 1–5 days before earthquakes, especially for M ≥ 6.8 and M ≥ 7.0. In general, the observed negative or positive precursors are consistent with the result of Chen et al. (2015). It should be noticed there are also higher positive abnormal proportion on 7–19 days before earthquakes, implying that the observed TEC tend to be relatively larger during this period. Therefore, if using the previous 15 days as the background, the upper and lower

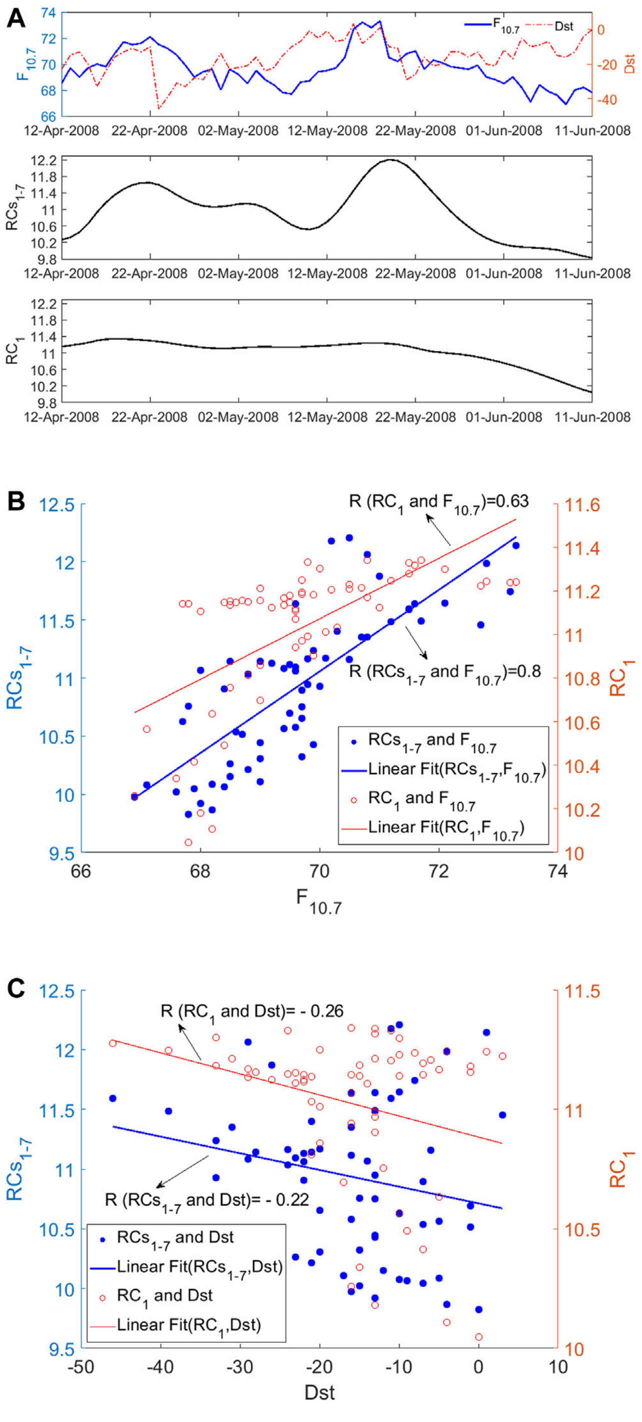

FIGURE 3 | The correlation between reconstructed components and $F_{10.7}$/Dst of 30 days before and after the Wenchuan earthquake. **(A)** The solar activity time series $F_{10.7}$, Dst, the reconstructed components 1–7 and reconstructed component 1 of TEC data at the fixed point (35°N, 90°E) from April 12 to 11 June, **(B)** correlation of reconstructed components 1–7 and $F_{10.7}$ indices (in blue color), and correlation of reconstructed component 1 and $F_{10.7}$ indices (in red color), and **(C)** correlation of reconstructed components 1–7 and Dst indices (in blue color), and correlation of reconstructed component 1 and Dst indices (in red color).

bounds of the dynamic ranges for TEC anomaly detection will become high. This might lead to more negative (below the lower bound) and less positive (above the upper bound) in the subsequent days. The proportion of anomalies overall in (Chen et al., 2015) is higher than that in our study, implying that the TEC anomalies reduce after applying SSA. This is consistent with the results of (He et al., 2012) that the ranges of TEC anomalies decreased on the global scale after removing background variations produced by solar radiations.

Even if the results in **Figure 5** can be deemed to remove the influence of solar activity after SSA method, we redefine an anomaly hour when the TEC exceeds the upper or lower bound and both geomagnetic and solar activity are quiet (Dst index is more than −30 nT and $F_{10.7}$ is <100 SFU). If 3 h or more in the 0600–1000 LT occurred negative or positive anomalies, it is counted as a negative or positive anomaly day. **Figure 6** shows results after ruling out the anomalies when geomagnetic or solar activities are not quiet. Negative anomalies are still dominant in 1–5 days before earthquakes, but the proportion decreased compared to that in **Figure 5**.

DISCUSSION AND CONCLUSIONS

A number of studies have shown the ionospheric TEC changes prior to great/mega earthquakes worldwide (e.g., Heki, 2011; Guo et al., 2015; He and Heki, 2016; Iwata and Umeno, 2016; He and Heki, 2017; Liu et al., 2018). As suggested by He et al. (2012), one of the key points is the elimination of ionospheric effect from solar radiation. In this study, we demonstrate another possible approach of SSA to eliminate such solar effects. By using SSA, the GIM-TEC anomalies prior to 56 M ≥ 6.0 earthquakes in the Chinese mainland during 1998–2013 have been revealed. Our findings agree with previous studies that negative anomalies are dominant during 1–5 days before earthquakes at the fixed point (Chen et al., 2015). The results persist after removing the data during intense geomagnetic and solar activity. As shown in both **Figures 5** and **6**, overall, the proportion of precursory days increases with the rise of earthquake magnitude, implying that the GIM-TEC anomalies are more likely to cooperate with stronger events.

Due to the ionospheric dynamic complexity, the earthquake-related perturbations might be far less than the seasonal and diurnal variations in the TEC data. Most studies took the previous 15/30 days as a reference and built the bounds for the TEC variation on the target day. As shown in **Figure 2B**, there are long-term trends in the TEC data. It may overestimate the background using the previous 15-day data if the TEC is on a downswing. On the contrary, the background may be underestimated if the TEC is in an uptrend. These may cause bias in detecting anomalies in the TEC data. As an attempt, we apply SSA to extract long-term, diurnal, and semi-diurnal variations. The residual ΔTEC contains errors, and possible perturbations induced by earthquakes and geomagnetic activities. By using the RMS as a threshold, we could remove

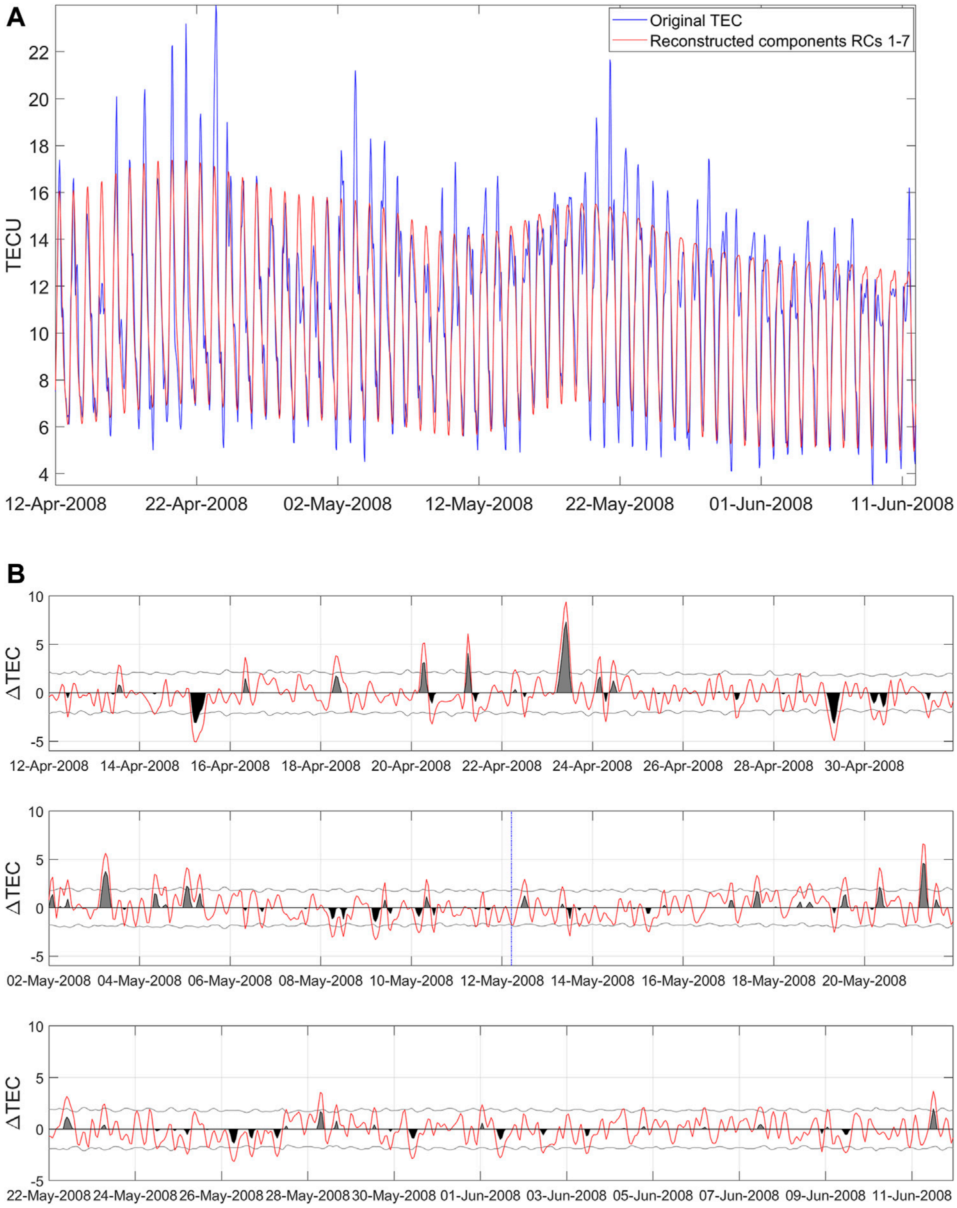

FIGURE 4 | The ΔTEC time series of the point (35°N, 90°E) over a period of time for the 2008 Ms8.0 Wenchuan earthquakes **(A)**The contrast of original TEC and reconstructed by 1–7 components, **(B)** time series of ΔTEC and the upper or lower bounds. The red curve is the ΔTEC, denoted later by O. The two gray curves are the associated upper bound (UB) and lower bound (LB). The gray and black shaded areas denote differences of O-UB and LB-O, respectively.

the influences of computing errors to a certain degree, as the RMS gives the precision of the TEC data. The approach based on SSA and RMS have an advantage in identifying anomalous changes in TEC variation (Guo et al., 2019).

It should be noticed that some earthquakes' epicenters may be far from the point at the GIM map that we used to analyze pre-seismic TEC variations, especially for the M6–M6.5 earthquakes, some of them are outside the Dobrovolsky earthquake preparation zone, leading to unobvious ionosphere reaction on the GIM selected point. Thus, we also take into account the pre-earthquake anomalies over the epicenter of the 56 earthquakes. **Figure 7** shows the ΔTEC of the point which is closest to epicenter for the Wenchuan earthquake and its upper/lower bounds with ±RMS, here we use the same method above to extract the main components. There are more obvious positive and negative anomalies compared to **Figure 4B**, especially positive abnormal enhancement on May 9, which are in line with the results of Liu et al. (2009).

In our statistical results, we focus on the time of 0600–1000 LT, if one-third of the time in the 0600–1000 LT (3 h or more) occurred negative or positive anomalies, we count it a negative or positive anomaly day (following Chen

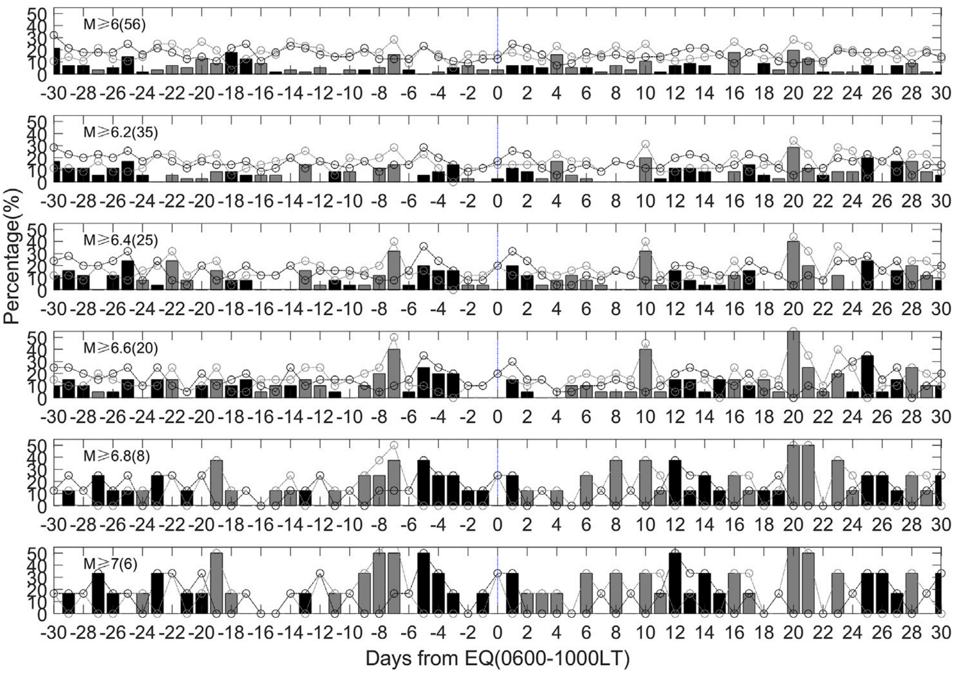

FIGURE 5 | Percentages of the earthquakes with negative (black dot) and positive (gray dot) precursory days that appear 30 days before and after the earthquakes in China during 1998–2013 in the 0600–1000 LT. The black bar represents the amount of percentage in which negative anomaly is over positive anomaly, while the gray bar denotes the amount of percentage in which positive anomaly is over negative anomaly.

et al., 2015). For 1–5 days before M ≥ 6.0 earthquakes, the highest proportion of both positive and negative anomalies is about 23%, as shown in **Figure 5**. After ruling out the anomalies when intense geomagnetic or solar activities occur, the highest proportion of negative and positive anomalies are 19 and 13%, respectively, as seen in **Figure 6**. The proportion decreases compared to that in **Figure 5** but negative anomalies are still dominant on 1–5 days before earthquakes. **Figure 8** displays the percentages of the earthquakes with negative and positive precursory days over epicenter and gives which kind of precursor is dominated. In **Figure 8**, when using the TEC data close to the epicenter, the highest proportion of negative and positive anomalies increase to 28 and 34% on 1–5 days before M ≥ 6.0 earthquakes. The percentage is higher than those based on the TEC data in a fixed area in **Figure 5**, and the proportion increases with the magnitude. The proportions reach up to 100% (negative anomalies) and 33% (positive anomalies) for M ≥ 7.0 earthquakes. The results display that the anomalous variations are more significantly enhanced near the epicenter area. After ruling out the anomalies when intense geomagnetic or solar activities occur, the highest proportion of negative and positive anomalies are 15 and 18% respectively on 1–5 days before M ≥ 6.0 earthquakes, as shown in **Figure 9**, the proportion decreases compared to that in **Figure 8** but negative anomalies are still dominant on 5 days before. The positive anomalies become obvious on 2–4 days before M ≥ 7.0 earthquakes, showing agreement with the positive abnormal enhancement on May 9, 3 days before the Wenchuan earthquake (Liu et al., 2009).

The characteristics of pre-earthquake TEC changes were quite different in different areas. For example, the negative anomalies are found to be dominant 1–6 days before earthquakes in China (Liu et al., 2006; Chen et al., 2015); while the positive anomalies were considered prominent 1–5 days before earthquakes in Japan (Kon et al., 2011). If the earthquake samples are analyzed together, one may not find clear results as the correlation between either negative or positive anomalies and earthquakes will decrease. This might be the reason why no significant anomalies for global earthquakes were detected in some studies (Zhu and Jiang, 2020). In addition, the RMS of GIM-TEC data is different at different places due to the uneven distribution of GPS stations. The level of uncertainty is high if using the GIM-TEC with large RMS, so the data accuracy should be also considered when doing global statistical analysis.

As for the physical mechanism of ionospheric anomalies associated earthquake, there are several ideas have been proposed by some scholars in the previous studies. The internal gravity waves (IGWs) mechanism has been provided by Pertsev and Shalimov (1996), which origin from seismogenic zone with period of 1–3 h due to inflowing of lithosphere gases into the atmosphere before earthquake. Liu et al. (2016) indicated that the triggered acoustic and/or gravity waves in the atmosphere near the surface can be activated by vertical ground motions, which is considered coseismic phenomenon of Tohoku earthquake (Liu et al., 2016). Some scholars described the formation mechanism of earthquake ionospheric precursors by seismogenic electric field with amplitude (Sorokin and Chmyrev, 1999; Pulinets and Boyarchuk, 2004), which charged aerosols

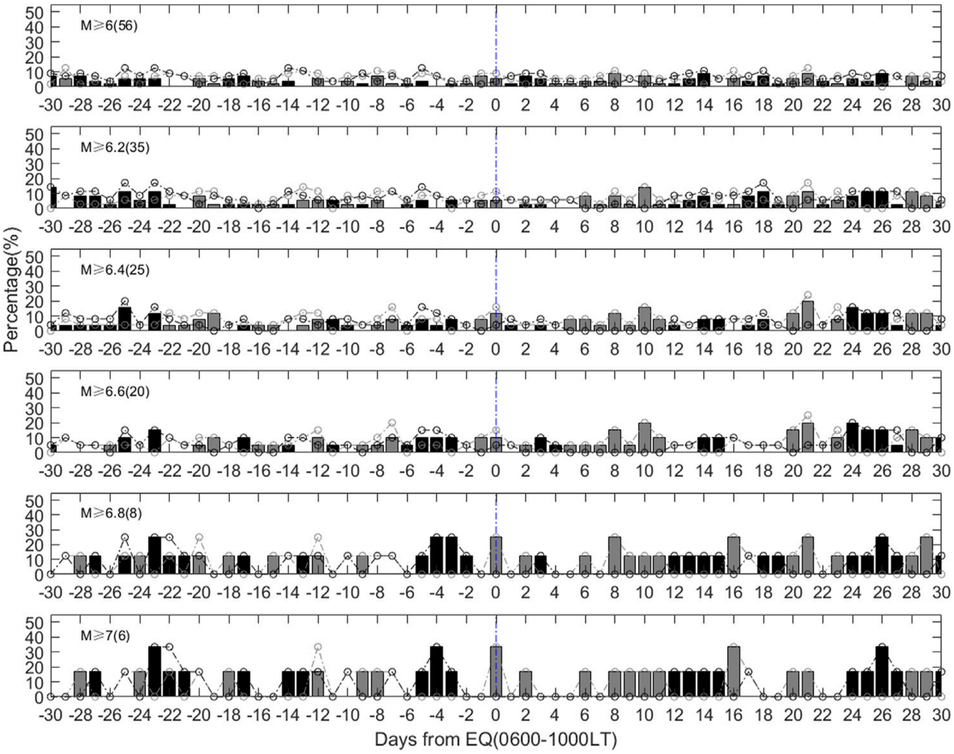

FIGURE 6 | Percentages of the earthquakes with negative (black dot) and positive (gray dot) precursory days after ruling out the anomalies when geomagnetic or solar activities are not quiet. The black bar represents the amount of percentage in which negative anomaly is over positive anomaly, while the gray bar denotes the amount of percentage in which positive anomaly is over negative anomaly.

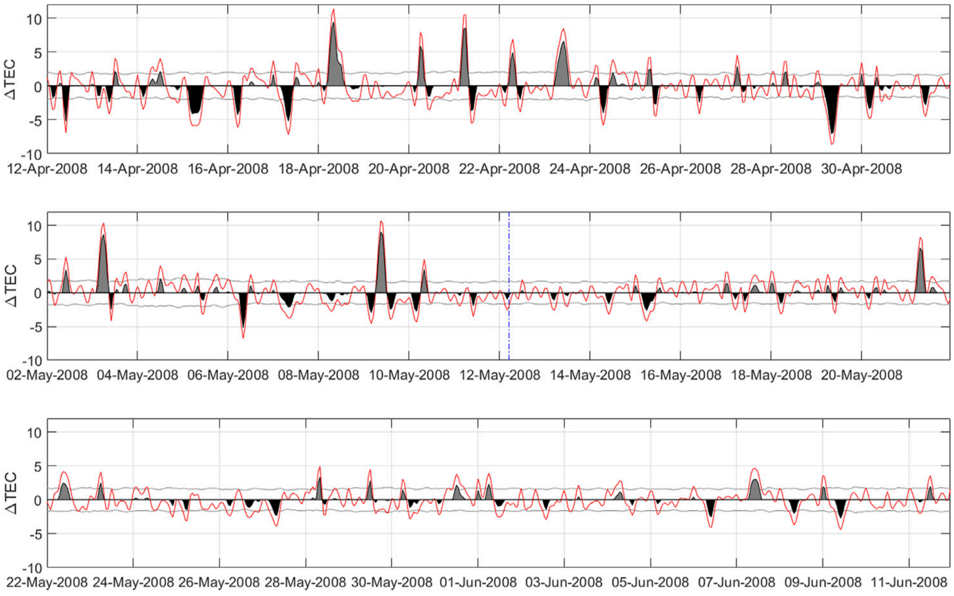

FIGURE 7 | The ΔTEC time series of the point (30°N, 105°E) closest to the epicenter over a period of time for the 2008 Ms8.0 Wenchuan earthquakes.

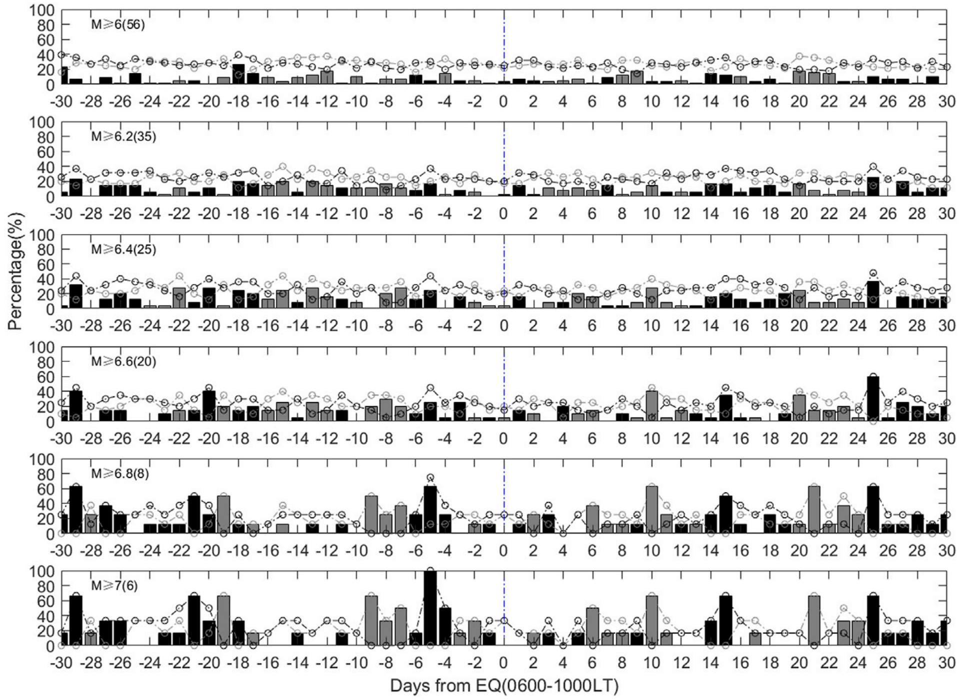

FIGURE 8 | Percentages of the earthquakes with negative (black dot) and positive (gray dot) precursory days over epicenter that appear 30 days before and after the earthquakes in China during 1998–2013 in the 0600–1000 LT. The black bar represents the amount of percentage in which negative anomaly is over positive anomaly, while the gray bar denotes the amount of percentage in which positive anomaly is over negative anomaly.

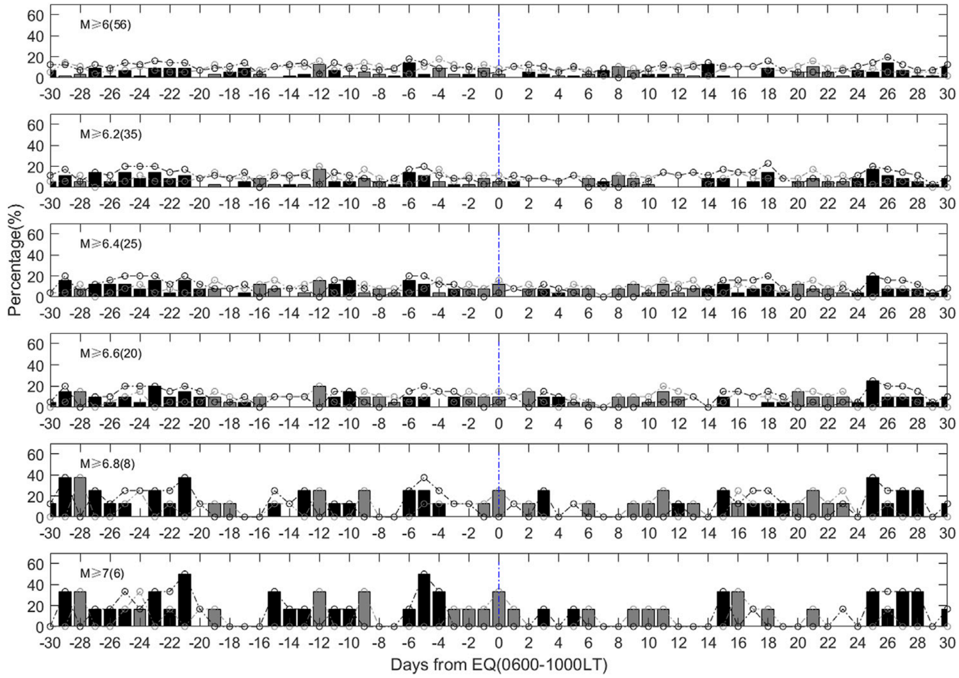

FIGURE 9 | Percentages of the earthquakes with negative (black dot) and positive (gray dot) precursory days over epicenter after ruling out the anomalies when geomagnetic or solar activities are not quiet. The black bar represents the amount of percentage in which negative anomaly is over positive anomaly, while the gray bar denotes the amount of percentage in which positive anomaly is over negative anomaly.

injected in the atmosphere and air ionization by radon followed by formation of large ion clusters of aerosol size during preparation. Namgaladze et al. (2009) proposed the most probable formation was the vertical transport of F2-region ionosphere plasma under action of zonal electric field (Namgaladze et al., 2009), some phenomena including geomagnetic conjugacy of the ionosphere precursors are the strong arguments in favor of this hypothesis. One more possible formation mechanism about the abnormal electromagnetic fields and emissions has been offered (Hayakawa and Molchanov, 2002), which originated from the ground due to certain mechanisms such as piezo-electric effects (Finkelstein et al., 1973), tribo-electric effect (Gershenzon et al., 1993) and positive holes (P-holes) (Freund, 2000), although this mechanism is found to be insufficient because of the weak intensity of lithosphere radio emissions (Hayakawa, 2007). Among the possible mechanisms, air ionization by natural ground radioactivity is considered more credible by some scholars (Pulinets, 2012; Guo et al., 2015), which is conform to the ionospheric characteristics of Chile and Wenchuan earthquakes (Pulinets and Davidenko, 2014).

In summary, by applying the SSA method, we extract the trend and periodical background components of GIM-TEC to analyze the pre-earthquake ionospheric anomalies associated with M ≥ 6.0 earthquakes in the Chinese Mainland during 1998–2013. The results are consistent with those of Chen et al. (2015) in general. It is confirmed that the negative anomalies are dominant 1–5 days before the earthquake at the fixed point (35°N, 90°E) during 0600–1000 LT. The anomalies are more obvious near the epicenter area. As there are considerable errors in the GIM-TEC data, it is worthwhile to analyze high-precision satellite observation data to obtain more accurate results.

DATA AVAILABILITY STATEMENT

Publicly available datasets were analyzed in this study. This data can be found here: "The TEC data are from the Center for Orbit Determination in Europe (ftp://ftp.unibe.ch/aiub/CODE), the solar radiation flux $F_{10.7}$ index are from Space Physics Data Facility (SPDF) of NASA (https://cdaweb.gsfc.nasa.gov/index.html/) and the Dst data are from the World Data Center for Geomagnetism (http://wdc.kugi.kyoto-u.ac.jp/)."

AUTHOR CONTRIBUTIONS

Conceptualization, PH and HC; methodology, HC and PH; software, HC; validation, HC, MM, YC, QW, XS, KH, and PH; formal analysis, HC; investigation, HC, QW, XS, KH, and PH; resources, HC, MM, and YC; data curation, QW, XS, KH, and PH; writing—original draft preparation, HC; writing—review and editing, XS, KH, and PH; visualization, HC; supervision, PH; All authors have read and agreed to the published version of the manuscript.

FUNDING

This research is partly supported by National Natural Science Foundation of China (41974083, 41804049), China Seismic Experimental Site (2019CSES0105), and Grand-in-Aids for Scientific Research of Japan Society for Promotion of Science (26249060), and the Ministry of Education, Culture, Sports, Science, and Technology (MEXT) of Japan, under its observation and Research Program for Prediction of Earthquakes and Volcanic Eruptions.

ACKNOWLEDGMENTS

We are very grateful to Orbit Determination in Europe (ftp://ftp.unibe.ch/aiub/CODE) for providing the GIM-TEC data. The solar radiation flux $F_{10.7}$ index were provided by Space Physics Data Facility (SPDF) of NASA (https://cdaweb.gsfc.nasa.gov/index.html/) and the Dst data were obtained from the World Data Center for Geomagnetism (http://wdc.kugi.kyoto-u.ac.jp/). We thank the reviewers for their useful comments and suggestions.

REFERENCES

Afraimovich, E. L., and Astafyeva, E. I. (2008). TEC Anomalies-Local TEC Changes Prior to Earthquakes or TEC Response to Solar and Geomagnetic Activity Changes? *Earth Planet. Sp.* 60 (9), 961–966. doi:10.1186/bf03352851

Astafyeva, E., and Heki, K. (2011). Vertical TEC over Seismically Active Region during Low Solar Activity. *J. Atmos. Solar-Terrestrial Phys.* 73 (13), 1643–1652. doi:10.1016/j.jastp.2011.02.020

Carter, B. A., Kellerman, A. C., Kane, T. A., Dyson, P. L., Norman, R., and Zhang, K. (2013). Ionospheric Precursors to Large Earthquakes: A Case Study of the 2011 Japanese Tohoku Earthquake. *J. Atmos. Solar-terrestrial Phys.* 102, 290–297. doi:10.1016/j.jastp.2013.06.006

Chen, Y.-I., Huang, C.-S., and Liu, J.-Y. (2015). Statistical Evidences of Seismo-Ionospheric Precursors Applying Receiver Operating Characteristic (ROC) Curve on the GPS Total Electron Content in China. *J. Asian Earth Sci.* 114, 393–402. doi:10.1016/j.jseaes.2015.05.028

Dautermann, T., Calais, E., Haase, J., and Garrison, J. (2007). Investigation of Ionospheric Electron Content Variations before Earthquakes in Southern California, 2003–2004. *J. Geophys. Res. Solid Earth* 12 (B2), 121. doi:10.1029/2006jb004447

de Boor, C. (1978). *A Practical Guide to Splines*. Berlin: Springer-Verlag. doi:10.1007/978-1-4612-6333-3

Elsner, J. B. (2002). Analysis of Time Series Structure: SSA and Related Techniques. *J. Am. Stat. Assoc.* 97 (460), 1207–1208. doi:10.1198/jasa.2002.s239

Finkelstein, D., Hill, R. D., and Powell, J. R. (1973). The Piezoelectric Theory of Earthquake Lightning. *J. Geophys. Res. (1896-1977).* 78 (6), 992–993. doi:10.1029/JC078i006p00992

Freund, F. (2000). Time-resolved Study of Charge Generation and Propagation in Igneous Rocks. *J. Geophys. Res.* 105 (B5), 11001–11019. doi:10.1029/1999JB900423

Gershenzon, N. I., Gokhberg, M. B., and Yunga, S. L. (1993). On the Electromagnetic Field of an Earthquake Focus. *Phys. Earth Planet. Interiors.* 77 (1), 13–19. doi:10.1016/0031-9201(93)90030-D

Golyandina, N., Nekrutkin, V., and Zhigljavsky, A. (2001). Analysis of Time Series Structure. *Monogr. Stat. Appl. Probab.* 90, 144. doi:10.1201/9781420035841

Gonzalez, W. D., Joselyn, J. A., Kamide, Y., Kroehl, H. W., Rostoker, G., Tsurutani, B. T., et al. (1994). What Is a Geomagnetic Storm? *J. Geophys. Res.* 99 (A4), 5771. doi:10.1029/93ja02867

Guo, J., Li, W., Yu, H., Liu, Z., Zhao, C., and Kong, Q. (2015). Impending Ionospheric Anomaly Preceding the Iquique Mw8.2 Earthquake in Chile on 2014 April 1. *Geophys. J. Int.* 203 (3), 1461–1470. doi:10.1093/gji/ggv376

Guo, J., Shi, K., Liu, X., Sun, Y., Li, W., and Kong, Q. (2019). Singular Spectrum Analysis of Ionospheric Anomalies Preceding Great Earthquakes: Case Studies of Kaikoura and Fukushima Earthquakes. *J. Geodynamics* 124, 1–13. doi:10.1016/j.jog.2019.01.005

Han, P., Hattori, K., Zhuang, J., Chen, C.-H., Liu, J.-Y., and Yoshida, S. (2017). Evaluation of ULF Seismo-Magnetic Phenomena in Kakioka, Japan by Using Molchan's Error Diagram. *Geophys. J. Int.* 208 (1), 482–490. doi:10.1093/gji/ggw404

Han, P., Zhuang, J., Hattori, K., Chen, C.-H., Febriani, F., Chen, H., et al. (2020). Assessing the Potential Earthquake Precursory Information in ULF Magnetic Data Recorded in Kanto, Japan during 2000-2010: Distance and Magnitude Dependences. *Entropy*. 22 (8), 859. doi:10.3390/e22080859

Hattori, K., and Han, P. (2018). Statistical Analysis and Assessment of Ultralow Frequency Magnetic Signals in Japan as Potential Earthquake Precursors. *Pre-Earthquake Process.* 14, 229–240. doi:10.1002/9781119156949.ch13

Hayakawa, M., and Molchanov, O. (2002). *Seismo Electromagnetics Lithosphere–Atomosphere–Ionosphere Coupling*. Tokyo, Japan: Terra Sci. Publ. Co.

Hayakawa, M. (2007). VLF/LF Radio Sounding of Ionospheric Perturbations Associated with Earthquakes. *Sensors*. 7, 1141–1158. doi:10.3390/s7071141

He, L., and Heki, K. (2017). Ionospheric Anomalies Immediately before M W 7.0-8.0 Earthquakes. *J. Geophys. Res. Space Phys.* 122 (8), 8659–8678. doi:10.1002/2017ja024012

He, L., and Heki, K. (2016). Three-dimensional Distribution of Ionospheric Anomalies Prior to Three Large Earthquakes in Chile. *Geophys. Res. Lett.* 43 (14), 7287–7293. doi:10.1002/2016gl069863

He, L., Wu, L., Pulinets, S., Liu, S., and Yang, F. (2012). A Nonlinear Background Removal Method for Seismo-Ionospheric Anomaly Analysis under a Complex Solar Activity Scenario: A Case Study of the M9.0 Tohoku Earthquake. *Adv. Space Res.* 50 (2), 211–220. doi:10.1016/j.asr.2012.04.001

He, Y., Yang, D., Qian, J., and Parrot, M. (2011). Response of the Ionospheric Electron Density to Different Types of Seismic Events. *Nat. Hazards Earth Syst. Sci.* 11, 2173–2180. doi:10.5194/nhess-11-2173-2011

Heki, K., and Enomoto, Y. (2015). M W Dependence of the Preseismic Ionospheric Electron Enhancements. *J. Geophys. Res. Space Phys.* 120 (8)**,** 7006–7020. doi:10.1002/2015JA021353

Heki, K. (2011). Ionospheric Electron Enhancement Preceding the 2011 Tohoku-Oki Earthquake. *Geophys. Res. Lett.* 38 (17), 77. doi:10.1029/2011gl047908

Hirooka, S., Ichikawa, T., Hattori, K., Han, P., Yoshino, C., and Liu, J.-Y. (2016). Spatial and Temporal Distribution of the Pre-seismic Ionospheric Anomaly Prior to the 2011 off the Pacific Coast of Tohoku Earthquake (Mw9.0). *IEEJ Trans. FM*. 136, 265–271. doi:10.1541/ieejfms.136.265

Iwata, T., and Umeno, K. (2016). Correlation Analysis for Preseismic Total Electron Content Anomalies Around the 2011 Tohoku-Oki Earthquake. *J. Geophys. Res. Space Phys.* 121 (9), 8969–8984. doi:10.1002/2016ja023036

Keppenne, C. L., and Ghil, M. (1992). Adaptive Filtering and Prediction of the Southern Oscillation index. *J. Geophys. Res.* 97 (D18), 20449–20454. doi:10.1029/92jd02219

Kon, S., Nishihashi, M., and Hattori, K. (2011). Ionospheric Anomalies Possibly Associated with M⩾6.0 Earthquakes in the Japan Area during 1998-2010: Case Studies and Statistical Study. *J. Asian Earth Sci.* 41 (4)**,** 410–420. doi:10.1016/j.jseaes.2010.10.005

Lazaridou-Varotsos, M. S. (2013). The VAN Earthquake Prediction Method in Other Countries: Current Views. in *Earthquake Prediction by Seismic Electric Signals: The success of the VAN Method over Thirty Years*. (Berlin, Heidelberg: Springer), 191–202. doi:10.1007/978-3-642-24406-3_23

Le, H., Liu, J. Y., and Liu, L. (2011). A Statistical Analysis of Ionospheric Anomalies before 736M6.0+ Earthquakes during 2002-2010. *J. Geophys. Res. Space Phys.* 116, 49. doi:10.1029/2010ja015781

Li, M., and Parrot, M. (2013). Statistical Analysis of an Ionospheric Parameter as a Base for Earthquake Prediction. *J. Geophys. Res. Space Phys.* 118 (6), 3731–3739. doi:10.1002/jgra.50313

Li, Z. S., Wang, N. B., Li, M., Zhou, K., and Yuan, H. (2017). Evaluation and Analysis of the Global Ionospheric TEC Map in the Frame of International GNSS Services. *Chin. J. Geophysics-Chinese Edition*. 60 (10), 3718–3729.

Lin, J., Y, W., Y, Z. F., J, Q. X., and Y. Y, Z. (2009). Wenchuan Earthquake Ionosphere TEC Anomaly Detected by GPS. *Chin. J. Geophysics-Chinese Edition* 52 (1), 297–300. doi:10.1007/s10291-018-0759-1

Liu, J., Chen, C.-H., Sun, Y.-Y., Tsai, H.-F., Yen, H.-Y., Chum, J., et al. (2016). The Vertical Propagation of Disturbances Triggered by Seismic Waves of the 11 March 2011 M9.0 Tohoku Earthquake over Taiwan. *Geophys. Res. Lett.* 43, 37. doi:10.1002/2015gl067487

Liu, J., Hattori, K., and Chen, Y.-I. (2018). *Application of Total Electron Content Derived from the Global Navigation Satellite System for Detecting Earthquake Precursors*. Berlin: Springer, 305–317.

Liu, J. Y., Chen, Y. I., Chen, C. H., Liu, C. Y., Chen, C. Y., Nishihashi, M., et al. (2009). Seismoionospheric GPS Total Electron Content Anomalies Observed before the 12 May 2008Mw7.9 Wenchuan Earthquake. *J. Geophys. Res.* 114, 3–9. doi:10.1029/2008ja013698

Liu, J. Y., Chen, Y. I., Chuo, Y. J., and Chen, C. S. (2006). A Statistical Investigation of Preearthquake Ionospheric Anomaly. *J. Geophys. Res.* 111 (A5), 304. doi:10.1029/2005JA011333

Liu, J. Y., Chen, Y. I., Chuo, Y. J., and Tsai, H. F. (2001). Variations of Ionospheric Total Electron Content during the Chi-Chi Earthquake. *Geophys. Res. Lett.* 28 (7), 151. doi:10.1029/2000gl012511

Liu, J. Y., Chuo, Y. J., Shan, S. J., Tsai, Y. B., Chen, Y. I., Pulinets, S. A., et al. (2004). Pre-earthquake Ionospheric Anomalies Registered by Continuous GPS TEC Measurements. *Ann. Geophys.* 22 (5), 1585–1593. doi:10.5194/angeo-22-1585-2004

Namgaladze, A. A., Klimenko, M. V., Klimenko, V. V., and Zakharenkova, I. E. (2009). Physical Mechanism and Mathematical Modeling of Earthquake Ionospheric Precursors Registered in Total Electron Content. *Geomagn. Aeron.* 49 (2), 252–262. doi:10.1134/S0016793209020169

Ouzounov, D., Pulinets, S., Hattori, K., and Taylor, P. (2018a). *Pre-earthquake Processes: A Multidisciplinary Approach to Earthquake Prediction Studies*. Hoboken: John Wiley & Sons.

Ouzounov, D., Pulinets, S., Liu, J., Hattori, K., and Han, P. (2018b). *Multiparameter Assessment of Pre-Earthquake Atmospheric Signals*. Hoboken: John Wiley & Sons.

Pancheva, D., and Lastovicka, J. (1989). *Solar or Meteorological Control of Lower Ionospheric Fluctuations (2-15 and 27 Days) in Middle Latitudes*. Cambridge: Cambridge Uiversity Press.

Pancheva, D., Schminder, R., and Laštovička, J. (1991). 27-day Fluctuations in the Ionospheric D-Region. *J. Atmos. Terrestrial Phys.* 53, 1145–1150. doi:10.1016/0021-9169(91)90064-e

Parrot, M. (2012). Statistical Analysis of Automatically Detected Ion Density Variations Recorded by DEMETER and Their Relation to Seismic Activity. *Ann. Geophys.* 55 (1), 149–155. doi:10.1007/s11589-011-0813-3

Pertsev, N., and Shalimov, S. L. (1996). Generation of Atmospheric Gravitational Waves in a Seismo-Active Region and its Influence on the Ionosphere. *Geomagn. Aeron.* 36, 111–118.

Pisa, D., Němec, F., SantolíK, O., Parrot, M., and Rycroft, M. (2013). Additional Attenuation of Natural VLF Electromagnetic Waves Observed by the DEMETER Spacecraft Resulting from Preseismic Activity. *J. Geophys. Res. Atmospheres* 118 (8), 5286–5295. doi:10.1002/jgra.50469

Pulinets, S. A., Legen"Ka, A. D., Gaivoronskaya, T. V., and Depuev, V. K. (2003). Main Phenomenological Features of Ionospheric Precursors of strong Earthquakes. *J. Atmos. Solar-Terrestrial Phys.* 65 (16–18), 1337–1347. doi:10.1016/j.jastp.2003.07.011

Pulinets, S., and Boyarchuk, K. (2004). *Ionospheric Precursors of Earthquakes*. Berlin: Springer.

Pulinets, S., and Davidenko, D. (2014). Ionospheric Precursors of Earthquakes and Global Electric Circuit. *Adv. Space Res.* 53 (5)**,** 709–723. doi:10.1016/j.asr.2013.12.035

Pulinets, S. (2012). Low-Latitude Atmosphere-Ionosphere Effects Initiated by Strong Earthquakes Preparation Process. *Int. J. Geophys.* 12, 1–14. doi:10.1155/2012/131842

Robert, V., Pascal, Y., and Michael, G. (1992). Singular-spectrum Analysis: A Toolkit for Short, Noisy Chaotic Signals. *Physica D Nonlinear Phenomena*. 58, 95–126. doi:10.1016/0167-2789(92)90103-t

Rozhnoi, A., Solovieva, M., Parrot, M., Hayakawa, M.P.-F., and Biagi (2015). VLF/LF Signal Studies of the Ionospheric Response to strong Seismic Activity in the Far Eastern Region Combining the DEMETER and Ground-Based Observations. *Phys. Chem. Earth. Parts A/B/C*. 85–86, 141–149. doi:10.1016/j.pce.2015.02.005

Sarkar, S., Tiwari, S., and Gwal, A. K. (2011). Electron Density Anomalies Associated with M≥5.9 Earthquakes in Indonesia during 2005 Observed by DEMETER. *J. Atmos. Solar-Terrestrial Phys.* 73 (16), 2289–2299. doi:10.1016/j.jastp.2011.06.004

Sarlis, N. V., Skordas, E. S., Christopoulos, S.-R. G., and Varotsos, P. A. (2020). Natural Time Analysis: The Area under the Receiver Operating Characteristic Curve of the Order Parameter Fluctuations Minima Preceding Major Earthquakes. *Entropy*. 22 (5), 583. doi:10.3390/e22050583

Sarlis, N. V., Skordas, E. S., Varotsos, P. A., Nagao, T., Kamogawa, M., Tanaka, H., et al. (2013). Minimum of the Order Parameter Fluctuations of Seismicity before Major Earthquakes in Japan. *Proc. Natl. Acad. Sci. USA* 110 (34), 13734–13738. doi:10.1073/pnas.1312740110

Saroso, S., Liu, J., Hattori, K., and Chen, C.-H. (2008). Ionospheric GPS TEC Anomalies and M ≧ 5.9 Earthquakes in Indonesia during 1993 - 2002. *Terrestrial Atmos. Oceanic Sci. TERR ATMOS OCEAN SCI*. 19, 481–488. doi:10.3319/TAO.2008.19.5.481(T)

Shah, M., Inyurt, S., Ehsan, M., Ahmed, A., Shakir, M., Ullah, S., et al. (2020). Seismo Ionospheric Anomalies in Turkey Associated with M ≥ 6.0 Earthquakes Detected by GPS Stations and GIM TEC. *Adv. Space Res.* 65 (11), 2540–2550. doi:10.1016/j.asr.2020.03.005

Shi, K., Guo, J., Liu, X., Liu, L., You, X., and Wang, F. (2020). Seismo-ionospheric Anomalies Associated with Mw 7.8 Nepal Earthquake on 2015 April 25 from CMONOC GPS Data. *Geosci. J.* 24 (4), 391–406. doi:10.1007/s12303-019-0038-3

Sorokin, V. M., and Chmyrev, V. (1999). Modification of the Ionosphere by Seismic Related Electric Field. *Atmos. Ionospheric Electromagn. Phenomena Assoc. Earthq.* 12, 805–818.

Tariq, M. A., Shah, M., Hernández-Pajares, M., and Iqbal, T. (2019). Pre-earthquake Ionospheric Anomalies before Three Major Earthquakes by GPS-TEC and GIM-TEC Data during 2015-2017. *Adv. Space Res.* 63 (7), 2088–2099. doi:10.1016/j.asr.2018.12.028

Thomas, J. N., Huard, J., and Masci, F. (2017). A Statistical Study of Global Ionospheric Map Total Electron Content Changes Prior to Occurrences of M ≥ 6.0 Earthquakes during 2000-2014. *J. Geophys. Res. Space Phys.* 122 (2), 2151–2161. doi:10.1002/2016ja023652

Xie, W., Hattori, K., and Han, P. (2019). Temporal Variation and Statistical Assessment of the B Value off the Pacific Coast of Tokachi, Hokkaido, Japan. *Entropy*. 21, 249. doi:10.3390/e21030249

Yao, Y., Chen, P., Wu, H., Zhang, S., and Peng, W. (2012). Analysis of Ionospheric Anomalies before the 2011 M W 9.0 Japan Earthquake. *Chin. Sci. Bull.* 57 (5), 500–510. doi:10.1007/s11434-011-4851-y

Zhang, X., Wang, Y., Boudjada, M., Liu, J., Magnes, W., Zhou, Y., et al. (2020). Multi-Experiment Observations of Ionospheric Disturbances as Precursory Effects of the Indonesian Ms6.9 Earthquake on August 05, 2018. *Remote Sensing*. 12 (24), 4050. doi:10.3390/rs12244050

Zhang, X., Zhao, S., Song, R., and Zhai, D. (2019). The Propagation Features of LF Radio Waves at Topside Ionosphere and Their Variations Possibly Related to Wenchuan Earthquake in 2008. *Adv. Space Res.* 63 (11), 3536–3544. doi:10.1016/j.asr.2019.02.008

Zhang, Y., Liu, X., Guo, J., Shi, K., Zhou, M., and Wang, F. (2021). Co-Seismic Ionospheric Disturbance with Alaska Strike-Slip Mw7.9 Earthquake on 23 January 2018 Monitored by GPS. *Atmosphere*. 12 (1), 83. doi:10.3390/atmos12010083

Zhu, F., and Jiang, Y. (2020). Investigation of GIM-TEC Disturbances before M ≥ 6.0 Inland Earthquakes during 2003-2017. *Sci. Rep.* 10 (1), 18038. doi:10.1038/s41598-020-74995-w

Conflict of Interest: Author YC was employed by the company BGRIMM Technology Group. The remaining authors declare that the research was conducted in the absence of any commercial or financial relationships that could be construed as a potential conflict of interest.

frontiers in Earth Science

REVIEW
published: 06 July 2021
doi: 10.3389/feart.2021.676766

A Critical Review of Ground Based Observations of Earthquake Precursors

Livio Conti[1,2*†], *Piergiorgio Picozza*[1,2,3†] *and Alessandro Sotgiu*[2,3†]

[1]Uninettuno University, Rome, Italy, [2]INFN - Sezione Roma Tor Vergata, Rome, Italy, [3]Department of Physics, University of Rome "Tor Vergata," Rome, Italy

OPEN ACCESS

Edited by:
Dimitar Ouzounov,
Chapman University, United States

Reviewed by:
Michel Parrot,
UMR7328 Laboratoire de Physique et Chimie de l'Environnement et de l'Espace (LPC2E), France
Angelo De Santis,
University of Studies G. d'Annunzio Chieti and Pescara, Italy
Sergey Alexander Pulinets,
Space Research Institute (RAS), Russia

***Correspondence:**
Livio Conti
livio.conti@uninettunouniversity.net

†These authors have contributed equally to this work

Specialty section:
This article was submitted to Geohazards and Georisks, a section of the journal Frontiers in Earth Science

Received: *08 March 2021*
Accepted: *16 June 2021*
Published: *06 July 2021*

Citation:
Conti L, Picozza P and Sotgiu A (2021) A Critical Review of Ground Based Observations of Earthquake Precursors. Front. Earth Sci. 9:676766. doi: 10.3389/feart.2021.676766

We aim at giving a short review of the seismo-associated phenomena detected on ground that in recent years have been investigated as possible earthquake precursors. The paper comes together with a companion article–published on this same volume by Picozza et al., 2021–devoted to summarize the space-based observation of earthquake–precursors by satellites missions. In the present work, we give an overview of the observations carried out on ground in order to identify earthquake precursors by distinguishing them from the large background constituted by both natural non-seismic and artificial sources. We start discussing the measurements of mechanical parameters and variations of geochemical fluids detected before earthquakes; then we review thermal and atmospheric oscillations; finally, observations of electromagnetic and ionospheric parameters possibly related to the occurrence of impeding earthquakes are discussed. In order to introduce a so large field of research, we focus only on some main case studies and statistical analyses together with the main hypotheses and models proposed in literature in order to explain the observed phenomenology.

Keywords: earthquake precursors, LAIC mechanism, preseismic phenomena, radon, AGW-acoustic gravity waves, DEMETER, Swarm, CSES

INTRODUCTION

Earthquake prediction is the Saint Graal of seismology, but the study of possible earthquake precursors should be better regarded in the framework of fundamental geophysics more than in trying to guess the future (Ouzounov et al., 2018; Hough, 2020). Several authors have analyzed data and many papers have been published with claims ranging from (by chance) observations of spatial and temporal correlations - cautiously interpreted as possible earthquake precursors - up to the proposal of methods and procedures (never confirmed) aimed at forecasting earthquakes. The realm of studied earthquake precursors includes a variety of physical parameters ranging from mechanical deformation up to gas emissions; from variations of groundwater levels up to fluctuations of electromagnetic field (in a large spectrum of frequencies, possibly radiated, induced or generated as secondary effect of other primary perturbations); from variations of ground temperature up to fluctuations of ionospheric and magnetospheric parameters. The first reports about correlation between impending earthquakes and electromagnetic emissions date back to Varotsos (1981) (even though highly debated), Gokhberg et al. (1982) and Warwick et al. (1982). About 50 years ago, the successful short-term prevision of the strong Haicheng (China) earthquake (Lomnitz, 1994) as well as the failure in forecasting the event of Tangshan (China) (Lomnitz, 1994)–even though of comparable intensity - have started a swinging wave of hopes and delusions about the possibility that seismic events could be effectively forecasted (Turcotte, 1991; Uyeda et al., 2009b). Many measurements, claimed as earthquake precursors, have been carried out (occasionally or even by systematic observation campaigns) on single earthquakes (case studies). Unfortunately, only a few of them were repeated/reproduced in occasion of other seismic events (such as for example Hattori et al., 2013; Liu et al., 2010; Davidenko and Pulinets, 2019) so that the observations of these cases studies are in some aspect often "unique" and scattered in the panorama of earthquake precursor investigations. For example, some early observations have suggested that, before strong earthquakes, the focal area could generate and radiate detectable electromagnetic signals in a large range of frequency. Two hours before the M = 9.2 Alaska earthquake of 1964 - one of the largest ever recorded seismic event in the era of regular seismological recording–Davies and Baker (1965) reported a strong ionospheric anomaly at about 4–5 MHz, recorded at Boulder, Colorado. Another "classical" case study was the measurement of fluctuations in magnetic field data (in ultra-low frequency range) carried out a couple of weeks (and then some hours) before the Loma Prieta earthquake (magnitude 7.1) on 1989 (Fraser-Smith et al., 1990). A less numerous type of analysis is constituted instead by statistical studies, performed by applying a given data analysis procedure to an ensemble (more or less statistically significant) of seismic events. In this framework, a systematic effort have been carried out by USGS along the San Andreas Fault at Parkfield, CA, by installing creep and strain meters, groundwater level detectors, magnetometers, etc. (Bakun and Lindh, 1985), but gathered data and results have not allowed to forecast any seismic event (Langbein et al., 2005). The most decidedly adverse perspective, mainly from the seismology and geodesy point of view, was summarized by Geller according to whom:<< results in nonlinear dynamics are consistent with the idea that earthquakes are inherently (or actually) unpredictable because of the highly sensitive nonlinear dependence on initial conditions>> (Geller, 1997), while indirectly Uyeda replied that: <<There are reasons for this pessimism because mere conventional seismological approach is not efficient for this aim. Overturning this situation is possible only through multi-disciplinary science>> (Uyeda et al., 2009b). This paper aims at presenting a critical overview of earthquake precursors observed on ground and the related analyses published in literature trying to point out their own characteristics (physical parameters, intensity, duration, background, etc.) and possible connection to the earthquake magnitude. We will also summarize some of the physical models proposed to reconcile the observed phenomenology with the physics of earthquake even though a scientific consensus of which could be preferable is still missing. We address the reader to the paper (Picozza et al., 2021) published in this same issue that provides a review of satellite-based observations and more in general of earthquake precursors in space.

SUMMARY OF CLAIMED GROUND-BASED EARTHQUAKE PRECURSORS

Even though our review does not pretend to be exhaustive of earthquake precursors on ground, we tried to select them between the most reliable ones published in literature. In the following, we will discuss several types of precursors that suggest an effective lithosphere-atmosphere-ionosphere-magnetosphere coupling, such as:

1) Seismicity that is the most extensively studied phenomenology before, during and after earthquakes (Mignan 2008; Hong et al., 2018; De Santis et al., 2019b). Also extreme low frequency acoustic emissions have been claimed (see for example Ihmlé and Jordan, 1994) to constitute earthquake precursors before the main rupture at a higher frequency.
2) Lithospheric mechanical deformations, such as those detectable with creep- and stain-meters (Niu et al., 2008; Langbein, 2015).
3) Variation of the groundwater level and composition, reported some weeks up to few hours before earthquakes (Hayakawa et al., 1997; Koizumi et al., 1999).
4) Gas exhalations, mainly (but not only) of radon or radioactive ions induced by gas-water release from earthquake preparation zone into the atmosphere (Khilyuk et al., 2000; Pulinets et al., 2003).
5) Fluctuations of temperature observed in temporal correlation with some earthquakes and possibly reconciled with variation of groundwater circulation and uplift or more recently with vapour condensation on surface (Tramutoli et al., 2005).
6) Propagation of acoustic gravity waves (AGW) (Molchanov and Hayakawa, 2008), A physical mechanism of seismo-ionospheric coupling including both AGW and radon exhalation has been recently suggested (Rapoport et al., 2020).
7) Fluctuation of electric and magnetic field components in a large range of frequencies [from ULF (Uyeda, et al., 2009b; Han et al. (2014)] to VHF (Sorokin et al., 2020). Many observations have been reported on ground and in space of (direct, induced and secondary) electromagnetic emissions localized on the earthquake area or measured along the related field line or spread around it.
8) Ground based observations of ionospheric parameters [such as Total Electron Content (TEC) (Liu et al., 2004; Liu, 2009), VLF reflection height (Hayakawa et al., 1996, 1997; Rodger et al., 1999), whistler dispersion (Hayakawa et al., 1993), critical frequency foF2 (Hobara and Parrot, 2005), etc.].

With the analysis of LEO satellite observations, the range of earthquake precursors investigations has been extended including measurements of disturbances of plasma parameters in the ionosphere-magnetosphere transition zone; thermal anomalies; AGW; precipitation of particles from the inner Van Allen belt (see Picozza et al., 2021 and references therein).

For each type of precursors listed above, we will try to discuss the main related information such as earthquake parameters (including time, location, magnitude and depth), time of the measured precursor, duration of the disturbance, amplitude, signal-to-noise ratio, distance from the epicentre, etc. Moreover, we have catalogued the physical models proposed in literature in order to verify which of them could better explain the phenomenology of the precursors and can reconcile the observed disturbances with the earthquake properties such as magnitude, momentum, focal mechanism, depth, etc.

POSSIBLE MECHANICAL, GEOCHEMICAL AND THERMAL PRECURSORS OF EARTHQUAKES

The earthquake precursors observed on ground can be generally categorized in two main groups: non-electromagnetic precursors and electromagnetic ones. In this section, we will review observations of the first type that includes mechanical, geochemical and thermal anomalies.

Seismicity and Observation of Local Mechanical Deformations

In the seismic sequence–often associated to large earthquakes–the main shock is frequently preceded by foreshocks of lower magnitude (Jones and Molnar, 1976; Reasenberg, 1999). Foreshocks occur within a variable time interval from the main earthquake (even though often with an increased frequency before the main shock) and spatially near to the epicentre of the main event (Sornette and Sornette, 1989; Ben-Zion et al., 2003). Scholz (2019) suggested that foreshocks are part of the nucleation process resulting in the main seismic event and that, in some sequence, dilatancy could induce seismic energy release and explain short-term quiescence just prior to the main event (Press and Siever, 1982; Allegri et al., 1983; Lomnitz, 1994; Sgrigna and Malvezzi, 2003). A systematic worldwide study of foreshock catalogues for low magnitude earthquakes is a challenge due to the uneven threshold in seismic measurements around the world. It has been suggested that the foreshock occurrence and the claimed earthquake precursors (such as radon release, electromagnetic anomalies, groundwater level variations, etc.) could be correlated through some physical mechanism (De Santis 2014; Varotsos et al., 2019). After a strong earthquake, the aftershock sequence normally decays and the occurrence probability of a subsequent larger event is of a few per cent Gulia, and Wiemer (2019). Anyway, this probability is a function of the stress conditions due to previous earthquakes and long-term tectonic conditions. In this framework, foreshocks can give valuable information about the process in action (see Console et al., 1993; Avlonitis and Papadopoulos 2014; and references therein), but earthquake catalogues are still uncomplete and foreshock interpretation for earthquake forecasting is highly debated. Attempts to predict the next large earthquake, based on physical models and Coulomb stress transfer, have been unsuccessful due in part to incomplete knowledge of the location of faults Nanjo (2020). Gulia and Wiemer (2019) suggested that in some cases it would be possible to distinguish between decaying aftershock sequences and foreshocks preceding a large event. Gulia and Wiemer (2019) proposed that the probability of larger subsequent event is higher for seismic sequences diverting from the generally observed increase of b value after a mainshock. Anyway, the authors consider preliminary their results due to the reduced number of events analyzed ($M > 6$ with high dense seismic networks coverage). More recently, Trugman and Ross (2019) suggested that more than 70% of all mainshocks in Southern California was preceded by foreshocks, but van den Ende and Ampuero (2020) objected that only a percentage between 18 and 33% of mainshocks were preceded by significantly elevated seismicity rates. Several authors have reported surface deformations, such as tilt, strain, uplifts and downdrops, etc., measured before earthquakes of medium and high magnitude (Rikitake, 1987; Lomnitz, 1994). Some mechanical models Tse and Rice (1986) and Lorenzetti and Tullis (1989), etc. have been proposed in order to predict surface deformation possibly associated to the earthquake preparation phase. They need to describe the fault mechanical dynamics through constitutive relationships and to study the friction along the fault (Dieterich 1978; Dieterich, 1979; Ruina, 1983) in order to estimate if the induced strain rate, displacement, velocity, etc. are below the detectability threshold for the available instruments and experimental methodology. The results suggest that–due to signal-to-noise ratio, with respect to the intrinsic background–the strain rate is the most reliable observable. These investigations today can take advantage of temporal high-frequency sampling and spatial high-resolution measurements with GPS and SAR interferometry with satellites, in particular at low orbit. In the case of Amatrice earthquake, Panza et al. (2018) reported an increase of the deformation velocity for a transect (500 km wide) moving eastward, along the direction of tectonic extension (from Tyrrhenian to Adriatic coast). The velocity gradient has a peak localized in the Amatrice area (not observed for transects to the North and South). For further case studies see for example (Wright, 2016; Moro et al., 2017; Panza et al., 2018) and references therein. Even though the intensity of the measured deviations–carried out within some hundreds of kilometres from the epicentres–seems related with the earthquake magnitude, the claimed identification of these observations as earthquake precursors is not conclusive.

Variation of Geochemical Fluids: Release of Gas and Groundwater Level Fluctuations

Starting from the sixties, several reports have been published about a claimed increase of radon concentration before earthquakes (Lomnitz, 1994). The hypothesis is that an increase of compressional stresses could open and/or close micro-fractures and cracks facilitating radon exhalation of radon up to the surface together with the flow of groundwater carbon dioxide, methane, helium, etc. (Wakita et al., 1980; Teng et al., 1981; Biagi et al., 2001b). The ^{222}Rn is the most stable radon isotope, a noble radioactive gas generated by the alpha decay of Radium 226, with a half-life of about 3.8 days (Bé et al., 2011). ^{222}Rn is water soluble, with low concentration in surface water–due to the continuous release in the atmosphere– and higher concentration in deep groundwater. For this reason, the variation of concentration of ^{222}Rn has been studied as a marker of tectonic processes and proposed as a possible short-term precursor of seismic events (see for example Richon et al., 2003; Omori et al., 2007; Alam et al., 2020).

Physical Mechanisms for Correlating Gas Exhalation and Seismic Activity

The variety of models suggested in order reconciling the observed radon exhalations with physical mechanisms driven by seismicity can be summarized into 1) releases induced by ultrasonic vibrations; 2) pressure-induced change of solubility; 3) collapses of pores; 4) development of new pores; and 5) fluid mixing in depth (Thomas, 1988).

1) According to the vibrational model, gas releases would be induced, or facilitated, by ultrasonic vibrations of rocks. Even though this mechanism has been tested in laboratory and during artificial explosions in seismic explorations, the power density of natural seismic spectra at high frequencies could not be enough for explaining the phenomenology of the seismo–associated exhalations. Moreover, releases induced by seismicity are more intense than the explosion induced ones, and these, besides, can follow (instead of precede) the rupture events.
2) It has been suggested that gases emissions could be induced by variations of solubility due to an increase of the fluids pressure during the earthquake preparation phase, but the mechanism would not be effective because the required increase seems too high to be transferred to the fluid phase (Cicerone et al., 2009).
3) The collapse of the pores volume due to the stress increase of the incoming earthquake region has been also claimed to induce gases release in groundwater. Even though observed in some laboratory tests, this mechanism is questionable because, generally, high stress values on porous rocks are effective in increasing the pores volume and the observed periodicity in the gas releases intensity is not easily reconcilable with the irreversible compression of pores.
4) A more effective role in gas exhalation could be played by the rocks dilatancy that can increase of tens and hundreds the rock porosity percentage (Brace, 1978; Bernabé et al., 2003; LongJohn et al., 2018): microfracturing both facilitates gas release from the rocks and increases the reaction ratio with ground waters through the growth of microscopic surfaces (Holub and Brady, 1981). On the other side, significant pores volume increases have been observed only near the rock failure strength, which would mean that the claimed mechanism could be effective only in the small volume of the seismic fault experiencing the rupture process, whereas gases releases have been observed even far from the epicentre (Pulinets and Ouzounov 2011).
5) The phenomenology of spread exhalations could be reconciled by invoking cracking due to corrosion and subs stage occurring at low stress with higher fluid content. Finally, it has been proposed that a mix of ground fluids and chemical elements between different aquifer systems could be the most effective mechanism for generating fluctuations (both positive and negative) of gas exhalation even because it explains also the temperature fluctuations some time measured together with radon exhalations (Byerlee, 1993). In this framework, the mechanism would have a role in the electrokinetic generation of low frequency electromagnetic emissions (Fenoglio et al., 1995) that will be discussed later.

All the physical models claimed to explain precursors share the hypothesis that fast and non-linear processes in the rocks along the seismic fault (such as deformation, dilatancy, fluids flow changes, pores volume variation, etc.) could originate the anomalous variations of observed parameters (Press and Siever, 1982; Lomnitz, 1994).

Radon Exhalations

The majority of the reports about significant variations of radon concentration was for moderate and strong magnitude seismic events (about $M \geq 4.0$), but fluctuations have been reported also for earthquakes of lower intensity. More than 80% of the measurements are constituted by increases of radon concentration with respect to the background reference value, with a distribution of the variations peaked between 50 and 100% and extending up to more than a thousand percent. The duration, as well as the beginning and ending time of the radon exaltation events, show a quite large variability–without a clear temporal distance with the claimed associated earthquake–that does not allow identifying time of radon exaltations as a sharp/reliable short-term earthquake precursor (Plastino and Bella 2001; Cicerone et al., 2009; Plastino et al., 2010; Sorokin et al., 2020). In fact, even though, in the majority of the cases, the anomalous fluctuations started within about one month before the earthquake and lasted less than about three months and a half, the statistics also includes radon exhalations ended before the earthquakes and/or continued after the seismic events (Pulinets and Ouzounov 2011). On the other side, Yasuoka et al. (2006) demonstrated that radon behaviour fits curve of the critical exponent (Sornette and Sammis, 1995).

The reported radon exhalations are more frequent near the epicentres, where also the highest variations have been measured. On the contrary, no significant correlation has been observed between the intensity and frequency of the gas exhalation from one side and the earthquake magnitude from the other one (Kissin and Grinevsky, 1990; Toutain and Baubron, 1999; Pulinets and Boyarchuk, 2005). That would suggest that, even though gas releases could be related to the seismic fault dynamics, their entity would not be correlated with the incoming earthquake intensity (Cicerone et al., 2009; Sorokin et al., 2020).

Both the advance in time of the radon exhalation (before the seismic event) and its duration are correlated with the earthquake magnitude, suggesting that bigger events are preceded by larger releases occurring more in advance (see for example the statistical study of Kissin and Grinevsky, 1990; Toutain and Baubron, 1999; as well as the most recent works Pulinets and Boyarchuk, 2005; Hartmann and Levy, 2005; Riggio and Santulin, 2015). This would furtherly support the Rikitake law of the empirical linearity between the logarithm of precursor time and the earthquake magnitude [see Figure 13 of Rikitake (1987)]. On the other side Pulinets and Ouzounov 2011 pointed out that the discrepancy between the claim that radon exhalations are a precursor to earthquakes (Toutain and Baubron, 1999; Omori et al., 2007; Pulinets, 2007) and the demonstration that radon releases are not a statistically reliable precursor (Geller, 1997) cannot be easily resolved with local measurement stations, due to the variety of measurement methods adopted worldwide and the uncertainty about the origin (crustal or mantle) of radon and the related transport models. Due to the difficulty of monitoring radon on the ground–with networks with high spatial resolution (İnan et al., 2008) over large areas (such as within and beyond the Dobrovolsky radius)–the authors suggested retrieving radon release (as well as methane, carbon dioxide and other geochemical fluids) indirectly, through remote sensing methods, from space-based observations of thermal infrared radiation, based on the LAIC model that correlates thermal anomalies with radon and other gas exhalations (Pulinets et al., 2006; Surkov, 2015; De Santis, et al., 2019b). However, the claim that closer to and on the eve of an earthquake a higher release should be observed is not yet confirmed and a statistical assessment of the true/false vs. positive/negative cases, through a reliable confusion-matrix based classification, is desirable. The recent statistical analysis of correlation between groundwater radon variations and seismo-tectonic activity of time series about the Wenchuan earthquake (Alam A. et al., 2020) would show a persistent trend with a notable upsurge just before and during the Wenchuan earthquake in the near stations not observed in the response of more distant monitoring stations.

Measurements of Other Gas Emissions

Radon is not the only gas studied looking for correlation between exhalations and earthquakes (Sugisaki, 1978; Chung, 1984; Sato et al., 1986; Claesson et al., 2004). The intensity of the exhalations strongly varies for different species such as methane, argon, carbon monoxide and di-oxide, helium, etc. (Kawabe, 1984; Satake et al., 1984; Varshal et al., 1984; Huixin and Zuhuang, 1986). Even though fewer and scattered (Tsunogai and Wakita, 1995; Toutain et al., 1997; Sugisaki et al., 1996; Amonte et al., 2021 and therein references), the measurements of other gases show statistical distributions and a functional dependences - from the (postulated) associated earthquake events - similar to those pointed out for the radon observations (Reimer, 1980; Reimer, 1990; O'Neil and King, 1980; Craig, 1980; Sugisaki and Sugiura, 1985; Sugisaki and Sugiura, 1986; Nagamine and Sugisaki, 1991). On the other side, whereas some gasses (such as hydrogen, helium to argon ratio and chlorine) show an increase, other ones (including helium, methane to argon ratio and nitrogen to argon ratio) decrease before earthquakes (Bella et al., 1995a; Bella et al., 1995b; Virk et al., 2001).

Based on the literature, at present, a quantitative estimation of the intensity of the correlation mechanism, as well as of the temporal and spatial distance between claimed anomalous gas releases and the occurrence of seismic events are still missing. Therefore, no firm conclusions can be drawn about the reliability of the hypothesis.

Aerosols and Bubbles Exhalations

Aerosol measurements showed anomalous variations before and after the Gujarat M 7.7 event on January 26th, 2001 (Okada et al., 2004)–that was also preceded by the anomalous disturbances of TEC, ions and electron density, electron temperature and VLF electric field– and before the Chile M 8.8 earthquake on February 27th, 2010 (Akhoondzadeh, 2015). By analysing data of Aerosol Optical Depth (AOD) (measured through absorption of light at 550 nm by MODIS of Terra and Aqua satellites) Qin et al. (2014) have shown a significant fluctuation along the active Longmenshan faults, seven days before the Wenchuan earthquake (May 12th, 2008) before whom several have been the detections of anomalous variations of electromagnetic, atmospheric and ionospheric parameters including air temperature, outgoing longwave radiation, relative humidity, etc. Similarly, Akhoondzadeh and Jahani Chehrebargh (2016) reported anomalies in the AOD detected by MODIS before 16 high magnitude earthquakes; Boyarchuk (1997) shown exhalation of metallic aerosols (Cu, Fe, Ni, Zn, Pb, Co, Cr and radon); King (1986) reported emissions of Rn, He, H, Co_2 up to 500 km far from the epicentre (from few weeks to hours) before the seismic event; several analyses (Alekseev and Alekseeva, 1992; Heinicke et al., 1995; Pulinets et al., 1997; Biagi, 2009) claimed an increase of up two orders of magnitude of the charged aerosols density and an enhancement of the local radioactivity from weeks to days before earthquakes (correlated with possible exhalations of radon and other radioactive species).

Increased gas release in seismic regions during the earthquake preparation phase has been observed not only on land near faults (King, 1986), but also near submarine faults (McCartney and Bary, 1965; Lyon, 1974) with an intense rise of gas bubbles (including vapour, CO_2, He, methane, etc.) due to volcanic activity (Marty et al., 1993; Nikolaeva et al., 2009). The bubbles of gas under the sea can carry small electric charge (10^{-14}–10^{-13}) C (Gak 2013) that can originate electric field in the atmosphere (Harper 1957; Blanchard, 1963). Even though the detailed balance of air-sea fluxes is still not completely known (Zavarsky et al., 2018), marine spray aerosol strongly contributes to an increase in aerosol optical depth (Revell et al., 2019) and winds spread aerosols into the atmosphere both over the land and over the sea. Based on that Sorokin et al. (2020) advanced the hypothesis that the electromagnetic environment on the lands and over the sea could be similarly affected by aerosol releases, as would be confirmed by the analyses of electric field perturbations detected by satellite, that don't show a significant difference for seismic events on land and at sea.

Groundwater Level and Vapour Variations

Studies about level variation of ground waters in occurrence with seismic events have been carried since long time ago and are particularly numerous (Hamilton, 1975; Kovach et al., 1975; Raleigh et al., 1977; Cai and Shi, 1980,; Merifield and Lamar 1981; Golenetskii et al., 1982; Wakita et al., 1985; Asteriadis and Livieratos, 1989; Liu et al., 2006). Between the end of last century and the begin of the current, the investigations extended including test campaigns in other countries (Kissin and Grinevsky, 1990; Igarashi et al., 1992; Igarashi et al., 1995; Roeloffs and Quilty, 1997; Koizumi et al., 1999; King, 1986; Chadha et al., 2003; Koizumi et al., 2004). In many cases, the reports about level variation of ground waters in occurrence with seismic events are not systematic and "scattered", making difficult comparisons and a statistical analysis. Nevertheless, the trend of the main characteristics (such as distribution, spatial and temporal distance, intensity, etc.) seems qualitatively similar in the gas releases and ground water level measurements suggesting a common driver in the earthquake preparation phase that, anyway, asks for further confirmations. In order to point out the correlation between variation of ground water level and seismic events it is needed to reject the background effect (Roeloffs, 1988) due to not seismic processes such as tidal effects (Bredehoeft, 1967); rainfalls, pressure variations and seasonal contributions (Rice and Cleary, 1976; Roeloffs and Quilty, 1997), oil and gas extractions, etc. Even though measurements of water level fluctuations are spread up to values of some meters, the most frequently absolute variations are within 1 m with a large majority of decreases before the earthquake. The statistical distribution of advance time between ground water level variation and seismic events ranges between less than one day up to years with a peak at about one month and half, while the largest anomalies would occur nearer to the earthquake time. In addition, the largest variations have been observed nearer the epicentre (with the majority within 200 km), but there is not a clear evidence of a correlation between the entity of the variation and the earthquake magnitude. More recent observations (see for example Plastino, 2006; De Luca et al., 2018) have confirmed the general picture of the impact of seismic activity on the groundwater level fluctuation. İnan et al. (2010) reported hydro-geochemical anomalies lasting for more than a month before an earthquake magnitude 4.8, in Western Turkey, detected within few tens of kilometers from the epicenter. A longer preparation phase seems confirmed also by the analysis of De Santis et al. (2020) of a precursory anomaly lasting almost a year (from September 2018 to July 2019) of ground water level data from a borehole located about 200 km from the epicenter of the July 6, 2019, M7.1 Ridgecrest earthquake and six USGS groundwater-monitoring sites.

Thermal Anomalies Possibly Associated With Seismic Events

In the framework of earthquake precursor's research, several analyses have investigated the existence of anomalous temperature variations before earthquakes (Tronin 1996; Carreno et al., 2001; Tronin et al., 2002b; Jing et al., 2013; Ouzounov and Freund 2004; Saraf and Choudhury 2005; Choudhury et al., 2006; Ouzounov et al., 2007; Panda et al., 2007; Bi et al., 2009; Saraf et al., 2009; Qin et al., 2013; Lu et al., 2016). Relatively few are the reports about such anomalies detected on ground before earthquakes, the reason being the reduced number of test campaigns devoted to such a measurements and the complexity of the study aimed at discriminating positive effects from those not related to earthquakes. Now day, the satellite remote sensing has extended the available dataset as well as the capability of detection.

How Earthquakes Could Generate Thermal Anomalies

The first hypothesis advanced in order to reconcile the possible appearance of a thermal anomaly in conjunction with earthquakes has been that such an anomaly would originate in depth during the seismic preparation phase (for example by frictional heating on fault surfaces) and would propagate up to the surface. Due to the low thermal conductivity of the rocks, the direct diffusion of an anomalous thermal fluctuation is quite inefficient in reaching the surface asking for some years even for diffusing of few meters. An alternative idea was that thermal fluctuations could be generated by fluids flow variation in depth–such as uplift or interruption of the hot geothermal groundwater circulation in volcanic regions and/or due to the volumetric variation of porous rocks due to dilatancy that facilitates fluids and gases flow–and then transported to the surface by the groundwater motion. The speed of the flow, the volume of groundwater involved as well as the depth variation would drive the temperature fluctuation intensity and temporal trend. Being the geothermal gradient of about 1.5–3.5°C per 100 m (but even higher for volcanic regions), a temperature variation of several degrees can be generated by the circulation trough rocks at some hundreds of meters. The hypothesis of a fluid driven propagation would explain why the majority of the claimed observations observed on ground has been carried out near thermal sources (in Greece and Japan, where significant subductions and geochemical activity take place) (Zheng et al., 2020); within few tens of kilometres from the epicentre; with a peak of the intensity distribution at less than one degree; before and during the seismic events. Anyway, it must be noticed that no such geothermal anomalous fluctuation have been reported along the Saint Andreas fault (Lachenbruch and Sass, 1992). Moreover, because thermal anomalies have observed both on ground and over the sea surface, Pulinets and Ouzounov (2011) ruled out thermal waters as a source to explain observed anomalies.

A further hypothesis has been advanced for the generation mechanism according to which the variation of tidal force could trigger shallow thrust fault earthquakes (Cochran et al., 2004). In fact, Tanaka et al. (2002) have found a correlation between temporal trend of tidal force and seismic events. It appears reasonable that the tectonic stress due to tidal force can contribute to reach the rock critical failure point (Heaton, 1975; McNutt and Beavan, 1981; Kilston and Knopoff, 1983) and then could be correlated with the earthquake nucleation (Weiyu et al., 2018). In this framework, it has been claimed that tidal force could generate some seismo-associated thermal anomalies (Ma et al., 2012; Ma et al., 2015; Yan Z. et al., 2017; Weiyu et al., 2018; Zhang et al., 2018). However, even this generation mechanism does not overcome the limits due to the inefficient propagation process up to the surface.

An interesting link could exist between thermal anomalies and radon exhalation. Even though Toutain and Baubron (1999) (see also references therein) have shown some systematic correlation between radon exaltation and seismic events, further investigations (for example İnan et al., 2008) have not confirmed previous results and other scientists (such as for example Geller, 1997) have demonstrated that the claim of using radon as earthquake precursor could be illusory. Pulinets and Ouzounov (2011) and Sorokin et al. (2020) proposed that the discrepancies between data, models and statistical accuracy could be due to the variety of instruments and methodology adopted for the measurements campaigns as well as to the mosaic-like distribution of radon exhalations that could appear randomly scattered in space and time. By assuming that radon exhalations would result into local increase of temperature, Pulinets and Ouzounov (2011) claim that the remote sensing of thermal anomalies (propagated from ground to upper atmosphere) would solve the difficulties of point like observations of radon on ground (Pulinets, 2007).

Detections of Thermal Anomalies

The prospective of investigating seismo-associated thermal anomalies has strongly changed with space-based observations. The Earth's surface naturally emits thermal radiation that is routinely measured by satellite sensors in the (8–14 μm) spectral range (Pergola et al., 2004; Genzano et al., 2007). Several different methods have been applied to identify thermal fluctuations. Tramutoli et al. (2001) suggested the RST (Robust Satellite Techniques) procedure; Ouzounov and Freund (2004) analyzed LST (land surface temperature) data; Bryant and Nathan (2003) suggested the NTG (Nighttime Thermal Gradient) method and finally Zhang et al. (2010) applied wavelet transformation to infrared data. On the other side, various thermal parameters and datasets, collected on ground and trough remote sensing have been studied (Heaton, 1975; Tanaka et al., 2002; Blackett et al., 2011). Several studies have analyzed TIR (Thermal InfraRed spectral radiations) measurements acquired by infrared sensors on board of several satellite missions such as MODIS (on Terra and Aqua), FY Chinese satellite, MSG-41 SEVIRI on MeteoSat missions, AVHRR on NOAA satellites, etc. (Weiyu, et al., 2018; Yan R. et al., 2017; Zhang and Meng, 2019; Zhang et al., 2021). A common feature of the cited processing methods is to statistically process long temporal series of remote sensing data in order to extract possible anomalies (Lisi, et al., 2010; Sannazzaro, et al., 2014). Even though this approach provides a better statistical robustness, on the other side it could prevent from detecting small but significant thermal anomalies (Weiyu et al., 2018). One of the last research paper on the geochemical and thermal seismo-associated anomalies by Martinelli et al. (2020a) provides also an interesting summary and further references on this subject.

Acoustic Gravity Waves

At the begin of 2000 several authors (Gokhberg and Shalimov, 2000; Molchanov et al., 2004; Korepanov, et al., 2009) suggested that the earthquake precursor's phenomenology could be explained by the emission of AGW oscillations in a range of 6–60 min generated by lithospheric oscillations or gas exhalations and amplified in their propagation from the Earth surface through the atmosphere up to the ionosphere. The model of Molchanov et al. (2004) is based on the emission of charged aerosol (including an increase of groundwater, stable/radioactive gases and heat flows) in the earthquake preparation phase that would generate local disturbances in the conductivity in the atmosphere-ionosphere circuit. The advantage of this approach would be its capability to explain the large variety of observed disturbance taking in to account anomalous electromagnetic ULF/ELF measurements on ground (Schekotov et al., 2006) and in space (Rozhnoi et al., 2004), small scale plasma irregularities (Molchanov, 2009) in the geomagnetic flux tubes possibly reconciled with earthquakes occurrence, thermal fluctuations (Molchanov et al., 2004) as well as the claimed preearthquake character of VHF measurements (Devi et al., 2012). The analyses of ultra-low frequency electric and magnetic field before earthquakes shown electromagnetic perturbations associated with growth of plasma density structures (with scales between 10 and 40 km) several days before earthquake in the magnetic tubes with the footprint over the epicentre (Zhang et al., 2009; Akhoondzadeh 2013) similarly to what occurs over tropical cyclones (Isaev et al., 2002; Sorokin et al., 2005). It has been suggested (Akhoondzadeh, 2013) that these seismo-associated plasma fluctuations would be generated by quasi-static electric field amplification due to AGWs instability for value of critical field greater than about 10 mV/m (Chmyrev et al., 1997; Sorokin et al., 1998, 2005). The plasma irregularities along the magnetic tube show variations of tens of percent and dimensions from few hundreds of meters to tens kilometres (Chmyrev et al., 2008) while amplitude of magnetic field fluctuation are of few nT and with frequencies from fraction of Hz up to few Hz (Chakraborty et al., 2018 and references therein). Beyond several advantages (Lizunov, et al., 2020), the models based on AGW and internal gravity waves suffer of the difficulty in explaining local disturbances (such as electromagnetic and plasma fluctuation over the epicentral zone) because the directional propagation of such a waves would shift the interaction zone with the ionosphere of a thousand of kilometres far from the epicentre (Hayakawa et al., 2011; Yang et al., 2019; Sorokin et al., 2020).

SEISMO-ELECTROMAGNETIC PERTURBATIONS DETECTED ON GROUND

As mentioned above, beyond the mechanical oscillations (of the ground surface or of the atmospheric layers), the geochemical fluids variations and the thermal anomalies, the list of proposed earthquake-precursors on ground includes many observations of electromagnetic disturbances. We will concentrate only on measurements on ground, addressing to the companion article by Picozza et al. (2021) on the same volume for a review of the space born detection of possible seismo-electromagnetic precursors.

One of the most cited, and now "classical", case study is the observation of the increase of the ULF (0.5–2.0 Hz) magnetic field amplitude stated one month before of the Loma Prieta (California) earthquake of October 17th, 1989 (Ms 7.1) registered 7 km far from the epicentre. The amplitude of the horizontal component intensified a couple of weeks before and then further strongly increased in the 0.01–0.5 Hz range some hours before the shock, when power was lost, (Fraser-Smith et al., 1990). Nevertheless, a detector operating 50 km far did not measure any anomalous signal in the same period. The hypothesis that the anomalous observations could have been originated by atmospheric natural background has been rejected, but on 2009 Campbell (2009)–by comparing geomagnetic indices trend with a portion of the magnetic measurements by Fraser-Smith et al. (1990)–claimed that, despite their large amplitudes and other unusual characteristics, the observations of Fraser-Smith et al. (1990) would merely represent natural magnetic disturbance fields. Instead, after a critical and careful reanalysis, (Fraser-Smith et al., 2011), confirmed that the large-amplitude fields observed before the Loma Prieta earthquake are fundamentally different from "natural magnetic disturbance fields" and that they may well have been precursor fields to the earthquake.

Looking for ULF and Higher Frequency Electromagnetic Precursors

On ground, Fraser-Smith et al. (1990), reported a SNR in the ULF frequency range up to 60. Instead, the SNR reported for satellite observations by Larkina et al. (1989), Serebryakova et al. (1992) and Parrot (1994) was limited to 10. Nevertheless, this value is significantly higher than the background noise suggesting the possibility to detect seismo-electromagnetic precursors also from space at least in some case of strong earthquakes. The alleged pre-earthquake magnetic ULF (lower than several Hz) signals have a skin depth (tens of kilometres for 1 Hz) larger than that at higher frequencies (hundreds of meters for 10 kHz); moreover, low frequency magnetic signals suffer of a reduced attenuation, which allows long-range detection. These are some of the reasons that have drawn much attention to low-frequency magnetic field anomalies as important earthquake precursors. In addition to the Loma Prieta observations, early studies of ULF precursors were done also on the 1988 Spitak M 6.9 earthquake (Kopytenko et al., 1993), 1993 Guam M8.0 (Hayakawa et al., 1996), 1996 Hetian M7.1 event (Du et al., 2002), 1997 Kagoshima M 6.5 earthquake (Hattori et al., 2002), etc. In order to take into account the dependence of the ULF magnetic anomalies from the magnitude and the hypocentre distance earthquake from the observation site (Hattori 2004; Schekotov et al., 2006), Hattori et al. (2006) and Hattori et al. (2013) suggested to consider the cumulative (daily sum) of the local energy of the earthquakes weighted by the squared distance from the measurement station. This method have been adopted also by Han et al. (2014), that have carried an interesting statistical study - based on a superposed epoch approach for a long time period (2001–2010)–by analysing data at 0.01 Hz measured night-time (LT 2:30–4:00 am) at the Kakioka (Japan) geomagnetic station and compared with Kanoya observatory, as a reference, in order to reduce background of artificial noises and global geomagnetic perturbations. The authors report an increased probability of ULF magnetic anomalies 1–2 weeks before medium and strong shallow earthquakes [confirming previous results by Hattori et al. (2013)] and pointed out that perturbations are more relevant for stronger and closer events. More recently, Han et al. (2016) have reported statistical significant anomalies in the geomagnetic diurnal variation (GDV) of the vertical component in a long-term observations from 17 Japanese stations about 2 months before the 2011 Tohoku earthquake (Mw 9.0) confirming results of Xu et al. (2013) and Han et al. (2015) on the same event. Liu et al. (2020) extended the study of the geomagnetic solar quiet daily (Sq) for the same Tohoku event: by analysing data from 20 geomagnetic observatories in the period 2009–2012 pointing out a relevant perturbation about one month and half before the earthquake.

In the same years, several studies have been carried out looking for possible precursors on ground. in frequency bands higher than ULF, in particular investigating the variability of well know and highly stable radio signals used for communication and geolocalization networks. By studying the attenuation of radio LF and VLF point-to-point transmissions over long distances, several authors (see for example Hayakawa, et al., 1996; Bella et al., 1998; Biagi et al., 2001a; Biagi et al., 2004) have reported cases of attenuation of broadcasted signal some days before seismic events occurred near the radio propagation path and suggested that preseismic ionospheric disturbances could have affected the conditions of transmission/reflection in the Earth-ionosphere waveguide. More recent investigations have claimed similar effects (Rozhnoi et al., 2009; Fidani, 2010; Biagi et al., 2011; Zhang et al., 2019).

One of the most controversial aspect of seismo-associated electromagnetic precursors is the large variety of observations even for the measurements possibly associated to the strongest events. For example, electromagnetic precursors have been detected, or claimed, only in some specific frequency bands and the spread in latitude and in longitude is different (or even opposite with a claimed clustering) in some analyses. We believe that, at present, many aspects of the seismo-electromagnetic phenomena must still be understood. Nevertheless, the studies seem to support the hypothesis that seismo-electromagnetic precursors can be observed several hours before medium and strong earthquakes and that their intensity seems higher near the epicentre.

The Turn of the Century

For an extended review of early observations and models, we must cite the precious works of Park et al. (1993) and Johnston (1997). Between the end of the last century and the beginning of the 2000s, we can register an increased interest in the investigation of seismo-electromagnetic precursors (see for example Jianguo et al., 2000; Nikiforova and Michnowski, 1995; Hao et al., 2000, Hattori et al., 2002; Liu et al., 2001; Liu et al., 2002; Liu et al., 2004; Korepanov et al., 2009; Sgrigna et al., 2004; Sgrigna and Conti, 2010; Ouzounov et al., 2006; Dudkin et al., 2010; Ramírez-Rojas and Flores-M árquez, 2013). In occasion of 1995 Kobe earthquake, seismo-electromagnetic emissions in ULF, ELF and VLF frequency ranges have been registered by Nagao et al. (2002), while Zafrir et al. (2003) reported measurements of radon and ULF emissions. Several research groups were active in Greece (Thanassoulas and Tselentis, 1993; Eftaxias et al., 2003; Hristopulos and Mouslopoulou, 2013) where (Varotsos et al., 2002; Varotsos et al., 2003a; Varotsos et al., 2003b; Varotsos et al., 2008) proposed the highly controversial VAN method (se also Uyeda et al., 2009b). Between the other national communities of scientists that set the standard at the beginning of this century we can cite: Italy (Biagi et al., 2001a, Tramutoli et al., 2005; Sgrigna et al., 2007; Sgrigna and Conti, 2012); France (Zlotnicki and Cornet, 1986; Parrot et al., 1993, Parrot, 995); Japan (Hattori, 2004, Hattori et al., 2006; Uyeda et al., 2009a; Uyeda et al., 2009b); URSS-Russia (Chirkov, 2004; Kotsarenko et al., 2005; Morozov, 2006; Namgaladze et al., 2009) with several observations have been carried out for example in Kamchatka area (Vershinin et al., 1999); etc. In this framework, several space projects have been proposed and developed such as DEMETER (Parrot, 2002), QuakeSat (Flagg et al., 2004), ESPERIA (Sgrigna et al., 2008a; Sgrigna et al., 2008b), VULKAN (Kuznetsov et al., 2011), CSES (Shen et al., 2018; Lin et al., 2018; Yan et al., 2018; Li et al., 2020; Sotgiu et al., 2021) and FORMOSAT-7/COSMIC-2 (Lin et al., 2020). The Earth remote sensing is the new frontier of seismo-electromagnetic investigation because it allows monitoring several regions worldwide that is a key ingredient for statistical studies including several seismic events occurring in different tectonic systems and geomagnetic conditions. If the space-based investigation will provide solid results, we will need of satellite constellations that can ensure a global coverage with enough spatial and temporal resolution (Sgrigna et al., 2004). For the reader interested in an in-depth study, we refer to Tanimoto et al. (2015) and Ouzounov et al. (2018) that provide an updated and extended summary of research in the field.

How Seismo-Associated Electromagnetic Disturbances Could be Generated

Several models have been proposed in literature in order to explain the observed phenomenology of seismo-electromagnetic field precursors. We can divide them in two main categories depending on whether they could explain the lower frequency precursors (ULF) (Uyeda, et al., 2009b) or generate the disturbances at higher frequency (mainly ELF/VLF but also higher bands up to HF).

Generation of Low Frequency Magnetic Fields

In order to explain the ULF precursory fluctuations, three main effects have been suggested such as 1) the magneto-hydrodynamic (MHD) effect (Draganov et al., 1991); 2) the piezomagnetic effect (Sasai, 2001) (Parrot, 1995) and 3) the electrokinetic effect (Nourbehecht, 1936-1963; Fitterman, 1979).

1) In the MHD effect, a conducting fluid moving in a magnetic field generates a secondary induced field. We can define a magnetic Reynold number Rm such as the ratio between the convective term (due to the resistance to flux change of magnetic field) and the diffusive one (due to Ohmic dissipation) in the MHD equation. From the formula $R_m = \mu_0 \sigma v L$ (where σ is the conductivity, v the velocity of the fluid and L is the characteristic length scale of the source) the induced field B_i can be estimated as a function of the external one: $B_i = R_m B$.
2) In the piezomagnetic mechanism, the applied stress would change the magnetization M of the ferromagnetic rocks inducing a secondary magnetic field. By solving the differential equation, that, in an isotropic material, we can write as $\Delta M_i = \beta T_{ij} M_j$–where β is the sensitivity to the stress and T_{ij} is a function of the stress tensor, of the displacement vector and of the material's parameters–it is possible to estimate the magnetic field at the surface due to piezomagnetic mechanism.
3) Finally, in the electrokinetic effect an electric current is generated not by an electric field gradient, but by a pressure gradient at the electrified interface of a solid-liquid boundary. The electrokinetic current would be responsible of an induced magnetic field according to the Biot-Savart law.

Draganov et al. (1991) reconciled the (Fraser-Smith et al., 1990) observations with an origin in the MHD effect. Nevertheless, this conclusion was obtained by using values of permeability and lithostatic pressure of about two orders of magnitude higher than that at the Loma Prieta hypocentre depth (Fenoglio et al., 1995). On the contrary, it can be argued that, due to the strong attenuation of the magnetic field intensity, which decreases as the third power of the distance, MHD effect would give a negligible contribution to the magnetic signal detected on ground. Even the contribution of the piezoelectric effect could be negligible (Fenoglio et al., 1995), being of about 10^{-2} nT, i.e. two order of magnitude less than the two or about 7 nT reported by (Fraser-Smith et al., 1990). Whereas the electrokinetic effect could be able to generate a signal of 5–10 nT of the same order of magnitude of the signals measured before the Loma Prieta earthquake (Fenoglio et al., 1995). Interesting is also the research activity that tries to apply/extend the lesson learned in laboratory to research on field (see for example Vallianatos and Tzanis, 1999; Tzanis and Vallianatos, 2002; Vallianatos et al., 2004).

Electromagnetic Emissions at Higher Frequency

In order to explain the generation of electromagnetic emissions detected before some earthquakes (mainly in the ELF/VLF range but also up to HF) several physical models have been proposed that can be summarized in 4 main typologies such as: contact electrification, separation electrification, piezo-electrification (Ogawa et al., 1985; Zlotnicki and Cornet 1986) and atmospheric electricity generated by radon exhalation (Pierce, 1976). The electric field emissions generated in granite samples under bending or impact/shock have been studied by Ogawa et al. (1985) that has reconciled the observed phenomenology with the electric dipole momentum due to contact/separation electrification or piezo-electrification that would induce a charge separation. At a distance r from the dipole momentum (p), the near-, induced- and radiated-field (associated with increasing frequency range) are proportional to p/r^3, $dp/dt/cr^2$ and $d^2p/dt^2/c^2r$ respectively.

Most Recent Hypotheses on the Generation of Electromagnetic Fields

Some authors such as Liperovsky et al. (2008a) suggested that the variety of variables and coupling mechanisms involved in generating precursors and the large phenomenology of observed anomalies could be reconciled claiming that different physical mechanisms can explain quite the same precursors. It is not necessary to quote Occam's razor to argue that the simplest explanation, with fewer parameters, is usually the correct one. However, a consistent unified model would certainly be preferable for more stringent checks of the variables involved. By summarizing results from literature (including cited works and also Kondo, 1968; Vershinin et al., 1999; Hao et al., 2000) the amplitude of on ground preseismic quasi-static electric field disturbances–detected on long spatial (hundreds of kilometers) and temporal scales (from 10 days up to few hours)–can be estimated never exceeding 100 V/m (even though sudden and more intense increases fluctuations have been reported on shorter distances). In space, these values reduce to about 10 mV/m (Zhang et al., 2014). The proposed hypotheses of an electrostatic origin of the lithosphere-atmosphere ionosphere coupling mechanism, through a direct propagation, have been ruled out by several authors such as Sorokin et al. (2020). Moreover, Denisenko (2015) and Denisenko et al. (2018) have demonstrated that the penetrations of both a lithospheric electric field and a current in the ionosphere is negligible. In order to explain preseismic electric field anomalies (Freund, 2010) proposed that they could be originated by tectonic stress applied to lithospheric rocks. In fact, laboratory experiments have pointed out that igneous rocks under stress are able to generate currents carried by both electrons and positive holes that can cause positive electric potential, ionization of air molecules and corona discharge on the rocks surface. This model has been criticized for two different points of view. The anomalies registered in space (of for example ionospheric plasma parameters, electromagnetic values, etc.) consist of both increase and decrease of the studied variable: some time the same variable can show an increase or a drop along the temporal series about a given seismic event. According with Pulinets and Ouzounov (2011) the "unipolar character" electric field suggested by Freund (2010) would be in contradiction with the experimental results of bidirectional behaviour of ionospheric preseismic effects and could be applicable only to earthquakes occurring on ground because the release of charges in atmosphere would need of solid rocks on the surface. Moreover, even though the mechanism proposed by Freund (2010) could contribute to explain short time electric field fluctuations (on the scale of about 10 min), Sorokin et al. (2020) argued that it would not be able to explain quasi-static electric field in space on a longer temporal scale.

Pulinets and Ouzounov (2011) proposed the so-called LAIC model that can be summarized as follows. Radioactive gases (mainly radon) exhalations would be responsible of the preseismic chain. In the first step, the higher radon concentration (through alpha decay) would increase the local ionization in lower atmosphere and consequently the attachment centers for water vapor condensation causing a higher release of latent heat (Garavaglia et al., 2000; Dey and Singh, 2003; Silva and Claro, 2005). The resulting anomalies in the gradient of temperature would: 1) propagate from ground up to the high atmosphere (as detected by the OLR measurements), and 2) generate a flow of clusters/condensation nuclei (Svensmark and Friis-Christensen, 1997; Svensmark et al., 2007) that will affect the clouds formation rate and morphology (Ondoh, 2004). Simultaneously, the conductivity of atmospheric layers would change affecting the Global Electric Circuit inducing fluctuations in the ionospheric parameters such as: height scale, temperature and density of electron and ions, ion composition, etc. According with the authors, the model results into: the formation of ionospheric irregularities, electromagnetic disturbances, and the precipitation of charged trapped magnetospheric particles. Finally, the model forecast a feedback process when precipitating electrons would increase the D layer ionization affecting: VLF reflection height, whistler dispersion and more in general the e. m. propagation conditions in the Earth-ionosphere. The "bipolar character" of Pulinets and Ouzounov (2011) model aims at reconciling in a consistent scheme the extended phenomenology of the preseismic observations: the positive or negative direction of anomalous electric field on the ground can induce both positive and negative variations observed for several physical parameters (such as the electric air conductivity over the earthquake, the ionospheric parameters, the cloud formation, etc.).

More recently, Sorokin and Hayakawa (2014) proposed that preseismic processes would originate a current source near to ground that modify the lower atmosphere properties by generating an EMF (electro-motive force) that will cause ionospheric electromagnetic and plasma disturbances. The model would allow explaining several aspects of the phenomenology such as: the existence of quasi-static electric field on ground and in space over the seismic regions, the increase of conductivity with altitude and a mechanism for limiting the vertical component of the electric field on ground. Associated with EMF enhancement, ionospheric instability can generate AGW, field-aligned currents and plasma irregularities along the magnetic tubes, spectral broadening of VLF transmitter signals, enhancement in space of ELF (due to scattering of with conductivity irregularities) and changes in Schuman resonance harmonics.

A common feature to the models [such as Pulinets and Ouzounov (2011) and Sorokin et al. (2020)] based on radon release is that they could be applicable both for in land and undersea earthquakes and potentially independently from the seismo-tectonic characteristics of the involved faults, as long as a sufficient radon exhalation takes place.

Ionospheric Disturbances

The ionosphere is a highly dynamic environment characterized by global structures (evolving under the solar periodic and irregular activity) as well as by local irregularities on different scales and times. The list of ionospheric parameters routinely monitored by ionosondes and GPS that have been studied in correlation with seismic activity includes total electron content (TEC); F2-layer critical frequency (foF2); electron temperature at F2-layer heights; LF radio signals etc. Some references can be for example: (Strakhov and Liperovsky, 1999; Ondoh, 2003; Ondoh, 2009; Trigunait et al., 2004; Hobara and Parrot, 2005; Liu et al., 2006; Maekawa et al., 2006; Ondoh and Hayakawa, 2006; Dabas et al., 2007; Chum et al., 2016).

Hayakawa et al. (2011) reported an increase of the amplitude and frequency shift of the fourth Schuman resonance before seismic events and proposed that this could be due to changes in the height of reflection and absorption of electromagnetic waves induced by variation of the ionization degree in the D layer.

Ondoh (2003) reported that changes in the altitudinal profile of ionospheric plasma density over a seismically active region could be accompanied by the formation of sporadic layers in the lower ionosphere. In addition, Pfaff et al. (2005) tried to reconcile the occurrence of sporadic E layer with seismic events, proposing that this would be induced by differential charging of top and bottom sides of clouds due to the migration of radon. Silina et al. (2001), Ondoh (2004), Ondoh and Hayakawa (2006) and Korsunova and Khegai (2006) and Korsunova and Khegai (2008) have identified ionospheric earthquake precursors by using sporadic Es layer. The method applied to ionosonde data has shown an increase of Es occurrence in conjunction with strong earthquakes ($M > 7$) in Japan and moderate earthquakes (with $5.5 \leq M$) in Italy (Perrone et al., 2010). Similarly, Perrone et al. (2018) have identified anomalous variations of the sporadic E-layer parameters (h′Es, foEs) and foF2 in occasion of earthquakes with magnitude $M \geq 6.0$ in Greece during the 2003–2015 period. By studying the foF2 variations, through ionosondes measurements, Hobara and Parrot (2005) have detected a decrease near the epicenter of the Hachinohe earthquake (magnitude 8.3) of 1968. A decrease of foF2 (greater than 25%) has been reported also by Liu et al. (2006) within 5 days before of more than 150 seismic events (of magnitude greater or equal than 5) occurred in a period of 5 years. The authors pointed out a correlation between the entity of the decrease and the earthquake magnitude, whereas the effect decreases far from the epicenter and is not more evident more than 150 km from the epicenter. In addition, Kandalyan and Alquran (2010) have investigated the existence of a possible correlation between the occurrence of strong earthquakes and ionospheric scintillations. Even though, many TEC anomalies, detected by GPS networks, have been correlated to seismic events (see also Tsai et al., 2006; Singh et al., 2009; Jhuang et al., 2010; Hasbi et al., 2011; Kon et al., 2011; Ma and Wu, 2012; Contadakis et al., 2012 and references therein) nevertheless, the debate is still intense because some authors (e.g., Rishbeth, 2006) highlighted that generally TEC perturbations could be caused by the natural ionospheric and geomagnetic variability and that the precursors analyses are generally carried out after the earthquake occurrence (e.g., Mulargia and Geller, 2003; Afraimovich and Astafyeva, 2008). For this reason, statistical analyses on long time series are particularly valuable. By analyzing changes in total electron content from the global ionosphere map (GIM) within 2.5° latitude and 5.0° longitude around the earthquake epicenter, Thomas et al. (2017) found no statistically significant TEC changes before the 1279 $M \geq 6.0$ earthquakes for the period 2000–2014 (after declustering for aftershocks). The Wenchuan earthquake on May 12th, 2008, 14:28 LT, occurred in the eastern edge of the Tibetian plateau, is remembered not only for its devastating consequences–with tens of thousands of death and the large-scale disruptions in the western Sichuan–but also for having given a further input to Chinese scientific community, involved in studying earthquake precursors, to develop the satellite CSES mission designed for remote sensing the Earth electromagnetic environment. Zhao et al. (2008) have studied TEC data from 58 GPS receivers installed nearby the epicenter of the Wenchuan earthquake. Whereas the enhancement observed on May 3rd have been mainly reconciled with geomagnetic storm occurred in the 00:00–10:00 UTC, the analysis has pointed out a TEC anomalous disturbances detected on May 9th over the southern China and its conjugate point in the southern hemisphere could be related to the Wenchuan earthquake. For specific techniques that allow discriminating between real seismo-ionospheric anomalies and artifacts see also (He et al., 2014). By analyzing VTEC measurements, during all of the 20 $M \geq 6.0$ earthquakes in the Taiwan area from September 1999 to December 2002, Liu et al. (2004) reported preseismic ionospheric anomalies (with respect a 15-days running average) before of the 80% of the analyzed earthquakes. More precisely, for the seismic events in the Taiwan, ionospheric VTEC remarkably decreased during 18:00–22:00 LT within 1–5 days before the earthquakes. Observations are in agreement with the 93% reported by Liu et al. (2000). In occasion of the Chi-Chi earthquake Liu et al. (2010) reported that the correlations between the co-located NmF2 and VTEC about one week before the event was extremely high (about 0.95) suggesting that TEC measurements *via* GPS receiver would allow monitoring preseismic ionospheric anomalies. Liu et al. (2004) suggested that the anomalies appear first near the Earth's surface and then extend to higher altitudes through an unknown mechanism such as diffusion, atmospheric gravity waves or due to some vertical preseismic electric field. Since a large amount of contribution comes from higher altitudes, the appearance of the diurnal VTEC features may be somewhat later than that of the NmF2 (or foF2).

By investigating TEC spatial distribution, Liu J. Y. (2009) and Zakharenkova et al. (2008) reported that preseismic TEC fluctuations seems accompanied by simultaneous changes of the electric field in the ionosphere [of the order of 1–10 mV/m, also in agreement with Klimenko et al. (2012)], but without variations on ground; the authors also estimated that an increase of several times of the aerosols concentration on ground could cause TEC variations of several tens of percent (see also Ruzhin et al., 2014).

According with Freund (2010), the rocks under stress would constitute a dynamo able to generate preseismic currents of electrons and positive holes. The author of Kuo et al. (2011) estimated that current density of about (10^{-7}–10^{-6}) A/m^2 would be able to generate a daytime TEC variations from 2% up to 25%. On the contrary, Sorokin et al. (2020) highlighted that this hypothesis would be incompatible with the measurements because: 1) the duration of the Freund currents (only several minutes) doesn't match with that of the TEC variations; for achieving the claimed current intensity it would be needed a vertical electric field of about (10^7–10^8) V/m that is higher than the values observed on ground in the seismic areas.

The investigation of seismo associated disturbances on a long temporal scale can be carried out by the study of the variations of amplitude and phase of VLF signals (between ground based transmitters and receivers) traveling over the preparation zone of seismic events (Biagi et al., 2004; Rozhnoi et al., 2004; Hayakawa et al., 2011). Amplitude and phase of such signals - generally very stable as a function of time–have shown variations of the scale of tens of minutes possibly induced by variations the height of the Earth-ionosphere waveguide due to local ionization or secondary effects induced by seismic sequence.

Multi-Parametric Analyses Looking for Earthquake Precursors

The common feature of the most recent models for investigating earthquake precursors is to assume a multi-parameter coupling mechanism (which also includes several feedback processes, see for example İnan et al., 2010; Pulinets and Ouzounov 2011; Freund 2013; Hayakawa et al., 2018; Ouzounov et al., 2018) according to which the exchange of energy and particles between the lithosphere and the lower and upper atmospheric layers of the ionosphere, during the earthquake preparation phase, causes a variety of precursor phenomena that should be considered as a whole [in the so called holistic approach of De Santis et al. (2019b)]. Therefore, one of the updated trends in precursor research is the simultaneous measurement of several physical variables [such as radon and other gas release, air temperature and humidity (e.g., Akhoondzadeh et al., 2018), thermal infrared emissions (e.g., Natarajan and Philipoff, 2018), electromagnetic fields and ionospheric parameters, including electron density (e.g., Zhang et al., 2011; De Santis et al., 2015) etc.] for a joint analysis of such complex and interrelated system (Ouzounov et al., 2018). Because data needed for these investigations are collected both on ground and by satellite, we address the reader to the companion article Picozza et al. (2021) and to therein references, where this topic is further discussed for space-based observations of precursors. The possible correlation between seismic events and fluctuation of water column content has been studied for example by Dey et al. (2004) for the 2001 M7.8 Gujarat earthquake; by Ma et al. (2010) for the Hengchun (Taiwan) M 7.2 event of 2006 and by Wu et al. (2016) for the 2009 M6.2 L'Aquila earthquake. Anomalies of ozone have been investigated for example by Akselevich and Tertyshnikov (1995) and by Tronin (2002a). In this framework, Piscini et al. (2017) proposed the CAPRI (Climatological Analysis for seismic PRecursor Identification) algorithm searching for anomalies of the time series of climatological parameters. The authors analyzed skin temperature, total water vapor column, and total ozone column for the period from two months prior to the entire Amatrice-Norcia seismic sequence (central Italy)–which began on August 24, 2016 with an M6 earthquake and included two other large quakes (i.e., an M5.9 earthquake on October 26 and then an M6.5 on October 30)–comparing the measurements with time series of data from the previous 37 years in order to remove the possible effect of global warming. The method was also extended to analyze the M 6.2 L'Aquila (2009) earthquake. Piscini et al. (2017) reported persistent anomalies that emerged simultaneously in all parameters analyzed, conclusions that would be confirmed by comparing the data with those of the same months in other seismically quiet years. On the other hand, the authors have commendably pointed out that a single anomaly, if present, of an individual climatological parameter would have low statistical significance as it could be caused by several sources unrelated to the earthquake. Moreover, weather phenomena could move and mix the substances released from underground into the atmosphere could mask precursors, if any, lowering their signal-to-noise ratio and shortening their persistence in the atmosphere (Marchetti et al., 2019). Similar results have been obtained by De Santis et al. (2020) that have applied a multi-parametric study to the 2019 M7.1 Ridgecrest earthquake, by analysing furthermore methane exhalations [as suggested by Cui et al. (2019)], electron density fluctuations, and magnetic field measurements from Swarm satellites (Friis-Christensen et al., 2006; Zhu et al., 2019). The results can be summarized as follows: 1) precursor times would be much longer than those identified by other papers (especially about ionospheric precursors which seem to occur only a few hours to days before large seismic events) (see for example Heki, 2011; He and Heki, 2017; Yan R. et al., 2017); 2) the preparation phase would be much longer than few days [as also suggested by Liu et al. (2020), Marchetti et al. (2019), Marchetti et al. (2020), Sugan et al. (2014), Giovambattista and Tyupkin (2004)]; claimed precursors would follow the empirical Rikitake (1987) law, recently confirmed for ionospheric precursors from the satellite by De Santis et al. (2019a). In any case, it is a complex task to monitor several or all atmospheric effects due to the LAIC mechanism that also include linear cloud structures (the "earthquake clouds" that would repeat the shape of the tectonic structure in the sky (Jones and Stewart, 1997; Nissen et al., 2012); OLR [Ongoing Longwave Radiation–infrared emission at 10–13 μm recorded above the clouds (Ouzounov et al., 2007)]; jet streams (Wu, 2007); etc. Even in a multi-parametric approach, the benefit of analysing the OLR–measured in the upper atmosphere - is that the OLR can take into account the cumulative effect of all thermal contributions possibly due to the earthquake, between the ground surface and the tropopause, according with the so-called "synergy of precursors" (Pulinets, 2011). Moreover, thanks to the long time series of data collected by the NASA Aqua and NOAA/AVHRR satellites, it is possible to compare the local and temporal variations of the OLR with a well-estimated reference background that would improve the statistical significance and reliability of pre-earthquake fluctuations of this parameter. Ouzounov et al. (2007) reported that a few days before the M 9.1 Sumatra earthquake of December 26, 2004, the OLR value was above 80 W/m^2 compatible with the estimate given by Kafatos et al. (2007). In general, the results of the multi-parameter analyses–also made possible by recent big data analysis techniques and large computational capacity–reinforce the idea of considering such an integrated anomaly recognition system as an effective tool for systematically finding earthquake precursors.

POSSIBLE APPROACHES FOR RECOGNIZING NATURAL AND ARTIFICIAL ELECTROMAGNETIC BACKGROUND

In order to identify electromagnetic earthquake precursors it is essential to reject carefully the background due to natural non-seismic sources and industrial electromagnetic noise. Although, the main driver of the electromagnetic Earth environment is the solar wind that shapes the magnetosphere and affects its dynamics, several other natural and artificial sources of electromagnetic emissions take place in the geomagnetic cavity. The terrestrial electromagnetic background noise of not-ionizing radiations (distributed–although not uniformly–in a broad range of power levels and frequencies from about mHz up to 300 GHz), is generated by a wide variety of natural (atmospheric thunderstorms (e.g., Neubert et al., 2008) or cosmic rays) and man-made (power line harmonic radiation, industrial and communications equipment, etc.) sources (Hayakawa, 1994). These emissions constitute a significant background with the respect to the elusive electromagnetic emissions and related ionospheric disturbances possibly caused by natural geophysical activities, such as earthquakes and volcanic eruptions (Hayakawa, et al., 2011).

Natural Non-Earthquake Electromagnetic Noise on Ground and in the Near Terrestrial Environment

Depending on the frequency, the natural electromagnetic noise in the magnetosphere arises from wave-particle interaction phenomena, while within the ionosphere originates from atmospheric electric discharges through several propagation mechanisms Simões et al. (2012). On ground, in some areas, the artificial noise generated by technological devices exceeded the natural one, while in the VLF-HF range, the atmospheric electromagnetic emissions exceed the artificial ones in rural areas (in the order of some tens of dB) and are comparable to them in industrialized zones. At higher frequencies, the electromagnetic noise induced by thunderstorms becomes less important, and that of cosmic origin (up to millimeter wavelength) prevails (Bianchi and Meloni 2007).

In the ULF band (from 1 mHz up to 1 Hz, i.e., from the lowest frequency that the magnetospheric cavity can support, up to the ions gyro-frequencies) are observed the geomagnetic pulsations and the “incoherent noise” (Lanzerotti et al., 1990; Jacobs et al., 1964). The low-frequency pulsations are generally originated by the Kelvin-Helmholtz instability in the magnetopause, through to the interaction of the solar wind with the magnetosphere, or by the waves “upstream” in the “foreshock” region. Wave-particle interactions in the magnetosphere give rise to the so-called “chorus” and “hiss” phenomena. The chorus are among the most intense electromagnetic emissions generated in the external magnetosphere and propagating up to the Earth surface where are observed at intermediate latitudes. The spectral characteristics of the chorus (from about 500 Hz to about 1.2 kHz) consist in a succession of tones - predominantly growing–that resemble to the birds chirping, that constitutes the origin of their name. Hiss are intense electromagnetic emissions, occurring mainly in the auroral zone, in a broad frequency band (from a few hundreds of Hz up to several tens of kHz). The most important electromagnetic phenomenon in the ELF band is the Schumann resonance, at about 7 Hz and higher harmonics, arising at the proper oscillation frequencies of the natural Earth-ionosphere waveguide (Polk, 1983). The tropospheric layers (with variable electrical conductivity) between the Earth crust and the ionosphere (both of them schematized as perfectly conductors) constitute an electromagnetic cavity in which electromagnetic radiation is trapped and waves can propagate. Waves constructive interference can excite resonances in the frequency band of about 6 ÷ 60 Hz in the above-mentioned Earth-ionosphere waveguide. Lightning are the main source of electromagnetic noise background in the ionosphere, where they generate emissions from ELF (about few Hz) up to VHF (about hundreds of MHz) although most of the energy is concentrated in the VLF band (from 0.1 to 10 kHz) with a typical power spectrum slope. Some thousands of storms are estimated to occur daily on the Earth (Shvets and Hayakawa, 2011), generating about 100 lightning per second, with discharges up to 10 kA per each and releasing an amount of energy from a few units up to a few tents of GJ, i.e., powers of the order of 0.1 ÷ 1 TW, for a total of 10^{19} J released yearly around the world. The natural electromagnetic phenomena relevant in the ELF-VLF frequency bands are the so-called sferics, tweeks and whistlers, generated by lighting electromagnetic pulsed signals (of a few ms), that travel with a low attenuation in the Earth-ionosphere waveguide for thousands of kilometres (Helliwell, 1965; Hitchcock and Patterson 1995). The propagation of the spherical waves is determined by the variable ionospheric conditions and the sferics can be observed with directional antennas and AM receivers as typical disordered sounds called “statics”. The tweeks (generally detected in the evening after the sunset) are sferics showing a spectral dispersion during their propagation and that, in acoustic spectra, sounds similar to birds singing with frequencies of about 1 ÷ 7 kHz. The higher harmonics penetrate in the ionosphere more in depth than the lower components that, being less attenuated, cover longer distances. Different paths imply different arrival times and the spectrograms show descending tones with a duration from about 25 ms up to about 150 ms. The whistlers are intense circular-polarized electromagnetic waves propagating at a frequency below the plasma frequency (from about 6 kHz up to a few hundred Hz), generated by lightning and perceived in radio receivers as characteristic decreasing tones. Whistler waves rotate clockwise propagating along the geomagnetic field lines through the ionosphere up to the magnetosphere, bouncing back and forth, and showing a significant spectral dispersion as function of the path length and the characteristics of the crossed medium. Also in the LF/MF/HF bands, up to the plasma frequency, the natural electromagnetic noise is mainly generated by atmospheric phenomena (with an amplitude decreasing at higher frequencies) and its propagation is affected by local ionospheric conditions and geometry of the paths. For frequencies higher than 15 ÷ 30 MHz the cosmic noise of astrophysical origin appears (Kraus, 1988; Erickson, 1990).

Anthropogenic Sources of Electromagnetic Emissions in the Near-Earth Space

The natural electromagnetic background is accompanied by the emissions due to human activities. The artificial noise originated by industrial technologies (power lines, radio and TV broadcasting stations, communications facilities, etc.) strongly depends on the distance from the sources, can vary also by many orders of magnitude, frequency and power, and show distinctive features such as continuous or impulsive regime, modulation and polarization. In the ELF band, the most powerful source of artificial noise (except Antarctica where the natural ELF emissions can be detected with few anthropogenic interference) is represented by power lines harmonic radiation (PLHR) which ideally operate at a single frequency of 50 Hz (60 Hz in the U.S.). At these frequencies, the electric and magnetic fields are virtually disconnected and (due to the multipolar configuration of the electric lines) decrease dramatically by increasing distance from the lines. Satellite observations show that PLHR can contribute–through non-linear interactions–to precipitation of Van Allen particles from the slot region in the radiation belts. The principal part of the PLHR energy dissipates in the lower ionosphere modifying ionospheric currents. Ground-based radio-navigation and communications VLF transmitters in the 10 ÷ 20 kHz frequency band can trigger new waves, ionospheric heating, wave-electron interactions, and particle precipitation *via* the cyclotron resonance. The wave and the particles interact when the Doppler-shifted wave frequency seen by the particles is close to the electron gyro-frequency. The trajectory of particles follows the magnetic field lines but the ray path of the injected waves is only field aligned if the wave is propagating in a whistler mode duct. The strongest interaction region is around the geomagnetic equator. Triggered emissions by coherent waves are related with non-linear wave growth caused by resonant particle trapping in a non-uniform magnetic field. At HF frequencies, powerful broadcasting stations can provoke ionospheric Joule heating by changing plasma temperature and density Erickson (1990). The dissipation in the ionosphere of the above-mentioned waves may contribute to the global warming of the Earth, since the change in global temperature increases the number of natural lightning discharges in the atmosphere and this produce more magnetospheric whistlers that may provoke heating and ionization in the lower ionosphere. This is a feedback mechanism since lightning are sources of NOx that influence the ozone concentration in the atmosphere contributing to the greenhouse effect. Moreover, precipitation of energetic electrons by anthropogenic waves may trigger other lightning discharges. This explains the importance in studying such anthropogenic electromagnetic emissions. For VHF or higher frequencies, that are relevant for radio astronomy observations Erickson (1990), the anthropogenic electromagnetic emissions are due to radio and television broadcasting stations, mobile communications, car ignition systems and industrial equipment, while radar and satellite devices, as well as highly directional SHF/EHF emitters, do not give a significant contribution to the electromagnetic noise background.

Rejecting Non-Earthquake Associated Effects From Data Analysis

The described features could allow distinguishing the effects of natural non-seismic, seismic and man-made electromagnetic emissions. In some frequency range (i.e., at 50 or 60 Hz or for signals from radio transmitters), it is easier to reject man-made electromagnetic emissions. On the other hand, in many cases, it is not straight to remove the background emissions due to magnetospheric disturbances and tropospheric sources aimed at identifying seismo-electromagnetic disturbances. This is particularly true for example in the statistical analyses (such as those based on the epochs overlap method) where data from different geographic regions (naturally exposed to different geomagnetic processes) are grouped and studied together.

In this framework, the analyses published in literature have adopted different strategies. Unfortunately, in many cases, the studies have not carefully excluded data collected in geomagnetically disturbed periods. A reduction of the background can be achieved by using magnetospheric and ionospheric indices. Some examples are the well-assessed (global or aerial) indices Kp, Ap, AE, Dst, etc. released with relatively low time resolution (hour or multi-hour scale). Other ones are the more detailed indices able to describe the geomagnetic perturbations at mid-latitudes as a function of longitudinally asymmetric (ASY) and symmetric (SYM) disturbances for both H and D components (respectively parallel and perpendicular to the geomagnetic dipole axis). A further filtering, more difficult to be applied but that can be investigated, is to take care of the metrological conditions and of the lightning activity in the area of the earthquake and in the conjugated one. Frequencies range around the band of the known VLF transmitters should be also rejected in the analyses of seismo-associated disturbance because the power of the artificial signals can overwhelm the natural and faint emissions possibly associated to earthquakes. On the other side the high stability in power and frequency of these transmitters, as well as of the radio broadcasting stations, have been and are investigated in order to point out fluctuation in the transmission parameters possibly due to seismo-electromagnetic disturbances occurred along the transmission path from the transmitter and a fixed receiver station. In addition, the polarization of eventually directional signals can give hints on the internal or external origin of detected measurements candidates to be associated to lithospheric processes. In general, a strong interdisciplinary approach, between different research fields, is mandatory to clean data, to reject background and to better distinguish such complex phenomena.

Hattori (2004) applied the principal component analysis (PCA) for decomposing and filtering time-domain series of observations in order to identify background signals (generated by DC noise, natural emitters and man–made devices) that could be removed in order to point out earthquake related anomalies (if any). The authors have applied the procedure to ground measurements of magnetic field (also including data gathered during strong geomagnetic disturbances) and reported that the first two principal components would be correlated to geomagnetic variation and anthropogenic sources, respectively, while the third component has been investigated in order to point out seismo-associated disturbances. By applying principal component analysis to magnetic data from six observatories (4 near Napa, California, together with two remote reference stations), Kappler et al. (2017) were able to identify and distinguish global geomagnetic signals (such as solar-generated noise) and anthropogenic signals.

Recently some authors have explored the application of machine learning methods for automatically classifying and recognizing earthquake precursors on ground and in space (see for example Rouet-Leduc et al., 2017; Li et al., 2018;

Akyol et al., 2020; Johnson et al., 2021; Xiong et al., 2020; Xiong et al., 2021). The field of research is very interesting, but asks for some caution. Even though the amount of available observations is huge, the supervised methods could suffer the difficulty of learning from a limited number of tagged measurement: because even for scientists the signature of possible precursors is still unclear, it is hard to define a clear "learning path" for an automatic recognition. On the other side, the unsupervised methods could help in extracting/clarifying the signature of precursors, but the artificial intelligence systems should be trained also in distinguishing spurious phenomena for the needed background rejection.

REPORTS OF EARTHQUAKE LIGHTS FROM WITNESSES AND ANOMALIES IN ANIMAL BEHAVIOUR

One of the most controversial debates about earthquake precursors is the presumed correlation between the occurrence of seismic events and: 1) observations of earthquake lights; 2) reports of anomalous animal behaviour. We highlight that these two groups of alleged precursors are significantly inhomogeneous and very different from each other. Nevertheless, we present them in the same paragraph not with the purpose of mixing such a broad phenomenology, but because they often share a non-instrumental method of observation (with some recent, but still rare and unclear exceptions of photo/video recording) and suffer from the high variability of sensory perceptions by biological organisms with the consequent inherent difficulty of assessing the statistical significance of the reports.

Reports on Earthquake Lights

Pre- and co-seismic visible luminescence phenomena (so-called earthquake lights, EQLs for short) have been reported by several authors such as Galli (1910), Terada (1930), Richter (1958) and Yasui (1968) that published the first photograph of EQL; Derr (1973), Derr (1986), Tsukuda (1997) for the Kobe earthquake; Papadopoulos (1999), Stothers (2004), St-Laurent (2000) and Omori et al. (2007). The reports refer primarily to shallow earthquakes of high magnitude, but in some cases, observations have also been collected on medium events with deeper epicentres. EQLs have been reported from a few up to several kilometers from the epicenter, across the visible spectrum, with durations ranging from a fraction of a second to several seconds. EQLs have been sighted both before (from several weeks to a few seconds, near the epicenter) and during earthquakes (even far from the epicentre). More recently, in his valuable catalog of evidence of eyewitnesses - ranging from 9 months before up to five months after the main shock of the 2009 L'Aquila earthquake–Fidani (2010) compiled a careful classification (and an attempt to locate) observations of lights, flames and other bright observations–reported in a wide area up to 50 km far the city of L'Aquila and along the Aterno valley–looking for a correlation with the occurrence of the earthquakes of the L'Aquila seismic sequence. Heraud and Lira (2011) reported some EQLs that would have occurred during the 2007 Pisco earthquake–also supported by a video recording, and apparently not induced by thunderstorms or electrical faults–suggesting that they would have been generated by some electrical phenomena not yet understood in the atmosphere above the epicentral area. In general, some of the EQLs reported in the literature seem less convincing, however, some characteristics of the EQLs (shapes, colours, flames, etc.) are recurrent in the evidences (such as in the L'Aquila, Saguenay, and Pisco events) and the quantity of observations ask for a careful consideration of this phenomenon. Persinger, (1983) suggested that co-seismic EQLs would be related to energy release during fracturing of rocks; (Brady and Rowell, 1986; Kato et al., 2010; Martinelli et al., 2020b) and other authors showed that under high-stress conditions rocks could emit electromagnetic radiation prior to fracture. Additional hypotheses have been proposed in order to explain the origin of EQLs (Mizutani et al., 1976; St-Laurent et al., 2006), including a generation due to gas and aerosol exhalation Liperovsky et al. (2005) and a high-frequency electromagnetic origin Liperovsky et al. (2008b). Analysing the observation of claimed EQLs potentially associated to about 65 earthquakes (38 from Europe and 27 from the Americas) in different geotectonic settings, Thériault et al. (2014) proposed an updated model for the origin of EQLs associated with both intraplate and interplate earthquakes, which is based on the generation of electron charge carriers under high-voltage conditions (see also Freund et al., 2009; Freund 2010). Their thesis is that EQLs may be predominantly associated with intraplaque earthquakes within or nearby rift-related structures. EQLs do not always appear to occur before all strong earthquakes, and they vary in rate. Freund et al. (2021) suggested a solid-state physics mechanism that could take into account the variety of phenomenology. The peroxy defects in igneous rocks–mainly in gabbroic rocks that fill the sub vertical dykes and would be preferentially located along boundaries or between adjacent mineral grains–would make them highly susceptible to ever so slight displacements of mineral grains. The propagation of seismic waves would activate peroxy bonds generating charges displacement. The co-seismic EQL would be caused by the rupture of peroxy bonds, a discharge from the top of the dyke, removing some of the charge carriers. Less evident is how the other processes (corona discharges, thermal infrared emissions, air ionization as well as ion and electron fluctuation in the ionosphere, and electro-magnetic anomalies) would be generated by such mechanism before the propagation of seismic mechanical waves. Within the already highly debated topic of earthquake precursors Hough (2016), the complexity of the observations of pre- and co-earthquake EQLs is even more controversial because analysing eyewitness observations is much more difficult than studying instrumental measurements. Moreover, the possibility of misinterpretations is not negligible, also because the survey of witnesses is generally based on questionnaires filled out and collected after tragic events in very difficult and stressful environmental conditions. Therefore, the statistical completeness of anecdotic or sparse datasets could strongly influence the interpretation of the collected data, the over- or under-estimation of outliers and the rejection of spurious cases. In addition, at least in some cases, data are collected and analysed much later than the seismic events, when eyewitness accounts may no longer be independent. Photographic and video evidences are certainly a valuable tool to support the reliability and objectivity of claimed observations, but published testimonies leave room for uncertainty and interpretation. Despite the large amount of testimony collected in published about EQLs (see also Lockner et al., 1983; Johnston, 1991; Whitehead and Ulusoy, 2015 and reference therein), it appears that the rate of observation by witnesses for EQLs is significantly lower than even the most conservative estimates of hallucination prevalence in the normative population. This consideration is neither a bias due to the authors' skepticism nor a preclusion against the investigation and existence of EQLs, but something that should be cautiously taken into account when assessing the reliability of this intriguing phenomenon. Indeed, it is worth noting that the prevalence of hallucinations is by no means negligible even in the general population (which may include psychotics, whether they know they are psychotic or not. Some estimates of prevalence in nonclinical samples are about 10% (Sidgwick, 1891; West, 1948; Posey and Losch, 1983; Asaad and Shapiro, 1986; Sidgwick et al., 1994). Tien (1991) suggested 10–30 cases per 1,000 people per year while for Ohayon (2000) (although the methodology adopted is open to criticism) up to 40% of the 13,000 subjects included in the study would have experienced daytime hallucinations, demonstrating how hallucinations can occur sporadically even in healthy subjects in normative populations (including all possible types of dis- or mis-perception). More recently, Temmingh et al. (2011) suggest a lifetime prevalence of 10–15% for vivid sensory hallucinations. Because of the difficult conditions of a post-earthquake survey, reports published in EQLs include limited information on some key witness parameters (such as education, occupation, alcohol and drug use, and cognitive status) that play a role in estimating the status of participants in psychological studies (e.g., Badcock et al., 2017; Eaton and Kessler, 1985), and that should, at least, not be ignored when collecting and evaluating data from witnesses of earthquake observations. Memories of witnesses and therefore a precise time location of the observations are key points in distinguishing EQL occurred during main shocks or before them (but possibly during foreshocks). If the co-seismic intense flashes of light bursting out of the ground could be "more easily" reconciled with the propagation of seismic waves (Freund, 2019), the preseismic luminous events are more debated, even though the supporters of EQLs claim a common origin of pre- and co-earthquake visible emissions. Therefore, filtering psychological uncertainty and the future instrumental proofs could help in cross-checking eyewitness testimonials and clarifying EQLs existence and origin. The need to consider all possible biases, including possible "human illusions," in the difficult task of distinguishing EQLs from background noise is relevant not only to reject spurious events, but also to estimate the possible rate of EQLs. According to Papadopoulos (1999), De Ballore (1913) and Mallet (1855) and Thériault et al. (2014), EQLs would occur in about 10% of earthquakes (5–6% at night, while they would be hardly visible during the day) but for Persenger and Derr (1984) this percentage would represent a lower limit because many observed EQLs would never be reported and published in the scientific literature, or are interpreted as unidentified flying objects (UFOs) (Devereux et al., 1983). All these aspects should be carefully evaluated in surveys (including those aimed at estimating EQLs) in populations exposed to long and highly stressful conditions–such as the seismic sequence that often precedes main earthquakes–which obviously have an impact on the psychological and psychiatric response to environmental stimuli (individual and social) possibly varying the threshold of reaction as well as the sensitivity of witnesses, even if sincere and in good faith!

Can Anomalies in Animal Behaviour be Reliably Correlated With Impending Earthquakes?

In the letter of 1949, recently published Dyer et al. (2021), in reference to the work of Karl von Frisch (Nobel Prize in Physiology in 1973) and the sensory perception of animals, A. Einstein wrote "It is conceivable that the investigation of the behaviour of migratory birds and homing pigeons may one day lead to the understanding of some physical process that is not yet known". A few words that show an insight into animal ethology and physiology that preceded by more than half a century the investigations and discoveries of our years about some animals capabilities (Wu and Dickman, 2012; Lambert et al., 2013; Mouritsen, 2018). But, can birds be sensitive to earthquakes as Yosef (1997) has suggested? It is well know that birds can use the Sun, stars, and magnetic field to orient themselves; young and adult turtles as well as salmon navigate using the geomagnetic field as a reference system (Lohmann, 2007; Lohmann and Lohmann, 2019); glass eels would have a magnetic compass linked to the tidal cycle (Cresci et al., 2017); cellular autofluorescence is sensitive to the magnetic field (Ikeya and Woodward, 2021); etc. Although, such research could also shed new light on the long-standing claim that animals are sensitive to earthquake precursors (see for example Ikeya, 2004; Freund and Stolc, 2013; Yamauchi et al., 2014; Grant et al., 2015 and therein references) however, this topic is highly debated to the point of overt skepticism even within the most open and convinced scientific community to investigate precursors. In their famous paper, Woith et al. (2018) analysed more than 700 reports of claimed correlation between earthquakes and "anomalies" in animal behaviour. Observations have been claimed for organisms belonging to more than one hundred different species–ranging from deep-sea fish (Orihara et al., 2019) to catfish (Musha, 1957), from mice (Ikeya et al., 1996) to elephants (Garstang, 2009), from pets to snakes (Tributsch, 1982), from cows (Fidani et al., 2014; Yamauchi et al., 2017) to mouse (Yokoi et al., 2003), etc.–published in nearly 200 papers. Hypotheses advanced to explain the claimed anomalous animal behaviours range from a high sensitivity (postulated but not demonstrated) of animals to earthquake-related mechanical oscillations to their claimed ability to sense magnetic field fluctuations of a few nanotesla (Li et al., 2009) (which should be cautiously verified, pre-earthquake magnetic anomalies being detected even below this threshold). The claimed observation distance varies from a few up to hundreds of kilometers, but most of them were observed within 100 km of the epicentre and about 70% within 50 km. Although the advance in time varies from a few minutes to months before the earthquake, the number of claimed observations increases close to the seismic event and almost 60% of the cases fall in the last 5 min. Observations of claimed abnormal animal behaviour have been reported for several earthquakes worldwide, but more than 50% of the reports relate to only 3 earthquakes out of the 160 analysed by Woith et al. (2018). Beyond the specific reports, the objective difficulties in analysing data (and screening publications) on putative earthquake precursors based on animal behaviour can be summarized as follows: 1) the common bias of categorizing animal behavior as anomalous events only ex post seismic events; 2) the often unclear distinction of normal/anomalous behavior when a threshold and quantitative criteria are missing (preventing a clear definition of the signal-to-noise ratio); 3) the frequent cases of (too) short or partially published time series [focusing only on the "relevant" (claimed) portion of the "anomalous" data]; 4) the partial or missing monitoring of environmental variables (such as meteorological parameters, moon phase illumination, ethological constraints/variabilities, human or predatory conditioning, animal health conditions, etc.) that may influence animal behavior even under normal conditions; 5) statistical uncertainty in looking for recurrence/exceptionality when comparing too short time series of biological cycles with external sporadic events. Some attempts have been made in the past to evaluate (systematically and independently) the reliability of some earthquake prediction approaches and methods, such as the IASPEI initiative (Wyss, 1997; Wyss and Dmowska, 1997), or the international Collaboratory for the Study of Earthquake Predictability (CSEP) (Jordan, 2006; Michael and Werner 2018), etc. However, regardless of the initiatives, these approaches cannot be fruitfully applied to control animal observations because of the incomplete description of the original observations, the lack of data, and the difficulty of repeating observations under similar and controlled seismic and environmental conditions (Fidani, 2013; Fidani et al., 2014). The combined effect of too short time series, the periodicity of biological cycles, phase shifts, and the temporal distribution of earthquakes in long seismic sequences (with the difficulty of distinguishing foreshocks and aftershocks) can lead to misinterpreting random coincidences for positive correlations. Indeed, for example, the 80% success rate of catfish in alerting for an incoming earthquake claimed by Hatai and Abe (1932) should be interpreted more carefully because on 85% of the observation days an earthquake occurred by chance. Similarly, the claimed anomalies in toad behaviour (Grant and Halliday, 2010) were observed in too short a time period compared to the overlap between their life cycle and the long sequence of the L'Aquila earthquake. The correlation between earthquake and anomalies in ant behavior suggested by Berberich et al. (2013) was not confirmed in the longer study, up to two years, by Apostol et al. (2014). And the list could be longer. Furthermore, modeling the reasons that might have driven the emergence of animal sensitivity to earthquake precursors is even more complex because it is unclear what ethological stressor might have driven the natural selection of individuals capable of recognizing earthquake-related phenomena. Even less clear is why and how this sensitivity appeared in many species (of different phylum, class, order, genus, and species) and living in such diverse environments (on land, in the sea, and in the air). Indeed, although earthquakes are disruptive to human constructions, their occurrence is relatively infrequent (even in the zone of maximum seismicity) and generally safe for animals, so it is difficult to justify that mechanical effects in the destruction of burrows or eggs can explain an adaptive response and (generalized) modification of the genome and/or ethology of animals. The hypotheses advanced can be summarized into two main groups. Adaptive evolution may have developed/increased the animals' sensitivity to early mechanical oscillations of P- and S-waves (Wikelski et al., 2020). This hypothesis has the advantage that the presumed increased ability would not necessarily be a specific response to seismic stimuli, but could simply be an increased sensitivity to noise and infrasonic waves, naturally evolved as a reaction to predator pressure (Kirschvink, 2000). On the other hand, it has been suggested that animals would be highly sensitive to fluctuations in earthquake-related parameters [such as magnetic field, humidity (Tichy and Loftus, 1996), temperature, etc.]. Although, by altering the magnetic field it has been experimentally demonstrated that it is possible to change the direction of flight of birds within a Faraday cage, it is not correct to infer the statement that all birds or animals in all circumstances are equally sensitive to the magnetic field (Kirschvink, et al., 2010). For example, even in the pigeon-which is not a migratory bird but tends to return to the dovecote-the orientation system is more complex and not yet fully understood. Mora et al. (2004) suggested that iron-rich cells in the beaks of pigeons were nerve cells containing magnetite and thus able to aid navigation through the Earth's magnetic field. However, Treiber et al. (2012) and Treiber et al. (2013) realized that the iron-rich cells are actually immune system cells (macrophages) and not neurons. Magrophages could probably have a function in orientation toward the dove, but not in orientation with respect to the magnetic field. Furthermore, while sensitivity to the quasi-static geomagnetic field, which allows animals to map and recognize their environment, may support orientation as well as migration, the postulated sensitivity of animals to even the highest frequency content of electromagnetic spectra (which could be relevant to earthquakes) is less convincing. More recently, some complex scenarios have been suggested about a putative mechanism of magnetoreception by electromagnetic induction in the inner ear of some birds (Nimpf et al., 2019). From this perspective, non-static magnetic field sensitivity would not be an evolutionary capacity driven by seismic events, but a collateral/derived capacity consisting of a lowered response threshold. To explain the biological effects of weak magnetic fields, some molecular transduction mechanisms have been proposed (Binhi and Prato 2018; Bialas et al., 2019). While for animal navigation/orientation, the main hypothesis is a specialized magnetic sense associated with pairs of radicals located in the retina of the eye, nonspecific effects could occur due to the interaction of magnetic fields with the magnetic moments of rotating molecules dispersed in the organism. Indeed, Binhi and Prato (2018) have shown that the precession of the magnetic moments of these rotating molecules can be slowed due to a mixing of the quantum levels of magnetic moments (LMMs) inducing a magnetic field dependence that is in good agreement with experiments in which biological effects arise in response to the reversal of magnetic field orientation. Although these studies would suggest a (potentially "common") sensitivity of biological organisms to the magnetic field, even under non-static conditions, nevertheless, at present, the purported response of animals to earthquake precursors seems a bit of a blanket statement. Indeed, such sensitivity-even greater than the instrumental sensitivity of measurements made in various test campaigns to study earthquake precursors-would cut across so many different species that they do not share other important sensory characteristics. Systematic monitoring campaigns with continuous bio-logging of animal collectives, including movements and physiological parameters - such as the experiments about ultra-sensitive measurement of micro-movement of cows in the stable and on pasture (see Brown et al., 2013; Wikelski, et al., 2020), and therein references–could yield valuable insights on this topic.

CONCLUSION

The hypothesis that before earthquake it could be possible to detect surface deformations is supported by the observation of dilatancy effects in labs experiments before rocks rupture. GPS and satellite-based SAR interferometry have given powerful tools for such a worldwide investigation both on local scale and on the continental one through the measurements carried out along the plate boundary. However the growth of the observed effects that would prelude to the earthquakes would not allow defining time and place of the occurrence.

All the physical models claimed to explain precursors share the hypothesis that fast and non-linear processes in the rocks along the seismic fault (such as deformation, dilatancy, fluids flow changes, pores volume variation, etc.) could originate the anomalous variations of observed parameters. Even though experiments and theoretical models give some hints about the possibility to reconcile the observed phenomenology with physical mechanisms operative in the active faults–and non-linear effects have been detected in laboratory tests–the scalability of results obtained in small-size labs experiments up to the large scale of real seismic fault dynamics is highly debated mainly for the large uncertainty about the values of many key parameters that are still barely known in the depth conditions of the faults.

The proposed models of a direct propagation of an electrostatic disturbance from ground to the upper atmosphere and then in the ionosphere have been ruled out by theoretical calculations and simulations. In this framework, it has been suggested that the lithosphere-atmosphere-ionosphere coupling could be due to atmospheric processes including acoustic gravity waves. It worth noting that the complexity of the observed phenomenology–and mainly the high variability of the spatial and temporal scales of the ionospheric preseismic fluctuations–could be hardly reconciled with only one single coupling mechanism prevailing over all the other proposed models. On this basis, the hypothesis that the lithosphere-atmosphere-ionosphere coupling is implemented by multiple physical mechanisms together seems reasonable. For example, the variation of geochemical species (mainly radon exhalations) proposed in order to explain atmospheric thermal anomalies could also generate atmospheric oscillations that can trigger AGW.

Even though the spatial distribution of preseismic geochemical fluids variations (groundwater level, vapour emissions, gases releases and radioactivity fluctuations) would be correlated with the geographical system of seismic faults, the timing of the anomalies could still be basically random as well as the earthquakes themselves and their foreshocks, generating a <<mosaic of precursors>> (Sorokin et al., 2020) function of depth and magnitude.

Up to now, in several proposed models, a key role seems played by radon emission that would vary atmospheric parameters (such as conductivity) inducing a reaction in the global electric circuits. From one side, this prospective avoids the difficulties of a direct propagation of electromagnetic signal. However, from another side, probably, these hypotheses, if confirmed, expose the research of earthquake precursors to further conceptual and practical difficulties due such as: the complexity of transport and diffusion processes; the effect of convection and turbulence in the atmosphere; the difficulty in distinguishing seismo-associated signals from the large electromagnetic noise due to thunderstorm electricity, artificial signals and geomagnetic activity. However, achieving a better understanding of the physics of earthquakes (before, during, and after the seismic event) deserves the efforts being made by the involved scientific community worldwide.

AUTHOR CONTRIBUTIONS

All authors listed have made a substantial, direct, and intellectual contribution to the work and approved it for publication.

ACKNOWLEDGEMENT

This work was supported by the Italian Space Agency in the framework of the "Accordo Attuativo 2020-32.HH.0 Limadou Scienza+" (CUP F19C20000110005).

REFERENCES

Afraimovich, E. L., and Astafyeva, E. I. (2008). TEC Anomalies-Local TEC Changes Prior to Earthquakes or TEC Response to Solar and Geomagnetic Activity Changes? *Earth Planet. Sp.* 60 (9), 961–966. doi:10.1186/BF03352851

Akhoondzadeh, M. (2015). Ant Colony Optimization Detects Anomalous Aerosol Variations Associated with the Chile Earthquake of 27 February 2010. *Adv. Space Res.* 55 (7), 1754–1763. doi:10.1016/j.asr.2015.01.016

Akhoondzadeh, M., De Santis, A., Marchetti, D., Piscini, A., and Cianchini, G. (2018). Multi Precursors Analysis Associated with the Powerful Ecuador (MW= 7.8) Earthquake of 16 April 2016 Using Swarm Satellites Data in Conjunction with Other Multi-Platform Satellite and Ground Data. *Adv. Space Res.* 61 (1), 248–263. doi:10.1016/j.asr.2017.07.014

Akhoondzadeh, M., and Jahani Chehrebargh, F. (2016). Feasibility of Anomaly Occurrence in Aerosols Time Series Obtained from MODIS Satellite Images during Hazardous Earthquakes. *Adv. Space Res.* 58 (6), 890–896. doi:10.1016/j.asr.2016.05.046

Akhoondzadeh, M. (2013). Novelty Detection in Time Series of ULF Magnetic and Electric Components Obtained from DEMETER Satellite Experiments above Samoa (29 September 2009) Earthquake Region. *Nat. Hazards Earth Syst. Sci.* 13 (1), 15–25. doi:10.5194/nhess-13-15-2013

Akselevich, V. I., and Tertyshnikov, A. V. (1995). METHODOLOGY OF ECOLOGICAL MONITORING DATA APPLICATION TO SEISMIC FORECASTING. *Atmos. Oceanic Opt.* 8 (7), 567–569.

Akyol, A. A., Arikan, O., and Arikan, F. (2020). A Machine Learning-Based Detection of Earthquake Precursors Using Ionospheric Data. *Radio Sci.* 55 (11), e2019RS006931. doi:10.1029/2019RS006931

Alam, A., Wang, N., Zhao, G., and Barkat, A. (2020). Implication of Radon Monitoring for Earthquake Surveillance Using Statistical Techniques: A Case Study of Wenchuan Earthquake. *Geofluids.*, 2020, 1–14. doi:10.1155/2020/2429165

Alekseev, V. A., and Alekseeva, N. G. (1992). Investigation of Metal Transfer in the Biosphere during Gaseous Emission in Zones of Tectonic Activity Using Methods of Nuclear-Physics. *Nucl. Geophys.* 6 (1), 99–110.

Allegri, L., Bella, F., Della Monica, G., Ermini, A., Improta, S., Sgrigna, V., et al. (1983). Radon and Rilt Anomalies Detected before the Irpinia (South Italy) Earthquake of November 23, 1980 at Great Distances from the Epicenter. *Geophys. Res. Lett.* 10 (4), 269–272. doi:10.1029/GL010i004p00269

Amonte, C., Asensio-Ramos, M., Melián, G. V., Pérez, N. M., Padrón, E., Hernández, P. A., et al. (2021). Hydrogeochemical Temporal Variations Related to Changes of Seismic Activity at Tenerife, Canary Islands. *Bull. Volcanol.* 83, 24. doi:10.1007/s00445-021-01445-4

Apostol, A., Moldovan, I.-A., Constantin, A. P., and Toader, V. E. (2014). "Are Red wood Ants Earthquake Predictors," in Proceedings of Second European Conference on Earthquake Engineering and Seismology 2nd ECEES), Istanbul, 1–3. http://www.eaee.org/Media/Default/2ECCES/2ecces_esc/2298.pdf.

Asaad, G., and Shapiro, B. (1986). Hallucinations: Theoretical and Clinical Overview. *Am. J. Psychiatry* 143 (Issue 9), 1088–1097. doi:10.1176/ajp.143.9.1088

Asteriadis, G., and Livieratos, E. (1989). Pre-seismic Responses of Underground Water Level and Temperature Concerning a 4.8 Magnitude Earthquake in Greece on October 20, 1988. *Tectonophysics* 170 (1–2), 165–169. doi:10.1016/0040-1951(89)90111-X

Avlonitis, M., and Papadopoulos, G. A. (2014). Foreshocks and B Value: Bridging Macroscopic Observations to Source Mechanical Considerations. *Pure Appl. Geophys.* 171 (10), 2569–2580. doi:10.1007/s00024-014-0799-6

Badcock, J. C., Dehon, H., and Larøi, F. (2017). Hallucinations in Healthy Older Adults: An Overview of the Literature and Perspectives for Future Research. *Front. Psychol.* 8 (JUL), 1134. doi:10.3389/fpsyg.2017.01134

Bakun, W. H., and Lindh, A. G. (1985). The Parkfield, California, Earthquake Prediction experiment. *Science* 229 (4714), 619–624. doi:10.1126/science.229.4714.619

Bé, M.-M., Coursol, N., Duchemin, B., Lagoutine, F., and Legrand, J. (2011). *Note Technique LNHB 2011/53*, Gif-sur-Yvette: CEA Saclay.

Bella, F., Biagi, P. F., Caputo, M., Cozzi, E., Della Monica, G., Ermini, A., et al. (1998). Field Strength Variations of LF Radio Waves Prior to Earthquakes in central Italy. *Phys. Earth Planet. Interiors* 105 (3–4), 279–286. doi:10.1016/S0031-9201(97)00097-6

Bella, F., Biagi, P. F., Caputo, M., Cozzi, E., Monica, G. D., Ermini, A., et al. (1995a). Helium Content in thermal Waters in the Caucasus from 1985 to 1991 and Correlations with the Seismic Activity. *Tectonophysics* 246 (4), 263–278. doi:10.1016/0040-1951(94)00260-G

Bella, F., Biagi, P. F., Caputo, M., Monica, G. D., Ermini, A., Manjgaladze, P. V., et al. (1995b). Possible Creep-Related Tilt Precursors Obtained in the Central Apennines (Italy) and in the Southern Caucasus (Georgia). *Pageoph* 144 (2), 277–300. doi:10.1007/bf00878635

Ben-Zion, Y., Eneva, M., and Liu, Y. (2003). Large Earthquake Cycles and Intermittent Criticality on Heterogeneous Faults Due to Evolving Stress and Seismicity. *J. Geophys. Res.* 108 (B6), 2307. doi:10.1029/2002jb002121

Berberich, G., Berberich, M., Grumpe, A., Wöhler, C., and Schreiber, U. (2013). Early Results of Three-Year Monitoring of Red Wood Ants' Behavioral Changes and Their Possible Correlation with Earthquake Events. *Animals* 3 (1), 63–84. doi:10.3390/ani3010063

Bernabé, Y., Mok, U., and Evans, B. (2003). Permeability-porosity Relationships in Rocks Subjected to Various Evolution Processes. *Pure Appl. Geophys.* 160 (5–6), 937–960. doi:10.1007/PL00012574

Bi, Y., Wu, S., Xiong, P., and Shen, X. (2009). A Comparative Analysis for Detecting Seismic Anomalies in Data Sequences of Outgoing Longwave Radiation. *Lecture Notes in Computer Science (Including Subseries Lecture Notes in Artificial Intelligence and Lecture Notes in Bioinformatics)*, Berlin: Springer, 5914, 285–296. doi:10.1007/978-3-642-10488-6_29

Biagi, P. F., Ermini, A., and Kingsley, S. P. (2001b). Disturbances in LF Radio Signals and the Umbria-Marche (Italy) Seismic Sequence in 1997-1998. *Phys. Chem. Earth, C: Solar, Terrestrial Planet. Sci.* 26 (10–12), 755–759. doi:10.1016/S1464-1917(01)95021-4

Biagi, P. F., Ermini, A., Kingsley, S. P., Khatkevich, Y. M., and Gordeev, E. I. (2001a). Difficulties with Interpreting Changes in Groundwater Gas Content as Earthquake Precursors in Kamchatka, Russia. *J. Seismology* 5 (4), 487–497. doi:10.1023/A:1012015317086

Biagi, P. F., Maggipinto, T., Righetti, F., Loiacono, D., Schiavulli, L., Ligonzo, T., et al. (2011). The European VLF/LF Radio Network to Search for Earthquake Precursors: Setting up and Natural/man-Made Disturbances. *Nat. Hazards Earth Syst. Sci.* 11 (2), 333–341. doi:10.5194/nhess-11-333-2011

Biagi, P. F., Piccolo, R., Castellana, L., Maggipinto, T., Ermini, A., Martellucci, S., et al. (2004). VLF-LF Radio Signals Collected at Bari (South Italy): A Preliminary Analysis on Signal Anomalies Associated with Earthquakes. *Nat. Hazards Earth Syst. Sci.* 4 (5–6), 685–689. doi:10.5194/nhess-4-685-2004

Biagi, P. F. (2009). "Pre and Post Seismic Disturbances Revealed on the Geochemical Data Collected in Kamchatka (Russia) during the Last 30 Years," in *Electromagnetic Phenomena Associated with Earthquakes*. Editor M. Hayakawa (Kerala: Transworld Research Network), 97–117.

Bialas, C., Barnard, D. T., Auman, D. B., McBride, R. A., Jarocha, L. E., Hore, P. J., et al. (2019). Ultrafast Flavin/tryptophan Radical Pair Kinetics in a Magnetically Sensitive Artificial Protein. *Phys. Chem. Chem. Phys.* 21 (25), 13453–13461. doi:10.1039/c9cp01916b

Bianchi, C., and Meloni, A. (2007). Natural and Man-Made Terrestrial Electromagnetic Noise: An Outlook. *Ann. Geophys.* 50 (3), 435–445. doi:10.4401/ag-4425

Binhi, V. N., and Prato, F. S. (2018). Rotations of Macromolecules Affect Nonspecific Biological Responses to Magnetic fields. *Sci. Rep.* 8 (1), 13495. doi:10.1038/s41598-018-31847-y

Blackett, M., Wooster, M. J., and Malamud, B. D. (2011). Exploring Land Surface Temperature Earthquake Precursors: A Focus on the Gujarat (India) Earthquake of 2001. *Geophys. Res. Lett.* 38 (15), 15303. doi:10.1029/2011GL048282

Blanchard, D. C. (1963). The Electrification of the Atmosphere by Particles from Bubbles in the Sea. *Prog. Oceanography* 1 (C), 73–202. doi:10.1016/0079-6611(63)90004-1

Boyarchuk, K. A. (1997). Kinetics of Elementary Ions in the Lower Atmosphere Acted upon by Ionizing Radiation. *Izvestiya. Atmos. Oceanic Phys.* 33 (2), 214–217.

Brace, W. F. (1978). Volume Changes during Fracture and Frictional Sliding: A Review. *Pure and Applied Geophysics PAGEOPH*, 116, 603–614. doi:10.1007/BF00876527

Brady, B. T., and Rowell, G. A. (1986). Laboratory Investigation of the Electrodynamics of Rock Fracture. *Nature* 321 (6069), 488–492. doi:10.1038/321488a0

Bredehoeft, J. D. (1967). Response of Well-Aquifer Systems to Earth Tides. *J. Geophys. Res.* 72 (12), 3075–3087. doi:10.1029/jz072i012p03075

Brown, D. D., Kays, R., Wikelski, M., Wilson, R., and Klimley, A. (2013). Observing the Unwatchable through Acceleration Logging of Animal Behavior. *Anim. Biotelemetry* 1 (1), 20. doi:10.1186/2050-3385-1-20

Bryant, N. A., and Nathan, R. B. (2003). "Observed Weather Satellite Thermal Responses Prior to and after Earthquakes," in AGU 2003 Fall Meeting, T52D-04, San Francisco, CA, (. AGU).

Byerlee, J. (1993). Model for Episodic Flow of High-Pressure Water in Fault Zones before Earthquakes. *Geology* 21 (4), 303. doi:10.1130/0091-7613(1993)021<0303:mfefoh>2.3.co;2

Cai, Z., and Shi, H. X. (1980). *An Introduction to Seismological Fluid Geology*. Beijing: Seismological Press.

Campbell, W. H. (2009). Natural Magnetic Disturbance fields, Not Precursors, Preceding the Loma Prieta Earthquake. *J. Geophys. Res. Space Phys.* 114 (A5), n/a. doi:10.1029/2008ja013932

Carreno, E., Capote, R., Yague, A., Tordesillas, J. M., Lopez, M. M., Ardizone, J., et al. (2001). "Observations of thermal Anomaly Associated to Seismic Activity from Remote Sensing." in General Assembly of European Seismology Commission, Portugal, Lisbon, Portugal, 265–269.

Chadha, R. K., Pandey, A. P., and Kuempel, H. J. (2003). Search for Earthquake Precursors in Well Water Levels in a Localized Seismically Active Area of Reservoir Triggered Earthquakes in India. *Geophys. Res. Lett.* 30 (7), 1416. doi:10.1029/2002GL016694

Chakraborty, S., Sasmal, S., Chakrabarti, S. K., and Bhattacharya, A. (2018). Observational Signatures of Unusual Outgoing Longwave Radiation (OLR) and Atmospheric Gravity Waves (AGW) as Precursory Effects of May 2015 Nepal Earthquakes. *J. Geodynamics* 113, 43–51. doi:10.1016/j.jog.2017.11.009

Chirkov, Y. B. (2004). The Study of Local Sources of ULF Geoelectric Signals with Steep Fronts. *Ann. Geophys.* 47 (1), 213–227. doi:10.4401/ag-3273

Chmyrev, V. M., Isaev, N. V., Serebryakova, O. N., Sorokin, V. M., and Sobolev, Y. P. (1997). Small-scale Plasma Inhomogeneities and Correlated ELF Emissions in the Ionosphere over an Earthquake Region. *J. Atmos. Solar-Terrestrial Phys.* 59 (9), 967–974. doi:10.1016/S1364-6826(96)00110-1

Chmyrev, V. M., Sorokin, V. M., and Shklyar, D. R. (2008). VLF Transmitter Signals as a Possible Tool for Detection of Seismic Effects on the Ionosphere. *J. Atmos. Solar-Terrestrial Phys.* 70 (16), 2053–2060. doi:10.1016/j.jastp.2008.09.005

Choudhury, S., Dasgupta, S., Saraf, A. K., and Panda, S. (2006). Remote Sensing Observations of Pre-earthquake thermal Anomalies in Iran. *Int. J. Remote Sensing* 27 (20), 4381–4396. doi:10.1080/01431160600851827

Chum, J., Liu, J.-Y., Laštovička, J., Fišer, J., Mošna, Z., Baše, J., et al. (2016). Ionospheric Signatures of the April 25, 2015 Nepal Earthquake and the Relative Role of Compression and Advection for Doppler Sounding of Infrasound in the Ionosphere. *Earth Planets Space* 68 (1), 1–12. doi:10.1186/s40623-016-0401-9

Chung, Y. (1985). Radon Variations at Arrowhead and murrieta Springs: Continuous and Discrete Measurements. *Pageoph* 122 (2–4), 294–308. doi:10.1007/BF00874600

Cicerone, R. D., Ebel, J. E., and Britton, J. (2009). A systematic compilation of earthquake precursors. *Tectonophy.* 476 (3-4), 371–396. doi:10.1016/j.tecto.2009.06.008

Claesson, L., Skelton, A., Graham, C., Dietl, C., Mörth, M., Torssander, P., et al. (2004). Hydrogeochemical Changes before and after a Major Earthquake. *Geol* 32 (8), 641. doi:10.1130/G20542.1

Cochran, E. S., Vidale, J. E., and Tanaka, S. (2004). Earth Tides Can Trigger Shallow Thrust Fault Earthquakes. *Science* 306 (5699), 1164–1166. doi:10.1126/science.1103961

Console, R., Murru, M., and Alessandrini, B. (1993). Foreshock Statistics and Their Possible Relationship to Earthquake Prediction in the Italian Region. *Bull. Seismological Soc. America* 83 (4), 1248–1263.

Contadakis, M. E., Arabelos, D. N., Pikridas, C., and Spatalas, S. D. (2012). Total Electron Content Variations over Southern Europe before and during the M 6.3 Abruzzo Earthquake of April 6, 2009. *Ann. Geophys.* 55 (1), 83–93. doi:10.4401/ag-5322

Craig, H., Chung, Y., Poreda, J., Lupton, J., and Damascene, S. (1980). Fluid-phase earthquake precursor studies in southern California. *Eos, Transactions, American Geophysical Union* 61 (1035), 1035.

Cresci, A., Paris, C. B., Durif, C. M. F., Shema, S., Bjelland, R. M., Skiftesvik, A. B., et al. (2017). Glass Eels (*Anguilla anguilla*) Have a Magnetic Compass Linked to the Tidal Cycle. *Sci. Adv.* 3 (6), e1602007. doi:10.1126/sciadv.1602007

Cui, J., Shen, X., Zhang, J., Ma, W., and Chu, W. (2019). Analysis of Spatiotemporal Variations in Middle-Tropospheric to Upper-Tropospheric Methane during the Wenchuan Ms = 8.0 Earthquake by Three Indices. *Nat. Hazards Earth Syst. Sci.* 19 (12), 2841–2854. doi:10.5194/nhess-19-2841-2019

Dabas, R. S., Das, R. M., Sharma, K., and Pillai, K. G. M. (2007). Ionospheric Precursors Observed over Low Latitudes during Some of the Recent Major Earthquakes. *J. Atmos. Solar-Terrestrial Phys.* 69 (15), 1813–1824. doi:10.1016/j.jastp.2007.09.005

Davidenko, D. V., and Pulinets, S. A. (2019). Deterministic Variability of the Ionosphere on the Eve of Strong (M ≥ 6) Earthquakes in the Regions of Greece and Italy According to Long-Term Measurements Data. *Geomagn. Aeron.* 59 (4), 493–508. doi:10.1134/S001679321904008X

Davies, K., and Baker, D. M. (1965). Ionospheric Effects Observed Around the Time of the Alaskan Earthquake of March 28, 1964. *J. Geophys. Res.* 70 (9), 2251–2253. doi:10.1029/jz070i009p02251

De Luca, G., Di Carlo, G., and Tallini, M. (2018). A Record of Changes in the Gran Sasso Groundwater before, during and after the 2016 Amatrice Earthquake, central Italy. *Sci. Rep.* 8 (1), 1–16. doi:10.1038/s41598-018-34444-1

De Santis, A., Abbattista, C., Alfonsi, L., Amoruso, L., Campuzano, S. A., Carbone, M., et al. (2019b). Geosystemics View of Earthquakes. *Entropy* 21 (4), 412. doi:10.3390/e21040412

De Santis, A., Cianchini, G., Marchetti, D., Piscini, A., Sabbagh, D., Perrone, L., et al. (2020). A Multiparametric Approach to Study the Preparation Phase of the 2019 M7.1 Ridgecrest (California, United States) Earthquake. *Front. Earth Sci.* 8, 478. doi:10.3389/feart.2020.540398

De Santis, A., De Franceschi, G., Spogli, L., Perrone, L., Alfonsi, L., Qamili, E., et al. (2015). Geospace Perturbations Induced by the Earth: The State of the Art and Future Trends. *Physics and Chemistry of the Earth, Parts A/B/C*, 85-86, 17–33. doi:10.1016/j.pce.2015.05.004

De Santis, A. (2014). Geosystemics, Entropy and Criticality of Earthquakes: A Vision of Our Planet and a Key of Access. *Nonlinear Phenomena in Complex Systems: From Nano to Macro Scale*. Dordrecht: Springer, 3–20. doi:10.1007/978-94-017-8704-8_1

De Santis, A., Marchetti, D., Pavón-Carrasco, F. J., Cianchini, G., Perrone, L., Abbattista, C., et al. (2019a). Precursory Worldwide Signatures of Earthquake Occurrences on Swarm Satellite Data. *Sci. Rep.* 9 (1), 1–13. doi:10.1038/s41598-019-56599-1

Denisenko, V. V., Boudjada, M. Y., and Lammer, H. (2018). Propagation of Seismogenic Electric Currents through the Earth's Atmosphere. *J. Geophys. Res. Space Phys.* 123 (5), 4290–4297. doi:10.1029/2018JA025228

Denisenko, V. V. (2015). Estimate for the Strength of the Electric Field Penetrating from the Earth's Surface to the Ionosphere. *Russ. J. Phys. Chem. B* 9 (5), 789–795. doi:10.1134/S199079311505019X

Derr, J. S. (1973). Earthquake Lights: a Review of Observations and Present Theories. *Bull. Seismological Soc. America* 63 (6–1), 2177–2187.

Derr, J. S. (1986). Rock Mechanics: Luminous Phenomena and Their Relationship to Rock Fracture. *Nature* 321 (6069), 470–471. doi:10.1038/321470a0

Deverux, P., McCartney, P., and Robins, D. (1983). Bringing UFOSs Down to Earth: many Reports of UFO Sightings Come from Areas Close to Geological Faults. Far from Being Spaceships from Other Worlds, Could the Explanation of UFOs Be Much More Earthbound? *New Scientist* 99 (1373), 627–630.

Devi, M., Barbara, A. K., Ruzhin, Y. Y., and Hayakawa, M. (2012). Over-the-Horizon Anomalous VHF Propagation and Earthquake Precursors. *Surv. Geophys.* 33 (5), 1081–1106. doi:10.1007/s10712-012-9185-z

Dey, S., Sarkar, S., and Singh, R. P. (2004). Anomalous Changes in Column Water Vapor after Gujarat Earthquake. *Adv. Space Res.* 33 (3), 274–278. doi:10.1016/S0273-1177(03)00475-7

Dey, S., and Singh, R. P. (2003). Surface Latent Heat Flux as an Earthquake Precursor. *Nat. Hazards Earth Syst. Sci.* 3 (6), 749–755. doi:10.5194/nhess-3-749-2003

Dieterich, J. H. (1979). Modeling of Rock Friction: 1. Experimental Results and Constitutive Equations. *J. Geophys. Res.* 84 (B5), 2161–2168. doi:10.1029/JB084iB05p02161

Dieterich, J. H. (1978). "Time-Dependent Friction and the Mechanics of Stick-Slip" in *Rock Friction and Earthquake Prediction*. Editors J. D. Byerlee and M. Wyss, Basel: Birkhäuser Verlag, 790–806. doi:10.1007/978-3-0348-7182-2_15

Draganov, A. B., Inan, U. S., and Taranenko, Y. N. (1991). ULF Magnetic Signatures at The Earth Surface Due to Ground Water Flow: A Possible Precursor to Earthquakes. *Geophy. Res. Letters* 18 (6), 1127–1130. doi:10.1029/91GL01000

Du, A., Huang, Q., and Yang, S. (2002). Epicenter Location by Abnormal ULF Electromagnetic Emissions. *Geophys. Res. Lett.* 29 (10), 94-1–94–3. doi:10.1029/2001gl013616

Dudkin, F., Arora, B. R., Korepanov, V., Leontyeva, O., Sharma, A. K., and Sharma, A. K. (2010). Application of Polarization Ellipse Technique for Analysis of ULF Magnetic fields from Two Distant Stations in Koyna-Warna Seismoactive Region, West India. *Nat. Hazards Earth Syst. Sci.* 10 (7), 1513–1522. doi:10.5194/nhess-10-1513-2010

Dyer, A. G., Greentree, A. D., Garcia, J. E., Dyer, E. L., Howard, S. R., and Barth, F. G. (2021). Einstein, von Frisch and the honeybee: a historical letter comes to light. *J. Comp. Physiol. A Neuroethol. Sens. Neural. Behav. Physiol.*, 1–8. doi:10.1007/s00359-021-01490-6

Eaton, W. W., and Kessler, L. G. (1985). Epidemiologic Field Methods in Psychiatry. *Epidemiologic Field Methods in Psychiatry: The NIMH Epidemiologic Catchment Area Program*. Elsevier, 1–379. doi:10.1016/C2009-0-02951-1

Eftaxias, K., Kapiris, P., Polygiannakis, J., Peratzakis, A., Kopanas, J., Antonopoulos, G., et al. (2003). Experience of Short Term Earthquake Precursors with VLF-VHF Electromagnetic Emissions. *Nat. Hazards Earth Syst. Sci.* 3 (3/4), 217–228. doi:10.5194/nhess-3-217-2003

Erickson, W. C. (1990). " Radio noise near the Earth in the 1 â € 30 MHz frequency range" in *Low frequency Astrophysics from Space*. Springer, 57–69.

Fenoglio, M. A., Johnston, M. J. S., and Byerlee, J. D. (1995). Magnetic and Electric fields Associated with Changes in High Pore Pressure in Fault Zones: Application to the Loma Prieta ULF Emissions. *J. Geophys. Res.* 100 (B7), 12951–12958. doi:10.1029/95jb00076

Fidani, C. (2013). Biological Anomalies Around the 2009 L'Aquila Earthquake. *Animals* 3 (3), 693–721. doi:10.3390/ani3030693

Fidani, C., Freund, F., and Grant, R. (2014). Cows Come Down from the Mountains before the (Mw = 6.1) Earthquake Colfiorito in September 1997; a Single Case Study. *Animals* 4 (2), 292–312. doi:10.3390/ani4020292

Fidani, C. (2010). The Earthquake Lights (EQL) of the 6 April 2009 Aquila Earthquake, in Central Italy. *Nat. Hazards Earth Syst. Sci.* 10 (5), 967–978. doi:10.5194/nhess-10-967-2010

Fitterman, D. V. (1979). Theory of Electrokinetic-Magnetic Anomalies in a Faulted Half-Space. *J. Geophys. Res.* 84 (B11), 6031–6040. doi:10.1029/JB084iB11p06031

Flagg, S., Bleier, T., Dunson, C., Doering, J., DeMartini, L., Clarke, P., et al. (2004). Using Nanosats as a Proof of Concept for Space Science Missions: QuakeSat as an Operational Example. 18th Annual AIAA/USU Conference on Small Satellites, SSC04-IX-4), Logan, 1–12. Available at: https://digitalcommons.usu.edu/cgi/viewcontent.cgi?article=1728andcontext=smallsat.

Fraser-Smith, A. C., Bernardi, A., McGill, P. R., Ladd, M. E., Helliwell, R. A., and Villard, O. G. (1990). Low-frequency Magnetic Field Measurements Near the Epicenter of the Ms7.1 Loma Prieta Earthquake. *Geophys. Res. Lett.* 17 (9), 1465–1468. doi:10.1029/GL017i009p01465

Fraser-Smith, A. C., McGill, P. R., and Bernardi, A. (2011). Comment on "Natural Magnetic Disturbance fields, Not Precursors, Preceding the Loma Prieta Earthquake" by Wallace H. Campbell. *J. Geophys. Res. Space Phys.* 116 (A8), n/a-n/a. doi:10.1029/2010ja016379

Freund, F. (2019). Co-seismic Earthquake Lights: The Underlying Mechanism. *Pure Appl. Geophys.* 176 (8), 3439–3450. doi:10.1007/s00024-019-02142-2

Freund, F. (2013). Earthquake Forewarning - A Multidisciplinary challenge from the Ground up to Space. *Acta Geophys.* 61 (4), 775–807. doi:10.2478/s11600-013-0130-4

Freund, F., Ouillon, G., Scoville, J., and Sornette, D. (2021). Earthquake Precursors in the Light of Peroxy Defects Theory: Critical Review of Systematic Observations. *Eur. Phys. J. Spec. Top.* 230 (1), 7–46. doi:10.1140/epjst/e2020-000243-x

Freund, F., and Stolc, V. (2013). Nature of Pre-earthquake Phenomena and Their Effects on Living Organisms. *Animals* 3 (2), 513–531. doi:10.3390/ani3020513

Freund, F. T., Kulahci, I. G., Cyr, G., Ling, J., Winnick, M., Tregloan-Reed, J., et al. (2009). Air Ionization at Rock Surfaces and Pre-earthquake Signals. *J. Atmos. Solar-Terrestrial Phys.* 71 (17–18), 1824–1834. doi:10.1016/j.jastp.2009.07.013

Freund, F. (2010). Toward a Unified Solid State Theory for Pre-earthquake Signals. *Acta Geophys.* 58 (5), 719–766. doi:10.2478/s11600-009-0066-x

Friis-Christensen, E., Lühr, H., and Hulot, G. (2006). Swarm: A Constellation to Study the Earth's Magnetic Field. *Earth Planet. Sp* 58 (4), 351–358. doi:10.1186/BF03351933

Galli, I. (1910). Raccolta e classificazione di fenomeni luminosi osservati nei terremoti. *Boll. Soc. Sismol. Ital.* XIV, 221–448.

Garavaglia, M., Dal Moro, G., and Zadro, M. (2000). Radon and Tilt Measurements in a Seismic Area: Temperature Effects. *Phys. Chem. Earth, A: Solid Earth Geodesy* 25 (3), 233–237. doi:10.1016/S1464-1895(00)00038-7

Garstang, M. (2009). Precursor Tsunami Signals Detected by Elephants. *Open Conservat. Biol. J.*, 3, 1–3.

Geller, R. J. (1997). Earthquake Prediction: a Critical Review. *Geophys. J. Int.* 131 (3), 425–450. doi:10.1111/j.1365-246X.1997.tb06588.x

Genzano, N., Aliano, C., Filizzola, C., Pergola, N., and Tramutoli, V. (2007). A Robust Satellite Technique for Monitoring Seismically Active Areas: The Case of Bhuj-Gujarat Earthquake. *Tectonophysics* 431 (1–4), 197–210. doi:10.1016/j.tecto.2006.04.024

Giovambattista, R. D., and Tyupkin, Y. S. (2004). Seismicity Patterns before the M=5.8 2002, Palermo (Italy) Earthquake: Seismic Quiescence and Accelerating Seismicity. *Tectonophysics* 384 (1–4), 243–255. doi:10.1016/j.tecto.2004.04.001

Gokhberg, M. B., Morgounov, V. A., Yoshino, T., and Tomizawa, I. (1982). Experimental Measurement of Electromagnetic Emissions Possibly Related to Earthquakes in Japan. *J. Geophys. Res.* 87 (B9), 7824–7828. doi:10.1029/JB087iB09p07824

Gokhberg, M. B., and Shalimov, S. L. (2000). Lithosphere--ionosphere Relation and its Modeling. *Russ. J. Earth Sci.* 2 (2), 95–108. doi:10.2205/2000ES000032

Golenetskii, S. I., Dem'yanovitch, M. G., Semenov, R. M., Vas' ko, V. G., Avdeev, V. A., Kashkin, V. F., et al. (1982). Seismicity of the Regions of the Orongoi Basins and the Earthquake of 2 October 1980 in Western Transbaikal. *Sov. Geol. Geophys.* 23, 39–46.

Grant, R. A., and Halliday, T. (2010). Predicting the Unpredictable; Evidence of Pre-seismic Anticipatory Behaviour in the Common Toad. *J. Zoolog.* 281 (4), no. doi:10.1111/j.1469-7998.2010.00700.x

Grant, R. A., Raulin, J. P., and Freund, F. T. (2015). Changes in Animal Activity Prior to a Major (M= 7) Earthquake in the Peruvian Andes. *Phys. Chem. Earth, Parts A/B/C* 85-86 (86), 69–77. doi:10.1016/j.pce.2015.02.012

Gulia, L., and Wiemer, S. (2019). Real-time Discrimination of Earthquake Foreshocks and Aftershocks. *Nature* 574 (7777), 193–199. doi:10.1038/s41586-019-1606-4

Hamilton, R. M. (1975). Earthquake Studies in China: A Massive Earthquake Prediction Effort Is Underway. *Earthquake Inf. Bull. (Usgs)* 7 (6), 3–8. Available at: http://pubs.er.usgs.gov/publication/70178910.

Han, P., Hattori, K., Hirokawa, M., Zhuang, J., Chen, C.-H., Febriani, F., et al. (2014). Statistical Analysis of ULF Seismomagnetic Phenomena at Kakioka, Japan, during 2001-2010. *J. Geophys. Res. Space Phys.* 119 (6), 4998–5011. doi:10.1002/2014JA019789

Han, P., Hattori, K., Huang, Q., Hirooka, S., and Yoshino, C. (2016). Spatiotemporal Characteristics of the Geomagnetic Diurnal Variation Anomalies Prior to the 2011 Tohoku Earthquake (Mw 9.0) and the Possible Coupling of Multiple Pre-earthquake Phenomena. *J. Asian Earth Sci.* 129, 13–21. doi:10.1016/j.jseaes.2016.07.011

Han, P., Hattori, K., Xu, G., Ashida, R., Chen, C.-H., Febriani, F., et al. (2015). Further Investigations of Geomagnetic Diurnal Variations Associated with the 2011 off the Pacific Coast of Tohoku Earthquake (Mw 9.0). *J. Asian Earth Sci.* 114, 321–326. doi:10.1016/j.jseaes.2015.02.022

Hao, J., Tang, T., and Li, D. (2000). Progress in the Research on Atmospheric Electric Field Anomaly as an index for Short-Impending Prediction of Earthquakes. *J. Earthquake Prediction Res.* 8 (3), 241–255.

Harper, W. R. (1957). The Generation of Static Charge. *Adv. Phys.* 6 (24), 365–417. doi:10.1080/00018735700101396

Hartmann, J., and Levy, J. K. (2005). Hydrogeological and Gasgeochemical Earthquake Precursors ? A Review for Application. *Nat. Hazards* 34 (3), 279–304. Springer. doi:10.1007/s11069-004-2072-2

Hasbi, A. M., Mohd Ali, M. A., and Misran, N. (2011). Ionospheric Variations before Some Large Earthquakes over Sumatra. *Nat. Hazards Earth Syst. Sci.* 11 (2), 597–611. doi:10.5194/nhess-11-597-2011

Hatai, S., and Abe, N. (1932). The Responses of the Catfish, Parasilurus Asotus, to Earthquakes. *Proc. Imperial Acad.* 8 (8), 375–378. doi:10.2183/pjab1912.8.375

Hattori, K., Akinaga, Y., Hayakawa, M., Yumoto, K., Nagao, T., and Uyeda, S. (2002). "ULF Magnetic Anomaly Preceding the 1997 Kagoshima Earthquakes," in *Seismo Electromagnetics: Lithosphere-Atmosphere-Ionosphere Coupling*. Editors M. Hayakawa and O. A. Molchanov (Terra Scientific Pub. Comp), 19–28.

Hattori, K., Han, P., Yoshino, C., Febriani, F., Yamaguchi, H., and Chen, C.-H. (2013). Investigation of ULF Seismo-Magnetic Phenomena in Kanto, Japan during 2000-2010: Case Studies and Statistical Studies. *Surveys in Geophysics*. 34 (3), 293–316. doi:10.1007/s10712-012-9215-x

Hattori, K., Serita, A., Yoshino, C., Hayakawa, M., and Isezaki, N. (2006). Singular Spectral Analysis and Principal Component Analysis for Signal Discrimination of ULF Geomagnetic Data Associated with 2000 Izu Island Earthquake Swarm. *Phys. Chem. Earth, Parts A/B/C* 31 (4–9), 281–291. doi:10.1016/j.pce.2006.02.034

Hattori, K. (2004). ULF Geomagnetic Changes Associated with Large Earthquakes. *Terr. Atmos. Ocean. Sci.* 15 (3), 329–360. doi:10.3319/tao.2004.15.3.329(ep)

Hayakawa, M., Asano, T., Rozhnoi, A., and Solovieva, M. (2018). "Very-low- and Low-Frequency Sounding of Ionospheric Perturbations and Possible Association with Earthquakes," in *Pre-Earthquake Processes: A Multidisciplinary Approach to Earthquake Prediction Studies*. Editors D. Ouzounov, S. Pulinets, K. Hattori, and P. Taylor (Hoboken: Wiley Online Library), 277–304.

Hayakawa, M., Hobara, Y., Ohta, K., and Hattori, K. (2011). The Ultra-low-frequency Magnetic Disturbances Associated with Earthquakes. *Earthq Sci.* 24 (6), 523–534. doi:10.1007/s11589-011-0814-2

Hayakawa, M., Kawate, R., Molchanov, O. A., and Yumoto, K. (1996). Results of Ultra-low-frequency Magnetic Field Measurements during the Guam Earthquake of 8 August 1993. *Geophys. Res. Lett.* 23 (3), 241–244. doi:10.1029/95GL02863

Hayakawa, M., Molchanov, O. A., Ondoh, T., and Kawai, E. (1997). "On the Precursory Signature of Kobe Earthquake on VLF Subionospheric Signals," in IEEE International Symposium on Electromagnetic Compatibility, Beijing, 72–75. doi:10.1109/elmagc.1997.617080

Hayakawa, M. (1994). Terrestrial Electromagnetic Noises. *Radiophys Quan. Electron* 37 (6), 464–467. doi:10.1007/BF01088657

Hayakawa, M., Yoshino, T., and Morgounov, V. A. (1993). On the Possible Influence of Seismic Activity on the Propagation of Magnetospheric Whistlers at Low Latitudes. *Phys. Earth Planet. Interiors* 77 (1–2), 97–108. doi:10.1016/0031-9201(93)90036-9

He, C., Dong, S., Santosh, M., and Chen, X. (2014). Seismic Structure of The Longmenshan Area in SW China Inferred From Receiver Function Analysis: Implications for Future Large Earthquakes. *J. Asian Earth Sci.* 96, 226– 236. doi:10.1016/j.jseaes.2014.09.026

He, L., and Heki, K. (2017). Ionospheric Anomalies Immediately before M W 7.0-8.0 Earthquakes. *J. Geophys. Res. Space Phys.* 122 (8), 8659–8678. doi:10.1002/2017JA024012

Heaton, T. H. (1975). Tidal Triggering of Earthquakes. *Geophys. J. Int.* 43 (2), 307–326. doi:10.1111/j.1365-246X.1975.tb00637.x

Heinicke, J., Koch, U., and Martinelli, G. (1995). CO2and Radon Measurements in the Vogtland Area (Germany) - A Contribution to Earthquake Prediction Research. *Geophys. Res. Lett.* 22 (7), 771–774. doi:10.1029/94GL03074

Heki, K. (2011). Ionospheric Electron Enhancement Preceding the 2011 Tohoku-Oki Earthquake. *Geophys. Res. Lett.* 38 (17), a–n. doi:10.1029/2011GL047908

Helliwell, R. A. (1965). *Whistlers and Related Ionospheric Phenomena*, Vol. 50. Calif: Stanford University Press Stanford.

Heraud, J. A., and Lira, J. A. (2011). Co-seismic Luminescence in Lima, 150 Km from the Epicenter of the Pisco, Peru Earthquake of 15 August 2007. *Nat. Hazards Earth Syst. Sci.* 11 (4), 1025–1036. doi:10.5194/nhess-11-1025-2011

Hitchcock, R. T., and Patterson, R. M. (1995). *Radio-frequency and ELF Electromagnetic Energies: A Handbook for Health Professionals*. New York: John Wiley & Sons.

Hobara, Y., and Parrot, M. (2005). Ionospheric Perturbations Linked to a Very Powerful Seismic Event. *J. Atmos. Solar-Terrestrial Phys.* 67 (7), 677–685. doi:10.1016/j.jastp.2005.02.006

Holub, R. F., and Brady, B. T. (1981). The Effect of Stress on Radon Emanation from Rock. *J. Geophys. Res.* 86 (B3), 1776–1784. doi:10.1029/JB086iB03p01776

Hong, T.-K., Lee, J., Park, S., and Kim, W. (2018). Time-advanced Occurrence of Moderate-Size Earthquakes in a Stable Intraplate Region after a Megathrust Earthquake and Their Seismic Properties. *Sci. Rep.* 8 (1), 13331. doi:10.1038/s41598-018-31600-5

Hough, S. E. (2016). *Predicting the Unpredictable: The Tumultuous Science of Earthquake Prediction*. Princeton: Princeton University Press. doi:10.1515/9781400883547

Hough, S. (2020). *The Great Quake Debate: The Crusader, the Skeptic, and the Rise of Modern Seismology*. Hough: University of Washington Press.

Hristopulos, D. T., and Mouslopoulou, V. (2013). Strength Statistics and The Distribution of Earthquake Interevent Times. *Phys. A: Stat. Mech. Appl.* 392, 485–496. doi:10.1016/j.physa.2012.09.011

Huixin, S., and Zuhuang, C. (1986). Geochemical Characteristics of Underground Fluids in Some Active Fault Zones in China. *J. Geophys. Res.* 91 (B12), 12282–12290. doi:10.1029/jb091ib12p12282

Igarashi, G., Saeki, S., Takahata, N., Sumikawa, K., Tasaka, S., Sasaki, Y., et al. (1995). Ground-water Radon Anomaly before the Kobe Earthquake in Japan. *Science* 269 (5220), 60–61. doi:10.1126/science.269.5220.60

Igarashi, G., Wakita, H., and Sato, T. (1992). Precursory and Coseismic Anomalies in Well Water Levels Observed for the February 2, 1992 Tokyo Bay Earthquake. *Geophys. Res. Lett.* 19 (15), 1583–1586. doi:10.1029/92GL01422

Ihmlé, P. F., and Jordan, T. H. (1994). Teleseismic Search for Slow Precursors to Large Earthquakes. *Science* 266 (5190), 1547–1551. doi:10.1126/science.266.5190.1547

Ikeya, M. (2004). *Earthquakes and Animals*. Singapore: World Scientific. doi:10.1142/5382 Earthquakes and Animals

Ikeya, M., Furuta, H., Kajiwara, N., and Anzai, H. (1996). Ground Electric Field Effects on Rats and Sparrows: Seismic Anomalous Animal Behaviors (SAABs). *Jpn. J. Appl. Phys.* 35 (8), 4587–4594. doi:10.1143/jjap.35.4587

Ikeya, N., and Woodward, J. R. (2021). Cellular Autofluorescence Is Magnetic Field Sensitive. *Proc. Natl. Acad. Sci. USA* 118 (3), e2018043118. doi:10.1073/pnas.2018043118

Inan, S., Akgül, T., Seyis, C., Saatçilar, R., Baykut, S., Ergintav, S., et al. (2008). Geochemical Monitoring in the Marmara Region (NW Turkey): A Search for Precursors of Seismic Activity. *J. Geophys. Res. Solid Earth* 113 (3), 3401. doi:10.1029/2007JB005206

Inan, S., Ertekin, K., Seyis, C., Şimşek, Ş., Kulak, F., Dikbaş, A., et al. (2010). Multidisciplinary Earthquake Researches in Western Turkey: Hints to Select Sites to Study Geochemical Transients Associated to Seismicity. *Acta Geophysica* 58 (5), 767–813. doi:10.2478/s11600-010-0016-7

Isaev, N. V., Sorokin, V. M., Chmyrev, V. M., Serebryakova, O. N., and Ovcharenko, O. Y. (2002). "Electric Field Enhancement in the Ionosphere above Tropical Storm Region," in *Seismo Electromagnetics: Lithosphere-Atmosphere-Ionosphere Coupling*. Editors M. Hayakawa and O. A. Molchanov, (Tokyo: TERRAPUB), 313–315.

Jacobs, J. A., Kato, Y., Matsushita, S., and Troitskaya, V. A. (1964). Classification of Geomagnetic Micropulsations. *J. Geophys.*, 8 (3), 341–342. doi:10.1111/j.1365-246X.1964.tb06301.x

Jhuang, H.-K., Ho, Y.-Y., Kakinami, Y., Liu, J.-Y., Oyama, K.-I., Parrot, M., et al. (2010). Seismo-ionospheric Anomalies of the GPS-TEC Appear before the 12 May 2008 Magnitude 8.0 Wenchuan Earthquake. *Int. J. Remote Sensing* 31 (13), 3579–3587. doi:10.1080/01431161003727796

Jianguo, H., Tianming, T., and Derui, L. (2000). Progress in the Research on Atmospheric Electric Field Anomaly as an index for Short-Impending Prediction of Earthquakes. *J. Earthquake Prediction Res.* 8 (3), 241–255.

Jing, F., Shen, X. H., Kang, C. L., and Xiong, P. (2013). Natural Hazards and Earth System Sciences Variations of Multi-Parameter Observations in Atmosphere Related to Earthquake. *Hazards Earth Syst. Sci.* 13, 27– 33. doi:10.5194/nhess-13-27-2013

Johnson, P. A., Rouet-Leduc, B., Pyrak-Nolte, L. J., Beroza, G. C., Marone, C. J., Hulbert, C., Howard, A., Singer, P., Gordeev, D., Karaflos, D., Levinson, C. J., Pfeiffer, P., Puk, K. M., and Reade, W. (2021). “Laboratory Earthquake Forecasting: A Machine Learning Competition,” in Proceedings of the National Academy of Sciences of the United States of America (National Academy of Sciences), 118 Issue 5, e2011362118. doi:10.1073/pnas.2011362118

Johnston, A. C. (1991). Light from Seismic Waves. *Nature* 354, 361, 1991 . Nature Publishing Group. doi:10.1038/354361a0

Johnston, M. J. S. (1997). Review of Electric and Magnetic fields Accompanying Seismic and Volcanic Activity. *Surveys in Geophysics*, Netherlands: Springer. 18. Issue 5, 441–476. doi:10.1023/a:1006500408086

Jones, L., and Molnar, P. (1976). Frequency of Foreshocks. *Nature* 262 (5570), 677–679. doi:10.1038/262677a0

Jones, R. H., and Stewart, R. C. (1997). A Method for Determining Significant Structures in a Cloud of Earthquakes. *J. Geophys. Res.* 102 (B4), 8245–8254. doi:10.1029/96jb03739

Jordan, T. H. (2006). Earthquake Predictability, Brick by Brick. *Seismological Res. Lett.* 77 (1), 3–6. doi:10.1785/gssrl.77.1.3

Kafatos, M., Ouzounov, D., Pullinets, S., Cervone, G., and Singh, R. P. (2007). “Energies Associated with the Sumatra Earthquakes of December 26, 2004 and March 28, 2005,” in AGU Fall Meeting Abstracts, San Francisco, S42B–S04.2007

Kandalyan, R. A., and AlQuran, M. K. (2010). Ionosphere Scintillation and Earthquakes. *Jordan J. Phys.* 3 (2), 69–76.

Kappler, K. N., Schneider, D. D., MacLean, L. S., and Bleier, T. E. (2017). Identification and Classification Of Transient Pulses Observed in Magnetometer Array Data by Time-Domain Principal Component Analysis Filtering. *Earthquake Sci.* 30, 193–207. doi:10.1007/s11589-017-0191-6

Kato, M., Mitsui, Y., and Yanagidani, T. (2010). Photographic Evidence of Luminescence during Faulting in Granite. *Earth Planet. Sp* 62 (5), 489–493. doi:10.5047/eps.2010.02.004

Kawabe, I. (1985). Anomalous Changes of CH4/Ar Ratio in Subsurface Gas Bubbles as Seismogeochemical Precursors at Matsuyama, Japan. *Pageoph* 122 (2–4), 194–214. doi:10.1007/BF00874593

Khilyuk, L. F., Robertson, J. O., Jr, Endres, B., and Chilingarian, G. V. (2000). *Gas Migration: Events Preceding Earthquakes*. Huston: Elsevier.

Kilston, S., and Knopoff, L. (1983). Lunar-solar Periodicities of Large Earthquakes in Southern California. *Nature* 304 (5921), 21–25. doi:10.1038/304021a0

King, C.-Y. (1986). Gas Geochemistry Applied to Earthquake Prediction: An Overview. *J. Geophys. Res.* 91 (B12), 12269–12281. doi:10.1029/jb091ib12p12269

Kirschvink, J. L. (2000). Earthquake Prediction by Animals: Evolution and Sensory Perception. *Bull. Seismological Soc. America* 90 (2), 312–323. doi:10.1785/0119980114

Kirschvink, J. L., Winklhofer, M., and Walker, M. M. (2010). Biophysics of Magnetic Orientation: Strengthening the Interface between Theory and Experimental Design. *Journal of the Royal Society Interface*, 7 Suppl. 2. doi:10.1098/rsif.2009.0491.focus

Kissin, I. G., and Grinevsky, A. O. (1990). Main Features of Hydrogeodynamic Earthquake Precursors. *Tectonophy.* 178, 277– 286. doi:10.1016/0040-1951(90)90154-Z

Klimenko, M. V., Klimenko, V. V., Zakharenkova, I. E., and Pulinets, S. A. (2012). Variations of Equatorial Electrojet as Possible Seismo-Ionospheric Precursor at the Occurrence of TEC Anomalies before strong Earthquake. *Adv. Space Res.* 49 (3), 509–517. doi:10.1016/j.asr.2011.10.017

Koizumi, N., Kitagawa, Y., Matsumoto, N., Takahashi, M., Sato, T., Kamigaichi, O., et al. (2004). Preseismic Groundwater Level Changes Induced by Crustal Deformations Related to Earthquake Swarms off the East Coast of Izu Peninsula, Japan. *Geophys. Res. Lett.* 31 (10), a–n. doi:10.1029/2004GL019557

Koizumi, N., Tsukuda, E., Kamigaichi, O., Matsumoto, N., Takahashi, M., and Sato, T. (1999). Preseismic Changes in Groundwater Level and Volumetric Strain Associated with Earthquake Swarms off the East Coast of the Izu Peninsula, Japan. *Geophys. Res. Lett.* 26 (23), 3509–3512. doi:10.1029/1999GL005381

Kon, S., Nishihashi, M., and Hattori, K. (2011). Ionospheric Anomalies Possibly Associated with M⩾6.0 Earthquakes in the Japan Area during 1998-2010: Case Studies and Statistical Study. *J. Asian Earth Sci.* 41 (4–5), 410–420. doi:10.1016/j.jseaes.2010.10.005

Kondo, G. (1968). The Variation of The Atmospheric Electric Field at The Time of Earthquake. *Mem. Kakioka Magnet. Observ.* 12, 11–23.

Kopytenko, Y. A., Matiashvili, T. G., Voronov, P. M., Kopytenko, E. A., and Molchanov, O. A. (1993). Detection of Ultra-low-frequency Emissions Connected with the Spitak Earthquake and its Aftershock Activity, Based on Geomagnetic Pulsations Data at Dusheti and Vardzia Observatories. *Phys. Earth Planet. Interiors* 77 (1–2), 85–95. doi:10.1016/0031-9201(93)90035-8

Korepanov, V., Hayakawa, M., Yampolski, Y., and Lizunov, G. (2009). AGW as a Seismo-Ionospheric Coupling Responsible Agent. *Phy. Chem. Earth* 34, 485–495. doi:10.1016/j.pce.2008.07.014

Korsunova, L. P., and Khegai, V. V. (2008). Analysis of Seismoionospheric Disturbances at the Chain of Japanese Stations for Vertical Sounding of the Ionosphere. *Geomagn. Aeron.* 48 (3), 392–399. doi:10.1134/S0016793208030134

Korsunova, L. P., and Khegai, V. V. (2006). Medium-term Ionospheric Precursors to strong Earthquakes. *Int. J. Geomagn. Aeron.* 6, 3005. doi:10.1029/2005GI000122

Kotsarenko, A., Molchanov, O., Hayakawa, M., Koshevaya, S., Grimalsky, V., Pérez Enríquez, R., et al. (2005). Investigation of ULF Magnetic Anomaly during Izu Earthquake Swarm and Miyakejima Volcano Eruption at Summer 2000, Japan. *Nat. Hazards Earth Syst. Sci.* 5 (1), 63–69. doi:10.5194/nhess-5-63-2005

Kovach, R. L., Nur, A., Wesson, R. L., and Robinson, R. (1975). Water-level Fluctuations and Earthquakes on the San Andreas Fault Zone. *Geol* 3 (8), 437. doi:10.1130/0091-7613(1975)3<437:wfaeot>2.0.co;2

Kraus, J. D. (1988). *Antennas*. McGraw-Hill.

Kuo, C. L., Huba, J. D., Joyce, C. L., and Lee, L. C. (2011). Ionosphere Plasma Bubbles and Density Variations Induced by Pre-Earthquake Rock Currents and Associated Surface Charges. *J. Geophys. Res. Space Phys.* 116, 10317. doi:10.1029/2011JA016628

Kuznetsov, V. D., Bodnar, L., Garipov, G. K., Danilkin, V. A., Degtyar, V. G., Dokukin, V. S., et al. (2011). Orbital Monitoring of the Ionosphere and Abnormal Phenomena by the Small Vulkan-Compass-2 Satellite. *Geomagn. Aeron.* 51 (3), 329–341. doi:10.1134/S001679321103011X

Lachenbruch, A. H., and Sass, J. H. (1992). Heat Flow from Cajon Pass, Fault Strength, and Tectonic Implications. *J. Geophys. Res.* 97 (B4), 4995–5015. doi:10.1029/91JB01506

Lambert, N., Chen, Y.-N., Cheng, Y.-C., Li, C.-M., Chen, G.-Y., and Nori, F. (2013). Quantum Biology. *Nat. Phys* 9 (1), 10–18. doi:10.1038/nphys2474

Langbein, J., Borcherdt, R., Dreger, D., Fletcher, J., Hardebeck, J. L., Hellweg, M., et al. (2005). Preliminary Report on the 28 September 2004, M 6.0 Parkfield, California Earthquake. *Seismological Res. Lett.* 76 (1), 10–26. doi:10.1785/gssrl.76.1.10

Langbein, J. (2015). Borehole Strainmeter Measurements Spanning the 2014 M W 6.0 South Napa Earthquake, California: The Effect from Instrument Calibration. *J. Geophys. Res. Solid Earth* 120 (10), 7190–7202. doi:10.1002/2015jb012278

Lanzerotti, L. J., Maclennan, C. G., and Fraser-Smith, A. C. (1990). Background Magnetic Spectra: ~10−5to ~105Hz. *Geophys. Res. Lett.* 17 (10), 1593–1596. doi:10.1029/GL017i010p01593

Larkina, V. I., Migulin, V. V., Molchanov, O. A., Kharkov, I. P., Inchin, A. S., and Schvetcova, V. B. (1989). Some Statistical Results on Very Low Frequency Radiowave Emissions in the Upper Ionosphere over Earthquake Zones. *Phys. Earth Planet. Interiors* 57 (1–2), 100–109. doi:10.1016/0031-9201(89)90219-7

Li, M., Shen, X., Parrot, M., Yu, C., Zhang, X., Yan, R., et al. (2020). Primary Joint Statistical Seismic Influence on Ionospheric Parameters Recorded by the CSES and DEMETER Satellites. doi:10.1002/ESSOAR.10502965.1

Li, X. Q., Xu, Y. B., An, Z. H., Liang, X. H., Wang, P., Zhao, X. Y., et al. (2019). The High-Energy Particle Package Onboard CSES. *Radiat. Detect. Technol. Methods* 3 (3), 1–11. doi:10.1007/s41605-019-0101-7

Li, Y., Liu, Y., Jiang, Z., Guan, J., Yi, G., Cheng, S., et al. (2009). Behavioral Change Related to Wenchuan Devastating Earthquake in Mice. *Bioelectromagnetics* 30 (8), 613–620. doi:10.1002/bem.20520

Li, Z., Meier, M.-A., Hauksson, E., Zhan, Z., and Andrews, J. (2018). Machine Learning Seismic Wave Discrimination: Application to Earthquake Early Warning. *Geophys. Res. Lett.* 45 (10), 4773–4779. doi:10.1029/2018GL077870

Lin, C. Y., Lin, C. C. H., Liu, J. Y., Rajesh, P. K., Matsuo, T., Chou, M. Y., et al. (2020). The Early Results and Validation of FORMOSAT-7/COSMIC-2 Space Weather Products: Global Ionospheric Specification and Ne-Aided Abel

Electron Density Profile. *J. Geophys. Res. Space Phys.* 125 (10), e2020JA028028. doi:10.1029/2020JA028028

Lin, J., Shen, X., Hu, L., Wang, L., and Zhu, F. (2018). CSES GNSS Ionospheric Inversion Technique, Validation and Error Analysis. *Sci. China Technol. Sci.* 61 (5), 669–677. doi:10.1007/s11431-018-9245-6

Liperovsky, V. A., Meister, C.-V., Liperovskaya, E. V., and Bogdanov, V. V. (2008b). On the Generation of Electric Field and Infrared Radiation in Aerosol Clouds Due to Radon Emanation in the Atmosphere before Earthquakes. *Nat. Hazards Earth Syst. Sci.* 8 (5), 1199–1205. doi:10.5194/nhess-8-1199-2008

Liperovsky, V. A., Meister, C.-V., Liperovskaya, E. V., Davidov, V. F., and Bogdanov, V. V. (2005). On the Possible Influence of Radon and Aerosol Injection on the Atmosphere and Ionosphere before Earthquakes. *Nat. Hazards Earth Syst. Sci.* 5 (6), 783–789. doi:10.5194/nhess-5-783-2005

Liperovsky, V. A., Pokhotelov, O. A., Meister, C.-V., and Liperovskaya, E. V. (2008a). Physical Models of Coupling in the Lithosphere-Atmosphere-Ionosphere System before Earthquakes. *Geomagn. Aeron.* 48 (6), 795–806. doi:10.1134/s0016793208060133

Lisi, M., Filizzola, C., Genzano, N., Grimaldi, C. S. L., Lacava, T., Marchese, F., et al. (2010). A Study on the Abruzzo 6 April 2009 Earthquake by Applying the RST Approach to 15 Years of AVHRR TIR Observations. *Nat. Hazards Earth Syst. Sci.* 10 (2), 395–406. doi:10.5194/nhess-10-395-2010

Liu, J. Y., Chen, C. H., Chen, Y. I., Yang, W. H., Oyama, K. I., and Kuo, K. W. (2010). A Statistical Study of Ionospheric Earthquake Precursors Monitored by Using Equatorial Ionization Anomaly of GPS TEC in Taiwan during 2001-2007. *J. Asian Earth Sci.* 39 (1–2), 76–80. doi:10.1016/j.jseaes.2010.02.012

Liu, J. Y., Chen, Y. I., Chuo, Y. J., and Chen, C. S. (2006). A Statistical Investigation of Preearthquake Ionospheric Anomaly. *J. Geophys. Res.* 111 (5), 5304. doi:10.1029/2005JA011333

Liu, J. Y., Chen, Y. I., Chuo, Y. J., and Tsai, H. F. (2001). Variations of Ionospheric Total Electron Content during the Chi-Chi Earthquake. *Geophys. Res. Lett.* 28 (7), 1383–1386. doi:10.1029/2000GL012511

Liu, J. Y., Chen, Y. I., Pulinets, S. A., Tsai, Y. B., and Chuo, Y. J. (2000). Seismo-ionospheric Signatures Prior to M≥6.0 Taiwan Earthquakes. *Geophys. Res. Lett.* 27 (19), 3113–3116. doi:10.1029/2000GL011395

Liu, J. Y., Chuo, Y. J., Pulinets, S. A., Tsai, H. F., and Zeng, X. (2002). "A Study on the TEC Perturbations Prior to the Rei-Li, Chi-Chi and Chia-Yi Earthquakes," in *Seismo-Electromagnetics: Lithosphere-Atmosphere-Ionosphere Coupling*. Editors M. Hayakawa and O. A. Molchanov (Terra Scientific Pub. Comp), 297–301.

Liu, J. Y., Chuo, Y. J., Shan, S. J., Tsai, Y. B., Chen, Y. I., Pulinets, S. A., et al. (2004). Pre-earthquake Ionospheric Anomalies Registered by Continuous GPS TEC Measurements. *Ann. Geophys.* 22 (5), 1585–1593. doi:10.5194/angeo-22-1585-2004

Liu, J. Y. (2009). "Earthquake Precursors Observed in the Ionospheric F-Region," in *Electromagnetic Phenomena Associated with Earthquakes*. Editor M. Hayakawa (Trivandrum: Transworld Research Network), 187–204.

Liu, X., Hattori, K., Han, P., Chen, H., Chie, Y., and Zhao, X. (2020). Possible Anomalous Changes in Solar Quiet Daily Geomagnetic Variation (Sq) Related to the 2011 off the Pacific Coast of Tohoku Earthquake (Mw 9.0). *Pure Appl. Geophys.* 177 (1), 333–346. doi:10.1007/s00024-018-02086-z

Lizunov, G. V., Skorokhod, T. V., Skorokhod, T. V., and Korepanov, V. Y. (2020). Atmospheric Gravity Waves Among Other Physical Mechanisms of Seismic-Ionospheric Coupling. *Kosm. Nauka Tehnol.* 26 (3), 55–80. doi:10.15407/knit2020.03.055

Lockner, D. A., Johnston, M. J. S., and Byerlee, J. D. (1983). A Mechanism to Explain the Generation of Earthquake Lights. *Nature* 302 (5903), 28–33. doi:10.1038/302028a0

Lohmann, K. J., and Lohmann, C. M. F. (2019). There and Back Again: Natal Homing by Magnetic Navigation in Sea Turtles and salmon. *J. Exp. Biol.* 222 (Suppl. l_1). doi:10.1242/jeb.184077

Lohmann, K. J. (2007). Sea Turtles: Navigating with Magnetism. *Curr. Biol.* 17 (3), R102–R104. Elsevier. doi:10.1016/j.cub.2007.01.023

Lomnitz, C. (1994). *Fundamentals of Earthquake Prediction*. Wiley.

LongJohn, T., Morgan, J. K., and Dugan, B. (2018). Microstructural Evolution of Porosity and Stress during the Formation of Brittle Shear Fractures: A Discrete Element Model Study. *J. Geophys. Res. Solid Earth* 123 (3), 2228–2245. doi:10.1002/2017JB014842

Lorenzetti, E., and Tullis, T. E. (1989). Geodetic Predictions of a Strike-Slip Fault Model: Implications for Intermediate- and Short-Term Earthquake Prediction. *J. Geophys. Res.* 94 (B9), 12343–12361. doi:10.1029/jb094ib09p12343

Lu, X., Meng, Q. Y., Gu, X. F., Zhang, X. D., Xie, T., and Geng, F. (2016). Thermal Infrared Anomalies Associated with Multi-Year Earthquakes in the Tibet Region Based on China's FY-2E Satellite Data. *Adv. Space Res.* 58 (6), 989–1001. doi:10.1016/j.asr.2016.05.038

Lyon, G. L. (1974). Geothermal Gases. in *Natural Gases in Marine Sediments*. Editors I. R. Kaplan. (Boston: Springer US), 141–150. doi:10.1007/978-1-4684-2757-8_9Geothermal Gases.

Ma, T., and Wu, Z. (2012). Precursor-Like Anomalies Prior to the 2008 Wenchuan Earthquake: A Critical-But-Constructive Review. *Int. J. Geophys.*, 2012, 1–13. doi:10.1155/2012/583097

Ma, W., Kong, X., Kang, C., Zhong, X., Wu, H., Zhan, X., et al. (2015). Research on the Changes of the Tidal Force and the Air Temperature in the Atmosphere of Lushan (China) MS7.0 Earthquake. *Therm. Sci.* 19, 487–493. doi:10.2298/TSCI150403148M

Ma, W. Y., Wang, H., Li, F. S., and Ma, W. M. (2012). Relation between the Celestial Tide-Generating Stress and the Temperature Variations of the Abruzzo M = 6.3 Earthquake in April 2009. *Nat. Hazards Earth Syst. Sci.* 12 (3), 819–827. doi:10.5194/nhess-12-819-2012

Ma, Y., Zhao, Y., Liu, S., and Wu, L. (2010). Possible Abnormal Phenomenon of the Atmospheric Water Vapor before Hengchun Earthquake. *PIERS Online* 6 (1), 21–25. doi:10.2529/PIERS090907094618

Maekawa, S., Horie, T., Yamauchi, T., Sawaya, T., Ishikawa, M., Hayakawa, M., et al. (2006). A Statistical Study on the Effect of Earthquakes on the Ionosphere, Based on the Subionospheric LF Propagation Data in Japan. *Ann. Geophys.* 24 (8), 2219–2225. doi:10.5194/angeo-24-2219-2006

Mallet, R. (1855). Report of the 24th meeting of the British Association for the Advancement of Science, Liverpool, September 1854. in *Third report on the facts of earthquake phenomena, Catalogue of recorded earthquakes from 1606 B.C. to A.D. 1850 (continued from report for 1853)*, . John Murray, 2-326.

Marchetti, D., De Santis, A., D'Arcangelo, S., Poggio, F., Piscini, A., Campuzano, S. A., et al. (2019). Pre-earthquake Chain Processes Detected from Ground to Satellite Altitude in Preparation of the 2016-2017 Seismic Sequence in Central Italy. *Remote Sensing Environ.* 229, 93–99. doi:10.1016/j.rse.2019.04.033

Marchetti, D., De Santis, A., Shen, X., Campuzano, S. A., Perrone, L., Piscini, A., et al. (2020). Possible Lithosphere-Atmosphere-Ionosphere Coupling Effects Prior to the 2018 Mw = 7.5 Indonesia Earthquake from Seismic, Atmospheric and Ionospheric Data. *J. Asian Earth Sci.* 188, 104097. doi:10.1016/j.jseaes.2019.104097

Martinelli, G., Facca, G., Genzano, N., Gherardi, F., Lisi, M., Pierotti, L., et al. (2020a). Earthquake-Related Signals in Central Italy Detected by Hydrogeochemical and Satellite Techniques. *Front. Earth Sci.* 8, 529. doi:10.3389/feart.2020.584716

Martinelli, G., Plescia, P., and Tempesta, E. (2020b). Electromagnetic Emissions from Quartz Subjected to Shear Stress: Spectral Signatures and Geophysical Implications. *Geosciences* 10 (4), 140. doi:10.3390/geosciences10040140

Marty, B., Meynier, V., Nicolini, E., Griesshaber, E., and Toutain, J. P. (1993). Geochemistry of Gas Emanations: A Case Study of the Réunion Hot Spot, Indian Ocean. *Appl. Geochem.* 8 (2), 141–152. doi:10.1016/0883-2927(93)90030-K

McCartney, B. S., and Bary, B. M. (1965). Echo-sounding on Probable Gas Bubbles from the Bottom of Saanich Inlet, British Columbia. *Deep Sea Res. Oceanographic Abstr.* 12 (3), 285–294. doi:10.1016/0011-7471(65)90002-1

McNutt, S. R., and Beavan, R. J. (1981). Volcanic Earthquakes at Pavlof Volcano Correlated with the Solid Earth Tide. *Nature* 294 (5842), 615–618. doi:10.1038/294615a0

Merifield, P. M., and Lamar, D. L. (1981). Anomalous Water-Level Changes and Possible Relation with Earthquakes. *Geophys. Res. Lett.* 8 (5), 437–440. doi:10.1029/GL008i005p00437

Michael, A. J., and Werner, M. J. (2018). Preface to the Focus Section on the Collaboratory for the Study of Earthquake Predictability (CSEP): New Results and Future Directions. *Seismological Research Letters* 89 (4), 1226–1228. doi:10.1785/0220180161

Mignan, A. (2008). The Stress Accumulation Model: Accelerating Moment Release and Seismic Hazard. *Advances in Geophysics*, 49, 67–201. doi:10.1016/S0065-2687(07)49002-1

Mizutani, H., Ishido, T., Yokokura, T., and Ohnishi, S. (1976). Electrokinetic Phenomena Associated with Earthquakes. *Geophys. Res. Lett.* 3 (7), 365–368. doi:10.1029/GL003i007p00365

Molchanov, O. A., and Hayakawa, M. (2008). *Seismo-electromagnetics and Related Phenomena: History and Latest Results*, Vol. 189. Tokyo: Terrapub.

Molchanov, O. A. (2009). "Lithosphere-atmosphere-ionosphere Coupling Due to Seismicity," in *Electromagnetic Phenomena Associated with Earthquakes*. Editor M. Hayakawa (Trivandrum: Transworld Research Network), 255–279.

Molchanov, O., Fedorov, E., Schekotov, A., Gordeev, E., Chebrov, V., Surkov, V., et al. (2004). Lithosphere-atmosphere-ionosphere Coupling as Governing Mechanism for Preseismic Short-Term Events in Atmosphere and Ionosphere. *Nat. Hazards Earth Syst. Sci.* 4 (5–6), 757–767. doi:10.5194/nhess-4-757-2004

Mora, C. V., Davison, M., Martin Wild, J., and Walker, M. M. (2004). Magnetoreception and its Trigeminal Mediation in the Homing pigeon. *Nature* 432 (7016), 508–511. doi:10.1038/nature03077

Moro, M., Saroli, M., Stramondo, S., Bignami, C., Albano, M., Falcucci, E., et al. (2017). New Insights into Earthquake Precursors from InSAR. *Sci. Rep.* 7 (1), 1–11. doi:10.1038/s41598-017-12058-3

Morozov, V. N. (2006). The Influence of Convective Current Generator on the Global Current. *Nonlin. Process. Geophys.* 13 (2), 243–246. doi:10.5194/npg-13-243-2006

Mouritsen, H. (2018). Long-distance Navigation and Magnetoreception in Migratory Animals. *Nature* 558 (7708), 50–59. Nature Publishing Group. doi:10.1038/s41586-018-0176-1

Mulargia, F., and Geller, R. J. (2003). in *Earthquake Science and Seismic Risk Reduction*. Editors F. Mulargia and R. J. Geller (Dordrecht: Springer Science & Business Media), Vol. 2.

Musha, K. (1957). *Jishin Namazu (Earthquake and Catfish)*. Tokyo: Toyo Tosho.

Nagamine, K., and Sugisaki, R. (1991). Coseismic Changes of Subsurface Gas Compositions Disclosed by an Improved Seismo-Geochemical System. *Geophys. Res. Lett.* 18 (12), 2221–2224. doi:10.1029/91GL02710

Nagao, T., Enomoto, Y., Fujinawa, Y., Hata, M., Hayakawa, M., Huang, Q., et al. (2002). Electromagnetic Anomalies Associated with 1995 Kobe Earthquake. *J. Geodynamics* 33 (4–5), 401–411. doi:10.1016/S0264-3707(02)00004-2

Namgaladze, A. A., Klimenko, M. V., Klimenko, V. V., and Zakharenkova, I. E. (2009). Physical Mechanism and Mathematical Modeling of Earthquake Ionospheric Precursors Registered in Total Electron Content. *Geomagn. Aeron.* 49 (2), 252–262. doi:10.1134/S0016793209020169

Nanjo, K. Z. (2020). Were Changes in Stress State Responsible for the 2019 Ridgecrest, California, Earthquakes? *Nat. Commun.* 11 (1), 1–10. doi:10.1038/s41467-020-16867-5

Natarajan, V., and Philipoff, P. (2018). Observation of Surface and Atmospheric Parameters Using "NOAA 18" Satellite: a Study on Earthquakes of Sumatra and Nicobar Is Regions for the Year 2014 (M ≥ 6.0). *Nat. Hazards* 92 (2), 1097–1112. doi:10.1007/s11069-018-3242-y

Neubert, T., Rycroft, M., Farges, T., Blanc, E., Chanrion, O., Arnone, E., et al. (2008). Recent Results from Studies of Electric Discharges in the Mesosphere. *Surveys in Geophysics*, 29 Issue 2. Netherlands: Springer, 71–137. doi:10.1007/s10712-008-9043-1

Nikiforova, N. N., and Michnowski, S. (1995). Atmospheric Electric Field Anomalies Analysis during Great Carpatian Earthquake at Polish Observatory SwiderIUGG XXI General Assembly Abstracts in *IUGG XXI General Assembly Abstracts VA11D-16*. Boulder, Colorado: IUGG.

Nikolaeva, N. A., Derkachev, A. N., and Obzhirov, A. I. (2009). Characteristic Features of the Occurrence of Gas-Fluid Emanations on the Northeastern Slope of Sakhalin Island, Sea of Okhotsk. *Russ. J. Pac. Geol.* 3 (3), 234–248. doi:10.1134/S181971400903004X

Nimpf, S., Nordmann, G. C., Kagerbauer, D., Malkemper, E. P., Landler, L., Papadaki-Anastasopoulou, A., et al. (2019). A Putative Mechanism for Magnetoreception by Electromagnetic Induction in the Pigeon Inner Ear. *Curr. Biol.* 29 (23), 4052–4059. doi:10.1016/j.cub.2019.09.048

Nissen, E., Krishnan, A. K., Arrowsmith, J. R., and Saripalli, S. (2012). Three-dimensional Surface Displacements and Rotations from Differencing Pre- and post-earthquake LiDAR point Clouds. *Geophys. Res. Lett.* 39 (16), a–n. doi:10.1029/2012GL052460

Niu, F., Silver, P. G., Daley, T. M., Cheng, X., and Majer, E. L. (2008). Preseismic Velocity Changes Observed from Active Source Monitoring at the Parkfield SAFOD Drill Site. *Nature* 454 (7201), 204–208. doi:10.1038/nature07111

Nourbehecht, B. (1936-1963). Irreversible Thermodynamic Effects in Inhomogeneous media and Their Applications in Certain Geoelectric Problems [Massachusetts Institute of Technology]. Available at: https://dspace.mit.edu/handle/1721.1/11576.

Ogawa, T., Oike, K., and Miura, T. (1985). Electromagnetic Radiations from Rocks. *J. Geophys. Res.* 90 (D4), 6245–6249. doi:10.1029/jd090id04p06245

Ohayon, M. M. (2000). Prevalence of Hallucinations and Their Pathological Associations in the General Population. *Psychiatry Res.* 97 (2–3), 153–164. doi:10.1016/S0165-1781(00)00227-4

Okada, Y., Mukai, S., and Singh, R. P. (2004). Changes in Atmospheric Aerosol Parameters after Gujarat Earthquake of January 26, 2001. *Adv. Space Res.* 33 (3), 254–258. doi:10.1016/S0273-1177(03)00474-5

Omori, Y., Yasuoka, Y., Nagahama, H., Kawada, Y., Ishikawa, T., Tokonami, S., et al. (2007). Anomalous Radon Emanation Linked to Preseismic Electromagnetic Phenomena. *Nat. Hazards Earth Syst. Sci.* 7 (5), 629–635. doi:10.5194/nhess-7-629-2007

Ondoh, T. (2004). Anomalous Sporadic-E Ionization before a Great Earthquake. *Adv. Space Res.* 34 (8), 1830–1835. doi:10.1016/j.asr.2003.05.044

Ondoh, T. (2003). Anomalous Sporadic-E Layers Observed before M7.2 Hyogo-Ken Nanbu Earthquake; Terrestrial Gas Emanation Model. *Adv. Polar Upper Atmosphere Res.* 17, 96–108. doi:10.15094/00006365

Ondoh, T., and Hayakawa, M. (2006). Synthetic Study of Precursory Phenomena of the M7.2 Hyogo-Ken Nanbu Earthquake. *Phys. Chem. Earth, Parts A/B/C* 31 (4–9), 378–388. doi:10.1016/j.pce.2006.02.017

Ondoh, T. (2009). Investigation of Precursory Phenomena in the Ionosphere, Atmosphere and Groundwater before Large Earthquakes of M>6.5. *Adv. Space Res.* 43 (2), 214–223. doi:10.1016/j.asr.2008.04.003

O'Neil, J. R., and King, C. Y. (1980). Deuterium Anomalies in Groundwater as Precursors to Seismic Activity in California. *Eos, Trans. Am. Geophys. Union* 61 (46), 1033, 1980 . Available at: https://eurekamag.com/research/018/717/018717545.php.

Orihara, Y., Kamogawa, M., Noda, Y., and Nagao, T. (2019). Is Japanese Folklore Concerning Deep-Sea Fish Appearance a Real Precursor of Earthquakes? *Bull. Seismological Soc. America* 109 (4), 1556–1562. doi:10.1785/0120190014

Ouzounov, D., Bryant, N., Logan, T., Pulinets, S., and Taylor, P. (2006). Satellite thermal IR Phenomena Associated with Some of the Major Earthquakes in 1999-2003. *Phys. Chem. Earth, Parts A/B/C* 31 (4–9), 154–163. doi:10.1016/j.pce.2006.02.036

Ouzounov, D., and Freund, F. (2004). Mid-infrared Emission Prior to strong Earthquakes Analyzed by Remote Sensing Data. *Adv. Space Res.* 33 (3), 268–273. doi:10.1016/S0273-1177(03)00486-1

Ouzounov, D., Liu, D., Chunli, K., Cervone, G., Kafatos, M., and Taylor, P. (2007). Outgoing Long Wave Radiation Variability from IR Satellite Data Prior to Major Earthquakes. *Tectonophysics* 431 (1–4), 211–220. doi:10.1016/j.tecto.2006.05.042

Ouzounov, D., Pulinets, S., Hatori, K., and Taylor, P. (2018). *Pre-Earthquake Processes: A Multidisciplinary Approach to Earthquake Prediction Studies*. Hoboken: Wiley. John Wiley & Sons. Available at: https://www.wiley.com/en-us/Pre+Earthquake+Processes%3A+A+Multidisciplinary+Approach+to+Earthquake+Prediction+Studies-p-9781119156932.

Panda, S. K., Choudhury, S., Saraf, A. K., and Das, J. D. (2007). MODIS Land Surface Temperature Data Detects thermal Anomaly Preceding 8 October 2005 Kashmir Earthquake. *Int. J. Remote Sensing* 28 (20), 4587–4596. doi:10.1080/01431160701244906

Panza, G. F., Peresan, A., Sansò, F., Crespi, M., Mazzoni, A., and Nascetti, A. (2018). How Geodesy Can Contribute to the Understanding and Prediction of Earthquakes. *Rend. Fis. Acc. Lincei* 29 (1), 81–93. doi:10.1007/s12210-017-0626-y

Papadopoulos, G. A. (1999). "Luminous and Fiery Phenomena Associated with Earthquakes in the East Mediterranean. Atmospheric and Ionospheric Electromagnetic Phenomena Associated with Earthquakes," in *Atmospheric and Ionospheric Electromagnetic Phenomena Associated with Earthquakes*. Editor M. Hayakawa (Tokyo: Terra Scientific Pub. Comp), 559–575.

Park, S. K., Johnston, M. J. S., Madden, T. R., Morgan, F. D., and Morrison, H. F. (1993). Electromagnetic Precursors to Earthquakes in the Ulf Band: A Review of

Observations and Mechanisms. *Reviews of Geophysics* 31 (2), 117–132. doi:10.1029/93RG00820

Parrot, M., Achache, J., Berthelier, J. J., Blanc, E., Deschamps, A., Lefeuvre, F., et al. (1993). High-frequency Seismo-Electromagnetic Effects. *Phys. Earth Planet. Interiors* 77 (1–2), 65–83. doi:10.1016/0031-9201(93)90034-7

Parrot, M. (1994). Statistical Study of ELF/VLF Emissions Recorded by a Low-Altitude Satellite during Seismic Events. *J. Geophys. Res. Space Phys.* 99 (12), 23339–23347. doi:10.1029/94JA02072

Parrot, M. (2002). The Micro-satellite DEMETER. *J. Geodynamics* 33 (4–5), 535–541. doi:10.1016/S0264-3707(02)00014-5

Parrot, M. (1995). Use of Satellites to Detect Seismo-Electromagnetic Effects. *Adv. Space Res.* 15 (11), 27–35. doi:10.1016/0273-1177(95)00072-M

Pergola, N., Marchese, F., and Tramutoli, V. (2004). Automated Detection of thermal Features of Active Volcanoes by Means of Infrared AVHRR Records. *Remote Sensing Environ.* 93 (3), 311–327. doi:10.1016/j.rse.2004.07.010

Perrone, L., De Santis, A., Abbattista, C., Alfonsi, L., Amoruso, L., Carbone, M., et al. (2018). Ionospheric Anomalies Detected by Ionosonde and Possibly Related to Crustal Earthquakes in Greece. *Annales Geophysicae* 36 (2), 361–371. doi:10.5194/angeo-36-361-2018

Perrone, L., Korsunova, L. P., and Mikhailov, A. V. (2010). Ionospheric Precursors for Crustal Earthquakes in Italy. *Ann. Geophysicae* 28 (4), 941–950. doi:10.5194/angeo-28-941-2010

Persenger, M. A., and Derr, J. S. (1984). Geophysical Variables and Human Behavior: XIX. Strong Temporal Relationships between Inclusive Seismic Measures and UFO Reports within Washington State. *Perceptual Mot. Skills* 59 (2), 551–566. doi:10.2466/pms.1984.59.2.551

Persinger, M. A. (1983). The Tectonic Strain Theory of Luminosities. *Pursuit* 16 (1), 21–35.

Pfaff, R., Freudenreich, H., Yokoyama, T., Yamamoto, M., Fukao, S., Mori, H., et al. (2005). Electric Field Measurements of DC and Long Wavelength Structures Associated with Sporadic-E Layers and QP Radar Echoes. *Ann. Geophysicae* 23 (7), 2319–2334. doi:10.5194/angeo-23-2319-2005

Picozza, P., Conti, L., and Sotgiu, A. (2021). Looking for Earthquake Precursors from Space: a Critical Review, In "*Geospace Observation of Natural Hazards*", Frontiers in Earth Science, Section Geohazards and Georisks. doi:10.3389/feart.2021.676775

Pierce, E. T. (1976). Atmospheric Electricity and Earthquake Prediction. *Geophys. Res. Lett.* 3 (3), 185–188. doi:10.1029/GL003i003p00185

Piscini, A., De Santis, A., Marchetti, D., and Cianchini, G. (2017). A Multi-Parametric Climatological Approach to Study the 2016 Amatrice–Norcia (Central Italy) Earthquake Preparatory Phase. *Pure Appl. Geophys.* 174 (10), 3673–3688. doi:10.1007/s00024-017-1597-8

Plastino, W. (2006). Monitoring Of Geochemical And Geophysical Parameters In The Gran Sasso Aquifer. *J. Environ. Radioact.*, 8, 335–341. doi:10.1016/S1569-4860(05)08027-7Monitoring of Geochemical and Geophysical Parameters in the Gran Sasso Aquifer.

Plastino, W., and Bella, F. (2001). Radon Groundwater Monitoring at Underground Laboratories of Gran Sasso (Italy). *Geophys. Res. Lett.* 28 (14), 2675–2677. doi:10.1029/2000GL012430

Plastino, W., Povinec, P. P., De Luca, G., Doglioni, C., Nisi, S., Ioannucci, L., et al. (2010). Uranium Groundwater Anomalies and L'Aquila Earthquake, 6th April 2009 (Italy). *J. Environ. Radioactivity* 101 (1), 45–50. doi:10.1016/j.jenvrad.2009.08.009

Polk, C. (1983). Natural and Man-Made Noise in the Earth-Ionosphere Cavity at Extremely Low Frequencies (Schumann Resonances and Man-Made 'interference'). *Space Sci. Rev.* 35 (1), 83–89. doi:10.1007/BF00173695

Posey, T. B., and Losch, M. E. (1983). Auditory Hallucinations of Hearing Voices in 375 Normal Subjects. *Imagination, Cogn. Personal.* 3 (2), 99–113. doi:10.2190/74v5-hnxn-jey5-dg7w

Press, F., and Siever, R. (1982). *Earth*. San Francisco: W. H. Freeman. Available at: https://www.abebooks.co.uk/servlet/BookDetailsPL?bi=30754169047andsearchurl=kn%3DEarth%2BPress%252C%2BFrank%2Band%2BSiever%252C%2BRaymond%26sortby%3D17andcm_sp=snippet-_-srp1-_-title1.

Pulinets, S. A., Alekseev, V. A., Legen'ka, A. D., and Khegai, V. V. (1997). Radon and Metallic Aerosols Emanation before strong Earthquakes and Their Role in Atmosphere and Ionosphere Modification. *Adv. Space Res.* 20 (11), 2173–2176. doi:10.1016/S0273-1177(97)00666-2

Pulinets, S. A., Legen'ka, A. D., Gaivoronskaya, T. V., and Depuev, V. K. (2003). Main Phenomenological Features of Ionospheric Precursors of strong Earthquakes. *J. Atmos. Solar-Terrestrial Phys.* 65 (16–18), 1337–1347. doi:10.1016/j.jastp.2003.07.011

Pulinets, S. A. (2007). Natural Radioactivity, Earthquakes, and the Ionosphere. *Eos* 88 (20), 217–218. doi:10.1029/2007EO200001

Pulinets, S. A., Ouzounov, D., Karelin, A. V., Boyarchuk, K. A., and Pokhmelnykh, L. A. (2006). The Physical Nature of thermal Anomalies Observed before strong Earthquakes. *Phys. Chem. Earth* 31 (4–9), 143–153. doi:10.1016/j.pce.2006.02.042

Pulinets, S., and Boyarchuk, K. (2005). *Ionospheric Precursors of Earthquakes*. Springer Berlin Heidelberg. doi:10.1007/b137616

Pulinets, S., and Ouzounov, D. (2011). Lithosphere-Atmosphere-Ionosphere Coupling (LAIC) Model - an Unified Concept for Earthquake Precursors Validation. *J. Asian Earth Sci.* 41 (4–5), 371–382. doi:10.1016/j.jseaes.2010.03.005

Pulinets, S. (2011). The Synergy of Earthquake Precursors. *Earthquake Sci.* 24 (6), 535–548. doi:10.1007/s11589-011-0815-1

Qin, K., Wu, L. X., Zheng, S., Bai, Y., and Lv, X. (2014). Is There an Abnormal Enhancement of Atmospheric Aerosol before the 2008 Wenchuan Earthquake? *Adv. Space Res.* 54 (6), 1029–1034. doi:10.1016/j.asr.2014.04.025

Qin, K., Wu, L., Zheng, S., and Liu, S. (2013). A Deviation-Time-Space-Thermal (DTS-T) Method for Global Earth Observation System of Systems (GEOSS)-based Earthquake Anomaly Recognition: Criterions and Quantify Indices. *Remote Sensing* 5 (10), 5143–5151. doi:10.3390/rs5105143

Raleigh, C. B., Molnar, P., Hanks, T., Nur, A., Wu, F., Savage, J., et al. (1977). Prediction of the Haicheng Earthquake. *Eos, Trans. Am. Geophys. Union* 58 (5), 236. doi:10.1029/eo058i005p00236amd

Ramírez-Rojas, A., and Flores-Márquez, E. L. (2013). Order Parameter Analysis of Seismicity of the Mexican Pacific Coast. *Physica A: Stat. Mech. Its Appl.* 392 (10), 2507–2512. doi:10.1016/j.physa.2013.01.034

Rapoport, Y., Grimalsky, V., Krankowski, A., Pulinets, S., Fedorenko, A., and Petrishchevskii, S. (2020). Algorithm for Modeling Electromagnetic Channel of Seismo-Ionospheric Coupling (SIC) and the Variations in the Electron Concentration. *Acta Geophysica* 68 (1), 253–278. doi:10.1007/s11600-019-00385-0

Reasenberg, P. A. (1999). Foreshock Occurrence before Large Earthquakes. *J. Geophys. Res. Solid Earth* 104 (B3), 4755–4768. doi:10.1029/1998jb900089

Reimer, G. M. (1990). *Geophysical Research Letters*, (John Wiley & Sons) 17 Issue 6, 799. doi:10.1029/GL017i006p00799 The Occurrence and Transport of Radon in the Natural Environment.

Reimer, G. M. (1980). Use of Soil-Gas Helium Concentrations for Earthquake Prediction: Limitations Imposed by Diurnal Variations (Colorado, Wyoming, California). *J. Geophys. Res.* 85 (B6), 3107–3114. doi:10.1029/JB085iB06p03107

Revell, L. E., Kremser, S., Hartery, S., Harvey, M., Mulcahy, J. P., Williams, J., et al. (2019). The Sensitivity of Southern Ocean Aerosols and Cloud Microphysics to Sea spray and Sulfate Aerosol Production in the HadGEM3-GA7.1 Chemistry-Climate Model. *Atmos. Chem. Phys.* 19 (24), 15447–15466. doi:10.5194/acp-19-15447-2019

Rice, J. R., and Cleary, M. P. (1976). Some Basic Stress Diffusion Solutions for Fluid-saturated Elastic Porous media with Compressible Constituents. *Reviews of Geophysics* 14 (2), 227–241. doi:10.1029/RG014i002p00227

Richon, P., Sabroux, J. C., Halbwachs, M., Vandemeulebrouck, J., Poussielgue, N., Tabbagh, J., et al. (2003). Radon Anomaly in the Soil of Taal Volcano, the Philippines: A Likely Precursor of the M 7.1 Mindoro Earthquake (1994). *Geophys. Res. Lett.* 30 (9). doi:10.1029/2003GL016902

Richter, C. F. (1958). *Elementary Seismology*. San Francisco: W. H. Freeman and Company. Available at: https://www.abebooks.it/Elementary-Seismology-1958-Freeman-Company-San/879247410/bd.

Riggio, A., and Santulin, M. (2015). Earthquake Forecasting: a Review of Radon as Seismic Precursor. *Bollettino Di Geofisica Teorica e Applicata* 56 (2), 95–114. Available at: http://www3.ogs.trieste.it/bgta/provapage.php?id_articolo=650.

Rikitake, T. (1987). Earthquake Precursors in Japan: Precursor Time and Detectability. *Tectonophysics* 136 (3–4), 265–282. doi:10.1016/0040-1951(87)90029-1

Rishbeth, H. (2006). Ionoquakes: Earthquake Precursors in the Ionosphere? *Eos* 87 (32), 316. doi:10.1029/2006eo320008

Rodger, C. J., Clilverd, M. A., and Thomson, N. R. (1999). Modeling of Subionospheric VLF Signal Perturbations Associated with Earthquakes. *Radio Sci.* 34 (5), 1177–1185. doi:10.1029/1999RS900061

Roeloffs, E. A. (1988). Hydrologic Precursors to Earthquakes: A Review. *Pure Appl. Geophys. PAGEOPH* 126 (2–4), 177–209. doi:10.1007/bf00878996

Roeloffs, E., and Quilty, E. (1997). Water Level and Strain Changes Preceding and Following the August 4, 1985 Kettleman Hills, California, Earthquake. *Pure Appl. Geophys.* 149 (1), 21–60. doi:10.1007/BF00945160

Rouet-Leduc, B., Hulbert, C., Lubbers, N., Barros, K., Humphreys, C. J., and Johnson, P. A. (2017). Machine Learning Predicts Laboratory Earthquakes. *Geophys. Res. Lett.* 44 (18), 9276–9282. doi:10.1002/2017GL074677

Rozhnoi, A., Solovieva, M., Molchanov, O., Schwingenschuh, K., Boudjada, M., Biagi, P. F., et al. (2009). Anomalies in VLF Radio Signals Prior the Abruzzo Earthquake (M=6.3) on 6 April 2009. *Nat. Hazards Earth Syst. Sci.* 9 (5), 1727–1732. doi:10.5194/nhess-9-1727-2009

Rozhnoi, A., Solovieva, M. S., Molchanov, O. A., and Hayakawa, M. (2004). Middle Latitude LF (40 kHz) Phase Variations Associated with Earthquakes for Quiet and Disturbed Geomagnetic Conditions. *Phys. Chem. Earth* 29 (4–9), 589–598. doi:10.1016/j.pce.2003.08.061

Ruina, A. (1983). Slip Instability and State Variable Friction Laws. *J. Geophys. Res.* 88 (B12), 10359–10370. doi:10.1029/JB088iB12p10359

Ruzhin, Y. Y., Sorokin, V. M., and Yashchenko, A. K. (2014). Physical Mechanism of Ionospheric Total Electron Content Perturbations over a Seismoactive Region. *Geomagnetism and Aeronomy* 54 (3), 337–346. doi:10.1134/S001679321403013X

Sannazzaro, F., Filizzola, C., Marchese, F., Corrado, R., Paciello, R., Mazzeo, G., et al. (2014). Identification Of Dust Outbreaks On Infrared MSG-SEVIRI Data By Using A Robust Satellite Technique (RST). *Acta Astronautica* 93, 64–70. doi:10.1016/j.actaastro.2013.07.003

Saraf, A. K., and Choudhury, S. (2005). NOAA-AVHRR Detects thermal Anomaly Associated with the 26 January 2001 Bhuj Earthquake, Gujarat, India. *International Journal of Remote Sensing* 26 (6), 1065–1073. doi:10.1080/01431160310001642368

Saraf, A. K., Rawat, V., Choudhury, S., Dasgupta, S., and Das, J. (2009). Advances in Understanding of the Mechanism for Generation of Earthquake thermal Precursors Detected by Satellites. *Int. J. Appl. Earth Observation Geoinformation* 11 (6), 373–379. doi:10.1016/j.jag.2009.07.003

Sasai, Y. (2001). Tectonomagnetic Modeling Based on the Piezomagnetism: A Review. *Ann. Geophys.* 44 (2), 361–368. doi:10.4401/ag-3602

Satake, H., Ohashi, M., and Hayashi, Y. (1984). Discharge of H2 from the Atotsugawa and Ushikubi Faults, Japan, and its Relation to Earthquakes. *Pure Appl. Geophys. PAGEOPH* 122 (2–4), 185–193. doi:10.1007/BF00874592

Sato, M., Sutton, A. J., McGee, K. A., and Russell-Robinson, S. (1986). Monitoring of Hydrogen along the San Andreas and Calaveras Faults in central California in 1980-1984. *J. Geophys. Res. Solid Earth* 91 (B12), 12315–12326. doi:10.1029/jb091ib12p12315

Schekotov, A., Molchanov, O., Hattori, K., Fedorov, E., Gladyshev, V. A., Belyaev, G. G., et al. (2006). Seismo-ionospheric Depression of the ULF Geomagnetic Fluctuations at Kamchatka and Japan. *Phys. Chem. Earth* 31 (4–9), 313–318. doi:10.1016/j.pce.2006.02.043

Scholz, C. H. (2019). *The Mechanics of Earthquakes and Faulting*. (Cambridge: Cambridge University Press). doi:10.1017/9781316681473 The Mechanics of Earthquakes and Faulting.

Serebryakova, O. N., Bilichenko, S. V., Chmyrev, V. M., Parrot, M., Rauch, J. L., Lefeuvre, F., et al. (1992). Electromagnetic ELF Radiation from Earthquake Regions as Observed by Low-altitude Satellites. *Geophys. Res. Lett.* 19 (2), 91–94. doi:10.1029/91GL02775

Sgrigna, V., Buzzi, A., Conti, L., Guglielmi, A. V., and Pokhotelov, O. A. (2004). Electromagnetic Signals Produced by Elastic Waves in the Earth's Crust. *Nuovo Cimento Della Societa Italiana Di Fisica C* 27 (2), 115–132. doi:10.1393/ncc/i2002-10009-y

Sgrigna, V., Buzzi, A., Conti, L., Picozza, P., Stagni, C., and Zilpimiani, D. (2007). Seismo-induced Effects in the Near-Earth Space: Combined Ground and Space Investigations as a Contribution to Earthquake Prediction. *Tectonophysics* 431 (1–4), 153–171. doi:10.1016/j.tecto.2006.05.034

Sgrigna, V., Buzzi, A., Conti, L., Picozza, P., Stagni, C., and Zilpimiani, D. (2008a). The ESPERIA Satellite Project for Detecting Seismo-Associated Effects in the Topside Ionosphere. First Instrumental Tests in Space. *Earth, Planets and Space* 60 (5), 463–475. doi:10.1186/bf03352813

Sgrigna, V., Console, R., Conti, L., Galper, A. M., Malvezzi, V., Parrot, M., et al. (2008b). The ESPERIA Project: a Mission to Investigate the Near-Earth Space. *Earth Observation with CHAMP*. (Berlin: Springer-Verlag), 407–412. doi:10.1007/3-540-26800-6_65

Sgrigna, V., and Conti, L. (2012). A Deterministic Approach to Earthquake Prediction. *Int. J. Geophys.* 2012, 1–20. doi:10.1155/2012/406278

Sgrigna, V., and Conti, L. (2010). Earthquake Preparation and Warning: Science, Methods and Technologies. *Advances in Environmental Research*, (New York: Nova Science Publishers, Inc.) 7, 1–38.

Sgrigna, V., and Malvezzi, V. (2003). Preseismic Creep Strains Revealed by Ground Tilt Measurements in central Italy on the Occasion of the 1997 Umbria-Marche Apennines Earthquake Sequence. *Pure Appl. Geophys.* 160 (8), 1493–1515. doi:10.1007/s00024-003-2357-5

Shen, X. H., Zhang, X. M., Yuan, S. G., Wang, L. W., Cao, J. Bin., Huang, J. P., et al. (2018). The State-Of-The-Art of the China Seismo-Electromagnetic Satellite mission. *Sci. China Technol. Sci.* 61 (5), 634–642. doi:10.1007/s11431-018-9242-0

Shvets, A., and Hayakawa, M. (2011). Global Lightning Activity on the Basis of Inversions of Natural ELF Electromagnetic Data Observed at Multiple Stations Around the World. *Surv. Geophys.* 32 (6), 705–732. doi:10.1007/s10712-011-9135-1

Sidgwick, H. (1891). A CENSUS OF HALLUCINATIONS. *New Rev.* 4 (20), 52–59.

Sidgwick, H., Johnson, A., Myers, F. W. H., Podmore, F., and Sidgwick, E. M. (1994). "Report on the Census of Hallucinations," in Proceedings of the Society for Psychical Research, 25–422. https://www.scopus.com/record/display.uri?eid=2-s2.0-0000483685andorigin=inwardandtxGid=9d0afbfad00a3800114515bbe534e6cd.10

Silina, A. S., Liperovskaya, E. V., Liperovsky, V. A., and Meister, C. V. (2001). Ionospheric Phenomena before strong Earthquakes. *Nat. Hazards Earth Syst. Sci.* 1 (3), 113–118. doi:10.5194/nhess-1-113-2001

Silva, A. A., and Claro, L. H. (2005). Surface Air Radon Progeny at São José Dos Campos, Brazil. *Atmos. Environ.* 39 (26), 4619–4625. doi:10.1016/j.atmosenv.2005.04.025

Simões, F., Pfaff, R., Berthelier, J. J., and Klenzing, J. (2012). A Review of Low Frequency Electromagnetic Wave Phenomena Related to Tropospheric-Ionospheric Coupling Mechanisms. In *Space Science Reviews* (Vol. 168, Issues 1–4, pp. 551–593). Springer. doi:10.1007/s11214-011-9854-0

Singh, O. P., Chauhan, V., Singh, V., and Singh, B. (2009). Anomalous Variation in Total Electron Content (TEC) Associated with Earthquakes in India during September 2006-November 2007. *Phys. Chem. Earth* 34 (6–7), 479–484. doi:10.1016/j.pce.2008.07.012

Sornette, A., and Sornette, D. (1989). Self-organized Criticality and Earthquakes. *EPL* 9 (3), 197–202. doi:10.1209/0295-5075/9/3/002

Sornette, D., and Sammis, C. G. (1995). Complex Critical Exponents from Renormalization Group Theory of Earthquakes: Implications for Earthquake Predictions. *J. de Physique* 5 (5), 607–619. doi:10.1051/jp1:1995154

Sorokin, V., and Hayakawa, M. (2014). Plasma and Electromagnetic Effects Caused by the Seismic-Related Disturbances of Electric Current in the Global Circuit. *Mod. Appl. Sci.* 8 (4), 61–83. doi:10.5539/mas.v8n4p61

Sorokin, V. M., Chmyrev, V. M., and Hayakawa, M. (2020). A Review on Electrodynamic Influence of Atmospheric Processes to the Ionosphere. *Open J. Earthquake Res.* 09 (02), 113–141. doi:10.4236/ojer.2020.92008

Sorokin, V. M., Chmyrev, V. M., and Isaev, N. V. (1998). A Generation Model of Small-Scale Geomagnetic Field-Aligned Plasma Inhomogeneities in the Ionosphere. *J. Atmos. Solar-Terrestrial Phys.* 60 (13), 1331–1342. doi:10.1016/S1364-6826(98)00078-9

Sorokin, V. M., Isaev, N. V., Yaschenko, A. K., Chmyrev, V. M., and Hayakawa, M. (2005). Strong DC Electric Field Formation in the Low Latitude Ionosphere over Typhoons. *J. Atmos. Solar-Terrestrial Phys.* 67 (14), 1269–1279. doi:10.1016/j.jastp.2005.06.014

Sotgiu, A., De Donato, C., Fornaro, C., Tassa, S., Scannavini, M., Iannaccio, D., et al. (2021). Control and Data Acquisition Software of the High-Energy Particle Detector on Board the China Seismo-Electromagnetic Satellite Space mission. *Softw. - Pract. Experience* 51 (6), 1459–1480. doi:10.1002/spe.2947

St-Laurent, F., Derr, J. S., and Freund, F. T. (2006). Earthquake Lights and the Stress-Activation of Positive Hole Charge Carriers in Rocks. *Phys. Chem. Earth* 31 (4–9), 305–312. doi:10.1016/j.pce.2006.02.003

St-Laurent, F. (2000). The Saguenay, Québec, Earthquake Lights of November 1988-January 1989: A Comparative Study with Reference to the Geoatmospheric Lights Classification Proposed by Montandon in 1948, and a Description Put Forward by Yasui in 1968. *Seismological Research Letters*, 71 (2), 160–174. doi:10.1785/gssrl.71.2.160

Stothers, R. B. (2004). Ancient and Modern Earthquake Lights in Northwestern Turkey. *Seismological Res. Lett.* 75 (2), 199–204. doi:10.1785/gssrl.75.2.199

Strakhov, V. N., and Liperovsky, V. A. (1999). *Short-term Forecast of Catastrophic Earthquakes Using Radiophysical Ground-Based and Space Methods*. (Moscow: Inst Earth Phys).

Sugan, M., Kato, A., Miyake, H., Nakagawa, S., and Vuan, A. (2014). The Preparatory Phase of the 2009 Mw 6.3 L'Aquila Earthquake by Improving the Detection Capability of Low-Magnitude Foreshocks. *Geophys. Res. Lett.* 41 (17), 6137–6144. doi:10.1002/2014GL061199

Sugisaki, R. (1978). Changing He/Ar and N2/Ar Ratios of Fault Air May Be Earthquake Precursors. *Nature* 275 (5677), 209–211. Nature Publishing Group. doi:10.1038/275209a0

Sugisaki, R., Ito, T., Nagamine, K., and Kawabe, I. (1996). Gas Geochemical Changes at mineral Springs Associated with the 1995 Southern Hyogo Earthquake (M = 7.2), Japan. *Earth Planet. Sci. Lett.* 139 (1–2), 239–249. doi:10.1016/0012-821x(96)00007-6

Sugisaki, R., and Sugiura, T. (1986). Gas Anomalies at Three mineral Springs and a Fumarole before an Inland Earthquake, central Japan. *J. Geophys. Res. Solid Earth* 91 (B12), 12296–12304. doi:10.1029/jb091ib12p12296

Sugisaki, R., and Sugiura, T. (1985). Geochemical Indicator of Tectonic Stress Resulting in an Earthquake in central Japan, 1984. *Science* 229 (4719), 1261–1263. doi:10.1126/science.229.4719.1261

Surkov, V. V. (2015). Pre-seismic Variations of Atmospheric Radon Activity as a Possible Reason for Abnormal Atmospheric Effects. *Ann. Geophys.* 58 (5), 554. doi:10.4401/ag-6808

Svensmark, H., and Friis-Christensen, E. (1997). Variation of Cosmic ray Flux and Global Cloud Coverage - A Missing Link in Solar-Climate Relationships. *J. Atmos. Solar-Terrestrial Phys.* 59 (11), 1225–1232. doi:10.1016/S1364-6826(97)00001-1

Svensmark, H., Pedersen, J. O. P., Marsh, N. D., Enghoff, M. B., and Uggerhøj, U. I. (2007). Experimental Evidence for the Role of Ions in Particle Nucleation under Atmospheric Conditions. *Proc. R. Soc. A: Math. Phys. Eng. Sci.* 463, 385–396. doi:10.1098/rspa.2006.1773.2078

Tanaka, S., Ohtake, M., and Sato, H. (2002). Spatio-temporal Variation of the Tidal Triggering Effect on Earthquake Occurrence Associated with the 1982 South Tonga Earthquake of Mw 7.5. *Geophys. Res. Lett.* 29 (16), 3-1–3–4. doi:10.1029/2002gl015386

Tanimoto, T., Heki, K., and Artru-Lambin, J. (2015). Interaction of Solid Earth, Atmosphere, and Ionosphere. *Treatise on Geophysics* 4, 421–443. doi:10.1016/B978-0-444-53802-4.00083-X

Temmingh, H., Stein, D. J., Seedat, S., and Williams, D. R. (2011). The Prevalence and Correlates of Hallucinations in a General Population Sample: Findings from the South African Stress and Health Study. *Afr. J. Psychiatry (South Africa)* 14 (3), 211–217. doi:10.4314/ajpsy.v14i3.4

Teng, T. -l., Sun, L. -f., and McRaney, J. K. (1981). Correlation of Groundwater Radon Anomalies with Earthquakes in the Greater Palmdale Bulge Area. *Geophys. Res. Lett.* 8 (5), 441–444. doi:10.1029/GL008i005p00441

Terada, T. (1930). On Luminous Phenomena Accompanying Earthquakes. *Proc. Imperial Acad.* 6 (10), 401–404. doi:10.2183/pjab1912.6.401

Thanassoulas, C., and Tselentis, G. (1993). Periodic Variations in the Earth's Electric Field as Earthquake Precursors: Results from Recent Experiments in Greece. *Tectonophysics* 224 (1–3), 103–111. doi:10.1016/0040-1951(93)90061-N

Thériault, R., St-Laurent, F., Freund, F. T., and Derr, J. S. (2014). Prevalence of Earthquake Lights Associated with Rift Environments. *Seismological Res. Lett.* 85 (1), 159–178. doi:10.1785/0220130059

Thomas, D. (1988). Geochemical Precursors to Seismic Activity. *Pure Appl. Geophys. PAGEOPH* 126 (2–4), 241–266. doi:10.1007/BF00878998

Thomas, J. N., Huard, J., and Masci, F. (2017). A Statistical Study of Global Ionospheric Map Total Electron Content Changes Prior to Occurrences of M ≥ 6.0 Earthquakes during 2000–2014. *J. Geophys. Res. Space Phys.* 122 (2), 2151–2161. doi:10.1002/2016JA023652

Tichy, H., and Loftus, R. (1996). Hygroreceptors in Insects and a Spider: Humidity Transduction Models. *Naturwissenschaften* 83 (6), 255–263. doi:10.1007/BF01149598

Tien, A. Y. (1991). Distribution of Hallucinations in the Population. *Soc. Psychiatry Psychiatr. Epidemiol.* 26 (6), 287–292. doi:10.1007/BF00789221

Toutain, J. P., and Baubron, J. C. (1999). Gas Geochemistry and Seismotectonics: A Review. *Tectonophysics* 304 (1–2), 1–27. doi:10.1016/S0040-1951(98)00295-9

Toutain, J. P., Munoz, M., Poitrasson, F., and Lienard, A. C. (1997). Springwater Chloride Ion Anomaly Prior to a ML = 5.2 Pyrenean Earthquake. *Earth Planet. Sci. Lett.* 149 (1–4), 113–119. doi:10.1016/s0012-821x(97)00066-6

Tramutoli, V., Cuomo, V., Filizzola, C., Pergola, N., and Pietrapertosa, C. (2005). Assessing the Potential of thermal Infrared Satellite Surveys for Monitoring Seismically Active Areas: The Case of Kocaeli (İzmit) Earthquake, August 17, 1999. *Remote Sensing Environ.* 96 (3–4), 409–426. doi:10.1016/j.rse.2005.04.006

Tramutoli, V., Di Bello, G., Pergola, N., and Piscitelli, S. (2001). Robust Satellite Techniques for Remote Sensing of Seismically Active Areas. *Ann. Geophys.* 44 (2), 295–312. doi:10.4401/ag-3596

Treiber, C. D., Salzer, M., Breuss, M., Ushakova, L., Lauwers, M., Edelman, N., et al. (2013). High Resolution Anatomical Mapping Confirms the Absence of a Magnetic Sense System in the Rostral Upper Beak of Pigeons. *Communicative Integr. Biol.* 6 (4). doi:10.4161/cib.24859

Treiber, C. D., Salzer, M. C., Riegler, J., Edelman, N., Sugar, C., Breuss, M., et al. (2012). Clusters of Iron-Rich Cells in the Upper Beak of Pigeons Are Macrophages Not Magnetosensitive Neurons. *Nature* 484 (7394), 367–370. doi:10.1038/nature11046

Tributsch, H. (1982). *When the Snakes Awake*. (Cambridge, Massachusetts: The MIT Press). Available at: https://mitpress.mit.edu/books/when-snakes-awake.

Trigunait, A., Parrot, M., Pulinets, S., and Li, F. (2004). Variations of the Ionospheric Electron Density during the Bhuj Seismic Event. *Ann. Geophysicae* 22 (12), 4123–4131. doi:10.5194/angeo-22-4123-2004

Tronin, A. A. (2002a). "Atmosphere-lithosphere Coupling. Thermal Anomalies on the Earth Surface in Seismic Processes," in *Seismo Electromagnetics: Lithosphere-Atmosphere-Ionosphere Coupling*. Editors M. Hayakawa and O. A. Molchanov (Tokyo: TERRAPUB), 173–176.

Tronin, A. A., Hayakawa, M., and Molchanov, O. A. (2002b). Thermal IR Satellite Data Application for Earthquake Research in Japan and China. *J. Geodynamics* 33 (4–5), 519–534. doi:10.1016/S0264-3707(02)00013-3

Tronin, A. A. (1996). Satellite thermal Survey—A New Tool for the Study of Seismoactive Regions. *Int. J. Remote Sensing* 17 (8), 1439–1455. doi:10.1080/01431169608948716

Trugman, D. T., and Ross, Z. E. (2019). Pervasive Foreshock Activity across Southern California. *Geophys. Res. Lett.* 46 (15), 8772–8781. doi:10.1029/2019GL083725

Tsai, Y. Ben., Liu, J. Y., Ma, K. F., Yen, H. Y., Chen, K. S., Chen, Y. I., et al. (2006). Precursory Phenomena Associated with the 1999 Chi-Chi Earthquake in Taiwan as Identified under the iSTEP Program. *Phys. Chem. Earth* 31 (4–9), 365–377. doi:10.1016/j.pce.2006.02.035

Tse, S. T., and Rice, J. R. (1986). Crustal Earthquake Instability in Relation to the Depth Variation of Frictional Slip Properties. *J. Geophys. Res.* 91 (B9), 9452. doi:10.1029/jb091ib09p09452

Tsukuda, T. (1997). Sizes and Some Features of Luminous Sources Associated with the 1995 Hyogo-Ken Nanbu Earthquake. *J. Phy. Earth* 45 (2), 73–82. doi:10.4294/jpe1952.45.73

Tsunogai, U., and Wakita, H. (1995). Precursory Chemical Changes in Ground Water: Kobe Earthquake, Japan. *Science* 269 (5220), 61–63. doi:10.1126/science.269.5220.61

Turcotte, D. L. (1991). Earthquake Prediction. *Annu. Rev. Earth Planet. Sci.* 19 (1), 263–281. doi:10.1146/annurev.ea.19.050191.001403

Tzanis, A., and Vallianatos, F. (2002). "A Physical Model of Electrical Earthquake Precursors Due to Crack Propagation and the Motion of Charged Edge Dislocations," in *Seismo Electromagnetics: Lithosphere-Atmosphere-Ionosphere Coupling*. Editors M. Hayakawa and O. A. Molchanov (Tokyo: TERRAPUB), 117–130.

Uyeda, S., Kamogawa, M., and Tanaka, H. (2009a). Analysis of Electrical Activity and Seismicity in the Natural Time Domain for the Volcanic-Seismic Swarm Activity in 2000 in the Izu Island Region, Japan. *J. Geophys. Res. Solid Earth* 114 (2). doi:10.1029/2007JB005332

Uyeda, S., Nagao, T., and Kamogawa, M. (2009b). Short-term Earthquake Prediction: Current Status of Seismo-Electromagnetics. *Tectonophysics* 470 (3–4), 205–213. doi:10.1016/j.tecto.2008.07.019

Vallianatos, F., Triantis, D., Tzanis, A., Anastasiadis, C., and Stavrakas, I. (2004). Electric Earthquake Precursors: From Laboratory Results to Field Observations. *Phys. Chem. Earth* 29 (4–9), 339–351. doi:10.1016/j.pce.2003.12.003

Vallianatos, F., and Tzanis, A. (1999). On Possible Scaling Laws between Electric Earthquake Precursors (EEP) and Earthquake Magnitude. *Geophys. Res. Lett.* 26 (13), 2013–2016. doi:10.1029/1999GL900406

van den Ende, M. P. A., and Ampuero, J. P. (2020). On the Statistical Significance of Foreshock Sequences in Southern California. *Geophys. Res. Lett.* 47 (3), e2019GL086224. doi:10.1029/2019GL086224

Varotsos, P. A., Sarlis, N. V., and Skordas, E. S. (2003b). Electric fields that "Arrive" before the Time Derivative of the Magnetic Field Prior to Major Earthquakes. *Phys. Rev. Lett.* 91 (14), 148501. doi:10.1103/PhysRevLett.91.148501

Varotsos, P. A., Sarlis, N. V., Skordas, E. S., and Lazaridou, M. S. (2008). Fluctuations, under Time Reversal, of the Natural Time and the Entropy Distinguish Similar Looking Electric Signals of Different Dynamics. *J. Appl. Phys.* 103 (1), 014906. doi:10.1063/1.2827363

Varotsos, P. A., Sarlis, N. V., and Skordas, E. S. (2002). Long-range Correlations in the Electric Signals that Precede Rupture. *Phys. Rev. E - Stat. Phys. Plasmas Fluids Relat. Interdiscip. Top.* 66 (1), 011902. doi:10.1103/PhysRevE.66.011902

Varotsos, P. A., Sarlis, N. V., and Skordas, E. S. (2003a). Long-range Correlations in the Electric Signals that Precede Rupture: Further Investigations. *Phys. Rev. E - Stat. Phys. Plasmas Fluids Relat. Interdiscip. Top.* 67 (2), 13. doi:10.1103/PhysRevE.67.021109

Varotsos, P. A., Sarlis, N. V., and Skordas, E. S. (2019). Phenomena Preceding Major Earthquakes Interconnected through a Physical Model. *Ann. Geophysicae* 37 (3), 315–324. doi:10.5194/angeo-37-315-2019

Varotsos, P. (1981). Seismic Electric Currents. *Prakt. Akad. Athenon* 56, 277–286.

Varshal, G. M., Sobolev, G. A., Barsukov, V. L., Koltsov, A. V., Kostin, B. I., Kudinova, T. F., et al. (1984). Separation of Volatile Components from Rocks under Mechanical Loading as the Source of Hydrogeochemical Anomalies Preceding Earthquakes - Results of a Large-Scale Model experiment. *Pure Appl. Geophys. PAGEOPH* 122 (2–4), 463–477. doi:10.1007/BF00874612

Vershinin, E. F., Buzevich, A. V., Yumoto, K., Saita, K., and Tanaka, Y. (1999). "Correlations of Seismic Activity with Electromagnetic Emissions and Variations in Kamchatka Region," in *Atmospheric and Ionospheric Electromagnetic Phenomena Associated with Earthquakes*. Editor M. Hayakawa (Terra Scientific Publishing Company), 513–517.

Virk, H. S., Walia, V., and Kumar, N. (2001). Helium/radon Precursory Anomalies of Chamoli Earthquake, Garhwal Himalaya, India. *J. Geodynamics* 31 (2), 201–210. doi:10.1016/S0264-3707(00)00022-3

Wakita, H., Nakamura, Y., Notsu, K., Noguchi, M., and Asada, T. (1980). Radon Anomaly: A Possible Precursor of the 1978 Izu-Oshima-Kinkai Earthquake. *Science* 207 (4433), 882–883. doi:10.1126/science.207.4433.882

Wakita, H., Nakamura, Y., and Sano, Y. (1985). Groundwater Radon Variations Reflecting Changes in Regional Stress Fields. *Practical Approaches to Earthquake Prediction and Warning*. (Netherlands: Springer), 545–557. doi:10.1007/978-94-017-2738-9_19

Warwick, J. W., Stoker, C., and Meyer, T. R. (1982). Radio Emission Associated with Rock Fracture: Possible Application to the Great Chilean Earthquake of May 22, 1960. *J. Geophys. Res.* 87 (B4), 2851–2859. doi:10.1029/JB087iB04p02851

Weiyu, M., Xuedong, Z., Liu, J., Yao, Q., Zhou, B., Yue, C., et al. (2018). Influences of Multiple Layers of Air Temperature Differences on Tidal Forces and Tectonic Stress before, during and after the Jiujiang Earthquake. *Remote Sensing Environ.* 210, 159–165. doi:10.1016/j.rse.2018.03.003

West, D. J. (1948). A Mass Observation Questionnaire on Hallucinations. *J. Soc. Psychical Res.* 34 (644–645), 187–195.

Whitehead, N. E., and Ulusoy, Ü. (2015). Origin of Earthquake Light Associated with Earthquakes in Christchurch, New Zealand, 2010-2011. *Earth Sci. Res. J.* 19 (2), 113–120. doi:10.15446/esrj.v19n2.47000

Wikelski, M., Mueller, U., Scocco, P., Catorci, A., Desinov, L. V., Belyaev, M. Y., et al. (2020). Potential Short-Term Earthquake Forecasting by Farm Animal Monitoring. *Ethology* 126 (9), 931–941. doi:10.1111/eth.13078

Woith, H., Petersen, G. M., Hainzl, S., and Dahm, T. (2018). Review: Can Animals Predict Earthquakes? *Bull. Seismological Soc. America* 108 (3A), 1031–1045. doi:10.1785/0120170313

Wright, T. J. (2016). The Earthquake Deformation Cycle. *Astron. Geophys.* 57 (4), 4.20–4.26. doi:10.1093/astrogeo/atw148

Wu, H. (2007). AGU Fall Meeting Abstracts, S13B–S1302.Jet Stream Converges Prior to 6.8 M Niigata Chuetsu-Oki Earthquake of Japan on 2007/07/16*2007*

Wu, L. Q., and Dickman, J. D. (2012). Neural Correlates of a Magnetic Sense. *Science* 336 (6084), 1054–1057. doi:10.1126/science.1216567

Wu, L., Zheng, S., De Santis, A., Qin, K., Di Mauro, R., Liu, S., et al. (2016). Geosphere Coupling and Hydrothermal Anomalies before the 2009 Mw 6.3 L'Aquila Earthquake in Italy. *Nat. Hazards Earth Syst. Sci.* 16 (8), 1859–1880. doi:10.5194/nhess-16-1859-2016

Wyss, M. (1997). Cannot Earthquakes Be Predicted? *Science* 278 (5337), 487–490. doi:10.1126/science.278.5337.487

Wyss, M., and Dmowska, R. (1997). Earthquake Prediction - State of the Art. *Pure and Applied Geophysics*, Vol. 149 Issue 1. (Pure and Applied Geophysics (PAGEOPH)).

Xiong, P., Long, C., Zhou, H., Battiston, R., Zhang, X., and Shen, X. (2020). Identification of Electromagnetic Pre-earthquake Perturbations from the Demeter Data by Machine Learning. *Remote Sensing* 12 (21), 1–27. doi:10.3390/rs12213643

Xiong, P., Tong, L., Zhang, K., Shen, X., Battiston, R., Ouzounov, D., et al. (2021). Towards Advancing the Earthquake Forecasting by Machine Learning of Satellite Data. *Sci. Total Environ.* 771, 145256. doi:10.1016/j.scitotenv.2021.145256

Xu, G., Han, P., Huang, Q., Hattori, K., Febriani, F., and Yamaguchi, H. (2013). Anomalous Behaviors of Geomagnetic Diurnal Variations Prior to the 2011 off the Pacific Coast of Tohoku Earthquake (Mw9.0). *J. Asian Earth Sci.* 77, 59–65. doi:10.1016/j.jseaes.2013.08.011

Yamauchi, H., Hayakawa, M., Asano, T., Ohtani, N., and Ohta, M. (2017). Statistical Evaluations of Variations in Dairy Cows' Milk Yields as a Precursor of Earthquakes. *Animals* 7 (3), 19. doi:10.3390/ani7030019

Yamauchi, H., Uchiyama, H., Ohtani, N., and Ohta, M. (2014). Unusual Animal Behavior Preceding the 2011 Earthquake off the pacific Coast of Tohoku, Japan: A Way to Predict the Approach of Large Earthquakes. *Animals* 4 (2), 131–145. doi:10.3390/ani4020131

Yan, R., Guan, Y., Shen, X., Huang, J., Zhang, X., Liu, C., et al. (2018). The Langmuir Probe Onboard CSES: Data Inversion Analysis Method and First Results. *Earth Planet. Phys.* 2 (6), 1–10. doi:10.26464/epp2018046

Yan, R., Parrot, M., and Pinçon, J. L. (2017). Statistical Study on Variations of the Ionospheric Ion Density Observed by DEMETER and Related to Seismic Activities. *J. Geophys. Res. Space Phys.* 122 (12), 12421–12429. doi:10.1002/2017JA024623

Yan, Z., Chunli, K., Weiyu, M., and Qi, Y. (2017). The Change in Outgoing Longwave Radiation before the Ludian Ms6. 5 Earthquake Based on Tidal Force Niche Cycles. *Earthquake Res. China* 3, 422–430.

Yang, S. S., Asano, T., and Hayakawa, M. (2019). Abnormal Gravity Wave Activity in the Stratosphere Prior to the 2016 Kumamoto Earthquakes. *J. Geophys. Res. Space Phys.* 124 (2), 1410–1425. doi:10.1029/2018JA026002

Yasui, Y. (1968). A Study on the Luminous Phenomena Accompanied with Earthquake (Part I). *Mem. Kakioka Magnet. Observ.* 13, 25–61.

Yasuoka, Y., Igarashi, G., Ishikawa, T., Tokonami, S., and Shinogi, M. (2006). Evidence of Precursor Phenomena in the Kobe Earthquake Obtained from Atmospheric Radon Concentration. *Appl. Geochem.* 21 (6), 1064–1072. doi:10.1016/j.apgeochem.2006.02.019

Yokoi, S., Ikeya, M., Yagi, T., and Nagai, K. (2003). Mouse Circadian Rhythm before the Kobe Earthquake in 1995. *Bioelectromagnetics* 24 (4), 289–291. doi:10.1002/bem.10108

Yosef, R. (1997). Reactions of Birds to an Earthquake. *Bird Study* 44 (1), 123–124. doi:10.1080/00063659709461047

Zafrir, H., Ginzburg, B., Hrvoic, I., Shirman, B., Gazit-Yaari, N., Steinitz, G., and Wilson, M. (2003). "Ultra Sensitive Monitoring of the Geomagnetic Field Combined with Radon Emanation as a Tool for Studying Earthquake Related Phenomena," in AGU Fall Meeting Abstracts, San Francisco, T51E–T0206.

Zakharenkova, I. E., Shagimuratov, I. I., Tepenitzina, N. Y., and Krankowski, A. (2008). Anomalous Modification of the Ionospheric Total Electron Content Prior to the 26 September 2005 Peru Earthquake. *J. Atmos. Solar-Terrestrial Phys.* 70 (15), 1919–1928. doi:10.1016/j.jastp.2008.06.003

Zavarsky, A., Booge, D., Fiehn, A., Krüger, K., Atlas, E., and Marandino, C. (2018). The Influence of Air-Sea Fluxes on Atmospheric Aerosols during the Summer Monsoon over the Tropical Indian Ocean. *Geophys. Res. Lett.* 45 (1), 418–426. doi:10.1002/2017GL076410

Zhang, X., Kang, C., Ma, W., Ren, J., and Wang, Y. (2018). Study on thermal Anomalies of Earthquake Process by Using Tidal-Force and Outgoing-Longwave-Radiation. *Therm. Sci.* 22 (2), 767–776. doi:10.2298/TSCI161229153Z

Zhang, X., Shen, X., Zhao, S., Yao, L., Ouyang, X., and Qian, J. (2014). The Characteristics of Quasistatic Electric Field Perturbations Observed by DEMETER Satellite before Large Earthquakes. *J. Asian Earth Sci.* 79 (PA), 42–52. doi:10.1016/j.jseaes.2013.08.026

\Zhang, X., Zeren, Z., Parrot, M., Battiston, R., Qian, J., and Shen, X. (2011). ULF/ELF Ionospheric Electric Field and Plasma Perturbations Related to Chile Earthquakes. *Adv. Space Res.* 47 (6), 991–1000. doi:10.1016/j.asr.2010.11.001

Zhang, X., Zhao, S., Song, R., and Zhai, D. (2019). The Propagation Features of LF Radio Waves at Topside Ionosphere and Their Variations Possibly Related to Wenchuan Earthquake in 2008. *Adv. Space Res.* 63 (11), 3536–3544. doi:10.1016/j.asr.2019.02.008

Zhang, Y., Feng, W. P., Xu, L. S., Zhou, C. H., and Chen, Y. T. (2009). Spatio-temporal Rupture Process of the 2008 Great Wenchuan Earthquake. *Sci. China, Ser. D: Earth Sci.* 52 (2), 145–154. doi:10.1007/s11430-008-0148-7

Zhang, Y., and Meng, Q. (2019). A Statistical Analysis of TIR Anomalies Extracted by RSTs in Relation to an Earthquake in the Sichuan Area Using MODIS LST Data. *Nat. Hazards Earth Syst. Sci.* 19 (3), 535–549. doi:10.5194/nhess-19-535-2019

Zhang, Y., Meng, Q., Ouillon, G., Zhang, L., Hu, D., Ma, W., et al. (2021). Long-term Statistical Evidence Proving the Correspondence between Tir Anomalies and Earthquakes Is Still Absent. *Eur. Phys. J. Spec. Top.* 230 (1), 133–150. doi:10.1140/epjst/e2020-000248-4

Zhang, Y. S., Guo, X., Zhong, M. J., Shen, W. R., Li, W., and He, B. (2010). Wenchuan Earthquake: Brightness Temperature Changes from Satellite Infrared Information. *Chin. Sci. Bull.* 55 (18), 1917–1924. doi:10.1007/s11434-010-3016-8

Zhao, B., Wang, M., Yu, T., Wan, W., Lei, J., Liu, L., et al. (2008). Is an Unusual Large Enhancement of Ionospheric Electron Density Linked with the 2008 Great Wenchuan Earthquake? *J. Geophys. Res. Space Phys.* 113 (11), 11304. doi:10.1029/2008JA013613

Zheng, S., Qin, K., Wu, L., An, Y., Yin, Q., and Lai, C. (2020). Hydrothermal Anomalies of the Earth's Surface and Crustal Seismicity Related to Ms8.0 Wenchuan EQ. *Nat. Hazards* 104 (3), 2097–2114. doi:10.1007/s11069-020-04263-7

Zhu, K., Li, K., Fan, M., Chi, C., and Yu, Z. (2019). Precursor Analysis Associated with the Ecuador Earthquake Using Swarm A and C Satellite Magnetic Data Based on PCA. *IEEE Access* 7, 93927–93936. doi:10.1109/ACCESS.2019.2928015

Zlotnicki, J., and Cornet, F. H. (1986). A Numerical Model of Earthquake-Induced Piezomagnetic Anomalies. *J. Geophys. Res.* 91 (B1), 709–718. doi:10.1029/JB091iB01p00709

Conflict of Interest: The authors declare that the research was conducted in the absence of any commercial or financial relationships that could be construed as a potential conflict of interest.

frontiers in Earth Science

REVIEW
published: 14 July 2021
doi: 10.3389/feart.2021.676775

Looking for Earthquake Precursors From Space: A Critical Review

Piergiorgio Picozza[1,2,3]*, *Livio Conti*[2,3] *and Alessandro Sotgiu*[1,2]

[1]University of Rome Tor Vergata, Rome, Italy, [2]INFN - Sezione Roma Tor Vergata, Rome, Italy, [3]Uninettuno University, Rome, Italy

Starting from late seventies, many observations have been reported about observations in space of signals reconciled with earthquakes and claimed as possible preseismic measurements. The detected parameters range from electromagnetic field components (in a large band of frequencies) to plasmas parameters; from particles detection to thermal anomalies; etc. Up to the DEMETER mission, the analyses have been carried out on datasets gathered by not devoted satellites. Even beyond the results obtained, the DEMETER mission has constituted a milestone for space-based investigations of seismo-associated phenomena drawing a baseline for next missions with respect instruments, observational strategy and measurements uncertainty. Nowadays, the CSES-01 satellite – developed within a sino-italian collaboration with the participation also of Austrian Institutes – represents the most advanced mission for investigating near-Earth electromagnetic environment aimed at extending the observation of earthquake precursors to a long time series. The benefit of the mission is even higher by considering that CSES-01 is the first of a program of several LEO small satellites, the second of which will be launched on 2023 with the same instruments and orbit of CSES-01, but with a shift of half of an orbit in order to monitor each trace twice per orbit. The article gives a short survey of space-based observations of preseismic phenomena from the early studies up to the more recent ones, critically reviewing results, hypotheses and trends in this research field. The supposed physical processes proposed to explain the observations are still unable to explain the large variety of the phenomenology, the statistical significance of the results are highly debated, and more in general a common consensus is still missing. Anyway, the investigation of the seismo-associated phenomena from space is a challenge for near future Earth observation.

Keywords: earthquake precursors, trapped particles, space weather, DEMETER, CSES, acoustic gravity waves, HEPD

Edited by:
Dimitar Ouzounov,
Chapman University, United States

Reviewed by:
Angelo De Santis,
University of Studies G. d'Annunzio Chieti and Pescara, Italy
Michel Parrot,
UMR7328 Laboratoire de physique et chimie de l'environnement et de l'Espace, France

***Correspondence:**
Piergiorgio Picozza
Piergiorgio.Picozza@roma2.infn.it

Specialty section:
This article was submitted to Geohazards and Georisks, a section of the journal Frontiers in Earth Science

Received: *08 March 2021*
Accepted: *28 June 2021*
Published: *14 July 2021*

Citation:
Picozza P, Conti L and Sotgiu A (2021) Looking for Earthquake Precursors From Space: A Critical Review. Front. Earth Sci. 9:676775. doi: 10.3389/feart.2021.676775

INTRODUCTION

The key ingredient for studying the earthquake preparation process - and ideally for forecasting its occurrence - is to point out the existence of possible earthquake precursors (on long, middle, or short temporal scale) as well as their detection as a function of the distance (from the focal area of the impinging event). An extended review can be found for example in Tronin (2006), Hayakawa (2015), Pulinets and Ouzounov (2018), Parrot (2018), Ouzounov et al. (2018), Pulinets and Ouzounov (2018). Beyond the classification as a function of the time delay with respect the seismic event, precursors can be further distinguished on the spatial scale as a function of the detection distance and their localization or diffusion. In fact, some processes, candidate to be considered such as precursors, can be detected around the seismic focal area (local precursors) even though eventually at significant distance. Due to the topology of the geomagnetic field, other possible precursors can be detected not only over the epicentre, but also near to its magnetically conjugated region or along the field line with footprint on the epicentre (diffused precursors). Finally, a further class of precursors could be constituted by fluctuations detectable not only along a geomagnetic flux tube associated to the epicentre, but spread in suitable iono-magnetospheric "shell" (distributed precursors). Nowadays, earthquake forecasting is far from being reached and the debated about earthquake precursors is still open. Nevertheless, even though not conclusive results have been obtained, a large amount of measurements have been gathered worldwide with a large variety of methodology and the investigations of many different physical quantities and parameters, both on ground and in space. Unexpectedly, there is a problem of repeatability and confirmation of claimed results by different authors using the same methodology and/or analyzing the same parameters. Whereas the co-seismic effects in the atmosphere are well-established (Tanimoto et al., 2015), the possible pre-earthquake phenomena on the surface as well as the coupling between lithosphere, atmosphere and ionosphere (called LAIC for short, hereafter) are still disputed (e.g., Geller, 1997, Geller et al., 1997; Hough, 2020 and references therein). As it is very difficult to detail a debate (in which facts and views are sometimes mixed), we summarize only some of the main recent "trends" of discussion. A general skepticism about ground and space precursors (including thermal anomalies due to their "natural variability" and more in general for the "a posteriori" findings of the anomalies) is advocated by Jordan et al. (2011), Nakatani (2020) and - especially for seismic precursors - by Scholz (2019), although more recent results (e.g., Gulia and Wiemer, 2019) might change the perspective. Wang and Burgmann (2019) have questioned the reliability of precursory gravity changes; Helman (2020) has written in favor of the pre-seismic character of electrical signals, while Warden et al. (2020) support a critical view on ULF anomalies. Woith (2015) reviewed the "complexity" of investigating radon anomalies both as precursors to earthquakes and beyond this specific interpretation. In the debate on preseismic ionospheric anomalies, negative positions have been expressed by Dautermann et al. (2007), Thomas et al. (2012), Kamogawa and Kakinami (2013), Masci et al. (2015), Masci et al. (2017) and an analysis of the statistical reliability of some TEC anomalies can be found in Ikuta et al. (2020) and Tozzi et al. (2020). However, in a larger and reliable perspective, Kato and Ben-Zion (2021) and Pritchard et al. (2020) have highlighted the potential of precursors. Uchida and Bürgmann (2021) have discussed the importance of short-term earthquake anomalies for more accurately establishing the seismic hazard of giant impending earthquake (although the same authors do not believe that such an event can be predicted with high confidence level). In this framework, this article presents a review of the main observations, hypotheses and models about the phenomenology of earthquake precursors observed in space, which, in our opinion, are valuable insights - that deserve to be investigated with the utmost precision and highest statistical accuracy - of the coupling mechanism existing between the lithosphere and the near-Earth environment (De Santis et al., 2015). For a review about the main earthquake precursors observed on ground (and further references about ground-space multi-parametric analyses) the interested reader is addressed to the twin article of Conti et al. (2021) in this same issue. The layout of the article is as follow. We will adopt a quasi-chronological approach discussing observations carried out in space before (section *Seismo-Electromagnetic Perturbations Detected in Space by Non-Dedicated Missions*) and after (section *DEMETER Satellite Observations*) the DEMETER mission that has been the first satellite devoted to investigate precursors from space. Then we will present the first results from the CSES satellite (section *First Analyses From the CSES Satellite Mission*) that is the first mission of a program including several satellites devoted to investigate seismo-induced phenomena in the near-Earth electromagnetic environment. Finally, in section *Connecting Perturbations on Ground and in Space* we will summarize some ideas about the physical mechanism for coupling lithosphere with lower and upper layers of the atmosphere up to the ionosphere.

SEISMO-ELECTROMAGNETIC PERTURBATIONS DETECTED IN SPACE BY NON-DEDICATED MISSIONS

Seismic events are the last stage of a long preparation process generated by a continuous and variable tectonic stress (Scholz, 2002; Olaiz et al., 2009). Many attempts have been done in order to monitor on ground the earthquake preparation phase and the underlying physical processes on specific fault systems (Kanamori, 2003), but the involved processes are deep, slow and complex. Since some tens of years, the possibility to remote sensing earthquakes though their effects in the near-Earth space has been explored. In order to explain the effects of the LAIC, Pulinets and Ouzounov (2011) proposed a model - based on rising of gas and fluid toward the surface in the seismic preparation phase - that could take into account the last stages of the long-term seismic phase. Other hypotheses have been suggested by Sorokin et al. (2001), Hayakawa and Molchanov (2002), Liperovsky et al. (2008a), De Santis et al. (2017), De Santis et al. (2019a); etc. Freund (2011) proposed a mechanism, successfully tested in laboratory (Freund et al., 2007), based on the theory of positive holes that could locally ionize the lower atmosphere and create instability in the ionosphere. Finally Kuo et al. (2011), Kuo et al. (2014) proposed a coupling mechanism that, through the effect of the geomagnetic field of the Earth, would induce perturbation in the ionosphere.

Early Observations of Electromagnetic Perturbations

Several authors have reported measurements of seismo-electromagnetic precursors detected on ground or on board of satellite missions. After the early publications - mainly focused on analyzing electric and magnetic field variations - other studies have also discussed fluctuations of plasma parameters, precipitation of high-energy charged particles from the inner Van Allen belt, etc.

On 1982 were published the first observations of seismo-electromagnetic disturbances from space. Although some analyses of ionospheric disturbances that might occur before an earthquake - based on ground-based ionosonde data - were reported in the early 1970s [see e.g., Antselevich (1966); Datchenko et al. (1972)], the first results on satellite surveys of low-frequency electromagnetic emissions before earthquakes were obtained on data from the Intercosmos 19 satellite (Migulin et al., 1982; Gokhberg et al., 1983; Larkina et al., 1983); Aureol 3 mission (Larkina et al., 1984); while, the detection of VLF noise in the region magnetically conjugate to the earthquake zone was reported by Gokhberg et al. (1983) and Parrot et al. (1985) using observations from the geostationary satellites GEOS 1 and 2. Larkina et al. (1989) authored an analysis of Intercosmos 19 satellite data, detected at 800 and 4,650 Hz, from about 8 h before up about 3 h after some earthquakes, within 2 degrees of latitude and 60 degrees of longitude around the epicentres. Chmyrev et al. (1989) reported an anomalous variation of 3–7 mV/m in the quasi DC component of the vertical electric field measured by the Intercosmos-Bulgaria 1300 satellite at the altitudes of about 800 km over the magnetically conjugate zone of the epicentre, about 15 min before an event of magnitude 4.8 in the Pacific Ocean.

Few years later, COSMOS-1809 detected anomalous electromagnetic emissions at frequencies below 450 Hz, up to few hours before the seismic event, in more than 92% of the satellite traces, within 6 degree of longitude from the epicentre and about 4–10° of latitude to the South of the Armenia earthquake of 1988 (Serebryakova et al., 1992). AUREOL-3 satellite data confirmed the observations, on the same region and events. By studying the seismic sequence of the Armenia earthquake of 1988, Kopytenko et al. (1993) and Serebryakova et al. (1992) reported some anomalous fluctuation of ULF magnetic and electric field measurements recorded on ground about 200 km far from the epicentre and some hours before the main event and some aftershocks.

Two years of AUREOL-3 satellite data, gathered in the ELF/VLF frequency range, have been analyzed also by Parrot (1994) in the first statistical study published on space based observations of earthquake precursors. Through the superposed epoch and space method, applied to more than 300 seismic events of magnitude higher than 5, the analysis has pointing out a significant fluctuation of the electromagnetic field intensity within 10 degrees of longitude from the epicentres (of all latitudes), but without discriminating the temporal series of observations as pre-, co- and post-seismic detections.

More recently, by re-analyzing data from Intercosmos-Bulgaria 1300 for hundreds earthquakes (Gousheva et al., 2008; Gousheva et al., 2009), estimated that the amplitude of preseismic quasi DC electric field disturbances in space was of the order of 10 mV/m over seismic events both in land and in sea.

From Ground to Space: can be Radon the Root of the Coupling Mechanism?

From space, several seismo-associated parameters can be measured such as lithospheric deformation, temperature fluctuation, gas and aerosol exhalation and electromagnetic field. While the co-seismic (horizontal and vertical) deformations can be significant (tens centimeters and meters) and can be monitored with InSAR with high precision and reliability (Moro et al., 2017; Zhao et al., 2018; Xu et al., 2020), the preseismic deformations are lower and more complex to be investigated from space (Tronin, 2006; Cenni et al., 2015; Moro et al., 2017; Nardò et al., 2020). Only in few cases, deformations have been detected both before and after seismic events (Massonnet et al., 1993; Kuzuoka and Mizuno, 2004; Tronin, 2006). Remote sensing observations allow also to measure concentrations of gases and aerosol in the atmosphere potentially involved in preseismic phenomena. Dey and Singh (2003) reported increase of surface latent heat flux before the Gujarat earthquake and some other coastal earthquakes. After the observations on ground of nighttime ionospheric fluorescence emissions by (Fishkova et al., 1985), that were correlated with physics of the E layer (85–110 km), Morozova (1996) reported an increase of the intensity of oxygen lines 5577 and 6300 A a few hours before seismic events.

One of the most debated issue in the physics of earthquake precursors includes the role of the seismo-induced radon exhalation in the generation of electromagnetic disturbances (Wakita et al., 1980; Teng et al., 1981; Cicerone et al., 2009). It has been proposed that the enhancement of total rock surface due to failure would increase the emissions of radon and other gases from grains and migration (Conti et al., 2021). This would be in agreement with: 1) the enhancement of radon concentration observed in aftershocks and 2) some laboratory experiments (Koike et al., 2015) aimed at verifying the growth of radon emissions of granites under compressional stress. Also in extensional tectonic regime, rock deformation can create cracks facilitating the radon and other gases exhalation (Reddy and Nagabhushanam, 2011) as demonstrated by Fu et al. (2017) by studying the variation of soil Rn concentration in shallow earthquakes (<15 km) in the extensional regime. Moreover, several authors have reported a temporal correlation between local variation of stress/strain and anomalous fluctuation of radon concentration in groundwater (Biagi et al., 2001; Ingebritsen and Manga 2014). It has been claimed that, due to radon exhalation from the soil, local fair-weather conductivity could increase up to 50%, whereas the electric field could decrease of 30% (Pierce, 1976). In this framework, Pulinets and Ouzounov (2011) and Pulinets et al. (2018) proposed a LAIC model that explains the synergy between earthquake activity and its precursors. According to this LAIC model, the relative movement of tectonic blocks leads to the generation of tectonic stresses with the release of gases (including radon) along seismically active faults. Radon can generate local ionization in the lower layers of the atmosphere that can facilitate water vapor condensation with: 1) release of latent heat exhalation (that could explain thermal fluctuations) and

2) local variation of the conductivity that would impact on the global electric circuit over the earthquake preparation zone generating the observed seismo-associated ionospheric anomalies. Anyway, the radon exhalation seems cannot explain a direct generation of electromagnetic anomalies at higher frequency. We address the interested reader to the paper (Conti et al., 2021) published in this same issue, that provides a short review of models and ground based observations. In this framework, candidate precursor analyses have been performed on data from dedicated missions (DEMETER, CSES), multi-payload spacecraft (such as NOAA 14,15,16,17, other Sun-synchronous LEO missions, weather and Earth observation satellites), Swarm satellites and for ionospheric sounding (as those of the FORMOSAT series). A summary of the main results will be given in the following sections.

Ionospheric Disturbances

The large variety of atmospheric, ionospheric, and magnetospheric anomalies claimed as possibly being related to earthquakes shows the importance of both ground-based measurements of ionospheric parameters and satellite-based Earth remote sensing for investigating earthquake precursors (see Ondoh (2003); Ouzounov and Freund (2004); Pulinets and Boyarchuk (2005); Ondoh and Hayakawa (2006); Liu et al. (2006); Zhao et al. (2008); Ondoh, (2009); Kakinami et al. (2010); Perrone et al. (2010); Kandalyan and AlQuran (2010); Liou et al. (2010) and references therein). Anyway, it must be highlighted that many studies of seismo-ionospheric precursors are cases studies (seldom reproduces in further investigations carried out in "similar" conditions) and that many times the statistical significance is low. In general, the level of reliability changes significantly between the analyses and even in the scientific community involved in studying earthquake precursors the consensus is highly debated.

For the observations from ground of ionospheric preseismic phenomena, see Conti et al., 2021. For observations from space, in this section we just cite some of the earliest studies of plasma disturbances and observations from experiments different from DEMETER and CSES. Results from these latter missions will be discussed in the devoted *DEMETER Satellite Observations* and *First Analyses From the CSES Satellite Mission*.

Only few are the studies of plasma parameters detected by satellite in the early investigations of precursors. By analyzing data of IC-B 1300 satellite the authors of (Sorokin and Chmyrev, 1999) reported a dissipative instability of acoustic-gravity waves 15 min before an earthquake with M = 4.8 and suggested that it would be due to an increased injection into the atmosphere of radioactive gas such as radon. Galperin et al. (1992) reported perturbations in electron profile and ion composition of the plasma, together with VLF anomalies, in a large extension of some degrees of longitude around the epicentral zone. Sharma et al. (2021) have analyzed 160 earthquakes in North East Indian region by studying GPS/TEC measurements, reporting TEC precursors in 46.5% of the Mw <5 earthquakes, in more than 81.5% of Mw = 5–6 events and all the Mw >6 earthquakes.

When several variables must be studied in order identify the "prevailing" ones and possible correlations, the principal component analysis (PCA) could be adopted for analyzing time series of observations and to reject background noise. After Hattori et al. (2004), that applied PCA to ground based observation of magnetic data, more recently, Zhu et al. (2019) applied PCA to Swarm satellite (Friis-Christensen et al., 2008) magnetic field data successfully finding seismo-related anomalies. Another recent examples of possible ionospheric electron density enhancement detected before large earthquakes (M = 7.0–8.0) have been reported by (He and Heki, 2017) by analyzing vertical total electron contents (VTEC) data observed by GNSS stations near the epicentres. In eight of the 32 earthquakes studied, possible preseismic anomalies were observed starting 10–20 min before the event. De Santis et al. (2019a) have analyzed 4.7 years of electron density (Ne sampled at 2 Hz) and magnetic field (mainly Y component at low frequency) data measured by Swarm three-satellite constellation (Friis-Christensen et al., 2008). By using a worldwide statistical correlation analysis, through a superposed epoch approach, they have statistically studied the possible spatial and temporal correlation between the earthquakes and ionospheric disturbances. The authors reported a concentration of electron density and magnetic anomalies from more than two months up to some days before the seismic events with magnitude greater equal 5.5 and hypocentral depth up to 50 km, studied in a time window from 90 days before up to 30 days after each event. A further interesting aspect of the performed analysis is that it would provide a confirmation based on space based measurements - from Swarm data, investigated in a time interval of 500 days before the seismic event - of the Rikitake empirical law for earthquake precursors (Rikitake, 1987), proposed in the earliest' 80s for precursors on ground. The law, summarized by the formulas $\mathrm{Log}_{10}\,(\Delta T) = a + b\,M$ (where ΔT is the precursor time, M is the earthquake magnitude and a and b are fit parameters) claims that the precursor time is a function of the earthquake magnitude: the larger the magnitude, the longer the precursor time. Interestingly, by analyzing ionospheric data (Ne and Y magnetic component), the authors of (De Santis et al., 2019a) estimated values of the a and b parameters compatible with those proposed for ground magnetic observations by (Rikitake, 1987). The authors argue that the Rikitake law could take into account the LAIC. By assuming a lithospheric process of stress diffusion (Shapiro et al., 1997) across the Dobrovolsky strain radius (Dobrovolsky et al., 1979), the authors also obtained an estimation of the coefficient of diffusion too much higher than a reasonable value for the crust, but anyway of the same order of magnitude of the diffusivity found for slow earthquakes when a diffusion model is considered (Ide et al., 2007). Between the more recent analyses of ionospheric anomalies before strong earthquakes based on satellites observations we can cite also as significant examples Natarajan and Philipoff (2018), Zhang X. et al. (2019b), De Santis et al. (2020).

Thermal Anomalies

Several authors [see Tronin (2006), Conti et al. (2021) and references therein] have suggested that the earthquake preparation process can generate variation of temperature (induced by flow/exhalation of geochemical fluids in the deep lithosphere and/or by secondary effects of the friction and displacement along the seismic faults) that can affect the energy budget in the LAIC in seismic sequences (Qin et al., 2021). Only relatively few test campaigns have been carried out on ground and articles published about measurements of temperature variations before earthquakes that explains the small amount of this type of data and the large uncertainty on the subject (Cicerone et al., 2009). From one side, in volcanic areas, where also large earthquakes can take place, the temperature variations sometime observed before seismic events have been associated to groundwater level variations and gas releases, on the other side no anomalous temperature fluctuations have been detected for example in the investigations performed in the areas of the San Andreas fault. The most up-to-date hypothesis for reconciling thermal fluctuations and seismic activity involves gas emissions due to the stress field in the earthquake preparation phase (e.g., Tramutoli et al., 2013). Preseismic processes could result in the release of radon and optically active gases (including carbon dioxide and methane) whose concentration could influence the thermal radiation emitted from the ground (Sorokin et al., 2005). In addition, the density ratio between released volatiles and air would influence the distribution pattern of thermal anomalies, which could be more concentrated for chemical species heavier than the air and more diffuse for lighter ones.

In the last years, the possibility to identify, on global scale, seismo-associated thermal anomalies has been enormously facilitated by continuous satellite monitoring. What is generically called thermal anomalies refer to anomalous fluctuations of several different parameters such as atmospheric temperature (at various altitudes), Brightness Temperature (BT), Surface Latent Heat Flux (SLHF), Outgoing Longwave Radiation (OLR), etc. For example, Qin et al. (2011) have found preseismic anomalies of SLHF (i.e., the heat released by phase changes that is function of several meteorological parameters including surface temperature, relative humidity, wind speed etc.) and Qin et al. (2012) reported surface temperature anomalies before two major earthquakes occurred in Emilia (Italy) on May 20, 2012, 2:03 UTC (ML 5.9) and on May 29, 2012, 7:00 UTC (ML 5.8). In this framework, Piscini et al. (2017) applied a multi-parametric analysis looking for anomalies in time series of climatological parameters (including skin temperature, total water vapor column, and total ozone column) and reported persistent anomalies during the Amatrice-Norcia seismic sequence (central Italy, 2016) that emerged simultaneously in all parameters analyzed.

In order to select seismo-associated TIR (Thermal InfraRed) anomalies with respect to not earthquake fluctuations due to natural and/or measurement failures, the RST (Robust Satellite Techniques) method has been proposed (Tramutoli, 1998; Bryant and Nathan, 2003; Tramutoli et al., 2005) aimed at distinguishing spatial and temporal outliers in long-term series of satellite observations. In this framework, the RETIRA (Robust Estimator of TIR Anomalies) index has been proposed (Filizzola et al., 2004; Tramutoli et al., 2005). RETIRA classifies the pixels of satellite images (not affected by cloudiness by means the OCA procedure (Cuomo et al., 2004) based on the number of standard deviations of the TIR brightness temperature with respect to the spatial and temporal mean value. By applying these approaches to several seismic sequences (with magnitudes between 4.0 and 7.9 occurred in different seismo-tectonic conditions) Tramutoli (2007) and Tramutoli et al. (2015) reported that TIR anomalies could be detected in a large areas (up to thousand square kilometers) around the epicenter from about one month before up to a few days after the earthquake. Even though RETIRA allows minimizing the fluctuations [due to natural features (such as topography and land cover); measurement method (including illumination and satellite view angle) and regular variations (i.e., daily, seasonal, and inter-annual cycle)] Martinelli et al. (2020) highlighted that the procedure is intrinsically not protected by the proliferation of signal outliers. Weiyu et al. (2018) have studied air temperature variations in multiple layers before, during and after the Jiujiang (China) earthquake [of magnitude 5.7 occurred at 00:49 (UTC) on November 26, 2005], and reported some pre-seismic increase of temperature in the atmosphere before earthquake, with heat flow propagating from ground to higher altitude where finally dissipates. Finally, several authors reported that - because remote sensing of thermal infrared anomalies is clearly affected by cloud coverage (Blackett et al., 2011) - it is hard to discriminate thermal contribution emitted by ground possibly connected to seismic activity in cloudy conditions [see for example Zhang and Meng (2019) for the study in the Sichuan area]. Thermal anomalies and related multi-instrumental observations will be furtherly discussed also in R*emote Sensing and Multi-Parametric Approach*.

Acoustic Gravity Waves

Between the several hypotheses proposed to reconcile the observed anomalies on ground and in space with seismic activity, it has been proposed that acoustic (AW) and acoustic gravity waves (AGW) could be responsible of the coupling between lithospheric processes and tropo-ionospheric disturbances (Korepanov et al., 2009). Molchanov and Hayakawa (1998) and (Molchanov et al., 2001) suggested that the variation of the morning/evening terminator times - observed in the plots of amplitude and phase of the ground-based VLF measurements in Japan, before the Kobe earthquake on 1995 - could be induced by lithospheric oscillations through the occurrence of planetary waves with periods from few up to 10 days. Theses authors suggested that the modulation of VLF terminator time as well as the reduction of the amplitude and the enhanced dispersion of VLF intensity (observed during nightime, a few days before seismic events, in a statistical analysis including 7 years of earthquakes in the Japan area) could be induced by a decrease of a few km in the VLF reflection height possibly caused by AGW. It is interesting to notice that this effect is confirmed by Němec et al. (2009) and Píša et al. (2013) (see the following *Electromagnetic Field Anomalies*) that show a decrease of the wave intensity of electric field measured by ICE on board of DEMETER (more intense when the magnitude is larger) in a frequency range close to 1.7 kHz. If the intensity of the electric field decreases, it means that the cut-off frequency is increasing and then, it means that the height of the ionosphere is statistically lower above epicenter. Therefore, it is particularly relevant that all these studies (Molchanov and Hayakawa, 1998; Molchanov et al., 2001; Němec et al., 2009; Píša et al., 2013) based on two very different experiments, support the common idea that at the bottom of the ionosphere, above epicentre of impending earthquake, there is a statistically relevant excess of ionization. Changes of ground motion and/or temperature and pressure would induce oscillations in the atmosphere over the earthquake preparation zone that can propagate up to the ionosphere (Molchanov et al., 2001; Miyaki et al., 2002; Korepanov et al., 2009; Muto et al., 2009; Hayakawa et al., 2011). Through a wavelet analysis, Nakamura et al. (2013) showed that the fluctuations in the period of 10–100 min (which is in the range of AGW) were enhanced before the Niigata-Chuetsu earthquake (M = 6.8) of 2004. Endo et al. (2013) extended the study to AW and AGW (with a period of 1–10 min) rising the conclusion that before two earthquakes (Niigata-Chuetsu Oki (M = 6.8) 2007, and Iwate-Miyagi (M = 7.2) 2008) the oscillations would have been enhanced when the lower ionosphere was perturbed. Based on GPS measurements, Kamiyama et al. (2016) claimed a temporal correlation between seismic crustal oscillations before the 2011 Tohoku (M 9.0) earthquake and ULF magnetic and VLF/LF ionospheric disturbances observed for this earthquake by several authors (Maekawa et al., 2006; Hayakawa et al., 2012; Hayakawa et al., 2013a, 2013b; Ohta et al., 2013; Schekotov et al., 2013). Phanikumar et al. (2018) suggested that earthquake precursors could involve not only charged ionospheric components but also neutral atmospheric species. In fact, the authors pointed out an anomalous and simultaneous fluctuation at mesospheric altitude - corresponding to the VLF reflection height - of the ozone density (measured by the TIMED satellite of the NASA’s Solar Terrestrial Probes program) together with VLF signals detected on ground, before two earthquakes of 7.8 and 7.3 magnitude occurred on 2015 near Gorkha (Nepal). The hypothesis of a correlation between preseismic processes, tropo-ionospheric oscillations and thermal fluctuation has been supported also by the studies of Chakraborty et al. (2018). Starting from 3 to 4 days before the M7.3 earthquake of Gorkha (Nepal), the authors have found three correlated phenomena: 1) an anomalous fluctuation of the OLR satellite data (that can be related to thermal anomalies); 2) the occurrence of AGW of period of about 1 h and 3) ground-based detection of VLF disturbances. More recently the correlation between the occurrence of AW/AGW and the observation of TEC, plasma and VLF disturbances has been reported by several authors (such as for example Rozhnoi et al., 2013; Hayakawa et al., 2018; Piersanti et al., 2020) and further support to the AGW hypothesis has been provided by Yang et al. (2019) and Lizunov et al. (2020). On the other side, it has been argued that, as the geo-chemical and the electromagnetic hypotheses, also that of the preseismic occurrence of AW/AGW is not able to explain all the phenomenology of the LAIC process, since the observations are not conclusive in supporting/excluding any of the proposed models (Pulinets and Boyarchuk, 2005; Liperovsky et al., 2008b; Oyama et al., 2016). It can be believed that different mechanisms could coexist and contribute together in different conditions on several spatial/temporal scales.

Electromagnetic Field Measurements

Zhang et al. (2012) have analyzed two series of electric field measurements before the Wenchuan earthquake of May 12, 2008, M8.0: a long time series (since March 2008) detected on ground, and a shorter series (1–2 days) measured by ICE on board of DEMETER satellite. The time occurrence and spatial distribution of ground- and space-based measurements are consistent between them for long and short time series. The authors have found that the amplitude of measured electric field anomalies (detected a few days before the earthquake was: from about 3 mV/km up to 100 mV/km (on ground) and of about 3–5 mV/m at frequencies <0.5 Hz (relative variation >4%) (for space data). The amplitudes differ largely between ground and satellite observations, so that it is difficult to reconcile ground and space-based measurements *via* a direct propagation of electromagnetic waves from the lithosphere through the atmosphere up to the ionosphere. Bortnik and Bleier (2004) and Bortnik et al. (2010) have shown that seismo-electromagnetic signals generated in the lithosphere at frequencies <20 Hz could be able to cross the ionosphere, with the most severe attenuation occurring in the propagation under the ground and in the D-region. For frequencies in the range of 0.1–1 Hz, the attenuation of the signals seems to be moderate (about 0.01%), which means that if such signals are generated by earthquakes at the assumed location (depth of about 10 km), these signals should contain sufficient power to be detected aboard satellite. Bortnik and Bleier (2004) suggested an electromagnetic signal in the focal depth of the order of 300.000 mV/km, but this is much higher than the 3–100 mV/km observed in the three ground stations before the Wenchuan earthquake. The anomalous electric field measured on ground are often from a few tens mV/km up to a few hundred mV/km (Xiong, 1992). It means that the amplitude of ground observed electromagnetic emissions would be still far lower than that detected in space: amplitudes detected by ICE were of about 3 mV/m. Consequently a “simple” wave propagation cannot explain the observed phenomenology.

By considering the exponential damping of the electromagnetic spectrum intensity vs. frequency, several authors (such as Hayakawa et al., 1999; Smirnova et al., 2001; Molchanov et al., 2004; Hobara and Parrot, 2005; Hayakawa et al., 2009; Imamura et al., 2010) have shown that (for ground and space-based observations) the electric field spectrum (SE) before strong earthquakes has a typical fractal feature: $SE = a \times f^{-b}$ (with a and b fit parameters). Zhang et al. (2010) have pointed out that the electric field Intensity detected by ICE in the Chile area before several earthquakes would show the same dependency from the frequency. The authors have analyzed ICE data in the frequency range 19.5–250 Hz and earthquakes near the Chile area, with M >6.0, from 2004 to 2010, in nighttime, in a time window of 5 days around the earthquakes. The study has pointed out that in two thirds of the earthquakes in this region, ULF/ELF electric field perturbations have been detected and that Ne, dNe/Ne, Te, dTe/Te have always varied simultaneously with ELF electromagnetic fluctuations. More recently, by studying two months of Swarm magnetic data around the M 7.8 Nepal earthquake (April 25, 2015, 06:26 UTC), De Santis et al. (2017) reported that the cumulative number of magnetic anomalies (measured nighttime, in geomagnetically quiet conditions) shows a power-law behavior typical of a critical system (with the approach to the critical time and the recovery phase). Based on the similarity of this behavior with that of seismic data, the authors suggest that the LAIC has generated the reported anomalies during the preparation phase of Nepal earthquake.

Particle Precipitations From the Van Allen Belts

In the Earth magnetosphere, the magnetic field is able to trap charged particles (electron, positrons, protons and ions) up to energies of tens or hundreds of MeV generating the so-called inner and outer radiation belts separated by the slot region originated by particle flux depletion due to interactions with whistler waves. The inner Van Allen belt is mainly constituted by protons and electrons through the decay of albedo neutrons (Zhang K. et al., 2019) originated by cosmic rays impinging the upper atmosphere (CRAND process). Electrons are the main constituent of the outer belts eventually energized through wave-particle interactions. Whistlers are the main source of particles precipitation *via* the so-called whistler electron precipitation (WEP) (Dungey, 1963; Rodger et al., 2003) due to the resonant interaction between circularly polarized VLF (3–30 kHz) waves traveling along the geomagnetic field lines and trapped electrons resulting in their deflection in the loss cone and the consequent precipitation. The Sun is the main driver of the magnetospheric particles dynamics, but precipitation can be induced also by nuclear explosions (that can originated also long-term trapped artificial belt); by the already cited VLF emissions generated by lightning; by artificial radio signals (Sauvaud et al., 2008) and possibly by electromagnetic emission due to seismic activity. Such precipitations of electrons and protons can be observed by satellite detectors as sudden increases of the particles fluxes on the scale from few up to tens of seconds. It has been suggested that, the stable motion of high-energy trapped and quasi-trapped Van Allen particles can be perturbed also by seismo-associated electromagnetic emissions (Aleshina et al., 1992; Galperin et al., 1992). These authors suggested that electromagnetic emissions eventually generated in the preparation phase of an earthquake could modify the particles pitch angle, inducing the lowering of their mirror points and finally causing particles precipitation that are detected as sudden particles flux increase with LEO detectors. During precipitation, such burst of particles could still follow partially their longitudinal drift, that would increase the satellite capability of their detection in space not only over the hypocentral zones, but also even far from the area of the preparation earthquake. Russian scientists carried out the earliest analyses of these correlations with measurements of: MARIA detector installed on the SALYUT-7 station (Chesnokov et al., 1987; Voronov, 1990), MARIA-2 experiment on board MIR; ELECTRON experiments carried out on the INTERCOSMOS-BULGARIA-1300 and METEOR-3 satellites (Galper et al., 1989); GAMMA detector, etc. At the beginning of this century, Aleksandrin et al. (2003) and Sgrigna et al. (2005b) have published careful analyses of such phenomenon on data collected by the PET experiment on board the SAMPEX NASA satellite, obtaining a statistically reliable temporal correlation between seismic events and charged particle precipitation from the lower boundary of the inner Van Allen radiation belt. Particle Burst (PB) are defined such as anomalous increases of the count rates beyond the background fluctuation. By studying the distribution of the time difference between earthquakes and anomalous particle detections, ±36 h around the earthquake time, the authors of Aleksandrin et al. (2003) and Sgrigna et al. (2005b) have observed a peak at about 4–5 h with a significance of 5 sigma out of the mean, showing that the burst precipitation would occur before the earthquakes. This result was obtained using data driven algorithms - independent from specific LAIC model - and by considering together the all SAMPEX database. The result provides a good evidence (with a high statistical significance) of particle precipitation induced by seismic activity. Fidani and Battiston (2008) and Battiston and Vitale (2013) have extended the study on a larger time period with a different methods for background rejections. The authors have investigated the correlations between precipitation of low energy electrons ($E > 0.3$ MeV) from the NOAA satellites (POES 15, 16, 17 and 18) and about 18,000 earthquakes of magnitude greater than 5 (from USGS) along 13 years. The distribution of time differences between earthquakes and detected particle bursts is uniform (mean = 8.3, SD = 2.9) within the statistical errors, but the authors observe a large excess at -1.25 ± 0.25 h (i.e., after the earthquakes time). The temporal correlation, i.e., the possibility to measure anomalous particle burst with space based detectors before/after the seismic events, depends on the particles longitudinal drift period (around the Earth). For electrons of 300 KeV the drift period is of about 4 h, that allowed the authors to conclude that the observed peak is anyway due to a preseismic phenomenon detected by the satellite after the earthquake occurrences. The statistical significance of the found correlation peak is of 5.7 sigma, corresponding to a probability of 1.2×10^{-6} of being a statistical fluctuation. Further studies are in progress (Fidani, 2018) in order to reconstruct the spatial area of the wave-particle interaction (that has induced the precipitation events) based on the detection point and features of the precipitating particles. By studying the distribution of earthquakes with magnitude $M > 5$, as a function of the McIlwain L-shell and time, the research group of the AGILE satellite found an enhancement of particle bursts detected by the AGILE satellite, with a significance of 4 sigma, during the period August 5–September 3, 2007 (De Santis et al., 2015). The particle flux increase was in apparent coincidence with the earthquake shower in Peru that started with the M = 8 event on August 15, 2007 (Ica event). In general, even though several authors have published reports of correlations between seismic events and anomalous particles precipitation - that would precede of few hours the occurrence of earthquake of moderate and strong magnitude - the phenomenon is still asking for a large and well-assessed statistical confirmation that is one of the purposes of the experiments carried out on the CSES satellite, the most advanced satellite devoted to investigate precursors phenomena from space.

Remote Sensing and Multi-Parametric Approach

The investigation of earthquake precursors from space not only shows the advantage of worldwide coverage of seismic areas, but also offers the possibility of exploiting new methods. Remote sensing makes it possible to monitor multiple parameters for precursor signatures in the simultaneous variation of several physical variables (above the epicenter, around it and in its conjugate zone), but also to survey large areas that could be affected by the earthquake preparation process but cannot be monitored with the network of scattered ground stations (see for example Hayakawa, 2009; Ouzounov et al., 2018; De Santis et al., 2019b). In this framework, Pulinets et al. (2006) have highlighted that because the peak of preseismic radon exhalation would occur 4–10 days before the earthquake, the time scale of radon variations and that of the observed air temperature variations are comparable (Inan et al., 2008) that is compatible with their multi-parametric analysis of the anomalies of surface temperature, latent heat flux, air temperature and relative humidity observed before the Colima (Mexico) earthquake (M7.6) of 2003; the M7.1 Hector Mine (United States) event of 1999 and the Parkfield (United States) earthquake (M6) of 2004.

The potential of a multi-parameter statistical analysis of satellite data was highlighted by the joint study, published by De Santis et al. (2019c), on electron density and magnetic field measured during 2.5 years by the Swarm satellite (with quiet geomagnetic conditions) in a time window of one-month before and after 12 strong earthquakes. The authors report that the detected anomalies (limited to the Dobrovolsky area, statistically defined and normalized with respect to the number of satellite background tracks) show a linear dependence on the earthquake magnitude, which may support the hypothesis of their seismic origin and exclude a random correlation.

Between the multi-parametric analyses, several studies have been devoted the outgoing long-wave radiation (OLR). OLR is the flux of thermal radiation (between about 4 and 100 μm) emitted from the Earth to space and is measured by satellites such as NOAA14, 15, 16 and 17. In the global system of heating/cooling of the Earth, OLR is the main way in which the planet loses energy and includes the integrated effect of atmospheric species, cloud formation, aerosol balance, ocean whitecap, albedo, emissions from land and sea surfaces, etc. There are several advantages of investigating earthquake precursors through OLR because the data are available worldwide and OLR takes into account the (large spatially integrated) contributions of all soil-atmosphere coupling processes, including direct and indirect effects of earthquakes (such as radon release, ionization, latent heat release, etc.) that may occur over large areas around the epicenter, but that would be difficult to monitor with a network of local stations. Ouzounov et al. (2007) studied the OLR anomaly of the eddy field with respect to reference values averaged over months and years (in the period 1999–2004) before and after several seismic events, at different spatial resolutions [$1^\circ \times 1^\circ$ and $2.5^\circ \times 2.5^\circ$ in latitude and longitude. The eddy field is defined as the sum of the differences of the OLR measured value between adjacent points in the analyzed period (day/month) (Liu et al., 1999; Liu, 2000; Kang and Liu, 2001). Ouzounov et al. (2007) report transient OLR anomalies (in the range 10 and 13 μm) before several strong events: ΔOLR ~ +6 W/m^2, 5 days before the Bhuj (India) earthquake of M7.9, January 26, 2001); ΔOLR ~ +10 W/m^2, the month before the M6.8 event in Boumerdes, (Algeria), May 21, 2003; several anomalous OLR increases in the months before the M6.6 Iran earthquake, December 26, 2003 (with the largest ΔOLR of +22 W/m^2, occurring about two weeks before the event); several OLR anomalies before the M9.0 Sumatra earthquake, December 26, 2004 (including the largest one of +80 W/m^2, on 21 December). Above the epicenter of the Sumatra event, Ouzounov et al. (2005) also reported anomalies of surface latent heat flux and GPS/TEC, also about 5 days before the earthquake. Based on the joint observation of several variations of thermal, atmospheric and ionospheric parameters, Ouzounov et al. (2007) suggested that the observed pre-earthquake OLR anomalies could be explained by the chain of phenomena of LAIC model triggered by the radon release (Pulinets and Boyarchuk, 2005; Pulinets et al., 2006; Pulinets and Ouzounov, 2011). Starting from the Ouzounov et al. (2007) seminal work, OLR anomalies have been observed for many other seismic events, such as for example before (from 19 to December 24, 2009) the M7.0 Haiti earthquake of January 12, 2010 (Xiong et al., 2010); before the M7.7 Awaran (Pakistan) earthquake of September 24, 2013 (Venkatanathan and Natyaganov, 2014); before the M7.0 Jiuzhaigou (China) earthquake, August 8, 2017 and the M 7.1 Mexico earthquake occurred on September 20, 2017 (Zhai et al., 2020). Fu et al. (2020) have recently applied the analysis of OLR data for studying ten years (2009–2019) of earthquakes in the Taiwan area. With an epoch-superimposed method, the authors have found consecutive anomalies before strong events (M ≥ 6.0). Particularly interesting is the advance time of the temporal profile of daily OLR anomalies index (analyzed in a time-window of 25 days before and after the earthquake, see Figure 4 of Fu et al. (2020) that shows a peak 2–15 days before the events regardless of being in the daytime or the nighttime. The authors claim that, after removing the background due to typhoon's occurrence, OLR anomalies have been observed before about 77% of the earthquakes while weak seems the correlation between the number of OLR anomalies index and the earthquake's magnitude (apparently, the increasing intensity of OLR anomalies would not be associated with increased magnitude). An important multi-parametric analysis of atmospheric and ionospheric data collected on ground and from space (OLR, GPS/TEC, LEO ionospheric tomography and critical frequency foF2) has been carried out for the M9 Tohoku (Japan) earthquake of March 11, 2011 (Ouzounov et al., 2011). The authors report a chain of anomalies in the days before the earthquake: an OLR anomalies near the epicenter (on March 7th), an anomalous increase of electron density (GPS/TEC data, from March 8th), and a large increase in electron concentration detected in all 4 Japanese ground-based ionosondes (from March 3 to 11), which returned to normal a few days after the main shock of March 11. Some of the recorded TEC anomalies occurred between two minor/moderate geomagnetic storms, while the major increase (on March 8) was measured during a geomagnetically quiet period. Based on the long duration of the detected disturbances over the Sendai region, the authors excludes a meteorological or geomagnetic activity origin and suggested a preseismic character of the observed phenomenology.

De Santis et al. (2020) carried out an analysis, paradigmatic of the multi-parametric approach - by correlating ground and space-based data of seismicity, atmospheric temperature, water vapor, aerosol, methane, ionosonde measurements as well as electron density and magnetic field observations from Swarm satellite - studying the seismic sequence of Ridgecrest (CA, United States) 2019, started on July 4 and culminating with the M7.1 event of 6 July (that included also several large foreshocks of M6.4, M5 and M5.4). The results suggested a chain of multiple precursor anomalies during a preparation phase (September 2018 to July 2019) much longer than that identified by many other works, particularly on ionospheric precursors, which appeared to be limited to only a few hours to days before large earthquakes (e.g., Heki, 2011; He and Heki, 2017; Yan et al., 2017). The same long preparation phase is confirmed for example by Liu et al. (2020c), Marchetti et al. (2019, 2020). In particular, ionospheric anomalies (from ionosonde and Swarm satellite data) reported by De Santis et al. (2020), were detected from five months before the mainshock; at around 2 months before and finally on 2–3 June 2019 (under very quiet geomagnetic conditions). The authors pointed out that: 1) anticipation time, distance and features of the ionospheric anomalies were in agreement with the values estimated by using the Korsunova and Khegai (2006, 2008) method as a function of the magnitude of incoming earthquake (for M = 6–7, the distance would be less than 600 km, and the advance time from 1 to 6 days); 2) the results seem support the hypothesis that the observed percursors can be due to the release of ionized particles from the lithosphere (see Freund, 2011; Pulinets and Ouzounov, 2011; Hayakawa et al., 2018).

DEMETER SATELLITE OBSERVATIONS

In the previous century, the analyses of earthquake precursors in space were carried out with data collected by non-devoted satellites. The increasing interest in studying these phenomena resulted in the proposal of several missions - deigned for investigating the phenomenology with multi-instrumental payloads - such as DEMETER (Parrot, 2002), QuakeSat (Flagg et al., 2004), ESPERIA (Sgrigna et al., 2005a; Sgrigna et al., 2007; Sgrigna et al., 2008), VULKAN (Kuznetsov et al., 2011), CSES (Shen et al., 2018) and FORMOSAT-7/COSMIC-2 (Liu et al., 2020a). Between them, the French satellite DEMETER has been the first satellite devoted to investigate seismo-electromagnetic and volcanic phenomena (Lagoutte et al., 2006). The mission–started on 2004 and ended on 2010–was based on a payload including: a detector (ICE) of electric field components from quasi DC up to 3.5 MHz; a three axis search-coil magnetometer IMSC (from a few Hz up to 18 kHz); a couple of instruments for plasma investigations (ISL and IAP); and a high energy particle detector (IDP). The orbit was quasi Sun-synchronous circular with an inclination of about 98°, ascending node at 22:15 LT, altitude between about 710 km (up to 2005) and about 660 km (after 2005). All the instruments operated in two data acquisition modes (named survey and burst, at low and high data sampling rate respectively) between ± 65 degrees of invariant latitude. It is neither possible to discuss in detail nor to summarize all published results based on DEMETER data. Therefore, in this review, we will mainly concentrate on the statistical studies and on the most assessed analysis methods, even though this will exclude to discuss some other interesting analyses. For the purpose of this review, we privilege presenting results obtained on many events with a procedure adopted by several authors.

Electromagnetic Field Anomalies

By analyzing quasi-static electric field data detected night-time by DEMETER for high magnitude earthquakes of Indonesia and Chile regions (Zhang et al., 2014), reported perturbations from 1.5 to 16 mV/m, over the epicentre or at the end of seismic faults within 2000 km from the epicentre, before (in a time window of -7/+1 day around the events) of 27 earthquakes. This value of about 10 mV/m measured in space should be reconciled with that measured on ground that is several order of magnitude higher, but never exceeding 100 V/m over an area of 100–1,000 km around the epicentre and for middle-time observations (days) (Kondo, 1968; Vershinin et al., 1999; Hao et al., 2000; Rulenko, 2000). On 2010, DEMETER has detected an enhancement of ULF emissions two months around the Haiti earthquake (M7.0, January 12th, 21:53 UTC) (Athanasiou et al., 2011) and in occasion of the Chile event (M8.8, February 27th, 2010, 6:34 UTC), when also ELF and ionospheric perturbations were detected simultaneously (Zhang et al., 2011).

Probably the most significant result obtained with the DEMETER data is the statistical analysis - through the superposed epoch and space method - of the disturbances of the electric field power spectrum density (PSD) measured by the ICE experiment as function of the seismic activity (Němek et al., 2008, 2009, 2010; Píša et al., 2013) According to this method, all earthquake occurrences and locations are placed at the origin of the resulting time-space diagram (time = 0 and distance = 0). The relative intensity of the electric PSD (evaluated by subtracting the background and normalizing by the SD) is plotted as a function of spatial and temporal distance between the satellite and the position and time for each analyzed earthquake. The first results of such a study of ICE data, published on 2008, included 2.5 years of observations, whereas the last analysis of 2013 was executed on 6.5 years, i.e., all the DEMETER database. Starting from the larger band of 1–2 kHz, analyzed on 2008, the study has been refined on 2009 by restricting to PSD at 1.7 ± 200 Hz (i.e., cantered on the waveguide cut-off frequency, see below for details). On 2013 the investigation have been extended to the whole range below 10 kHz (with 16 bands of about 117 Hz each) in order to reduce the interference from VLF transmitters. In the most updated version of the study, only isolated earthquakes have been selected by excluding aftershocks as well as by filtering events belonging to seismic sequences preceding the main shock. Earthquakes have been classified in several categories as a function of magnitude and hypocentral depth. The temporal series of ICE data detected around each seismic event has been grouped in bins of 4 h, since five days before up to three days after the earthquake. Geomagnetic conditions have been taken in account by categorizing data in four classes, based on Kp values, and by excluding data collected in geomagnetically perturbed periods. The impact of magnetic local time has also been investigated. By distinguishing dayside and nightside, a positive correlation has been found only for night-time data. Finally, observations have been tested against random dataset of earthquakes (casually shifted in time and longitude). The authors claim a very small but statistically significant decrease of the electric PSD at about 1.7 kHz, which starts a few hours before the earthquakes. The "peak" in the 2009 analysis includes 2068 "points" (observations) from 64 earthquakes and 2952 "points" from 369 earthquakes for the 2013 analysis. The involved distance of the claimed decrease is of less than 350 km on 2008 analysis (with a bin of 140 km) and less than 440 km in the 2013 study. It worth to highlight that these results would be "compatible" with a raw estimation of the area involved in the mechanical precursors that could be done on the basis of the Dobrovolsky radius $r \leq 10^{4.3M}$ km (Dobrovolsky et al., 1979) that is of about 140 and 380 km for earthquake magnitude M = 5 and 6 respectively. The frequency of 1.7 kHz, where the decrease of wave intensity was observed, corresponds to the low-frequency cutoff for propagation in the Earth-ionosphere waveguide at night (Budden, 1961; Harrison et al., 2010). This frequency is inversely proportional to the height of lower boundary of the ionosphere. Electromagnetic waves generated by lightning in thunderstorms are a crucial source of VLF radiation (including whistlers) during the nighttime. Local variations of the electromagnetic conditions over the area of earthquake preparation could vary the cutoff frequency of the Earth-ionosphere waveguide affecting the electromagnetic spectrum observed by DEMETER at frequencies of about 1.7 kHz. A hypothesis could be that additional ionization of air molecules at the Earth's surface prior to earthquakes could increase the electrical conductivity of the lower troposphere. The height of the lower boundary of the ionosphere exhibits a seasonal variation, and it depends on the position of observation (Toledo-Redondo et al., 2012). It is therefore hard to compare observations of absolute values of VLF wave intensity, which depend on the positions and on season. In this framework, seasonal effects have been studied by dividing the ICE dataset in groups of three months. Even though non conclusive, the PSD analyses seem pointing out some dependence from the seasonal variation of lightning activity - that is globally larger between March and August - that could maximize the possibility to detect seismo-electromagnetic fluctuations. The decrease of wave intensity found in the cited ICE-DEMETER studies is of about 4–6 dB for the analysis of 2008, about 2.4–3.6 dB for the study published on 2009 and about 2 dB for the results of 2013. It is a small, but significant decrease of wave intensity as compared to the normal variability of about 11 dB (2009), and ± 7.5 dB (2013). The decrease does not occur directly above the earthquake epicentre, but is shifted about 2° in the westward direction. Several hypothesis have been suggested for explaining this latitudinal shift such as aerosol drift, Coriolis contribution, ion drift, etc. (2009). The effect appears higher for higher geomagnetic latitudes (greater than 20°) (for analysis of 2010 and 2013). The decrease occurs more often close to shallower earthquakes: events with depth less than 40 km. The effect is larger for larger magnitude: M > 5.0 (2009); M > 5.5 and threshold effect at M = 4 (2013). With respect to the investigation of the effect of earthquakes occurring under sea/land, no dependence has been found in the analyses of 2008–2009, whereas a greater effect has been pointed out for undersea earthquakes in the 2013 investigation. The statistical significance of the claimed observations has reduced from the initial value (more than 3σ) (for 2008, 2009) obtained with 2.5 years up to the last published analysis carried out on the whole DEMETER database (2013). The ICE study disagrees with previous ones that mostly reported an increase in the ELF/VLF activity (Parrot et al., 1985; Larkina et al., 1989; Parrot and Mogilevsky, 1989; Serebryakova et al., 1992; Molchanov et al., 1993). However, we should cite that early studies have not used "control set of data" in order to estimate statistical significance of the observed effects. It is worth highlighting that, with a conservative and very laudable approach, the authors of the 2009 analysis wrote: « [. . .] although the correlation between seismic activity and intensity of electromagnetic waves is statistically significant, it is observed only due to the large number of the analyzed events. Therefore even if there is on average a decrease of wave intensity related to large surface earthquakes, individual events may exhibit rather different behavior; the natural fluctuations of intensity of electromagnetic waves are large and the observed effect is relatively weak as compared to them». Finally, it is worth highlighting that, even though the DEMETER studies have pointed out the evidence of electric field fluctuations, no effect has been found for magnetic field measurements carried out simultaneously by the same satellite.

The authors of (Parrot and Pinçon 2020) studied the existence of a spatial and temporal correlation between seismic activity and the whistler waves detected by the RNF neural network of DEMETER. On ground, Hayakawa, et al. (1993) have found a correlation between earthquakes and the occurrence of the anomalous whistlers, i.e., whistlers with anomalous dispersion. Whistlers are ELF-VLF right hand polarized emissions generated by lightning that can propagate in the Earth-ionosphere waveguide as well as through the ionosphere and the magnetosphere mainly ducted along the geomagnetic field lines. The authors reported a statistical increase of about 10% of the whistler rate the day before the earthquake (with M ≥ 5.5 and depth ≤20 km, at a distance less than 200 km) with respect to the background (evaluated between -15 and 5 days around the earthquake time). On the other side, no significant correlation was observed for earthquakes of magnitude lower or equal to 5.2, which could point out both the difficulty and the sensitivity of the applied overlapping epoch's method to identify such an increase. It is worth highlighting the prudence of the authors when they remarks that even though their observation confirms the detectability from space of a LAIC mechanism prior to large and shallow earthquakes, their studies cannot support any forecast or deterministic association of anomalies detection with the occurrence of a single seismic events. The existence of LAIC coupling mechanism is an excellent reason to study short-term precursors.

Ion and Electron Density Fluctuations

Several analyses of DEMETER satellite data have shown an increase of the number and intensity of the ionospheric perturbations detected before the occurrence of strong earthquakes as well as an increase of the perturbations amplitude as a function of the magnitude (Parrot, 2011). In particular, Píša et al. (2011) has pointed out a significant increase of the plasma density detected by DEMETER tens of days before the main shock of the Chile earthquake on February 27, 2010.

Li and Parrot (2012) have analyzed ion density (defined as the sum of H+, He+, O+ from IAP)) and the electron density (from ISL) data collected in the whole DEMETER activity along 6.5 years and registered only for night-time. The authors have selected 21.863 earthquakes from the USGS catalog, with magnitude grater or equal than 4.8 and distance between DEMETER and the epicentre ≤1,500 km, with a time window of 15 days before earthquake and measurements collected in quiet days ($Kp < 3$). In addition, observations have been tested against random dataset of earthquakes (casually shifted in time of one month, in the same season, and in longitude of 25°). The ion density perturbations mainly consist of an increase. The fraction of precursor observations increases of few percent with the earthquake magnitude. The mean number of perturbations per earthquake is larger for stronger events. Both the good detections and the number of false alarms decrease as a function of the perturbations amplitude (whatever is the magnitude of the earthquakes). This means that the amplitude of the perturbations is not well related to the magnitude. By studying the mean and median values of perturbations amplitude plotted vs. magnitude, the authors claim that: stronger earthquake apparently show larger perturbations; this effect is only evident for very large magnitude and other earthquake parameters (different from magnitude) could play a role. Results for electron density are similar to those for ion density. In order to analyze of the effect of the earthquakes location, the epicentres have been classified such as inland, below sea (water depth >1 km), and close coast (depth <1 km). The author's conclusions are that the percentage of good detections increases with the magnitude whatever is the earthquake location. The percentage of good detections is larger for earthquake occurring below the sea. Earthquake taking place near coasts have the lowest percentage of good detections. The mean number of perturbations smoothly increase the days before the seismic event. Anyway, the authors emphasize that - beyond the spatial and temporal correlation between observations and seismic events - there is no further way to assert a causal relationship between earthquakes and observed anomalies. Ryu et al. (2014) and Ryu et al. (2016) have studied the statistical impact of earthquakes, of $M > 5.0$ and $M \geq 6.0$ respectively, (mainly occurring in the equatorial region) on the electron density data measured by the DEMETER satellite in the period 2005–2010. By correlating the indices of daily seismic activity and the EIA (equatorial ionization anomaly) intensity, the authors obtained statistically significant values of the lagged cross-correlation function. The results show the existence of ionospheric precursors of low-latitude earthquakes and that their concur in enhancing the equatorial anomaly.

More recently, machine-learning methods have been applied for the automatic identification of earthquake precursors (Xiong et al., 2020; Xiong et al., 2021). The new research field is extremely interesting and further results can be achieved. DEMETER data have been analyzed in hundreds of publications. For a summary, we address the reader to the general review Parrot (2018) and to the specific articles (such as for example Parrot, 2012; Zlotnicki et al., 2010; Zlotnicki et al., 2013; Parrot, and Li, 2015; Liu et al., 2015; Ho et al., 2018; Parrot and Li, 2018; Parrot et al., 2021).

FIRST ANALYSES FROM THE CSES SATELLITE MISSION

As described in previous sections, after the earliest studies with not devoted satellites, the DEMETER observations have supported an increasing number of studies claiming the existence of seismo-associates ionospheric and magnetospheric perturbations occurring from two weeks up to few hours before earthquakes. In this framework, the CSES satellite is the second mission designed for investigating seismo-associated phenomena from space, which has successfully been launched on February 2018. CSES payload includes nine instruments: a particle detector from China constituted by three sub-units [the HEPP-L, -H and -X detectors (Li M. et al., 2019) for measuring low- and high-energy charged particles and X rays]; the Italian HEPD high-energy particle detector (Alfonsi et al., 2017; Ambrosi et al., 2018, 2020; Picozza et al., 2019; Bartocci et al., 2020; Sotgiu et al., 2021); two magnetometers [HPM (Cheng et al., 2018) for low and SCM (Cao et al., 2018) for high frequencies respectively]; the EFD detector (Huang et al., 2018) (for measuring electric field components); a Langmuir probe (LAP) (Yan et al., 2018a; Liu et al., 2019) and a plasma detector PAP (Liu et al., 2019b); a three bands beacon transmitter and a occultation receiver (Chen et al., 2018; Lin et al., 2018). After two years of data acquisitions, the temporal series starts to be enough long to allow carrying out statistical studies. In the following, we discuss some of the last published results.

Yan et al. (2018b) reported the observations by CSES of unusual ionospheric irregularities of (electromagnetic field, plasma, and energetic particle fluxes) over the epicentral area and before four earthquakes of magnitude greater than 7. Perturbations have been recorded by several CSES instruments (such as EFD, SCM, LAP, PAP and HEPP) during night-time orbits. The authors claim a correlation with the earthquake hypocentral depth (the deeper the earthquake hypocentre was the fewer were the anomalous irregularities observed) and with the magnitude (the greater was the magnitude, the greater were the observed electromagnetic disturbances). In the analysis, measurements gathered in geomagnetically disturbed period (i.e., Kp index greater than 3 or the Dst index lower than −20 nT) have been excluded. The studied earthquakes occurred all at low latitude on August 2018 in: New Caledonia (M = 7.1), Venezuela (M = 7.3), Fiji islands (M = 8.1) and Peru (M = 7.1). Unfortunately, for the studied earthquakes none observations have been carried out spatially and temporally near to the epicentres. Therefore, the claimed perturbations have been evaluated as anomalous with respect a background level computed with a spatial resolution of some degrees (i.e., on the basis of measurements done quite far from the epicentre) and with a poor temporal resolution (i.e., there is not a temporal series of repeated measurements before/after the events in the same place). Recently, Zhu et al. (2021) published the most up-to-date CSES data analysis (over more than 2.5 years of electron density and temperature measurements) that would support a temporal and spatial correlation between the occurrence of earthquakes with Ms ≥ 4.8 and the observation of positive variations of Ne and negative variations of Te (during nighttime hours), approximately one and two weeks before the seismic events, at a distance of less than about 200 km from the epicenters (apparently within the Dobrovolsky's radius). However, the authors declare, similarly to other reports on earthquake precursors, the anomalous variation of parameters has not been revealed in all studied earthquakes and the perturbations seems can occur at various temporal and spatial distances from the epicentre. On the other side, the ionospheric and geomagnetic dynamics driven by the solar activity cannot rule out other possibilities as sources of the observed anomalies.

Several authors (Pulinets, 2012; Parrot, 2013; Kuo et al., 2014; Oikonomou et al., 2016) have suggested that the increase of ionization over the zone of impending earthquake (registered by ground-based TEC measurements and electron density satellite observations) could have a significant impact on the equatorial ionospheric anomaly (EIA). Marchetti et al. (2020) have studied the anomalies (defined with respect to the EIA background variability) of the electron density measured by CSES and Swarm in eight months preceding the M = 7.5 Indonesia earthquake occurred on September 28th, 2018. An increase of atmospheric (mainly in aerosol optical thickness, skin temperature and water vapor) and ionospheric anomalies were reported about 3.7 and 2.7 months respectively before the mainshock, while on August 2, 2018 an anomaly was detected simultaneously in atmosphere (aerosol content), topside ionosphere (electron density detected by CSES) and in the Swarm magnetic field. Finally, on August 19th, 2018 an enhancement of the electron density was detected by Swarm and CSES over the area of the preparing earthquake and in the conjugated zone (during nighttime). These observations confirm the DEMETER analyses of Ryu et al. (2014), Ryu et al. (2016) about the impact of the earthquake preparation phase on the EIA.

In the article Xuhui, et al. (2020) recently published, CSES measurements possibly reconciled with 12 earthquakes with magnitude M ≥ 7 have been analyzed. The authors report the observation of various anomalies of several parameters measured by the on board instruments, on different spatial and temporal scales (from days to weeks before the events). In particular, in occasion of the Ms = 7.1 earthquake - occurred in Mexico on February 17, 2018 - the authors report: 1) disturbances of low-frequency PSD of the electric field (at 155.5 and 1.405 kHz) one and two days before the seismic event; 2) fluctuations of ionospheric parameters (such as electrons density and temperature, and NO+ density) two days before the event. The article is a short report aimed at summarizing the results of the CSES program (that will be published in further specific reports) that does not allow a complete comprehension of the achieved results.

Li et al. (2020) have analyzed electron and ion oxygen density measured by ISL and IAP (Li and Parrot, 2012) on board the DEMETER mission (in about 6.5 years) and by LAP and PAP on board of the CSES satellite (in more than one year). The authors have searched for correlations with seismic events occurred within a distance less than 1,500 km from the satellite ground trace and in a time window of 15 days before the earthquakes. The authors claim that the detection rate of seismo-ionospheric perturbations increases as a function of: 1) the time resolution of satellite data acquisition and 2) the earthquake magnitude; whereas decreases as the epicentral depth of seismic events increases. They also claim that the occurrence rate of these ionospheric variations is the highest the day of the earthquake and then gradually decreases the day before. More precisely, in some areas, the observed ionospheric perturbations mainly occur about 6–7 days prior to earthquakes confirming the observations of (Akselevich and Tertyshnikov, 1995) and (Liu et al., 2009) and the analysis of Li M. et al. (2019) who found that ionospheric variations gain a high climax 3 days before the Wenchuan main event on May 12, 2008.

Even though up to now, the reported CSES analyses are not conclusive, the large amount of observations from instruments will significantly help in studying frequencies, amplitudes and characteristics of ionospheric perturbations related to earthquakes and possibly their generation mechanisms.

CONNECTING PERTURBATIONS ON GROUND AND IN SPACE

As previously mentioned the value of preseismic quasi-static electric field amplitude measured in space is of about 10 mV/m (Zhang et al., 2014) while that measured on ground is several order of magnitude higher, but never exceeding 100 V/m over an area of 100–1,000 km around the epicentre and for middle-time observations (days) Kondo (1968); Vershinin et al. (1999); Hao et al. (2000); Rulenko (2000). In order to reconcile such ground-based and space-based observations, Sorokin et al. (2001) suggested that radon gas exhalations in the atmosphere would generate a flow of large negative aerosol particles moving upward with a velocity of a few cm/s together with smaller positive aerosol particles moving at lower velocity. The difference of speeds between the two fluxes would cause a local electric field impulse of tens kV/m on a temporal scale of less than tens of minutes (Liperovsky et al., 2008b) but, because this electric field is confined between such layers of aerosols clouds, it will not affect regions external to the layers. Therefore, this mechanism would not be able to explain the quasi-static electric field observed in the ionosphere before earthquakes on the scale of hundreds or thousands of kilometres. In general, the hypothesis that ionospheric quasi-static electric field could be induced by radon emissions is highly debated. The releases of gas, aerosol and other radioactive sources can vary the local ionization - through alpha and gamma decays - which could change up to two times the conductivity of the lower layers of the atmosphere (Omori et al., 2009). Anyway, by assuming a radon exhalation of 10 Bq/m^3, Omori et al. (2009) estimated an increase of the conductivity of only 1.5 times, not enough to generate a significant variation the background electric field up to about 10 mV/m observed in the ionosphere. Similarly, even doubling the ionization rate by radon will result into a variation 10% of the electric field between Earth and ionosphere (Harrison, et al., 2010).

More in general, a direct propagation of an electric field from the lithosphere up to the ionosphere seems in contradiction with observations. The value of the electric field in the ionosphere have been estimated by several authors (Kim and Hegai, 1999; Denisenko et al., 2008) by assuming a given value on ground as well as different geometries, distributions and conditions. In night-time, the intensity of quasi-static electric field on ground needed to obtain the observed intensity of 10 mV/m in space would be at least one order of magnitude higher than the maximum one observed at the surface in the preparation zone. In daytime, when the conductivity in the ionosphere is one or two orders of magnitude larger than in night-time, the electric field value in space would be of the order of 10^{-3} mV/m, well lower than the observed value of 10 mV/m. This conclusion seems confirmed by the estimation of the damping of the electric field from ground to the ionosphere observed about intense thunderstorm events (Park and Dejnakarintra 1973). In fact, measurements of quasi-static electric field during tropical cyclones can be of about (1–10) kV/m on ground (Park and Dejnakarintra 1973) and in space up to about 25 mV/m, as recorder at an altitude of about 950 km over intense thunderstorms by the COSMOS-1809 satellite (together with plasma density fluctuation of about 6%) (Isaev et al., 2002; Sorokin et al., 2005). Therefore, the amplitude of the quasi-static electric field on ground during intense thunderstorms is of some order of magnitude higher than the highest ever measured/claimed on ground about earthquakes.

CONCLUSION

It is extremely hard to take conclusions in a so large field with this variety of observations, methods, hypothesis, models and sometime speculations. Therefore, we will limit to draw some considerations.

- Variability of electromagnetic precursors

The interpretation of claimed electromagnetic precursors is promising, but still in some early stage: there is a large variability of the detected intensity, frequencies, spatial and temporal distribution, spreading or clustering around the epicentre or along geomagnetically connected areas, etc. After the early sparse observations, even with the most recent devoted missions such as DEMETER, CSES, and FORMOSAT the phenomenology is still barely understood.

- What transfers the information from ground to space?

Based on the observations of an enhancement of VLF fluctuations in the range of acoustic gravity waves measured before some earthquakes, the link between AW/AGW and VLF disturbances seems quite well assessed. On the other side the conclusion that the observed phenomenology has a preseismic character asks for further confirmations, because the connection is still indirect. Several reports are in favor of a LAIC due to the chain of ionization, changes of conductivity and feedback phenomena originated by radon emissions.

- Correlation between earthquake magnitude, depth and amplitude of possible precursors

The published analyses about groundwater level variations and radon gas exhalations seems suggest a correlation between the earthquakes magnitude and the amplitude and spatial/temporal distributions of their claimed precursors. Reports about electromagnetic precursors seem not univocal, but the variation of the electric field intensity at the ionospheric cut-off is more intense when the magnitude is higher (Němec et al., 2009; Píša et al. (2013). Nevertheless the vast majority (if not all) of the analyses cited in this review that found precursors were conducted on earthquakes of magnitude greater than 5, and a significant percentage of the case studies cited were for even higher magnitudes (6 or greater). This consideration - which remains generally valid for the vast literature on the subject - shows that magnitude should be a key parameter in precursor identification. A similar role is played by hypocentral depth: most reports of seismic precursors concern shallow earthquakes, although we do not have a clear or unique threshold for depth, partly because differences in the specific seismic-tectonic conditions of different areas should not be overlooked. Thus, we could summarize that the larger the magnitude and the smaller the depth of the earthquake, the greater the chances of detecting the earthquake effects at satellite altitudes. Otherwise, it would be rather difficult (if not impossible) to detect these ionospheric or magnetospheric effects. Obviously, it cannot be ignored that, the dependence from the earthquake magnitude can cause a threshold of detectability and that unfortunately, the cut on magnitude reduces significantly the statistics, which can affect the significance of the conclusions. However, a clear proportionality between the earthquake intensity and the numerousness, frequency and/or amplitude of the presumed pre-seismic anomalies is necessary to link together the two kind of phenomena. Higher-sensitivity instruments foreseen for next satellites will allow a better definition of this correlation.

- Extent of the spatial scale of the precursors

The densification of precursor observations within few hundreds of kilometres from the epicentre - i.e., near the larger earthquake deformations - seems coherent with the postulated dependence of the precursor generation mechanism from the size of the involved faults and the magnitude of the resulting earthquake. The distance of ionospheric precursors could be correlated with magnitude [see for example the model of Korsunova and Khegai (2006), Korsunova and Khegai (2008)]. However, is still missing an estimation of the area that could be involved in the generation mechanism of various (not only mechanical) earthquake-precursors as well as of the extension of detectability region in which the signal to noise ratio would allow a reliable precursors recognition.

- Temporal advance and clustering of anomalous observations

The largest electromagnetic anomalies (measured hours or days before large events) seem occur more frequently in time and with larger amplitude close to the incoming earthquake. Moreover, it is worth highlighting the recent hypothesis (and first confirmations) that also ionospheric precursors would follow Rikitake's law that larger earthquakes should be associated with a longer precursor times. This could be reconciled with the critical nature of the process originating the earthquake in the preparation phase along the fault before the rupture.

The variety of phenomena associated with earthquakes requires the simultaneous observation of many parameters. The need for statistical studies that increase the reliability of results by reducing background effects asks for increasing the number of seismic events analyzed worldwide. Both of these requirements, for a global coverage system, can only be met from space through satellite remote sensing. In this framework will be particularly valuable the new multi-spacecraft missions.

On 2019 have been launched the six small satellites of the FORMOSAT-7/COSMIC-2 constellation (Lin et al., 2020). The satellites - initially deployed into a circular orbit at 720 km - will take about 16 months to reach the mission orbit at 550 km with 24 degrees of inclination. The satellites are equipped with a radio occultation system (TGRS) designed for 3D sounding of electron density; the IVM instrument (for *in-situ* observations of ion density, temperature, and drift); and a RF beacon. From IVM measurements of the ion velocity, it is also possible to estimate the electric field. The FORMOSAT-7/COSMIC-2 mission offers the unique capabilities: 1) to carry simultaneously both vertical soundings of the ionospheric and *in-situ* plasma observations; and 2) to provide measurements with a constellation of six satellites (Ho et al., 2020). These features will allow investigating pre-, co- and post-seismic phenomena with a high-resolution (in time and space) measurements at low latitude (Liu et al., 2020b). Some preliminary results - about the Bitung Indonesia earthquake of November 14, 2019, M7.1 (with an increase of TEC, NmF2 and HmF2 over the epicentre on 25–26 October 2019) - appear already interesting (Liu et al., 2020b).

On 2023 will be launched CSES-02, the second mission of the CSES series, with the same multi-instrumental payload and similar orbital parameters of the first satellite, that will allow reducing the revisit time between the consecutive observations of the same geographic region.

Earthquake precursors are extremely elusive and difficult to be observed, immersed as they are in a variety of other natural and anthropogenic signals - with amplitudes even orders of magnitude greater - that can cover them and easily induce erroneous interpretations. However, the set of observed precursors is remarkable and so varied to provide confidence to the efforts of the vast scientific community that deals with them. Observations from space, especially with multi-satellite missions and constellations, will be able to contribute significantly to clarifying this picture.

AUTHOR CONTRIBUTIONS

All authors listed have made a substantial, direct, and intellectual contribution to the work and approved it for publication.

FUNDING

This work was supported by the Italian Space Agency in the framework of the "Accordo Attuativo 2020-32.HH.0 Limadou Scienza+" (CUP F19C20000110005)

REFERENCES

Akselevich, V. I., and Tertyshnikov, A. V. (1995). Methodology of Ecological Monitoring Data Application to Seismic Forecasting. *Atmospheric Oceanic. Optics C/C Optika Atmosphri Okena* 8, 567–569.

Aleksandrin, S. Y., Galper, A. M., Grishantzeva, L. A., Koldashov, S. V., Maslennikov, L. V., Murashov, A. M., et al. (2003). High-energy Charged Particle Bursts in the Near-Earth Space as Earthquake Precursors. *Ann. Geophys.* 21 (2), 597–602. doi:10.5194/angeo-21-597-2003

Aleshina, M. E., Voronov, S. A., Gal'Per, A. M., Koldashov, S. V., and Maslennikov, L. V. (1992). Correlation between Earthquake Epicenters and Regions of High-Energy Particle Precipitations from the Radiation belt. *Cosmic Res.* 30 (1), 65–68.

Alfonsi, L., Ambroglini, F., Ambrosi, G., Ammendola, R., Assante, D., Badoni, D., et al. (2017). The HEPD Particle Detector and the EFD Electric Field Detector for the CSES Satellite. *Radiat. Phys. Chem.* 137, 187–192. doi:10.1016/j.radphyschem.2016.12.022

Ambrosi, G., Bartocci, S., Basara, L., Battiston, R., Burger, W. J., Campana, D., et al. (2020). Beam Test Calibrations of the HEPD Detector on Board the China Seismo-Electromagnetic Satellite. *Nucl. Instr. Methods Phys. Res. Section A: Acc. Spectrometers, Detectors Associated Equipment* 974, 164170. doi:10.1016/j.nima.2020.164170

Ambrosi, G., Bartocci, S., Basara, L., Battiston, R., Burger, W. J., Carfora, L., et al. (2018). The HEPD Particle Detector of the CSES Satellite mission for Investigating Seismo-Associated Perturbations of the Van Allen Belts. *Sci. China Technol. Sci.* 61 (5), 643–652. doi:10.1007/s11431-018-9234-9

Antselevich, M. G. (1966). The Influence of Tashkent Earthquake on the Earth's Magnetic Field and the Ionosphere. *Tashkent Earthquake* 26, 187–188.

Athanasiou, M. A., Anagnostopoulos, G. C., Iliopoulos, A. C., Pavlos, G. P., and David, C. N. (2011). Enhanced ULF Radiation Observed by DEMETER Two Months Around the strong 2010 Haiti Earthquake. *Nat. Hazards Earth Syst. Sci.* 11 (4), 1091–1098. doi:10.5194/nhess-11-1091-2011

Bartocci, S., Battiston, R., Burger, W. J., Campana, D., Carfora, L., Castellini, G., et al. (2020). Galactic Cosmic-Ray Hydrogen Spectra in the 40-250 MeV Range Measured by the High-Energy Particle Detector (HEPD) on Board the CSES-01 Satellite between 2018 and 2020. *ApJ* 901 (1), 8. doi:10.3847/1538-4357/abad3e

Battiston, R., and Vitale, V. (2013). First Evidence for Correlations between Electron Fluxes Measured by NOAA-POES Satellites and Large Seismic Events. *Nucl. Phys. B - Proc. Supplements* 243-244, 249–257. doi:10.1016/j.nuclphysbps.2013.09.002

Biagi, P. F., Ermini, A., Kingsley, S. P., Khatkevich, Y. M., and Gordeev, E. I. (2001). Difficulties with Interpreting Changes in Groundwater Gas Content as Earthquake Precursors in Kamchatka, Russia. *J. Seismology* 5 (4), 487–497. doi:10.1023/A:1012015317086

Blackett, M., Wooster, M. J., and Malamud, B. D. (2011). Exploring Land Surface Temperature Earthquake Precursors: A Focus on the Gujarat (India) Earthquake of 2001. *Geophys. Res. Lett.* 38 (15), 15303. doi:10.1029/2011GL048282

Bortnik, J., Bleier, T. E., Dunson, C., and Freund, F. (2010). Estimating the Seismotelluric Current Required for Observable Electromagnetic Ground Signals. *Ann. Geophys.* 28 (8), 1615–1624. doi:10.5194/angeo-28-1615-2010

Bortnik, J., and Bleier, T. (2004). *Full Wave Calculation of the Source Characteristics of Seismogenic Electromagnetic Signals as Observed at LEO Satellite Altitudes*. San Francisco: AGU Fall Meeting Abstracts.

Bryant, N. A., and Nathan, R. B. (2003). *Observed Weather Satellite Thermal Responses Prior to and after Earthquakes*, T52D–04. San Francisco: AGU Fall Meeting Abstracts.

Budden, K. G. (1961). *The Wave-Guide Mode Theory of Wave Propagation*. London: Logos Press.

Cao, J., Zeng, L., Zhan, F., Wang, Z., Wang, Y., Chen, Y., et al. (2018). The Electromagnetic Wave experiment for CSES mission: Search Coil Magnetometer. *Sci. China Technol. Sci.* 61 (5), 653–658. doi:10.1007/s11431-018-9241-7

Cenni, N., Viti, M., and Mantovani, E. (2015). Space Geodetic Data (GPS) and Earthquake Forecasting: Examples from the Italian Geodetic Network. *Bollettino di Geofisica Teorica ed Applicata* 56 (2), 129–150. doi:10.4430/bgta0139

Chakraborty, S., Sasmal, S., Chakrabarti, S. K., and Bhattacharya, A. (2018). Observational Signatures of Unusual Outgoing Longwave Radiation (OLR) and Atmospheric Gravity Waves (AGW) as Precursory Effects of May 2015 Nepal Earthquakes. *J. Geodynamics* 113, 43–51. doi:10.1016/j.jog.2017.11.009

Chen, L., Ou, M., Ou, M., Yuan, Y., Sun, F., Yu, X., et al. (2018). Preliminary Observation Results of the Coherent Beacon System Onboard the China Seismo-Electromagnetic Satellite-1. *Earth Planet. Phys.* 2 (6), 1–10. doi:10.26464/epp2018049

Cheng, B., Zhou, B., Magnes, W., Lammegger, R., and Pollinger, A. (2018). High Precision Magnetometer for Geomagnetic Exploration Onboard of the China Seismo-Electromagnetic Satellite. *Sci. China Technol. Sci.* 61 (5), 659–668. doi:10.1007/s11431-018-9247-6

Chesnokov, V. Y., Galper, A. M., Kirillov-Ugryumov, V. G., Koldashov, S. V., Mikhailov, V. V., Popov, A. V., et al. (1987). Registration of Sporadic Increase of High Energy Particle Flux Near the Brazilian Anomaly Region. *Int. Cosmic Ray Conf.* 4, 451.

Chmyrev, V. M., Isaev, N. V., Bilichenko, S. V., and Stanev, G. (1989). Observation by Space-Borne Detectors of Electric fields and Hydromagnetic Waves in the Ionosphere over an Earthquake centre. *Phys. Earth Planet. Interiors* 57 (1–2), 110–114. doi:10.1016/0031-9201(89)90220-3

Cicerone, R. D., Ebel, J. E., and Britton, J. (2009). A Systematic Compilation of Earthquake Precursors. *Tectonophysics.* 476, 371–396. doi:10.1016/j.tecto.2009.06.008

Conti, L., Picozza, P., and Sotgiu, A. (2021). A Critical Review of Ground Based Observations of Earthquake Precursors. *Front. Earth Sci. Sec. Geohazards Georisks*. doi:10.3389/feart.2021.676766

Cuomo, V., Filizzola, C., Pergola, N., Pietrapertosa, C., and Tramutoli, V. (2004). A Self-Sufficient Approach for GERB Cloudy Radiance Detection. *Atmos. Res.* 72 (1–4), 39–56. doi:10.1016/j.atmosres.2004.03.030

Datchenko, E. A., Ulomov, V. I., and Chernyshova, C. P. (1972). Electron Density Anomalies as the Possible Precursor of Tashkent Earthquake. *Dokl. Uzbek. Acad. Sci.* 12, 30–32.

Dautermann, T., Calais, E., Haase, J., and Garrison, J. (2007). Investigation of Ionospheric Electron Content Variations before Earthquakes in Southern California, 2003-2004. *J. Geophys. Res.* 112 (2). doi:10.1029/2006JB004447

De Santis, A., Abbattista, C., Alfonsi, L., Amoruso, L., Campuzano, S. A., Carbone, M., et al. (2019a). Geosystemics View of Earthquakes. *Entropy* 21 (4), 412. doi:10.3390/e21040412

De Santis, A., Balasis, G., Pavón-Carrasco, F. J., Cianchini, G., and Mandea, M. (2017). Potential Earthquake Precursory Pattern from Space: The 2015 Nepal Event as Seen by Magnetic Swarm Satellites. *Earth Planet. Sci. Lett.* 461, 119–126. doi:10.1016/j.epsl.2016.12.037

De Santis, A., Cianchini, G., Marchetti, D., Piscini, A., Sabbagh, D., Perrone, L., et al. (2020). A Multiparametric Approach to Study the Preparation Phase of the 2019 M7.1 Ridgecrest (California, United States) Earthquake. *Front. Earth Sci.* 8, 478. doi:10.3389/feart.2020.540398

De Santis, A., De Franceschi, G., Spogli, L., Perrone, L., Alfonsi, L., Qamili, E., et al. (2015). Geospace Perturbations Induced by the Earth: The State of the Art and Future Trends. *Phys. Chem. Earth, Parts A/B/C* 85-86, 17–33. doi:10.1016/j.pce.2015.05.004

De Santis, A., Marchetti, D., Pavón-Carrasco, F. J., Cianchini, G., Perrone, L., Abbattista, C., et al. (2019b). Precursory Worldwide Signatures of Earthquake Occurrences on Swarm Satellite Data. *Sci. Rep.* 9 (1), 20287. doi:10.1038/s41598-019-56599-1

De Santis, A., Marchetti, D., Spogli, L., Cianchini, G., Pavón-Carrasco, F. J., Franceschi, G. D., et al. (2019c). Magnetic Field and Electron Density Data Analysis from Swarm Satellites Searching for Ionospheric Effects by Great Earthquakes: 12 Case Studies from 2014 to 2016. *Atmosphere* 10 (7), 371. doi:10.3390/atmos10070371

Denisenko, V. V., Boudjada, M. Y., Horn, M., Pomozov, E. V., Biernat, H. K., Schwingenschuh, K., et al. (2008). Ionospheric Conductivity Effects on Electrostatic Field Penetration into the Ionosphere. *Nat. Hazards Earth Syst. Sci.* 8 (5), 1009–1017. doi:10.5194/nhess-8-1009-2008

Dey, S., and Singh, R. P. (2003). Surface Latent Heat Flux as an Earthquake Precursor. *Nat. Hazards Earth Syst. Sci.* 3 (6), 749–755. doi:10.5194/nhess-3-749-2003

Dobrovolsky, I. P., Zubkov, S. I., and Miachkin, V. I. (1979). Estimation of the Size of Earthquake Preparation Zones. *Pageoph.* 117 (5), 1025–1044. doi:10.1007/BF00876083

Dungey, J. W. (1963). Loss of Van Allen Electrons Due to Whistlers. *Planet. Space Sci.* 11 (6), 591–595. doi:10.1016/0032-0633(63)90166-1

Endo, T., Kasahara, Y., Hobara, Y., Sue, T., and Hayakawa, M. (2013). A Note on the Correlation of Seismo-Ionospheric Perturbations with Ground Motions as Deduced from F-Net Seismic Observations. *Jae* 33 (1), 69–76. doi:10.1541/jae.33.69

Fidani, C., and Battiston, R. (2008). Analysis of NOAA Particle Data and Correlations to Seismic Activity. *Nat. Hazards Earth Syst. Sci.* 8 (6), 1277–1291. doi:10.5194/nhess-8-1277-2008

Fidani, C. (2018). Improving Earthquake Forecasting by Correlations between strong Earthquakes and NOAA Electron Bursts. *Terr. Atmos. Ocean. Sci.* 29 (2), 117–130. doi:10.3319/TAO.2017.10.06.01

Filizzola, C., Pergola, N., Pietrapertosa, C., and Tramutoli, V. (2004). Robust Satellite Techniques for Seismically Active Areas Monitoring: a Sensitivity Analysis on September 7, 1999 Athens's Earthquake. *Phys. Chem. Earth, Parts A/B/C* 29 (4–9), 517–527. doi:10.1016/j.pce.2003.11.019

Fishkova, L. M., Gokhberg, M. B., and Pilipenko, V. A. (1985). Relationship between Night Airglow and Seismic Activity. *AnGeo* 3, 689–694. Available at: https://ui.adsabs.harvard.edu/abs/1985AnGeo...3..689F/abstract.

Flagg, S., Bleier, T., Dunson, C., Doering, J., DeMartini, L., Clarke, P., et al. (2004). "Using Nanosats as a Proof of Concept for Space Science Missions: QuakeSat as an Operational Example," in Annual AIAA/USU Conference on Small Satellites (Logan: SSC04-IX-4), 1–12. Available at: https://digitalcommons.usu.edu/cgi/viewcontent.cgi?article=1728andcontext=smallsat.

Freund, F. (2011). Pre-earthquake Signals: Underlying Physical Processes. *J. Asian Earth Sci.* 41 (4–5), 383–400. doi:10.1016/j.jseaes.2010.03.009

Freund, F. T., Takeuchi, A., Lau, B. W. S., Al-Manaseer, A., Fu, C. C., Bryant, N. A., et al. (2007). Stimulated Infrared Emission from Rocks: Assessing a Stress Indicator. *eEarth* 2 (1), 7–16. www.electronic-earth.net/2/7/2007/. doi:10.5194/ee-2-7-2007

Friis-Christensen, E., Lühr, H., Knudsen, D., and Haagmans, R. (2008). Swarm - an Earth Observation Mission Investigating Geospace. *Adv. Space Res.* 41 (1), 210–216. doi:10.1016/j.asr.2006.10.008

Fu, C.-C., Lee, L.-C., Ouzounov, D., and Jan, J.-C. (2020). Earth's Outgoing Longwave Radiation Variability Prior to M ≥6.0 Earthquakes in the Taiwan Area during 2009-2019. *Front. Earth Sci.* 8, 364. doi:10.3389/feart.2020.00364

Fu, C.-C., Yang, T. F., Chen, C.-H., Lee, L.-C., Wu, Y.-M., Liu, T.-K., et al. (2017). Spatial and Temporal Anomalies of Soil Gas in Northern Taiwan and its Tectonic and Seismic Implications. *J. Asian Earth Sci.* 149, 64–77. doi:10.1016/j.jseaes.2017.02.032

Galper, A. M., Dimitrenko, V. B., Nikitina, N. V., Grachev, V. M., and Ulin, S. E. (1989). Interrelation between High-Energy Charged Particle Fluxes in the Radiation belt and Seismicity of the Earth. *Cosmic Res.* 27, 789.

Galperin, Y. I., Gladyshev, V. A., Dzhordzhio, N. V., Larkina, V. I., and Mogilevskij, M. M. (1992). Energetic Particles Precipitation from the Magnetosphere above the Epicenter of Approaching Earthquake. *Kosmicheskie Issledovaniya* 30 (1), 89–106.

Geller, R. J. (1997). Earthquake Prediction: a Critical Review. *Geophys. J. Int.* 131 (3), 425–450. doi:10.1111/j.1365-246X.1997.tb06588.x

Geller, R. J., Jackson, D. D., Kagan, Y. Y., and Mulargia, F. (1997). Earthquakes Cannot Be Predicted. *Science* 275 (5306), 1616. doi:10.1126/science.275.5306.1616

Gokhberg, M. B., Pilipenko, V. A., and Pokhotelov, O. A. (1983). Satellite Observation of Electromagnetic Radiation over the Epicentral Region of an Incipient Earthquake. *Dokl. Akad. Nauk. SSSR Earth Sci. Ser. Engl. Transl.* 268 (1), 5–7.

Gousheva, M., Danov, D., Hristov, P., and Matova, M. (2009). Ionospheric Quasi-Static Electric Field Anomalies during Seismic Activity in August-September 1981. *Nat. Hazards Earth Syst. Sci.* 9 (1), 3–15. doi:10.5194/nhess-9-3-2009

Gousheva, M., Danov, D., Hristov, P., and Matova, M. (2008). Quasi-static Electric fields Phenomena in the Ionosphere Associated with Pre- and post Earthquake Effects. *Nat. Hazards Earth Syst. Sci.* 8 (1), 101–107. doi:10.5194/nhess-8-101-2008

Gulia, L., and Wiemer, S. (2019). Real-time Discrimination of Earthquake Foreshocks and Aftershocks. *Nature* 574 (7777), 193–199. doi:10.1038/s41586-019-1606-4

Hao, J., Tang, T., and Li, D. (2000). Progress in the Research on Atmospheric Electric Field Anomaly as an index for Short-Impending Prediction of Earthquakes. *J. Earthquake Prediction Res.* 8 (3), 241–255.

Harrison, R. G., Aplin, K. L., and Rycroft, M. J. (2010). Atmospheric Electricity Coupling between Earthquake Regions and the Ionosphere. *J. Atmos. Solar-Terrestrial Phys.* 72 (5–6), 376–381. doi:10.1016/j.jastp.2009.12.004

Hattori, K., Serita, A., Gotoh, K., Yoshino, C., Harada, M., Isezaki, N., et al. (2004). ULF Geomagnetic Anomaly Associated with 2000 Izu Islands Earthquake Swarm, Japan. *Phys. Chem. Earth, Parts A/B/C* 29 (4–9), 425–435. doi:10.1016/j.pce.2003.11.014

Hayakawa, M., Asano, T., Rozhnoi, A., and Solovieva, M. (2018). "Very-low-and Low-Frequency Sounding of Ionospheric Perturbations and Possible Association with Earthquakes," in *Pre-Earthquake Processes: A Multidisciplinary Approach To Earthquake Prediction Studies*. Editors D. Ouzounov, S. Pulinets, K. Hattori, and P. Taylor (Hoboken: Wiley Online Library), 277–304.

Hayakawa, M. (1999). *Atmospheric and Ionospheric Electromagnetic Phenomena Associated with Earthquakes*. Tokyo: Terra Scientific Publishing Company.

Hayakawa, M. (2015). *Earthquake Prediction with Radio Techniques*. Singapore: Wiley Blackwell, 1–294. doi:10.1002/9781118770368

Hayakawa, M., Hobara, Y., Rozhnoi, A., Solovieva, M., Ohta, K., Izutsu, J., et al. (2013b). The Ionospheric Precursor to the 2011 March 11 Earthquake Based upon Observations Obtained from the japan-pacific Subionospheric VLF/LF Network. *Terr. Atmos. Ocean. Sci.* 24 (3), 393–408. doi:10.3319/TAO.2012.12.14.01(AA10.3319/tao.2012.12.14.01(aa)

Hayakawa, M., Hobara, Y., Yasuda, Y., Yamaguchi, H., Ohta, K., Izutsu, J., et al. (2012). Possible Precursor to the March 11, 2011, Japan Earthquake: Ionospheric Perturbations as Seen by Subionospheric Very Low Frequency/Low Frequency Propagation. *Ann. Geophys.* 55 (1), 95–99. doi:10.4401/ag-5357

Hayakawa, M., Ito, T., and Smirnova, N. (1999). Fractal Analysis of ULF Geomagnetic Data Associated with the Guam Earthquake on August 8, 1993. *Geophys. Res. Lett.* 26 (18), 2797–2800. doi:10.1029/1999GL005367

Hayakawa, M., Kasahara, Y., Nakamura, T., Hobara, Y., Rozhnoi, A., Solovieva, M., et al. (2011). Atmospheric Gravity Waves as a Possible Candidate for Seismo-Ionospheric Perturbations. *Jae* 31 (2), 129–140. doi:10.1541/jae.31.129

Hayakawa, M., Liu, J.-Y., Hattori, K., and Telesca, L. (2009). Electromagnetic Phenomena Associated with Earthquakes and Volcanoes. *Phys. Chem. Earth* 34 (6), 341–515. doi:10.1016/j.pce.2008.12.003

Hayakawa, M., and Molchanov, O. A. (2002). *Seismo Electromagnetics: Lithosphere - Atmosphere - Ionosphere Coupling*. Tokyo: TERRAPUB.

Hayakawa, M., Rozhnoi, A., Solovieva, M., Hobara, Y., Ohta, K., Schekotov, A., et al. (2013a). The Lower Ionospheric Perturbation as a Precursor to the 11 March 2011 Japan Earthquake. *Geomatics, Nat. Hazards Risk* 4 (3), 275–287. doi:10.1080/19475705.2012.751938

Hayakawa, M., Sue, Y., and Nakamura, T. (2009). The Effect of Earth Tides as Observed in Seismo-Electromagnetic Precursory Signals. *Nat. Hazards Earth Sys. Sci.* 9 (5), 1733–1741. doi:10.5194/nhess-9-1733-2009

Hayakawa, M., Yoshino, T., and Morgounov, V. A. (1993). On the Possible Influence of Seismic Activity on the Propagation of Magnetospheric Whistlers at Low Latitudes. *Phys. Earth Planet. Interiors* 77 (1–2), 97–108. doi:10.1016/0031-9201(93)90036-9

He, L., and Heki, K. (2017). Ionospheric Anomalies Immediately before M W 7.0-8.0 Earthquakes. *J. Geophys. Res. Space Phys.* 122 (8), 8659–8678. doi:10.1002/2017JA024012

Heki, K. (2011). Ionospheric Electron Enhancement Preceding the 2011 Tohoku-Oki Earthquake. *Geophys. Res. Lett.* 38 (17), a–n. doi:10.1029/2011GL047908

Helman, D. S. (2020). Seismic Electric Signals (SES) and Earthquakes: A Review of an Updated VAN Method and Competing Hypotheses for SES Generation and Earthquake Triggering. *Phys. Earth Planet. Interiors* 302, 106484. doi:10.1016/j.pepi.2020.106484

Ho, S.-P., Zhou, X., Shao, X., Zhang, B., Adhikari, L., Kireev, S., et al. (2020). Initial Assessment of the COSMIC-2/FORMOSAT-7 Neutral Atmosphere Data Quality in NESDIS/STAR Using *In Situ* and Satellite Data. *Remote Sensing* 12 (24), 4099. doi:10.3390/rs12244099

Ho, Y.-Y., Jhuang, H.-K., Lee, L.-C., and Liu, J.-Y. (2018). Ionospheric Density and Velocity Anomalies before M ≥ 6.5 Earthquakes Observed by DEMETER Satellite. *J. Asian Earth Sci.* 166, 210–222. doi:10.1016/j.jseaes.2018.07.022

Hobara, Y., and Parrot, M. (2005). Ionospheric Perturbations Linked to a Very Powerful Seismic Event. *J. Atmos. Solar-Terrestrial Phys.* 67 (7), 677–685. doi:10.1016/j.jastp.2005.02.006

Hough, S. (2020). *The Great Quake Debate: The Crusader, the Skeptic, and the Rise of Modern Seismology*. Seattle: University of Washington Press.

Huang, J., Lei, J., Lei, J., Li, S., Zeren, Z., Li, C., et al. (2018). The Electric Field Detector (EFD) Onboard the ZH-1 Satellite and First Observational Results. *Earth Planet. Phys.* 2 (6), 469–478. doi:10.26464/epp2018045

Ide, S., Beroza, G. C., Shelly, D. R., and Uchide, T. (2007). A Scaling Law for Slow Earthquakes. *Nature* 447 (7140), 76–79. doi:10.1038/nature05780

Ikuta, R., Hisada, T., Karakama, G., and Kuwano, O. (2020). Stochastic Evaluation of Pre-Earthquake TEC Enhancements. *J. Geophys. Res. Space Phys.* 125 (11), e2020JA027899. doi:10.1029/2020JA027899

Imamura, T., Ida, Y., Kasahara, Y., Nakamura, T., Hobara, Y., and Hayakawa, M. (2010). Fractal Analysis of Subionospheric LF Propagation Data and Consideration of the Lithosphere-Atmosphere-Ionosphere Coupling. *Nat. Hazards Earth Syst. Sci.* 10 (4), 901–906. doi:10.5194/nhess-10-901-2010

Inan, S., Akgül, T., Seyis, C., Saatçilar, R., Baykut, S., Ergintav, S., et al. (2008). Geochemical Monitoring in the Marmara Region (NW Turkey): A Search for Precursors of Seismic Activity. *J. Geophys. Res. Solid Earth* 113 (3), 3401. doi:10.1029/2007JB005206

Ingebritsen, S. E., and Manga, M. (2014). Hydrogeochemical Precursors. *Nat. Geosci.* 7 (10), 697–698. doi:10.1038/ngeo2261

Isaev, N. V., Sorokin, V. M., Chmyrev, V. M., Serebryakova, O. N., and Ovcharenko, O. Y. (2002). "Electric Field Enhancement in the Ionosphere above Tropical Storm Region," in *Seismo Electromagnetics: Lithosphere-Atmosphere-Ionosphere Coupling* (Tokyo: TERRAPUB), 313–315.

Jordan, T. H., Chen, Y. T., Gasparini, P., Madariaga, R., Main, I., Marzocchi, W., et al. (2011). Operational Earthquake Forecasting: State of Knowledge and Guidelines for Utilization. *Ann. Geophys.* 54 (4), 319–391. doi:10.4401/ag-5350

Kakinami, Y., Liu, J.-Y., Tsai, L.-C., and Oyama, K.-I. (2010). Ionospheric Electron Content Anomalies Detected by a FORMOSAT-3/COSMIC Empirical Model before and after the Wenchuan Earthquake. *Int. J. Remote Sensing* 31 (13), 3571–3578. doi:10.1080/01431161003727788

Kamiyama, M., Sugito, M., Kuse, M., Schekotov, A., and Hayakawa, M. (2016). On the Precursors to the 2011 Tohoku Earthquake: Crustal Movements and Electromagnetic Signatures. *Geomatics, Nat. Hazards Risk* 7 (2), 471–492. doi:10.1080/19475705.2014.937773

Kamogawa, M., and Kakinami, Y. (2013). Is an Ionospheric Electron Enhancement Preceding the 2011 Tohoku-Oki Earthquake a Precursor? *J. Geophys. Res. Space Phys.* 118 (4), 1751–1754. doi:10.1002/jgra.50118

Kanamori, H. (2003). Earthquake prediction: An overview. *Int. Geophys.* 81, 1205–1216. doi:10.1016/S0074-6142(03)80186-9

Kandalyan, R. A., and AlQuran, M. K. (2010). Ionosphere Scintillation and Earthquakes. *Jordan J. Phys.* 3 (2), 69–76.

Kang, C., and Liu, D. (2001). The Applicability of Satellite Remote Sensing in Monitoring Earthquake. *Sci. Surv. Mapp.* 26 (3), 46–48.

Kato, A., and Ben-Zion, Y. (2021). The Generation of Large Earthquakes. *Nat. Rev. Earth Environ.* 2 (1), 26–39. doi:10.1038/s43017-020-00108-w

Kim, V. P., and Hegai, V. V. (1999). "A Possible Presage of strong Earthquakes in the Night-Time Mid-latitude F2 Region Ionosphere," in *Atmospheric and Ionospheric Electromagnetic Phenomena Associated with Earthquakes*. Editor M. Hayakawa (Tokyo: Terrapub), 619.

Koike, K., Yoshinaga, T., Suetsugu, K., Kashiwaya, K., and Asaue, H. (2015). Controls on Radon Emission from Granite as Evidenced by Compression Testing to Failure. *Geophys. J. Int.* 203 (1), 428–436. doi:10.1093/gji/ggv290

Kondo, G. (1968). The Variation of the Atmospheric Electric Field at the Time of Earthquake. *Mem. Kakioka Magnet. Observ.* 12, 11–23.

Kopytenko, Y. A., Matiashvili, T. G., Voronov, P. M., Kopytenko, E. A., and Molchanov, O. A. (1993). Detection of Ultra-low-frequency Emissions Connected with the Spitak Earthquake and its Aftershock Activity, Based on Geomagnetic Pulsations Data at Dusheti and Vardzia Observatories. *Phys. Earth Planet. Interiors* 77 (1–2), 85–95. doi:10.1016/0031-9201(93)90035-8

Korepanov, V., Hayakawa, M., Yampolski, Y., and Lizunov, G. (2009). AGW as a Seismo-Ionospheric Coupling Responsible Agent. *Phys. Chem. Earth, Parts A/B/C* 34 (6–7), 485–495. doi:10.1016/j.pce.2008.07.014

Korsunova, L. P., and Khegai, V. V. (2008). Analysis of Seismoionospheric Disturbances at the Chain of Japanese Stations for Vertical Sounding of the Ionosphere. *Geomagn. Aeron.* 48 (3), 392–399. doi:10.1134/S0016793208030134

Korsunova, L. P., and Khegai, V. V. (2006). Medium-term Ionospheric Precursors to strong Earthquakes. *Int. J. Geomagn. Aeron.* 6 (3), 1–8. doi:10.1029/2005gi000122

Kuo, C. L., Huba, J. D., Joyce, G., and Lee, L. C. (2011). Ionosphere Plasma Bubbles and Density Variations Induced by Pre-earthquake Rock Currents and Associated Surface Charges. *J. Geophys. Res.* 116 (10), a–n. doi:10.1029/2011JA016628

Kuo, C. L., Lee, L. C., and Huba, J. D. (2014). An Improved Coupling Model for the Lithosphere-Atmosphere-Ionosphere System. *J. Geophys. Res. Space Phys.* 119 (4), 3189–3205. doi:10.1002/2013JA019392

Kuznetsov, V. D., Bodnar, L., Garipov, G. K., Danilkin, V. A., Degtyar, V. G., Dokukin, V. S., et al. (2011). Orbital Monitoring of the Ionosphere and Abnormal Phenomena by the Small Vulkan-Compass-2 Satellite. *Geomagn. Aeron.* 51 (3), 329–341. doi:10.1134/S001679321103011X

Kuzuoka, S., and Mizuno, T. (2004). "Land Deformation Monitoring Using PSInSAR Technique," in *International Symposium on Monitoring, Prediction and Mitigation of Disasters by Satellite Remote Sensing, MPMD-2004*, Hyogo, 176–181.

Lagoutte, D., Brochot, J. Y., de Carvalho, D., Elie, F., Harivelo, F., Hobara, Y., et al. (2006). The DEMETER Science Mission Centre. *Planet. Space Sci.* 54 (5), 428–440. doi:10.1016/j.pss.2005.10.014

Larkina, V. I., Migulin, V. V., Molchanov, O. A., Kharkov, I. P., Inchin, A. S., and Schvetcova, V. B. (1989). Some Statistical Results on Very Low Frequency Radiowave Emissions in the Upper Ionosphere over Earthquake Zones. *Phys. Earth Planet. Interiors* 57 (1–2), 100–109. doi:10.1016/0031-9201(89)90219-7

Larkina, V. I., Nalivayko, A. V., Gershenzon, N. I., Gokhberg, M. B., Liperovskiy, V. A., and Shalimov, S. L. (1983). Observations of VLF Emission, Related with Seismic Activity, on the Interkosmos-19 Satellite. *Geomagnetism and Aeronomy* 23 (5), 684.

Larkina, V., Migulin, V., Mogilevsky, M., Molchanov, O., Galperin, Y., Jorjio, N., et al. (1984). Earthquake Effects in the Ionosphere According to Intercosmos-19 and Aureol-3 Satellite Data. *Results ARCAD-3 Project Recent Programmes Magnetospheric Ionospheric Phys.* 685–699.

Li, M., Lu, J., Zhang, X., and Shen, X. (2019). Indications of Ground-Based Electromagnetic Observations to A Possible Lithosphere-Atmosphere-Ionosphere Electromagnetic Coupling before the 12 May 2008 Wenchuan MS 8.0 Earthquake. *Atmosphere* 10 (7), 355. doi:10.3390/atmos10070355

Li, M., and Parrot, M. (2012). "Real Time Analysis" of the Ion Density Measured by the Satellite DEMETER in Relation with the Seismic Activity. *Nat. Hazards Earth Syst. Sci.* 12 (9), 2957–2963. doi:10.5194/nhess-12-2957-2012

Li, M., Shen, X., Parrot, M., Zhang, X., Zhang, Y., Yu, C., et al. (2020). Primary Joint Statistical Seismic Influence on Ionospheric Parameters Recorded by the CSES and DEMETER Satellites. *J. Geophys. Res. Space Phys.* 125 (12), e2020JA028116. doi:10.1029/2020JA028116

Li, X. Q., Xu, Y. B., An, Z. H., Liang, X. H., Wang, P., Zhao, X. Y., et al. (2019). The High-Energy Particle Package Onboard CSES. *Radiat. Detect. Technol. Methods* 3 (3), 1–11. doi:10.1007/s41605-019-0101-7

Lin, C. Y., Lin, C. C. H., Liu, J. Y., Rajesh, P. K., Matsuo, T., Chou, M. Y., et al. (2020). The Early Results and Validation of FORMOSAT-7/COSMIC-2 Space Weather Products: Global Ionospheric Specification and Ne-Aided Abel Electron Density Profile. *J. Geophys. Res. Space Phys.* 125 (10), e2020JA028028. doi:10.1029/2020JA028028

Lin, J., Shen, X., Hu, L., Wang, L., and Zhu, F. (2018). CSES GNSS Ionospheric Inversion Technique, Validation and Error Analysis. *Sci. China Technol. Sci.* 61 (5), 669–677. doi:10.1007/s11431-018-9245-6

Liou, Y.-A., Kar, S. K., and Chang, L. (2010). Use of High-Resolution Formosat-2 Satellite Images for post-earthquake Disaster Assessment: A Study Following the 12 May 2008 Wenchuan Earthquake. *Int. J. Remote Sensing* 31 (13), 3355–3368. doi:10.1080/01431161003727655

Liperovsky, V. A., Meister, C.-V., Liperovskaya, E. V., and Bogdanov, V. V. (2008b). On the Generation of Electric Field and Infrared Radiation in Aerosol Clouds Due to Radon Emanation in the Atmosphere before Earthquakes. *Nat. Hazards Earth Syst. Sci.* 8 (5), 1199–1205. doi:10.5194/nhess-8-1199-2008

Liperovsky, V. A., Pokhotelov, O. A., Meister, C.-V., and Liperovskaya, E. V. (2008a). Physical Models of Coupling in the Lithosphere-Atmosphere-Ionosphere System before Earthquakes. *Geomagn. Aeron.* 48 (6), 795–806. doi:10.1134/S0016793208060133

Liu, C., Guan, Y., Zheng, X., Zhang, A., Piero, D., and Sun, Y. (2019). The Technology of Space Plasma *In-Situ* Measurement on the China Seismo-Electromagnetic Satellite. *Sci. China Technol. Sci.* 62 (5), 829–838. doi:10.1007/s11431-018-9345-8

Liu, D.-F., Peng, K.-Y., Liu, W.-H., Li, L.-Y., and Hou, J.-S. (1999). Thermal Omens before Earthquakes. *Acta Seimol. Sin.* 12 (6), 710–715. doi:10.1007/s11589-999-0072-8

Liu, D. (2000). Anomalies Analyses on Satellite Remote Sensing OLR before Jiji Earthquake. *Geo-Information Sci.* 2 (1), 33–36.

Liu, J.-Y. G., Chang, F. Y., Lin, C.-Y., and Chen, Y.-I. (2020b). *Ionospheric Earthquake Precursors and Space Weather Observed by FORMOSAT-7/COSMIC-2*. AGU Fall Meeting Abstracts.

Liu, J.-Y. G., Chang, F. Y., Lin, C. C. H., and Lin, C.-Y. (2020a). *Advances in Low-Latitude Ionosphere Observed by FORMOSAT-7/COSMIC-2*. AGU Fall Meeting Abstracts, SA038–04.

Liu, J. Y., Chang, F. Y., Oyama, K. I., Kakinami, Y., Yeh, H. C., Yeh, T. L., et al. (2015). Topside Ionospheric Electron Temperature and Density along the Weddell Sea Latitude. *J. Geophys. Res. Space Phys.* 120 (1), 609–614. doi:10.1002/2014JA020227

Liu, J. Y., Chen, Y. I., Chen, C. H., Liu, C. Y., Chen, C. Y., Nishihashi, M., et al. (2009). Seismoionospheric GPS Total Electron Content Anomalies Observed before the 12 May 2008Mw7.9 Wenchuan Earthquake. *J. Geophys. Res.* 114 (4), a–n. doi:10.1029/2008JA013698

Liu, J. Y., Chen, Y. I., Chuo, Y. J., and Chen, C. S. (2006). A Statistical Investigation of Preearthquake Ionospheric Anomaly. *J. Geophys. Res.* 111 (5), 5304. doi:10.1029/2005JA011333

Liu, Q., De Santis, A., Piscini, A., Cianchini, G., Ventura, G., and Shen, X. (2020c). Multi-Parametric Climatological Analysis Reveals the Involvement of Fluids in the Preparation Phase of the 2008 Ms 8.0 Wenchuan and 2013 Ms 7.0 Lushan Earthquakes. *Remote Sensing* 12 (10), 1663. doi:10.3390/rs12101663

Lizunov, G. V., Skorokhod, T. V., Skorokhod, T. V., and Korepanov, V. Y. (2020). Atmospheric Gravity Waves Among Other Physical Mechanisms of Seismic-Ionospheric Coupling. *Kosm. Nauka Tehnol.* 26 (3), 55–80. doi:10.15407/knit2020.03.055

Maekawa, S., Horie, T., Yamauchi, T., Sawaya, T., Ishikawa, M., Hayakawa, M., et al. (2006). A Statistical Study on the Effect of Earthquakes on the Ionosphere, Based on the Subionospheric LF Propagation Data in Japan. *Ann. Geophys.* 24 (8), 2219–2225. doi:10.5194/angeo-24-2219-2006

Marchetti, D., De Santis, A., D'Arcangelo, S., Poggio, F., Piscini, A., A. Campuzano, S., et al. (2019). Pre-earthquake Chain Processes Detected from Ground to Satellite Altitude in Preparation of the 2016-2017 Seismic Sequence in Central Italy. *Remote Sensing Environ.* 229, 93–99. doi:10.1016/j.rse.2019.04.033

Marchetti, D., De Santis, A., Shen, X., Campuzano, S. A., Perrone, L., Piscini, A., et al. (2020). Possible Lithosphere-Atmosphere-Ionosphere Coupling Effects Prior to the 2018 Mw = 7.5 Indonesia Earthquake from Seismic, Atmospheric and Ionospheric Data. *J. Asian Earth Sci.* 188, 104097. doi:10.1016/j.jseaes.2019.104097

Martinelli, G., Facca, G., Genzano, N., Gherardi, F., Lisi, M., Pierotti, L., et al. (2020). Earthquake-Related Signals in Central Italy Detected by Hydrogeochemical and Satellite Techniques. *Front. Earth Sci.* 8, 529. doi:10.3389/feart.2020.584716

Masci, F., Thomas, J. N., and Secan, J. A. (2017). On a Reported Effect in Ionospheric TEC Around the Time of the 6 April 2009 L'Aquila Earthquake. *Nat. Hazards Earth Syst. Sci.* 17 (9), 1461–1468. doi:10.5194/nhess-17-1461-2017

Masci, F., Thomas, J. N., Villani, F., Secan, J. A., and Rivera, N. (2015). On the Onset of Ionospheric Precursors 40 Min before strong Earthquakes. *J. Geophys. Res. Space Phys.* 120 (2), 1383–1393. doi:10.1002/2014JA020822

Massonnet, D., Rossi, M., Carmona, C., Adragna, F., Peltzer, G., Feigl, K., et al. (1993). The Displacement Field of the Landers Earthquake Mapped by Radar Interferometry. *Nature* 364 (6433), 138–142. doi:10.1038/364138a0

Migulin, V., Larkina, V., Molchanov, O., Nalivaiko, A., Gokhberg, M., Liperovsky, V., et al. (1982). Detection of the Earthquake Effects on the VLF-ELF Noises in the Upper Ionosphere. *Preprint IZMIRAN, Institute of Terrestrial Magnetism, Ionosphere and Radio Wave Propagation (IZMIRAN), USSR Academy of Sciences, Moscow* 25 (390), 28.

Miyaki, K., Hayakawa, M., and Molchanov, O. A. (2002). "The Role of Gravity Waves in the Lithosphere-Ionosphere Coupling, as Revealed from the Subionospheric LF Propagation Data," in *Seismo Electromagnetics: Lithosphere-Atmosphere-Ionosphere Coupling*. Editors M. Hayakawa and O. A. Molchanov (Tokyo: TERRAPUB), 229–232.

Molchanov, O. A., Hayakawa, M., and Miyaki, K. (2001). VLF/LF Sounding of the Lower Ionosphere to Study the Role of Atmospheric Oscillations in the Lithosphere-Ionosphere Coupling. *Adv. Polar Upper Atmos. Res.* 15, 146–158.

Molchanov, O. A., and Hayakawa, M. (1998). Subionospheric VLF Signal Perturbations Possibly Related to Earthquakes. *J. Geophys. Res.* 103 (A8), 17489–17504. doi:10.1029/98ja00999

Molchanov, O. A., Mazhaeva, O. A., , et al.Molchanov, O. A., Mazhaeva, O. A., Golyavin, A. N., et al. (1993). Observation by the Intercosmos-24 Satellite of ELF-VLF Electromagnetic Emissions Associated with Earthquakes. *AnGeo* 11 (5), 431–440. Available at: https://ui.adsabs.harvard.edu/abs/1993AnGeo..11..431M/abstract.

Molchanov, O., Fedorov, E., Schekotov, A., Gordeev, E., Chebrov, V., Surkov, V., et al. (2004). Lithosphere-atmosphere-ionosphere Coupling as Governing Mechanism for Preseismic Short-Term Events in Atmosphere and Ionosphere. *Nat. Hazards Earth Syst. Sci.* 4 (5–6), 757–767. doi:10.5194/nhess-4-757-2004

Moro, M., Saroli, M., Stramondo, S., Bignami, C., Albano, M., Falcucci, E., et al. (2017). New Insights into Earthquake Precursors from InSAR. *Sci. Rep.* 7 (1), 1–11. doi:10.1038/s41598-017-12058-3

Morozova, L. I. (1996). Features of Atmo-Lithmospheric Relationships during Periods of strong Asian Earthquakes. *Fizika Zemli N.* 5, 63–68.

Muto, F., Kasahara, Y., Hobara, Y., Hayakawa, M., Rozhnoi, A., Solovieva, M., et al. (2009). Further Study on the Role of Atmospheric Gravity Waves on the Seismo-Ionospheric Perturbations as Detected by Subionospheric VLF/LF Propagation. *Nat. Hazards Earth Syst. Sci.* 9 (4), 1111–1118. doi:10.5194/nhess-9-1111-2009

Nakamura, T., Korepanov, V., Kasahara, Y., Hobara, Y., and Hayakawa, M. (2013). An Evidence on the Lithosphere-Ionosphere Coupling in Terms of Atmospheric Gravity Waves on the Basis of a Combined Analysis of Surface Pressure, Ionospheric Perturbations and Ground-Based ULF Variations. *Jae* 33 (1), 53–68. doi:10.1541/jae.33.53

Nakatani, M. (2020). Evaluation of Phenomena Preceding Earthquakes and Earthquake Predictability. *J. Disaster Res.* 15 (Issue 2), 112–143. doi:10.20965/jdr.2020.p0112

Nardò, S., Ascione, A., Mazzoli, S., Terranova, C., and Vilardo, G. (2020). PS-InSAR Data Analysis: Pre-seismic Ground Deformation in the 2009 L'Aquila Earthquake Region. *Bollettino di Geofisica Teorica ed Applicata* 61 (1), 41–56. doi:10.4430/bgta0251

Natarajan, V., and Philipoff, P. (2018). Observation of Surface and Atmospheric Parameters Using "NOAA 18" Satellite: a Study on Earthquakes of Sumatra and Nicobar Is Regions for the Year 2014 (M ≥ 6.0). *Nat. Hazards* 92 (2), 1097–1112. doi:10.1007/s11069-018-3242-y

Němec, F., Santolík, O., and Parrot, M. (2009). Decrease of Intensity of ELF/VLF Waves Observed in the Upper Ionosphere Close to Earthquakes: A Statistical Study. *J. Geophys. Res. Space Phys.* 114 (4), 4303. doi:10.1029/2008JA013972

Němec, F., Santolík, O., Parrot, M., and Rodger, C. J. (2010). Relationship between Median Intensities of Electromagnetic Emissions in the VLF Range and Lightning Activity. *J. Geophys. Res. Space Phys.* 115 (8), 8315. doi:10.1029/2010JA015296

Němek, F., Santolík, O., Parrot, M., and Berthelier, J. J. (2008). Spacecraft Observations of Electromagnetic Perturbations Connected with Seismic Activity. *Geophys. Res. Lett.* 35 (5), 5109. doi:10.1029/2007GL032517

Ohta, K., Izutsu, J., Schekotov, A., and Hayakawa, M. (2013). The ULF/ELF Electromagnetic Radiation before the 11 March 2011 Japanese Earthquake. *Radio Sci.* 48 (5), 589–596. doi:10.1002/rds.20064

Oikonomou, C., Haralambous, H., and Muslim, B. (2016). Investigation of Ionospheric TEC Precursors Related to the M7.8 Nepal and M8.3 Chile Earthquakes in 2015 Based on Spectral and Statistical Analysis. *Nat. Hazards* 83 (1), 97–116. doi:10.1007/s11069-016-2409-7

Olaiz, A. J., Muñoz-Martín, A., De Vicente, G., Vegas, R., and Cloetingh, S. (2009). European Continuous Active Tectonic Strain-Stress Map. *Tectonophysics* 474 (1–2), 33–40. doi:10.1016/j.tecto.2008.06.023

Omori, Y., Nagahama, H., Kawada, Y., Yasuoka, Y., Ishikawa, T., Tokonami, S., et al. (2009). Preseismic Alteration of Atmospheric Electrical Conditions Due to Anomalous Radon Emanation. *Phys. Chem. Earth, Parts A/B/C* 34 (6–7), 435–440. doi:10.1016/j.pce.2008.08.001

Ondoh, T. (2003). Anomalous Sporadic-E Layers Observed before M7.2 Hyogo-Ken Nanbu Earthquake; Terrestrial Gas Emanation Model. *Adv. Polar Upper Atmosphere Res.* 17, 96–108. doi:10.15094/00006365

Ondoh, T., and Hayakawa, M. (2006). Synthetic Study of Precursory Phenomena of the M7.2 Hyogo-Ken Nanbu Earthquake. *Phys. Chem. Earth, Parts A/B/C* 31 (4–9), 378–388. doi:10.1016/j.pce.2006.02.017

Ondoh, T. (2009). Investigation of Precursory Phenomena in the Ionosphere, Atmosphere and Groundwater before Large Earthquakes of M>6.5. *Adv. Space Res.* 43 (2), 214–223. doi:10.1016/j.asr.2008.04.003

Ouzounov, D., and Freund, F. (2004). Mid-infrared Emission Prior to strong Earthquakes Analyzed by Remote Sensing Data. *Adv. Space Res.* 33 (3), 268–273. doi:10.1016/S0273-1177(03)00486-1

Ouzounov, D., Liu, D., Chunli, K., Cervone, G., Kafatos, M., and Taylor, P. (2007). Outgoing Long Wave Radiation Variability from IR Satellite Data Prior to Major Earthquakes. *Tectonophysics* 431 (1–4), 211–220. doi:10.1016/j.tecto.2006.05.042

Ouzounov, D., Pulinets, S., Cervone, G., Singh, R., and Taylor, P. (2005). *Atmospheric Processes in Reaction of Northern Sumatra Earthquake Sequence Dec 2004-Apr 2005*. New Orleans: AGU Spring Meeting Abstracts.

Ouzounov, D., Pulinets, S., Hatori, K., and Taylor, P. (2018). *Pre-Earthquake Processes: A Multidisciplinary Approach to Earthquake Prediction Studies*. Hoboken: John

Wiley & Sons. Available at: https://www.wiley.com/en-us/Pre+Earthquake+Processes%3A+A+Multidisciplinary+Approach+to+Earthquake+Prediction+Studies-p-9781119156932

Ouzounov, D., Pulinets, S., Romanov, A., Romanov, A., Tsybulya, K., Davidenko, D., et al. (2011). Atmosphere-ionosphere Response to the M9 Tohoku Earthquake Revealed by Multi-Instrument Space-Borne and Ground Observations: Preliminary Results. *Earthq. Sci.* 24 (6), 557–564. doi:10.1007/s11589-011-0817-z

Oyama, K.-I., Devi, M., Ryu, K., Chen, C. H., Liu, J. Y., Liu, H., et al. (2016). Modifications of the Ionosphere Prior to Large Earthquakes: Report from the Ionosphere Precursor Study Group. *Geosci. Lett.* 3 (1), 6. doi:10.1186/s40562-016-0038-3

Park, C. G., and Dejnakarintra, M. (1973). Penetration of Thundercloud Electric fields into the Ionosphere and Magnetosphere: 1. Middle and Subauroral Latitudes. *J. Geophys. Res.* 78 (28), 6623–6633. doi:10.1029/ja078i028p06623

Parrot, M. (1994). Statistical Study of ELF/VLF Emissions Recorded by a Low-Altitude Satellite during Seismic Events. *J. Geophys. Res. Space Phys.* 99 (12), 23339–23347. doi:10.1029/94JA02072

Parrot, M. (2018). "DEMETER Satellite and Detection of Earthquake Signals," in *Natural Hazards: Earthquakes, Volcanoes, and Landslides*. Editors R. Singh and D. Bartlett (New York: CRC Press), 115–138. doi:10.1201/9781315166841-6

Parrot, M., Lefeuvre, F., Parrot, M., and Lefeuvre, F. (1985). Correlation between GEOS VLF Emissions and Earthquakes. *AnGeo* 3, 737–747. https://ui.adsabs.harvard.edu/abs/1985AnGeo...3..737P/abstract.

Parrot, M., and Li, M. (2015). DEMETER Results Related to Seismic Activity. *Radio Sci. Bull.* 355, 18–25. https://www.ursi.org/content/RSB/RSB_355_2015_12.pdf.

Parrot, M., and Li, M. (2018). "Statistical Analysis of the Ionospheric Density Recorded by the DEMETER Satellite during Seismic Activity," in *Pre-Earthquake Processes: A Multidisciplinary Approach to Earthquake Prediction Studies*. Editors D. Ouzounov, S. Pulinets, K. Hattori, and P. Taylor (Hoboken: John Wiley & Sons - American Geophysical Union (AGU)), 319–328. doi:10.1002/9781119156949.ch18

Parrot, M., and Mogilevsky, M. M. (1989). VLF Emissions Associated with Earthquakes and Observed in the Ionosphere and the Magnetosphere. *Phys. Earth Planet. Interiors* 57 (1–2), 86–99. doi:10.1016/0031-9201(89)90218-5

Parrot, M., and Pinçon, J.-L. (2020). Is There an Earthquake Weather? *Ojer* 09 (02), 69–82. doi:10.4236/ojer.2020.92005

Parrot, M. (2013). "Satellite Observations of Ionospheric Perturbations Related to Seismic Activity," in *Earthquake Prediction Stud. Seismo Electromagnetics*. Editor M. Hayakawa (Tokyo: TERRAPUB), 1–16.

Parrot, M. (2012). Statistical Analysis of Automatically Detected Ion Density Variations Recorded by DEMETER and Their Relation to Seismic Activity. *Ann. Geophys.* 55 (1), 149–155. doi:10.4401/ag-5270

Parrot, M. (2011). Statistical Analysis of the Ion Density Measured by the Satellite DEMETER in Relation with the Seismic Activity. *Earthq. Sci.* 24 (6), 513–521. doi:10.1007/s11589-011-0813-3

Parrot, M. (2002). The Micro-satellite DEMETER. *J. Geodynamics* 33 (4–5), 535–541. doi:10.1016/S0264-3707(02)00014-5

Parrot, M., Tramutoli, V., Liu, T. J. Y., Pulinets, S., Ouzounov, D., Genzano, N., et al. (2021). Atmospheric and Ionospheric Coupling Phenomena Associated with Large Earthquakes. *Eur. Phys. J. Spec. Top.* 230 (1), 197–225. doi:10.1140/epjst/e2020-000251-3

Perrone, L., Korsunova, L. P., and Mikhailov, A. V. (2010). Ionospheric Precursors for Crustal Earthquakes in Italy. *Ann. Geophys.* 28 (4), 941–950. doi:10.5194/angeo-28-941-2010

Phanikumar, D. V., Maurya, A. K., Kumar, K. N., Venkatesham, K., Singh, R., Sharma, S., et al. (2018). Anomalous Variations of VLF Sub-ionospheric Signal and Mesospheric Ozone Prior to 2015 Gorkha Nepal Earthquake. *Sci. Rep.* 8 (1), 1–9. doi:10.1038/s41598-018-27659-9

Picozza, P., Battiston, R., Ambrosi, G., Bartocci, S., Basara, L., Burger, W. J., et al. (2019). Scientific Goals and In-Orbit Performance of the High-Energy Particle Detector on Board the CSES. *ApJS* 243 (1), 16. doi:10.3847/1538-4365/ab276c

Pierce, E. T. (1976). Atmospheric Electricity and Earthquake Prediction. *Geophys. Res. Lett.* 3 (3), 185–188. doi:10.1029/GL003i003p00185

Piersanti, M., Materassi, M., Battiston, R., Carbone, V., Cicone, A., D'Angelo, G., et al. (2020). Magnetospheric-Ionospheric-Lithospheric Coupling Model. 1: Observations during the 5 August 2018 Bayan Earthquake. *Remote Sensing* 12 (20), 3299. doi:10.3390/rs12203299

Píša, D., Němec, F., Santolík, O., Parrot, M., and Rycroft, M. (2013). Additional Attenuation of Natural VLF Electromagnetic Waves Observed by the DEMETER Spacecraft Resulting from Preseismic Activity. *J. Geophys. Res. Space Phys.* 118 (8), 5286–5295. doi:10.1002/jgra.50469

Píša, D., Parrot, M., and Santolík, O. (2011). Ionospheric Density Variations Recorded before the 2010 Mw 8.8 Earthquake in Chile. *J. Geophys. Res. Space Phys.* 116 (8), 8309. doi:10.1029/2011JA016611

Piscini, A., De Santis, A., Marchetti, D., and Cianchini, G. (2017). A Multi-Parametric Climatological Approach to Study the 2016 Amatrice-Norcia (Central Italy) Earthquake Preparatory Phase. *Pure Appl. Geophys.* 174 (10), 3673–3688. doi:10.1007/s00024-017-1597-8

Pritchard, M. E., Allen, R. M., Becker, T. W., Behn, M. D., Brodsky, E. E., Bürgmann, R., et al. (2020). "New Opportunities to Study Earthquake Precursors. *Seismol. Res. Letters.* 91, 2444–2447. doi:10.1785/0220200089

Pulinets, S. A., Ouzounov, D., Karelin, A. V., Boyarchuk, K. A., and Pokhmelnykh, L. A. (2006). The Physical Nature of thermal Anomalies Observed before strong Earthquakes. *Phys. Chem. Earth, Parts A/B/C* 31 (4–9), 143–153. doi:10.1016/j.pce.2006.02.042

Pulinets, S., and Boyarchuk, K. (2005). "Ionospheric Precursors of Earthquakes," in *Ionospheric Precursors of Earthquakes* (Berlin: Springer), 1–315. doi:10.1007/b137616

Pulinets, S. (2012). Low-latitude Atmosphere-Ionosphere Effects Initiated by strong Earthquakes Preparation Process. *Int. J. Geophys.* 2012, 1–14. doi:10.1155/2012/131842

Pulinets, S., Ouzounov, D., Karelin, A., and Davidenko, D. (2018). Lithosphere-Atmosphere-Ionosphere-Magnetosphere Coupling-A Concept for Pre-earthquake Signals Generation. *Preâ€Earthquake Processes: A Multidisciplinary Approach to Earthquake Prediction Studies*. Editors D. Ouzounov, S. Pulinets, K. Hattori, and P. Taylor (Hoboken: John Wiley & Sons), 77–98. doi:10.1002/9781119156949.ch6

Pulinets, S., and Ouzounov, D. (2011). Lithosphere-Atmosphere-Ionosphere Coupling (LAIC) Model - an Unified Concept for Earthquake Precursors Validation. *J. Asian Earth Sci.* 41 (4–5), 371–382. doi:10.1016/j.jseaes.2010.03.005

Pulinets, S., and Ouzounov, D. (2018). *The Possibility of Earthquake Forecasting: Learning from Nature*. Bristol: IOP Publishing. doi:10.1088/978-0-7503-1248-6

Qin, K., Wu, L., De Santis, A., and Wang, H. (2011). Surface Latent Heat Flux Anomalies before the M S 7.1 New Zealand Earthquake 2010. *Chin. Sci. Bull.* 56, 3273–3280. doi:10.1007/s11434-011-4680-z

Qin, K., Wu, L. X., De Santis, A., and Cianchini, G. (2012). Preliminary Analysis of Surface Temperature Anomalies that Preceded the Two Major Emilia 2012 Earthquakes (Italy). *Annal. Geophys.* 55, 4. doi:10.4401/ag-6123

Qin, K., Zheng, S., Wu, L., and Wang, Y. (2021). Quasi-synchronous Multi-Parameter Anomalies before Wenchuan and Yushu Earthquakes in China. *Eur. Phys. J. Spec. Top.* 230 (1), 263–274. doi:10.1140/epjst/e2020-000253-3

Reddy, D. V., and Nagabhushanam, P. (2011). Groundwater Electrical Conductivity and Soil Radon Gas Monitoring for Earthquake Precursory Studies in Koyna, India. *Appl. Geochem.* 26 (5), 731–737. doi:10.1016/j.apgeochem.2011.01.031

Rikitake, T. (1987). Earthquake Precursors in Japan: Precursor Time and Detectability. *Tectonophysics* 136 (3–4), 265–282. doi:10.1016/0040-1951(87)90029-1

Rodger, C. J., Clilverd, M. A., and McCormick, R. J. (2003). Significance of Lightning-Generated Whistlers to Inner Radiation belt Electron Lifetimes. *J. Geophys. Res.* 108 (A12), 1462. doi:10.1029/2003JA009906

Rozhnoi, A., Solovieva, M., and Hayakawa, M. (2013). *Earthquake Prediction Studies: Seismo Electromagnetics*. Tokyo: TERRAPUB, 31–48.VLF/LF Signals Method for Searching of Electromagnetic Earthquake Precursors

Rulenko, O. P. (2000). Operative Precursors of Earthquakes in the Near-Ground Atmosphere Electricity. *J. Volcanol. Seismol.* 4, 57–68.

Ryu, K., Lee, E., Chae, J. S., Parrot, M., and Pulinets, S. (2014). Seismo-ionospheric Coupling Appearing as Equatorial Electron Density Enhancements Observed *via* DEMETER Electron Density Measurements. *J. Geophys. Res. Space Phys.* 119, 8524–8542. doi:10.1002/2014JA020284

Ryu, K., Oyama, K.-I., Bankov, L., Chen, C.-H., Devi, M., Liu, H., et al. (2016). Precursory Enhancement of EIA in the Morning Sector: Contribution from

Mid-latitude Large Earthquakes in the north-east Asian Region. *Adv. Space Res.* 57 (1), 268–280. doi:10.1016/j.asr.2015.08.030

Sauvaud, J.-A., Maggiolo, R., Jacquey, C., Parrot, M., Berthelier, J.-J., Gamble, R. J., et al. (2008). Radiation belt Electron Precipitation Due to VLF Transmitters: Satellite Observations. *Geophys. Res. Lett.* 35 (9), 9101. doi:10.1029/2008GL033194

Schekotov, A., Fedorov, E., Hobara, Y., and Hayakawa, M. (2013). ULF Magnetic Field Depression as a Possible Precursor to the 2011/3.11 Japan Earthquake. *Jae* 33 (1), 41–51. doi:10.1541/jae.33.41

Scholz, C. H. (2019). "Earthquake Prediction and hazard Analysis," in *The Mechanics of Earthquakes and Faulting*. 3rd Edn. (Cambridge: Cambridge University Press), 337–380.

Scholz, C. H. (2002). *The Mechanics of Earthquakes and Faulting*. 2nd Edn. Cambridge: Cambridge University Press. doi:10.1017/cbo9780511818516

Serebryakova, O. N., Bilichenko, S. V., Chmyrev, V. M., Parrot, M., Rauch, J. L., Lefeuvre, F., et al. (1992). Electromagnetic ELF Radiation from Earthquake Regions as Observed by Low-Altitude Satellites. *Geophys. Res. Lett.* 19 (2), 91–94. doi:10.1029/91GL02775

Sgrigna, V., Buzzi, A., Conti, L., Picozza, P., Stagni, C., and Zilpimiani, D. (2007). Seismo-induced Effects in the Near-Earth Space: Combined Ground and Space Investigations as a Contribution to Earthquake Prediction. *Tectonophysics* 431 (1–4), 153–171. doi:10.1016/j.tecto.2006.05.034

Sgrigna, V., Buzzi, A., Conti, L., Picozza, P., Stagni, C., and Zilpimiani, D. (2008). The ESPERIA Satellite Project for Detecting Seismo-Associated Effects in the Topside Ionosphere. First Instrumental Tests in Space. *Earth Planet. Sp* 60 (5), 463–475. doi:10.1186/BF03352813

Sgrigna, V., Carota, L., Conti, L., Corsi, M., Galper, A. M., Koldashov, S. V., et al. (2005a). Correlations between Earthquakes and Anomalous Particle Bursts from SAMPEX/PET Satellite Observations. *J. Atmos. Solar-Terrestrial Phys.* 67 (15), 1448–1462. doi:10.1016/j.jastp.2005.07.008

Sgrigna, V., Console, R., Conti, L., Galper, A. M., Malvezzi, V., Parrot, M., et al. (2005b). "The ESPERIA Project: A mission to Investigate the Near-Earth Space," in *Earth Observation with CHAMP: Results from Three Years in Orbit* (Berlin: Springer-Verlag), 407–412. doi:10.1007/3-540-26800-6_65

Shapiro, S. A., Huenges, E., and Borm, G. (1997). Estimating the Crust Permeability from Fluid-Injection-Induced Seismic Emission at the KTB Site. *Geophys. J. Int.* 131 (2), F15–F18. doi:10.1111/j.1365-246X.1997.tb01215.x

Sharma, G., Saikia, P., Walia, D., Banerjee, P., and Raju, P. L. N. (2021). TEC Anomalies Assessment for Earthquakes Precursors in North-Eastern India and Adjoining Region Using GPS Data Acquired during 2012-2018. *Quat. Int.* 575-576 (576), 120–129. doi:10.1016/j.quaint.2020.07.009

Shen, X., Zhang, X., Yuan, S., Wang, L., Cao, J., Huang, J., et al. (2018). The State-Of-The-Art of the China Seismo-Electromagnetic Satellite mission. *Sci. China Technol. Sci.* 61 (5), 634–642. doi:10.1007/s11431-018-9242-0

Smirnova, N., Hayakawa, M., Gotoh, K., and Volobuev, D. (2001). Scaling Characteristics of ULF Geomagnetic fields at the Guam Seismoactive Area and Their Dynamics in Relation to the Earthquake. *Nat. Hazards Earth Syst. Sci.* 1 (3), 119–126. doi:10.5194/nhess-1-119-2001

Sorokin, V. M., and Chmyrev, V. M. (1999). "Modification of the Ionosphere by Seismic Related Electric Field," in *Atmospheric and Ionospheric Electromagnetic Phenomena Associated with Earthquakes*. Editor M. Hayakawa (Tokyo: Terra Sci. Publ. Co.), 805–818.

Sorokin, V. M., Chmyrev, V. M., and Yaschenko, A. K. (2001). Electrodynamic Model of the Lower Atmosphere and the Ionosphere Coupling. *J. Atmos. Solar-Terrestrial Phys.* 63 (16), 1681–1691. doi:10.1016/s1364-6826(01)00047-5

Sorokin, V. M., Isaev, N. V., Yaschenko, A. K., Chmyrev, V. M., and Hayakawa, M. (2005). Strong DC Electric Field Formation in the Low Latitude Ionosphere over Typhoons. *J. Atmos. Solar-Terrestrial Phys.* 67 (14), 1269–1279. doi:10.1016/j.jastp.2005.06.014

Sotgiu, A., De Donato, C., Fornaro, C., Tassa, S., Scannavini, M., Iannaccio, D., et al. (2021). Control and Data Acquisition Software of the High-energy Particle Detector on Board the China Seismo-Electromagnetic Satellite Space mission. *Softw. Pract. Exper* 51 (6), 1459–1480. doi:10.1002/spe.2947

Tanimoto, T., Heki, K., and Artru-Lambin, J. (2015).Interaction of Solid Earth, Atmosphere, and Ionosphere. *Treatise Geophys.* 4. 421–443. doi:10.1016/B978-0-444-53802-4.00083-X

Teng, T.-l., Sun, L.-f., and McRaney, J. K. (1981). Correlation of Groundwater Radon Anomalies with Earthquakes in the Greater Palmdale Bulge Area. *Geophys. Res. Lett.* 8 (5), 441–444. doi:10.1029/GL008i005p00441

Thomas, J. N., Love, J. J., Komjathy, A., Verkhoglyadova, O. P., Butala, M., and Rivera, N. (2012). On the Reported Ionospheric Precursor of the 1999 Hector Mine, California Earthquake. *Geophys. Res. Lett.* 39 (6), a–n. doi:10.1029/2012GL051022

Toledo-Redondo, S., Parrot, M., and Salinas, A. (2012). Variation of the First Cut-Off Frequency of the Earth-Ionosphere Waveguide Observed by DEMETER. *J. Geophys. Res.* 117 (4), a–n. doi:10.1029/2011JA017400

Tozzi, R., Masci, F., and Pezzopane, M. (2020). A Stress Test to Evaluate the Usefulness of Akaike Information Criterion in Short-Term Earthquake Prediction. *Sci. Rep.* 10 (1), 1–9. doi:10.1038/s41598-020-77834-0

Tramutoli, V., Aliano, C., Corrado, R., Filizzola, C., Genzano, N., Lisi, M., et al. (2013). On the Possible Origin of thermal Infrared Radiation (TIR) Anomalies in Earthquake-Prone Areas Observed Using Robust Satellite Techniques (RST). *Chem. Geology.* 339, 157–168. doi:10.1016/j.chemgeo.2012.10.042

Tramutoli, V., Corrado, R., Filizzola, C., Genzano, N., Lisi, M., and Pergola, N. (2015). From Visual Comparison to Robust Satellite Techniques: 30 Years of thermal Infrared Satellite Data Analyses for the Study of Earthquake Preparation Phases. *Bollettino Di Geofisica Teorica e Applicata* 56 (2), 167–202. Available at: http://www3.ogs.trieste.it/bgta/provapage.php?id_articolo=654.

Tramutoli, V., Cuomo, V., Filizzola, C., Pergola, N., and Pietrapertosa, C. (2005). Assessing the Potential of thermal Infrared Satellite Surveys for Monitoring Seismically Active Areas: The Case of Kocaeli (İzmit) Earthquake, August 17, 1999. *Remote Sensing Environ.* 96 (3–4), 409–426. doi:10.1016/j.rse.2005.04.006

Tramutoli, V. (1998). Robust AVHRR Techniques (RAT) for Environmental Monitoring: Theory and Applications. *Earth Surf. Remote Sensing* 3496, 101–113.

Tramutoli, V. (2007). "Robust Satellite Techniques (RST) for Natural and Environmental Hazards Monitoring and Mitigation: Theory and Applications." in Proceedings of MultiTemp 2007 - 2007 International Workshop on the Analysis of Multi-Temporal Remote Sensing Images (Leuven: IEEE), 1–6. doi:10.1109/MULTITEMP.2007.4293057

Tronin, A. A. (2006). Remote Sensing and Earthquakes: A Review. *Phys. Chem. Earth, Parts A/B/C* 31 (4–9), 138–142. doi:10.1016/j.pce.2006.02.024

Uchida, N., and Bürgmann, R. (2021). A Decade of Lessons Learned from the 2011 Tohoku-Oki Earthquake. *Rev. Geophys.* 59 (2), e2020RG000713. doi:10.1029/2020rg000713

Venkatanathan, N., and Natyaganov, V. (2014). Outgoing Longwave Radiations as Pre-earthquake Signals: Preliminary Results of 24 September 2013 (M 7.7) Earthquake. *Curr. Sci.* 106 (9), 1291–1297. Available at: http://www.jstor.org/stable/24102346.

Vershinin, E. F., Buzevich, A. V., Yumoto, K., Saita, K., and Tanaka, Y. (1999). "Correlations of Seismic Activity with Electromagnetic Emissions and Variations in Kamchatka Region," in *Atmospheric and Ionospheric Electromagnetic Phenomena Associated with Earthquakes* (Tokyo: Terra Scientific Publishing Company), 513–517.

Voronov, S. A. (1990). Increases in High Energy Charged Particle Fluxes Near the South Atlantic Magnetic Anomaly and the Seismicity of the Earth. *Cosmic Res.* 28, 789–791.

Wakita, H., Nakamura, Y., Notsu, K., Noguchi, M., and Asada, T. (1980). Radon Anomaly: A Possible Precursor of the 1978 Izu-Oshima-Kinkai Earthquake. *Science* 207 (4433), 882–883. doi:10.1126/science.207.4433.882

Wang, L., and Burgmann, R. (2019). Statistical Significance of Precursory Gravity Changes before the 2011 M W 9.0 Tohoku-Oki Earthquake. *Geophys. Res. Lett.* 46 (13), 7323–7332. doi:10.1029/2019GL082682

Warden, S., MacLean, L., Lemon, J., and Schneider, D. (2020). Statistical Analysis of Pre-earthquake Electromagnetic Anomalies in the ULF Range. *J. Geophys. Res. Space Phys.* 125 (10), e2020JA027955. doi:10.1029/2020JA027955

Weiyu, M., Xuedong, Z., Liu, J., Yao, Q., Zhou, B., Yue, C., et al. (2018). Influences of Multiple Layers of Air Temperature Differences on Tidal Forces and Tectonic Stress before, during and after the Jiujiang Earthquake. *Remote Sensing Environ.* 210, 159–165. doi:10.1016/j.rse.2018.03.003

Woith, H. (2015). Radon Earthquake Precursor: A Short Review. *Eur. Phys. J. Spec. Top.*, 224, 611–627. doi:10.1140/epjst/e2015-02395-9

Xiong, P., Long, C., Zhou, H., Battiston, R., Zhang, X., and Shen, X. (2020). Identification of Electromagnetic Pre-earthquake Perturbations from the DEMETER Data by Machine Learning. *Remote Sensing* 12 (21), 3643. doi:10.3390/rs12213643

Xiong, P., Shen, X. H., Bi, Y. X., Kang, C. L., Chen, L. Z., Jing, F., et al. (2010). Study of Outgoing Longwave Radiation Anomalies Associated with Haiti Earthquake. *Nat. Hazards Earth Syst. Sci.* 10 (10), 2169–2178. doi:10.5194/nhess-10-2169-2010

Xiong, P., Tong, L., Zhang, K., Shen, X., Battiston, R., Ouzounov, D., et al. (2021). Towards Advancing the Earthquake Forecasting by Machine Learning of Satellite Data. *Sci. Total Environ.* 771, 145256. doi:10.1016/j.scitotenv.2021.145256

Xiong, Z. (1992). Electromagnetic Modeling of 3-D Structures by the Method of System Iteration Using Integral Equations. *Geophysc.* 57 (12), 1556–1561. doi:10.1190/1.1443223

Xu, X., Sandwell, D. T., and Smith-Konter, B. (2020). Coseismic Displacements and Surface Fractures from sentinel-1 InSAR: 2019 Ridgecrest Earthquakes. *Seismological Res. Lett.* 91 (4), 1979–1985. doi:10.1785/0220190275

Xuhui, S., Zhima, Z., Jianping, H., Yanyan, Y., Shufan, Z., Rui, Y. A. N., et al. (2020). Current Status and Main Scientific Results of In-Flight CSES Mission. *Chin. J. Space Sci.* 40 (5), 662. doi:10.11728/cjss2020.05.662

Yan, R., Guan, Y., Guan, Y., Shen, X., Huang, J., Zhang, X., et al. (2018a). The Langmuir Probe Onboard CSES: Data Inversion Analysis Method and First Results. *Earth Planet. Phys.* 2 (6), 1–10. doi:10.26464/epp2018046

Yan, R., Parrot, M., and Pinçon, J.-L. (2017). Statistical Study on Variations of the Ionospheric Ion Density Observed by DEMETER and Related to Seismic Activities. *J. Geophys. Res. Space Phys.* 122 (12), 421–12,429. doi:10.1002/2017JA024623

Yan, R., Shen, X., Shen, X., Huang, J., Wang, Q., Chu, W., et al. (2018b). Examples of Unusual Ionospheric Observations by the CSES Prior to Earthquakes. *Earth Planet. Phys.* 2 (6), 515–526. doi:10.26464/epp2018050

Yang, S. S., Asano, T., and Hayakawa, M. (2019). Abnormal Gravity Wave Activity in the Stratosphere Prior to the 2016 Kumamoto Earthquakes. *J. Geophys. Res. Space Phys.* 124 (2), 1410–1425. doi:10.1029/2018JA026002

Zhai, D., Zhang, X., and Xiong, P. (2020). Detecting thermal Anomalies of Earthquake Process within Outgoing Longwave Radiation Using Time Series Forecasting Models. *Ann. Geophys.* 63 (5), 1–18. doi:10.4401/ag-8057

Zhang, K., Li, X., Zhao, H., Schiller, Q., Khoo, L. Y., Xiang, Z., et al. (2019). Cosmic Ray Albedo Neutron Decay (CRAND) as a Source of Inner Belt Electrons: Energy Spectrum Study. *Geophys. Res. Lett.* 46 (2), 544–552. doi:10.1029/2018GL080887

Zhang, X., Chen, H., Liu, J., Shen, X., Miao, Y., Du, X., et al. (2012). Ground-based and Satellite DC-ULF Electric Field Anomalies Around Wenchuan M8.0 Earthquake. *Adv. Space Res.* 50 (1), 85–95. doi:10.1016/j.asr.2012.03.018

Zhang, X., Shen, X., Zhao, S., Yao, L., Ouyang, X., and Qian, J. (2014). The Characteristics of Quasistatic Electric Field Perturbations Observed by DEMETER Satellite before Large Earthquakes. *J. Asian Earth Sci.* 79 (PA), 42–52. doi:10.1016/j.jseaes.2013.08.026

Zhang, X., Zeren, Z., Parrot, M., Battiston, R., Qian, J., and Shen, X. (2011). ULF/ELF Ionospheric Electric Field and Plasma Perturbations Related to Chile Earthquakes. *Adv. Space Res.* 47 (6), 991–1000. doi:10.1016/j.asr.2010.11.001

Zhang, X., Zhao, S., Song, R., and Zhai, D. (2019). The Propagation Features of LF Radio Waves at Topside Ionosphere and Their Variations Possibly Related to Wenchuan Earthquake in 2008. *Adv. Space Res.* 63 (11), 3536–3544. doi:10.1016/j.asr.2019.02.008

Zhang, Y., Guo, X., Zhong, M., Shen, W., Li, W., and He, B. (2010). Wenchuan Earthquake: Brightness Temperature Changes from Satellite Infrared Information. *Chin. Sci. Bull.* 55 (18), 1917–1924. doi:10.1007/s11434-010-3016-8

Zhang, Y., and Meng, Q. (2019). A Statistical Analysis of TIR Anomalies Extracted by RSTs in Relation to an Earthquake in the Sichuan Area Using MODIS LST Data. *Nat. Hazards Earth Syst. Sci.* 19 (3), 535–549. doi:10.5194/nhess-19-535-2019

Zhao, B., Wang, M., Yu, T., Wan, W., Lei, J., Liu, L., et al. (2008). Is an Unusual Large Enhancement of Ionospheric Electron Density Linked with the 2008 Great Wenchuan Earthquake? *J. Geophys. Res.* 113 (11), a–n. doi:10.1029/2008JA013613

Zhao, D., Qu, C., Shan, X., Gong, W., Zhang, Y., and Zhang, G. (2018). InSAR and GPS Derived Coseismic Deformation and Fault Model of the 2017 Ms7.0 Jiuzhaigou Earthquake in the Northeast Bayanhar Block. *Tectonophysics* 726, 86–99. doi:10.1016/j.tecto.2018.01.026

Zhu, K., Li, K., Fan, M., Chi, C., and Yu, Z. (2019). Precursor Analysis Associated with the Ecuador Earthquake Using Swarm A and C Satellite Magnetic Data Based on PCA. *IEEE Access* 7, 93927–93936. doi:10.1109/ACCESS.2019.2928015

Zhu, K., Zheng, L., Yan, R., Shen, X., Zeren, Z., Xu, S., et al. (2021). Statistical Study on the Variations of Electron Density and Temperature Related to Seismic Activities Observed by CSES. *Nat. Hazards Res.* 2 (1). doi:10.1016/j.nhres.2021.06.001

Zlotnicki, J., Li, F., and Parrot, M. (2013). Ionospheric Disturbances Recorded by DEMETER Satellite over Active Volcanoes: From August 2004 to December 2010. *Int. J. Geophys.* 2013, 1–17. doi:10.1155/2013/530865

Zlotnicki, J., Li, F., and Parrot, M. (2010). Signals Recorded by DEMETER Satellite over Active Volcanoes during the Period 2004 August-2007 December. *Geophys. J. Int.* 183 (3), 1332–1347. doi:10.1111/j.1365-246X.2010.04785.x

Conflict of Interest: The authors declare that the research was conducted in the absence of any commercial or financial relationships that could be construed as a potential conflict of interest.

frontiers
in Earth Science

ORIGINAL RESEARCH
published: 05 August 2021
doi: 10.3389/feart.2021.673105

West Pacific Earthquake Forecasting Using NOAA Electron Bursts With Independent *L*-Shells and Ground-Based Magnetic Correlations

Cristiano Fidani*

Central Italy Electromagnetic Network, Fermo, Italy

Recent advances in statistical correlations between strong earthquakes and several non-seismic phenomena have opened the possibility of formulating warnings within days or even hours. The retrieved correlations have been discovered for those ionospheric physical observations which lasted a long time and realized using the same instruments, including multi-satellite recordings. One of those regarded the electron burst phenomena detected by NOAA, for which the conditional probability of a seismic event was calculated. Then an earthquake probability greater than its frequency was assigned when a satellite realized such a phenomenological observation. This approach refers to the correlations obtained between high-energy electrons detected using the NOAA POES and strong Indonesian and Philippine earthquakes. It is reformulated here to realize a test of earthquake forecasting. The fundamental step is obtained by using a unique electron *L*-shell interval of $1.21 \leq L \leq 1.31$, which decouples the electron parameters from the earthquake parameters. Then, the optimized correlation was recalculated to be 1.5–3.5 h early, between electron bursts and an increased number of seismic events with $M \geq 6$, therein improving the significance too. Moreover, this methodology is reconnected to the frequency theory, and to Molchan's error diagram, by the probability gain, where a comparison among the significances of various methods is given. The previously proposed physical link between the crust and the ionosphere through magnetic interaction, presumably operating 4–6 h before strong earthquakes, is examined quantitatively on the basis of recent magnetic pulse measurements. Consequently, the probability gain of earthquake forecasting is hypothetically calculated for both the dependent measurements of electron bursts using NOAA satellites and possible ground-based magnetic pulse detection. This method of combining probability gains for earthquake forecasting is general enough that it can be applied to any pair of observables from space and the ground.

Keywords: strong earthquakes, near-seismic precursors, electron bursts, magnetic pulses, ionosphere, statistical correlations, probability gain

OPEN ACCESS

Edited by:
Dimitar Ouzounov,
Chapman University, United States

Reviewed by:
Sergey Alexander Pulinets,
Space Research Institute (RAS), Russia
Dedalo Marchetti,
Jilin University, China

***Correspondence:**
Cristiano Fidani
c.fidani@virgilio.it

Specialty section:
This article was submitted to Environmental Informatics and Remote Sensing, a section of the journal Frontiers in Earth Science

Received: *03 March 2021*
Accepted: *16 June 2021*
Published: *05 August 2021*

Citation:
Fidani C (2021) West Pacific Earthquake Forecasting Using NOAA Electron Bursts With Independent L-Shells and Ground-Based Magnetic Correlations. Front. Earth Sci. 9:673105. doi: 10.3389/feart.2021.673105

INTRODUCTION

Different phenomena, possibly connected with seismic activity, have been reported in recent years by many authors researching anomalies, both geoscientific (Rikitake, 1976; Rikitake, 1987) and macroscopic (Rikitake, 2003). Their research has reported instrumentally repeated observations occurring with strong earthquakes (EQs), and this has permitted them to identify important statistical behavior (Rikitake, 2003). However, in the absence of a recording network, almost all the results are dependent on individual properties of recording, and this renders it rather difficult to obtain an estimation on reasonable statistics (Molchanov and Hayakawa, 2008). The limited number of observatories on the ground and their punctual observations, even when operative (Console, 2001), reduce the number of considered strong EQs, making it too small to calculate a statistical correlation over several decades. Only when moderate magnitude EQs are considered, a statistical correlation is currently calculated for ULF geomagnetic fluctuations at ground stations (Schekotov et al., 2006; Hattori et al., 2013; Han et al., 2014; Han et al., 2017). In other studies, Pc1 anticipated EQs by 6–7 days (Bortnik et al., 2008), VLF noise by 2 days (Oike and Yamada, 1994), lightning activities 17–19 days before EQs (Liu et al., 2015), and geoelectric fields with lead times from days to weeks (An et al., 2020). A review of several correlation increases corresponding to 3 days between ELF Q-bursts and the Kanchakta EQs has been reported with the possible associated physical models (Hayakawa et al., 2019). A method to predict the time, epicenter, and magnitude of such events has been suggested (Schekotov et al., 2019) based on the works cited above.

Observations made by low-orbit satellites are able to monitor large portions of the ground in a few hours, allowing the monitoring of the area affected by each seismic event (Barnhart et al., 2019), and to consider all, or a large portion, of strong EQs. Satellite detection techniques and communication developments are made using electromagnetic instruments and have therefore been immediately used to monitor electromagnetic fields in the ionosphere. Electromagnetic fields measured in the low Earth orbits were associated with strong EQ occurrence for the first time in the 1980s, with regard to electric and magnetic intensity in the range of 1 Hz–10 kHz, when satellites arrived close to EQ epicentres (Larkina et al., 1983; Parrot and Lefeuvre, 1985; Larkina et al., 1989; Parrot and Mogilevsky, 1989; Mikhaylova et al., 1991; Serebryakova et al., 1992). A space-borne system for short-term EQ warning has been suggested (Pulinets, 1998a; Parrot, 2002; Pulinets, 2006), and as ionospheric perturbations measured using satellites are not only due to EQs and are not found for all EQs, a statistical analysis of a possible influence of the seismic activity on the ionosphere is preferred (Parrot, 2011). Statistical results were obtained in 1993 using the Intercosmos-24 satellite (Molchanov, 1993), where the probability of charged particle burst observations was from 6 to 24 h before the event increased by 50%, and the DE-2 satellite (Henderson et al., 1993), where no significant differences occurred between EQ orbits and control orbits. Moreover, the average wave intensity received on board the AUREOL-3 satellite (Parrot, 1994) increased with seismic activity, resulting in an extension in the latitude direction but not in the longitude, with respect to EQ epicentres. The ISIS 1 and 2 satellites have been used to identify the spectra of electromagnetic radiation of seismic events under control data (Rodger et al., 1996), showing no significant evidence for differences between data sets of the EQs and control orbits. A statistical study of intensity for VLF electromagnetic waves has been realized in the vicinity of EQ epicentres using the micro-satellite DEMETER (Nemec et al., 2008). It has evidenced a significant decrease in the measured wave intensity, 0–4 h before strong EQs. A confirmation of this result, on a longer set of data, was obtained (Nemec et al., 2009), suggesting that a significant decrease is occurring for larger EQs, is stronger for shallower EQs, and does not seem to depend on whether the EQ occurs below an ocean or not.

Anomalies appearing in electron densities of the ionospheric F-region a few days before strong EQs were observed (Pulinets 1998b; Liu et al., 2000; Pulinets and Boyarchuk, 2004; Liu et al., 2006). These anomalies concern the electron densities recorded using local ionosondes, where the critical frequency of the F2-peak, foF2, significantly decreased days before several EQs. Moreover, decreasing electron densities, days before strong EQs in Taiwan, had been compared with the total electron content (TEC) calculated using ground-based GPS receivers and satellite transmitters (Liu et al., 2004). Anomalous TEC signals were observed in Southern California, but no statistically significant correlations regarding time and space between these TEC anomalies and the occurrence of seismic events resulted (Thomas et al., 2007). On the other hand, positive results for the correlation of EQ from 2 to 5 days after TEC fluctuations have been obtained (Li and Parrot, 2013). Study results from Taiwan support the result that the equatorial ionization anomaly crest significantly moves equatorward 1–5 days before strong EQs (Liu et al., 2010). A statistical analysis carried out on TEC data from the global ionosphere map evidenced that the largest occurrence rates of anomalies were for those EQs with larger magnitudes and lower depths 1–5 days before the EQs (Liu et al., 2011; Zhu et al., 2014). This was confirmed by Japanese (Kon et al., 2011) and Chinese (Ke et al., 2016) studies. Vertical TEC positive and negative anomalies aligned parallel with the local geomagnetic field were repeatedly observed 20–40 min before three $M > 8$ Chilean EQs (He and Heki, 2016). Concentrations of electron density and magnetic anomalies for more than two months to some days before the EQ occurrences have been reported worldwide (De Santis et al., 2019). However, a 14-year analysis of data did not reveal any statistically significant changes prior to EQs when considering all of the 1,279 EQs together (Thomas et al., 2017). Using GPS TEC measurements, a statistical analysis and comparison of the temporal and spatial distributions for the pre-EQ ionospheric anomalies before the $1,339\, M \geq 6.0$ EQs, which occurred globally between January 2003 and December 2014, did not provide reliable evidence of pre-EQ changes on the global ionospheric map of TEC data (Zhu et al., 2018).

Ionospheric perturbations with seismic activity have included wave paths of VLF and LF transmitters (Molchanov and

Hayakawa, 1998; Biagi et al., 2001). The VLF and LF amplitude observations are connected with the entire path covered by waves, even if they are obtained in a punctual station, thus representing an intermediate type of observation between the purely punctual and the completely diffused realized using satellites. Seismo-ionospheric effects on long sub-ionospheric paths have been investigated in amplitude variations of signals and have used the VLF terminator time method (Clilverd et al., 1999), indicating that the occurrence rate of successful EQ predictions using it cannot be distinguished with respect to a random one. Statistical results obtained by the superimposed epoch analysis in Japan (Maekawa et al., 2006) yielded that the ionosphere was definitively disturbed in terms of both amplitude and dispersion. For an integrated energy, released within the interested area for the LF wave path, the amplitude is depleted and the dispersion is very much enhanced for about one week to a few days before the EQ. A statistical correlation between EQs and VLF/LF signals over 10 years or so, obtained by means of the Japanese VLF/LF network, revealed perturbations 3–6 days prior to wave paths (Hayakawa et al., 2010).

A correlation analysis between earthquakes and atmospheric temperature variations over several months observed using a portable meteostation obtained a time anticipation of about one day (Molchanov et al., 2003). Consequently, thermal infrared anomalies have also been observed with strong EQs from space. A complete review has reported the main contributions and results achieved over 30 years (Tramutoli et al., 2015). Molchan's error diagram analysis computed for different classes of magnitude and significant sequences of thermal infrared anomalies has suggested a prognostic probability gain when compared to random guess results, both for strong EQs in Greece (Eleftheriou et al., 2016) and in the Sichuan area (Zhang and Meng, 2019).

Sudden variations in high-energy charged particle fluxes near the South Atlantic Anomaly have also been associated with seismic activity (Voronov et al., 1989). In fact, numerous experiments followed the discovery of the Van Allen Belts (Van Allen, 1959) to determine safe conditions for near-Earth space exploration. Further detection of charged particle flux variations associated with strong EQs was obtained using the Intercosmos-24 satellite (Galperin et al., 1992; Boskova et al., 1994), resulting in precipitating particles which escaped the trapped conditions of the geomagnetic field. High-energy precipitating particle fluxes have been statistically analyzed in relation to seismic activity in various near-Earth space experiments such as the MIR orbital station and the METEOR-3, GAMMA, and SAMPEX satellites, which have shown particle bursts 2–5 h before EQs (Aleksandrin et al., 2003). A reanalysis of the more recent and extended SAMPEX database has also shown a 3–4 h correlation with precipitating high-energy electrons anticipating strong EQs (Sgrigna et al., 2005). The NOAA-15 satellite particle database, which has been collecting data since 1998, has been systematically studied (Fidani et al., 2010). Sudden variations in high-energy charged particles have been connected with strong EQs in periods of weak solar activity (Fidani, 2015). This statistical correlation analysis evidenced that exceptional increases in electron fluxes occurring 2–3 h prior to the largest quakes had struck the Indonesian and Philippine investigated areas between 1998 and 2014. The correlated EQs occurred at a depth less than 200 km, independent of sea or land. Precipitating particles have been detected far from EQ geographical positions, so the possible disturbances above the EQ epicenters due to particle drift have been estimated to be in the range of 4–6.5 h before strong seismic events (Fidani, 2018).

Definitely, several studies' results have suggested that ionospheric phenomena appear to statistically precede strong earthquakes by up to a week, and some studies even propose longer anticipation times. However, the demonstration of the physical link between the two phenomena is essential to affirm that one of the two is more than a candidate precursor for the other. Moreover, short-term EQ precursors are thought to precede by 1–2 days to several weeks, and near-seismic precursors are thought to precede by several hours to 1–2 days (Molchanov and Hayakawa, 2008). Therefore, electromagnetic fluctuations detected using satellites both in the ELF and VLF bands, together with particle precipitation, may belong to the class of near-seismic candidate precursors, whereas TEC, together with both VLF and LF path amplitude depletion, and geoelectric ULF fields may belong to the class of short-term candidate precursors. As for ground observations, VLF noise belongs to the class of near-seismic candidate precursors, and Pc1 pulsations and lightning activity may belong to the class of short-term candidate precursors, while ELF Q-bursts, Schumann resonances, and ULF magnetic depressions may belong to both classes. The recent results on EQ observations, carried out using low Earth orbit satellites, can be found in a publication by Ouzounov et al. (2018).

Given the possibility reported above to observe physical phenomena that recurrently, and with statistical significance, anticipate strong EQs, a verification of EQ forecasting has been formulated on the basis of schemes already used, starting from the statistical study of seismicity (Console, 2001). In particular, the previously calculated correlations between NOAA electron precipitations and EQs are examined in the fundamental steps, showing what remains ambiguous for electron identification, in *Reviewing NOAA Electrons' Statistical Correlations*. A reproduction of the statistical correlation between completely decoupled NOAA electron precipitations and EQs, so as to define the precursor phenomenon unambiguously (Wyss, 1997), is obtained in *Unambiguous NOAA Electrons' Statistical Correlation*. NOAA correlations are reviewed using classic statistical frequency techniques, and their statistical significance is calculated using recent methods of error diagrams in *Forecasting Methodologies* and *Evaluating Significance*, where a complete equivalence among these approaches is demonstrated. The objective is to define a methodology to introduce one or more statistically verified precursors in EQ forecasting using conditional probabilities. *Prediction Model* is devoted to building a prediction scenario following the work of Console (2001). A discussion of any possible relevance to the improvement of the probability gain derived from dependent precursors used together, observed both on the Earth's surface and from space, is presented in *Dependent Observables*. Finally, the electron precipitations' possible dependence on magnetic pulses is shown using a physical model in *Different Precursors Combined*, and a hypothetical experiment demonstrates the probability gain due to these two dependent observations. The conclusion is reported in *Conclusion* with a sequence of steps that combine interdependent observations for EQ forecasting.

MATERIALS AND METHODS

To systematically test methodologies of precursors, for which a statistical analysis of past cases is feasible, the conditional probability of occurrence (Aki, 1981) is a desirable parameter that should supplement the usual time–location–magnitude parameters of the prediction (Console, 2001). Several physical observations on the Earth's surface and from space have been successfully correlated with EQs. However, a conditional probability has only been obtained from the analysis of the NOAA satellites' precipitating electrons (Fidani, 2018; Fidani, 2019; Fidani, 2020), so it would be the most suitable methodology to be tested.

Reviewing NOAA Electrons' Statistical Correlations

NOAA polar satellites use particle detectors which monitor fluxes of protons and electrons in polar orbits at altitudes between 807 and 854 km (Davis, 2007). The particle detectors (Space Environment Monitor SEM-2) consist of the total energy detector (TED) and the medium energy proton and electron detector (MEPED). The MEPED is composed of eight solid-state detectors measuring proton and electron fluxes from 30 keV to 200 MeV (Evans and Greer, 2004) which include the radiation belt populations, energetic solar particle events, and the low-energy portion of the galactic cosmic ray population. Data can be downloaded at the link http://www.ngdc.noaa.gov/stp/satellite/poes/dataaccess.html. As all of the sets of orbital parameters are provided every 8 s, this value was chosen as the basic time step for our study (Fidani and Battiston, 2008). Consequently, all other variables were defined with respect to the 8-s step. Thus, 8-s averages of the counting rates (CRs), latitude, longitude, MEPED, and omnidirectional data were calculated. Unreliable CRs with negative values were labeled and excluded from the analysis.

To systematically test the methodology proposed for NOAA data, a quantitative and rigorous definition of the concerned precursor (Console, 2001) was established. The daily averages of particle CRs exiting the entrapment in the geomagnetic field (precipitations) were calculated, and then the condition for which a CR fluctuation was not likely, due to possible statistical fluctuations, was set. This calculation was formulated with a probability larger than 99% (Fidani et al., 2010). The sudden increase in particle flux that satisfies this condition was named particle burst (Sgrigna et al., 2005), and for electrons, the same condition was named electron burst (EB). According to a previous work (Aleksandrin et al., 2003), the daily averages of CRs were calculated in the invariant coordinate space. Together with the *L*-shell and the pitch angle, it was necessary to take into account the CR amplitudes and their variations versus geomagnetic coordinates, since the spatial gradient of particle fluxes near the South Atlantic Anomaly (SAA) is too large (Fidani and Battiston, 2008). CR distributions inside invariant areas are compatible with a Poisson distribution. Being so, an amplitude threshold was introduced for the CRs to define the conditions for which a CR is a non-Poissonian fluctuation with 99% probability. Furthermore, NOAA satellites measure variations of ionospheric parameters not only due to EQs; indeed, they are principally due to solar activity (Sgrigna et al., 2005; Parrot, 2011). To reduce the effects of solar activity, both low values in Dst variations (http://wdc.kugi.kyoto-u.ac.jp/dst_final/index.html) and geomagnetic Ap indexes (https://www.ngdc.noaa.gov/geomag/data.shtml) were chosen to exclude CR data corresponding to the Sun's influence (Fidani, 2015).

To conclude the quantification of the precursor (Console, 2001), the *L*-shell invariant parameter was considered to define the magnetic line where a physical interaction, whatever it is, can connect the seismic and ionospheric activities. Following the works by Aleksandrin et al. (2003) and Sgrigna et al. (2005), particle bursts were considered only when their *L*-shell values referred to $M \geq 6$ EQ epicenter projections that occurred on the magnetic lines. This is equivalent to imagining that the physical interaction can occur in the same region near the vertical. The correlation was calculated by filling a histogram with the time differences Δt between the EQs and EBs, which was indicated by $\sum_{\{EQ;EB\}}(EQ \times EB)$ following the work of Fidani (2015). This approach was performed by considering only EB on magnetic lines identified as projecting EQ coordinates at different altitudes with respect to EQ epicenters, from −600 km up to 3,200 km in increments of 100 km. A correlation peak at $\Delta t = 2-3$ h started to be significant only for 30–100-keV EBs when considering magnetic line altitudes above 1,400 km and was maximized for 2,200 km (Fidani, 2015) (see **Figure 1**). Correlations were maximized by using EQs with magnitudes $M \geq 6$ downloaded at the link https://earthquake.usgs.gov/earthquakes/search/, located in both the Indonesian and the Philippine regions, having 90°–150° longitudes, with few events in South America. The EBs were detected high off the shore of the United States and the west coasts of South America, at longitudes between 200° and 280°. These different electron positions were associated in a causal way, due to the fact that electrons drift eastward and the EQ positions were located west of the EB detection positions (Fidani, 2018; Fidani, 2020). Being so, if the disturbances which caused electron precipitations from inner radiation belts occurred above the EQ epicenters in the ionosphere, they most likely anticipated the EQ times by 4–6.5 h.

However, to consider EB *L*-shells around the *L*-shells corresponding to the EQ epicenter projected at several altitudes constitutes an ambiguity in defining the phenomena that preceded EQs. In fact, the *L*-shell parameter to choose EB involves both EB and EQ events and each EQ event with a multiplicity of altitude projections. So, the request for the *L*-shell parameter, which is only related to EBs, is lost and EB cannot be chosen unambiguously. Furthermore, if the condition of *L*-shell similarity between considered EB detection and EQ projections is not satisfied, the correlation cannot be found. In conclusion, the

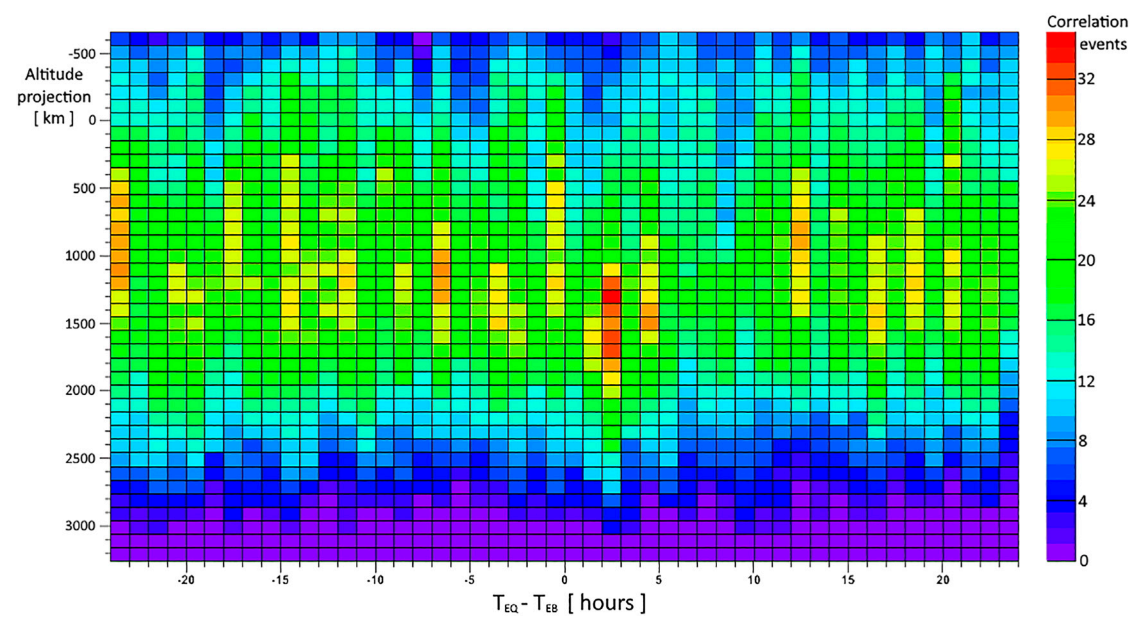

FIGURE 1 | Complete correlation histogram between EBs and EQs obtained between −24 and 24 h and projecting the EQ epicenters between −600 and 3,200 km. The correlation event palette on the right provides the number of EQs that contributed to the correlation. A positive $\Delta t = T_{EQ} - T_{EB}$ means that the time of an EQ is greater than the time of an EB, highlighting that the EB anticipated the EQ.

steps used to calculate any statistical correlation between EBs and EQs are ambiguous, so they cannot be used to define a phenomenon that anticipates strong EQs. In particular, the step involving the *L*-shell of EBs needs to be modified for the EQ forecasting.

Unambiguous NOAA Electrons' Statistical Correlation

The NOAA-15 MEPED telescope used to monitor the electron flux coming from the zenith in three energy bands in the range of 30 keV–2.5 MeV (Evans and Greer, 2004) has been used. The energy detected for the electrons is a cumulative sum over three thresholds: $E_1 = 30\,\mathrm{keV}$, $E_2 = 100\,\mathrm{keV}$, and $E_3 = 300\,\mathrm{keV}$. Since different energies determine different behaviors in particle dynamics, new energy channels were derived from the difference of the energy thresholds to obtain electrons detected in the intervals 30–100 keV, 100–300 keV, and 300–2.5 MeV. CRs were then corrected for proton contamination (Rodger et al., 2010) from the lower energy range, based on both observations (Asikainen and Mursula, 2008) and simulations (Yando et al., 2011), and using software downloaded from the Virtual Radiation Belt Observatory (http://virbo.org/POES#Processing). Furthermore, the escaping conditions from trapped electrons were determined, thus selecting particles perturbed from the inner Van Allen Belts. These precipitating electrons were identified by calculating their minimum mirror point altitudes, $h_{\min}$, through the UNILIB libraries (Krunglanski, 2003). In fact, if $h_{\min} < 100\,\mathrm{km}$ along the drift period, the electrons having energies between 30 keV and 3 MeV are ensured to be absorbed in the residual atmosphere. This occurs at the SAA longitudes due to the geomagnetic field asymmetry. Then, electrons drifting eastward and escaping the trapped conditions can be found by enforcing the condition $h_{\min} < 100\,\mathrm{km}$ on detected CRs. Such electrons cross the NOAA altitudes and are thus able to be detected, up to the 80° longitude from the westward edge of the SAA.

The dynamics of electrons were described using adiabatic invariants such as the geomagnetic field at mirror points $B_m = B/\cos 2\alpha$, where B is the geomagnetic field, the pitch angle α is the difference between the electron velocity and geomagnetic field directions and the *L*-shell parameter. CRs of precipitating electrons were thus represented in a 4-dimensional matrix $(t; L; \alpha; B)$ including time. The introduction of B was useful for describing the strong spatial variability of the CRs when the satellite entered the SAA (Asikainen and Mursula, 2008). B covered the range of 16–47 μT which was divided into nine nonidentical intervals, shorter where the CR was higher, to better describe the CR spatial variations, and larger where the CR was less frequent, to have a greater number of samples (Fidani and Battiston, 2008). The considered intervals in B were as follows: 16.0–17.5, 17.5–19.0, 19.0–20.5, 20.5–22.0, 22.0–25.0, 25.0–28.0, 28.0–32.5, 32.5–37.0, and 37.0–47.0 μT. Having the SEM-2 detectors with a finite aperture of 30°, the α interval was chosen to be of 15°, dividing the complete excursion into 12 equal intervals. The *B*-field and the *L*-shell were re-evaluated on the NOAA-15 orbit using the International Geomagnetic Reference Field (IGRF-12) model (http://www.ngdc.noaa.gov/IAGA/vmod/igrf.html) (Finlay et al., 2015). To concentrate the analysis in the inner Van Allen Belts, L was restricted at the interval of 1.0–2.2 with *L*-shell steps of 0.1 defining 12 equal intervals. To realize a measure of precipitating electrons which are disturbed from an

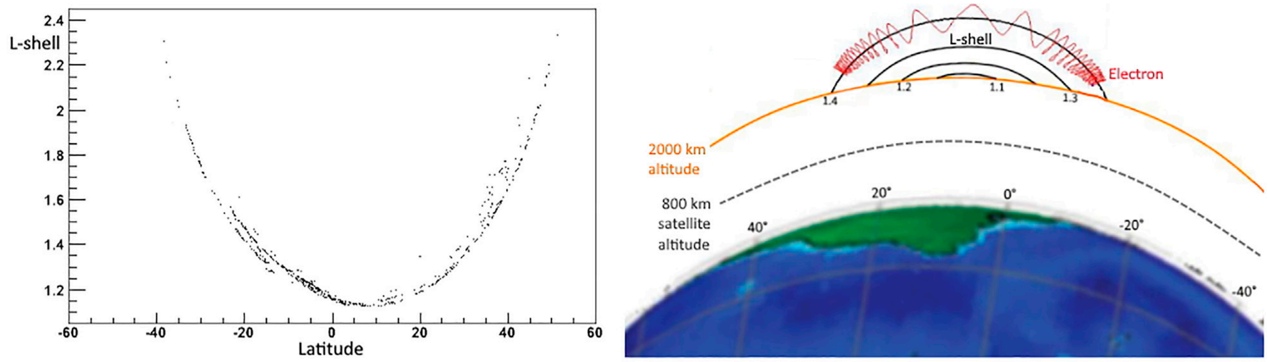

FIGURE 2 | L_{EB} dependence by the EQ latitudes which are considered for the correlation calculus when the L_{EQ} at some altitude projection of the EQ epicenter is near L_{EB}, on the left. The parable gives a quadratic dependence. The cause of this dependence is shown on the right where the L_{EB} covers the expected interval, around 2,000 km of altitude above the EQ latitudes. The satellite altitude at the corresponding longitudes is well under the Van Allen Belts; the satellite altitude will approach the L_{EB} interval at least 60° further east.

action coming from the Earth's surface, external Van Allen Belts are excluded by limiting L under 2.2, and the SAA is also excluded by a minimum value in $B = 20.5\ \mu T$.

CRs were summed on 8-s time intervals and associated to each adiabatic interval in B, α, and L. CR histograms were created, and their distributions at all the adiabatic regions resulted as Poissonian. Therefore, to obtain less than 1% probability that a CR fluctuation was of a statistical origin, the condition Poisson $(CR) < 0.01$ had to be satisfied for the average value corresponding to the same adiabatic coordinates of that CR. Thus, such a CR was considered to be a significant fluctuation with a probability greater than 99%, corresponding to the same adiabatic intervals. The small geometric acceptance $(\sim 0.1\ \mathrm{cm}^2\mathrm{sr})$ of NOAA detectors required a long time and large adiabatic intervals to obtain sufficient statistics for daily averages. However, in order to obtain a more accurate reading of the particle dynamics, small cell dimensions of adiabatic invariants should be preferred. Being so, an interpolated average value for each adiabatic interval was used to map L and B continuously from the centers of their intervals. In this way, cell sizes were not reduced, and daily averages were accepted only for those cells having at least 20 satellite passages a day. Furthermore, as CRs strongly increase near the SAA, a cubic nonlinear algorithm was used to better interpolate the averages. Starting from averages and variances, it was possible to verify if the NOAA MEPED detected any significant CR fluctuations along the entire satellite orbit.

Electron loss is primarily induced by solar activity; thus, time intervals, when the solar activity influences electron motion inside the internal Van Allen Belts, are excluded from the analysis. The exclusions are obtained by excluding time intervals when the Ap index overcame a threshold which is variable with seasons and years due to the solar cycle. The threshold was fixed by the year and the day of the year using the relation $Ap = 11.1 + 0.8 \sin[0.37(year - 1996)] + \{2.1 - 0.1 \sin[0.37(year - 1996)]\} \cos[0.0172(day - 27)]$, where a clear phase shift was defined with the minimum of the Sun's activity in 1996 and the 27-day modulation due to the Sun's rotation. Moreover, being that the electron flux was related to substorm activity (Lam et al., 2010), CRs were not considered for the analysis when the Dst index was lower than −27 nT satisfying these conditions. The sudden increase of electron CRs were considered EBs influenced by the Earth' surface, and more EBs detected along the same semi-orbit were considered as one EB.

The correlation between EBs and EQs was calculated after defining L-shells for an EQ (L_{EQ}) by projecting the EQ coordinates to different altitudes and then requiring the condition $|L_{EQ} - L_{EB}| \leq 0.1$. This was discussed in *Reviewing NOAA Electrons' Statistical Correlations* as a problem for discriminating EBs unambiguously, and another criterion is needed. Moreover, the L-shell condition is equivalent to setting a position above the future EQ epicenter where the detected EB passed. So, it might be the position where electrons escaped the trapped conditions following some remote interaction with the EQ preparation zone in the ground (Fidani, 2020). Given that each L-shell is associated with a well-defined altitude at each geographical point and a physical link is reasonably able to reach a certain maximal altitude, it is plausible that for each L-shell, there corresponds a more-or-less defined interval of geographical coordinates. A plot of EQ latitudes with respect to the L_{EB} indicates this correspondence in **Figure 2** (left). The plot shows a quadratic dependence of L_{EB} on the EQ latitude with a minimum around 10°. This depends on the shape of the internal Van Allen Belts above the EQ epicenters (see **Figure 2**; right) that crosses the altitude around 2,000 km with an increasing L-shell, as the latitude moves away from 10°. This asymmetry around the equator is produced by the inclination of the geomagnetic field with respect to the rotational axes. Being so, it is enough to select only EBs with L_{EB} in a well-defined interval to guarantee that they correlate with strong EQs in Indonesia and the Philippines.

To verify the validity of the new EB condition, a correlation was recalculated between EQs and EBs, which now includes only EB parameters, with the L_{EB} being in a restricted interval. After a complete study to maximize the correlation with respect to many EQ and EB parameters, the validity of the new condition was

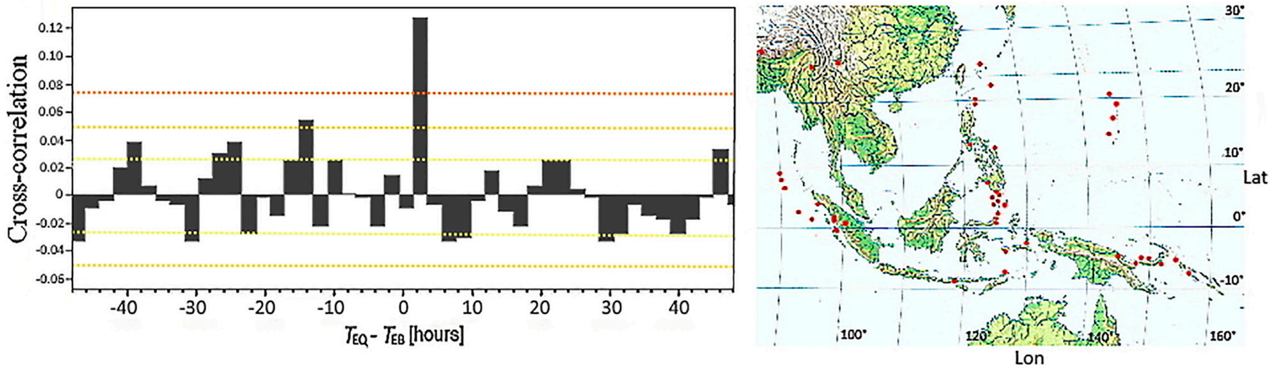

FIGURE 3 | Pearson's cross correlation between EBs and EQs recalculated using the new condition on L_{EB} for 16.5 years of data is shown on the left; the 1 σ, 2 σ, and 3 σ thresholds are indicated by yellow, orange, and red dotted lines, respectively. The Indonesian and the Philippine strong EQs producing the 1.5–3.5-h correlation peak are shown on the right.

confirmed by choosing EBs with the following: $1.21 \le L_{EB} \le 1.31$, pitch angles $56° \le \alpha \le 74°$ and $108° \le \alpha \le 126°$, and positions −35° to 15° in latitudes and 230°–280° in longitudes. For EQs, the depth must be less than 200 km, the latitude in the −6° to 26° interval, and the longitude in the 90°–170° interval. The correlation was defined by filling the histogram $\sum_{\{EQ;EB\}} (EQ \times EB)$ with the differences $\Delta t = T_{EQ} - T_{EB}$ between the EQ time T_{EQ} and the EB time T_{EB}, only for those EBs with L in the interval 1.21–1.31. The correlation was also optimized according to both the time binning and the time shift. The optimization corresponded to the $\Delta t = 1.5–3.5$ h interval. Here, the time difference interval, used as the binning, was suggested as the time necessary for the EB to cover the EQ longitude interval of 80° for a 60-keV electron drifting eastward at $L = 1.26$, which was found to be about 2 h. After it, the number of correlation events is increased to 44, thus improving the correlation significance. The updated correlation is shown in **Figure 3** (left), and the geographical distribution of correlated EQs is shown on the right. L_{EB} and the EB geographic position were found to be the critical parameters to reveal EB true alarms, and the $\Delta t = 1.5–3.5$ h interval is used from here on out. It should be noted that the peaks around 48 h and around 0 h are consistent with the results of the study by Anagnostopoulos et al. (2012), even if with a low significance.

Forecasting Methodologies

Following a work by Fidani (2018), the conditional probability of a strong EQ, given the EB measurement, can be calculated using the relation between the covariance and cross correlation (Billingsley, 1995). Moreover, this discussion is valid for binary events using any physical observation other than the EB, which is correlated with the EQ. If applied to the EQ and EB unitary events, the binary correlation is as follows:

$$corr(EQ, EB) = \frac{cov(EQ, EB)}{\sqrt{P(EQ)[1 - P(EQ)]P(EB)[1 - P(EB)]}}, \tag{1}$$

where the $cov(EQ, EB) = [P(EQ \cap EB) - P(EQ)P(EB)]$ can be explicated throughout the histogram of the EQ to EB coincidences $\sum_{\{EQ;EB\}} (EQ \times EB)$ in the following population formula:

$$cov(EQ, EB) = \frac{N_h \sum_{\{EQ;EB\}} (EQ \times EB) - N_{EQ} N_{EB}}{N_h^2}, \tag{2}$$

where N_{EQ} and N_{EB} are the number of EQs and EBs that participated in the correlation, respectively, while N_h is the number of total hours divided by two considered for the correlation. Being so, the probabilities of single events are $P(EQ) = N_{EQ}/N_h$ and $P(EB) = N_{EB}/N_h$. The binary correlation histogram is then calculated as follows:

$$corr(EQ, EB) = \frac{\sum_{\{EQ;EB\}} (EQ \times EB) \big/ N_h - P(EQ)P(EB)}{\sqrt{P(EQ)[1 - P(EQ)]P(EB)[1 - P(EB)]}}. \tag{3}$$

Being the joint probability by definition of the covariance and from **Eq. 1**, we have the following:

$$\begin{aligned} P(EQ \cap EB) = {} & P(EQ)P(EB) \\ & + corr(EQ, EB)\sqrt{P(EQ)[1 - P(EQ)]P(EB)[1 - P(EB)]}. \end{aligned} \tag{4}$$

The conditional probability $P(EQ|EB) = P(EQ \cap EB)/P(EB)$ can be rewritten as follows:

$$\begin{aligned} P(EQ|EB) &= P(EQ) + corr(EQ, EB)\sqrt{\frac{P(EQ)[1 - P(EQ)][1 - P(EB)]}{P(EB)}} \\ &= \frac{\sum_{\{EQ;EB\}} (EQ \times EB)}{N_{EB}}. \end{aligned} \tag{5}$$

which means that if a correlation exists between EQs and EBs which is $\max_{\Delta t} [\sum_{\{EQ;EB\}} (EQ \times EB)]$ and the time difference Δt between EQ and EB is chosen to be that of correlations, the probability of an EQ with M ≥ 6 is increased by a term proportional to the correlation.

An equivalent approach to test the results obtained using NOAA particle data refers to the work by Console (2001). Here, a simple definition of an EQ forecasting hypothesis was suggested with a particular sub-volume of the total time–space volume, called the alarm volume, within which the probability of occurrence of strong EQs is higher than the average. Following the work by Console, the prediction related to the detection of a precursor consists in the occurrence of an EQ event of minimal magnitude in the alarm volume. In this framework, the performance of a specific method is carried out through the statistical parameters that can be evaluated in this example, such as the success rate N_S/N_A, the false alarm rate $(N_A - N_S)/N_A$, the alarm rate N_S/N_E, the failure rate $(N_E - N_S)/N_E$, and the probability gain (Console, 2001), as shown below:

$$G = \frac{N_S}{N_A V_A} \frac{V_T}{N_E}, \tag{6}$$

where N_S is the success number, N_A is the alarm number, N_E is the EQ number, V_A is the alarm volume, and V_T is the total volume. It should be noted that this description is completely equivalent to the previous being $N_S = \max_{\Delta t}[\sum_{\{EQ;EB\}}(EQ \times EB)]$, $N_A = N_{EB}$, $N_E = N_{EQ}$, $V_A = A \cdot N_h$, where A is the Indonesian and Philippine areas and $V_A = 2A$ is for the alarm duration of 2 h. V_A based on NOAA particle data is constant for all the alarms. Thus, the success rate is exactly $P(EQ|EB)$, the false alarm rate is $1 - P(EQ|EB)$, the alarm rate is $\max_{\Delta t}[\sum_{\{EQ;EB\}}(EQ \times EB)]/N_{EQ}$, the failure rate is $1 - \max_{\Delta t}[\sum_{\{EQ;EB\}}(EQ \times EB)]/N_{EQ}$, and the probability gain is as follows:

$$\begin{aligned} G &= \frac{P_{\Delta t}(EQ|EB)}{P(EQ)} \\ &= 1 + corr_{\Delta t}(EQ, EB)\sqrt{[1/P(EQ) - 1][1/P(EB) - 1]}, \end{aligned} \tag{7}$$

where $corr_{\Delta t}(EQ, EB)$ is the particular correlation and $P_{\Delta t}(EQ|EB)$ is the particular conditional probability, both corresponding to a Δt of 1.5–3.5 h.

Evaluating Significance

A criterion for considering one model more valid than another can be made through the log-likelihood of observing that particular realization of the EQ process: under the hypothesis defining the probabilities of occurrence in P sub-volumes p_i, and c_i being the digital occurrence of at least one event in the sub-volume, the following is the case (Console, 2001):

$$\log(L) = \sum_{i=1}^{P}\{c_i \log[p_i/(1 - p_i)] - \log(1 - p_i)\}. \tag{8}$$

The geographical regions of Indonesia and the Philippines are considered, where strong $(M \geq 6)$ EQs occurred over 16.5 years from July 1998, which were correlated with the NOAA EBs. The space–time alarm sub-volumes are in this case disjointed and separated in time only, each completely covering both areas for 2-h time intervals from 1.5 to 3.5 h after the EB observations. If so, the complete volume covers N_h hours, of which N_{EQ} are those where an EQ occurred with $c_i = 1$, N_{EB} are those where an alarm occurred with $p_i = P(EQ|EB)$, $N_h - N_{EB}$ are those where no alarm occurred with $p_i = P(EQ)$, and $\sum_{\{EQ;EB\}}(EQ \times EB)$ are those where an EQ followed an alarm and where $p_i = P(EQ|EB)$. The log-likelihood histogram is as follows:

$$\begin{aligned} \log(L) = {} & \log\left[\frac{P(EQ|EB)}{1 - P(EQ|EB)}\right]\sum_{\{EQ;EB\}}(EQ \times EB) \\ & + \left[N_{EQ} - \sum_{\{EQ;EB\}}(EQ \times EB)\right]\log\left[\frac{P(EQ)}{1 - P(EQ)}\right] \\ & + N_{EB}\log[1 - P(EQ|EB)] \\ & + (N_h - N_{EB})\log[1 - P(EQ)], \end{aligned} \tag{9}$$

and it is possible to compare this forecasting hypothesis with a simpler model, called the null hypothesis, that is, the Poisson hypothesis. The success rate of this model is constantly $P(EQ)$ and the probability gain is always $G = 1.0$, so that the log-likelihood is calculated as follows:

$$\log(L_0) = N_{EQ}\log[P(EQ)] + (N_h - N_{EQ})\log[1 - P(EQ)]. \tag{10}$$

The log-likelihood ratio (Martin, 1971) can now be calculated to test the near-Earth space influence hypothesis against the null hypothesis for Δt of the maximum correlation, evaluating the following:

$$\begin{aligned} \log\left(\frac{L_{\Delta t}}{L_0}\right) = {} & \max_{\Delta t}\left[\sum_{\{EQ;EB\}}(EQ \times EB)\right]\log\left[\frac{P_{\Delta t}(EQ|EB)}{P(EQ)}\right] \\ & + \left\{N_{EB} - \max_{\Delta t}\left[\sum_{\{EQ;EB\}}(EQ \times EB)\right]\right\} \\ & \times \log\left[\frac{1 - P_{\Delta t}(EQ|EB)}{1 - P(EQ)}\right]. \end{aligned} \tag{11}$$

Moreover, the statistical link between EQs and EBs was tested for its significance, starting from their correlation distribution (Fidani, 2015). In the work by Fidani et al. (2010), it was reported that the EQ-to-EB correlation histogram (**Eq. 3**), obtained collecting $\sum_{\{EQ;EB\}}(EQ \times EB)$ for many time differences, can satisfy a Poissonian process when only main shock EQs and semi-orbit EBs are used. Then, indicating the average correlation histogram with Ave, the standard deviation histogram is $\sigma = \sqrt{Ave}$. Being so, the number of standard deviations N_σ relative to Δt, which is shown in **Figure 4** of the work by Fidani (2015) for a Δt lasting 2–3 h with respect to altitude projections, can be evaluated by calculating $Ave_{\Delta t}$ and $\sigma_{\Delta t}$ for the same Δt as follows:

$$N_\sigma = \frac{\max_{\Delta t}\left[\sum_{\{EQ;EB\}}(EQ \times EB)\right] - Ave_{\Delta t}}{\sigma_{\Delta t}}. \tag{12}$$

The significance in terms of N_σ is shown in **Figure 4** for the entire interval of altitude projections corresponding to **Figure 1**. The significance α_{corr} in terms of N_σ can be obtained using tables of Poisson probabilities. The significance of the new correlation was also evaluated using N_σ. The maximum obtained $N_\sigma = 5.4$ corresponded to a probability $< 0.1\%$, not being a statistical fluctuation. A summary of the correlation calculated using **Eq. 3**, time interval Δt and probability gains calculated using **Eq. 7**, and number of events and N_σ calculated using **Eq. 12**, corresponding to the altitude projections and to the new model based on L_{EB} only, are reported in columns 2, 3, 4, 5, and 6 of **Table 1**, respectively. The values of significance calculated using tables starting from **Eq. 12** are also reported in column 7 of **Table 1**.

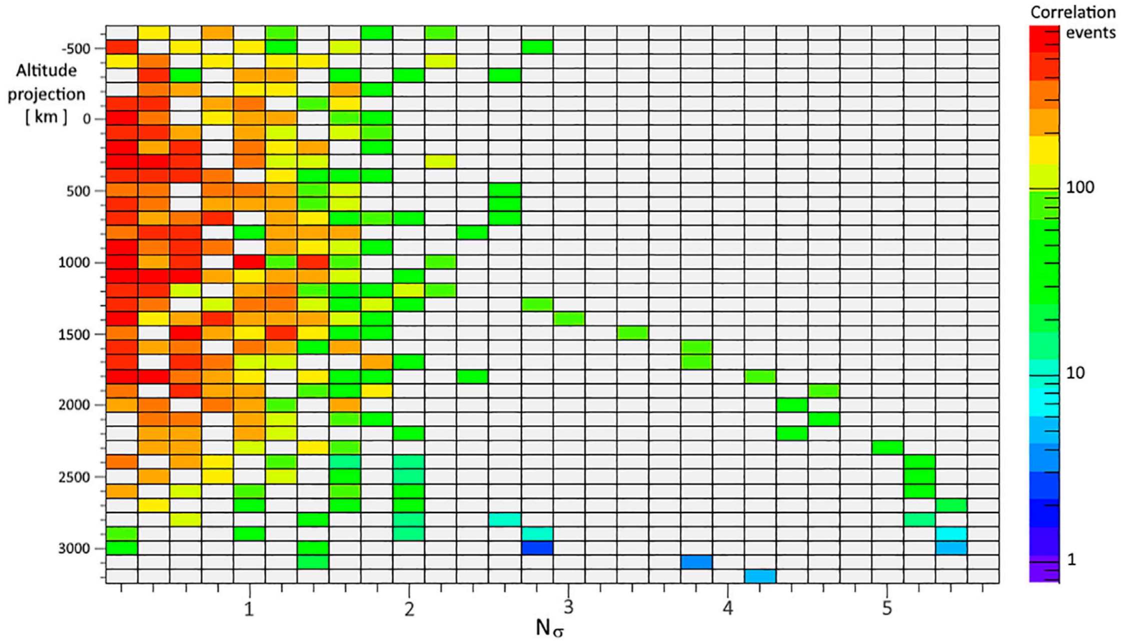

FIGURE 4 | Half of the significance histogram of the correlations in **Figure 1** between EBs and EQs obtained between −72 and 72 h and projecting the EQ epicenters between −600 and 3,200 km. The other half of the significance histogram concerns the negative N_σ values which have shown no anticorrelations till date. The correlation event palette on the right provides the number of EQs that contributed to that significance bin. Noteworthily, the correlation starts to be significant for altitude projections above 1,400 km, even if the maximum number of total events is reached around 1,000 km (see **Figure 1**).

Precursory information can be evaluated using Molchan's error diagram (Molchan, 2003). The quantities needed to characterize the predictive properties of a strategy in an interval $(0, T)$ are the relative number of failures to predict for an EQ magnitude greater than M, as follows:

$$\nu = \frac{1}{N(T)} \sum_{0<t<T} [1 - D_e(t)] dN(t), \tag{13}$$

and the relative alert time is as follows:

$$\tau = \frac{1}{T} \sum_{0<t<T} D_e(t) t_a, \tag{14}$$

where t_a is the alert time, $N(t)$ is the number of seismic events in the interval $(0, t)$, $dN(t) = N(t + t_a) - N(t) = \{0 \; or \; 1\}$ is the number of events in the alert time interval, and D_e is a decision alert which can be $\{0 \; or \; 1\}$ in the interval $(t, t + t_a)$. In the NOAA electron statistical results, $t_a = 2\,\mathrm{h}$, $N(T) = N_{EQ}$, the relative number of failures is the failure rate in the study of Console (2001), being $\nu_{EB} = 1 - \max_{\Delta t}[\sum_{\{EQ;EB\}}(EQ \times EB)]/N_{EQ}$, and the relative alert time is $\tau_{EB} = P(EB)$. The statistical significance α_{Molch} of a given point (ν_{EB}, τ_{EB}) on the Molchan's error diagram can be tested using the random probability of the Poisson model, which is the diagonal of the Molchan's diagram, and is given by the binomial distribution (Kossobokov, 2006) as follows:

$$B[N_{EQ}(1 - \nu_{EB}) | N_{EQ}, \tau_{EB}] = C[N_{EQ}; N_{EQ}(1 - \nu_{EB})] \times {\tau_{EB}}^{N_{EQ}} \left(\frac{1}{\tau_{EB}} - 1 \right)^{N_{EQ}\nu_{EB}}. \tag{15}$$

In light of this, the probability of obtaining $N_{EQ}(1 - \nu_{EB})$ or more hits by chance, as there have been N_{EQ} observed target EQs, is described by the following:

$$\alpha_{Molch} = \sum_{n=m}^{N} B[n | N_{EQ}, \tau_{EB}], \tag{16}$$

which produces the confidence bounds and where the index $m = \max_{\Delta t}[\sum_{\{EQ;EB\}}(EQ \times EB)]$. G on the Molchan's error diagram is the slope of the line connecting $(0, 1)$ to (τ_{EB}, ν_{EB}) (Zechar and Jordan, 2008), and it is simply calculated as $G = (1 - \nu_{EB})/\tau_{EB}$ (Molchan, 1991), which is identical to **Eq. 7**.

RESULTS

The EQ prediction model analyzing the EBs detected using NOAA satellites can now be represented following the more general work by Console (2001). Thus, the recent forecasting results obtained in the work by Fidani (2020) using annual averages must be redefined, in order to fit this more general representation. Subsequently, the final assessment of the hypothesis validity should be carried out *via* a test on a new and independent set of observations (Console, 2001).

Prediction Model

The scenario representing the model of EQ prediction needs to define volumes where EQs occur, where the target volume V_T is

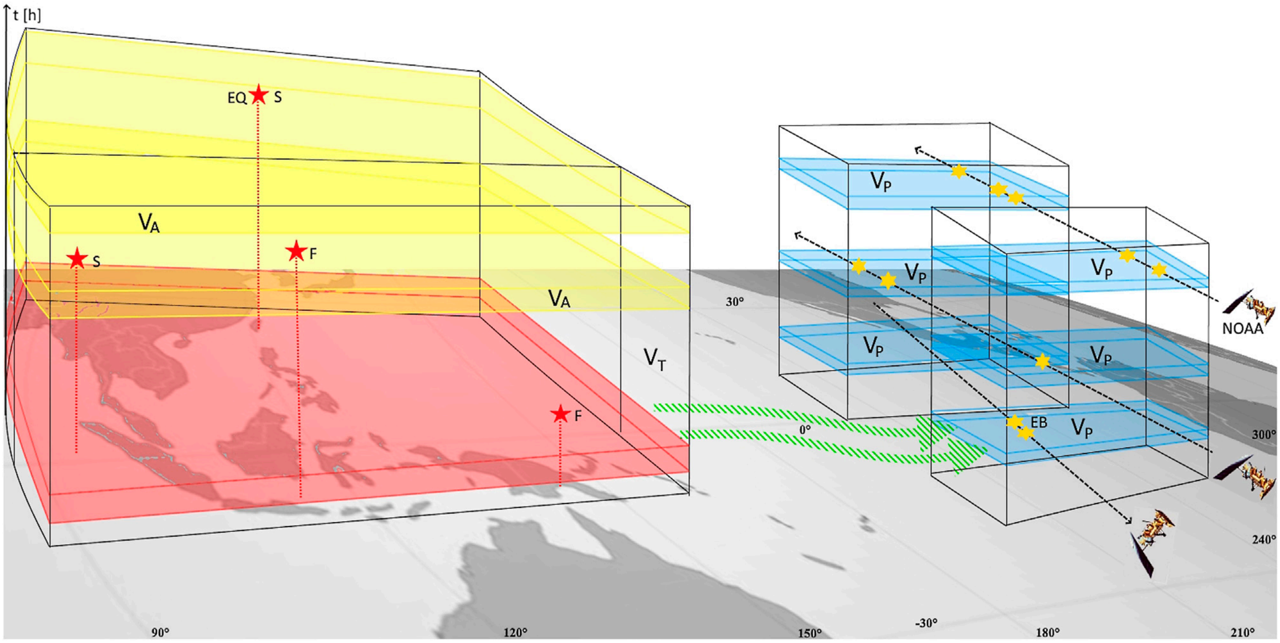

FIGURE 5 | Volume representation where the forecasting model can be tested is delimited by the product among the geographical coordinates of EQs and EBs and the time of observations. V_T, V_A, and V_P are all discontinuous volumes in time as the EB analysis is suitable for EQ forecasting when the solar activity is very low. Moreover, the alarm duration is 2 h. V_T and V_A cover the entire West Pacific area, and V_P covers the different geographical areas on the western North American and South American coasts. The causal link between EQ disturbance and EB measurement events is represented by green dashed arrows. The possible precursor volume due to a hypothetical physical action on the ionosphere above the epicenters of the earthquakes is represented in red.

2-d space + 1-d time–space. In this volume, the points of EQ occurrence can be identified, together with alarm volumes V_A, as success (S) and failure of prediction (F) events that are EQs occurring inside or outside V_A, respectively. In this case, a precursor volume V_P containing the alarm events must be defined, which is generally different from V_T; V_P is the volume of the area where EB detection using NOAA satellites occurs, multiplied by the time of EB observations. An EB detection in V_P is an alarm event which defines V_A. With regard to the correlation mentioned above, for the Indonesian and Philippine latitudes and longitudes, V_T is obtained by multiplying this area by the time spanned by the EQ observations. In this scenario, the occurrence of an EQ event is considered only with M above a magnitude threshold M_0, where $M_0 = 6$. Unlike the models that consider EQs as precursors themselves, in this model, the EB precursor events are detected at different latitudes and longitudes, with respect to those of EQs. Correlations between EBs and EQs occurred for EB detection in the area to the west of the South Atlantic Anomaly. Thus, V_T concerns the longitude interval of 90°–170° and the latitude interval of −6°–26° multiplied by the time interval of the analysis, whereas V_P concerns the area of 230°–280° in longitude and the area of −35°–15° in latitude multiplied by the time interval of the analysis. V_A is generated by an observation of one EB in V_P. It has the same area as V_T multiplied by a duration $T = 2$ h, which results in the width of the correlation peak, occurring over the next 1.5–3.5 h, which is found to be the time position of the correlation peak. In this case, the alarm volume V_A is constant for all alarms. A success is added if an EQ with $M \geq 6$ occurs in the V_A. A failure is added if an EQ occurs out of the V_A, which means not included in the time intervals, and any alarm EB not followed by EQ is classified as a false alarm. The described model can be represented by the three-dimensional space of geographical coordinates and time reported in **Figure 5**. Performance of the NOAA EB detection is conditioned by a V_P which is not continuous. In fact, as reported above, only a low number of days are magnetically calm enough to be used for the analysis. Moreover, the NOAA satellites go into the detection area west of the South Atlantic Anomaly intermittently, thus further reducing the total time of observations.

TABLE 1 | Numerical values for the cross correlations corresponding to different altitudes, from 1,200 to 2,800 km, and the L_{EB} condition, plus their corresponding correlations, Δ*t*, gain, number of events, and sigmas and α_{corr} significance.

km/*L*-shell	$corr_{\Delta t}$	Δt [h]	G_{EB}	Events	N_σ	α_{corr}
1,200	4.6 10−2	2–3	1.9	30	2.2	0.03
1,400	4.8 10−2	2–3	1.9	32	3.2	0.01
1,600	5.1 10−2	2–3	2.2	35	3.9	<0.01
1,800	5.3 10−2	2–3	2.5	34	4.3	<0.01
2,000	5.8 10−2	2–3	2.9	30	4.5	<0.01
2,200	6.5 10−2	2–3	4.7	27	4.8	<0.01
2,400	7.6 10−2	2–3	7.4	24	5.3	<0.01
2,600	7.3 10−2	2–3	28	19	5.2	<0.01
2,800	7.1 10−2	2–3	69.1	12	5.3	<0.01
L_{EB} only	0.13	1.5–3.5	3	44	5.4	<0.01

This is the cause of a noncontinuous V_T, where V_A appears to fill the same geographical area as V_T for a time interval of 2 h. A V_A within V_T is generated 1.5 h after an EB is observed in V_P. This is different from the model based exclusively on seismic activity, where the causal link between V_A and the precursor is near the vertical, given the seismic properties to cluster. The causal link between V_A and the EB observation event is represented near the horizontal. This causal link is the eastward electron drift, according to the electron energy, which is represented in **Figure 5** by green thick arrows moving according to the longitude. The vertical distance between the starting point of arrows above the EQ epicenters and the base of V_A is the time anticipation of a possible physical interaction relating the EQ preparation volume to the ionosphere. In the analysis of 16.5 years of NOAA data, V_T concerned only the Indonesian and the Philippine areas multiplied by $N_h = 6,953$ h. It should be noted that this value and the following are different from those reported in past publications (Fidani, 2020), as the past reports were rough estimates. In this volume, the following occurred: a total number $N_{EQ} = N_E = 600$ of EQs with $M \geq 6$, a total number $N_{EB} = N_A = 1,892$ of alarms, and a total number $N_S = 44$ of success. Being so, the success rate of this model is $N_S/N_A = 0.023$, the false alarm rate is $1 - (N_S/N_A) = 0.977$, the alarm rate is $N_S/N_E = 0.073$, the failure rate is $1 - (N_S/N_E) = 0.927$, and the $G = 3.0$.

Here, the target volume is subdivided into nonoverlapping sub-volumes with time intervals of a day that fill V_T completely. For each day sub-volume, the probability of occurrence of at least one target event is estimated to be equal to $P(EQ)$ with no EB observed and $P(EQ|EB)$ with one EB. Analyzing the data, days with more than one burst can be found with a frequency of about 20%. These bursts can be far away in time when the time difference is more than 10,000 s (~2.8 h) or neighbors when the time difference is 5,000–7,000 s (~1.4–2.0 h); in the latter case, they belong to successive orbits according to NOAA POES orbit parameters. It should be remembered that all EBs in a semi-orbit were considered as only one EB to be counted for the correlation calculus (Fidani, 2015). When two bursts are far away, the time alarm of the first ends before the beginning of the second detection, so two disjoint V_A with the same increasing of the conditional probabilities occur. When detected bursts belong to successive orbits, the V_A time interval of 2 h is greater than the range of 5,000–7,000 s, and a partial overlapping between two consecutive alarms will also occur. The few cases of overlapping for NOAA alarms are not considered here and will be presented in a future publication.

Dependent Observables

Bayes' theorem allows us to compute the probability that a hypothesis is true, provided that one knows the probable truth of all supporting arguments. It reverses the conditional probabilities and defines the probability of the hypothesis given the evidence. It shows that there is a significant probability gain in using precursors for prediction, even if a phenomenological occurrence is not the proof of a precursor. However, starting from the correlation results (Fidani, 2015), Bayes' theorem, as shown below,

$$P(EB|EQ) = \frac{P(EB)\,P(EQ|EB)}{P(EQ)}, \tag{17}$$

can be employed using statistical bases (**Eq. 5**). Being so, the alarm rate can be rewritten as $P(EB|EQ)$, the failure rate as $1 - P(EB|EQ)$, and the probability gain as follows:

$$G_{EB} = \frac{P(EB|EQ)}{P(EB)} = G. \tag{18}$$

Bayes theorem allows us to compute the probability of an EB given the measurement of an EQ. If calculated, it appears surprisingly high, equal to 0.8 for the correlation. However, this result must not be misinterpreted. In fact, the probability gain remains the same, suggesting that the high probability of detecting an EB when an EQ is observed is due to its greater frequency of EB occurrence.

Bayes' theorem tests hypotheses and can be updated on the basis of new information. If used under the condition of many independent precursors *EB, EC, ED* …, the EQ conditional probability in a small time interval of a given area after the simultaneous detection of one *EB*, one *EC*, one *ED* ... can be approximated by (Aki, 1981) the following:

$$P(EQ|EB \cap EC \cap ED \cap \ldots) \simeq P(EQ)G_{EB}G_{EC}G_{ED}\cdots. \tag{19}$$

It is the product among the unconditional probability and the probability gains of each precursor; those are the ratios between the conditional probability of each precursor and unconditional probability. However, the condition of independent precursors is difficult to prove, and from the studies reported in the Introduction, a set of physical links for only a part of them is suspected (see, for example, the study by Pulinets et al. (2015)). Therefore, it seems that dependent candidate precursors represent the most common occurrence. Therein, the conditional probability of an *EQ* with a magnitude greater than M_0 is not increased by a product of a further probability gain of another detected precursor, if this has a certain degree of dependence on the first to be detected. Thus, the conditional probability cannot be approximated by **Eq. 19**; it must be recalculated. Starting with only two dependent precursors *EB* and *EC* that generate alarms in the same V_T, the conditional probability on *EQ*, given the observations of both precursors *EB* and *EC*, can be expressed using the relations (**Eq. 7**) and (**Eq. 1**) as follows:

$$G_{EB\cap EC} = 1 + \frac{cov(EQ, EB \cap EC)}{P(EQ)P(EB \cap EC)}, \tag{20}$$

where the covariance can be explicated throughout the histogram of *EQ* to *EB*∩*EC* coincidences $\sum_{\{EQ;EB\cap EC\}}[EQ \times (EB \wedge EC)]$, and by considering the total number $N_{EB\cap EC}$ of correlated precursor events. Finally, $P(EB|EC)$ can be calculated through the $corr(EB, EC)$ of the relation (**Eq. 5**), as with all the other conditional probabilities. However, a more interesting question might arise upon using two observation networks whose observables are dependent: what is the overall probability gain upon using observations without differentiating them? In this case, the warning corresponds to a detection from the set of dependent observables $EB\cup EC$, which means that the probability, as shown below,

$$P(EQ|EB\cup EC)=\frac{P(EQ\cap(EB\cup EC))}{P(EB\cup EC)}, \tag{21}$$

is conditioned by the observation of an EB or an EC or of both an EB and an EC, indifferently. Then, using simple algebra with $P(EQ\cap(EB\cup EC)) = P((EQ\cap EB))\cup(EQ\cap EC))$, we obtain the following:

$$P(EQ|EB\cup EC)=\frac{P(EQ\cap EB)+P(EQ\cap EC)-P(EQ\cap EB\cap EC)}{P(EB)+P(EC)-P(EB\cap EC)}, \tag{22}$$

where $P(EQ\cap EB) = P(EQ|EB)P(EB)$, $P(EQ\cap EC) = P(EQ|EC)P(EC)$, $P(EB\cap EC) = P(EB|EC)P(EC)$, $P(EQ\cap EB\cap EC) = P(EQ|EB\cap EC)P(EB\cap EC)$. Considering the relation (**Eq. 7**), the probability gain due to the observation of an event in $EB\cup EC$ is as follows:

$$G_{EB\cup EC}=\frac{G_{EB}P(EB)+[G_{EC}-G_{EB\cap EC}P(EB|EC)]P(EC)}{P(EB)+[1-P(EB|EC)]P(EC)}, \tag{23}$$

where G_{EB} and G_{EC} are the probability gains of the single precursor EB and the single precursor EC, respectively. $G_{EB\cap EC}$ is the probability gain (**Eq. 20**) due to the observation of both EB and EC events that are correlated between them. Alternatively, using the relations (**Eq. 7**) and (**Eq. 1**), we obtain the following:

$$G_{EB\cup EC}=1+\frac{cov(EQ,EB\cup EC)}{P(EQ)P(EB\cup EC)}, \tag{24}$$

where the covariance can be explicated throughout the histogram of EQ to $EB\cup EC$ coincidences $\sum_{\{EQ;EB\cup EC\}}[EQ\times(EB\vee EC)]$, and by considering the total number $N_{EB\cup EC} = N_{EB} + N_{EC} - N_{EB\cap EC}$.

Different Precursors Combined

It needs to be highlighted that a statistical correlation between the two time series does not generally mean that they are physically related (Aldrich, 1995). A causal link has been hypothesized between EB measurements and EQ occurrence (Fidani, 2018; 2020), which supports the validity of the hypothesis. Although the $\Delta t = T_{EQ} - T_{EB}$ time difference of the correlation is in agreement with the physical migration of electrons eastward, this migration has not yet been observed for EBs correlated with EQs. Furthermore, a physical link between the EQ preparation zone and the ionosphere above the future epicenter, separated by about 2,000 km, has not been demonstrated. Finally, the existence of some physical phenomena occurring at the future EQ epicenter, which is enough to influence the ionosphere, remains only a hypothesis until all of these passages have been fully demonstrated. To discover EBs with the correct times at different longitudes, which would satisfy their physical migration in the ionosphere, more satellites are needed. This verification is currently possible for EBs, as different NOAA satellites fly together, even though cases having suitable satellite positions must be found. Till date, this has not been calculated, as no correlations have been found with EBs selected using other satellite databases during the same periods.

Regarding a physical link, able to cover more than 2,000 km between the Earth's crust and the ionosphere throughout the atmosphere, magnetic pulses have been hypothesized to influence the high-energy charged particles' motion by pitch angle diffusion (Galper et al., 1995). Even if other processes have been proposed more recently, such as the injection of radioactive substances and charged aerosols into the atmosphere, leading to a change in the vertical electric current in the atmosphere and to a modification of the electrical field in the ionosphere (Sorokin et al., 2001), from a solid-state physics perspective (Freund, 2011), and radioactive ionization to model the lithosphere–atmosphere–ionosphere–magnetosphere coupling by the latent heat flux (Pulinets et al., 2015), by AGW (Yang et al., 2019; Piersanti et al., 2020). Recent measurements of magnetic pulses on the occasions of strong EQs (Bleier et al., 2009; Orsini, 2011; Nenovski, 2015) have suggested an efficient process which may influence the ionosphere (Fidani et al., 2020). In this latter work, the magnetic data analysis at the Chieti Station of the Central Italy Electromagnetic Network, performed using two independent sample systems of the same signal, showed that a large number of pulses were recorded in the ELF band below 10 Hz with amplitudes mostly in the range of 2.5–80 nT. Specifically, the model proposed for analyzing magnetic pulses consisted of diffused underground electrical currents throughout a conductive strip between the Apennines and the Adriatic Sea. The current required to induce detected pulses is greater than $i = 40$ kA for the strongest pulses. Unipolar magnetic pulses can be, for example, generated deep in the rock column by peroxy defects when rocks are subjected to increasing deviatoric stresses (Freund et al., 2021). The proposed strip of diffuse current constitutes the electromagnetic source of ULF waves, which is able to produce low intensities of magnetic inductions on the Earth's surface, even if it is measurable both near and far from the EQ epicenter. The strip of diffuse current is able to produce significant fields, also far from the ground by integration. To demonstrate this and calculate magnetic induction in the ionosphere, two simple models can be considered. An infinitely long strip of about 6-km-thick and 150-km-large conductive soil has been considered to calculate the magnetic induction very close to the larger strip surface. In a real case, a finite-length strip should be utilized, which gives a correct result even for a coil magnetometer very close to the strip. Referring to **Figure 6**, on the left side, where the lines of induction are generated by a not-finite strip and wire lengths are compared, it is possible to see that the B intensities near the strip are lower than those near the wire. This is due to the current density differences flowing near the observational point. Relations (**Eq. 2**) and (C4) of the study by Fidani et al. (2020) were used for the wire and the strip, respectively. Moving away from the current density, magnetic inductions generated by the wire and the strip become equal, when the distance overcomes the strip width. However, currents which are not of finite length deviate too much from the real case at large distances. So, a finite length l of the wire is considered and the magnetic induction is simply calculated as follows:

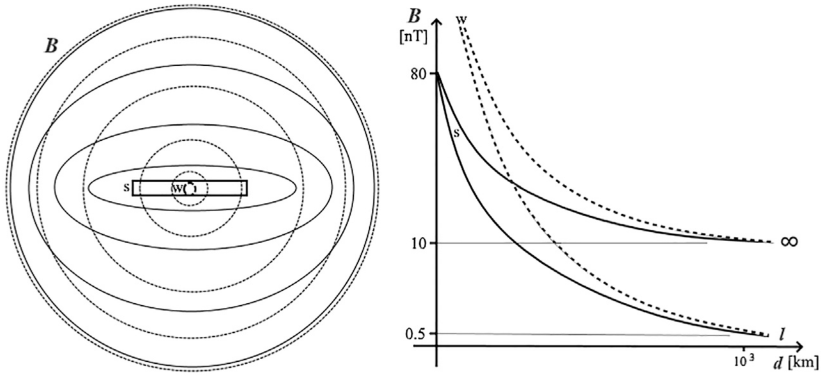

FIGURE 6 | Comparison of magnetic induction lines produced by the rectangular and circular sections in the center on the left; continuous lines are generated by the rectangular strip (s), whereas the dotted lines are generated by the wire (w). *B* dependence, from the distance at half of the strip width of the currents, is shown on the right for both conductors that are infinitely long or of length *l* using the relation (**Eq. 25**) and the relation (**Eq. 2**) of the study by Fidani et al. (2020).

$$B = \frac{\mu_o i l}{4\pi d\sqrt{(d^2 + l^2)}}, \tag{25}$$

where d is the distance. **Figure 6**, on the right side, depicts a comparison of B intensities of the two models with the distance. The B intensity results are limited to 0.2 nT at distances of 1,000 km with a total current of 40 kA. This is in agreement with the intensities obtained from the theoretical calculations, which have shown that only a magnetic type source with frequency < 10–20 Hz can be effective for the penetration of fields into the upper ionosphere and magnetosphere (Molchanov et al., 1995). Moreover, magnetic disturbances were observed above moderate EQ epicenters for the frequency band of 0.1–10 Hz (Strakhov et al., 1994). From the upper ionosphere, these waves travel as Alfven waves further along the geomagnetic field line and reach the inner boundary of the inner Van Allen Belt. Alfven waves are thought to resonantly interact with trapped charged particles; this process is most intensive in the equatorial part of the magnetosphere, for L-shell values equal to or less than 2 (Molchanov and Mazhaeva, 1993). In fact, the measured pulse frequency under 10 Hz is around the bouncing resonance of electrons with energies between 30 and 100 keV (Walt, 1994); it is exactly as measured on board NOAA satellites. This means that energy can be efficiently transferred from magnetic pulses producing electron pitch angle disturbances (Galper et al., 1995). Furthermore, the B intensity due to an Earth surface strip of current is a very low value, compared to an example of geomagnetic activity. However, the frequency range of geomagnetic activity is about 0.0001–0.01 Hz (Francia and Villante, 1997), so that the B rate is out of resonance. Finally, currents produced by lightning are generally lower in intensity, around $i = 10$ kA, with frequency emissions in the upper part of the ELF band and the VLF band still out of bouncing resonance (Inan et al., 2010).

Indeed, magnetic signals have been correlated with strong EQs in different regions of the world such as Japan (Ohta et al., 2013), Kamchactka (Schekotov et al., 2019), and California (Kappler et al., 2019). The Japanese and Kamchactka studies obtained correlations with time differences of 2–5 days before seismic events, and probability gains of about 1.6 (Han et al., 2014) to 2.6 (Hayakawa et al., 2019) were reported. Magnetic pulses, from here on identified with ECs, have been hypothesized to induce EBs, and therefore, they may be considered dependent events for hypothesis. The relation (**Eq. 23**) can be used to calculate the probability gain of EQ probability due to possible observations of both EBs and ECs. This possibility can be useful as the observation of ECs on the Earth's surface can occur when a NOAA satellite is not in a suitable position to reveal the possibly induced EBs. Moreover, magnetic detectors cannot be installed at some positions offshore or are not able to detect ECs where there are EQs. In other words, EBs and ECs can compensate for the gaps on each other in a forecasting experiment, where V_T is very large, as for the West Pacific. The magnetic pulse precursor can be represented by the red volume of **Figure 5**. Being so, the mutual interrelation of the sets of EBs, ECs, and EQs is a completely real case, which can be studied for a total probability gain with the expression (**Eq. 23**). To show the advantage in using two dependent observables, a forecasting experiment can be imagined where both EB and EC data are available. Here, one can imagine the presence of a magnetometer network distributed on several islands of the West Pacific. Although not still existent, this network is currently achievable. We suppose that it exists and is able to obtain a $G_{EC} = 1.6$ for EQs within a certain distance around the stations, with a time advance of ECs of 4–6 h with respect to EQs. $P(EC)$ is necessary for **Eq. 23** and is supposed to be 0.05, which means $N_{EC} = 324$ magnetic pulses, or sets of magnetic pulses, considered as magnetic alarms on the same time interval as for EBs. For what concerns the NOAA observable, a $G_{EB} = 3$ was found from the correlation analysis. However, even if ECs from days with the Ap index above the previously defined threshold were excluded as for EBs, the daily NOAA observation time was always half a day (Fidani, 2020) due to the satellite's orbit crossing the EB detection region. Being so, the probability gain should be evaluated on a double time interval and being able to detect the same number of EBs. The probability gain is

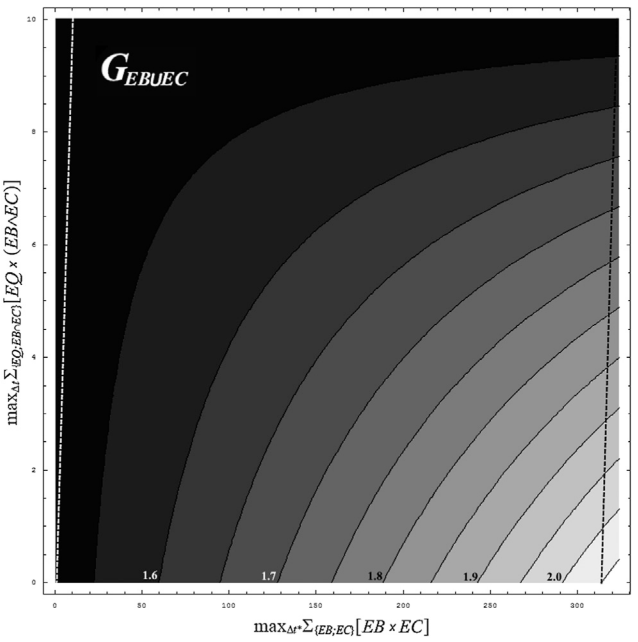

FIGURE 7 | Probability gain (**Eq. 23**) due to the contribution of EB and EC detection, where in this case ECs are ULF magnetic pulses. This gain is calculated with respect to the maximum event correlation between EBs and ECs on the abscissa, which comes from $P(EB|EC)$, and to the maximum event correlation between EQ and $EB\cap EC$ on the ordinate, which is derived from $P(EQ|EB\cap EC)$. $\Delta t* = T_{EB} - T_{EC}$ is thought to be the drifting time of electrons from the ionosphere above the epicenter to the cross with the NOAA satellite. Therefore, $G_{EB\cup EC}$ is described by the contours if Δt of EB-to-EC correlation is shifted by $\Delta t*$, that is, the dependence between EBs and ECs. The white dotted line on the left and the black one on the right represent $G_{EB\cup EC}$ limits of validity.

thus approximately $G_{EB} = 1.5$. With regard to $P(EB|EC)$, the correlation between EBs and ECs would need to be calculated using observational data. $P(EB|EC)$ depends on the histogram maximum $\max_{\Delta t*}[\sum_{\{EB;EC\}}(EB \times EC)]$, where $\Delta t* = 4(6) - \Delta t$ is such that the total time in advance of ECs with respect to EQs is 4–6 h. This could be chosen in the range from 0, no correlation, to 324, complete correlation, the N_{EB} being a much higher number, in order to consider a range of possibilities. Concerning $G_{EB\cap EC}$, the correlation between EQ and $EB\cap EC$ would need to be calculated utilizing observational data for $\max_{\Delta t}[\sum_{\{Eq;EB\cap EC\}}(EQ \times (EB\wedge EC))]$. If $EB\cap EC$ at Δt are the set of events EB and EC related by chance, $\sum_{\{EB;EC\}}(EB \times EC)$ should be a low value with $G_{EB\cup EC} \simeq [G_{EB}P(EB) + G_{EC}P(EC)]/[P(EB) + P(EC)]$. The dependence between EBs and ECs can be introduced in **Eq. 23** by fixing a time shift in ECs of $\Delta t*$ so that the number of correlation events is $\max[\sum_{\{EB;EC\}}(EB \times EC)] = \max_{\Delta t*}[\sum_{\{EB;EC\}}(EB \times EC)]$. It would also be necessary in this case to consider a range of possibilities from 0, no correlation between EQ and $EB\cap EC$, to 10 common events. The probability gain improvements that are obtainable thanks to a network of EC measurements added to the NOAA satellite EB detection are reported in the contour plot of **Figure 7**.

The maximum value of $G_{EB\cup EC} = 2.05$ is obtained for 314 ECs which are correlated with EBs, but none of these EBs are correlated with EQs, shown by point (314, 0) of **Figure 7**, which means that 10 ECs are correlated with EQs and another part of EBs not correlated with ECs is correlated with EQs; thus, the total number of different observations correlated with EQs is increased by 10. $G_{EB\cup EC}$ is a minimum when the correlation events between EBs and ECs are $\max_{\Delta t*}[\sum_{\{EB;EC\}}(EB \times EC)] = 0$, shown by the point (0, 0) of **Figure 7**. That is, when there are no ECs correlated with EQs nor with EBs, and $G_{EB\cup EC}$ is slightly less than 1.6 because it is a weighted average between G_{EB} and G_{EC}. When the EB-to-EC correlation increases to 10 events, a maximum of 10 correlations with EQs can happen, as shown by point (10, 10) of **Figure 7**, where $G_{EB\cup EC}$ is still lower due to redundancy. $G_{EB\cup EC}$ does not exist to the left of the white dotted line and on the right of the black dotted line. When the EB-to-EC correlation is at the maximum and the correlation of such ECs with EQs reaches 10 events, as shown by point (324, 10) of **Figure 7**, $G_{EB\cup EC}$ returns as near 1.5 due to the low number of correlated EQ events.

CONCLUSION

A complete EQ forecasting methodology has been considered in this study based on NOAA satellite high-energy electron detection. It utilizes recently discovered correlations existing between EBs selected from the NOAA database and strong EQs collected at the USGS (Fidani, 2015), which can be classified as an electromagnetic phenomenon and a near-seismic precursor. This correlation, concerning EBs anticipating main shocks, has been obtained also thanks to the geomagnetic disturbance database of the Ap and Dst indexes, as well as the IGRF model. The methodology has been represented by the volumes of target, alarm, and precursor, for testing EQ forecast hypotheses (Console, 2001).

To systematically test this methodology, a quantitative and rigorous definition of the anomaly is given according to a statistical criterion with respect to the Poisson distribution of electron CRs. Here, electrons must be escaping the trapping conditions, that is, precipitating, probably due to a disturbance. Finally, novel in relation to previous publications (Fidani, 2015; Fidani, 2018; Fidani, 2020), the parameter L-shell of the electrons has been disentangled from apparent L-shells associated to EQs. In fact, the condition of the difference $|L_{EB} - L_{EQ}| \le 0.1$ in previous publications was substituted with the $1.21 \le L_{EB} \le 1.31$, which was deduced from the correspondence between electron L-shells at around 2,000 km and EQ latitudes. This disentangling between anomalies and EQs is essential to provide a precise definition of the observed phenomenon (Wyss, 1997) in order to carry out a forecast.

The statistical correlation between EBs and EQs has been extended to a time difference of 1.5–3.5 h, thanks to the hypothesized causal connection of drifting electrons. Maximizing the significance of this correlation indicated that EQs still belong to the Indonesian and the Philippine areas, collecting more seismic events from the West Pacific. These EQs occurred as in the previous analysis, mainly in the sea, with a depth up to 200 km to correlate with EBs. Regarding EBs, the pitch angle intervals were restricted, even if the number of EBs increased. To demonstrate that the correlation calculus is completely equivalent to the frequency approach of Console (2001), the probability gain was recalculated in terms of conditional probability and correlation for digital events.

After having stressed that a statistical correlation between two time series does not generally mean that they are physically related (Aldrich, 1995), the hypothesis concerning a physical link between EBs and EQs was studied. A recent observation of magnetic pulses recorded before strong EQs in Central Italy provided recorded magnetic intensities with a diffuse current model (Fidani et al., 2020). This model can push back to the hypocenter region the causal connection of physical events, even if the deduced magnetic inductions in the ionosphere must be demonstrated to be able to modify the electron pitch angles. Being magnetic pulses measurable on the Earth's surface, they might be precursors, and indeed, statistical correlation of magnetic pulses was found (Han et al., 2014; Hayakawa et al., 2019). However, given their possible causal link with EBs, magnetic pulses and EBs could not be independent precursors. Thus, starting from Bayes' theorem, a more general relationship of the probability gain due to the combination of two precursors is expressed in terms of single probability gains of each precursor and the correlation between the precursors. An example of improvement in the probability gain due to a couple of digital dependent precursors is tentatively calculated for the first time. A dependence between the precursors is introduced in the probability gain (**Eq. 23**) by a time shift which correlates the precursors. The best probability gain is obtained for the maximum correlation between precursors not correlated with EQs.

Finally, this methodology is general enough that it could be adapted to the combinations of observations from both the Earth's surface and space, such as electromagnetic, seismic, or other physical observables. To do this, a series of steps must be performed: 1) collect data from the same instrument(s) with the same environmental conditions for many years, 2) search for anomalies of a physical observable with a statistical rigor, following a physical idea of possible equilibrium disturbances, 3) calculate a statistical correlation between EQs and anomalies by selecting physical parameters disentangled from EQ parameters, following a physical idea of possible interaction, 4) calculate the correlation significance, or the likelihood, or the Molchan's error diagram and optimize it with respect to the physical parameters, 5) use the more relevant parameters to determine the correlation significance, or the likelihood, or the Molchan's error diagram for a physical model refinement, 6) demonstrate the Δt and $\Delta t*$ agreement of the two observables using a unified physical model, and 7) calculate the probability gain to one or more precursors and to their combinations, and verify the results in a target volume of future times or different databases. If step 6 is not obtained, the probability gain (**Eq. 23**) can be maximized with respect to Δt and $\Delta t*$ to suggest a probable unified physical model. Moreover, an experiment for the EQ forecasting test in Indonesia and the Philippines is currently feasible using the NOAA-15 satellite, given the presence of the United States West Coast antennas (Fidani, 2020). This could be concluded over a few years with a reasonable response, due to the high frequency of strong seismicity in Indonesia and the Philippines.

DATA AVAILABILITY STATEMENT

Publicly available datasets were analyzed in this study. This data can be found here: http://www.ngdc.noaa.gov/stp/satellite/poes/dataaccess.html; http://wdc.kugi.kyoto-u.ac.jp/dst_final/index.html; https://www.ngdc.noaa.gov/geomag/data.shtml; https://earthquake.usgs.gov/earthquakes/search/.

AUTHOR CONTRIBUTIONS

CF: scientific analysis and manuscript writing.

REFERENCES

Aki, K. (1981). "A Probabilistic Synthesis of Precursory Phenomena," in *Earthquake Prediction, an International Review, Maurice Ewing Vol. 4*. Editors D.W. Simpson and P. G. Richards (Washington, DC: AGU), 566–574.

Aldrich, J. (1995). Correlations Genuine and Spurius in Pearson and Yule. *Stat. Sci.* 10 (4), 364–376. doi:10.1214/ss/1177009870

Aleksandrin, S. Y., Galper, A. M., Grishantzeva, L. A., Koldashov, S. V., Maslennikov, L. V., Murashov, A. M., et al. (2003). High-energy Charged Particle Bursts in the Near-Earth Space as Earthquake Precursors. *Ann. Geophys.* 21, 597–602. doi:10.5194/angeo-21-597-2003

An, Z., Zhan, Y., Fan, Y., Chen, Q., Chen, Q., and Liu, J. (2019). Investigation of the Characteristics of Geoelectric Filed Earthquake Precursors: a Case Study of the Pingliang Observation Station, China. *Ann. Geophys.* 62 (5), 545. doi:10.4401/ag-7982

Anagnostopoulos, G. C., Vassiliadis, E., and Pulinets, S. (2012). Characteristics of Flux-Time Profiles, 20 Temporal Evolution, and Spatial Distribution of Radiation-belt Electron Precipitation Bursts in the Upper Ionosphere before Great and Giant Earthquakes. *Ann. Geophys.* 55, 21–36. doi:10.4401/ag-5365

Asikainen, T., and Mursula, K. (2008). Energetic Electron Flux Behavior at Low L-Shells and its Relation to the South Atlantic Anomaly. *J. Atmos. Solar-Terrestrial Phys.* 70, 532–538. doi:10.1016/j.jastp.2007.08.061

Barnhart, W. D., Hayes, G. P., and Wald, D. J. (2019). Global Earthquake Response with Imaging Geodesy: Recent Examples from the USGS NEIC. *Remote Sensing* 11, 1357. doi:10.3390/rs11111357

Biagi, P. F., Ermini, A., and Kingsley, S. P. (2001). Disturbances in LF Radio Signals and the Umbria-Marche Seismic Sequence in 1997-1998. *Phys. Chem. Earth (C)* 26 (10-12), 755. doi:10.1016/s1464-1917(01)95021-4

Billingsley, P. (1995). *Probability and Measure*. 3rd ed. New York: John Wiley & Sons.

Bleier, T., Dunson, C., Maniscalco, M., Bryant, N., Bambery, R., and Freund, F. (2009). Investigation of ULF Magnetic Pulsations, Air Conductivity Changes, and Infra Red Signatures Associated with the 30 October Alum Rock M5.4 Earthquake. *Nat. Hazards Earth Syst. Sci.* 9, 585–603. doi:10.5194/nhess-9-585-2009

Bortnik, J., Cutler, J. W., Dunson, C., and Bleier, T. E. (2008). The Possible Statistical Relation of Pc1 Pulsations to Earthquake Occurrence at Low Latitudes. *Ann. Geophys.* 26, 2825–2836. doi:10.5194/angeo-26-2825-2008

Bošková, J., Šmilauer, J., Tříska, P., and Kudela, K. (1994). Anomalous Behaviour of Plasma Parameters as Observed by the Intercosmos 24 Satellite Prior to the Iranian Earthquake of 20 June 1990. *Stud. Geophys. Geod.* 38, 213–220. doi:10.1007/bf02295915

Clilverd, M. A., Rodger, C. J., and Thomson, N. R. (1999). Investigating Seismo-Ionospheric Effects on a Long Sub-ionospheric Path. *J. Geophys. Res.* 104 (A12), 171–179. doi:10.1029/1999ja900285

Console, R. (2001). Testing Earthquake Forecast Hypotheses. *Tectonophysics* 338, 261–268. doi:10.1016/s0040-1951(01)00081-6

Dautermann, T., Calais, E., Haase, J., and Garrison, J. (2007). Investigation of Ionospheric Electron Content Variations before Earthquakes in Southern California, 2003-2004. *J. Geophys. Res.* 112, B02106. doi:10.1029/2006JB004447

Davis, G. (2007). History of the NOAA Satellite Program. *J. Appl. Remote Sens* 1, 012504. doi:10.1117/1.2642347

De Santis, A., Marchetti, D., Pavón-Carrasco, F. J., Cianchini, G., Perrone, L., Abbattista, C., et al. (2019). Precursory Worldwide Signatures of Earthquake Occurrences on Swarm Satellite Data. *Sci. Rep.* 9, 20287. doi:10.1038/s41598-019-56599-1

Eleftheriou, A., Filizzola, C., Genzano, N., Lacava, T., Lisi, M., Paciello, R., et al. (2016). Long-Term RST Analysis of Anomalous TIR Sequences in Relation with Earthquakes Occurred in Greece in the Period 2004-2013. *Pure Appl. Geophys.* 173, 285–303. doi:10.1007/s00024-015-1116-8

Evans, D. S., and Greer, M. S. (2004). *Polar Orbiting Environmental Satellite Space Environment Monitor – 2: Instrument Descriptions and Archive Data Documentation, NOAA Technical Memorandum January, Version 1.4*, 155.

Fidani, C., and Battiston, R. (2008). Analysis of NOAA Particle Data and Correlations to Seismic Activity. *Nat. Hazards Earth Syst. Sci.* 8, 1277–1291. doi:10.5194/nhess-8-1277-2008

Fidani, C., Battiston, R., and Burger, W. J. (2010). A Study of the Correlation between Earthquakes and NOAA Satellite Energetic Particle Bursts. *Remote Sensing* 2, 2170–2184. doi:10.3390/rs2092170

Fidani, C. (2015). Particle Precipitation Prior to Large Earthquakes of Both the Sumatra and Philippine Regions: A Statistical Analysis. *J. Asian Earth Sci.* 114, 384–392. doi:10.1016/j.jseaes.2015.06.010

Fidani, C. (2018). Improving Earthquake Forecasting by Correlations between Strong Earthquakes and NOAA Electron Bursts. *Terr. Atmos. Ocean. Sci.* 29 (2), 117–130. doi:10.3319/tao.2017.10.06.01

Fidani, C. (2019). *From the Bayes Theorem to a Model of the Geomagnetic Interaction between strong Earthquakes in the Indonesian Archipelagos and Particle Data Detected by NOAA Satellites.* Bologna: SIF2019, L'Aquila, atticon11779 IV-C-9.

Fidani, C. (2020). Probability, Causality and False Alarms Using Correlations between Strong Earthquakes and NOAA High Energy Electron Bursts. *Ann. Geophys.* 63 (5), 543. doi:10.44101/ag-7957

Fidani, C., Orsini, M., Iezzi, G., Vicentini, N., and Stoppa, F. (2020). Electric and Magnetic Recordings by Chieti CIEN Station during the Intense 2016-2017 Seismic Swarms in Central Italy. *Front. Earth Sci.* 8, 536332. doi:10.3389/feart.2020.536332

Finlay, C. C., Olsen, N., and Tøffner-Clausen, L. (2015). DTU Candidate Field Models for IGRF-12 and the CHAOS-5 Geomagnetic Field Model. *Earth Planet. Sp* 67. doi:10.1186/s40623-015-0274-3

Francia, P., and Villante, U. (1997). Some Evidence of Ground Power Enhancements at Frequencies of Global Magnetospheric Modes at Low Latitude. *Ann. Geophys.* 15, 17–23. doi:10.1007/s00585-997-0017-2

Freund, F. (2011). Pre-earthquake Signals: Underlying Physical Processes. *J. Asian Earth Sci.* 41, 383–400. doi:10.1016/j.jseaes.2010.03.009

Freund, T. F., Heraud, J. A., Centa, V. A., and Scoville, J. (2021). Mechanism of Unipolar Electromagnetic Pulses Emitted from the Hypocenters of Impending Earthquakes. *Eur. Phys. J.* 230, 47–65. doi:10.1140/epjst/e2020-000244-4

Galper, A. M., Koldashov, S. V., and Voronov, S. A. (1995). High Energy Particle Flux Variations as Earthquake Predictors. *Adv. Space Res.* 15 (11), 131–134. doi:10.1016/0273-1177(95)00085-s

Galperin, Y. I., Gladyshev, V. A., Jorjio, N. V., Larkina, V. I., and Mogilevsky, M. M. (1992). Energetic Particles Precipitation from the Magnetosphere above the Epicentre of Approaching Earthquake. *Cosmic Res.* 30, 89–106.

Han, P., Hattori, K., Hirokawa, M., Zhuang, J., Chen, C.-H., Febriani, F., et al. (2014). Statistical Analysis of ULF Seismomagnetic Phenomena at Kakioka, Japan, during 2001-2010. *J. Geophys. Res. Space Phys.* 119 (6), 4998–5011. doi:10.1002/2014ja019789

Han, P., Hattori, K., Zhuang, J., Chen, C.-H., Liu, J.-Y., and Yoshida, S. (2017). Evaluation of ULF Seismo-Magnetic Phenomena in Kakioka, Japan by Using Molchan's Error Diagram. *Geophys. J. Int.* 208, 482–490. doi:10.1093/gji/ggw404

Hattori, K., Han, P., Yoshino, C., Febriani, F., Yamaguchi, H., Chen, C.-H., et al. (2013). Investigation of ULF Seismo-Magnetic Phenomena in Kanto, Japan during 2000-2010: Case Studies and Statistical Studies. *Surv. Geophys.* 34, 293–316. doi:10.1007/s10712-012-9215-x

Hayakawa, M., Kasahara, Y., Nakamura, T., Muto, F., Horie, T., Maekawa, S., et al. (2010). A Statistical Study on the Correlation between Lower Ionospheric Perturbations as Seen by Subionospheric VLF/LF Propagation and Earthquakes. *J. Geophys. Res.* 115, A09305. doi:10.1029/2009ja015143

Hayakawa, M., Schekotov, A., Izutsu, J., and Nickolaenko, A. P. (2019). Seismogenic Effects in ULF/ELF/VLF Electromagnetic Waves. *Int. J. Elect. Appl. Res.* 6 (2), 1–86. doi:10.33665/ijear.2019.v06i02.001

He, L., and Heki, K. (2016). Three-dimensional Distribution of Ionospheric Anomalies Prior to Three Large Earthquakes in Chile. *Geophys. Res. Lett.* 43, 7287–7293. doi:10.1002/2016gl069863

Henderson, T. R., Sonwalkar, V. S., Helliwell, R. A., Inan, U. S., and Fraser-Smith, A. C. (1993). A Search for ELF/VLF Emissions Induced by Earthquakes as Observed in the Ionosphere by the DE 2 Satellite. *J. Geophys. Res.* 98, 9503. doi:10.1029/92ja01533

Inan, U. S., Cummer, S. A., and Marshall, R. A. (2010). A Survey of ELF and VLF Research on Lightning-Ionosphere Interactions and Causative Discharges. *J. Geophys. Res.* 115, A00E36. doi:10.1029/2009ja014775

Kappler, K. N., Schneider, D. D., MacLean, L. S., Bleier, T. E., and Lemon, J. J. (2019). An Algorithmic Framework for Investigating the Temporal Relationship of Magnetic Field Pulses and Earthquakes Applied to California. *Comput. Geosciences* 133, 104317. doi:10.1016/j.cageo.2019.104317

Ke, F., Wang, Y., Wang, X., Qian, H., and Shi, C. (2016). Statistical Analysis of Seismo-Ionospheric Anomalies Related to Ms > 5.0 Earthquakes in China by GPS TEC. *J. Seismol* 20, 137–149. doi:10.1007/s10950-015-9516-x

Kon, S., Nishihashi, M., and Hattori, K. (2011). Ionospheric Anomalies Possibly Associated with $M \geqslant 6.0$ Earthquakes in the Japan Area during 1998-2010: Case Studies and Statistical Study. *J. Asian Earth Sci.* 41, 410–420. doi:10.1016/j.jseaes.2010.10.005

Kossobokov, V. G. (2006). Testing Earthquake Prediction Methods: "The West Pacific Short-Term Forecast of Earthquakes with Magnitude MwHRV≥5.8". *Tectonophysics* 413, 25–31. doi:10.1016/j.tecto.2005.10.006

Krunglanski, M. (2003). UNILIB Reference Manual, Belgisch Instituut Voor Ruimte –Aeronomie, Which Can Be Downloaded Together to the Library from. Available at: http://www.oma.be/NEEDLE/unilib.php/.

Lam, M. M., Horne, R. B., Meredith, N. P., Glauert, S. A., Moffat-Griffin, T., and Green, J. C. (2010). Origin of Energetic Electron Precipitation >30 keV into the Atmosphere. *J. Geophys. Res.* 115, A4. doi:10.1029/2009JA014619

Larkina, V. I., Migulin, V. V., Molchanov, O. A., Kharkov, I. P., Inchin, A. S., and Schvetcova, V. B. (1989). Some Statistical Results on Very Low Frequency Radiowave Emissions in the Upper Ionosphere over Earthquake Zones. *Phys. Earth Planet. Interiors* 57, 100–109. doi:10.1016/0031-9201(89)90219-7

Larkina, V. I., Nalivayko, A. V., Gershenzon, N. I., Gokhberb, M. B., Liperovsky, V. A., and Shamilov, S. (1983). Observations of VLF Emission, Related with Seismic Activity on the Interkosmos-19 Satellite. *Geomagn. Aeronomy* 23, 684–687.

Li, M., and Parrot, M. (2013). Statistical Analysis of an Ionospheric Parameter as a Base for Earthquake Prediction. *J. Geophys. Res. Space Phys.* 118 (6), 3731–3739. doi:10.1002/jgra.50313

Liu, J.-Y., Chen, C.-H., Lin, C.-H., Tsai, H.-F., Chen, C.-H., and Kamogawa, M. (2011). Ionospheric Disturbances Triggered by the 11 March 2011M9.0 Tohoku Earthquake. *J. Geophys. Res.* 116, A6. doi:10.1029/2011JA016761

Liu, J.-Y., Chen, Y.-I., Jhuang, H.-K., and Lin, Y.-H. (2004). Ionospheric foF2 and TEC Anomalous Days Associated with M >= 5.0 Earthquakes in Taiwan during 1997-1999. *Terr. Atmos. Ocean. Sci.* 15, 371–383. doi:10.3319/tao.2004.15.3.371(ep)

Liu, J. Y., Chen, C. H., Chen, Y. I., Yang, W. H., Oyama, K. I., and Kuo, K. W. (2010). A Statistical Study of Ionospheric Earthquake Precursors Monitored by Using Equatorial Ionization Anomaly of GPS TEC in Taiwan during 2001-2007. *J. Asian Earth Sci.* 39, 76–80. doi:10.1016/j.jseaes.2010.02.012

Liu, J. Y., Chen, Y. I., Chuo, Y. J., and Chen, C. S. (2006). A Statistical Investigation of Preearthquake Ionospheric Anomaly. *J. Geophys. Res.* 111, A05304. doi:10.1029/2005JA011333

Liu, J. Y., Chen, Y. I., Huang, C. H., Ho, Y. Y., and Chen, C. H. (2015). A Statistical Study of Lightning Activities and $M \geq 5.0$ Earthquakes in Taiwan during 1993-2004. *Surv. Geophys.* 36, 851–859. doi:10.1007/s10712-015-9342-2

Liu, J. Y., Chen, Y. I., Pulinets, S. A., Tsai, Y. B., and Chuo, Y. J. (2000). Seismo-ionospheric Signatures Prior to $M \geq 6.0$ Taiwan Earthquakes. *Geophys. Res. Lett.* 27, 3113–3116. doi:10.1029/2000gl011395

Maekawa, S., Horie, T., Yamauchi, T., Sawaya, T., Ishikawa, M., Hayakawa, M., et al. (2006). A Statistical Study on the Effect of Earthquakes on the Ionosphere, Based on the Subionospheric LF Propagation Data in Japan. *Ann. Geophys.* 24, 2219–2225. doi:10.5194/angeo-24-2219-2006

Martin, B. R. (1971). *Statistics for Physicists Academic.* San Diego, Calif., 209.

Mikhaylova, G. A., Golyavin, A. M., and Mikhaylov, Yu. M. (1991). Dynamic Spectra of VLF-Radiation in the Outer Ionosphere Associated with the Iranian Earthquake of June 21, 1990 (Intercosmos2 4 Satellite). *Geomagn. A.eron., Engl. Transl.* 31, 647.

Molchan, G. M. (1991). Structure of Optimal Strategies in Earthquake Prediction. *Tectonophysics* 193, 267–276. doi:10.1016/0040-1951(91)90336-q

Molchan, G. M. (2003). "Earthquake Prediction Strategies: a Theoretical Analysis," in *Nonlinear Dynamics of the Lithosphere and Earthquake Prediction*. Editors V.I. Keilis-Borok and A.A. Soloviev (Berlin-Heidelberg: Springer-Verlag), 209–237. doi:10.1007/978-3-662-05298-3_5

Molchanov, O. A. (1993). "Wave and Plasma Phenomena inside the Ionosphere and Magnetosphere Associated with Earthquakes," in *Review of Radio Science 1990–1992*. Editor W Ross Stone (Oxford: Oxford University Press), 591–600.

Molchanov, O. A., and Mazhaeva, O. A. (1993). Resonance Interaction of ULF and VLF Waves with High-Energy Protons in Magnetospheric Plasma. *Cosmic Res.* 31 (2), 108–119.

Molchanov, O. A., and Hayakawa, M. (1998). Subionospheric VLF Signal Perturbations Possibly Related to Earthquakes. *J. Geophys. Res.* 103, 17,489–17,504. doi:10.1029/98ja00999

Molchanov, O. A., and Hayakawa, M. (2008). *Seismo-Electromagnetics and Related Phenomena*. Tokyo: Terrapub.

Molchanov, O., Schekotov, A., Fedorov, E., Belyaev, G., and Gordeev, E. (2003). Preseismic ULF Electromagnetic Effect from Observation at Kamchatka. *Nat. Hazards Earth Syst. Sci.* 3, 203–209. doi:10.5194/nhess-3-203-2003

Němec, F., Santolík, O., Parrot, M., and Berthelier, J. J. (2008). Spacecraft Observations of Electromagnetic Perturbations Connected with Seismic Activity. *Geophys. Res. Lett.* 35, L05109. doi:10.1029/2007GL032517

Němec, F., Santolík, O., and Parrot, M. (2009). Decrease of Intensity of ELF/VLF Waves Observed in the Upper Ionosphere Close to Earthquakes: A Statistical Study. *J. Geophys. Res.* 114, A4. doi:10.1029/2008JA013972

Nenovski, P. (2015). Experimental Evidence of Electrification Processes during the 2009 L'Aquila Earthquake Main Shock. *Geophys. Res. Lett.* 42 (18), 7476–7482. doi:10.1002/2015GL065126

Ohta, K., Izutsu, J., Schekotov, A., and Hayakawa, M. (2013). The ULF/ELF Electromagnetic Radiation before the 11 March 2011 Japanese Earthquake. *Radio Sci.* 48, 589–596. doi:10.1002/rds.20064

Oike, K., and Yamada, T. (1994). "Relationship between Shallow Earthquakes and Electromagnetic Noises in the LF and VLF Ranges," in *Electromagnetic Phenomena Related to Earthquake Prediction* (Tokyo: Terra Scientific Publishing Company), 115–130.

Orsini, M. (2011). Electromagnetic Anomalies Recorded before the Earthquake of L'Aquila on April 6, 2009. *Bollettino di Geofisica Teorica e Applicata* 52 (1), 123–130.

Ouzounov, D., Pulinets, S., Hattori, K., and Taylor, P. (2018). *Pre-Earthquake Processes: A Multidisciplinary Approach to Earthquake Prediction Studies, AGU Geophysical Monograph*. Wiley, 365 p. doi:10.1002/9781119156949

Parrot, M., and Lefeuvre, F. (1985). Correlation between GEOS VLF Emissions and Earthquakes. *Ann. Geophys.* 3 (6), 733–748.

Parrot, M., and Mogilevsky, M. M. (1989). VLF Emissions Associated with Earthquakes and Observed in the Ionosphere and the Magnetosphere. *Phys. Earth Planet. Interiors* 57, 86–99. doi:10.1016/0031-9201(89)90218-5

Parrot, M. (1994). Statistical Study of ELF/VLF Emissions Recorded by a Low-Altitude Satellite during Seismic Events. *J. Geophys. Res.* 99 (A12), 339–347. doi:10.1029/94ja02072

Parrot, M. (2002). The Micro-satellite DEMETER. *J. Geodynamics* 33, 535–541. doi:10.1016/s0264-3707(02)00014-5

Parrot, M. (2011). Statistical Analysis of the Ion Density Measured by the Satellite DEMETER in Relation with the Seismic Activity. *Earthq. Sci.* 24, 513–521. doi:10.1007/s11589-011-0813-3

Piersanti, M., Materassi, M., Battiston, R., Carbone, V., Cicone, A., D'Angelo, G., et al. (2020). Magnetospheric-Ionospheric-Lithospheric Coupling Model. 1: Observations during the 5 August 2018 Bayan Earthquake. *Remote Sensing* 12, 3299. doi:10.3390/rs12203299

Pulinets, S. A., and Boyarchuk, K. A. (2004). *Ionospheric Precursors of Earthquakes*. Berlin: Springer, 315.

Pulinets, S. A., Ouzounov, D. P., Karelin, A. V., and Davidenko, D. V. (2015). Physical Bases of the Generation of Short-Term Earthquake Precursors: a Complex Model of Ionization-Induced Geophysical Processes in the Lithosphere-Atmosphere-Ionosphere-Magnetosphere System. *Geomagn. Aeron.* 55 (4), 521–538. doi:10.1134/s0016793215040131

Pulinets, S. A. (1998b). Seismic Activity as a Source of the Ionospheric Variability. *Adv. Space Res.* 22, 903–906. doi:10.1016/S0273-1177(98)00121-5

Pulinets, S. A. (2006). Space Technologies for Short-Term Earthquake Warning. *Adv. Space Res.* 37, 643–652. doi:10.1016/j.asr.2004.12.074

Pulinets, S. A. (1998a). Strong Earthquake Prediction Possibility with the Help of Topside Sounding from Satellites. *Adv. Space Res.* 21 (3), 455–458. doi:10.1016/s0273-1177(97)00880-6

Rikitake, T. (1976). *Earthquake Prediction*. Amsterdam: Elsevier Scientific Publishing Company, 381.

Rikitake, T. (1987). Earthquake Precursors in Japan: Precursor Time and Detectability. *Tectonophysics* 136, 265–282. doi:10.1016/0040-1951(87)90029-1

Rikitake, T. (2003). *Predictions and Precursors of Major Earthquakes*. Tokyo: Terra Scientific Publishing Company.

Rodger, C. J., Clilverd, M. A., Green, J., and Lam, M.-M. (2010). Use of POES SEM-2 Observations to Examine Radiation belt Dynamics and Energetic Electron Precipitation in to the Atmosphere. *J. Geophys. Res.* 115, A04202. doi:10.1029/2008ja014023

Rodger, C. J., Thomson, N. R., and Dowden, R. L. (1996). A Search for ELF/VLF Activity Associated with Earthquakes Using ISIS Satellite Data. *J. Geephys. Res.* 13, 369–378. doi:10.1029/96JA00078

Schekotov, A., Chebrov, D., Hayakawa, M., Belyaev, G., and Berseneva, N. (2019). Short-term Earthquake Prediction in Kamchatka Using Low-Frequency Magnetic fields. *Nat. Hazards* 100, 735–755. doi:10.1007/s11069-019-03839-2

Schekotov, A., Molchanov, O., Hattori, K., Fedorov, E., Gladyshev, V. A., Belyaev, G. G., et al. (2006). Seismo-ionospheric Depression of the ULF Geomagnetic Fluctuations at Kamchatka and Japan. *Phys. Chem. Earth, Parts A/B/C* 31, 313–318. doi:10.1016/j.pce.2006.02.043

Serebryakova, O. N., Bilichenko, S. V., Chmyrev, V. M., Parrot, M., Rauch, J. L., Lefeuvre, F., et al. (1992). Electromagnetic ELF Radiation from Earthquake Regions as Observed by Low-Altitude Satellites. *Geophys. Res. Lett.* 19, 91–94. doi:10.1029/91gl02775

Sgrigna, V., Carota, L., Conti, L., Corsi, M., Galper, A. M., Koldashov, S. V., et al. (2005). Correlations between Earthquakes and Anomalous Particle Bursts from SAMPEX/PET Satellite Observations. *J. Atmos. Solar-Terrestrial Phys.* 67, 1448–1462. doi:10.1016/j.jastp.2005.07.008

Sorokin, V. M., Chmyrev, V. M., and Yaschenko, A. K. (2001). Electrodynamic Model of the Lower Atmosphere and the Ionosphere Coupling. *J. Atmos. Solar-Terrestrial Phys.* 63 (16), 1681–1691. doi:10.1016/s1364-6826(01)00047-5

Strakhov, V. N., Gladyshev, V. A., Molchanov, O. A., and Pokhotelov, O. A. (1994). "On the Perspectives of Monitoring of the Seismic Activity on Board the Satellite ("Demeter" Project)," in *Electromagnetic Phenomena Related to Earthquake Prediction*. Editors M. Hayakawa and Y. Fujinawa (Tokyo: TERRAPUB), 475–481.

Thomas, J. N., Huard, J., and Masci, F. (2017). A Statistical Study of Global Ionospheric Map Total Electron Content Changes Prior to Occurrences of M ≥ 6.0 Earthquakes during 2000-2014. *J. Geophys. Res. Space Phys.* 122, 2151–2161. doi:10.1002/2016JA023652

Tramutoli, V., Corrado, R., Filizzola, C., Genzano, N., Lisi, M., and Pergola, N. (2015). From Visual Comparison to Robust Satellite Techniques: 30 Years of thermal Infrared Satellite Data Analyses for the Study of Earthquake Preparation Phases. *Boll. Geof. Teor. Appl.* 56, 167–202. doi:10.4430/bgta0149

Van Allen, J. A. (1959). The Geomagnetically Trapped Corpuscular Radiation. *J. Geophys. Res.* 64, 1683–1689. doi:10.1029/jz064i011p01683

Voronov, S. A., Galper, A. M., and Koldashov, S. V. (1989). Observation of High-Energy Charged Particle Flux Increases in SAA Region in 10 September 1985. *Cosmic Res.* 27 (4), 629–631.

Walt, M. (1994). *Introduction to Geomagnetically Trapped Radiation*. Cambridge: Cambridge University, 168.

Wyss, M. (1997). Second Round of Evaluations of Proposed Earthquake Precursors. *Pageoph.* 149, 3–16. doi:10.1007/bf00945158

Yando, K., Millan, R. M., Green, J. C., and Evans, D. S. (2011). A Monte Carlo Simulation of the NOAA POES Medium Energy Proton and Electron Detector Instrument. *J. Geophys. Res.* 116, A10231. doi:10.1029/2011ja016671

Yang, S. S., Asano, T., and Hayakawa, M. (2019). Abnormal Gravity Wave Activity in the Stratosphere Prior to the 2016 Kumamoto Earthquakes. *J. Geophys. Res. Space Phys.* 124 (2), 1410–1425. doi:10.1029/2018ja026002

Zechar, J. D., and Jordan, T. H. (2008). Testing Alarm-Based Earthquake Predictions. *Geophys. J. Inter.* 172 (2), 715–724. doi:10.1111/j.1365-246X.2007.03676.x

Zhang, Y., and Meng, Q. (2019). A Statistical Analysis of TIR Anomalies Extracted by RSTs in Relation to an Earthquake in the Sichuan Area Using MODIS LST Data. *Nat. Hazards Earth Syst. Sci.* 19, 535–549. doi:10.5194/nhess-19-535-2019

Zhu, F., Su, F., and Lin, J. (2018). Statistical Analysis of TEC Anomalies Prior to M6.0+ Earthquakes during 2003-2014. *Pure Appl. Geophys.* 175, 3441–3450. doi:10.1007/s00024-018-1869-y

Zhu, F., Zhou, Y., Lin, J., and Su, F. (2014). A Statistical Study on the Temporal Distribution of Ionospheric TEC Anomalies Prior to M7.0+ Earthquakes during 2003-2012. *Astrophys Space Sci.* 350 (2), 449–457. doi:10.1007/s10509-014-1777-2

Conflict of Interest: The author declares that the research was conducted in the absence of any commercial or financial relationships that could be construed as a potential conflict of interest.

frontiers in Earth Science

ORIGINAL RESEARCH
published: 12 August 2021
doi: 10.3389/feart.2021.656216

Discriminating the Multi-Frequency Microwave Brightness Temperature Anomalies Relating to 2017 Mw 7.3 Sarpol Zahab (Iran-Iraq Border) Earthquake

Yifan Ding[1,2], **Yuan Qi**[1,2]*, **Lixin Wu**[1,2]*, **Wenfei Mao**[1,2] **and Yingjia Liu**[1,2]

[1]School of Geosciences and Info-Physics, Central South University, Changsha, China, [2]Laboratory of Geo-hazards Perception, Cognition and Prediction, Central South University, Changsha, China

A Mw 7.3 earthquake occurred near the Iran-Iraq border on November 12, 2017, as the result of oblique-thrust squeezing of the Eurasian plate and the Arabian plate. By employing the spatio-temporally weighted two-step method (STW-TSM) and microwave brightness temperature (MBT) data from AMSR-2 instrument on board Aqua satellite, this paper investigates carefully the spatiotemporal features of multi-frequency MBT anomalies relating to the earthquake. Soil moisture (SM), satellite cloud image, regional geological map and surface landcover data are utilized to discriminate the potential MBT anomalies revealed from STW-TSM. The low-frequency MBT residual images shows that positive anomalies mainly occurred in the mountainous Urmia lake and the plain region, which were 300 km north and 200 km southwest about to the epicenter, respectively. The north MBT anomaly firstly appeared 51 days before the mainshock and its magnitude increased over time with a maximum of about +40K. Then the anomaly disappeared 3 days before, reappeared 1d after and diminished completely 10 days after the mainshock. Meanwhile, the southwest MBT anomaly firstly occurred 18 days before and peaked 3 days before the mainshock with a maximum of about +20K, and then diminished gradually with aftershocks. It is speculated that the positive MBT anomaly in the Urmia lake was caused by microwave dielectric property change of water body due to gas bubbles leaking from the bottom of the lake disturbed by local crust stress alteration, while the southwest MBT positive anomaly was caused by microwave dielectric constant change of shallow surface due to accumulation of seismically-activated positive charges originated at deep crust. Besides, some accidental abnormal residual stripes existed in line with satellite orbit, which turned out to be periodic data errors of the satellite sensor. High-frequency MBT residual images exhibit some significant negative anomalies, including a narrow stripe pointing to the forthcoming epicenter, which were confirmed to be caused by synchronous altostratus clouds. This study is of guidance meaning for distinguishing non-seismic disturbances and identifying seismic MBT anomaly before, during and after some large earthquakes.

Keywords: Sarpol Zahab earthquake, earthquake anomaly, microwave brightness temperature, STW-TSM, multi-frequency data, remote sensing

OPEN ACCESS

Edited by:
Dimitar Ouzounov,
Chapman University, United States

Reviewed by:
Angelo De Santis,
University of Studies G d'Annunzio Chieti and Pescara, Italy
Feng Jing,
China Earthquake Administration, China

***Correspondence:**
Yuan Qi
weloveqy@163.com
Lixin Wu
wulx66@csu.edu.cn

Specialty section:
This article was submitted to Geohazards and Georisks, a section of the journal Frontiers in Earth Science

Received: *20 January 2021*
Accepted: *02 August 2021*
Published: *12 August 2021*

Citation:
Ding Y, Qi Y, Wu L, Mao W and Liu Y (2021) Discriminating the Multi-Frequency Microwave Brightness Temperature Anomalies Relating to 2017 Mw 7.3 Sarpol Zahab (Iran-Iraq Border) Earthquake. Front. Earth Sci. 9:656216. doi: 10.3389/feart.2021.656216

INTRODUCTION

Microwave radiative signals are capable of penetrating thick fog and clouds, and do not rely on the Sun as the source for illumination. These particular attributes allow microwave radiation monitoring of the Earth's surface become valid under almost all-weather conditions (Ulaby and Long, 2015). Since 2008, satellite microwave brightness temperature (MBT) has been preliminarily adopted for thermal anomaly monitoring of volcanic and earthquake activities (Maeda and Takano, 2008; Takano and Maeda, 2009). Afterwards, Maeda and Takano (2009, 2010) used MBT data at 18.7 GHz from AMSR-E instrument to detect microwave radiation anomaly associated with 2008 Wenchuan earthquake and 2004 Morocco earthquake, and found obvious abnormal microwave signals distributing along the seismogenious faults or near the epicenter region. Subsequently, Chen and Jin (2010) proposed a radiation anomaly index to analyze microwave radiation anomaly of 2010 Yushu earthquake, and revealed a MBT anomaly area behaving great spatial correlation with the main faults 2 days before the mainshock; Jing et al. (2020) detected the anomalous MBT associated with three strong earthquakes occurred in Sichuan province, China, and also found that the MBT anomalies distributed around the forthcoming epicenter or along the main faults. Recently, Qi et al. (2020a) proposed the spatio-temporally weighted two-step method (STW-TSM) and validated its effectiveness by revealing and analyzing the spatiotemporal evolution of MBT anomalies of 2008 Wenchuan earthquake sequence (Qi et al., 2020a, b) and 2015 Nepal earthquake sequence (Qi et al., 2020c). Although current studies are based on different methods and various microwave satellite data, they have uncovered valuable seismic-related thermal anomalies before, during and after the earthquakes. This indicates that it is a feasible and promising way to use satellite MBT data to reveal particular phenomena and to explore geophysical mechanism of seismic thermal anomaly.

The Mw 7.3 Sarpol Zahab earthquake, occurred on November 12, 2017, was caused by the oblique-thrust faulting beneath the Iran-Iraq border (Yang et al., 2018). The epicenter located at the small town named Sarpol Zahab, with a depth of about 17.9 km, south of the Zagros Mountains that is seismically active (Berberian and King, 1981). So far, there are some relevant studies reported about the possible anomaly before this significant earthquake. Tariq et al. (2019) analyzed the time series of total electron content (TEC) in Iran-Iraq area, and found that there were anomalies several days before the earthquake, among which the anomalies 5days before the earthquake were caused by magnetic storms, and the ionospheric anomalies 8–11 days before the earthquake were thought to be related to the earthquake. Akhoondzadeh et al. (2019) studied the TEC and four atmospheric parameters (skin temperature, vertical column water vapor, aerosol optical thickness and sulfur dioxide) near the epicenter. They found that TEC 11 days before the earthquake enhanced obviously, while most atmospheric parameters presented abnormal in different times before the ionospheric anomaly. The sulfur dioxide anomaly, total aerosol thickness (AOT) anomaly, and skin temperature (SKT) anomaly occurred 9–19 days, 9–17 days and 14–15 days before the earthquake, respectively. These parameters all appeared before the ionospheric anomaly, which exhibited the potential effect of lithosphere-atmosphere-ionosphere (LAI) coupling (Pulinets and Ouzounov, 2011). Zhou, (2019) combined multi-parameter of land surface, near-surface, upper atmosphere and ionosphere to analyze abnormal precursor information in each geosphere before the earthquake, and further analyzed and confirmed the coupling effects between different geospheres.

However, the above researches mainly focus on atmospheric and ionospheric parameters, the coversphere (including water bodies, snow and ice, soil and sand layers, deserts, and vegetation) as well as the surface thermal radiative parameter is overlooked. The Iran-Iraq area is featured with simple land cover such as flat terrain, lifted mountain and sparse vegetation, and with stable climate (Saraf et al., 2008). It is regarded that the coversphere modifies the geo-electromagnetic signals from the deep crust and underground to the Earth's surface (Wu et al., 2012, 2016). The physical properties of the Earth's surface are critical to the microwave radiative capacity and satellite thermal observation. Therefore, monitoring seismic thermal anomaly using satellite MBT data will be less disturbed in the Iran-Iraq border area, which is worthy of detailed exploratory research.

This research aims to uncover the spatiotemporal evolution of MBT anomalies relating to the Sarpol Zahab earthquake by employing STW-TSM. Based on regional crust stress variations, existing theories and experiments, the uncovered MBT anomalies in the northern Urmia lakes and in the southwestern study area before and after the Sarpol Zahab earthquake are interpreted. By using soil moisture (SM) and satellite cloud images, as well as contrast analysis of low-high frequency MBT residual images, occasional positive abnormal stripes and characteristic negative anomalies are ruled out of possible seismic anomalies, which is of instructive significance for discriminating seismic MBT anomalies using multiple source auxiliary data.

STUDY AREA

The Iran-Iraq region is located at the junction of the Eurasian plate and the Arabian plate, and has a tropical desert climate with large areas of deserts and plateaus (Salahi and Asareh, 2008). As shown in **Figure 1**, the Caspian Sea is located to the northeast of the study area, while the Zagros mountains are in the middle, with undulating terrain; and the Mesopotamia plain is in the southwest, with quite flat terrain. The Arabian plate subducted under the Eurasian plate at a speed of about 30 mm per year, which caused the Eurasian plate to constantly rise and form Zagros mountains (Reilinger et al., 2006), and also made the Iran-Iraq region one of the most frequent seismic regions in the world. The Sarpol Zahab earthquake occurred at 18:18:25 (UTC) on November 12, 2017, near the border between Iran and Iraq ($34.911^{\circ}N, 45.959^{\circ}E$), south of the Zagros fault, with a depth

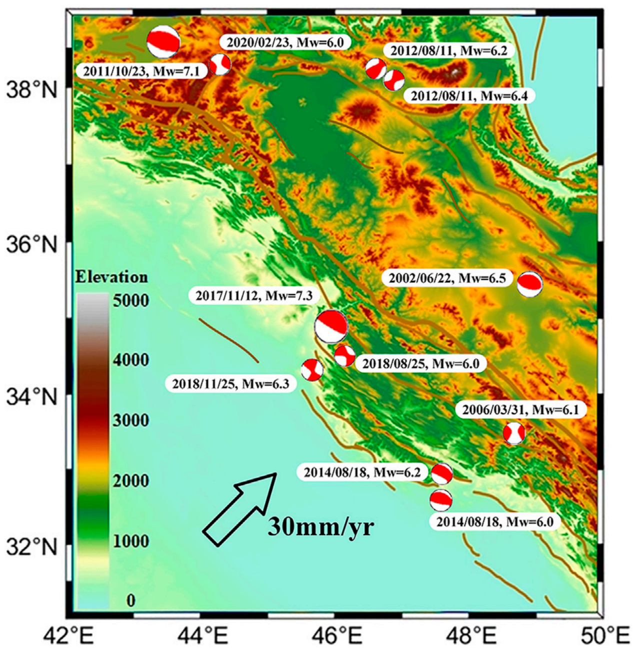

FIGURE 1 | The terrain of Zagros mountains and eastern Mesopotamia plain.

of 17.9 km and a magnitude of 7.3, which was the largest earthquake to strike the Iran-Iraq region this century. We collected earthquakes (Mw > 4.5) in the study area (as shown in subgraph in **Figure 2**) from 2015 to 2019 (data from USGS). The temporal seismicity in the study area from 2015 to 2019 is shown in **Figure 2**. The black dots represent magnitude and the blue bars denote the number of earthquakes per day. It can be seen from the figure that the seismicity in the area was less frequent from 2015 to May 2017, but more frequent from July 2017 to 2019. Rare seismic activity in this region before Sarpol Zahab earthquake might imply that the energy in the crust was in a state of accumulation. After the strong earthquake, the accumulated energy of the Earth's crust was constantly released, which made the seismic activity in this region more frequent.

MATERIALS AND METHOD

The Advanced Microwave Scanning Radiometer-2 (AMSR-2), a successor of AMSR on the Advanced Earth Observing Satellite-II and AMSR for EOS (AMSR-E) on NASA's Aqua satellite, is a single mission instrument on GCOM-W1 (Imaoka et al., 2012). The AMSR-2 is a five-frequency microwave radiometer system with dual polarization capability (Vertical and Horizontal, i.e., H & V in brief) for all frequency bands. The observations from AMSR-2 occur between approximately 1:30 a.m. and 2:30 a.m. (descending mode), 1:30 p.m. and 2:30 p.m. (ascending mode) local time. Basic characteristics of AMSR-2 instrument are shown in **Table 1**.

Low-frequency microwave signal has a certain penetration to the arid and desert areas, while high-frequency microwave signal has a certain sensitivity to the possible cloud and rain in the study area. The MBT data of 89 GHz has two channels with different incident angles, in which the incident angle of channel A is consistent with that of the low frequency. So that MBT of 89 GHz with channel-A is adopted to ensure the consistency of the incidence angle of the lower bands. In addition, soil moisture (SM) data retrieved from 10.65 GHz MBT data, satellite cloud images at nighttime derived from Meteosat-8, SRTM-DEM dataset with 30 m resolution, geological map provided by the Geological Survey of Canada (GSC), and land cover data with 30 m spatial resolution provided by the National Geomatics Center of China (NGCC) are also used in this research, in order to conduct the discriminating analysis using multi-source auxiliary data.

The diameter of preparation zone of Mw 7.3 earthquake calculated from Dobrovolsky's equation (Dobrovolsky et al., 1979) is about 2750 km, which is much large than the swath width of AMSR-2 data (1450 km). It is impossible to cover the entire preparation zone for a single swath of the observation. Therefore, the study area is selected as $42^\circ \sim 50^\circ E, 31^\circ \sim 39^\circ N$ in consideration of both the size of Dobrovolsky's zone and the spatial coverage of AMSR-2 swath. Historical earthquakes

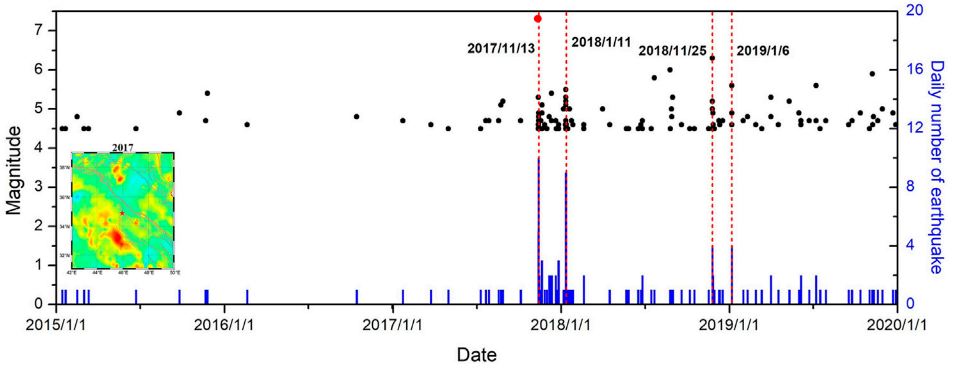

FIGURE 2 | Time series of seismicity (Mw ≥ 4.5) in study area. The red dashed line represents the date of the data.

TABLE 1 | Major performances and characteristics of AMSR-2.

Parameter	Performance and characteristic					
Observation frequency (GHz)	10.65	18.7	23.8	36.5	89.0(A)	89.0(B)
Observation Polarization	Vertical and horizontal polarizations (H & V)					
Measuring range (K)	2.7–340					
Spatial resolution (km)	50	25		15	5	
NEΔT (K)	<0.7	<0.7	<0.6	<0.7	<1.2	<1.2
IFOV (km)	42 × 24	22 × 14	26 × 15	12 × 7	5 × 3	5 × 3
Swath width (km)	1,450					
Incidence angle (°)	-	-	55.0	-	-	54.5
Off-nadir angle (°)	-	-	47.5	-	-	47.0

of magnitude greater than or equal to 6.0 in the study are listed in **Table 2**. In order to avoid the impact of other strong earthquakes and ensure the adequacy of MBT data for constructing historical background, historical MBT data for a month before and a month after a strong earthquake (Mw 6.0 on November 22, 2013; Mw 5.7 on October 15, 2014; Mw 6.3 on November 25, 2018; Mw 5.9 on November 7, 2019) were removed in data preprocessing.

STW-TSM is employed in this research for seismic anomaly detection. The principle of the STW-TSM is to obtain the basic residuals of the Earth surface MBT by removing the inherent general and stable trend with a temporally weighted background in the first step as in following equation:

$$T_{\omega}(x,y,t_{\xi}) = \frac{\sum_{i=1}^{n}\left[\exp\left(-\frac{(\varphi_i-\xi)^2}{D_1^2}\right)\cdot T(x,y,t_i)\right]}{\sum_{i=1}^{n}\left[\exp\left(-\frac{(\varphi_i-\xi)^2}{D_1^2}\right)\right]} \tag{1}$$

$$\Delta T(x,y,t_{\xi}) = T(x,y,t_{\xi}) - T_{\omega}(x,y,t_{\xi}) \tag{2}$$

where φ_i denotes any non-seismic year and its serial number is i, ξ is the earthquake year, D_1 is the maximum number of time interval years between all non-seismic years and shocking year, t_{ξ} is any day in the seismogenic year and t_i is the same day as t_{ξ} in the non-seismogenic year, $T(x,y,t_i)$ and $T_{\omega}(x,y,t_{\xi})$ represent the observed MBT values of pixels (x,y) on day t_i and day t_{ξ}, respectively, $T_{\omega}(x,y,t_{\xi})$ is the weighted reference value calculated from all $T(x,y,t_i)$, and $\Delta T(x,y,t_{\xi})$ is the basic residual value of the pixel (x,y) on day t_{ξ}.

Then, to retain the cleaned MBT residuals by eliminating the internal short-term variable effects in the study area with a spatially weighted background in the second step as in the following equation:

TABLE 2 | Historical earthquakes (Mw ≥ 6.0) from 2012 to 2019 in the study area (from USGS).

Location	Time (UTC)	Magnitude (mw)	Depth (km)
Ahar Varzaghan	2012.08.11	6.4	11.0
Murmuri	2014.08.18	6.2	10.2
Sarpol Zahab	2017.11.12	7.3	19.0
Javanrud	2018.08.25	6.0	10.0
Sarpol Zahab	2018.11.25	6.3	18.0

$$T_m(x,y,t_{\xi}) = \frac{\sum_{k=1}^{p}\left[\exp\left(-\frac{(i_k-x)^2+(i_k-y)^2}{D_2^2}\right)\cdot T(i_k,i_k,t_{\xi})\right]}{\sum_{k=1}^{p}\left[\exp\left(-\frac{(i_k-x)^2+(i_k-y)^2}{D_2^2}\right)\right]} \tag{3}$$

$$\Delta\Delta T(x,y,t_{\xi}) = \Delta T(x,y,t_{\xi}) - T_m(x,y,t_{\xi}) \tag{4}$$

where k is the sequence number of any pixel in the far field, p is the number of far-field pixels, (i_k, j_k) is any geographical position of the far field in the study area, D_2 is the diagonal length of the study area, $T_m(x,y,t_{\xi})$ represents the interpolated value of the far field pixel of point (x,y) on any day of t_{ξ} in the shocking year, and $\Delta\Delta T(x,y,t_{\xi})$ is the cleaned residual value (Qi et al., 2020a). A detailed description of this method is demonstrated in Qi et al., 2020a. Ultimately, the obtained cleaned MBT residual maps are adopted for performing comparative analysis to discriminating multiple MBT anomalies relating to the 2017 Sarpol Zahab earthquake.

RESULTS

Spatiotemporal Features of Low-High Frequency MBT Residuals

Figure 3 shows the spatiotemporal evolution of cleaned MBT residuals with 10.65 and 89 GHz at H polarization. As for the low-frequency (10.65 GHz) results, positive MBT anomaly mainly concentrated in the northern mountainous Urmia Lake and southwestern plain area (bare land and cultivated land) near the epicenter. Besides, there also existed several fortuitous strip-shaped abnormal MBT residuals, which were in line with the direction of satellite orbit (i.e., on September 21, October 7, November 8, and November 22).

The positive MBT anomaly in the northern mountainous Urmia Lake firstly appeared 51 days before the Mw 7.3 earthquake (September 21, 2017), and the amplitude and range of the anomaly increased with the approaching of the earthquake with a maximum of about 40K. From 3 days before (November 9) the earthquake, the positive anomaly of the lake region significantly reduced until it disappeared 1 day before the earthquake (November 11). Then the anomaly reoccurred 1d after the earthquake (November 13) but maintained relative low level compared with that before the earthquake until 5 days after the earthquake (November 17). Subsequently, the anomaly began

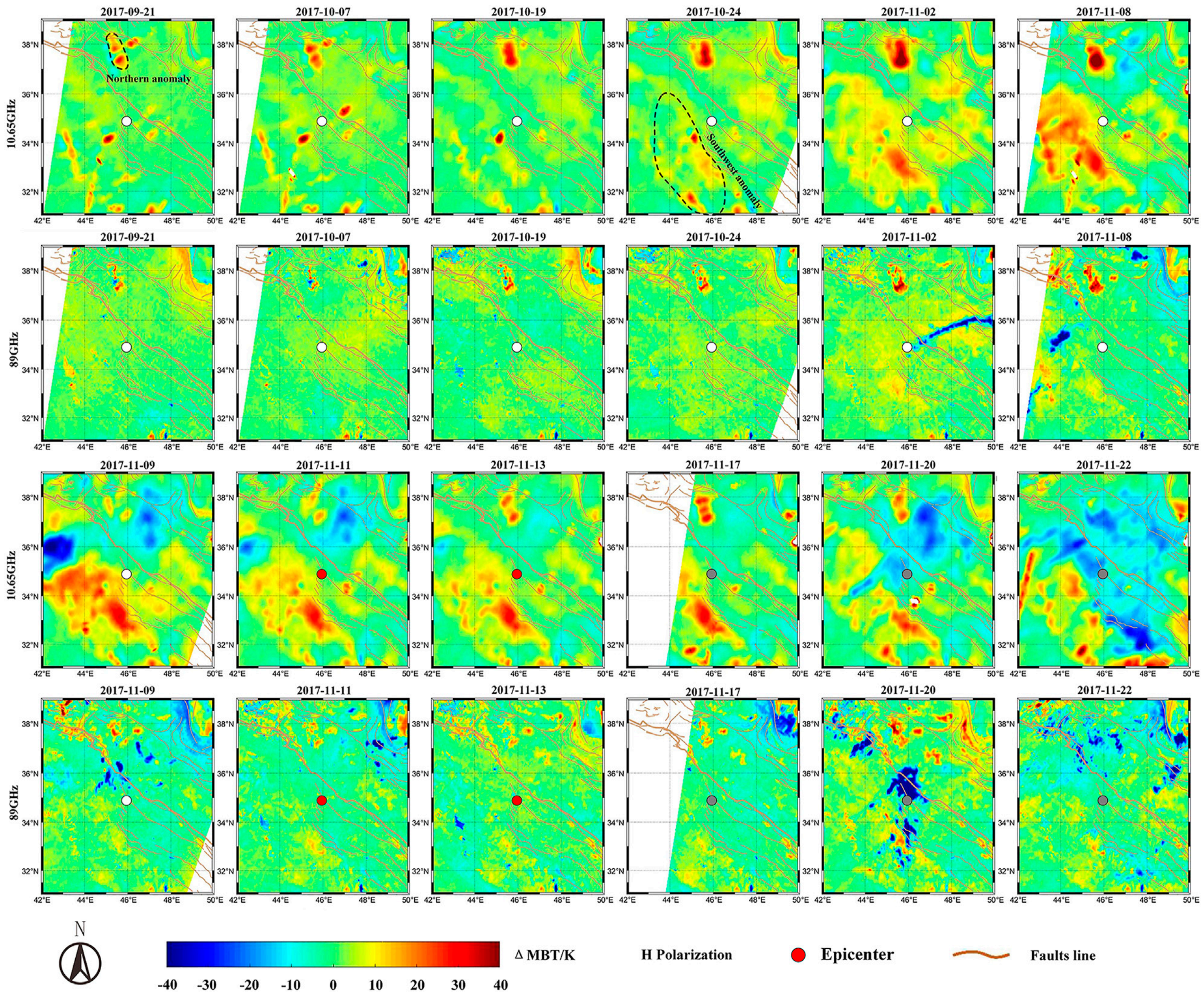

FIGURE 3 | Spatiotemporal evolution of the MBT residuals with 10.65 and 89 GHz at H polarization. The circle dots mark the epicenters of the shock, with white, red, and gray color for the days before earthquake, during earthquake, and after earthquake, respectively.

to fade gradually and disappeared completely 10 days after the earthquake (November 22). The evolution pattern of MBT anomaly in the Urmia Lake behaved as: occurring and continuously strengthening before the earthquake, reaching to the peak and then immediately disappearing during the short-impending of the earthquake, reoccurring and gradually dissipating after the earthquake.

The positive MBT anomaly in the southwest plain area firstly appeared 18 days before the earthquake (October 24, 2017), and also strengthened over time. The amplitude and range of the south anomaly achieved the peak 3 days before the earthquake (November 9) with a maximum of about 20K, and then started to decay on November 11. Slight positive anomaly persisted in this area until early February of the next year (see **Supplementary Figure S1**). The evolution pattern of the southwest MBT anomaly behaved as: occurring before the earthquake, strengthening continuously and reaching the peak during the short-impending of the earthquake, decaying gradually shortly before and after the earthquake.

As for the high-frequency (89 GHz) results, positive MBT anomaly in the northern mountainous Urmia lake behaved the same spatiotemporal pattern as that of low-frequency results, but the amplitude and range of the anomaly were relatively weak and small. However, the high-frequency MBT data failed to reveal positive regional anomaly in the southwest plain area. Meanwhile, there existed an obvious strip-shaped negative anomaly pointing at the forthcoming epicenter from east to west on November 2, and a regional negative anomaly almost overlapping with the epicenter on November 20. The negative anomalies are very characteristic and deserves further attention.

As described above, there are four types of MBT anomalies in the revealed residual images, including positive anomaly in the Urmia lake at both low-frequency and high-frequency bands, regional positive anomaly in the southwest plain area at low-frequency band, occasional abnormal positive stripes at low-frequency band, and significant negative abnormal residuals at high-frequency band.

Meteorological Disturbance and Negative Anomaly Discrimination

The MBT data of 89 GHz has better performance to reflect the influence from atmospheric clouds and heavy rains, for microwave signals at this band have shorter wavelength and better susceptibility to atmosphere (Eastman et al., 2019). Therefore, the possible causes of the negative MBT anomalies are analyzed, using multi-source remote sensing data involving original MBT observations, SM data and infrared satellite cloud images (nighttime). The comparative results are presented as in **Figure 4**.

As one can see, in the first row of **Figure 4**, an evident negative MBT residual stripe pointed at the epicenter from east to west on November 2, 2017, which also could be reflected as a negative stripe in the MBT image and as a high value stripe in the SM image. Checking the synchronous infrared satellite cloud images, it is easy to find a linear cloud in the area where the negative MBT anomaly was located. Besides, from the second row of **Figure 4**, the featured negative phenomena are visible in the black dotted box on November 20, 2017, which were consistent in space with low values in MBT image, high values in SM image, and thick clouds in the infrared cloud images. Obviously, we can draw a preliminary conclusion that the negative anomalies in high-frequency residual images were related with the synchronous clouds. However, the cloud images in **Figure 4** also indicate that only part of the clouds corresponded well with the negative anomalies, and what attributes of clouds were responsible for the negative residual values needs further analysis.

Figure 5 shows the cloud amount at three different altitude in the study area on November 2 and November 20, 2017. It can be found that the cloud on November 2 was mostly concentrated in the middle layer, but the cloud corresponding to the negative MBT residuals mainly existed in the high layers. On November 20, most of the clouds were concentrated in the middle and high layers, but the cloud corresponding to the negative MBT residuals mainly existed in the high layers. It is known that altostratus clouds are mainly composed of small ice crystals (Zhao et al., 2002), and the influence of solid particles such as snow, ice and haze are suggested reduce the microwave radiation of cloud comparing with cloudless conditions (Gu et al., 2016). Therefore, cloud at high altitude (altostratus cloud) are considered to cause the negative MBT anomalies at high frequency in this study.

ATTRIBUTION ANALYSIS

Periodical Positive MBT Residual Stripes

As mentioned above, there existed some positive stripes in the MBT residual images, which are marked with black dotted boxes in **Figure 6**. The stripes are in the same direction with the satellite orbit and have strict periodicity in recurrence time. According to their geolocations, the stripes can be divided into four categories, naming A, B, C, and D (see **Figure 6**). As one can see, stripe A and D both occurred on October 30 and November 15, 2017, stripe B occurred on November 6 and November 22, 2017, while stripe C occurred on November 8 and November 24, 2017. The time intervals of the reoccurrence of the respective stripes are all 16 days, which is exactly consistent with the revisit cycle of the AMSR-2 instrument. The MBT images in **Figure 6** show that four types of stripes actually come from the original satellite observations, which are not in harmony with normal observations.

Simplify taking stripe A and D as an example, the positive MBT residuals with five different bands (10.65, 18.7, 23.8, 36.5 and 89 GHz) are compared in **Figure 7**. It could be found that the abnormal stripes existed only in the results of 10.65 GHz. **Figure 8** exhibits the stripes A and D with 10.65 GHz at H and V polarization, and the abnormal stripes existed only in the results at H polarization. Furthermore, we extended the time range from months before the earthquake to months after the earthquake, to examine the periodicity and persistence of the four abnormal stripes, and the results proved the phenomena stated.

From above comparative analysis, it is known that the abnormal stripes existed only in MBT residual maps with 10.65 GHz at H polarization, and the interval time of reoccurrence were all 16 days. It can be deduced that the abnormal stripes may be data errors caused by sensor failures, which has nothing to do with seismic activity.

Positive MBT Residuals in the Mountainous Urmia Lake

Referring to microwave remote sensing physics, MBT can be expressed as the product of microwave emissivity and physical temperature (Ulaby et al., 1981). As one can note from above results that the original MBT observations in the Urmia lake are at low level, which is because the physical temperature and emissivity of the water body all are low. Contrastively, in the revealed MBT residual images, the residual values in the lake area are much higher than that of surrounding land area. It was regarded that rock mass friction and collisions between the fault planes might cause the physical temperatures of ground surface to rise during the preparation phase of an earthquake (Wu et al., 2006). Nevertheless, such temperature changes in the deep crust are difficult to affect the remote coversphere, especially the water body, and physical temperature changes of up to tens of K are theoretically impossible. Therefore, alterations in emissivity of lake area are essential except for the potential minor contribution of physical temperature rise.

Microwave signals of low frequency have certain penetrability to the object surface, and can reflect the radiation characteristics of water body to a certain depth. Microwave satellite observations are proved very sensitive to the physical properties of the water bodies through the effects on the microwave dielectric constant and the emissivity (Ulaby and

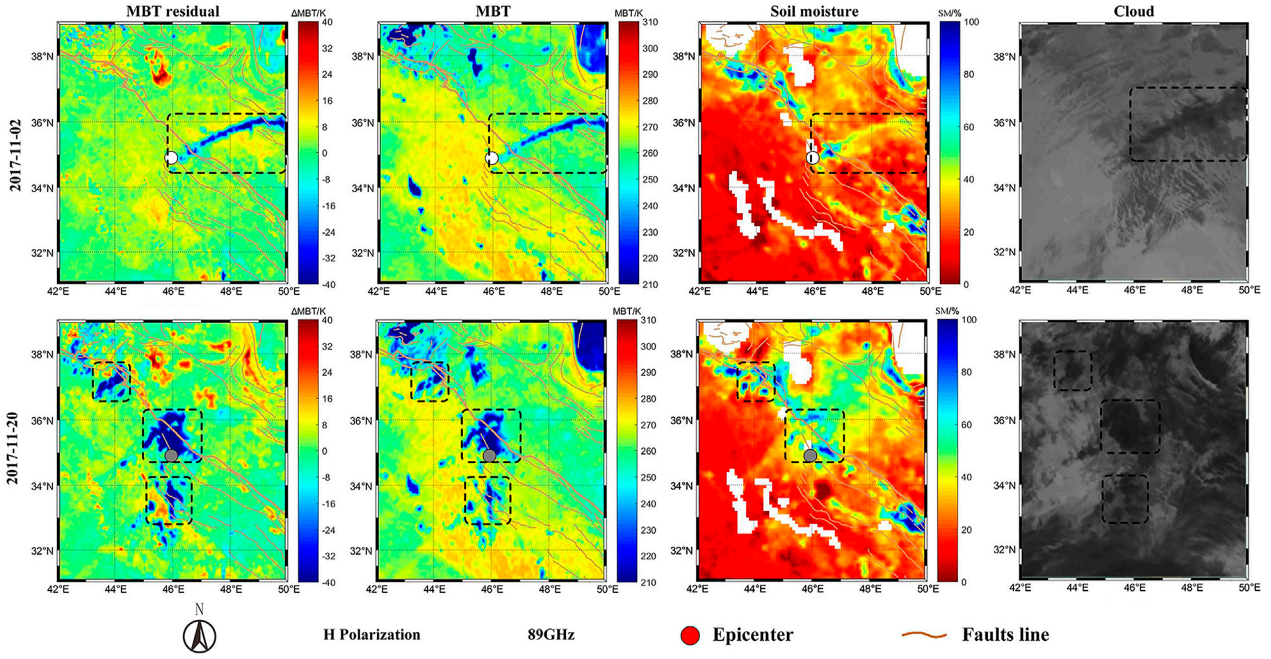

FIGURE 4 | Negative MBT residual images, MBT original observations, soil moisture, and satellite cloud images on November 2 and November 20, 2017.

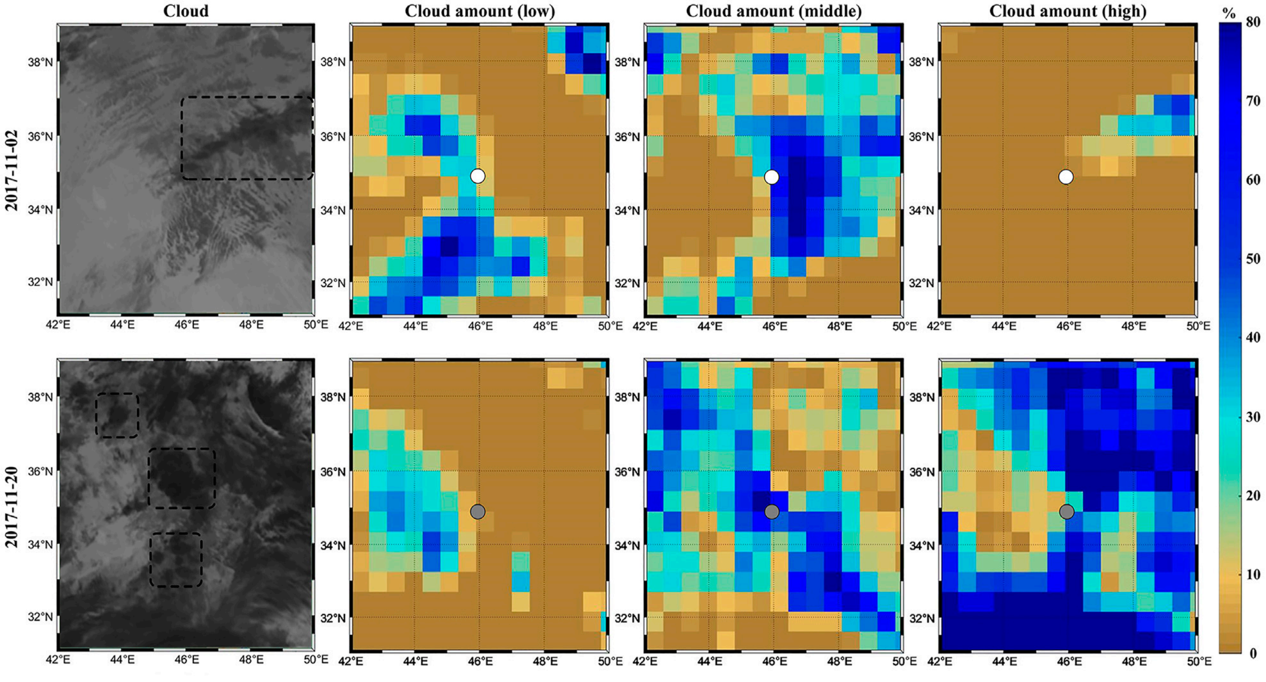

FIGURE 5 | Cloud amount at different altitudes.

Long, 2015). According to Ziolkowski, (1998), the change in stress before an earthquake would cause the gas to swell and contract under the action of still water, resulting in bubbles and then floating from the bottom to the surface under the action of gravity. The bubbles inside the water body or on the water surface would be able to change the dielectric property of lake water, thus affecting its scattering and radiation characteristics. The Urmia lake, north to the epicenter of the Sarpol Zahab

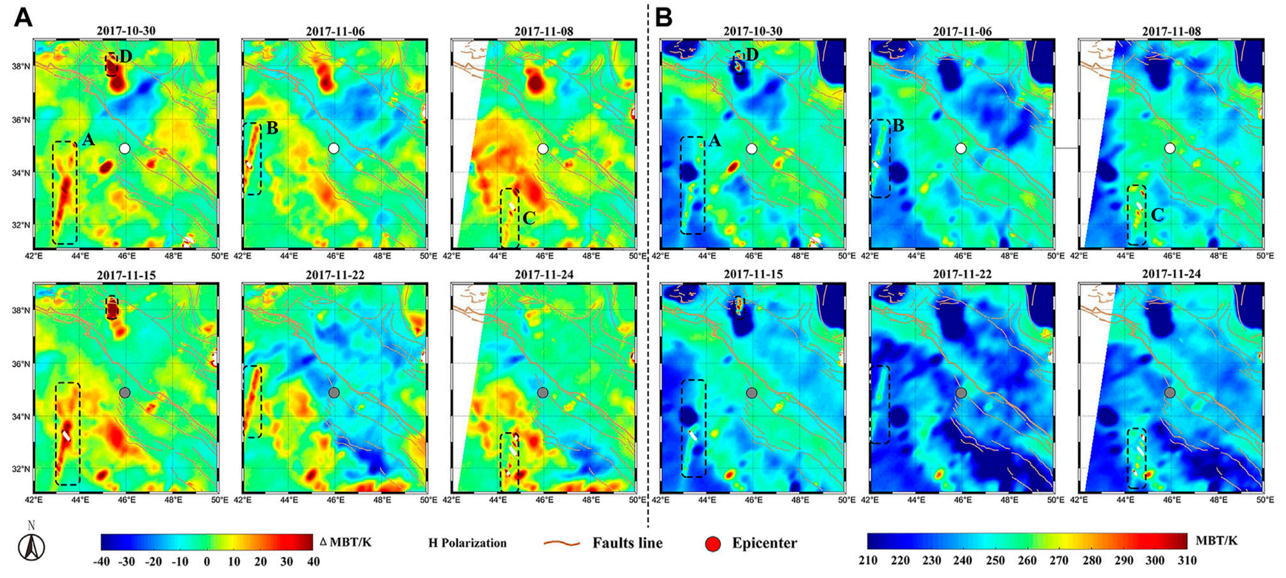

FIGURE 6 | Periodic positive abnormal stripes in residual MBT images **(A)** and original MBT images **(B)** with 10.65 GHz at H polarization.

earthquake, is the largest lake in Iran and the third largest saltwater lake in the world. According to Ma et al. (1999), the Urmia lake contained a large number of Na and Br ions, and the salinity of the lake was increasing continuously due to numerous water conservancy projects and continuous climate drought. Moreover, it was found by Camps et al. (2005) that with the same aeration rate, the thickness of foam layer on the sea surface raised with the increase of salinity. Williams (1971) experimentally measured the microwave emissivity of the artificial foam layer on different substrates at 9.4 GHz frequency using waveguide technology, and found that the foam covering the water surface had a high microwave emissivity, and the emissivity was positively correlated with the thickness of the foam layer. Therefore, both bubbles inside shallow water and possible foams above water surface of Urmia lake were able to reduce the dielectric constant of lake water, thus lifted the microwave emissivity and led to the rise of MBT.

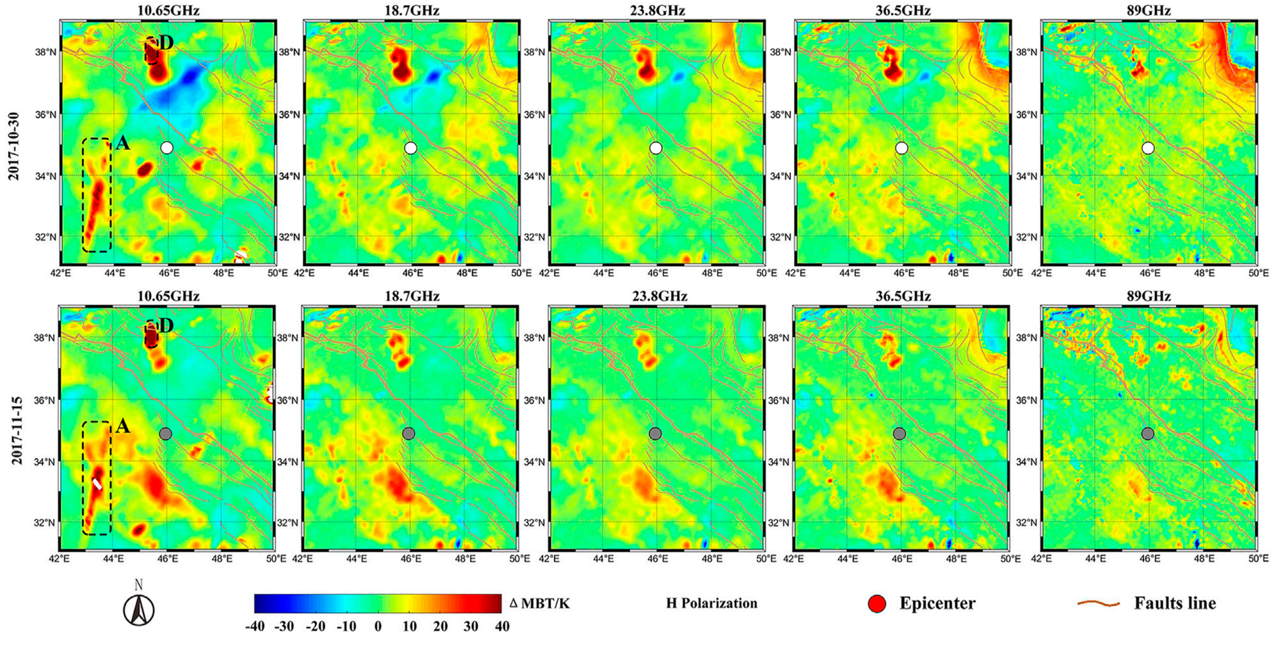

FIGURE 7 | Residual MBT images of different frequency (10.65, 18.7, 23.8, 36.5, and 89 GHz) at H polarization.

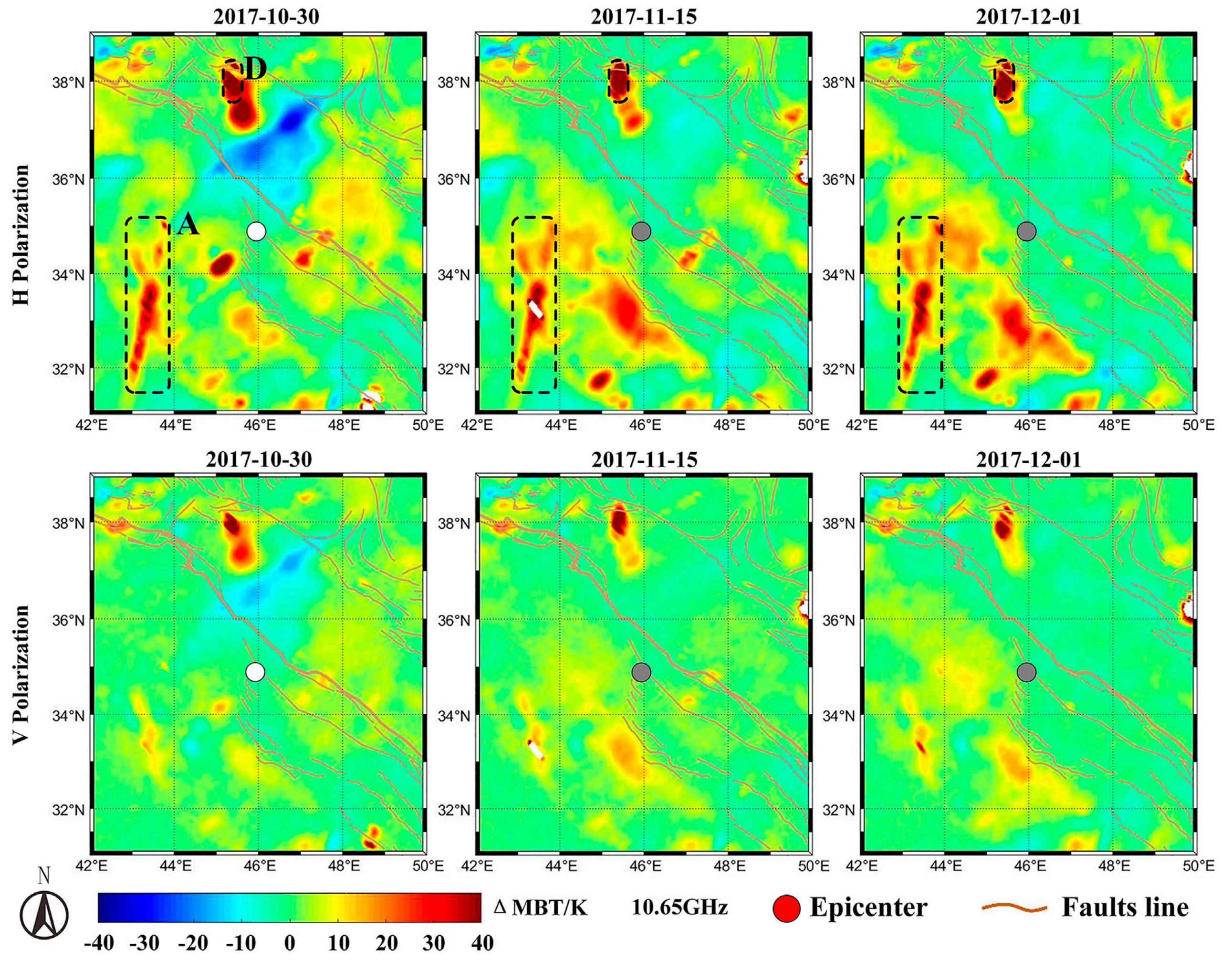

FIGURE 8 | Residual MBT images with 10.65 GHz at H and V polarization.

Taghipour et al. (2018) found that the Eastern Lake Fault on the east side of the Urmia Lake and the Eastern Salmas Fault on the west side of the Urmia Lake had the same strike and were both dextral strike-slip, and a linear geomorphic feature across the lake ascertained by satellite images divided the lake into north and south parts with different depths. This investigation shows that there is a possible geomorphic linkage between the faults. From **Figure 9**, it is known that the long-term trend of plate movement within the study area is approximately from south to north along the Mountain Front Flexure (MFF) (Vernant et al., 2004). According to the coseismic deformation field from D-InSAR and MAI measurements (Wang et al., 2019), the area north to the epicenter was squeezed from NE to SW. This suggested that the movement direction of the area around the Urmia Lake and the area north near to the epicenter may be inconsistent.

FLAC-3D software was used to make a numerical simulation of the seismogenious process during this earthquake. The results are shown in **Figure 10**, in which the fault structure was adapted from Vergés et al. (2011). The distribution of tectonic stress on the Main Recent Fault (MRF), which passes western through the Urmia lake, were presented by the simulation. It is found that during the northeast squeezing process of the Arabian cover and Arabian basement toward the MFF, the stress state in MRF region were divided into six stages. In the first stage, the MRF region appeared as a tensile zone. In the second stage, the area of tensile zone in MRF region decreased. In the third stage, the area of tensile zone in MRF region further reduced. In the fourth stage, the tensile zone in MRF region disappeared, and the whole study area was in a state of compression. In the fifth stage, a small tensile zone appeared on the northeast side of the MRF region, and in the sixth stage, the MRF region reappeared as a tensile zone. It is also shown that a non-squeezing zone appeared, disappeared and reappeared on the ground or coversphere along the MRF.

The simulation indicated that the mountainous Urmia Lake area, through which the MRF-ELF-ESF passes (as in **Figure 10**), was in a stretched state several days before the shocking (Stage 1–3). So that the underground passages or channels could be opened owing to tensile stress at the bottom of the Urmia lake,

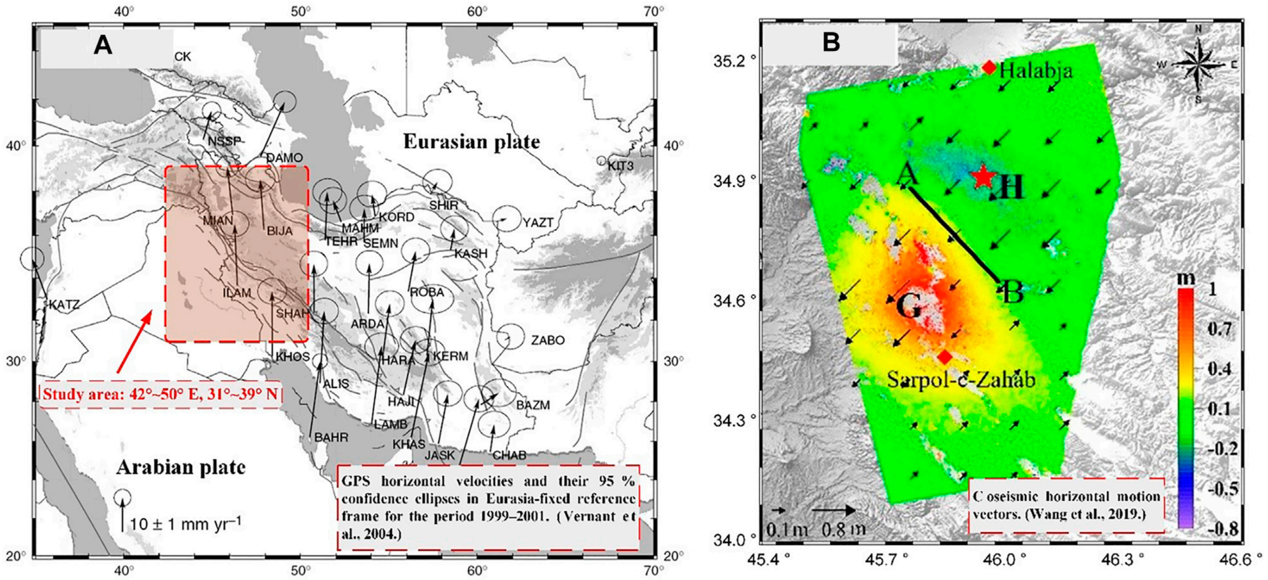

FIGURE 9 | Historical horizontal displacement **(A)** and coseismic horizontal motion vectors **(B)** in the study area adapted from Vernant et al. (2004) and Wang et al. (2019).

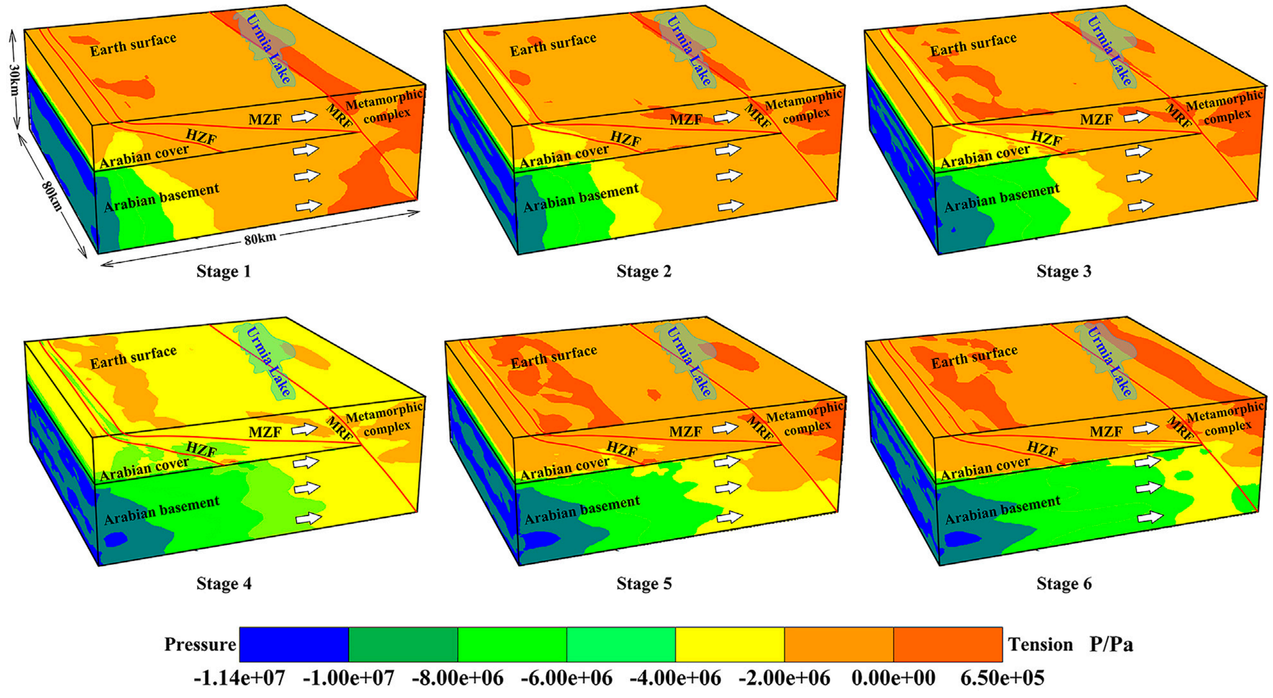

FIGURE 10 | Simulated dynamic stress state of local plate movement. The elastic model was applied to define the constitutive models of Arabian basement and metamorphic complex, and the Mohr-Coulomb model was applied to the Arabian cover. The interfaces were generated with respect to the main faults presented with red lines. In addition to the pre-set gravity, compressive stress of 10 MPa was initially applied at the depth from 0 to 10 km, while the initially applied compressive stress was 1 MPa at depth from 10 to 30 km on the left boundary surface.

through which underground gas (such as CH4, CO2) could be released to produce bubbles and possible foams, which in consequence led to positive MBT anomaly in the lake area (from 51 days before the earthquake to 3 days before the earthquake). However, during the impending period (2 days before) of the earthquake (Stage 4), crust stress was blocked in the hypocenter area, and the continuous movement of the Eurasian plate from NE to SW caused the plates at the bottom of the lake to be squeezed. Therefore, the underground passages through which the gas raised from lake bottom got closed, and consequently the positive MBT anomaly disappeared shortly before the earthquake. With the occurrence of the earthquake, the stress around the Zagros Mountains was partially adjusted, and the underground stress state of the ELF-ESF at the lake region might return to that of the earthquake impending (Stage 5–6). Therefore, the lake region was abnormal again (1d after the earthquake). With the departure of the shocking day, the lake region returned to its usual state, i.e., MRF was compressed and the gas passages are closed. Therefore, it is presented that the positive MBT anomaly in Urmia lake area were mainly produced by the uniformly distributed and altering crust stress field in the seismogenic area, which created good conditions for underground gas to escape from the lake floor and ELF-ESF, and then reduced the dielectric properties of the Urmia lake water, which led to an increment of MBT of Urmia lake.

Southwest Positive MBT Residuals Near the Epicenter

From **Figure 3**, it is known that positive MBT residuals existed also in the expansive plain southwest to the epicenter. The evolution of the abnormal positive residuals here fluctuates in range and amplitude, but the position remains unchanged over time. The most prominent area of the positive MBT residuals distributed along the southwest front of the Zagros mountains. By comparing the land cover and geological map of the study area with the MBT residual images, it is clear that the positive MBT anomaly area, bare land and cultivated land, and the Quaternary are in good spatial correspondence (see **Figure 11**). According to Freund's laboratory experiments, stress-activated charge carriers, known as P-hole, are able to appear in deep rock mass under compressively loading (Freund, 2000, 2011). The activated P-holes are mobile and capable of flowing down stress gradients and finally accumulating on the surface of distant unstressed rock, thus leading to additional electric field in the rock subsurface (King and Freund, 1984), even on the surface of a sand layer or a soil layer above the rock (Freund, 2010). The accumulation of P-holes will result in a positive surface e-potential and reduce the regional dielectric constant of the superficial rock mass. Thus, the microwave emissivity and the microwave radiation of rock surface would be enhanced. In addition, experimental studies have confirmed that the microwave dielectric constant of the rock surface reduced significantly during compressively loading (Mao, 2019), and the microwave radiation of sand layers overburdened the compressed rock specimen increased during rock loading process (Mao et al., 2020).

The peroxy defects are widespread in the mineral grains of the igneous and metamorphic rocks, which are susceptive to compressive stress. The Arabian basement is comprised of gneissose granites, schists, limestones, migmatites and mudstone (Bahroudi and Talbot, 2003), among which gneissose granites, schists, and migmatites are also peroxy rich. During the last preparation phase of Sarpol Zahab earthquake, the compression of plates caused the stress concentration of rock mass at the forthcoming hypocenter, a large number of micro-fractures were presented to had occurred at this period. The vast peroxy bonds embedded in the crust rock mass were broken, thus positive charges were activated in the stress concentration zone, showing a trend of propagating along crust stress gradient. Quaternary strata are usually characteristic by loose lithology, and mainly consist of gravel, sand, soil, and clay (Cao, 1995). The lithology of Arabian basement consists of fragments of intermediate-to-

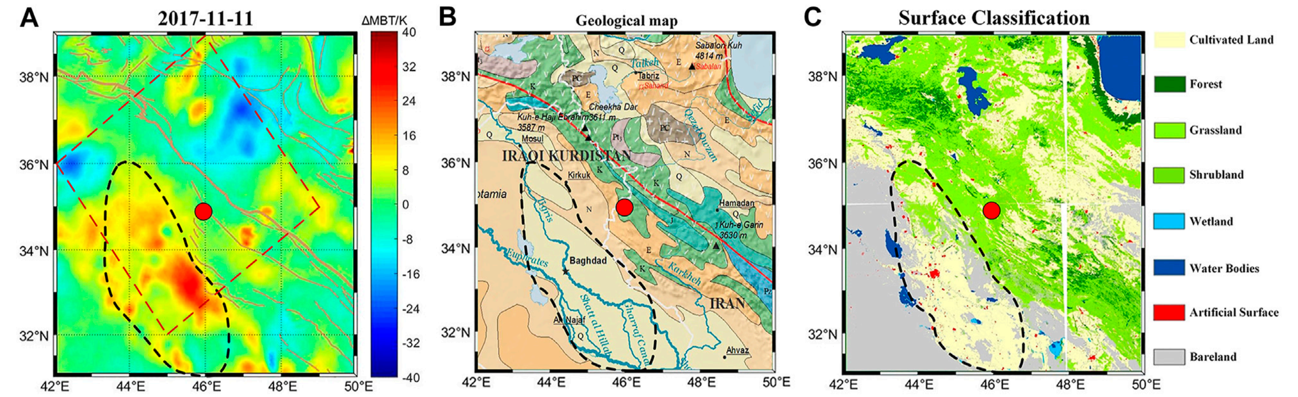

FIGURE 11 | Southwestern positive MBT anomaly, Geological map, and land cover.

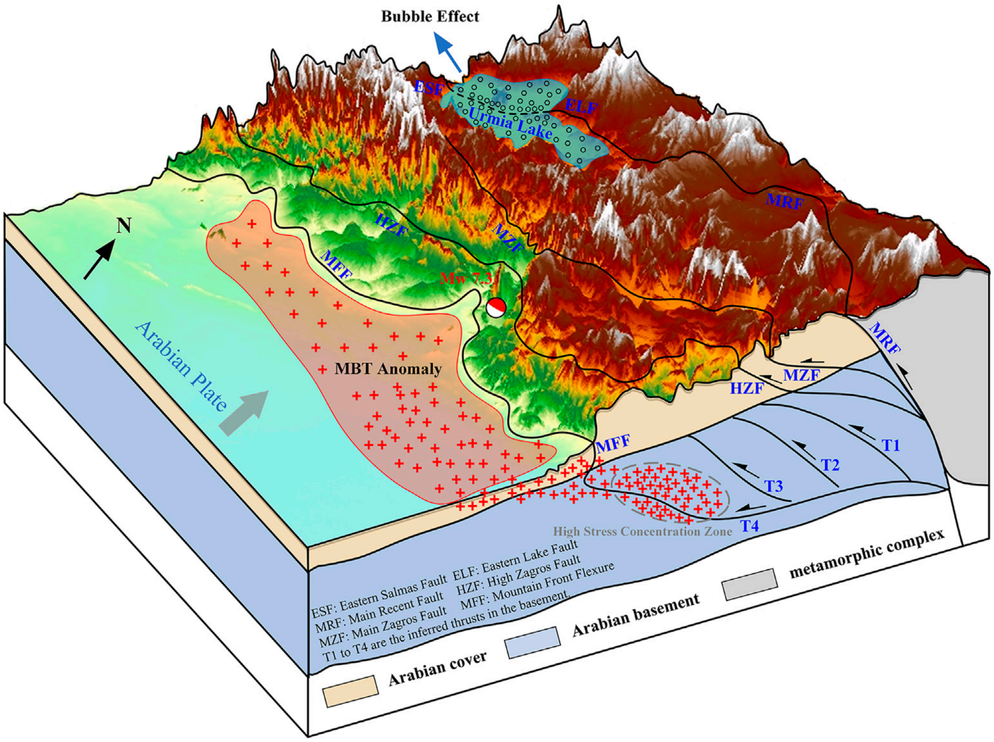

FIGURE 12 | Geologic section across the Zagros Mountains (interpreted from Vergés et al., 2011 and Yang et al., 2018) and conceptual diagram of P-hole transferring as well as bubble swelling.

high grade metamorphic rocks, which played a good medium for P-hole producing and propagating from the deep crust (T4, see **Figure 12**) to the Quaternary strata. Therefore, the local geological conditions allowed perfectly for the transfer of P-holes from MFF and Arabian cover to the northwest bare land and cultivated land, which resulting in the positive MBT anomaly here. The schematic diagram of this chain process is shown in **Figure 12**, of which the geographical range is marked in the red dotted box of the first subgraph in **Figure 11**. This effect induced by seismically activated P-holes reached its peak 2 days before the earthquake, and persisted with the stress adjustment and the occurrence of aftershocks.

The southwest anomaly lasted until the early February of the following year, with a relatively lower level than that before the Sarpol Zahab earthquake. During this period, more than 40 middle-large aftershocks (Mw ≥ 4.5) occurred near the epicenter of the Mw7.3 Sarpol Zahab earthquake. This means that the crust stress was in a state of continue adjustment until several months after the main shock. It is also worthy to note that the positive MBT anomaly in the Urmia lake occurred earlier than the southwest MBT anomaly, but with shorter duration. This might be owing to the ununiformly distribution of crust stress in the whole earthquake preparation zone, dynamic alteration of the crust stress field, and the different response of the regional faults system to the great earthquake.

CONCLUSION AND DISCUSSION

In this research, the spatiotemporal evolution of multi-frequency MBT anomalies associated with the 2017 Mw7.3 Sarpol Zahab earthquake is carefully investigated and analyzed. The uncovered MBT anomalies are divided into four featured categories, including the negative anomalies existing in the high-frequency result, the occasional positive abnormal stripes in line with satellite orbit, the significant positive anomaly in northern mountainous Urmia lake, and the extensive positive anomaly in Quaternary plain southwest to the epicenter.

Through comparative analysis of synchronous cloud image and SM data, the negative MBT anomalies of high-frequency were uncovered being attributed to the influence of high-altitude clouds, and were firstly excluded from being related to the impeding earthquake. We reach that not all atmospheric clouds are responsible for the negative MBT anomaly, only the altostratus (high clouds) can be reflected in the satellite MBT observations, which should be firstly excluded from the precursor study.

There existed also some abnormal stripes in the low-frequency MBT residuals. The geolocations of the stripes remain the same, and the reoccurrence time interval keep consistent with the revisit time of AMSR-2 instrument. We discovered that the abnormal stripes appeared in the results only with 10.65 GHz at H polarization. In addition, part of the Urmia lake behaved MBT over 300 K when the stripes existed with 16days reoccurrence, which is not in accordance with the natural phenomenon. It is daring but reasonable to attribute the abnormal stripes to data errors of the satellite instrument. Such periodically recurrent abnormal phenomenon requires careful identification in the study of seismic MBT anomaly.

The positive MBT anomaly in the northern mountainous Urmia lake existed both in the results of high-frequency and low-frequency, and behaved the same pattern in space and time. The positive MBT anomaly appeared 51 days before the earthquake and enhanced over time, but disappeared suddenly during the short-impending of the earthquake. Then the anomaly reoccurred 1 d after the earthquake and diminished gradually. Referring to the existing theory and microwave remote sensing physics, the amplitude of the positive MBT anomaly, with a maximum of 40K about, in the lake area might be caused by seismic-disturbed bubbles swelling from the lake bottom and ELF-EFF fault to water surface. Thus, the dielectric constant of lake surface water got reducing and the microwave radiative capacity got enhanced, which led to the positive MBT anomaly of the lake area.

The large-scale positive anomaly in the southwest plain appeared 18 days before the Sarpol Zahab earthquake, and the range and amplitude got larger with the approaching of the earthquake. The southwest MBT anomaly weakened also just 1 d before the impending earthquake, and continued to weaken until all aftershocks disappeared in the early February of 2018. Referring to the P-hole theory, seismogenic mechanism and microwave remote sensing physics, the southwest MBT positive anomaly, with a maximal amplitude of 20K about, was considered to be caused by seismic-activated positive charges transferring down the stress gradient from the deep crust to the Quaternary strata, which reduced the dielectric constant and lifted the microwave radiation there. Bare land and sand layers might have amplified the microwave signals from the crust to the atmosphere, thus to increase the significance of potential seismic MBT anomaly.

It is also essential to note that, from **Figure 2**, the seismicity in the study area was less frequent from 2015 to May 2017, but more frequent from July 2017 to 2019. The MBT data of 2015 and 2016 are selected for confutation analysis, and reach that no obvious positive MBT anomaly occurred in 2015. However, in 2016, positive MBT anomaly appeared also in the southwest plain area on October 25 and disappeared on December 24 (see **Supplementary Figure S2**). It can be seen from **Supplementary Figure S2** that the number of earthquakes in the study area in 2016 was much greater than that in 2015, and the epicenter was mostly located near the positive anomaly. By analyzing the distribution of earthquakes in this period, we believe that there was a certain spatial correlation between the location of positive anomalies and the coming epicenters in seismogenic process.

The epicenter of the Sarpol Zahab earthquake located at the boundary of two subzones with relatively uneven stress distribution, and MRF is the most active seismotectonic structure in the Zagros region (Khanban et al., 2021). The dynamic alteration of local stress in lithosphere might have been much more activated prior to the Sarpol Zahab earthquake, which led to the preseismic deformation (Vaka et al., 2019) and micro cracks of deep-to-shallow rock mass. The carbonaceous gas (such as CH_4 and CO_2) enclosed in the lithosphere might escape through the produced-and-opened micro cracks, which might cause MBT variations in Urmia lake since 51 days before the earthquake, and the accumulation of stress-activated P-holes on ground surface led to the MBT variations in plain area 18 days before, and then skin temperature got rise 15 days before the earthquake (Akhoondzadeh et al., 2019). Meanwhile, these up-swelling carbonaceous gases would had changed the composition of the atmosphere near ground surface accompanied by greenhouse effect, air-water condensation and aerosol generation, thus AOT and the water vapor behaved anomaly from 17 to 9 days and 6 to 4 days preceding the earthquake, respectively (Akhoondzadeh et al., 2019). The air ionization from possible radon gas emission was also supposed, and it could had ultimately disturbed the TEC in the ionosphere from 11 to 8 days preceding the earthquake (Akhoondzadeh et al., 2019; Tariq et al., 2019; Senturk et al., 2020). **Supplementary Figure S3** shows the temporal distribution of seismic precursor anomalies. As one can see from the figure, the occurrence time of precursor anomalies in each sphere generally presents a “slope” structure. In other words, anomalies in the coversphere appeared first, followed by those in the atmosphere, and those in the ionosphere appeared last. All the abnormal phenomena occurred in the multiple geospheres might reflect some coupling effect in the final phase of Sarpol Zahab seismogenic process. Through the analysis of the anomalies related with this earthquake, we found that the time of the anomaly occurred in each sphere was reasonable, which further proved the rationality of MBT anomaly in coversphere.

DATA AVAILABILITY STATEMENT

Publicly available datasets were analyzed in this study. This data can be found here: The datasets generated for this study are available on request from the first corresponding author, and from the National Aeronautics and Space Administration (NASA) for SRTM DEM data (https://earthexplorer.usgs.gov), the Japan Aerospace Exploration Agency (JAXA) for MBT data and soil moisture data (https://www.jaxa.jp), and European Meteorological Satellite website for cloud images (https://www.eumetsat.int).

AUTHOR CONTRIBUTIONS

YD: scientific analysis, data collection and manuscript writing. YQ and LW: scientific analysis, article organization and revising. LW: initiative thought and research supervisor; WM: numerical simulation; WM and YL: data processing and article improving.

FUNDING

This work was synergic supported by the National Key R and D Program of China under Grant 2018YFC15035, the Key Program of the National Natural Science Foundation of China under Grant 41930108, the innovation leading program of Central South University under Grant 506030101, and the Talents Gathering Program of Hunan Province, China under Grant 2018RS3013.

ACKNOWLEDGMENTS

We acknowledge the European Space Agency and NASA's Earth Observing System Data and Information System for making AMSR-2 images, SM data, SRTM DEM data and satellite cloud images free available to various researchers and communities. And we would also like to thank the reviewers for their hard work on this article.

SUPPLEMENTARY MATERIAL

The Supplementary Material for this article can be found online at: https://www.frontiersin.org/articles/10.3389/feart.2021.656216/full#supplementary-material

Supplementary Figure S1 | Spatiotemporal evolution of the MBT residuals with 10.65 GHz and 89 GHz at H polarization (following the **Figure 3**). The circle dots mark the epicenters of the shock, with gray color for the days after shock.

Supplementary Figure S2 | Seismic distribution (Mw >4.0) and spatiotemporal evolution of MBT residuals with 10.65 GHz at H polarization from October to December in 2015 and 2016. The circle dots mark the epicenters of the different magnitude shock, with white, red, and gray color for the days before the earthquake, during the earthquake, and after the earthquake, respectively.

Supplementary Figure S3 | Time distribution of reported earthquake anomalies at multiple geosphere. The dashed line and solid line indicate the intermittent and continuous abnormality, respectively. The light blue dashed line represents the point in time when the anomalies appeared and disappeared.

REFERENCES

Akhoondzadeh, M., De Santis, A., Marchetti, D., Piscini, A., and Jin, S. (2019). Anomalous Seismo-LAI Variations Potentially Associated with the 2017 Mw = 7.3 Sarpol-E Zahab (Iran) Earthquake from Swarm Satellites, GPS-TEC and Climatological Data. *Adv. Space Res.* 64 (1), 143–158. doi:10.1016/j.asr.2019.03.020

Bahroudi, A., and Talbot, C. J. (2003). The Configuration of the Basement beneath the Zagros basin. *J. Pet. Geol* 26 (3), 257–282. doi:10.1111/j.1747-5457.2003.tb00030.x

Berberian, M., and King, G. C. P. (1981). Towards a Paleogeography and Tectonic Evolution of Iran. *Can. J. Earth Sci.* 18 (2), 210–265. doi:10.1139/e81-019

Camps, A., Vall-llossera, M., Villarino, R., Reul, N., Chapron, B., Corbella, I., et al. (2005). The Emissivity of Foam-Covered Water Surface at L-Band: Theoretical Modeling and Experimental Results from the FROG 2003 Field experiment. *IEEE Trans. Geosci. Remote Sensing* 43 (5), 925–937. doi:10.1109/TGRS.2004.839651

Cao, B. (1995). *Geomorphology Quaternary Geology*. Beijing: Geosciences Press.

Chen, H., and Jin, Y. (2010). A Preliminary Detection of Anomalous Radiation of Rock Failures Related with Yushu Earthquake by Using Satellite-Borne Microwave Radiometers. *Remote Sens. Technol. Appl.* 25 (6), 860–866. doi:10.3724/SP.J.1087.2010.02819

Dobrovolsky, I. P., Zubkov, S. I., and Miachkin, V. I. (1979). Estimation of the Size of Earthquake Preparation Zones. *Pageoph* 117 (5), 1025–1044. doi:10.1007/BF00876083

Eastman, R., Lebsock, M., and Wood, R. (2019). Warm Rain Rates from AMSR-E 89-GHz Brightness Temperatures Trained Using CloudSat Rain-Rate Observations. *J. Atmos. Ocean Tech.* 36 (6), 1033–1051. doi:10.1175/JTECH-D-18-0185.1

Freund, F. (2011). Pre-earthquake Signals: Underlying Physical Processes. *J. Asian Earth Sci.* 41 (4-5), 383–400. doi:10.1016/j.jseaes.2010.03.009

Freund, F. (2000). Time-resolved Study of Charge Generation and Propagation in Igneous Rocks. *J. Geophys. Res.* 105 (B5), 11001–11019. doi:10.1029/1999JB900423

Freund, F. (2010). Toward a Unified Solid State Theory for Pre-earthquake Signals. *Acta Geophys.* 58 (5), 719–766. doi:10.2478/s11600-009-0066-x

Gu, C., Wang, Y., Zhang, X., Zhong, B., and Ma, X. (2016). Effects of Parameter on Brightness Temperature Computation in Microwave Band. *J. Appl. Meteorol. Sci.* 27 (3), 380–384. doi:10.11898/1001-7313.20160313

Imaoka, K., Maeda, T., Kachi, M., Kasahara, M., Ito, N., and Nakagawa, K. (2012). "Status of AMSR-2 Instrument on GCOM-W1," in *Earth Observing Missions and Sensors: Development, Implementation, and Characterization II* (Kyoto, Japan: International Society for Optics and Photonics), 8528, 852815.

Jing, F., Singh, R. P., Cui, Y., and Sun, K. (2020). Microwave Brightness Temperature Characteristics of Three strong Earthquakes in Sichuan Province, China. *IEEE J. Sel. Top. Appl. Earth Observations Remote Sensing* 13, 513–522. doi:10.1109/JSTARS.2020.2968568

Khanban, M. A., Pakzad, M., Mirzaei, N., Moradi, A., Mehramuz, M., and Mahmoud, M. (2021). The Present-day Stress Field in the Zagros Fold-Thrust Belt of Iran, from Inversion of Focal Mechanisms. *J. Geodynamics* 143, 101812. doi:10.1016/j.jog.2020.101812

King, B. V., and Freund, F. (1984). Surface Charges and Subsurface Space-Charge Distribution in Magnesium Oxides Containing Dissolved Traces of Water. *Phys. Rev. B* 29 (10), 5814–5824. doi:10.1103/PhysRevB.29.5814

Ma, P., Li, H., and Zhang, P. (1999). Comprehensive Utilization of Urmia Salt lake Resources. *J. Salt Lake Res.* 7 (1), 11–20. doi:10.3969/j.issn.1008-858X.1999.01.002

Maeda, T., and Takano, T. (2010). Detection Algorithm of Earthquake-Related Rock Failures from Satellite-Borne Microwave Radiometer Data. *IEEE Trans. Geosci. Remote Sensing* 48 (4), 1768–1776. doi:10.1109/TGRS.2009.2036008

Maeda, T., and Takano, T. (2009). Detection of Microwave Signals Associated with Rock Failures in an Earthquake from Satellite-Borne Microwave Radiometer Data. *Proc. Int. Geosci. Remote Sens. Symp.*, 61–64. doi:10.1109/IGARSS.2009.5418159

Maeda, T., and Takano, T. (2008). Discrimination of Local and Faint Changes from Satellite-Borne Microwave-Radiometer Data. *IEEE Trans. Geosci. Remote Sensing* 46 (9), 2684–2691. doi:10.1109/TGRS.2008.919144

Mao, W. (2019). *Pressure Effects on the Microwave Radiation and Dielectric Property of Rocks: Experiments and Mechanisms*. dissertation's thesis] (Shenyang: Northeastern University). doi:10.33737/gpps19-bj-086

Mao, W., Wu, L., Liu, S., Gao, X., Huang, J., Xu, Z., et al. (2020). Additional Microwave Radiation from Experimentally Loaded Granite Covered with Sand Layers: Features and Mechanisms. *IEEE Trans. Geosci. Remote Sensing* 58, 5008–5022. doi:10.1109/TGRS.2020.2971465

Pulinets, S., and Ouzounov, D. (2011). Lithosphere-Atmosphere-Ionosphere Coupling (LAIC) Model - an Unified Concept for Earthquake Precursors Validation. *J. Asian Earth Sci.* 41 (4-5), 371–382. doi:10.1016/j.jseaes.2010.03.005

Qi, Y., Wu, L., Ding, Y., and Mao, W. (2020c). Microwave Brightness Temperature Anomalies Associated with the 2015 Mw 7.8 Gorkha and Mw 7.3 Dolakha Earthquakes in Nepal. *IEEE Trans. Geosci. Remote Sensing*, 1–11. doi:10.1109/TGRS.2020.3036079

Qi, Y., Wu, L., He, M., and Mao, W. (2020a). Spatio-temporally Weighted Two-step Method for Retrieving Seismic MBT Anomaly: May 2008 Wenchuan Earthquake Sequence Being a Case. *IEEE J. Sel. Top. Appl. Earth Observations Remote Sensing* 13, 382–391. doi:10.1109/JSTARS.2019.2962719

Qi, Y., Wu, L., Mao, W., Ding, Y., and He, M. (2021b). Discriminating Possible Causes of Microwave Brightness Temperature Positive Anomalies Related with

May 2008 Wenchuan Earthquake Sequence. *IEEE Trans. Geosci. Remote Sensing* 59, 1903–1916. doi:10.1109/TGRS.2020.3004404

Reilinger, R., Mcclusky, S., Vernant, P., Lawrence, S., Ergintav, S., Cakmak, R., et al. (2006). GPS Constraints on continental Deformation in the Africa-Arabia-Eurasia continental Collision Zone and Implications for the Dynamics of Plate Interactions. *J. Geophys. Res.* 111 (B5), a–n. doi:10.1029/2005JB004051

Salahi, A., and Asareh, M. (2008). "Iran and its Natural Resources Features," in *Review of Forests, wood Products and wood Biotechnology of Iran and Germany, Part II* (Göttingen: Universitätsverlag Göttingen).

Saraf, A. K., Rawat, V., Banerjee, P., Choudhury, S., Panda, S. K., Dasgupta, S., et al. (2008). Satellite Detection of Earthquake thermal Infrared Precursors in Iran. *Nat. Hazards* 47, 119–135. doi:10.1007/s11069-007-9201-7

Senturk, E., Inyurk, S., and Sertcelik, I. (2020). Ionospheric Anomalies Associated with the Mw 7.3 Iran-Iraq Border Earthquake and a Moderate Magnetic Storm. *Ann. Geophys.* 38, 1031–1043. doi:10.5194/angeo-38-1031-2020

Taghipour, K., Khatib, M. M., Heyhat, M., Shabanian, E., and Vaezihir, A. (2018). Evidence for Distributed Active Strike-Slip Faulting in NW Iran: The Maragheh and Salmas Fault Zones. *Tectonophysics* 742-743, 15–33. doi:10.1016/j.tecto.2018.05.022

Takano, T., and Maeda, T. (2009). Experiment and Theoretical Study of Earthquake Detection Capability by Means of Microwave Passive Sensors on a Satellite. *IEEE Geosci. Remote Sensing Lett.* 6 (1), 107–111. doi:10.1109/LGRS.2008.2005735

Tariq, M. A., Shah, M., Hernández-Pajares, M., and Iqbal, T. (2019). Pre-earthquake Ionospheric Anomalies before Three Major Earthquakes by GPS-TEC and GIM-TEC Data during 2015-2017. *Adv. Space Res.* 63 (7), 2088–2099. doi:10.1016/j.asr.2018.12.028

Ulaby, F., and Long, D. (2015). *Microwave Radar and Radiometric Remote Sensing*. Fitchburg: Artech House.

Ulaby, F. T., Moore, R. K., and Fung, A. K. (1981). "Microwave Remote Sensing: Active and Passive," in *Remote Sensing Fundamentals and Radiometry* (Boston, MA, USA: Addison-Wesley), 186–254.

Vaka, D. S., Rao, Y. S., and Bhattacharya, A. (2019). Surface Displacements of the 12 November 2017 Iran-Iraq Earthquake Derived Using SAR Interferometry. *Geocarto Int.* 36, 660–675. doi:10.1080/10106049.2019.1618927

Vergés, J., Saura, E., Casciello, E., Fernàndez, M., Villaseñor, A., Jiménez-munt, I., et al. (2011). Crustal-scale Cross-Sections across the NW Zagros belt: Implications for the Arabian Margin Reconstruction. *Geol. Mag.* 148 (5-6), 739–761. doi:10.1017/S0016756811000331

Vernant, P., Nilforoushan, F., Hatzfeld, D., Abbassi, M. R., Vigny, C., Masson, F., et al. (2004). Present-day Crustal Deformation and Plate Kinematics in the Middle East Constrained by GPS Measurements in Iran and Northern Oman. *Geophys. J. Int.* 157 (1), 381–398. doi:10.1111/j.1365-246X.2004.02222.x

Wang, Z., Zhang, R., and Liu, Y. (2019). 3D Coseismic Deformation Field and Source Parameters of the 2017 Iran-Iraq Mw7.3 Earthquake Inferred from DInSAR and MAI Measurements. *Remote Sensing* 11 (19), 2248. doi:10.3390/rs11192248

Williams, G. (1971). Microwave Emissivity Measurements of Bubbles and Foam. *IEEE Trans. Geosci. Electron.* 9 (4), 221–224. doi:10.1109/TGE.1971.271504

Wu, L.-x., Qin, K., and Liu, S.-j. (2012). GEOSS-based thermal Parameters Analysis for Earthquake Anomaly Recognition. *Proc. IEEE* 100 (10), 2891–2907. doi:10.1109/JPROC.2012.2184789

Wu, L., Liu, S., and Wu, H. (2006). The experiment Evidences for Tectonic Earthquake Forecasting Based on Anomaly Analysis on Satellite Infrared Image. *IEEE Int. Symp. Geosci. Remote Sens.* 2158–2162. doi:10.1109/IGARSS.2006.558

Wu, L., Zheng, S., De Santis, A., Qin, K., Di, Mauro, R., Liu, S., et al. (2016). Geosphere Coupling and Hydrothermal Anomalies before the 2009 Mw 6.3 L'Aquila Earthquake in Italy. *Nat. Hazards Earth Syst. Sci.* 16 (8), 1859–1880. doi:10.5194/nhess-16-1859-2016

Yang, Y. H., Hu, J. C., Yassaghi, A., Tsai, M. C., Zare, M., Chen, Q., et al. (2018). Midcrustal Thrusting and Vertical Deformation Partitioning Constraint by 2017 Mw 7.3 Sarpol Zahab Earthquake in Zagros Mountain Belt, Iran. *Seismol. Res. Lett.* 89 (6), 2204–2213. doi:10.1785/0220180022

Zhao, S., Chen, W., and Hang, H. (2002). Analysis on Precipitation Altostratus Microphsical Structure in spring over North-East Qinghai. *plateau meteorology* 21 (3), 281–287. doi:10.1002/mop.10502

Zhou, Y. (2019). Muti-parameter Remote Sensing Pre-seismic Anomalies over Iran-Iraq Area. Master's thesis. Shenyang: Northeastern University. doi:10.1109/igarss.2019.8898238

Ziolkowski, A. (1998). Measurement of Air-gun Bubble Oscillations. *Geophysics* 63 (6), 2009–2024. doi:10.1190/1.1444494

Conflict of Interest: The authors declare that the research was conducted in the absence of any commercial or financial relationships that could be construed as a potential conflict of interest.

frontiers in Earth Science

ORIGINAL RESEARCH
published: 03 November 2021
doi: 10.3389/feart.2021.730162

On the Origin of ULF Magnetic Waves Before the Taiwan Chi-Chi 1999 Earthquake

Georgios Anagnostopoulos *

Space and Telecommunications Sector, Department of Electrical and Computer Engineering, Demokritos University of Thrace, Xanthi, Greece

The ultra low frequency (ULF) electromagnetic (EM) wave activity usually recorded on Earth's ground has been found to depend on various types of space weather. In addition ULF waves observed before an earthquake have been hypothesized to be a result of geotectonic processes. In this study we elaborate for the first time the origin of sub-ULF (<1 msec) magnetic field waves before an earthquake (Chi-Chi/Taiwan, 20.9.1999) by comparing simultaneously obtained measurements in the interplanetary space (ACE satellite) and on the Earth's ground (Taiwan). The most striking result of our data analysis, during a period of 7 weeks, is that the detection of four groups of sub-ULF waves in Taiwan coincide in time with the quasi-periodic detection of two solar wind streams by the satellite ACE with approximately the solar rotation period (~28 days). The high speed solar wind streams (HSSs) in the interplanetary space were accompanied by sub-ULF Alfvén wave activity, quasi-periodic southward IMF and solar wind density perturbations, which are known as triggering agents of magnetic storm activity. The four HSSs were followed by long lasting decreases in the magnetic field in Taiwan. The whole data set examined in this study strongly suggest that the subULF magnetic field waves observed in Taiwan before the Chi-Chi 1999 earthquake is a normal consequence of the incident of HSSs to the magnetosphere. We provide some observational evidence that the sub-ULF electromagnetic radiation on the Earth was most probably a partner to (not a result of) geotectonic processes preparing the Taiwan 1999 earthquake.

Keywords: ULF waves, earthquake generation process, space weather, earthquake electromagnetic precursors, earthquake prediction, sun-earth relationships, environmental electromagnetism

Edited by:
Dimitar Ouzounov,
Chapman University, United States

Reviewed by:
Georgios Balasis,
National Observatory of Athens, Greece
Sergey Alexander Pulinets,
Space Research Institute (RAS), Russia

***Correspondence:**
Georgios Anagnostopoulos
ganagno@ee.duth.gr

Specialty section:
This article was submitted to Environmental Informatics and Remote Sensing,
a section of the journal
Frontiers in Earth Science

Received: *24 June 2021*
Accepted: *03 August 2021*
Published: *03 November 2021*

Citation:
Anagnostopoulos G (2021) On the Origin of ULF Magnetic Waves Before the Taiwan Chi-Chi 1999 Earthquake.
Front. Earth Sci. 9:730162.
doi: 10.3389/feart.2021.730162

INTRODUCTION

The Origin of Terrestrial Ultra Low Frequency Electromagnetic Waves and the Taiwan Chi-Chi 7.7M_w 1999 Earthquake

Ultra low frequency (ULF) waves observed by terrestrial observatories is a matter of scientific research of great interest. ULF waves provide significant information about geomagnetic processes and earthquake (EQ) preparation processes and they have significant influence on biological organisms (Reichmanis et al., 1979; Pilipenko, 1990; Poole, 1993; Kivelson and Russell, 1995; Poole et al., 1993; McPherron, 2005; Pulinets and Boyarchuk, 2004; Grimalsky et al., 2010; Anagnostopoulos. 2015, 2016). Despite the extensive research done so far, there exist many open questions about their generating mechanisms. For instance, sub-ULF (<1 msec) waves have been reported before several earthquakes. However, low geomagnetic storm activity has been considered as a criterion of their terrestrial origin, without any other direct evidence. Therefore the question is: is it possible that sub-ULF (<1 msec) wave activity and moderate or low geomagnetic storm activity are related with solar activity and subsequent space weather? The answer to this question is positive from the side of space science. However, there is not, as far as we know, any study which directly compares space weather and terrestrial observations to address the above question of ULF activity before a particular earthquake. For this reason, in this case study, the subULF wave activity before the great Taiwan 1999 earthquake is reexamined in order to elaborate its origin.

The Taiwan 7.7 M_w earthquake (EQ) was one of the most catastrophic earthquake of the 20th century in Taiwan (Ma et al., 1999). The EQ struck the small town Chi-Chi at 1:47 local time (17:47 UT), 21 September (20 September), 1999. The earthquake epicenter was located at geographic latitude 23.85^0N and longitude 120.78^0E, with a depth of 8.0 km. In this earthquake, approximately 2500 lives were lost, about 11,305 people injured, more than 100,000 people made homeless, thousands of buildings were destroyed and NT$300 billion worth of damage was done. One month after the disastrous Chi-Chi earthquake (October 22, 199) another great EQ (*M*w 6.4) occurred in Chia-yi, in southern Taiwan (Chang and Wang, 2002; Huang et al., 2006).

Several investigators have reported various types of precursory electromagnetic (EM) phenomena, which occurred before the Chi-Chi 1999 earthquake. Almost all of the relative studies suggested that the precursory electromagnetic signals were the results of terrestrial processes. Since most researchers accept the hypothesis that seismic activity is a phenomenon related with a physical process in the interior of Earth, no systematic research has been made on the space weather and its possible effects on the Chi-Chi pre-EQ EM signals as well. The presence of a "weak" geomagnetic activity before the Chi-Chi EQ was hypothesized as an evidence of non space effects in Taiwan before the great 1999 EQ (Yen et al., 2004), according to the generally accepted geocentric paradigm.

Today the situation is different in understanding the importance of space weather on the planet Earth. In this respect, several studies have recently provided overwhelming evidence that the quiet Sun producing "weak" storms is a significant agent provoking terrestrial seismicity (Anagnostopoulos et al., 2021 and references therein). However, despite the great achievements in space weather, the scientific literature lacks any studies examining the possible space origin of any pre-EQ electromagnetic (EM) precursory signals based on a direct comparison of simultaneously obtained space and terrestrial measurements.

The Sun is the principal source of energy in our Solar System and the agent of many physical processes taking place in Earth's magnetosphere, ionosphere, atmosphere, lithosphere and biosphere (Odintsov et al., 2007; Gray et al., 2010; Vencloviene et al., 2012; Anagnostopoulos and Papandreou, 2012; Anagnostopoulos et al., 2015; Patsourakos et al., 2016; Kumar, A., and Kumar, S., 2018; Firoz, 2019; Tsurutani et al., 2020). Moreover, nowadays our knowledge about the Sun-Earth electromagnetic relationships allows a new insight into important physical and biological phenomena of great social interest (Anagnostopoulos et al., 2021; Zenchenko and Breus, 2021).

The solar wind-magnetospheric interaction is one of the most important issues in space research. In particular, space science has provided significant information on the role of solar wind turbulence on the energy and momentum transfer from the Sun to the Earth's environment (Dungey, 1961; Borovsky and Valdivia 2018). Moreover, in recent years, rich information has been accumulated concerning the impact of high speed solar wind streams (HSSs) on the status of the geomagnetosphere, and, in particular, on the trapped radiation belts (Kataoka, R. and Miyoshi, Y. 2006; Borovsky and Denton, 2006; Potapov, 2013, Baker et al., 2018; Richardson, 2018). Furthermore, HSSs periods were found to be related with enhanced seismicity occurring during "quiet" geomagnetic periods (Anagnostopoulos et al., 2021 and references therein).

This paper is devoted to elaborating on the space processes preceding a great earthquake. To this end, we investigate, for the first time, simultaneously obtained space and terrestrial observations for a specific earthquake, in order to extract information on the space weather – seismicity relationship additional to that received from our previous statistical study (Anagnostopoulos et al., 2021). We address the question of whether the ULF waves (<1 msec) recorded by the magnetic field observatories in Taiwan some weeks before the Chi-Chi EQ could be the result of space weather, during a quiet Sun.

THEORETICAL AND OBSERVATIONAL FRAMEWORK

Ultra Low Frequency Electromagnetic Waves in Space and on the Ground

ULF waves in the magnetosphere and on Earth, known as Pc or Pi pulsations (McPherron, 2005), are one of the most known phenomena in space science. There is a wide variety of ULF types, which are classified according to their form and frequency band.

ULF waves of different frequencies and polarizations observed on the ground may originate from different regions of the magnetosphere, the distant space or the Sun's environment. Ultra-low frequency waves are detected on the ground as geomagnetic pulsations, ranging in frequency from some Hz to less than 1 mHz and numerous theories have been proposed to explain their origin (Pilipenko, 1990; McPherron, 2005; Pulinets and Boyarchuk, 2004; Grimalsky et al., 2010)

On the other hand, there have been many reports of ULF waves observed before an earthquake, which have been considered as originating from tectonic processes. Many other electromagnetic EM field changes have also been reported before earthquakes on the ground, in the atmosphere and in a wide range of frequency of the EM spectrum as sub-ULF, ULF/ELF, VLF, IR (Hayakawa and Fujinawa, 1994; Molchanov and Hayakawa, 1998; Ouzounov and Freund, 2004; Hattori, 2004; Liu et al., 2004; Balasis and Mandea, 2007; Hayakawa et al., 2010; Uyeda et al., 2009, Pulinets and Ouzounov, 2011; Athanasiou et al., 2011, 2014; Freund et al., 2012; ZhangShen et al., 2012; Tramutoli et al., 2015, De Santis et al., 2015, 2017; Ouzounov et al., 2018; Han, 2020). Furthermore, some characteristic charged particle variations have been reported in the ionosphere and the inner radiation belt before great EQs, as, for instance, variations in TEC and in radiation belt electron precipitation as well as ionospheric plasma perturbations (Lui et al., 2000, 2001; Pulinets and Boyarchuk, 2004; Akhoondzadeh et al., 2010; Pulinets and Ouzounov, 2011; Sidiropoulos et al., 2011; Anagnostopoulos et al., 2012). Broad band VLF wave activity is related with electron precipitation from the inner radiation belts. Extensive summary of pre-earthquake phenomena have been reported by Ouzounov et al. (2018) and Pulinets and Ouzounov, 2018.

Enhanced ULF EM activity has been considered to be a significant earthquake precursory signal (Hattori, 2004; Hayakawa et al., 2007; Zhang et al., 2012; Athanasiou et al., 2014). In general, the detection of various electromagnetic perturbations before fault ruptures has been proposed as a useful way to monitor activities of Earth's crust.

An increasing number of investigators have used electromagnetic methods in the last two decades in order to achieve earthquake prediction. Furthermore, satellite observations have been extensively used in earthquake prediction research. The first space mission dedicated to the detection of pre-EQ EM emissions was the French satellite DEMETER (Parrot et al., 2006; Sauvaud et al., 2006), during the years 2004–2010. DEMETER mission greatly aided the scientific community in improving its methodologies on earthquake prediction research. Similarly, a second space mission, the Chinese satellite CSES (Shen et al., 2018) is currently in orbit around the Earth and provides us with current data.

In the scientific community the ultra low frequency electromagnetic radiation has been considered to be an important earthquake precursor, because of its deeper skin depths (Hattori and Han, 2018). ULF magnetic field activity has been recognized as a precursor to well-known and broadly discussed earthquakes, such as in Loma Prieta, Guam, Sumatra 2004, and Haiti 2010 (Fraser-Smith et al., 1994; Hayakawa et al., 1996; Athanasiou et al., 2011).

A short discussion about the origin of ULF wave activity before an EQ was made in the case of the Loma Prieta earthquake. Campbell (2009) compared magnetic field records from Fresno, Bolder and Tucson with magnetic field observations from Stanford University (Fraser-Smith et al., 1994) near Loma Prieta, and he found that a similar trend for the ULF wave activity characterized all these locations. Campbell concluded that the ULF waves recorded before the Loma Prieta earthquake was not a local signal originated from local preparation processes.

Thus, we think that we should address the following questions: 1) Are all types of pre-EQ ULF magnetic field waves the result of tectonic stresses? 2) Is it possible for some types of preearthquake ULF wave activity to originate from tectonic processes and some other types from some space phenomena? 3) Is there any observational evidence supporting the space origin of the subULF electromagnetic radiation observed before the Chi-Chi 1999 earthquake?

Space Weather and Solar Wind Ultra Low Frequency Waves

There is increasing evidence that supports the concept of two supplementary sources contributing to the generation of earthquakes: tectonic stresses and space weather phemomena. There are several studies, which have provided significant evidence that seismicity is related with solar cycle (SC) phase (Simpson, 1967; Gousheva et al., 2003; Bakhmutov et al., 2007; Odintsov et al., 2007; Khain and Khalilov, 2008; Straser and Cataldi, 2015) and geomagnetic activity (Sobolev et al., 2001; Duma and Ruzhin, 2003; Bakhmutov et al., 2007; Urata et al., 2018). Love and Thomas (2013) disputed the solar-terrestrial interaction in triggering great earthquakes, but they tested an incorrect hypothesis (active Sun affects seismicity) and wrong time scale (1 year) of averaged sunspot number (Anagnostopoulos et al., 2021).

The long-term (1964–2013) relationship between the occurrence of earthquakes with magnitudes M ≥ 5 was investigated by Gulyaeva (2014); it was found that the global number of earthquakes tends to grow towards the solar cycle minimum.

Anagnostopoulos et al. (2021) performed various statistical studies based on solar, space and seismological data between 1900 and 2017 and we also found strong evidence that both the great earthquakes as well as high global seismic energy release occur during the rising and the decay phase of SC as well as at specific times of the maximum solar cycle phase with temporal (# months) weak solar activity. In general, the analysis of monthly averaged solar sunspot number (SSN) confirms a systematic and significant negative correlation of the seismic activity with the SSN (Gulyeva, 2014; Rekapali, 2014; Anagnostopoulos et al., 2021).

During periods with small SSNs, coronal hole (CH) driven-recurrent HSSs and corotating interaction regions (CIRs) rotate in space with the solar rotation period of ~27 days. This periodicity is clear in various kinds of observations in the interplanetary space, the terrestrial magnetosphere and the ionosphere. For instance, solar wind speed and auroral electron power exhibit solar rotational periodicities (Emery et al., 2009). Since the ~27-days period recurrent solar wind structures influences Earth via EM interactions, the ~27 days-periodicity might be found in seismological data. Indeed, the power spectrum analysis of 4-h averaged global energy release values demonstrated a ~27-days periodicity during the decay phase of SC22 and SC23 and at the maximum of SC23 (Anagnostopoulos et al., 2021). This result is consistent with the concept that HSSs, which emanate from the coronal hole of the quiet Sun, provoke seismic activity on the planet Earth.

Since we found strong evidence that the impact of CH-driven HSSs/CIRs on the Earth's magnetosphere trigger earthquakes, the next question is how the magnetosphere mediates the energy transfer of the solar wind plasma to the ionosphere and the lithosphere. Anagnostopoulos et al. (2021) put forward the hypothesis that solar wind magnetohydrodynamic (MHD) waves, which are transformed into electromagnetic waves in the ionosphere, may mediate space weather with seismicity. Indeed, Alfvèn waves are present in the environment of HSSs and CIRs (McPherron, 2005; Richarson, 2018).

Alfvèn waves often reach the Earth's magnetosphere in a quasi-periodic southward direction, which is a condition for triggering magnetospheric storms (Dungey, 1961). HSSs and CIRs, which guide the Alfvèn waves, cause weak or moderate, but long lasting (several weeks to some months) geomagnetic storms, which are characterized by almost continuous UV

Auroras often covering the entire dayside and nightside auroral zones (Tsurutani and Gongalez, 1987). Under such space conditions, ionospheric electric fields and thermospheric winds from the high latitudes can affect the middle and the low latitude ionosphere (Abdu et al., 2006). At these times, magnetospheric and ionospheric EM variations produce electromagnetic effects on the ground (Marhavilas, 2007).

Since solar wind sub-ULF Alfvèn waves are transformed into sub-ULF electromagnetic waves reaching Earth's surface, they could probably mediate space weather with seismic activity. Furthermore, HSSs themselves are highly related to sub-ULF electromagnetic waves observed at Earth (Kim et al., 2002; McPherron, 2005).

Geomagnetic Ultra Low Frequency Waves Before the Taiwan Chi-Chi 1999 Earthquake

The first reason why we choose the Taiwan 1999 earthquake as a case study is the fact of CIRinduced extreme geomagnetic activity in late 1999 (Borovsky and Denton, 2006). A second reason is that sub-ULF waves were observed in Taiwan before the Chi-Chi 1999 EQ and they have been discussed in the scientific literature extensively. Geomagnetic sub-ULF fluctuations recorded by several stations in Taiwan before the 1999 Chi-Chi EQ have been reported and discussed among others by (Lin. 2013), Liu et al. (2000, 2004), Ohta et al. (2001), Akinaga et al. (2001); (Shin, 2004), Yen et al. (2004), Freund and Pilorz (2012), Tsai et al. (2018).

Yen et al. (2004) hypothesized that the geomagnetic sub-ULF fluctuations were connected to the process of accumulation and releases of crustal stress, and the subsequent severe surface ruptures. They noted that the mechanisms producing the geomagnetic fluctuations are not clearly understood.

Freund and Pilorz (2012), Tsai et al. (2018) suggested that the sub-ULF geomagnetic fluctuations before the Chi-Chi EQ, were the result of a large current generated by accumulation and release of crustal stress.

Pulinets and Boyarchuk (2004) noted that the near Chi-Chi earthquake magnetic anomalies were probably connected with effectiveness of solar events, while Anagnostopoulos et al. (2021) reported that HSSs/CIRs transferred Alfvèn waves in the magnetosphere before the Chi-Chi 1999 EQ.

Given that there exist several reports on the existence of ULF EM waves before the Chi-Chi earthquake, in this study we investigate the hypothesis that the ULF geomagnetic fluctuations in certain frequency bands may be originated from solar wind. To this end we reasonably address the question whether sub-ULF geomagnetic anomalies are not the result of the microseismicity observed for ~7 seven weeks before the Chi-Chi earthquake, but an agent of micro-earthquakes.

Geomagnetic Ultra Low Frequency Waves of Space Origin

ULF waves of space origin are observed on Earth, in particular at low frequencies around 1 mHz (Barnes, 1983). Some of these waves originate at the Sun and are both carried by, and propagate through the solar wind.

The location of the regions on the Earth where ULF waves are observed depends on the solar wind dynamic pressure, the interplanetary magnetic field, and the conductivity of the Earth underneath the observer (Kivelson and Russell, 1995; McPherron, 2005). Changes in orientation of the interplanetary magnetic field (IMF) or Alfvén waves in HSSs/CIRs have dramatic effects on the type of waves seen on the Earth.

Besides the ULF waves transferred by the solar wind, waves are also locally produced upstream from the Earth's bow shock, at the bow shock and the magnetopause and they are sources of ULF waves penetrating into the magnetosphere (McPherron, 2005). Another type of ULF waves is produced by oscillatory dynamic pressure fluctuations in the solar wind (Kepko et al., 2002).

Many observations obtained simultaneously by satellites in space and on the ground have shown that solar wind perturbations deeply penetrate into the magnetosphere. Furthermore, it was found that the lower-latitude data on the nightside are important in monitoring the external source variations (Kim et al., 2002; Villante and Tiberi, 2016). The ULF signal seen at the ground is an electromagnetic wave radiating from electric currents induced in the ionosphere (and not the magnetohydromagnetic waves themselves).

Russell et al. (1992) reported that the best correlation between ground level changes and the change in the solar wind dynamic pressure occurs at geomagnetic latitudes from 15^0 to 30^0.

Sarafopoulos (2005) demonstrated that sometimes monochromatic or quasi-periodic geomagnetic pulsations were exo-magnetospherically excited by a wave-source with a periodicity from ~3 to ~10 min and that the magnetosphere in these cases can respond to solar wind ULF waves in such small time scales as 2.7 min.

In the next section we compare space and terrestrial observations in order to identify the origin of the sub-ULF (<1 mHz) magnetic field waves observed before the catastrophic Taiwan 1999 earthquake.

RESULTS

In this section we compare space and terrestrial observations in order to test two hypotheses on the origin of the sub-ULF magnetic field waves observed before the occurrence of the Chi-Chi earthquake (21/20 September 1999), that is a space versus a geotectonic model of the magnetic field wave generation. To this end, we compare observations from the Advanced Composition Explorer (ACE) spacecraft (http://www.srl.caltech.edu/ACE/ace_mission.html), which is in orbit around the L1 Sun-Earth libration point, magnetic field observations in Taiwan, along with geomagnetic indexes (http://wdc.kugi.kyoto-u.ac.jp/ae_provisional/199809/index_19980913.html)

The ACE spacecraft was launched in 1997 and thereafter has been remained in a halo orbit about the L1 point.

The ACE instruments used in this study are the Electron, Proton, and Alpha Monitor (EPAM) (Gold et al., 1998), the Magnetometer Instrument (MAG) (Smith et al., 1998), and the Solar Wind Electron, Proton, and Alpha Monitor (SWEPAM) (McComas et al., 1998).

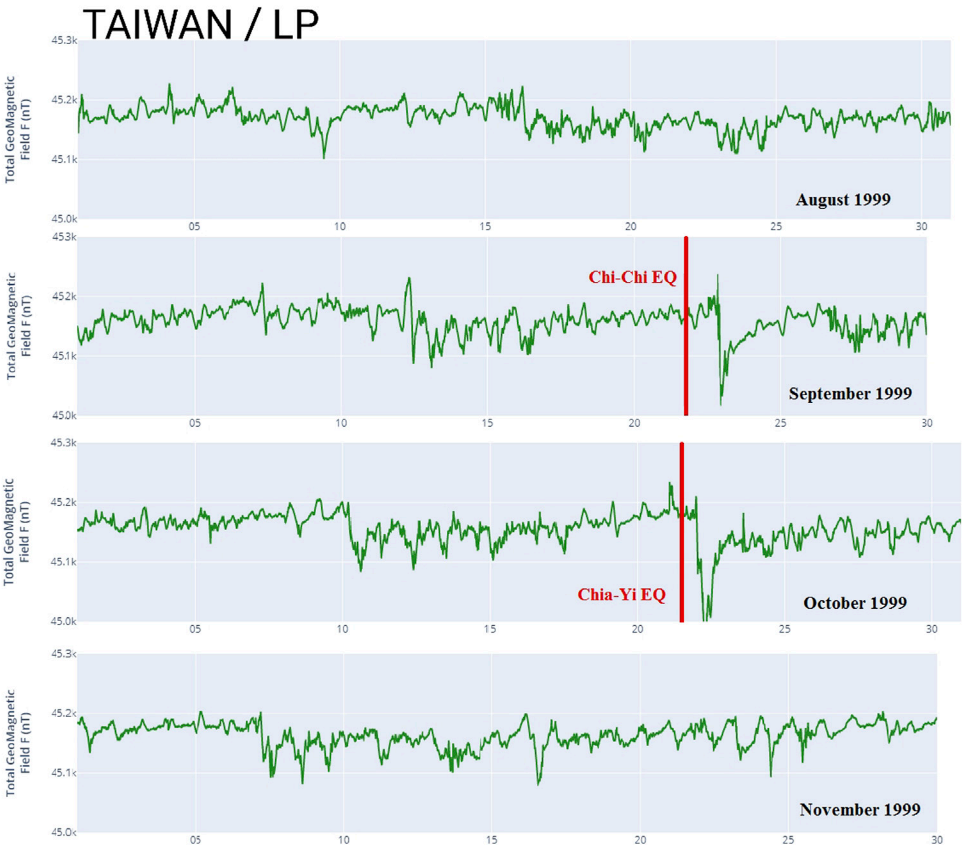

FIGURE 1 | Geomagnetic total intensity data recorded at the reference station (LP) from August to November 1999 adapted from Yen et al. (2004).

EPAM was constructed to investigate energetic ions and electrons, and it is composed of five telescope apertures of three different types; the Composition Aperture (CA), two low energy magnetically shielded telescopes (LEMS30 and LEMS120) and two low energy foil shielded telescopes (LEFS60 and LEFS150). The telescopes use the spin of the spacecraft to sweep the full sky. Solid-state detectors are used to measure the energy and composition of the incoming particles. ACE/EPAM data consist of electrons and ions in the energy range from ~50 keV to 5 MeV (Gold et al., 1998; Marvavilas et al., 2015).

The NASA Advanced Composition Explorer (ACE) ACE spacecraft is used, in a routine basis, in investigating space weather (https://www.swpc.noaa.gov/products/ace-real-time-solar-wind). The ACE satellite enables United States National Oceanic and Atmospheric Administration (NOAA) Space Weather Prediction Center (SWPC) to give advance warning of geomagnetic storms and recognize their types.

Test 1. A Space Origin of Magnetic Activity Before the Taiwan 1999 Earthquake Is Not Impossible

Geomagnetic Conditions Before the Chi-Chi Earthquake

The first question we examine relating to the origin of the sub-ULF (<1 mHz) magnetic field activity observed before the Taiwan 1999 earthquake (Akinaga et al., 2001; Yen et al., 2004; Freund and Pilorz, 2012) is whether there exists direct observational evidence that the sub-ULF magnetic field waves were produced by some tectonic process in the Earth's lithosphere.

Figure 1 shows the total geomagnetic intensity at the station LP, between mid-August and November 1999 (adapted from Yen et al., 2004). Yen et al. (2004) noted that a magnetic storm was observed ~2 days after the Chi-Chi earthquake and another one about 1 month later, at almost the time of occurrence of the Chia-Yi earthquake. These authors claimed that no other space-induced magnetic anomaly was observed except for these two storms and they concluded that the total geomagnetic intensity at the reference station LP did not show a disturbance at the times of the ChiChi earthquake and the Chia-Yi earthquake or times previous to the two EQs. However, this argumentation presupposes the unproven hypothesis that, beyond a terrestrial source, a space agent of the magnetic field wave activity could be a CME-induced short-lasting strong geomagnetic storm. Based on the absence of such a storm before the Chi-Chi and Chia-Yi EQs, a terrestrial origin is inferred.

The above argumentation follows the generally accepted hypothesis that only a short time great magnetic field variation might be an alternative physical process related with a future earthquake. However, it is well known from space science literature that there are two main types of geomagnetic storms

(Borovsky and Denton, 2006), which are followed by a similar magnetic field pattern on the ground: 1) a short time great magnetic field variation and 2) a weak or moderate long lasting but long lasting magnetic field depression.

Actually, in **Figure 1** we identify both types of imprints of geomagnetic storms. The two intense short lasting events (green arrows), which are obviously induced by Coronal Mass Ejections (CMEs) and three quasi-periodic (orange horizontal lines in **Figure 1**) long lasting moderate magnetic field depressions, which originate from a ~27-days recurrent HSS/CIR. Since, it is generally accepted that "in order to detect changes in the geomagnetic field associated with tectonic stress, it is necessary to eliminate the changes originating from external sources in the observed data", a space influence cannot be eliminated on the magnetic field data shown in **Figure 1** before both the Chi-Chi and Chia-Yi earthquakes.

In the next subsection we describe in some more detail the basic features of the two types of geomagnetic storms, since this information is crucial for the present study as well as the general research of the pre-EQ electromagnetic phenomena.

Coronal Mass Ejections and ~27-days Recurrent High Speed Solar Wind Streams Triggering Geomagnetic Storms

The most dramatic effect of the Sun in the interplanetary space is of course the Coronal Mass Ejections (CME). CMEs are large explosions of plasma and magnetic field from the Sun's corona, which are released into the solar wind and they often follow solar flares (Tsurutani et al., 2020). CMEs most often occur during solar maxima. On the other hand, the coronal holes are the least active regions of the Sun. They have magnetic fields opening freely into the heliosphere and they are associated with rapidly expanding open magnetic fields and the acceleration of the high-speed solar wind. They are the source of HSSs and CIRs, which are most often observed during the decay and the rising phase of the solar cycle (Richardson, 2018; Badruddin et al., 2018). During the year 1999 the solar activity was in the rising phase of solar cycle and in late 1999 (including July and August) ~27-days recurrent CIRs were noted as triggering long lasting storms (Borovsky and Denton, 2006).

However, despite the fact that dramatic solar flares and large CMEs are known to be associated with strong geomagnetic storms (Patsourakos et al., 2016 and references therein), the importance of the CH-driven HSSs in triggering geomagnetic storms is also significant (AGU collection of papers in Geophysical Monograph #167 edited by Alfvén, 1950; Kivelson and Russell, 1995; Tsurutani et al., 2006; Abdu et al., 2006; Kavanagh and Denton, 2007; Cranmer, 2009; Richardson and Cane, 2011; Tsurutani et al., 2011; Richardson and Cane, 2012a; Richardson and Cane, 2012b; Gerontidou et al., 2018; Richardson, 2018; Watari, 2018, and references therein).

HSSs dominate in the declining phase of the solar cycle, and in general during times of low SSNs, when polar CHs extend towards lower solar latitudes. Therefore, the flow of plasma from the solar corona is non-uniform in both time and space (Phillips et al., 1995). The fast solar wind emanating from a large coronal hole catches up with upstream slow solar wind and a compressive region is formed at the interface of the two streams. These structures reappear with the ~27-days rotation period of the Sun. When these CH-associated streams are long lasting, they lead to the formation of corotating interaction regions (CIRs) in the interplanetary space and when the CIRs are well developed, they are bound by fast forward (FS) and fast reverse (RS) shocks. It is interesting to note that HSSs and CIRs can drive important physical processes over longer periods than the more transient CMEs can (Tsurutani et al., 2006; Borovsky and Denton, 2006; Kavanagh and Denton, 2007).

The CME-driven storm is a strong, but short lived phenomenon, which usually lasts from a few hours to a few days (Tsurutani et al., 2006). The HSSs/CIRs cause weaker storms than the CMEs. However, the "weak" HSS-induced storms last for long times; the recovery phases of CIR-induced magnetic storms can last for a few up to 27 days. Furthermore, since during a quiet Sun, CH-driven HSSs corotate with the Sun's 27-days period, one or more HSSs, can affect semi-continuously the Earth's magnetosphere for several months. The important point to note is that during such long time periods, HSSs/CIRs can transfer much more energy in the magnetosphere than a single CME. During HSS-induced storms, the D_{st} value normally ranges between −25 nT and −75 nT and typically does not reach intensities of −100 nT.

Long-duration high-speed-stream-driven geomagnetic storms also lead to the strongest electron-radiation-belt radiation hazards, to the strongest plasma sheet spacecraft-charging hazards, and to the related spacecraft anomalies (Wrenn et al., 2002; Wrenn, 2009).

The semi-continuous arrival of HSS structures cause almost continuous UV Auroras, which often cover the entire dayside and nightside auroral zones for days to many weeks (Tsurutani and Gongalez, 1987). The Aurora phenomenon is known as High Intensity Long Duration Continuous Auroral Electrojet Activity (HILDCAAs).

Periodicities of ~14/27–28 days in Taiwan Geomagnetic Data in Late 1999

Imprints of the two types of storms, CIR-induced storm and CME-induced storm, on the geomagnetic field observed in Taiwan are evident in **Figure 1**, as we mentioned above. In particular, from **Figure 1** we see the imprints of a long-lasting storm between days 12–20.9.1999 before the ChiChi (September 20, 1999) EQ, and a short-lasting CME-induced storm after the EQ, on days 2223.9.1999. We also see a similar pattern in the magnetic field data before the Chia-Yi EQ.

The geomagnetic field data in Taiwan, which show a moderate, but long lasting magnetic field decrease with sub-ULF wave activity, between days 12–20 in September 1999 and ~27-days recurrent similar magnetic field patterns in October and November (**Figure 1**), during a period of ~27 days recurrent storms (Borovsky and Denton, 2006), suggest that we cannot reject the hypothesis that an external (space) agent might be the source of the sub-ULF waves between days 12–20.9.1999. On the contrary, since HSSs/CIRs trigger long-lasting weak to moderate magnetic storms, which produce sub-ULF EM waves at Earth, we infer that the presence of sub-ULF waves before the Chi-Chi EQ is consistent with a space source.

Since we cannot eliminate an external origin for the sub-ULF magnetic field waves before the Chi-Chi and Chia-Yi earthquakes, the question is: is there any direct observational evidence that they were the result of geotectonic processes? Freund and Pilorz (2012) compared the sub-ULF (<1 mHz) magnetic field waves with seismological data before the Chi-Chi earthquake, in order to directly test such a possibility. To this end, they compared the intensity of the ULF fluctuations by using LY/HL observatory 12-h running average data with the excess seismic energy output from August 1 to September 21,1999 (their Figure 19).

Their study suggested a dominant periodicity at ~14 days in the ULF magnetic activity. The periodicity was attributed to strong influence from the Earth's tides. However, if the ~14 days ULF periodicity was due to some gravitational effects of the Sun or the moon, then a clear argumentation on the correlation of the ULF ~14-days periodicity with the moon phase or the Sun-Earth relationship should be demonstrated. Instead, the authors noted that "Because the gravitational forces are relatively weak, the seemingly tight coupling between the Earth tides and both, ULF emission and regional seismicity, comes as a surprise». Therefore, we think that until a correlation between the ULF ~14-days periodicity and direct gravitational features can be shown, the attribution of the ULF ~14-days periodicity to gravitational forces cannot be accepted as a reliable explanation of the data.

A second argument by the same authors for a geotectonic source of the magnetic anomalies was based on the correlation between the curves of the ULF activity and the pre-EQ energy output excess between August 1-September 20, 1999. It was suggested that there exists a correlation and causal link between Earth tides, the frequency distribution of earthquakes, and the emission of ULF signals. However, in such a case, if the seismicity was the cause of the ULF fluctuations, the seismic energy release increase should have preceded the increase of the ULF activity.

However, the opposite pattern is obvious in Figure 19 of the paper by Freund and Pilorz. The pre-EQ excess seismic energy output curve E is shifted relative to the ULF line in such a way that both the onset and the maximum of the ULF activity reach earlier than the excess seismic energy E in all the four long lasting events analyzed (except for the onset of the last event, where the increases of the two parameters occurred almost simultaneously). Thus we cannot reject the hypothesis that space weather triggered the ULF EM waves at the LY station/Taiwan (red). Moreover, the time delay between ULF activity and seismic energy E are consistent with an external source of the ULF activity.

Test 2. The Taiwan Magnetic Activity Is Correlated to Geomagnetic Storm Activity

Here we check the hypothesis that the anomalous magnetic field activity in Taiwan and the geomagnetic storm may have a common space agent. For this reason we investigate the possible relation of the Taiwan magnetic field decrease associated with the sub-ULF magnetic activity between 12 and 21 September 1999 with the Earth's geomagnetic storm activity as provided by the global Dst index (Borovsky and Shprits, 2017), [http://wdc.kugi.kyotou.ac.jp/dst_final/199909/index.html].

For this reason, In **Figure 2** we compare the local B-field measurements by the LP/Taiwan observatory (Panel A) with the global geomagnetic index *Dst* (Borovsky and Shprits, 2017; http://wdc.kugi.kyoto-u.ac.jp/dst_final/199909/index.html) (panel B) during the whole of September.

The *Dst* index shows the strength of the Earth's ring current, which flows toroidally around the Earth, centered at the equatorial plane and at altitudes of-10,000–60,000 km. Changes in the ring current are responsible for global decreases in the Earth's surface magnetic field and reveals the occurrence of a geomagnetic storm (Daglis et al., 1999).

The Dst index also reacts to the partial ring current (Liemohn et al., 2001), the cross-tail current (Ohtani et al., 2001), and the Chapman-Ferraro dayside-magnetopause current (Burton et al., 1975) and is primarily a measure of plasma pressure in the bipolar magnetosphere (Dessler and Parker, 1959; Greenspan and Hamilton, 2000). *Dst* is also often used to define the duration of a storm, and to distinguish between quiet and disturbed geomagnetic conditions (Borovsky and Shprits, 2017). A *Dst* categorization that is often used to categorize storm intensity is (I) a weak storm (−30 nT > *Dst* > −50 nT), (II) a moderate storm (−50 nT > *Dst* > −100 nT), (III) a strong storm (−100 nT > *Dst* > −200 nT), (IV) a severe storm has (−200 nT > *Dst* > −350 nT), and a (V) great storm (*Dst* < 350 nT) (Loewe and Prolss, 1997). *Dst* is derived from a network of geomagnetic field observatories around the globe and its changes occur every time when Bz component of IMF B turns negative. The energy transfer is closely related to the B_z component of the IMF through a large-scale reconnection process, on the dayside, when a negative IMF meets the northward magnetic field of Earth's and a fraction of the available solar wind energy is able to penetrate our magnetosphere (Dungey, 1961).

Figure 2B reveals two different patterns of geomagnetic storms (Borovsky and Denton, 2006): 1) a long lasting CIR-induced Type II (moderate) storm, between 12 and 20.9.1999 and 2) a short time Type III CME-induced storm, on days 22–24.9.1999.

A comparison of Panels a and b suggests that the values in both panels follow a similar pattern during the whole of September 1999: 1) an increase between days 1–6, 2) a disturbance between days 7–11, 3) an abrupt decrease on day 12, 4) a general decrease along with a fluctuating profile between d. 12–16, 5) a recovery between d. 16–20, 6) an intense decrease on day 22, 7) a recovery phase until d. 26, and 8) a general small decrease between days 27–31. The impressive similarity of the local magnetic field in Taiwan with the index Dst, which reflects the global variation of magnetic field suggests that: 9) the magnetic field profile in Taiwan reflects not local physical processes but global variations in the Earth's magnetic field, and (b) the long lasting weak magnetic field decrease (days 12–20.9.1999) and the abrupt intense decrease (22–25.9.1999) in Taiwan reveals a CIR-induced storm and a CME-induced storm, respectively. In particular, we infer that the striking similarity of the profiles of two profiles strongly suggests a dependence of the local magnetic field before the Chi-Chi 1999 earthquake (days 12–20.9.1999) on space physical processes.

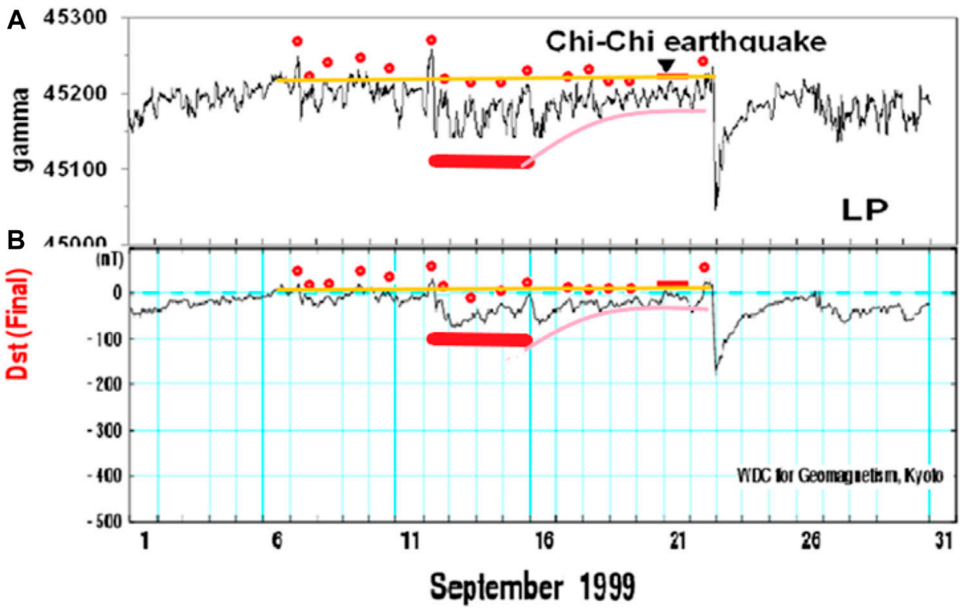

FIGURE 2 | Local magnetic field B at LP observatory, Taiwan (top panel) along with the Global *Dst* index of the geomagnetic storm activity in September 1999, including the time of the catastrophic Chi-Chi, 1999 earthquake. It is obvious that the two profiles are similar **(A, B)** during almost all September, and enhanced fluctuation occurs almost simultaneously in **(B)** and Dst values, during a general decrease in both profiles, before the time of the Chi-Chi earthquake (black arrow in **(A)**. The pre-earthquake magnetic profile in Taiwan obviously reflects the geomagnetic storm activity as indicated by the index Dst (see in the text).

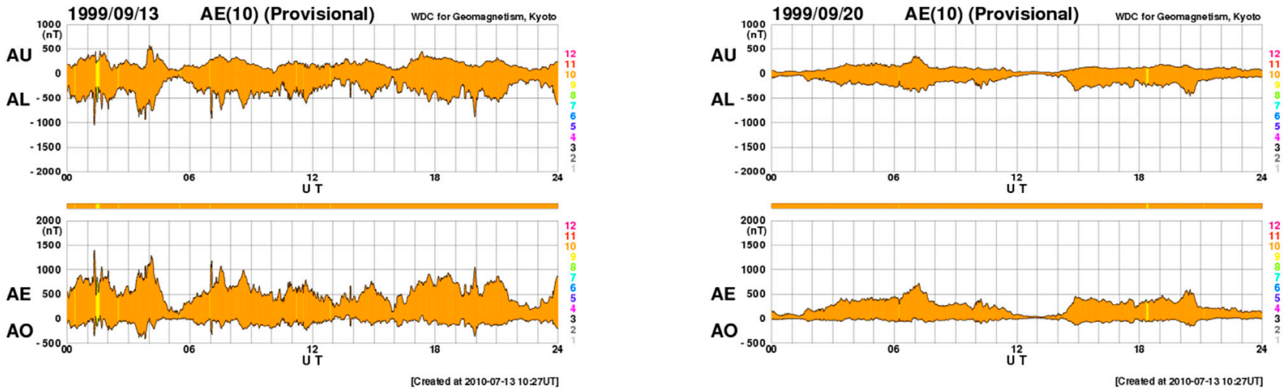

FIGURE 3 | Auroral Electrojet indexes on 13.9.1999, the day after the storm onset and during a day at its recovering phase of the long lasting storm occurred before the Chi-Chi earthquake.

In order to further check the nature of the magnetic field variations in September 1999, we also check the presence of geomagnetic storm activity at high latitudes by examining the auroral electrojet indeces AU, Al, AE and AO. The Auroral Electrojet indexes monitor the magnetic signature of the eastward and westward auroral electrojets in the Northern hemisphere and they have been usefully employed both qualitatively and quantitatively as a correlative index in studies of substorm morphology. To calculate the AE index, magnetograms of the H components of 12 observatories have been uniformly distributed over the longitude in the northern hemisphere at auroral or subauroral latitudes between 60° and 70° (Shadrina, 2017).

In **Figure 3** the AU, Al, AE and AO indexes are shown on a day near the beginning of the long lasting magnetic field disturbance in Taiwan (13.9.1999), and on a day at the recovery phase of the field. It is evident that the auroral electrojet indexes AU, Al, AE and AO show a strong storm activity on day 13 (http://wdc.kugi.kyoto-u.ac.jp/ae_provisional/199809/index_19980913.html and a weak activity on day 20.9.1999 (http://wdc.kugi.kyoto-u.ac.jp/ae_provisional/199809/index_19980910.html), in agreement with the Dst variations seen in **Figure 2B**. We infer that the local magnetic variations in Taiwan between days 12–20.9.1999 reflect the progress of a geomagnetic storm recorded at both the low and the high latitudes. The comparison of **Figure 3B** to **Figure 2B** and **Figure 3** confirm a space and not a local (terrestrial) physical process being the cause of the Taiwan magnetic field variations (including sub-ULF activity) for about 10 days before Chi-Chi EQ.

Test 3. The Magnetic Variations in Taiwan Is Controlled by Space Weather Conditions

We mentioned earlier that the flow of plasma from the solar corona is non-uniform in both time and space (Phillips et al., 1995), and a compressive region is often formed at the interface of the fast stream with the upstream slow stream. When these structures last for long times they form corotating interaction regions (CIRs) in the interplanetary space and when the CIRs are well developed, they are bound by a fast forward (FS) and fast reverse shock (RS).

The most typical variations of plasma parameters of a CIR are: 1) an increase in the solar wind plasma density N and the interplanetary magnetic field B, due to the 'pile-up' of material at the leading edge of the fast wind, 2) a long lasting high speed solar wind and 3) the presence of large amplitude low frequency (Alfvén) waves, in particular within the CIR, between the FS and the RS. When the CIR incident on the Earth's magnetosphere trigger long lasting weak or moderate magnetic storms (Tsurutani et al., 2006; Borovsky and Denton, 2006; Kavanagh and Denton, 2007; Richarson, 2018) and various other important phenomena in the Earth's environment. We investigate now the possible incident of a CIR as possible agent of the long duration time moderate geomagnetic storm (**Figure 2B** and **Figure 3**) and the subsequent magnetic field imprint in Taiwan (**Figure 1**), between September 1220, 1999.

In order to apply Test 3, that is the possible relation of the geomagnetic variations between 1220.9.1999 with the arrival of a CIR, we analyze space observations from the Advanced Composition Explorer (ACE) spacecraft, which is in orbit around the L1 Sun-Earth libration point, at a distance of ~220 R_E from Earth ($R_{E:}$ the Earth's radius). The ACE is a satellite, which is in general used in space weather studies in order to predict or explain space induced variations in the environment of Earth, as, for instance, geomagnetic storms, radiation belt electron variation status etc. (Stone et al., 1998).

Figure 4 shows magnetic field data in spherical coordinates (B, θ φ) in the three top panels, A, B and C, from the Magnetometer Instrument (MAG) (Smith et al., 1998) and solar wind density, temperature and speed in panels D, E and F from the Solar Wind Electron, Proton, and Alpha Monitor (SWEPAM), for the time interval September 8–22, 1999.

In this figure we can see characteristic features of a CIR structure bounded by a MHD FS on day 12 of September and a RS on day 15.9.1999. For instance, we can notice an increase in magnetic field magnitude B (panel A), in solar wind speed V_p (panel F) in solar wind density N_p (panel D), and proton density which indicate the arrival of the FS, on day 12th of September. Furthermore, we see a long lasting increase of the solar wind speed $V_{p,}$ which starts with the arrival of the CIR, on September 12, 1999 and drops to pre-CIR values on September 20, 1999, along with intense northsouth sub-ULF magnetic field direction fluctuations (values; panel B).

By comparing **Figures 1**, **2**, **4** we infer that both the long lasting geomagnetic storm and the magnetic field decrease in Taiwan started on day 12.9.1999 at almost the same time as the arrival of the CIR in the near Earth interplanetary space (ACE). Furthermore, the time interval of the most intense magnetic field fluctuations recorded in Taiwan coincides with the time interval of the CIR at ACE; the intense magnetic field fluctuations started on day, 12.9.1999, the day of FS and lasted until 15 September 1999, the day of RS (red bar in **Figure 1A**).

The ACE observations shown in **Figure 4** obviously confirm the hypothesis that the longlasting geomagnetic variations between 12 and 20.9.1999 in Taiwan and in the magnetosphere are related with the arrival of a CIR, which evidently was the cause of the magnetic field variations (Kavanagh and Denton, 2007; Badruddin et al., 2018; Richardson, 2018) observed in Taiwan between 1220.9.1999. Test 3 definitely confirms that a CIR was the cause of the long lasting geomagnetic storm (**Figures 2**, **3**) and of the related magnetic field anomalies in Taiwan (**Figure 1**) observed before the Chi-Chi earthquake.

Test 4. Magnetic Sub-Ultra Low Frequency Waves in Taiwan Are Related With Magnetohydrodynamic Wave Activity

Since we found strong observational evidence that the long lasting magnetic field decrease before the Chi-Chi EQ (12–20.9.1999) was a signature of the CIR incidence on the Earth's magnetosphere, we now further focus on the generation process of the pre-EQ sub-ULF magnetic field waves themselves.

In the previous (sub)sections we provided significant evidence that not only the pre-EQ magnetic field decreases, but also its general profile, including the sub-ULF magnetic field wave activity, is consistent with an external (space) cause. Now we investigate the exact generating mechanism of the sub-ULF magnetic field fluctuations between 12 and 20.9.1999.

It has been found that solar wind speed, solar wind ULF waves, the negative component B_z of the IMF and solar wind density perturbations are correlated with ULF magnetic pulsations on the ground (Bentley et al., 2018; Hynönen et al., 2020). Although solar wind speed has been considered as having the largest effect on the ground ULF power compared to the other parameters (solar wind ULF waves, the negative IMF component B_z and solar wind density perturbations), we examine here the (possible) contribution of the solar wind ULF Alfvén waves to the ground sub-ULF fluctuations before the Taiwan 1999 EQ. For this reason we compare here, for the first time, simultaneously obtained measurements in space, by the ACE spacecraft, and on Earth, by magnetic field observatories in Taiwan.

We have already mentioned that the solar wind is a source of MHD sub-ULF Alfvén waves, particularly at frequencies around 1 mHz (Barnes, 1983). In particular a series of studies has also confirmed that Alfvén waves are a ubiquitous feature of CIRs (Smith et al., 1995; Richardson, 2018) and that they have important implications for coupling of the interplanetary space

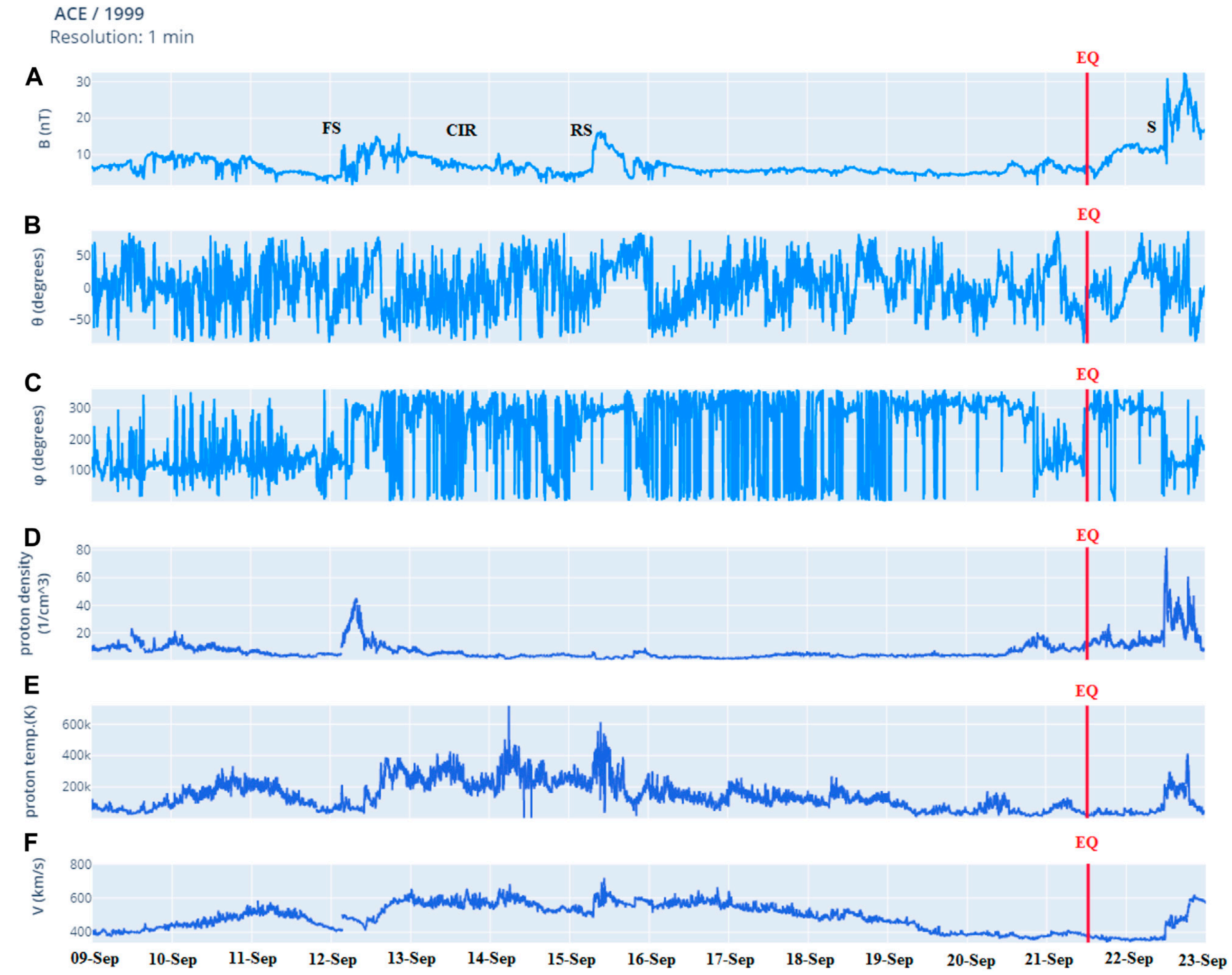

FIGURE 4 | Magnetic field data (B, θ φ) in spherical coordinates three top panels; **(A-C)**, Brms, and proton plasma density, temperature and speed three bottom panels; **(D-F)** as recorded by the ACE spacecraft, for the time interval September 9–22, 1999. The red normal line indicates the time of Taiwan earthquake occurrence, at the end of a corotating interaction region (CIR), which is accompanied by rich presence of ULF Alfvèn waves.

to the magnetosphere (Tsurutani et al., 2006). Two processes transform the ULF wave energy that enters the magnetosphere from outside: the field line resonance and the cavity resonance (Southwood and Hughes, 1983). The two processes interact with each other. Standing waves in the cavities feed energy to the field line resonances. Many of the pulsations seen at the ground are caused at the ends of field lines set into motion by a complex process involving coupling of the propagating waves to resonant cavities, and these, in turn coupling to field line resonances (McPherron, 2005). Furthermore, it has been confirmed that the 2–10 mHz EM power increases with an approximate power law dependence on solar wind speed, at all local times (Hynönen et al., 2020). Finally it worths noting that the space controlled signal seen at the ground is not the MHD waves themselves, but electromagnetic waves radiating from electric currents induced in the ionosphere by the external source (McPherron, 2005).

In **Figure 5** we compare magnetic field data obtained by the ACE spacecraft upstream from the Earth's bow shock (panels A and B) and by the LNP observatory in Taiwan (panels C and D) on day 13 September 1999, between 0 and 12UT. In particular, the two upper panels display the magnetic field magnitude (panel A) and the angle in polar coordinates (panel B), as measured by the magnetometer instrument MAG onboard ACE. The two bottom panels show the magnetic field component B_z (panel C) as well as the magnitude of the total magnetic field, as measured at LNP observatory in Taiwan.

We have seen that day 13 was characterized by intense geomagnetic storm activity (**Figure 3**), which was caused by the arrival of a CIR on day 12.9.1999 (**Figures 3**, **4**). **Figure 5** suggests that day 13, 0-12UT, was also a period of large amplitude magnetic field fluctuation at the position of the ACE spacecraft, far upstream from the Earth's magnetosphere. From **Figure 5** we also see that the magnetic field gradually decreases and it shows a

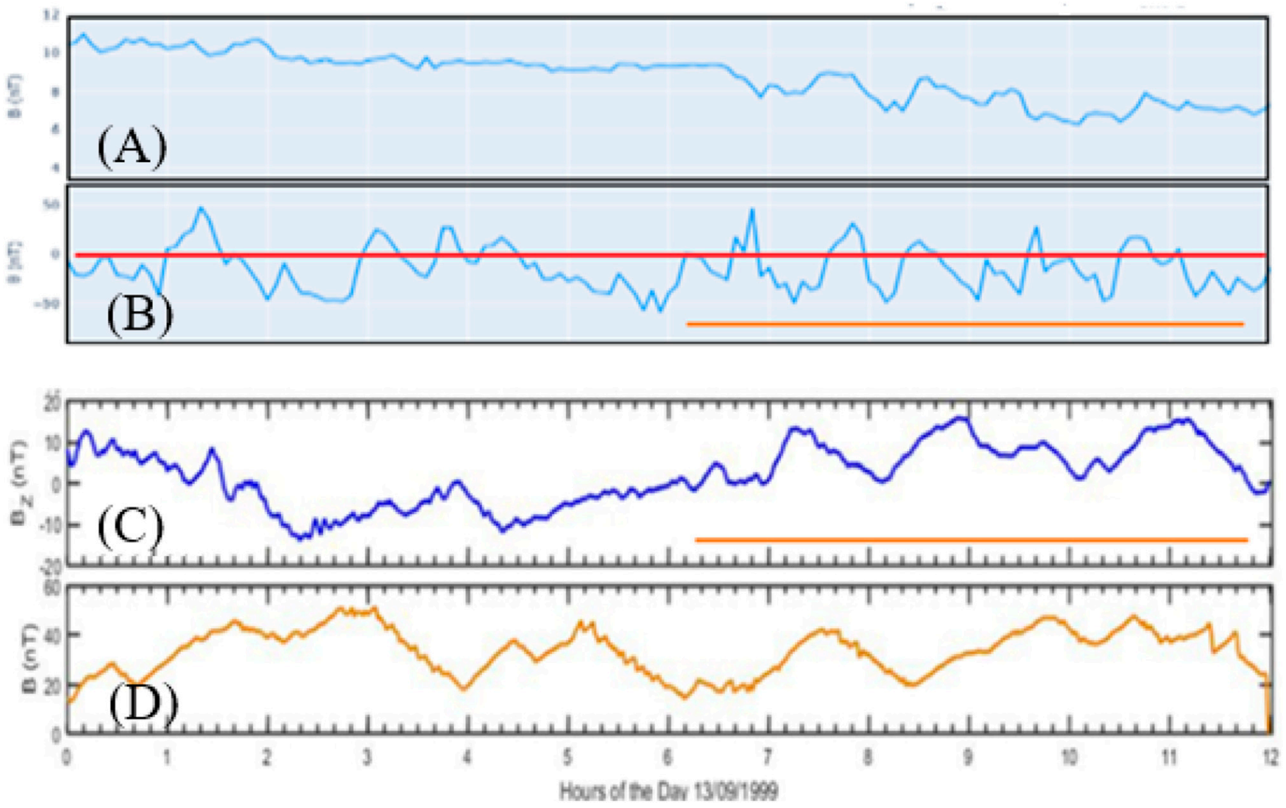

FIGURE 5 | The sub-ULF B wave activity in Taiwan **(C)** changes after ~7 UT following a change in the MHD Alfvén wave pattern at ACE satellite, in the interplanetary space **(A, B)**.

variable magnetic field direction during the whole 12-h period examined.

Panel b suggests that the magnetic field turns quasi-periodically in the southward direction. The southward IMF turning is the main condition that triggers geomagnetic storms (Dungey, 1961) and, indeed, we see that the storm activity is high at the same time period (**Figures 2**, **3**). The type of the waves are MHD Alfvén waves, as inferred from the almost stable magnetic field magnitude and the large variations of the azimuthal angle (Chen, 2016), which sometimes changes from ~−50^0 to ~+50^0 (panel b).

From the comparison of the curves in panels a, b, c, and d, we infer that the magnetic field at the LNO/Taiwan observatory also fluctuated. In particular, we see that the wavy pattern changes after ~6 UT both in the interplanetary space (ACE) and on the ground (LNO/Taiwan) in the first and the second part of the time period examined. After ~6 UT (horizontal orange lines in **Figure 4**) both the IMF and the terrestrial magnetic field become much more turbulent than between 0 and 6 UT; this evident when we compare the latitudinal magnetic field angle at ACE (panel B) and the northsouth magnetic field variation in Taiwan (panel C).

There is another interesting point to note in **Figure 5**. The increased magnetic field fluctuation at Earth after ~6 UT is preceded by successive southward turning of IMF, which is a cause of magnetic storms and a more turbulent magnetic field on Earth. Furthermore, some variations in the IMF magnitude, after ~07:00 UT, might contribute to geomagnetic triggering due to changes in the electromagnetic pressure on the Earth's magnetosphere (Takahashi et al., 2012). The magnetic field fluctuation variation at both sites, in the interplanetary space and in Taiwan, shows a period of ~1 h, that is a frequency <1 mHz (with somewhat longer period waves at Earth than at ACE).

We infer that the wave patterns in Taiwan and at ACE seen in **Figure 5** show remarkable relations. Since a variety of physical factors influence the propagation of an electromagnetic signal from the position of ACE, in the interplanetary space, to the Earth's surface, the above noted relations are remarkable and suggest that the sub-ULF activity in the solar wind made a significant contribution on the ground magnetic field waves (Fraser, 2009; Shi et al., 2020)

Test 5. The Geomagnetic Activity in Taiwan Is Correlated With a ~28-days Corotating Interaction Region of Solar Origin

Tests 1 to 4 support the concept that the sub-ULF magnetic field wave activity observed in Taiwan before the Chi-Chi EQ (12–20.1999) is consistent with a CIR-induced long lasting geomagnetic disturbance.

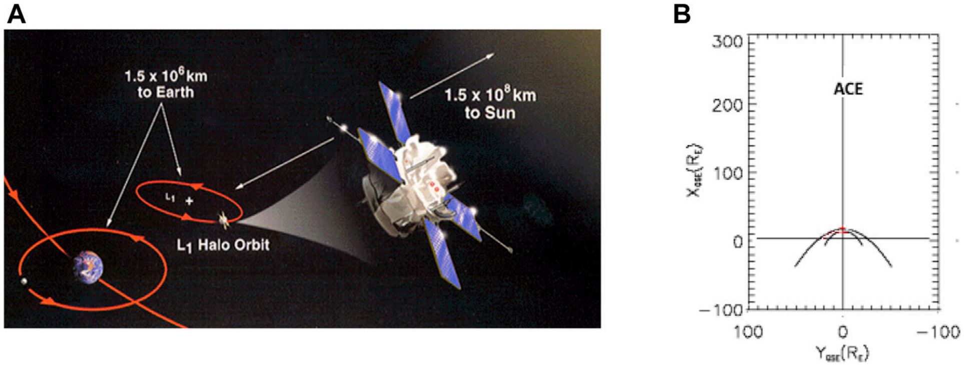

FIGURE 6 | ACE circulating around the L_1 Lagrangian point **(A)**, at a distance of ~220 R_E **(B)**.

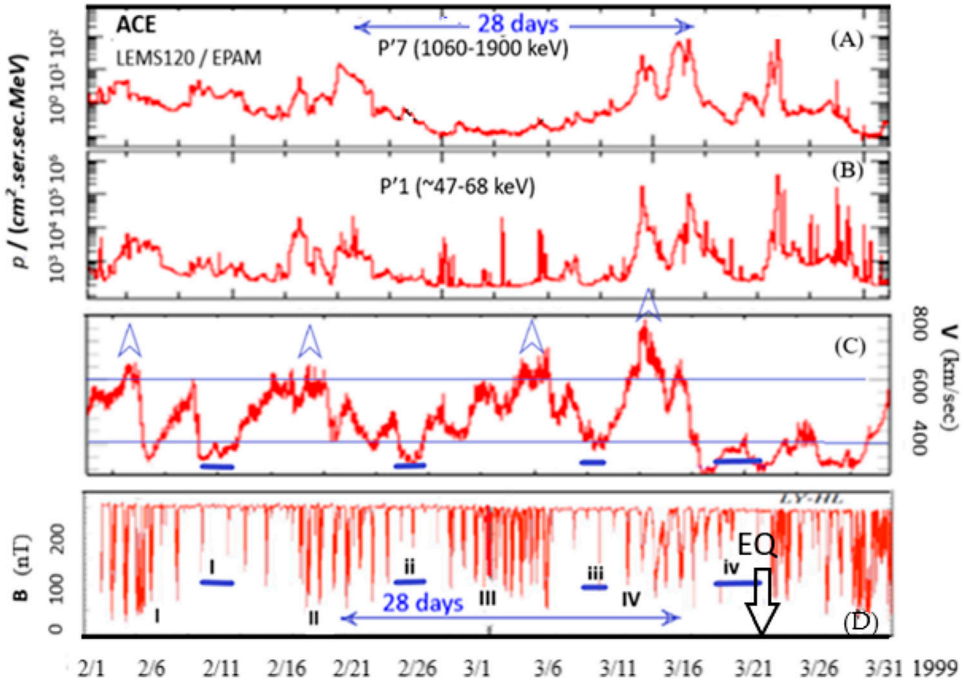

FIGURE 7 | From top to bottom: proton flux of low (ACE/LEMS120/P'2) and high (ACE/LEMS120/P'7) energy protons in the interplanetary space from the solar direction **(A, B)**, solar wind speed **(A)**, and **(D)** the magnetic field fluctuations. Tests 5, 6 and 7 are based on the comparison of simultaneous measurements obtained by the ACE spacecraft in the interplanetary space and by the magnetic field observatories in Taiwan for time long enough to cover at least two successive, about 28 days separated CIRs.

We now perform one more test concerning the space origin of the sub-ULF magnetic fluctuation before the M7.2 Chi-Chi EQ. Since 1) CIRs are a provoking agent of great EQs (Anagnostopoulos et al., 2021 and references therein), 2) CIRs-induced storms appear a characteristic ~27-days periodicity in the late 1999 (Borovsky and Denton, 2006) and 3) the CIRinduced storms are characterized by sub-ULF wave activity on the ground (McPherron, 2005; Shi et al., 2020), we examine the hypothesis that ULF wave activity in Taiwan follows the solar ~27/14 days periodicity of the CIRs. A correlation of the ground pre-EQ sub-ULF activity with CIRs in the interplanetary space would be an additional, very strong evidence of their space origin. The data in the interplanetary space were obtained by the ACE satellite (**Figure 6**).

For this reason, in **Figure 7**, we compare physical processes in interplanetary space, in the magnetosphere and on Earth (Taiwan) during a period of 7 weeks (from August 13 to September 30, 1999). The near Chi-Chi, Taiwan (adapted from Freund and Pilorz, 2012) from August 13 to September 30, 1999.

In particular, in **Figure 7**, we display, from top to bottom, 1) interplanetary space low and high energy proton flux measurements from the EPAM instrument onboard the ACE spacecraft (panels A and B) 2) the space plasma proton speed measured by the Solar Wind Electron, Proton, and Alpha Monitor (SWEPAM) onboard the same spacecraft, (panel C), and 3) the 12-h running average difference of magnetic field values measured at the LY station minus those at the HL station in Taiwan. (adapted from Figures 15A,B of Freund and Pilorz (2012). The 12-h running average difference of magnetic field values were used to emphasize the overall envelope. The energetic proton fluxes from channels P'1 (~47-68 kev), and P'7 (1060-1900 keV) were selected because of the general Sunward direction of the LEMS120/EPAM telescope (http://sdwww.jhuapl.edu/ACE/EPAM/idf.html), which allows investigation for particle streaming from the Sun.

When focusing on the time period before the Chi-Chi EQ (indicated by an arrow in panel E) we see a structure indicating an increased wave activity between days 12–19.9.1999 (ULF wave group marked IV), which correspond to the geomagnetic storm and the wave activity in Taiwan examined in the previous subsections (**Figures 1–5**; Tests 1–5). During this period the solar wind speed V (panel C) reached its highest values V = ~800 km/s that is ~2 times the normal value of solar wind speed.

Figure 7 also shows that, during days 12–20.9.1999, the enhanced solar wind speed values and the ULF wave group IV are also associated with enhanced proton fluxes showing two distinct peaks (panels A and B). These two flux peaks are related to the forward shock (FS) and the reverse shock (RS) of the CIR examined in **Figure 4**, and they reveal proton accelerating at the two edges of the CIR shocks (FS and RS). The coincidence of 1) the energetic particle flux enhancements (panels A and b), 2) the high solar wind speed structure (panel c), 3) the magnetic field profiles revealing the presence of a CIR (**Figure 3**) and (iv) the ULF wave group IV in Taiwan is in agreement with the CIR as a cause of the terrestrial magnetic field fluctuation at those times (Fraser, 2009; Richardson, 2018).

We examine now the hypothesis that the 27-days period corotating high solar wind speed streams/CIRs in late 1999 (Borovsky and Denton, 2006) may be related with the ULF wave activity in Taiwan. The observations in **Figure 6** (panels A–E) clearly show that the ULF wave group II preceded the ULF group IV by ~28 days, that is a time almost equal to the solar rotation period. The data in **Figure 7** also suggests the presence of: 1) a high speed solar wind stream (panel F) and 2) two peaks in energetic proton flux (panels a and b) associated with a FS and RS (data not shown here), during the ULF wave group II.

The time difference between ULF magnetic field wave groups II and IV and the appearance of a CIR structure at the times of the two wave groups II and IV suggest that the ULF wave groups II and group IV are related with the same CIR.

It is obvious that the two CIRs, which are associated in time with high solar wind speeds, strong magnetic storm activity and the ULF wave groups II and IV separated by a period of ~28 days, before the Chi-Chi EQ, strongly suggest that the two ULF magnetic field wave groups II and IV observed in Taiwan were caused by the incidence of a CIR on the Earth's magnetosphere (Kivelson and Russell, 1995; Fraser, 2009; Richardson, 2018).

TEST 6. Solar Wind Speed and Taiwan Sub-ULF Magnetic Field Fluctuation

The sub-ULF magnetic field fluctuation (i.e. Pc 5 pulsations, in the frequency band 2–7 mHz; Jacobs et al., 1964) correlate well with solar wind speed (Engebretson et al., 1998; Kessel, 2008, Pahud et al., 2009; Hynönen et al., 2020). However, solar wind speed has been considered to have the largest effect on the ground ULF power compared to the solar wind ULF waves, the negative component B_z of the IMF and the presence of solar wind density perturbations (Bentley et al., 2018; Hynönen et al., 2020).

Based on the above space weather-terrestrial relations, we apply an additional test for the origin of the Taiwan sub-ULF wave activity before the Chi-Chi EQ (TEST 6). Since it is known that the sub-ULF wave activity is a normal result on Earth related with high solar wind speeds, we elaborate on the whole period examined in **Figure 6**, the possible relation of the changes of the sub-ULF wave activity before the Chi-Chi EQ with changes in the solar wind speed as observed by ACE in the interplanetary space.

In order to do that we name the four groups of the sub-ULF magnetic field fluctuation by numbering I, II, III, IV and the periods with absence or weak magnetic field activity by i, ii, iii, iv. The quiet periods i, ii, iii, iv, at times when the solar wind speed falls below the usual limit of 400 km/s, for more than 1 day, are marked by horizontal bars (panels D and E) to facilitate the solar wind speeds-Taiwan ULF EM waves comparison.

Such a comparison reveals that (A) during the four groups I, I, III and IV the solar wind speed V reaches maximum values between 600 and ~800 km/sec (blue horizontal line) and (B) during the four periods of weak or absence of magnetic field wave activity (intervals called i, ii, iii and iv), the solar wind speed reaches its lowest values, below the usual level of 400 km/s (blue bars in panels D and E).

This correlation between the solar wind speed values and the presence/absence of the magnetic fluctuation in Taiwan, along with the previous Test 5, confirms that an external agent controls the sub-ULF magnetic fluctuations in Taiwan during 7 months before the Chi-Chi 1999 earthquake. This finding is consistent with recent statistical results (Gulyaeva, 2014; Rekapali, 2014; Anagnostopoulos et al., 2021)

Furthermore, it worths noting that the analysis of polarization (the ratio of vertical magnetic field component Z to the horizontal component G), that the polarization (Z/G) showed a significant enhancement for 2 months before the Chi-Chi earthquake. Akinaga et al. (2001) pointed out that this temporal evolution of polarization seems be associated with the Chi-Chi earthquake. These authors accepted as the generation mechanism of the sub-ULF (~0.01) Hz emissions the microfracturing model by Molchanov and Hayakawa (1995). However, the present study suggests that the temporal evolution of the polarization (Z/G) is related with the special space weather during the last 2 months before the Chi-Chi earthquake and most probably is the result of semi-continuous magnetic storm activity. However, this result should be further tested.

Test 7. Long Time ~14-days Periodicities in Space and in Taiwan

It is generally known that the ~27-days solar rotation controls many physical processes in the Earth's environment. The existence of a sole intense high speed solar wind stream emanating from the Sun causes ~27/28-days periodicities in various physical phenomena both in the near Earth environment and on the ground. The existence of more than one solar wind stream can produce additional periodicities. For instance a second high speed solar wind stream produces a ~13/14-days periodicity in the interplanetary space, in the Earth space and on Earth. Intense CIRs are observed as periodic (~27/28-days, ~13/14-days) phenomena even beyond the Earth's orbit, in the deep space (Burlaga, 1997; Anagnostopoulos et al., 2009).

The ~27/~13-days periodicity of high speed solar wind streams influence the Earth's magnetosphere in many ways. Among other phenomena, a power spectrum analysis recently revealed a ~27/13-days periodicity in the global seismic energy output, in particular during a quiet Sun (Anagnostopoulos et al., 2021).

The ~14 days-periodicity in sub-ULF activity is also seen in **Figure 6** in the ~14 days time separation of the four groups I, II, III and IV. This periodicity was also clear in the results of a Fourier Transform performed by Freund and Pirolz and (2012).

Since the four sub-ULF magnetic field wave groups I, II, III and IV are related with the arrival of the presence of high speed solar wind speed, we infer that the ~14 days-periodicity evaluated by Freund and Pirolz was of a clear space origin (and it is not due to the gravitational forces exerted by the moon and the Sun).

The space origin of the ~14 days-periodicity is also consistent with the fact that (both the onset and the maximum of) the four ULF groups I, II, III and IV earthquake reach earlier than the seismic energy E in all the four long lasting events before the Chi-Chi 1999 EQ.

The results from Tests 1–7 in a variety of observations in the interplanetary space and on the ground strongly suggest that the sub-ULF magnetic fluctuations in Taiwan during 7 months before the Chi-Chi 1999 earthquake are related with physical processes resulting from the interaction of high speed solar wind streams.

DISCUSSION

Great earthquakes as well as global seismic energy output have recently been confirmed as depending on solar activity and the subsequent space weather. Enhanced seismicity was found to be higher during times of a quiet Sun, when the sunspot number (SN) is low (but not in the deep minimum). Such solar conditions allow high solar wind speed streams to emanate from coronal holes and form structures rotating in the interplanetary space with the ~27-days period of solar rotation. Low SSN conditions and ~27-days corotating interaction regions (CIRs) are mostly observed in the decay phase throughout the ~11-years solar cycle, but also during the rising solar cycle phase as well as during short time intervals (some months) in the solar maximum phase. During such periods with small SN a ~27-days periodicity was revealed in seismic energy release at Earth (Anagnostopoulos et al., 2021). The seismic activity is in general anti-correlated to the SSN. One of the results of our previous paper is the finding that all of the 16 giant ($M \geq 8.5$) EQs between 1900 and 2017 occurred during the decay and the rising phase of the solar cycle or at times of a strong SN reduction.

The question raised from the above Solar-terrestrial relationship is which physical mechanism mediates space weather (CIRs) with the lithosphere in order to provoke great earthquakes or high global seismic energy release.

In the present case study we tested the hypothesis whether the sub-ULF (<1 mHz) magnetic field activity before a great EQ may be of a space origin, and therefore, a possible final agent of the EQ itself. The sub-ULF (<1 mHz) magnetic field activity is a well known phenomenon in the space community resulting from CIR incidence on the Earth's magnetosphere, while it has been also accepted as an earthquake precursor resulted from lithospheric processes, as we reported in *Theoretical and Observational Framework*.

As a case study we selected to investigate the great (7.7 M_w) Taiwan September 20, 1999 earthquake, which has been shown to be preceded by a long time period of sub-ULF (<1 mHz) magnetic field activity. To this end, we performed seven observational tests. Furthermore, for the first time in earthquake prediction scientific literature, we compared simultaneous space observations in the interplanetary space and magnetic field waves on the ground.

The enhanced sub-ULF (<1 mHz) magnetic field wave activity in Taiwan was previously attributed to tidal loading and unloading of the Earth's crust, due to the gravitational forces exerted by the moon and the Sun. However, it was also noted that since the gravitational forces are relatively weak, the seemingly tight coupling between the Earth tides and both ULF emission and regional seismicity, comes as a surprise (Freund and Pirolz, 2012).

The concept of gravitational tidal triggering has been known for more than 110 years (Schuster, 1897; Emter, 1997). However, several studies have reported either no correlation between the Earth's tide and earthquake occurrence (Heaton, 1982; Vidale et al., 1998; Kennedy et al., 2004) or small positive correlations (Tanaka et al., 2002; Cochran et al., 2004) under several restrictions, as for instance, for a particular geographic region (Tolstoy et al., 2002; Kasahara, 2002), earthquake magnitude range (Wilcock, 2001; Tanaka et al., 2002; Kasahara, 2002) and increasing tidal stress levels. Métivier et al. (2009) found that small magnitude (less than magnitude 4.0) EQs are more easily triggered by tides.

Our data analysis during the period of 7 weeks before the Taiwan 1999 earthquake provides significant information concerning the origin of ~27/28 and ~13-days ULF wave periodicity found by Freund and Pilorz (2012). Our analysis strongly suggests that the ~14-days periodic detection of four groups of ULF wave activity in Taiwan was the result of four almost simultaneous events of high speed solar wind streams observed by ACE in the interplanetary space. More studies are needed to further check the origin of sub-ULF (<1 mHz) magnetic field waves before other great earthquakes.

However, preliminary examination of several great earthquakes suggests that the pre-EQ sub-ULF (<1 mHz) magnetic field wave activity seems to be in general CIR-induced geomagnetic phenomena.

The data examined in the present study provide strong evidence that four groups of enhanced sub-ULF (<1 mHz) magnetic field waves in Taiwan were related in time with four groups (**Figure 6**; groups I, II, III, IV) of high speed solar wind streams for 7 weeks before the great September 21, 1999 E. The relation of magnetic storm activity, its imprints on the ground and the associated subULF magnetic fluctuation in Taiwan with the high speed solar wind streams and sub-ULF Alfvèn waves in the interplanetary space is consistent with space weather as the agent of ULF magnetic terrestrial fluctuation (Bentley et al., 2018; Hynönen et al., 2020) observed for 7 weeks before the Chi-Chi EQ.

Our study includes a more detailed data analysis for the fourth group of enhanced sub-ULF magnetic field activity (noted I **Figure 6** as IV), which was observed between days 12–20.9.1999. At almost the same time a strong CIR produced a significant reduction in magnetic field magnitude, which was recorded by observatories in Taiwan. The Chi-Chi EQ occurred at the end of the CIR, on day 20.9.1999, whereas another earthquake in southern Taiwan (Chia-Yi) occurred after a solar rotation, at the end of the next arrival of the CIR preceding the Chi-Chi EQ.

Enhanced solar wind speed, sub-ULF Alfvèn wave activity, magnetic pressure and southward IMF have been confirmed in space science to produce sub-ULF magnetic field activity at Earth (Fraser, 2009). In the time period we examined in this study, actually both enhanced solar wind speed (up to ~800 km/s) and intense sub-ULF Alfvèn wave activity were observed by the spacecraft ACE, almost simultaneously with the enhanced magnetic field activity in Taiwan during the four groups. Some observational evidence on day 13.9.1999, 0-12UT, during the main phase of the CIR-induced storm, suggests that when the pattern of the IMF wave activity changed, the terrestrial magnetic field wave activity changed as well. This observation suggests a principal role of the IMF wave activity at least at that time (day 13.9.1999, 0-12UT).

Our present results from the study of the precursory physical conditions before the Taiwan 7.7 M_w EQ provide evidence that the pre-EQ sub-ULF (<1 min) magnetic wave activity may indicate a potential cause and not the result of tectonic stresses. This hypothesis is consistent with the fact that MHD generators have been used to activate local earthquakes (Pulinets and Boyarchuk, 2004; Sorokin et al., 2012; Novikov et al., 2017). The impact of electrical pulses of DC current injected through emitting dipole into the earth crust on the spatial and temporal distribution of weak seismicity has been confirmed (Tarasova et al., 2000; Tarasov and Tarasova, 2002, 2004; Chelidze et al., 2006). Furthermore, modern laboratory studies of electric triggering of macro events (laboratory "earthquakes") were carried out at simplified slider system (Chelidze et al., 2002) and spring-block model simulated the seismogenic fault (Novikov et al., 2020).

The statistical results of Anagnostopoulos et al. (2021) and those of the present case study suggest that enhanced seismicity is preceded by CIRs and CIR-induced weak or moderate, but long lasting geomagnetic disturbances. In several cases examined, including the case of the present study (Taiwan 1999) some repeated CIRs, with a period of ~27 days, precede great EQs. We do believe that thereafter a good analysis of space weather should not be ignored in earthquake prediction research. In particular, a weak geomagnetic activity may be misleading criterion concerning the origin of EQ EM precursory phenomena. Recently, Biswas et al. (2020) presented a paper, where they tried to separate the contamination in ionospheric parameters due to geomagnetic storm and acoustics parameters.

Although, the CME-driven storm is usually a strong phenomenon, it lasts for a short time period; from a few hours to a few days (Tsurutani et al., 2006). The HSSs/CIRs cause weaker magnetic disturbances in Earth's magnetic field than the CMEs, but during a quiet Sun high speed solar wind streams corotate with the Sun's 27-days period. Under such conditions several CIRs can affect the Earth's magnetosphere semi-continuously for a long period of some months. During these long time periods, CIRs can transfer much more energy into the magnetosphere than a single CME (Tsurutani et al., 2006). For this reason high seismicity is well related with the presence of CIR–induced geomagnetic events around the minimum phase of the solar cycle (Gulyaeva, 2014; Rekapali, 2014; Anagnostopoulos et al., 2021). Other external sources, as for instance CME-driven events or Earth tides, possibly make some minor contribution to the preparation process of great earthquakes, but there is not such significant observational evidence.

We note that our understanding of the CIRs–induced sub-ULF electromagnetic radiation is a partner and not just a triggering agent of great earthquakes. This understanding comes, among other reasons, from the fact that all of the 16 giant (M ≥ 8.5) EQs between 1900 and 2017 occurred during the decay, minimum and the rising phase of the solar cycle or at times of a strong reduction, that is under space weather conditions of a quiet Sun.

In concluding, our recent results suggest that the planet Earth should not be considered as an autonomous body in earthquake prediction research, but we should think about the lithosphere as a boundary between two different cosmic regions, the planet Earth and space. This fact implies that EQ prediction research can gain much from complementary space weather research.

DATA AVAILABILITY STATEMENT

The original contributions presented in the study are included in the article/Supplementary Material, further inquiries can be directed to the corresponding author.

AUTHOR CONTRIBUTIONS

The author confirms being the sole contributor of this work and has approved it for publication

ACKNOWLEDGMENTS

The author thanks the PIs and the teams/Institutions providing the online data of the EPAM- MAG-SWEPAM onboard as well as World Data Center for Geomagnetism, Kyoto. The author also thanks his student P. Karagiorgas for his help in the construction of some figures.

REFERENCES

Abdu, M. A., de Souza, J. R., Sobral, J. H. A., and Batista, I. S. (2006). *Magnetic Storms Associated Disturbance Dynamo Effects in the Low and Equatorial Latitude Ionosphere, Magnetic Storms Caused by Corotating, Geophys. Res. Series 167, Recurrent Magnetic Streams*. Washington, DC: AGU, 283–304. doi:10.1029/167gm22

Akhoondzadeh, M., Parrot, M., and Parrot, M. (2010). Electron and Ion Density Variations before strong Earthquakes (M>6.0) Using DEMETER and GPS Data. *Nat. Hazards Earth Syst. Sci.* 10, 7–18. doi:10.5194/nhess-10-7-2010

Akinaga, Y., Hayakawa, M., Liu, J. Y., Yumoto, K., and Hattori, K. (2001). A Precursory ULF Signature for the Chi-Chi Earthquake in Taiwan. *Nat. Hazards Earth Syst. Sci.* 1 (33–36), 33–36. doi:10.5194/nhess-1-33-2001

Alfvén, H. (1950). *Cosmical Eletrodynamics (The International Series of Monographs on Physics)*. Clarendon Press. http://ia600703.us.archive.org/23/items/CosmicalElectrodynamics/Alfven-CosmicalElectrodynamics.pdf.

Anagnostopoulos, G. (2015). A Study of Correlation between Seismicity and Mental Health: Crete, 2008-2010. *Geomatics, Nat. Hazards Risk* 6, 145–175. doi:10.1080/19475705.2013.819385

Anagnostopoulos, G., Louri, I., Marhavilas, P., and Sarris, E. (2009). Jovian Periodicities (~10 H, ~40 Min) on Ulysses' Distant Jupiter Encounter Observations Around the Halloween CIR Events. *Adv. Space Res.* 43, 573–581. doi:10.1016/j.asr.2008.09.024

Anagnostopoulos, G., Menesidou, S. A., Vassiliadis, V., and Rigas, A. (2015) Correlation between Solar Particles and Temperature in North-East USA, Proceedings, 12th Hel.A.S Conference.

Anagnostopoulos, G., and Papandreou, A. (2012). Space Conditions during a Month of a Sequence of Six M > 6.8 Earthquakes Ending with the Tsunami of 26 December 2004. *Nat. Hazards Earth Syst. Sci.* 12, 1551–1559. doi:10.5194/nhess-12-1551-2012

Anagnostopoulos, G., Spyroglou, I., Rigas, A., Preka-Papadema, P., Mavromichalaki, H., and Kiosses, I. (2021). The Sun as a Significant Agent Provoking Earthquakes. *Eur. Phys. J. Spec. Top.* 230, 287–333. doi:10.1140/epjst/e2020-000266-2,

Anagnostopoulos, G., Vassiliadis, V., Basta, M., Rigas, A., and Vgontzas, A. (2016).Study of Seismogenic ULF Radiation with Satellites and Mental Diseases. Paphos, Cyprus: Fourth International Conference on Remote Sensing and Geoinformation of Environment.

Anagnostopoulos, G., Vassiliadis, E., and Pulinets, S. (2012). Characteristics of Flux-Time Profiles, Temporal Evolution, and Spatial Distribution of Radiation-belt Electron Precipitation Bursts in the Upper Ionosphere before Great and Giant Earthquakes. *Ann. Geophys.* 55, 21–36. Available at: https://www.annalsofgeophysics.eu/index.php/annals/article/view/5365/5677.

Athanasiou, M. A., Anagnostopoulos, G. C., and David Machairidis, C. N. G. G. (2014). The Ultra Low Frequency Electromagnetic Radiation Observed in the Topside Ionosphere above Boundaries of Tectonic Plates. *Res. Geophys.* 4, 5001.

Athanasiou, M. A., Anagnostopoulos, G. C., and Iliopoulos, A. C. (2011). Enhanced ULF Radiation Observed by DEMETER Two Months Around the strong 2010 Haiti Earthquake. *Nat. Hazards Earth Syst. Sci.* 11, 1091–1098. doi:10.5194/nhess-11-1091-2011

Avakyan, S. V., Voronin, N. A., and Nikol'sky, G. A. (2015). Response of Atmospheric Pressure and Air Temperature to the Solar Events in October 2003. *Aeron* 55 (8), 1180–1185. doi:10.1134/s0016793215080034

Badruddin, F., Mustajab, F., and Derouich, M. (2018). Relative Geoeffectiveness of High-Speed Solar Wind Streams from Different Solar Sources. *Adv. Space Res.* 62 (4), 765–784. doi:10.1016/j.asr.2018.05.024Mustajab

Baker, D., Erickson, P. J., Fennell, P., J. F., Foster, J., J. C., Jaynes, A. N., and Verronen, A., P. T. (2018). Space Weather Effects in the Earth's Radiation Belts. *Space Sci. Rev.* 214, 17. doi:10.1007/s11214-017-0452-7

Bakhmutov, V., Sedova, F., and Mozgovaya, T. (2007). Morphological Features in the Structure of Geomagnetic Variations in Relation to Earthquakes in Vrancea Publ. *Inst. Geophys. Pol. Acad. Sci.* 43, 931. doi:10.1134/s1069351307110031

Balasis, G., and Mandea, M. (2007). Can Electromagnetic Disturbances Related to the Recent Great Earthquakes Be Detected by Satellite Magnetometers. *Tectonophysics* 431, 173–195. doi:10.1016/j.tecto.2006.05.038

Barnes, A. (1983). "Hydromagnetic Waves, Turbulence, and Collisionless Processes in the Interplanetary Medium," in *Solar-Terrestrial Physics: Principles and Theoretical Foundations*. Editors R. L. Carovillano and J. M. Forbes, 155–199. doi:10.1007/978-94-009-7194-3_7

Bentley, S. N., Watt, C. E. J., Owens, M. J., and Rae, I. J. (2018). ULF Wave Activity in the Magnetosphere: Resolving Solar Wind Interdependencies to Identify Driving Mechanisms. *J. Geophys. Res. Space Phys.* 123 (4), 2745–2771. doi:10.1002/2017ja024740

Biswas, S., Kundu, S., Ghosh, S., Chowdhury, S., Yang, S., Hayakawa, M., et al. (2020). Contaminated Effect of Geomagnetic Storms on Pre-seismic Atmospheric and Ionospheric Anomalies during Imphal Earthquake. *Open J. Earthquake Res.* 9, 383–402. doi:10.4236/ojer.2020.95022

Borovsky, J. E., and Denton, M. H. (2006). Differences between CME-Driven Storms and CIR-Driven Storms. *J. Geophys. Res.* 111, A07S08. doi:10.1029/2005JA011447

Borovsky, J., and Valdivia, J. (2018). The Earth's Magnetosphere: A Systems Science Overview and Assessment. *Surv. Geophys.* 39 (5), 817–859. doi:10.1007/s10712-018-9487-x

Borovsky, Y., and Shprits, Y. (2017). Is the Dst Index Sufficient to Define All Geospace Storms. *J. Geophys. Res. Space Phys.* 122 (11), 11,543–11,611. doi:10.1002/2017JA024679

Burlaga, L. F., Ness, N. F., and Belcher, J. W. (1997). Radial Evolution of Corotating Merged Interaction Regions and Flows between _14AU and _43AU. *J. Geophys. Res.* 102 (4661–4), 671. doi:10.1029/96ja03629

Burton, R. K., McPherron, R. L., and Russell, C. T. (1975). An Empirical Relationship between Interplanetary Conditions and Dst. *J. Geophys. Res.* 80 (31), 4204–4214. doi:10.1029/JA080i031p04204

Błęcki, J., Parrot, M., and Wronowski, R. (2010). Studies of the Electromagnetic Field Variations in ELF Frequency Range Registered by DEMETER over the Sichuan Region Prior to the 12 May 2008 Earthquake. *Int. J. Remote Sens.* 31 (13), 3615–3629. doi:10.1080/01431161003727754

Campbell, W.H. (2009). Natural Magnetic Disturbance Fields, Not Precursors, Preceding the Loma Prieta Earthquake. *J. Geophy. Res. Space Phys.* 114, A05307. doi:10.1029/2008JA013932

Chang, S.-H., and Wang, W.-H. (2002). Estimates of Source Parameters of Two Large Aftershocks of the 1999 Chi-Chi, Taiwan, Earthquake in the Chia-Yi Area. Terr.. *Atmospheric Ocean. Sci.* 17 (2), 331–343. doi:10.3319/TAO.2006.17.2.331(T)

Chelidze, T., De Rubeis, V., Matcharshvili, T., and Tosi, P. (2006). Influence of strong Electromagnetic Discharges on the Dynamic of Earthquakes Time Distribution in the Bishkek Test Area (Central Asia). *Ann. Geophys.* 49 (4-5), 961–975.

Chelidze, T., Varamashvili, N., Devidze, M., Chelidze, Z., Chikladze, V., and Matcharashvili, T. (2002). Laboratory Study of Electromagnetic Initiation of Slip. *Ann. Geophys.* 45 (5), 587–598.

Chen, F. (2016). *Introduction to Plasma Physics and Controlled Fusion*. 3rd Ed. Springer.

ChenKuo, Y.-G. Y. T., Wu, Y-M., Chen, H.-L., Chang, C.-H., Chen, R.-Y., Lo, P.-W., et al. (2008). Seismology New Seismogenic Source and Deep Structures Revealed by the 1999 Chia-Yi Earthquake Sequence in Southwestern Taiwan. *Geophys. J. Int.* 172, 1049–1054. doi:10.1111/j.1365-246X.2007.03686.xGJI

Cranmer, S. (2009) Coronal Holes. *Living Rev. Sol. Phys.* 6 (3). doi:10.12942/lrsp-2009-3

Cochran, E. S., Vidale, J. E., and Tanaka, S. (2004). Earth Tides Can Trigger Shallow Thrust Fault Earthquakes. *Sci.* 306, 1164–1166.

Daglis, I., Thorne, R., Baumjohann, W., and Orsini, S. (1999). The Terrestrial Ring Current Origin, Formation, and Decay. *Rev. Geophys.* 37 (4), 407–438. doi:10.1029/1999rg900009

De Santis, A., Balasis, G., Pavón-Carrasco, F. J., Cianchini, G., and Mandea, M. (2017). Potential Earthquake Precursory Pattern from Space: The 2015 Nepal Event as Seen by Magnetic Swarm Satellites. *Earth Planet. Sci. Lett.* 461, 119–126. doi:10.1016/j.epsl.2016.12.037

De Santis, A., De Franceschi, G., Spogli, L., Perrone, L., Alfonsi, L., Qamili, E., et al. (2015). Geospace Perturbations Induced by the Earth: the State of the Art and Future Trends. *Phys. Chem. Earth Parts A/b/c 85*– 86, 17–33. doi:10.1016/j.pce.2015.05.004

Dessler, A. J., and Parker, E. N. (1959). Hydromagnetic Theory of Geomagnetic Storms. *J. Geophys. Res.* 64 (12), 2239–2252. doi:10.1029/JZ064i012p02239

Duma, G., and Ruzhin, Y. (2003). Diurnal Changes of Earthquake Activity and Geomagnetic SqvariationsNat. *Hazards Earth Syst. Sci.* 3, 171. doi:10.5194/nhess-3-171-2003

Dungey, J. W. (1961). Interplanetary Magnetic Field and Auroral Zones. *Phys. Rev. Lett.* 6 (2), 47–48. doi:10.1103/physrevlett.6.47

Emery, B., Richardson, I., Evans, D., and Rich, F. (2009). Solar Wind Structure Sources and Periodicities of Auroral Electron Power over Three Solar Cycles. *J. Atmosph. Solar-terrest. Phys.* 71, 10–11. doi:10.1016/j.jastp.2008.08.005

Emter, C. (1997). "Tidal Triggering of Earthquakes and Volcanic Events," in *Tidal Phenomena, Vol. 66 of Lecture Notes in Earth Sciences*. Editors H. Wilhem, W. Zürn, and H.-G. Wenzel (Springer-Verlag), 293–310.

Engebretson, M., Glassmeier, K.-H., Stellmacher, M., Hughes, W. J., and Lühr, H. (1998). The Dependence of High-Latitude Pc5 Wave Power on Solar Wind Velocity and on the Phase of High-Speed Solar Wind Streams. *J. Geophys. Res.* 103 (11), 26,271–26,283.

Firoz, K. (2019). On the Relation between Flare and CME during GLE-SEP and Non-GLE-SEP Events. *Ap. J.*, 883.

Fraser, B. (2009). ULF Waves: Exploring the Earth's Magnetosphere. *Adv. Geophys*, 1–32. doi:10.1142/9789812836205_0001

Fraser-Smith, A. C., McGill, P. R., and Helliwell, R. A. (1994). Ultra-Low Frequency Magnetic Field Measurements in Southern California during the Northridge Earthquake of 17 January. *Geophys. Res. Lett.* 21, 2195–2198.

Freund and Pilorz (2012). Electric Currents in the Earth Crust and the Generation of Pre-earthquake ULF Signals. *The Frontier of EQ Prediction Studies*. Nihon-Senmontosho-Shuppan, Tokyo: M. Hayakawa, 468–508.

Freund, F. T. (2013). Earthquake Forewarning – a Multidisciplinary challenge from the Ground up to Space. *Acta Geophys.* 61, 775–807. doi:10.2478/s11600-013-0130-4

Freund, F. T. (2010). Toward a Unified Solid State Theory for Pre-earthquake Signals. *Acta Geophysica* 58 (5), 719–766. doi:10.2478/s11600-009-0066-x

Gerontidou, M., Mavromichalaki, H., and Daglis, T. (2018). High-Speed Solar Wind Streams and Geomagnetic Storms during Solar Cycle 24. *Sol. Phys.* 293, 131. doi:10.1007/s11207-018-1348-8

Gold, R. E., Krimigis, S. M., Hawkins, S. E., Haggerty, D. K., Lohr, D. A., Fiore, E., et al. (1998). Electron, Proton, and Alpha Monitor on the Advanced Composition Explorer Spacecraft. *Space Sci. Rev.* 86, 541–562. doi:10.1007/978-94-011-4762-0_19

Gousheva, M. N., Georgiva, K. Y., Kirov, B. B., and Atanssov, D. (2003). On the Relation between Solar Activity and Seismicity. *Proc. Int. Conf. Recent Adv. Space Tech.*, 20–22. doi:10.1109/rast.2003.1303913

Gray, L., Beer, J., Geller, M., Haigh, J., Lockwood, M., Matthes, K., et al. (2010). Solar Influences on Climate. *Rev. Geophys.* 48, 1–53. doi:10.1029/2009RG000282

Greenspan, M. E., and Hamilton, D. C. (2000). A Test of the Dessler-Parker-Sckopke Relation during Magnetic Storms. *J. Geophys. Res.* 105 (A3), 5419–5430. doi:10.1029/1999JA000284

Grimalsky, V., Kotsarenko, A., Pulinets, S., and Perez-Enriquez, R. (2010). On the Modulation of Intensity of Alfven Resonances Before Earthquakes: Observations and Model. *J. Atmos. Sol.-Terr. Phys.* 72 (1), 1–6. doi:10.1016/j.jastp.2009.09.017

Gulyaeva, T. (2014). Association of Seismic Activity with Solar Cycle and Geomagnetic Activity, Developm. *Earth Sci.* 2, 14. http://www.seipub.org/des.

Han, P., Zhuang, J., Hattori, K., Chen, C-H., Febriani, F., Chen, H., et al. (2020). Assessing the Potential Earthquake Precursory Information in ULF Magnetic Data Recorded in Kanto, Japan during 2000–2010: Distance and Magnitude Dependences. *Entropy* 22, 859. doi:10.3390/e22080859

Hattori, K., and Han, P. (2018). "Statistical Analysis and Assessment of Ultralow Frequency Magnetic Signals in Japan as Potential Earthquake Precursors," in *Pre-Earthquake Processes*. Editors D. Ouzounov, S. Pulinets, K. Hattori, and P. Taylor. doi:10.1002/9781119156949.ch13

Hattori, K. (2004). ULF Geomagnetic Changes Associated with Large Earthquakes. *Terr. Atmos. Ocean. Sci.* 15, 329–360. doi:10.3319/tao.2004.15.3.329(ep)

Hayakawa, M., and Fujinawa, Y. (1994). *Electromagnetic Phenomena Related to Earthquake Prediction*. Tokyo: Terra Sci. Pub. Co., 67–71.

Hayakawa, M., Hattori, K., and Ohta, K. (2007). Monitoring of ULF (Ultra-low-frequency) Geomagnetic Variations Associated with Earthquakes. *Sensors* 7, 1108–1122. doi:10.3390/s7071108

Hayakawa, M., Kasahara, Y., Nakamura, T., Hobara, Y., Rozhnoi, A., Solovieva, M., et al. (2010). A Statistical Study on the Correlation between Lower Ionospheric Perturbations as Seen by Subionospheric VLF/LF Propagation and Earthquakes. *J. Geophys. Res. Atmospheres* 115, A9. doi:10.1029/2009JA015143

Hayakawa, M., Kawate, R., Oleg, A., Molchanov, O., and Yumoto, K. (1996). Results of Ultra-Low-Frequency Magnetic Field Measurements During the Guam Earthquake of 8 August 1993. *Geophys. Res. Lett.* 23(3), 241–244. doi:10.1029/95GL02863

Huang, M., Wang, J.-H., Hwang, R.-D., and Chen, K.-C. (2006). Mechanical Properties, Slip and Nucleation of the 1999 Chia-Yi Earthquake: the Question of Static Stress Influence from the 1999 Chi-Chi Earthquake. *Terr. Atmospheric Ocean. Sci.* 13(3), 299–312. doi:10.3319/TAO.2002.13.3.299(CCE)

Huzaimy, J., and Yumoto, K. (2011). Possible Correlation between Solar Activity and Global Seismicity. *Proceeding 2011 IEEE Int. Conf. Space Sci. Commun. (Iconspace)*, 138–141. doi:10.1109/IConSpace.2011.6015869

Hynönen, R., Tanskanen, E. I., and Francia, P. (2020). Solar Cycle Evolution of ULF Wave Power in Solar Wind and on Ground. *J. Space Weather Space Clim.* 10, 43. doi:10.1051/swsc/2020046

Jacobs, J., Kato, Y., Matsushita, S., and Troitskaya, V. (1964). Classification of Geomagnetic Micropulsations. *J. Geophys. Res. Space Sci.* 69, 1–181. doi:10.1029/JZ069i001p00180

Kasahara, J. (2002). Tides, Earthquakes and Volcanoes. *Sci.* 297, 348–349.

Kataoka, R., and Miyoshi, Y. (2006). Flux Enhancement of Radiation belt Electrons during Geomagnetic Storms Driven by Coronal Mass Ejections and Corotating Interaction Regions. *Space Weather* 4, S09004. doi:10.1029/2005SW000211

Kavanagh, A., and Denton, M. (2007). High-speed Solar-Wind Streams and Geospace Interactions. *Astron. Geophys.* 48 (6), 6.24–6.26. doi:10.1111/j.1468-4004.2007.48624.x

Kennedy, M., Vidale, J. E., and Parker, M. G. (2004). Earthquakes and the Moon: Syzygy Predictions Fail the Test. *Seismol. Res. Lett.* 75, 607–612. doi:10.1785/gssrl.75.5.607

Kepko, L., SpenceSinger, H. E. H. J., and Singer, H. J. (2002). ULF Waves in the Solar Wind as Direct Drivers of Magnetospheric Pulsations. *Geophys. Res. Lett.* 29 (8), 39–41. doi:10.1029/2001GL014405

Kessel, R. L. (2008). Solar Wind Excitation of Pc5 Fluctuations in the Magnetosphere and on the Ground. *J. Geophys. Res.* 113, A04202. doi:10.1029/2007JA012255

Khain, V. E., and Kalilov, E. N. (2008). About the Possible Influence of Solar Activity upon Seismic and Volcanic Activities: Long-Term Forecast, Science without Borders. *Trans. Inter. Acad. Sci. H&E., SWB* 3, 217–240.

Kim, K.-H., Cattell, C. A., Lee, D.-H., Takahashi, K., Yumoto, K., Shiokawa, K., et al. (2002). Magnetospheric Responses to Sudden and Quasiperiodic Solar Wind Variations. *J. Geophys. Res. Space Sci.* 107, A111–A112. doi:10.1029/2002JA009342

Kivelson, G. M., and Russell, C. T. (1995). *Introduction to Space Physics*. Cambridge University Press.

Kumar, A., and Kumar, S. (2018). Solar Flare Effects on D-Region Ionosphere Using VLF Measurements during Low- and High-Solar Activity Phases of Solar Cycle, 24. *Earth Planets Space* 70, 29. doi:10.1186/s40623-018-0794-8

Liemohn, M., Kozyra, W., Thomsen, J., Roeder, M., Lu, J., Borovsky, J., et al. (2001). Dominant Role of the Asymmetric Ring Current in Producing Storm Time Dst*. *J. Geophys. Res.* 106 (A6), 10,883–10,904. doi:10.1029/2000JA000326

Lin, J.-W. (2013). Taiwan' Chi-Chi Earthquake Precursor Detection Using Nonlinear Principal Component Analysis to Multi-Channel Total Electron Content Records. *J. Earth Sci.* 24, 244–253. doi:10.1007/s12583-013-0325-2

Liu, J., Chen, Y., Chuo, Y., and Tsai, H. (2001). Variations of Ionospheric Total Electron Content during the Chi-Chi Earthquake. *Geophys. Res. Lett.* 28 (7), 1383–1386. doi:10.1029/2000gl012511

Liu, J., Chen, Y., Pulinets, S., Tsai, Y., and Chuo, Y. (2000). Seismo-ionospheric Signatures Prior to M ≥ 6.0 Taiwan Earthquakes. *Geophys. Res. Lett.* 27 (19), 3113–3116. doi:10.1029/2000gl011395

Liu, J., Chuo, Y., Shan, S., Tsai, Y., Chen, Y., Pulinets, S., et al. (2004). Pre-Earthquake Ionospheric Anomalies Registered By Continuous Gps Tec Measurements. *Ann. Geophys.* 22, 1585–1593. doi:10.5194/angeo-22-1585-2004

Loewe, C. A., and Prolss, G. W. (1997). Classification of Mean Behavior of Magnetic Storms. *J. Geophys. Res.* 102 (A7), 14209–14214. doi:10.1029/96JA04020

Love, J.J., and Thomas, J.N. (2013). Insignificant Solar-Terrestrial Triggering of Earthquakes. *Geophys. Res. Lett.* 40, 1165. doi:10.1002/grl.50211

Ma, K. F., Lee, C. T., Tsai, Y. B., Shin, T. C., and Mori, J. (1999). The Chi-Chi, Taiwan Earthquake: Large Surface Displacements on an Inland Thrust Fault. *EOS Trans. Am. Geophys. Union* 80, 605–611. doi:10.1029/99eo00405

Marhavilas, P., Malandraki, O., and Anagnostopoulos, G. (2015). Survey of Caveats in Low-Energy Particle Measurements: Ulysses/HI-SCALE and ACE/EPAM Instruments, Planet. *Space Sci.* 117, 192206. doi:10.1016/j.pss.2015.06.010

Marhavilas, P. (2007). The Stormy Sun Affecting the Human Life and the Technology. *EGU Newsl.* 17, 13. Available at: https://cdn.egu.eu/static/e738470d/newsletter/eggs/eggs_19.pdf.

McPherron, R. (2005). Magnetic Pulsations: Their Sources and Relation to Solar Wind and Geomagnetic Activity. *Surv. Geophys.* 26, 545–592. doi:10.1007/s10712-005-1758-7

McComas, D., Bame, S., Barker, P., Feldman, W. C., Philips, J. L., Riley, P., et al. (1998). Solar Wind Electron Proton Alpha Monitor (SWEPAM) for the Advanced Composition Explorer. *Space Sci. Rev.* 86, 563–612. doi:10.1023/A:1005040232597

Métivier, L., de Viron, O., Conrad, C., Renault, S., Diament, M., and Patau, G. (2009). Evidence of Earthquake Triggering by the Solid Earth Tides. *Earth Planet. Sci. Lett.* 278, 370–375. doi:10.1016/j.epsl.2008.12.024

Molchanov, O. A., and Hayakawa, M. (1998). Subionospheric VLF Signal Perturbations Possibly Related to Earthquakes. *J. Geophys. Res.* 103 (17), 17489–17504. doi:10.1029/98ja00999

Molchanov, O., and Hayakawa, M. (1995). Generation of ULF Electromagnetic Emissions by Microfracturing. *Geohpys. Res. Lett.* 22, 3091–3094. doi:10.1029/95gl00781

Morley, S. K., Rouillard, A. P., and Freeman, M. P. (2008). Recurrent Substorm Activity during the Passage of a Corotating Interaction Region. *J. Atmosph. Solar-terrest. Phys.* 71, 10–11. doi:10.1016/j.jastp.2008.11.009

Novikov, V., Okunev, V., Klyuchkin, V., Liu, J., Ruzhin, Ya, Y., and Shen, X. (2017). Electrical Triggering of Earthquakes: Results of Laboratory Experiments at spring-block Models. *Earthq. Sci.* 30, 167–172. doi:10.1007/s11589-017-0181-8

Novikov, V., Ruzhin, Y., Sorokin, V., and Yaschenko, A. (2020). Space Weather and Earthquakes: Possible Triggering of Seismic Activity by strong Solar Flares. *Anal. Gelphys.* 63, 5. doi:10.4401/ag-7975

Odintsov, S. D., Ivanov-Klodonyi, G. S., and Gergieva, K. (2007). Solar Activity and Global Seismicity on Earth. *Bull. Russ. Aca. Sci. Phys.* 71 (4), 593–597. doi:10.3103/s1062873807040466

Ohta, K., Umeda, K., Watanabe, N., and Hayakawa, M. (2001). ULF/ELF Emissions Observed in Japan, Possibly Associated with the Chi-Chi Earthquake in Taiwan. *Nat. Hazards Earth Syst. Sci.* 1, 37–42. doi:10.5194/nhess-1-37-2001

Ohtani, S., Nose, M., Rostoker, G., Singer, H., Lui, A. T. Y., and Nakmura, M. (2001). Stormsubstorm Relationship: Contribution of the Tail Current to Dst. *J. Geophys. Res.* 106 (A10), 21. doi:10.1029/2000JA000400

Ouzounov, D., and Freund, F. (2004). Mid-infrared Emission Prior to strong Earthquakes Analyzed by Remote Sensing Data. *Adv. Space Res.* 33, 268–273. doi:10.1016/s0273-1177(03)00486-1

Ouzounov, D., Pulinets, S., Hattori, K., Taylor, P., and Ed's (2018). *Pre-Earthquake Processes: A Multidisciplinary Approach to Earthquake Prediction Studies*. American Geophysical UnionJohn Wiley & Sons, Inc., 385.

Ouzounov, D., Pulinets, S., Kafatos, M. C., and Taylor, P. (2018). "Thermal Radiation Anomalies Associated with Major Earthquakes," in *Pre-Earthquake Processes*. Editors D. Ouzounov, S. Pulinets, K. Hattori, and P. Taylor. doi:10.1002/9781119156949.ch15

PahudI, D., RaeI, J., Mann, K. R., Murphy, R., and Amalraj, V. (2009). Ground-based Pc5 ULF Wave 1057 Power: Solar Wind Speed and MLT Dependence. *J. Atmosph. Solar-Terr. Phys.* 71 (10–11), 1082–1092. doi:10.1016/j.jastp.2008.12.004

Parrot, M., Benoist, D., Berthelier, J. J., Blecki, J., Chapuis, Y., Colin, et al. (2006). The Magnetic Field experiment IMSC and its Data Processing Onboard DEMETER: scientific Objectives, Description and First Results. *Planet. Space Sci.* 54, 441–455. doi:10.1016/j.pss.2005.10.015

Patsourakos, S., Georgoulis, M. K., Vourlidas, A., Nindos, A., Sarris, T., Anagnostopoulos, G., et al. (2016). The Major Geoeffective 1067 Solar Eruptions of 2012 March 7: Comprehensive Sun-To-Earth Analysis. *Astrophys. J.* 817 (14), 114. doi:10.3847/0004-637x/817/1/14

Pilipenko, V. (1990). ULF Waves on the Ground and in Space. *J. Atm. Terrst. Phys.* 52 (12), 11931069–11931209.

Phillips, J. L., Bame, S. J., Barnes, A., Barraclough, B. L., Feldman, W. C., Goldstein, B. E., et al. (1995). Ulysses Solar Wind Plasma Observations from Pole to Pole. *Geophys. Res. Lett.* 22 (23), 3301–3304. doi:10.1029/95GL03094

Poole, C., Kavet, R., Funch, D. P., Donelan, K., Charry, J. M., and Dreyer, N. A. (1993). Depressive Symptoms and Headaches in Relation to Proximity of Residence to an Alternating-Current Transmission Line Right-Ofway. *Am. J. Epidemiol.* 137, 318–330. doi:10.1093/oxfordjournals.aje.a116679

Potapov, A. S. (2013). ULF Wave Activity in High-Speed Streams of the Solar Wind: Impact on the 1060 Magnetosphere. *J. Geophys. Res. Space Phys.* 118, 6465–6477. doi:10.1002/2013JA019119

Pulinets, S., and Boyarchuk, K. (2004). *Ionospheric Precursors of Earthquakes*. Springer.

Pulinets, S., and Ouzounov, D. (2011). Lithosphere-Atmosphere-Ionosphere Coupling (LAIC) Model—A Unified Concept for Earthquake Precursors Validation. *J. Asian Earth Sci.* 1073, 371–382. doi:10.1016/j.jseaes.2010.03.005

Pulinets, S., and Ouzounov, D. (2018). *The Possibility of Earthquake Forecasting: Learning from Nature*. Bristol, UK: Institute of Physics Books, IOP Publishing, 168.

Reichmanis, M., Perry, F. S., Marino, A. A., and Becker, R. O. (1979). Relation between Suicide and the 1078 Electromagnetic Field of Overhead Power Lines. *Physiol. Chem. Phys.* 11, 395–403.

Rekapali, R. (2014). Brief Communication: Correlation of Global Earthquake Rates with Temperature 1081 and sunspot Cycle, Natural Hazards and Earth Syst. *Sci.* doi:10.5194/nhessd-2-2851-2014

Richardson, I. G., and Cane, H. V. (2011). Geoeffectiveness (Dst and Kp) of Interplanetary Coronal Mass Ejections during 1995–2009 and Implications for Storm Forecasting. *Space Weather* 9, S07005. doi:10.1029/2011sw000670

Richardson, I. G., and Cane, H. V. (2012a). Solar Wind Drivers of Geomagnetic Storms during More Than Four Solar Cycles. *J. Space Weather Space Clim.* 2 (A01), A01–A09. doi:10.1051/swsc/2012001

Richardson, I. G., and Cane, H. V. (2012b). Near-earth Solar Wind Flows and Related Geomagnetic Activity during More Than Four Solar Cycles (1963-2011). *J. Space Weather Space Clim.* 2, A02. doi:10.1051/swsc/2012003

Richardson, I. G. (2018). Solar Wind Stream Interaction Regions throughout the Heliosphere. *Living Rev. Sol. Phys.* 15, 1. doi:10.1007/s41116-017-0011-z

Russell, C. T., Ginskey, M., Petrinec, S., and Le, G. (1992). The Effect of Solar Wind Dynamic Pressure Changes on Low and Mid-Latitude Magnetic Records. *Geophys. Res. Lett.* 19(12), 1227–1230. doi:10.1029/92GL0116

Sarafopoulos, D. V. (2005). Cases for Which the Earth's Magnetosphere Does not Act as a "Low-Pass Filter". *J. Atmos. Solar Terr. Phys.* 67, 1427.

Satoshi, I., Suguru, Y., and Tanaka, Y. (2016). Earthquake Potential Revealed by Tidal Influence on Earthquake Size–Frequency Statistics. *Nat. Geophys. Lett.* doi:10.1038/NGEO2796

Sauvaud, J., Moreau, T., Maggiolo, R., et al. (2006). High Energy Electron Detection Onboard DEMETER:the IDP Spectro-Meter, Description and First Results on the Inner belt. *Planet. Space Sci.* 54, 502–511. doi:10.1016/j.pss.2005.10.019

Schuster, A. (1897). On Lunar and Solar Periodicities of Earthquakes. *Proc. R. Soc. Lond.* 61, 455–465. doi:10.1098/rspl.1897.0060

Shadrina, L. (2017), Two Types of Geomagnetic Storms and Relationship between Dst and AE Indexes. In E3S Web of Conferences 20, 01010 Solar-Terrestrial Relations and Physics of Earthquake 1084 Precursors. doi:10.1051/e3sconf/20172001010

Shen, X., Zhang, X., and Yuan, S. (2018). The State-Of-The-Art of the China Seismo-Electromagnetic 1086 Satellite mission. *Sci. China Technol. Sci.* 61, 634–642. doi:10.1007/s11431-018-9242-0

Shi, Q., Shen, X.-C., Tian, A., Degeling, A., Zong, Q., Fu, S., et al. (2020). "Vortices, ULF Waves, and Aurorae, Magnetosphere Response to Solar Wind Dynamic Pressure Change,". Editors Q. Zong, P. Escoubet, D. Sibeck, G. Le, and H. Zhang. doi:10.1002/9781119509592

Shin, T.-C. (2004).An Overview of the 1999 Chi-Chi, Taiwan, Earthquake, Bulletin of the Seismolog. Albany, CA: Society of America, 5895. doi:10.1785/0120000738

Sidiropoulos, N., Anagnostopoulos, G., and Rigas, V. (2011). Comparative Study on Earthquake and Ground Based Transmitter Induced Radiation belt Electron Precipitation at Middle Latitudes. *Nat. Hazards Earth Syst. Sci.* 11, 1901. doi:10.5194/nhess-11-1901-2011

Simpson, J. F. (1967). Solar Activity as Triggering Mechanism for Earthquakes. *Earth Planet. Sci. Lett.* 3, 417–425. doi:10.1016/0012-821x(67)90071-4

Smith, E. J., Balogh, A., Neugebauer, M., and McComas, D. (1995). Ulysses Observations of Alfvén Waves in the Southern and Northern Solar Hemispheres. *Geophys. Res. Lett.* 22, 3381–3384. doi:10.1029/95gl03268

Smith, C. W., L'Heureux, J., Ness, N. F., Acuña, M. H., Burlaga, L. F., and Scheifele, J. (1998). The ACE Magnetic Fields Experiment. *Space Sci. Rev.* 86, 613–632. doi:10.1007/978-94-011-4762-0_21

Siscoe, G., McPherron, R., and Jordanova, V. K. (2005). K., Diminished Contribution of Ram Pressure to Dst during Magnetic Storms. *J. Geophys. Res. Atmospheres* 110 (A12), 1–7. doi:10.1029/2005JA011120

Sobolev, G. A., Zakrzhevskaya, N. A., and Kharin, E. P. (2001). On the Relation between Seismicity and Magnetic Storms. *Phys. Solid Earth, Russ. Acad. Sc.* 11, 62–72.

Sorokin, V, Yaschenko, A., Ruzhin, R., and Novikov, V. (2012).Model for Solar Flare Influence to the Seismic Activity. In Proc. EMSEV-2012 Workshop. Gotemba, Japan: Abstr, 3–10.

Sorokin, V. M., Yaschenko, A. K., and Novikov, V. A. (2019). A Possible Mechanism of Stimulation of Seismic Activity by Ionizing Radiation of Solar Flares. *Earthq Sci.* 32, 26–34. doi:10.29382/eqs-2019-0026-3

Southwood, D., and Hughes, W ((1983). Theory of Hydromagnetic Waves in the Magnetosphere. *Space Sci. Rev.* 35 (4), 301–366. doi:10.1007/bf00169231

Stone, E., Frandsen, A., Mewaldt, R., Christian, E., Margolies, D. D., Ormes, J., et al. (1998). The Advanced Composition Explorer. *Space Sci. Rev.* 86, 1–22. doi:10.1007/978-94-011-4762-0_1

Straser, V., and Cataldi, G. (2015). Solar Wind Ionic Variation Associated with Earthquakes Greater that Magnitude 6.0, *New Conc. Glob. Tect. J.* 3, 2.

Sytinskii, A. D. (1997). Influence of Interplanetary Disturbances on the Seismicity and Tmosphere of the Earth. *Geomagn. Aeron.* 37, 138–143.

Takahashi, K., Yumoto, K., Claudepierre, S. G., Sanchez, E. R., Troshichev, O. A., and Janzhura, A. S. (2012). Dependence of the Amplitude of Pc5-Band Magnetic Field Variations on the Solar Wind and Solar Activity. *J. Geophys. Res.* 117, a–n. doi:10.1029/2011JA017120

Tanaka, S., Ohtake, M., and Sato, H. (2002). Evidence for Tidal Triggering of Earthquakes as Revealed from Statistical Analysis of Global Data. *J. Geophys. Res.* 107 (5B10), 2211.

Tarasov, N., and Tarasova, N. (2004). Spatial-temporal Structure of Seismicity of the North Tien Shan and its Change under Effect of High Energy Electromagnetic Pulses. *Ann. Geoph.* 47, 199–212.

Tarasov, N., Tarasova, N., Zeigarnik, V., and Avagimov, A. (2000). The Effect of High Energy Electromagnetic Pulses on Seismicity in Central Asia and Kazakhstan. *J. Volcanol. Seismol.* 21, 627–639.

Tarasov, N. T., and Tarasova, N. V. (2002). The Effect of Geomagnetic Storms on the Seismicity. In Proc. of the 3rd International Workshop on Magnetic, Electric and Electromagnetic Methods in Seismology and Volcanology, 3. Moscow, Russia–6.

Tolstoy, M., Vernon, F., Orcutt, J., and Wyatt, F., (2002) Breathing of the Seafloor: Tidal Correlations of Seismicity at Axial Volcano. *Geol. Soc. Am.* 30(6), 503–506.

Tramutoli, V., Corrado, R., Filizzola, C., Genzano, N., Lisi, M., and Pergola, N. (2015). From Visual Comparison to Robust Satellite Techniques: 30 Years of thermal Infrared Satellite Data Analyses for the Study of Earthquake Preparation Phases. *B. Geofis. Teor. Appl.* 56, 167–202.

Tsai, Y-B., Liu, J-Y., Shin, T.-C., Yen, H.-Y., Chen, C-H., et al. (2018). Multidisciplinary Earthquake Precursor Studies in Taiwan, A Review and Future Prospects. Washington, DC: Pre-Earthquake Processes: A Multidisciplinary Approach to Earthquake Prediction Studies. doi:10.1002/9781119156949

Tsinganos, K. (1995). *Solar and Astrophysical Magnetohydrodynamic Flows*. Kluwer.

Tsurutani, B. T., Echer, E., Guarnieri, F. L., and Gonzalez, W. D. (2011). The Properties of Two Solar Wind High Speed Streams and Related Geomagnetic Activity during the Declining Phase of Solar Cycle 23. *J. Atmos. Solar-Terrestrial Phys.* 73, 164–177. doi:10.1016/j.jastp.2010.04.003

Tsurutani, B., Lakhina, G., and Hajra, R. (2020). The Physics of Space Weather/solar-Terrestrial Physics (STP): what We Know Now and what the Current and Future Challenges Are. *Nonlinear Process. Geoph.* 27 (1), 75–119. doi:10.5194/npg-27-75-2020

Tsurutani, B. T., and Gonzalez, W. D. (1987). The Cause of High-Intensity Long-Duration Continuous *AE* Activity (HILDCAAs): Interplanetary Alfvén Wave Trains. *Planet. Space Sci.* 35, 405–412. doi:10.1016/0032-0633(87)90097-3

Tsurutani, B. T., McPherron, R. L., Gonzalez, W. D., Lu, G., Gopalswamy, N., and Guarnieri, F. L. (2006). "Magnetic Storms Caused by Corotating Solar Wind Streams," in *Recurrent Magnetic Storms: Corotating Solar Wind*. Editor B. Tsurutani (Washington, DC: Geophysical Monographs, AGU), 167. doi:10.1029/167GM03

Urata, N., Duma, G. G., and Freund, F. (2018). Geomagnetic Kp Index and Earthquakes. *Open J. Earthq. Res.* 7, 39–52. Available at: http://www.scirp.org/journal/ojer. doi:10.4236/ojer.2018.71003

Uyeda, S., Nagao, T., and Kamogawa, M. (2009) Short-Term Earthquake Prediction: Current Status of Seismo-Electromagnetics, *Tectonophysics* 470, 205–213.

Vencloviene, J., Babarskiene, R., Slapikas, R., and Gintare Sakalyte, G. (2012). The Association between Phenomena on the Sun, Geomagnetic Activity, Meteorological Variables, and Cardiovascular Characteristic of Patients with Myocardial Infarction. *J. Biometeorol.* 57 (5), 797–804. doi:10.1007/s00484-012-0609-8

Villante, U., and Tiberi, P. (2016). Occurrence and Characteristics of Nighttime ULF Waves at Low Latitude: the Results of a Comprehensive Analysis.: Nighttime ULF Waves at Low Latitude. *J. Geophys. Res. Space Phys.* 121, 1. doi:10.1002/2015JA022137

Watari, S. (2018). Intense Geomagnetic Storms Associated with Coronal Holes under the Weak Solar-Wind Conditions of Cycle 24. *Sol. Phys.* 293, 23. doi:10.1007/s11207-018-1248-y

Wilcock, S. (2001). Tidal Triggering of Microearthquakes on the Juan de Fuca Ridge. *Geophys. Res. Lett.* 28(20), 3999–4002. doi:10.1029/2001GL013370

Wrenn, G. L. (2009). Chronology of "Killer" Electron: Solar Cycles 22 and 23. *J. Atmos. Solar - Terrestrial Phys.* 71 (10-11), 1210–1218. doi:10.1016/j.jastp.2008.08.002

Wrenn, G. L., Rodgers, D. J., and Ryden, K. A. (2002). A Solar Cycle of Spacecraft Anomalies Due to Internal Charging. *Ann. de Geophys.* 20 (7), 953–956. doi:10.5194/angeo-20-953-2002

Yen, H.-Y., Chen, C-H., Yeh, Y.-H., Liu, J.-Y., Lin, C.-R., and Tsai, Y.-B. (2004). Geomagnetic Fluctuations during the 1999 Chi-Chi Earthquake in Taiwan Horng-Yuan Zhang. *Earth Planets Space* 56, 39–45.

Zenchenko, T., and Breus, T. (2021). The Combined Effect of Space and Earth Weather Factors on Human Health and Well-Being. *Atmosphere* 12 (3), 346. doi:10.3390/atmos12030346

Zhang, X., Shen, X., Parrot, M., Zeren, Z., Ouyang, X., Liu, J., et al. (2012). Phenomena of Electrostatic Perturbations before strong Earthquakes (2005–2010) Observed on DEMETER. *Nat. Hazards Earth Syst. Sci.* 12 (), 75–83. doi:10.5194/nhess-12-75-2012

ZhangShen, X. X., Parrot, M., Zeren, Z., Ouyang, X., Liu, J., Qian, J., et al. (2012). Phenomena of Electrostatic Perturbations before strong Earthquakes (2005–2010) Observed on DEMETER. *Nat. Hazards Earth Syst. Sci.* 12, 75–83. doi:10.5194/nhess-12-75-2012

Conflict of Interest: The author declares that the research was conducted in the absence of any commercial or financial relationships that could be construed as a potential conflict of interest.

frontiers in Earth Science

ORIGINAL RESEARCH
published: 23 November 2021
doi: 10.3389/feart.2021.757358

Transient Effects in Atmosphere and Ionosphere Preceding the 2015 M7.8 and M7.3 Gorkha–Nepal Earthquakes

Dimitar Ouzounov[1]*, Sergey Pulinets[2], Dmitry Davidenko[2], Alexandr Rozhnoi[3†], Maria Solovieva[3], Viktor Fedun[4], B. N. Dwivedi[5,6], Anatoly Rybin[7], Menas Kafatos[1] and Patrick Taylor[8]

[1]Center of Excellence for Earth Systems Science and Observations, Chapman University, Orange, CA, United States, [2]Space Research Institute, RAS, Moscow, Russia, [3]The Schmidt Institute of Physics of the Earth, RAS, Moscow, Russia, [4]Plasma Dynamics Group, Department of Automatic Control and Systems Engineering, The University of Sheffield, Sheffield, United Kingdom, [5]Department of Physics, Indian Institute of Technology (BHU), Varanasi, India, [6]Rajiv Gandhi Institute of Petroleum Technology, Jais Amethi, India, [7]Research Station RAS, Bishkek, Kyrgyzstan, [8]NASA GSFC, Greenbelt, MD, United States

Edited by:
Dmitry Efremenko,
Helmholtz Association of German Research Centers (HZ), Germany

Reviewed by:
Angelo De Santis,
Istituto Nazionale di Geofisica e Vulcanologia (INGV), Italy
Dedalo Marchetti,
Jilin University, China
Lixin Wu,
Central South University, China
Oleg Zolotov,
Murmansk Arctic State University, Russia

***Correspondence:**
Dimitar Ouzounov
ouzounov@chapman.edu

†Deceased

Specialty section:
This article was submitted to Environmental Informatics and Remote Sensing,
a section of the journal Frontiers in Earth Science

Received: *12 August 2021*
Accepted: *29 October 2021*
Published: *23 November 2021*

Citation:
Ouzounov D, Pulinets S, Davidenko D, Rozhnoi A, Solovieva M, Fedun V, Dwivedi BN, Rybin A, Kafatos M and Taylor P (2021) Transient Effects in Atmosphere and Ionosphere Preceding the 2015 M7.8 and M7.3 Gorkha–Nepal Earthquakes. Front. Earth Sci. 9:757358. doi: 10.3389/feart.2021.757358

We analyze retrospectively/prospectively the transient variations of six different physical parameters in the atmosphere/ionosphere during the M7.8 and M7.3 earthquakes in Nepal, namely: 1) outgoing longwave radiation (OLR) at the top of the atmosphere (TOA); 2) GPS/TEC; 3) the very-low-frequency (VLF/LF) signals at the receiving stations in Bishkek (Kyrgyzstan) and Varanasi (India); 4) Radon observations; 5) Atmospheric chemical potential from assimilation models; and; 6) Air Temperature from NOAA ground stations. We found that in mid-March 2015, there was a rapid increase in the radiation from the atmosphere observed by satellites. This anomaly was located close to the future M7.8 epicenter and reached a maximum on April 21–22. The GPS/TEC data analysis indicated an increase and variation in electron density, reaching a maximum value during April 22–24. A strong negative TEC anomaly in the crest of EIA (Equatorial Ionospheric Anomaly) occurred on April 21, and a strong positive anomaly was recorded on April 24, 2015. The behavior of VLF-LF waves along NWC-Bishkek and JJY-Varanasi paths has shown abnormal behavior during April 21–23, several days before the first, stronger earthquake. Our continuous satellite OLR analysis revealed this new strong anomaly on May 3, which was why we anticipated another major event in the area. On May 12, 2015, an M7.3 earthquake occurred. Our results show coherence between the appearance of these pre-earthquake transient's effects in the atmosphere and ionosphere (with a short time-lag, from hours up to a few days) and the occurrence of the 2015 M7.8 and M7.3 events. The spatial characteristics of the pre-earthquake anomalies were associated with a large area but inside the preparation region estimated by Dobrovolsky-Bowman. The pre-earthquake nature of the signals in the atmosphere and ionosphere was revealed by simultaneous analysis of satellite, GPS/TEC, and VLF/LF and suggest that they follow a general temporal-spatial evolution pattern that has been seen in other large earthquakes worldwide.

Keywords: Nepal Earthquake, Natural hazards, precursors, thermal anomaly, ionospheric effects, GPS/TEC, VLF, LAIC

INTRODUCTION

The observational evidence of data from the last 3 decades from different parts of the world provides a significant pattern of transient anomalies preceding earthquakes (Tronin et al., 2002; Liu et al., 2004; Ouzounov et al., 2007; Němec et al., 2008; Parrot, 2009; Kon et al., 2010; Hayakawa et al., 2013; Tramutoli et al., 2013). Although there exists a great deal of experimental evidence on the presence of seismo-electromagnetic disturbances in the wide frequency range from Ultra Low to High Frequency and methods of observations stretch out from ground to satellite (Pulinets and Boyarchuk, 2004; Hayakawa 2015; Ouzounov et al., 2018a), the majority of the studies presented were obtained at one location, one wave path or only at the time of the events. It is rare to see "aseismic path" measurements, i.e., data from the receivers (*or outfit*) located far away from the earthquake epicenters. Long-term statistical analysis, or confutation analysis for other possible causes needs to be explored, which can produce the same signal anomalies. Sometimes there are demonstrations only on a single parameter and therefore many researchers have rational skepticism about pre-earthquake anomalies. We focus on the consistent multi-parameter data collection that could help to reveal the connection between atmospheric and ionospheric variations (or anomalies) associated with major earthquakes.

The 2015 earthquake sequence in Nepal has been studied with different methods for pre-earthquake anomalies. Several authors show precursory phenomena by using different satellite and ground observations: a/Satellite thermal anomalies (Ouzounov et al., 2015; Prakash et al., 2015; Shan et al., 2016); b/Microwave Brightness Temperature Anomalies (Qi et al., 2020); c/Radon anomalies (Deb et al., 2016); d/Ionospheric anomalies (Ouzounov et al., 2015; Maurya et al., 2016; Oikonomou et al., 2016; Li et al., 2016; De Santis et al., 2017); e/Gravity anomalies (Chen et al., 2015). We used a multi-parameter approach to search for pre-earthquake signals associated with the series of strong earthquakes in Nepal during April-May 2015. A network of different observations provides an opportunity to analyze signals over the same area with different methods. Our study analyzed ground and satellite data to record the atmospheric and ionospheric responses to the M7.8 and M7.3 earthquakes in Nepal in 2015. Immediately after the M7.8 on April 25, 2015, we could analyze and find anomalies in the atmosphere prospectively and acknowledge in advance the potential for the occurrence of M7.3 of May 12, 2015 (Ouzounov et al., 2015). We examined six different physical parameters characterizing the state of the atmosphere/ionosphere during the periods before and after the event: 1. Outgoing Longwave Radiation, OLR (infra-red 10–13 μm) measured at the top of the atmosphere; 2. GPS/TEC (Total Electron Content) ionospheric variability; 3. Very Low Frequency (VLF) over horizon propagation; 4. Radon observations; 5. Atmospheric chemical potential from assimilation models and 6. Air Temperature from NOAA ground stations. These results testify to the efficiency of combining different methods (Thermal, GPS/TEC, VLF/LF) for the revealing precursory activity associated with strong earthquakes, especially with multi-stationed observations.

EARTHQUAKES

The Nepal earthquake on April 25 was the strongest since 1934. The Mw = 7.8 (depth 15 km) earthquake with epicenter 28.230°N, 84.731°E occurred in the same area at 06:11 UT, 80 km from Kathmandu. A series of strong aftershocks began immediately after the mainshock, with one aftershock reaching Mw = 6.6 (depth = 10 km) within half an hour of the initial earthquake. A major aftershock of Mw = 6.9 occurred on April 26, 2015, in the same region at 07:08 UT. The weaker aftershocks were observed until the morning of April 28. According to the USGS, the earthquake was caused by a sudden thrust, or release of built-up stress, along the primary fault line where the Indian Plate is slowly diving underneath the Eurasian Plate, carrying much of Europe and Asia. The earthquake's effects were amplified in Kathmandu as it sits in the Kathmandu Basin, which contains about 600 m of sedimentary rocks, representing the infilling of an ancient lake.

Kathmandu, situated on a block of the crust of approximately 120 km wide and 60 km long, reportedly shifted 3 m to the south in a matter of just 30 s. This earthquake caused avalanches on Mount Everest. At least 19 people died, with 120 others injured or missing (Harris, 2015). In total there have been more than 8,669 victims and 17866 injured. Tens of hundred houses were destroyed, including several pagodas on Kathmandu Durbar Square (a UNESCO World Heritage Site) and the 60-m tower

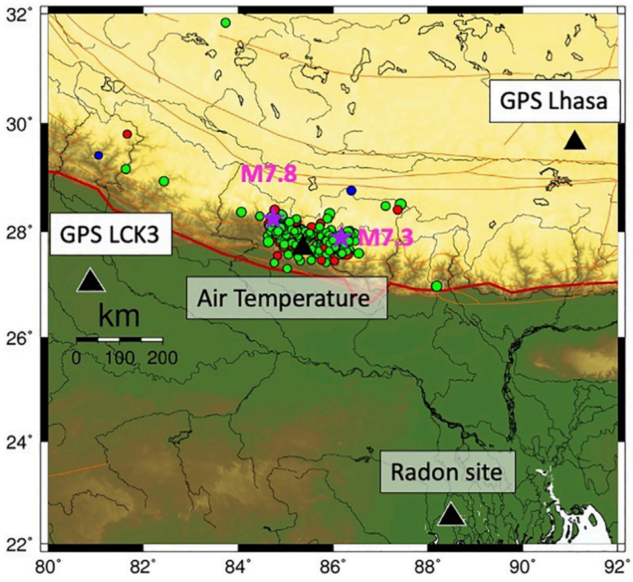

FIGURE 1 | Reference map of Nepal region, with the location of earthquakes >M4 for Jan–May 2015. The location of M7.8 of April 25 and M7.3 of May 12, 2015 are with purple stars. With black triangles are showing the location of the air Temperature station (katmandu) and GPS stations (Lhasa), radon site (Kolkata, India).

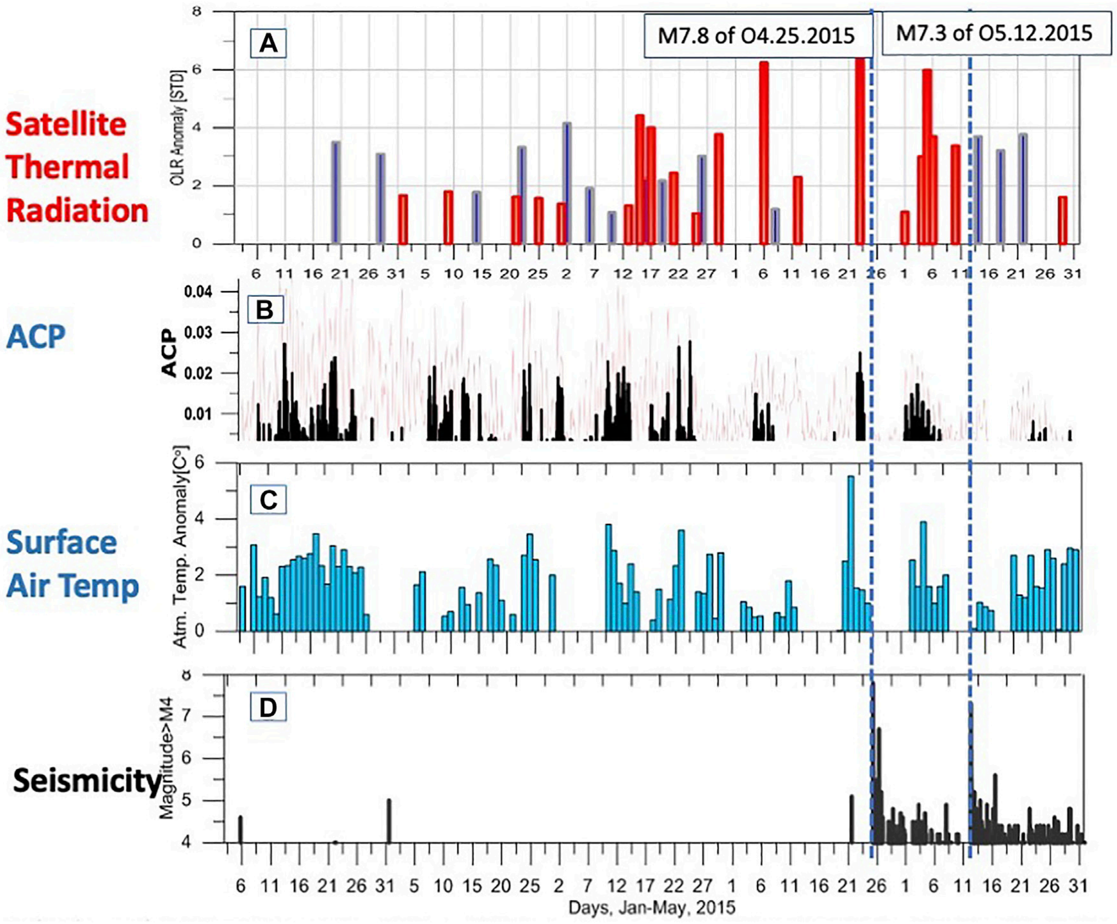

FIGURE 2 | Time series of atmospheric variability observed within a 200 km radius of the Nepal earthquake **(top to bottom)**: **(A)** Nighttime anomalous OLR over epicentral region from January 1–May 30, 2015 observed from NOAA AVHRR (red). Same location, same period a year before - Jan-Ma y 20 14 (black); **(B)** ACP time series over the epicentral areas. With pink color 2015 ACP 6 hourly data. With black the residual of 2015-20 14 6 hourly ACP data; **(C)** Air temperature anomaly from station Tribhuvan International Airport (blue) at 0600LT; **(D)** Seismicity (M>4.0), Jan–May 2015 within 200km radius of the M 7.8 epicenter (USGS).

Dharahara. More than half a million structures were damaged. The second Nepalese earthquake occurred on May 12, 2015, at 07: 05 UT with Mw = 7.3 (depth 18 km). This earthquake occurred on the same fault as the April 25, but further east than the original earthquake. Minutes later, another 6.3 magnitude earthquake hit Nepal, with its epicenter east of Kathmandu. The tremor caused new landslides and avalanches on Mount Everest and was felt at many places in northern India. It destroyed some of the buildings which survived the first earthquake. (**Figure 1**).

RESULTS

Air Temperature Observations

Multiyear day-by-day counts of nighttime temperatures were used to compute the daily temperature variations near the vicinity of the earthquake epicenter. Data near the ground surface were obtained from Tribhuvan International Airport, Nepal, through NOAA Surface Data Hourly Global Database. We analyzed surface air temperature and nighttime data for 2011–2015 close to the terminator time 0,500–0,600 LT to define the normal and abnormal state of the air temperature. The pre-terminator times have been found as one of the most sensitive indicators for buildup of thermal anomalies, because of the limited solar radiation impact during these hours (Ouzounov et al., 2006). The time series for January 1 to May 31, 2015, is shown in **Figure 2C**. We computed the residual values to distinguish between the current value and the multi-year year mean of the air temperature variability. The maximum offsets from the mean value reached near +5°C on April 20 and +4°C on May 5 (**Figure 2C**) with a confidence level of more than +2 sigma for all the observations from 2011 to 2015. This transient rapid increase in the surface air temperature is a little more significant than the remote satellite observations shown in **Figure 2A**, which agrees with the thermodynamic processes explained by the LAIC concept. (Pulinets and Ouzounov, 2011). To understand the day-by-day variability of the daytime and nighttime temperature during the earthquake events, we analyzed the hourly temperature near the epicenter in a new way. We used 3-h global surface air temperature data from the GEOS-5 assimilation (**Figure 2B**). The presence of ions in the atmosphere creates a possibility for water vapor molecules to join with these ions through the hydration process, which is different from condensation. The evaporation/condensation process, the phase transition of the first order, always occurs during the potential chemical equality. However, newly formed ions have different chemical potentials; what is to introduce should consider in the one-component approximation we introduce the correction to the chemical potential. The increase of the water molecules chemical potential indicates the strength of the nucleation process and can be used as an indicator of an imminent earthquake according to Boyarchuk et al., 2010 and demonstrated already within multiparameter analysis (Ouzounov et al., 2018a; Pulinets et al., 2020).

Radon Observation

Long-term array observations of radon anomalies have been used for pre-earthquake studies (Fu et al., 2011, 2015, Zoran et al., 2012; Giuliani et al., 2013, Karastathis et al., 2019). Anomalous radon variations occurred a few days to a few months before the earthquake and are likely to be associated with earthquake development's dilatancy and micro fracturing stages. Radon plays a crucial role in developing the lithosphere-atmosphere-ionosphere coupling (LAIC) concept (Scholz et al., 1973; Pulinets and Ouzounov, 2011; Pulinets et al., 2018) associated with the pre-earthquake process. During the 2015 earthquake sequences in Nepal, simultaneous measurements of soil radon-222 were recorded at the main campus of Jadavpur University, Kolkata, India. Deb et al. (2016) studied the precursory seismogenic radon. To observe coherent responses, the soil Rn222 concentration profiles were measured simultaneously at two nearby (~200 m apart) locations (**Figure 3A**), A and B, having uniformly clayey soil, within the Jadavpur University premises (22.5667°N, 88.3667°E). The soil moisture content at location A was lower than location B. It was expected that simultaneous recording of radon time series at these two locations would add confidence in identifying pre-seismic responses (**Figure 3b**). The 4-months time of their observations fortunately overlapped with the Nepal seismo-active period in 2015 (**Figure 3**). Their sensor, a solid-state nuclear track detector method, was used to detect the alpha-radiation in the radioactive radon gas. Two simultaneous 4-months of observations have been analyzed. During the observation period, four statistically significant anomalies (above the ±2σ level) were obtained on April 20, April 29, May 19, and May 29, 2015, simultaneously at both locations A and B. April 20 anomaly preceded the April 25 M7.8, and the April 29 was identified as precursors to the May 12. The May 29 radon anomaly is likely to be identified as a pre-seismic event to the M5.6 earthquake at Kokrajhar, Assam, on June 28, 2015 (Day et al. l, 2016). Despite that radon fluctuation on May 19 registered at locations A and B with >2σ significance, no earthquake occurred within a 1,000 km radius from Kolkata. Probably this anomaly is not associated with seismic origin but with geodynamics transition associated with the new Moon event on May 18, 2015, 1 day before the Radon anomaly occurrence. The connection between Lunar phases, geodynamics, and seismicity has been statistically established (Kolvankar et al., 2010). The overall interpolation of radon anomalies related to the Nepal 2015 earthquakes demonstrates that the reliable detection of radon anomaly due to seismicity requires simultaneous measurement of soil radon concentration by a broad network of radon/gamma sensors (Fu et al., 2011, 2015; Karastathis et al., 2019).

Atmospheric Chemical Potential

All thermodynamic models of the atmosphere, considering the phase transitions of water and latent heat fluxes, operate with latent heat (per mole or molecule) as a constant at a given temperature. It is equal to 0.422 eV per one water molecule. However, if one carefully deals with accurate data, one can often find that violations of the gas equation are observed (inexplicable additional variations in temperature, humidity, and pressure). We approached this phenomenon from a different approach different when studying the processes of ionization of the surface manner layer of the atmosphere by radon, the release of which from the Earth's crust sharply increases at the final stage of preparation for a strong earthquake. The detailed calculations could be found in Pulinets et al., (2015). Here we discuss the final findings. As it turned out, atmospheric ions formed during the ionization of atmospheric gases by energetic alpha particles emitted by radon during decay become instantly hydrated. Hydration is not equivalent to condensation because the process takes place at any relative humidity level and does not require saturated steam. However, all the same, a phase transition of water molecules from a free to a bound state takes place, and, just as during condensation, latent heat is released. It turned out that the released amount of latent heat is more significant at a high rate of ion production and high concentration of ions than for ordinary condensation. How much larger? For earthquakes, the value ranges from 0.01 to 0.1 eV, i.e., in extreme cases, it can reach about 25% of the latent heat constant. (it's the difference between the released latent heat during hydration and normal condensation). This difference we call the correction of the chemical potential of the water vapor in the atmosphere. We call it the atmospheric chemical potential (ACP) because, in the act of evaporation/condensation, the energy of the water molecule is equal to its chemical potential. To understand the day-by-day variability of ACP during the earthquake events, we analyzed 3 h global ACP data computed from the GEOS-5 assimilation (**Figure 2B**).

Earth Radiation Observation

One of the main parameters we used to characterize the Earth's radiation environment is outgoing long-wave-earth radiation (OLR). OLR has been associated with the top of the atmosphere (TOA) integrating the emissions from the ground, lower atmosphere, and clouds (Ohring G. and Gruber, 1982), and primarily was used to study the Earth's radiative budget and climate (Gruber and Krueger, 1984; Mehta and Susskind, 1999).

Daily OLR data were used to study the OLR variability in the zone of earthquake activity (Liu, 2000; Ouzounov et al., 2007, 2018b; Xiong et al., 2010). An augmentation in radiation and a transient change in OLR was proposed to be related to

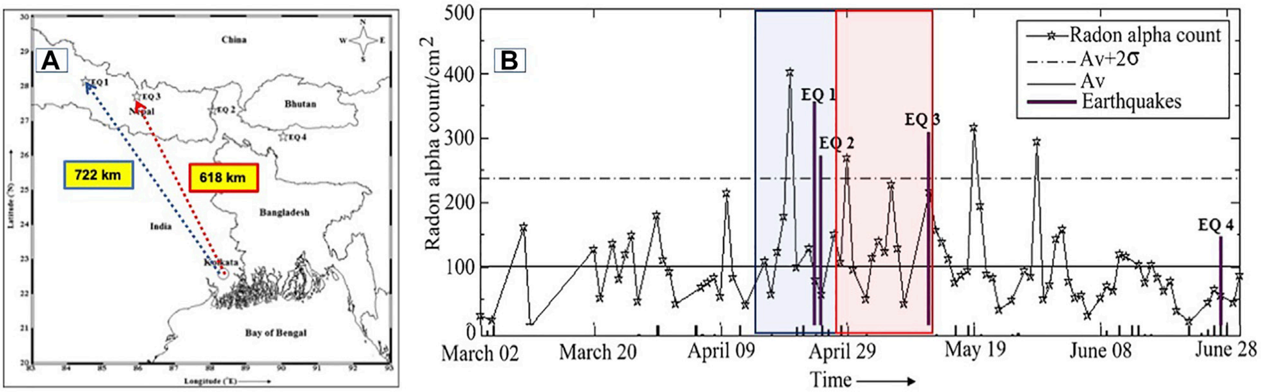

FIGURE 3 | Radon observation in Kolkata, India **(A)** Map indicating the monitoring sites in Kolkata and the MS+ earthquakes within 1000 km region. **(B)** Combined graph for radon-222 anomalies at location **(A)** and the corresponding earthquakes during the observation period from March 1 to June 30, 2015. EQ I -M7.8 of 04.25.2015; EQ2- M6.9 of 04.26.2015 and EQ3- M7.3 of OS.12.2015. (Deb at all, 2016).

thermodynamic processes in the atmosphere over seismically active regions. We can determine the atmospheric anomaly in Euler's reference frame as a first approximation by subtracting the mean. The average can be defined at the same day each year, local time, and location over 11 years (i.e., more than one solar cycle). The advantage of this approach is its efficiency in the presence of long-term satellite observations. The OLR anomalous variations were defined as an E_index (Ouzounov et al., 2007) as the statically defined maximum change in the rate of OLR for a specific spatial location and predefined times. They have constructed analogously to the anomalous thermal field proposed by (Tramutoli et al., 2005, 2013).

The E_index was defined as statically estimated variability in OLR values for specific locations and periods:

$$\text{E\_Index}_{i,j}(t) = \left(S^*\left(x_{i,j}, y_{i,j}, t\right) - \overline{S^*}\left(x_{i,j}, y_{i,j}, t\right)\right)/\sigma_{i,j} \qquad (1)$$

Where: t = 1, K days, $(S^*(x_{i,j}, y_{i,j}, t))$ is the current OLR and $\overline{S^*}(x_{i,j}, y_{i,j}, t)$ is the computed mean of the OLR field, defined for multiple years of observations over the same location and same local time, $\sigma_{i,j}$ is the standard deviation of S^*, and K is the total number of analyzed days. We use the Thermal radiation anomaly (TRA) index, a modified version of E_Index (**Eq. (1)**),

$$\text{TRA Anomaly}_{i,j}(t) = \left(A^*\text{E\_Index}_{i,j}(t)\right)/B \qquad (2)$$

A and B are regional coefficients, A—a mask, mainly defined by the regional seismo-tectonic patterns and TRA appearance frequency (A = 0.1–0.9). B normalizes each of NOAA 15 and 18-time series of OLR data to the same time coverage over 11 years averaging period (B = 1–3.5). The TRA indexes have been processed with additional preprocessing to avoid aliasing short wavelengths and spatial filtering based on a "minimum curvature" algorithm (Ouzounov et al., 2018a). We used OLR data from NOAA's Advanced Very High-Resolution Radiometer (AVHRR) for satellite thermal analysis over Nepal. The results of the 2015 Nepal earthquake showed that there was a rapid increase in transient infrared radiation in satellite data in mid-March 2015. An anomaly is observed near the epicenter; it peaked around April 4–7, about 2–3 weeks before the M7.8 earthquake (**Figure 4**, **Figure 6**). Further analysis revealed another temporary OLR anomaly on May 2–3. The second M7.3 event occurred on May 12, 2015. (Ouzounov et al., 2015). Our results show that long-wave radiation signals associated with earthquake processes were observed near the epicentral regions several days before the corresponding earthquakes. TRA hotspots appeared quickly, remained in the same regions for several hours, and then quickly dissipated. During March-May 2015, about TRA 15 anomalies were detected around the Nepali M7.3 epicentral areas (**Figures 5**,**6**). With red dots showing the anomaly locations, the date is given in the text, and a circle shows the confidence area. The centers TRA are computed based on **Eqs. (1), (2)**. The energetic threshold for determining the anomalous patterns was >2.5 sigma STD. TRAs on April 5, 23, and 29 are within the maximum level for the entire period inside the entire region. The possible reason for several TRA's is the activating of gas releases over Nepal and Central Asia. The triggered ionization inside the ABL generates zones of "thermal-bursts." The cross-section of several TRA areas probably indicates the spatial clustering of the degassing along joined tectonic lineaments. The appearance of TRA anomalies almost disappears after the May 12 Earthquakes. The spatial distribution indicates a large appearance area, but the distance from the epicenter is allowed inside the Dobrovolsky (Dobrovolsky et al., 1979) and Bowman et al., 1998 area ($R = 10^{0.43M}/R = 10^{0.44M}$), which is about 2,250 km according to Dobrovolsky. This rapid enhancement of radiation could be explained by an anomalous flux of the latent heat over the area of increased tectonic activity. (Pulinets and Ouzounov, 2011, 2018; De Santis et al., 2017). Analogous observations were observed within a few days before the most recent major earthquakes in Japan (M9, 2011), China (M7.9, 2008), Italy (M6.3, 2009), Samoa (M7, 2009), Haiti (M7, 2010), and Chile (M8.8, 2010) (Ouzounov et al., 2011b, c; Pulinets and Davidenko, 2014).

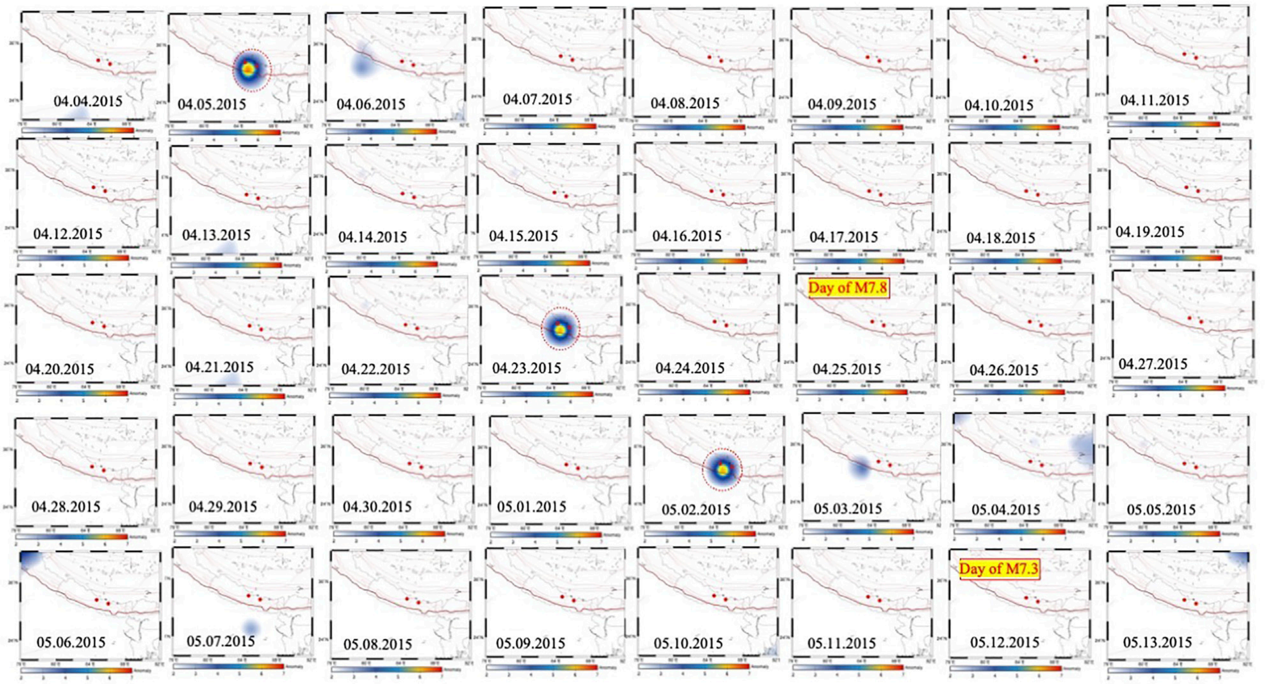

FIGURE 4 | Time series of night time TRA observed from NOANAVHRR, April 4–May 13, 2015. Tectonic plate boundaries are indicated with red lines and major faults by brown ones and earthquake location by red circles. Red circles show the spatial location of TRA within vicinity of M7.8 and M7.3.

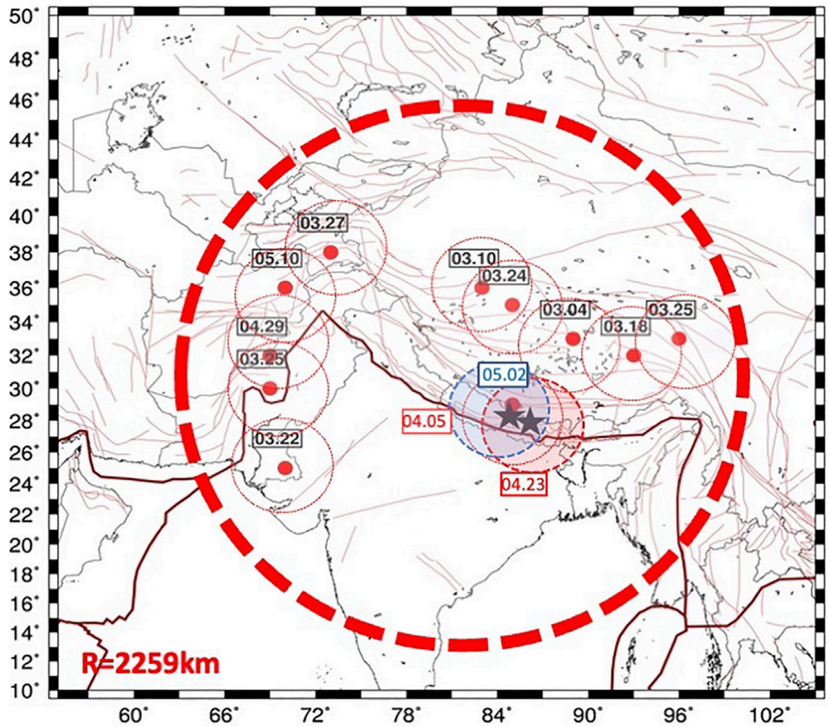

FIGURE 5 | Spatial distribution of Thermal Radiation Anomalies (TRA) March-May 2015 and Dobrvolsky estimated area for the earthquake preparation zone (red dash circle). With red shadowed circles 04.03 and 04.23 anomalies. With a blue shadowed circle 05.03.2015 anomaly. With red dots -the centers of TRA anomalies, with dash red circles, the confidence area of TRA. With black stars the epicenters of M7.8 04.25.2015 and M7.3 of05.12.20 15.

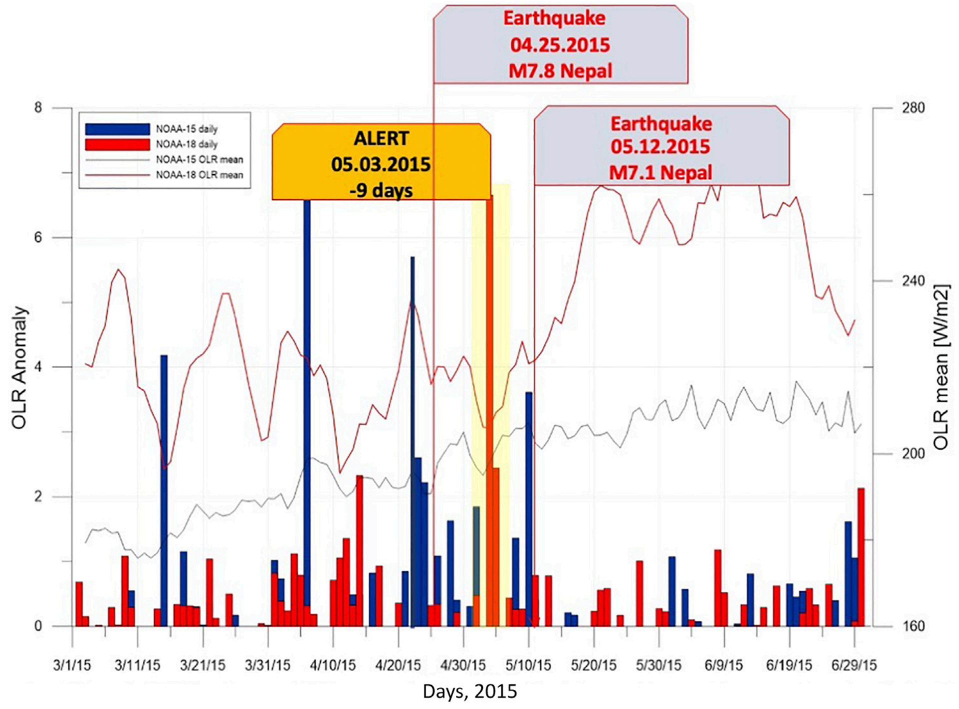

FIGURE 6 | TRA time series for March 2015- June 2015 over th'l: e'j\'Jr Gorkha epicentral area. On April 5, 2015 and April 23, were revealed transient anomalies (by retrospective analysis of satellite radiation) 21 and 3 days in advance to the M7.8 mainshock of April 25, 2015, earthquake. On May 3, 2015, the ongoing prospective analysis of satellite radiation revealed transient anomaly (9 days in advance, with yellow), associated with the M7.3 of May 12, 20 15, earthquake.

Pre-seismic Ionospheric Effects

For our analysis of ionospheric data, we used two sources of information: global maps of the total electron content in IONEX format provided by JPL and a time series of calculated vertical TEC of two GPS receivers in the region (lhaz and lck3). We also controlled the solar-geophysical conditions to purify the data from the possible solar-geomagnetic activity effects. Considering that we deal with the equatorial ionosphere, the primary source of geomagnetic activity was the equatorial geomagnetic index Dst provided by Kyoto World Data Center for Geomagnetism (http://wdc.kugi.kyoto- u.ac.jp/dstdir/index.html).

The epicenter of the M7.8 earthquake was at the outer slope of the northern crest of the Equatorial Ionization Anomaly (EIA). To detect the ionospheric precursors, it is necessary to carefully analyze the geophysical conditions around the time of the Nepal earthquakes. For this purpose, the Solar-geophysical conditions during April- May 2015 is shown in **Figure 7**, where the Solar radio flux F10.7 were analyzed. To put all parameters together (which are expressed in different values), all parameters were normalized. Where F10.7—it is Solar electromagnetic radiation on the Wavelength 10.7 cm: GEC—it is the Global ionospheric content which is the sum of all values in the IONEX table; REC (R5) - the Regional Ionospheric Content—is the sum of all values from the IONEX index within the 500 km radius circle; and REC (R10)—t is the Regional Ionospheric Content - is the sum of all values from the IONEX index within the 1,000 km radius circle.

In **Figure 7B** we plotted the Dst (equatorial geomagnetic) index for the same period. One can see that we are dealing with a moderately disturbed period. From the Dst we can conclude that we have three moderate (with Dst~−80 nT) geomagnetic storms: before the first earthquake and one started during the second earthquake. The other disturbances we can classify as small, not exceeding −30 nT (continuous line, bottom panel of **Figure 8**). The period is also characterized by the essential variations of F10.7 (min 100, max 155). Normalized F10.7 is shown as the green line in the upper panel of **Figure 7**. The F10.7 variations should be eliminated in the dTEC variations (defined in **Eq.(3)**) because they contribute to the running mean calculations. The first attempt to reveal the pre-earthquake variations having disturbed conditions is considering the difference between the Global TEC and Regional TEC (blue and red lines in **Figure 7**). As we see from the upper panel of **Figure 7**, the Global TEC follows the F10.7 with a delay of nearly 2 days (Afraimovich et al., 2008; Marchitelli, V et al., 2020). We exclude the difference in the vicinity of day 101 (April 10), which is a magnetic storm day. The most suspicious days are 111 (April 21) and 114 (April 24), when we may expect negative and positive anomalies. The differential GIM maps were computed for these days to check this supposition, which is presented in **Figure 8**. We see the strong negative (in crests) anomalies on April 21 and a powerful positive anomaly on April 24. The strength of the equatorial anomaly should change. Considering that the epicenter is inside the northern crest of EIA, we will express the strength of the TEC anomaly at the Northern crest to the TEC in the trough of EIA (**Figure 9**). We also

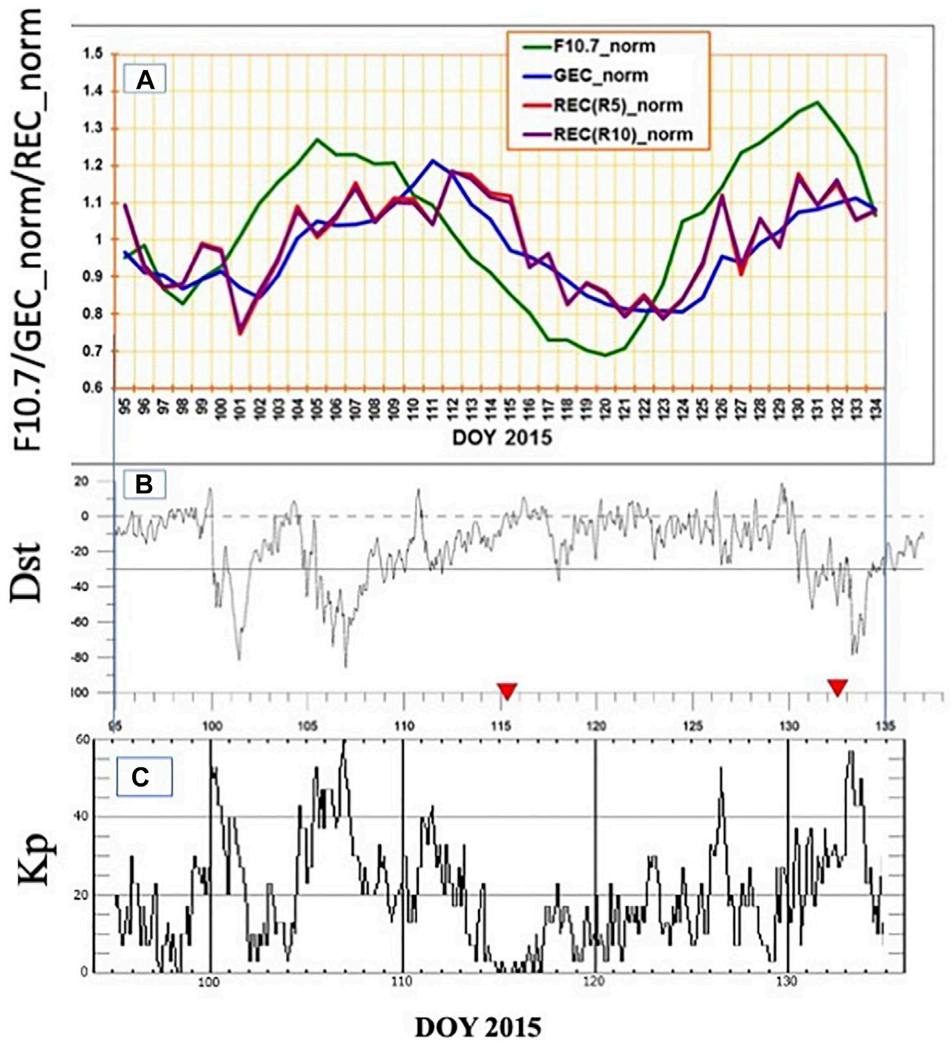

FIGURE 7 | Solar-geophysical conditions during April–May 2015. Al Normalized values of: Fl0.7—Solar electromagnetic radiation on the Wavelength 10.7 cm; GEC—Global ionospheric content, sum of all values in the IONEX table; REC (R5)—the Regional Ionospheric Content—within the 500 km radius circle; REC (RIO)—it is the Regional Ionospheric Content—Within the 1000 km radius circle; 8/ Dst equatorial geomagnetic index; Cl Planetary K-index (Kp* I 0, OMNI WEB Plus).

calculate S - the strength of EIA on undisturbed days as a relation between the TEC value in the crest of anomaly and in trough between crests. On day 111 (April 21), the EIA completely disappears which gives its strength less than 1: S = 0.98. S- It is the strength of equatorial anomaly (relation between the TEC value in crest of anomaly and in trough between crests). On day 114 (April 24), the anomaly strength is 1.69, and on disturbed days before the earthquake—day 98 (April 07) and after the earthquake - days 117 (April 27) and 120 (April 30), the strength varied from 1.22 to 1.39.

From the historical data of the ionosphere, monitoring has elaborated a conception of the precursor mask, which generalizes the pattern of ionosphere parameter variations (foF2 or GPS TEC) a few days before the earthquakes (Pulinets et al., 2007, 2018).

$$\Delta TEC = 100 \cdot (TEC - TEC_m)/TEC_m \tag{3}$$

Where TEC—is the Total Electron Content in TECU, where TECU = 10^{16} el/m^2, TEC$_m$ 15-days running average value of TEC. The precursor mask was developed based on the analysis of strong (M ≥ 6) earthquakes in Greece and Italy (Pulinets and Ouzounov, 2018; Davidenko and Pulinets, 2019). We used this approach to analyze the dTEC variations for the lhaz GPS receiver around the two Nepal earthquakes presented in **Figure 10**. The horizontal axis is the Day of Year 2015 of the mainshock designated by zero. Vertical axis—is the local time (LT), and VTEC deviation is color-coded in percentages relative to the 15-days mean. We can see that the positive anomaly appears near 8 PM and exists continuously up to 4 AM the next day. In the present figure, the anomalies appear 3 days before the mainshock. However, further analysis for other earthquakes revealed that such anomalies might appear up to 5 before the mainshock. We can see similar night-time positive deviations before both strong earthquakes lasting

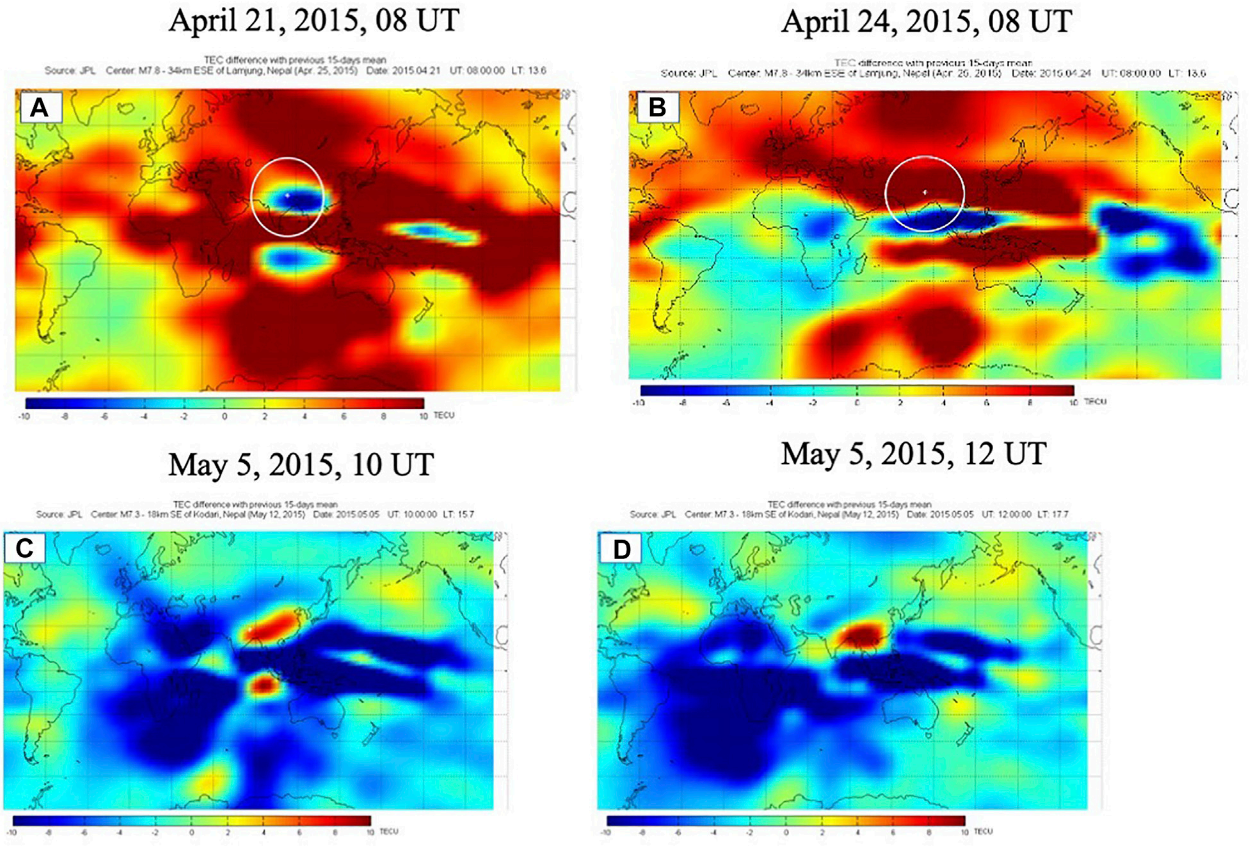

FIGURE 8 | GIM GPSffEC spatial analysis. **(A)** Differential TEC map of April 21, 2015, (−4 days) 09UT and **(B)** April 24, 2015, 08UT (−1 day) **(C)** Differential TEC map of May 5, 2015, (−7 days) !OUT and **(D)** May 5, 2015, 12UT (−7 day).

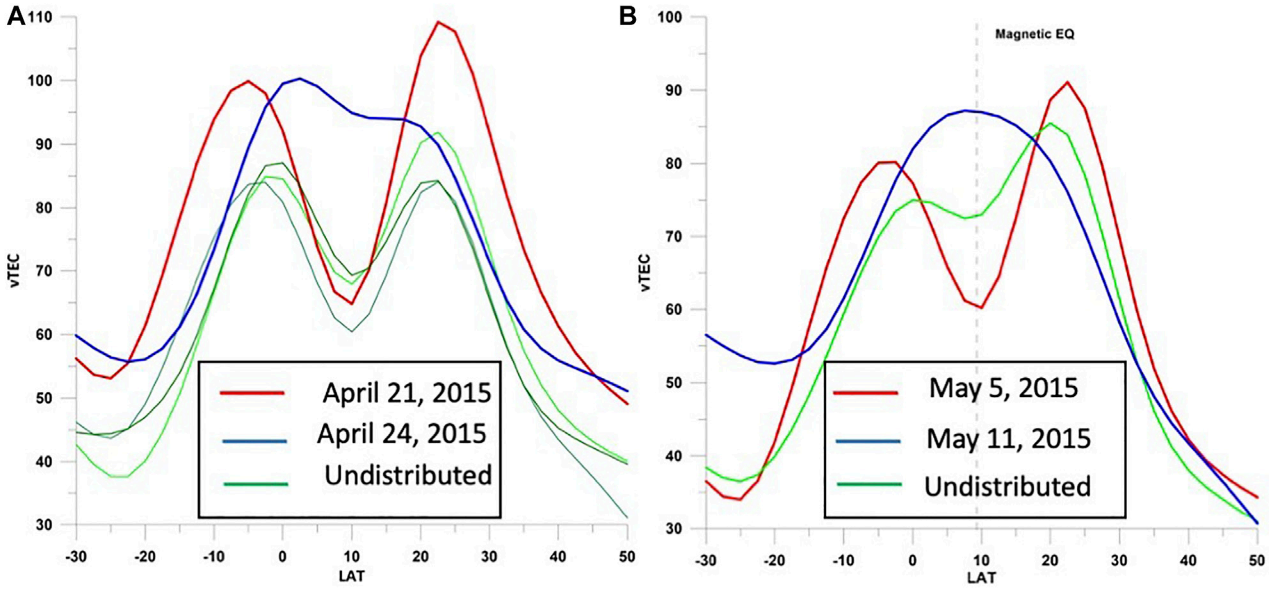

FIGURE 9 | dTEC variations (defined in **Eq. 3**) for the lhaz GPS/GLONASS receiver (**Figure 1**) for April 6–May 15, 2015.

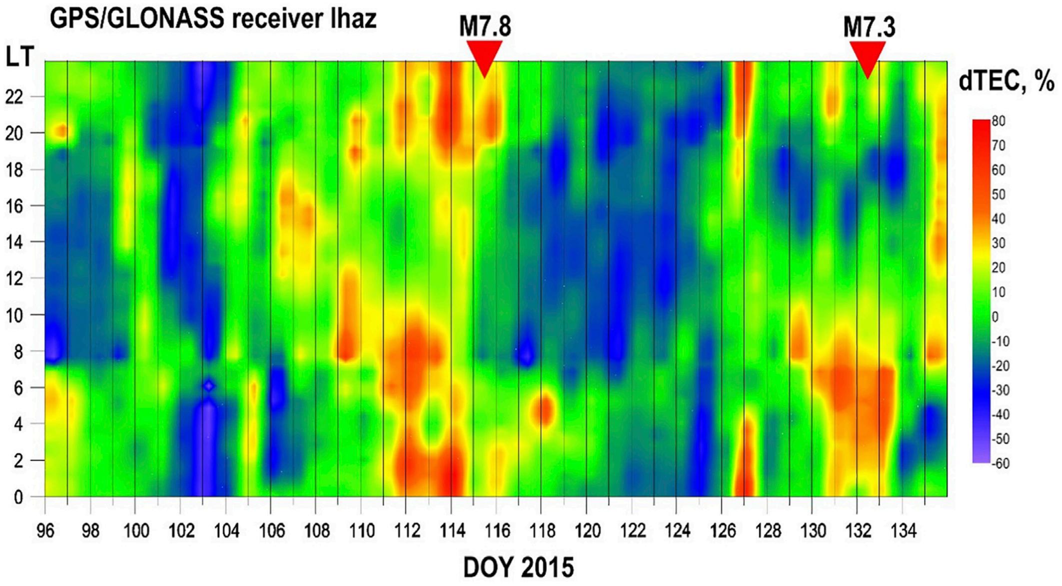

FIGURE 10 | GIM GPSffEC spatial analysis. **(A)** Differential TEC map of April 21, 2015, (–4 days) 09UT and **(B)** April 24, 2015, 08UT (–1 day) **(C)** Differential TEC map of May 5, 2015, (–7 days) ! OUT and **(D)** May 5, 2015, 12UT (–7 day).

more than 1 day and repeating every day at the same local time. The only difference with the pattern presented in **Figure 10** is that the favorable variations start at 6 PM and finish at 6 AM. It can relate to the different terminator times for Greece and Nepal (Zolotov, 2015).

Very Low Frequency/Low Frequency (VLF/LF) Probing

One of the possible experimental techniques that can monitor the ionization's perturbations within the lower ionosphere uses Very Low Frequency/Low Frequency (VLF/LF) probing. Waves in the VLF frequency range are trapped between the lower ionosphere and the Earth and are reflected by the D region at an altitude of ~65 km during the daytime and ~85 km during nighttime. The received signals contain information about the reflection height's region and its variability (Barr et al., 2000). The propagation of sub ionospheric VLF/LF (15–50 kHz) signals from navigation or time service transmitters over distances of thousands of kilometers (with low attenuation ~2–3 dB per Mm) enables remote sensing over large regions of the upper atmosphere in which ionospheric modifications lead to changes in the received amplitude and phase of the signals. The regular monitoring of many years at the Far East network, which operates in a highly seismic zones such as Japan and Kurile Islands, has established a statistical correlation between anomalies of the VLF/LF signal parameters in the nighttime and earthquakes with M ≥ 5.5. When observed, the possible time intervals of seismic-related phase and amplitude anomalies are about 1 week before an earthquake and 1 week after the event (Rozhnoi et al., 2004,2009,2015; Maekawa et al., 2006; Hayakawa et al., 2010, Biagi et al., 2011; Hayakawa 2015). Anomalies for such earthquakes were found in 20–25% of all cases. However, for strong earthquakes (M > 6.8), anomalies VLF/LF were observed in 60–70% of the earthquakes (Rozhnoi et al., 2013).

The VLF/LF receiving stations deployed both in Europe (Eastern Europe, Sheffield, Graz), the Far East (Kamchatka, Sakhalin, Kuril Islands), North America (Orange, CA) and Asia (Bishkek, Varanasi) are equipped with the UltraMSK receivers (http://ultramsk.com/). All the stations simultaneously receive the amplitude and phase of MSK (Minimum Shift Keying) modulated signals with fixed frequencies in a narrow band 50–100 Hz around the central frequency and adequate phase stability. The receivers can record signals with time resolutions ranging from 50 msec to 60 s. For our purpose, we use a sampling frequency of 20 s. The VLF/LF observation network is shown in **Figure 11A**, and the epicenters of earthquakes with M > 5 for the last 3 years. The analysis reported in this paper about earthquakes in Nepal in April-May 2015 is based on these data recorded by the VLF/LF stations in Bishkek (KGZ) and Varanasi (VAR).

Figure 11B, shows the relative positions of our observing stations and transmitters VTX (17.0 kHz) in India, NWC (19.8 kHz) in Australia, and JJY (40 kHz) in Japan, together with the positions of the epicenters of earthquakes in April-May 2015 in the region under analysis. The areas of earthquake preparation where precursors can be found (Dobrovolsky et al., 1979) are shown by the pink circle for the first strong earthquake on April 25 and the yellow circle for the second earthquake on May 12, 2015. The station in Varanasi (VAR) began a regular reception in April; therefore, analysis for both stations were made from the beginning of April. Two wave paths—NWC-KGZ and JJY-VAR pass directly above the epicenter of the Nepal earthquake. The signal from the JJI transmitter received at the Varanasi (VAR) station also passes above the epicenter, but it was

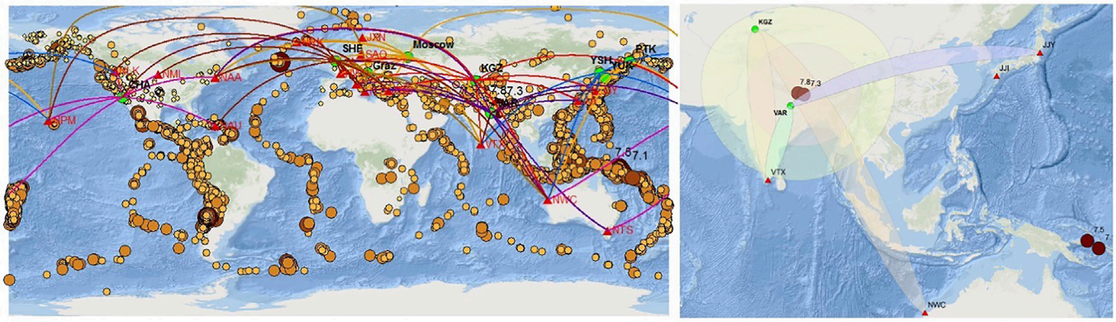

FIGURE 11 | The VLF/LF network. Green circles show the positions of receiving stations. Red triangles show transmitters. The lines are propagations paths from the transmitters to receivers. Brown circles show the epicenters of earthquakes with M > 5.5 for the period 2013-2015. Bl A map of the wave paths under analysis together with the epicenters of earthquakes with M > 7 (solid brown circles) occurred in April-May 2015. KGZ stands for the station in Bishkek (Kirgizstan), VAR means the station in Varanasi (India), YSH is the station in Yuzhno-Sakhalinsk (Sakhalin Island). The areas of earthquake preparation where precursors can be found are shown by the yellow circle for the first larger earthquake on April 25 and the pink circle for the second earthquake on May 12, 2015. The ellipses are projections of the third Fresnel sensitivity zone on the Earth's surface.

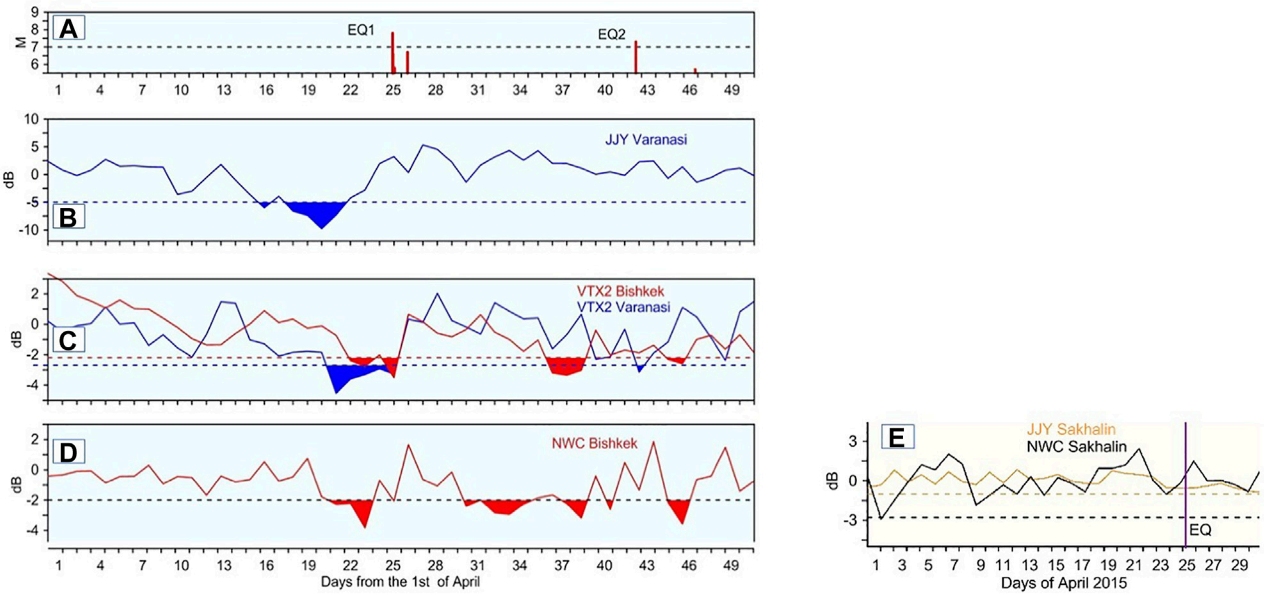

FIGURE 12 | (A–D) The results of the VLF/LF analysis. The average residual amplitudes of the VLF/LF signals in the nighttime are shown **(top to down)** for vrx (17.0 kHz)transmitter recorded in Bishkek (red) and Varanasi (blue), NWC (19.8 kHz) transmitter recorded in Bishkek, JN (40 kHz) transmitter recorded in Varanasi. The bottom panel shows JJY (yellow) and NWC (black) transmitter signals recorded in Yuzhno-Sakhalinsk stations (control "aseismic" paths). The upper panel shows the occurrence time of the earthquakes. The color-filled zones indicate values exceeding the –2a (a is the standard deviation) lEvel, indicated by the horizontal dotted lines. Fl the controlled pa1hs NWS Sakhalin and JJY Sakhalin.

not used for the analysis because it is very noisy. Two sub-ionospheric paths (VTX-KGZ and VTX-VAR) are outside the epicenter but inside the earthquake preparation area. We used a residual signal of amplitude calculated as the difference between the actual signal and the monthly averaged signal for our analysis.

The last was calculated using the data from undisturbed days. Since VLF/LF signals are very stable during daytime and are unaffected by any force except X-rays emitted during solar flares, the analysis was made only for nighttime. The results of these analyses are shown in **Figure 12A**. For validation of the results, we analyzed the signals from the same NWC and JJY transmitters propagating far away from the seismic zone, the significant negative nighttime amplitude anomalies for the four paths crossing the area where the possible precursors of the earthquake can be found 4–5 days before the first earthquake while the signals in the "aseismic" paths vary insignificantly (**Figure 12B**). Then after several days, when the signals were quiet, the second series of anomalies can be seen. These anomalies continue after the earthquake during the period of aftershock activity.

DISCUSSION

A joint analysis of atmospheric and ionospheric parameters during the M7.8 earthquake in Nepal has demonstrated correlated variations of atmospheric anomalies implying their connection with the earthquake preparation processes. One of the possible explanations for this relationship is the Lithosphere- Atmosphere-Ionosphere Coupling mechanism (Pulinets and Boyarchuk, 2004; Pulinets and Ouzounov, 2011, Pulinets et al., 2018), which provides the physical links between the different geochemical, atmospheric and ionospheric variations and tectonic activity. This phenomenon's primary process is the air ionization produced by increased radon emissions near active tectonic faults from the Earth's crust. Through the air ionization, triggered by radon level increases, latent surface heat (SLHF) (Cervone et al., 2010) was rapidly developed OLR anomaly was formed at the top of the Atmosphere (TOA) (Ouzounov et al., 2007; 2018b; Xiong et al., 2010). The distinct difference in the thermal atmospheric field over the earthquake preparation area automatically creates vertical air convection, which leads to a pressure anomaly. This pressure anomaly is probably responsible for the stationary behavior of the front end of the jet stream over the vicinity of the future epicentral area (Ouzounov et al., 2011; Wu and Tikhonov, 2014). At this point, we see the transition from atmospheric to electromagnetic effects. It is well established that the ion cluster size is essential for the Atmospheric Boundary Layer (ABL) of the Earth's atmosphere electric conductivity because of the different mobility of ions of different sizes (Hõrrak, 2001). The small and medium-size ions increase the ABL electric conductivity while the large ones if their concentration is high enough, will essentially decrease it. Considering the Global Electric Circuit conception (Pulinets and Davidenko, 2014), we can expect the increase of the vertical electric field gradient in the ABL conductivity drop, which will lead to the change of the ionosphere potential concerning the ground over the earthquake preparation area. As a high conductive media, the ionosphere will maintain its equipotentiality by modifying plasma concentration and temperature within the potential changes area. Due to high conductivity along the geomagnetic field lines, these irregularities will form the modified inner magnetosphere ducts. These ducts will trap the VLF emission inside the modified magnetospheric tube, creating an increased level of VLF noises within the modified tube.

Similarly, as for the Wenchuan earthquake, we observe the changes of the EIA strength and the latitudinal movements of the crests of EIA. During the adverse effect, the crest moved equatorward, and during the positive effect—poleward (**Figure 9**). We can conclude from this picture that this movement is at least 2.5°. As for many cases of other strong earthquakes analyzed, we observe the effect in the magnetically conjugated area of the southern hemisphere.

The maps and profiles of the equatorial anomaly were made using the Global Maps GIM TEC in the form of IONEX index. It is a product of IGS, which interpolates the data of all GPS receivers and inserts the model where we do not have receivers. The dTEC mask (**Figure 10**) was built using the data of Lhasa GPS receiver lhaz. Concerning the epicenter, the location of Lhaz is shown in **Figure 1**. The profiles of the equatorial anomaly were taken at the longitude of the epicenter. So, the IONEX and lhaz should not coincide exactly. There could be differences because of two factors: IONEX—interpolation map, and Lhaz are eastward from the epicenter, and ionospheric variations over there could be slightly different.

Regarding the external impact on the VLF/LF observations, the geomagnetic activities were during the middle of April 2020 (**Figure 7**; **Table 1**). A magnetic storm occurred on April, 17 to the 18th (UT) with Dst˜-79 nT. It was preceded by a proton burst and the relativistic electron fluxes recorded during the recovering stage of the storm. The storm itself does not influence signals propagation because the sudden commencement and main phase of the storm occurred when the analysis zone was sunlit. Another factor that can influence the behavior of the VLF/LF signals is atmospheric pressure fluctuations (Rozhnoi et al., 2014). According to data from the ground meteorological stations in Bishkek, Varanasi, no sharp changes in atmospheric pressure were recorded during the period when anomalies in the signals were detected. Unlike the first earthquake, the JJY signal was undisturbed before the second earthquake. It can relate to the signal's frequency (its frequency is twice higher than the frequencies of other signals) or the direction of propagation. This signature is lost due to the signal in the ionosphere irregularities during propagation. Therefore in **Figure 12B**, only the -2σ (σ is the standard deviation) level is shown for all the paths. The decrease of the NWC signal in the middle of May in the "aseismic" path NWC-YSH most probably was caused by two very strong Typhoons-Noul (1,506) and Dolphin (1,507), which followed one after another and crossed the path at that time. So, considering the possible influence of other factors which can produce perturbations in VLF/LF signals and rejecting them, also using "aseismic" paths, we may conclude that impending earthquakes caused observed anomalies. The preparation/activation zone estimate for both the M7.8 Nepal earthquake on April 24, and the M7.3 on May 12, 2015 follow the Dobrovolsky/Bowman estimates ($R = 10^{0.43M}/R = 10^{0.44M}$), are areas with a radius of 2,259/2,703 km and 1,377/1,629 km accordingly. The soil Rn222 concentration profiles measured simultaneously at two nearby sites at Jadavpur University, Kolkata, India, was at 625 km distance from the epicenter of the April 24 M7.7 Nepal earthquake (**Figure 3A**). During March-May 2015, about 15 TRA anomalies were detected around the Nepali M7.3 epicentral areas (**Figure 5**) were inside the 2,259 km zone. With the VLF/LF analysis, the area of earthquake preparation where precursors can be found is shown in **Figure 11B** by the pink circle for the first earthquake of M7.8 on April 25 and the yellow circle for the M7.3 n May 12, 2015. Although the radon variations, TRA and VLF, were observed far from epicentral areas, the anomalies are inside the Dobrovolsky-Bowman earthquake preparation area estimate. The pre-seismic ionospheric effects for the 2015 Nepal earthquakes are typical for low latitude earthquakes involving the equatorial ionospheric anomaly (EIA). The positive and negative effects are reflected in the conjugated hemisphere due to the charged particles that are influenced by the geomagnetic field lines. These effects should not be considered for Dobrovolsky's estimation. In addition, the equatorial effects are stretched along the longitude and exceed

TABLE 1 | Detection of joint anomalies for the M7.8 of 04.25.2015 Gorkha, Nepal and M7.3 of December 05, 2015 Kodari, Nepal.

#	Earthquakes	Anomalies and trends						
		Radon	TRA	Atm. Temp	ACP	VLF/LF	GIM TEC	EIA TEC
1	M7.8 of 04.25.2015 Gorkha, Nepal	April 20, 2015 strong (–5 days)	April 6, April 22, 2015 strong, (–19, –4 days)	April 4, 20 strong, (–21, 5 days)	March 11–12, April 4–5, April 20	April 22–23, 2015 strong (–2 days)	April 24, 2015 (–1 day)	April 24, 2015 (–1 day)
2	M7.3 of December 05, 2015 Kodari, Nepal	April 29, 2015 strong (–14 days)	May 3, 2015 strong (–9 days)	May 2, 2015 strong (–10 days)	May 2–62,015 Moderate (–6 days)	No anomaly	May 11, 2015 (–1 day)	May 11, 2015 (–1 day)

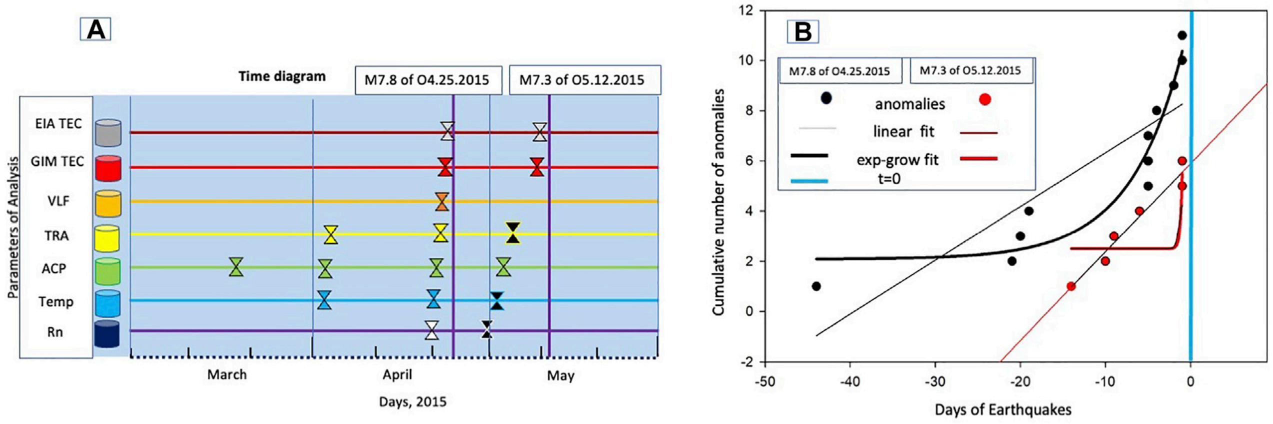

FIGURE 13 | (A) Fime diagram of multiparameter precursors analysis plotted with data shown in **Table 1**. The list of analyzed parameters **(bottom-up)**: Rn (Radon gas); Temp (Meteorological Atmospheric temperature); ACP (Atmospheric chemical potential); TRA (Thermal Radiation Anomaly); VLF (Vert low Frequency); GIM TEC (Global Ionospheric Model, Total Electronic Contents); EIA TEC (Equatorial Ionospheric Anomaly, Total Electronic Contents); **(B)** Cumulative number of all revealed precursory anomalies shown on Panel 13a (indicated here as black circles and lines associated with M7.8 of April 25, 2015, and with red circles and lines for M7.3 of May 12, 2015, as well.); Time origin t = O is the mainshock occurrence (blue line). With Red/Black, thick line curves show the exp-grow fit while Red/black is the straight line (thin lines). This graph confirms strong acceleration as the mainshocks approach both earthquakes.

the Dobrovolsky size. Only the latitudinal size over the earthquake preparation area should be considered (Klimenko et al., 2011, Kuo et al., 2014 Pulinets et al., 2014, 2021). The complex study of the synergetic behaviors of earthquake precursors helped to understand the direction of the process development leading to the critical state of the geosystems (Sornette and Sammis, 1995; Yasuoka et al., 2006,2009; De Santis et al., 2010; Pulinets 2011). As part of this study, the temporal behavior of earthquake precursors has been revealed as a sequencing pattern (Pulinets and Ouzounov, 2018), and the accelerated trend in the pre-earthquake anomalies has been identified (De Santis et al., 2017; De Santis et al., 2020). Here we demonstrate the temporal trend of the pre-earthquake and their accelerating pattern as the earthquake approaches (**Figure 13A**, **Figure 13B**). The cumulative number of all revealed precursory anomalies shown on the temporal trend is indicated in **Figure 13B** with black circles and lines associated with M7.8 of April 25, 2015, and red circles and lines for M7.3 of May 12, 2015, as well. The time origin (t = 0) is the mainshock occurrence (blue line). With Red/Black, thick line curves show the fit exponential -growth with Equation f = 2.0813 + 9.7166 *exp (0.1596 *x) for the black curve (April 5, 2015, earthquake) and with Equation f = 2.5 + 292.8693 *exp (4.5811 *x) for the red curve (May 12 Earthquake) while Red/black is the straight line (thin lines). This graph confirms strong acceleration as the mainshocks approaching both earthquakes. We see different patterns in the temporal (13a) and cumulative exponential -growth graphs (13b, Black vs. Red) before the mainshock (April 25, 2,915) and that before the major aftershock (May 12, 2015). The increased aftershock activities contributed to the difference in preparation time (shorter for the major aftershock) and into the much steeper pattern.

CONCLUSION

Our results show evidence that processes related to the Nepal earthquakes started at least in mid-March and were seen by satellite thermal observations (**Figure 6**; **Table 1**). On April 5, the atmospheric temperature had increased, which continued on April 23 with a thermal field build up on the top of the atmosphere (OLR) near the epicentral area (**Figure 4**). The ionosphere immediately reacts to these changes in the electric properties of the ground layer measured by GPS/TEC over the epicenter areas, which have been confirmed as a spatially localized increase in the dTEC on April 21 and 24 (Fig. 8,9,10,12). A similar scenario occurred for the M7.3 earthquake of May 12, 2015, with some delays in building the GPS/TEC, probably as a result of gas diffusion associated with the ground fracturing that occurred in the region during the first M7.8 earthquake. Ionospheric effects detected over the earthquake preparation zone, of the Nepal M7.8 earthquake, are very similar to those detected before the strong earthquakes in China (Wenchuan M7.9 earthquake on May 12, 2008, and Lushan M7.0 earthquake April 20, 2013) (Pulinets and Ouzounov, 2018). Configurations concerning the ionosphere morphology (position of the equatorial anomaly), is identical to the earthquakes that occurred in the Taiwanese region; because the Nepal earthquake's epicenter vertical projection is on the outer edge of the northern crest of the equatorial anomaly. So, except for the analysis of effect *per se*, we confirmed the results of previous studies on the ionospheric effects of strong earthquakes (Pulinets and Ouzounov, 2018; Ouzounov et al., 2018a).

Multi-parameter data recording atmospheric and ionospheric conditions during the M7.8 and M7.3 earthquakes in Nepal; using OLR monitoring on the top of the atmosphere, GIM-GPS/TEC maps, vertical TEC of lhaz GPS/GLONASS receiver in the region. The VLF/LF over NWC-KGZ and JJY-VAR paths for the first strong earthquake, and atmospheric temperature from ground measurements show the presence of anomalies in the atmosphere and ionosphere occurring consistently over the region near the 2015 Nepal earthquake epicenter. These results show evolutionally patterns in the appearance of pre-earthquake transient effects in the atmosphere and ionosphere, with a short time-lag from hours up to a few days (**Figure 13ab**; **Table 1**), and scalable with a magnitude estimate at their unusually far distance from the epicenter. The spatial characteristics of pre-earthquake anomalies were associated with the larger area but always inside the preparation-activation region estimated by Dobrovolsky-Bowman.

DATA AVAILABILITY STATEMENT

Not all the datasets presented in this article are readily available. Requests to access the datasets should be directed to ouzounov@chapman.edu.

AUTHOR CONTRIBUTIONS

DO, SP and VF provided the concepts of the manuscript. DO organized and wrote the manuscript with the help of SP, VF, ARo, MS and PT. MK, BND, ARy provided critical feedback. All authors contributed to the submitted version of the article.

ACKNOWLEDGMENTS

Thanks to ISC, USGS, EMSC for the seismic data. We thank NOAA/National Weather Service National Centers for Environmental Prediction Climate Prediction Center for providing OLR and surface temperature data. The IONEX data and RINEX data (for lhaz GPS/GLONASS receiver) in this study were acquired as part of NASA's Earth Science Data Systems and archived and distributed by the Crustal Dynamics Data Information System (CDDIS). The Dst index was provided by Kyoto World Data Center for Geomagnetism (http://wdc.kugi.kyoto- u.ac.jp/dstdir/index.html). DO and SP also thank ISSI (Bern) for support of the team "Multi-instrument Space-Borne Observations and Validation of the Physical Model of the Lithosphere-Atmosphere-Ionosphere-Magnetosphere Coupling" who initiated the research on the 2015 Nepalian earthquakes. BD thanks Abhishek Srivastava for his help in handling the data. Authors are grateful to all reviewers for their valuable comments and suggestions.

REFERENCES

Afraimovich, E. L., Astafyeva, E. I., Oinats, A. V., Yasukevich, Y. V., and Zhivetiev, I. V. (2008). A New conception to Track Solar Activity, *Ann. Geophys*. Global Electron Content, 26, 335–344.

Barr, R., Jones, D. L., and Rodger, C. J. (2000). ELF and VLF Radio Waves. *J. Atmos. Solar-Terrestrial Phys.* 62, 1689–1718. doi:10.1016/s1364-6826(00)00121-8

Biagi, P. F., Maggipinto, T., Righetti, F., Loiacono, D., Schiavulli, L., Ligonzo, T., et al. (2011).The European VLF/LF Radio Network to Search for Earthquake Precursors: Setting up and Natural/man-Made Disturbances, *Nat. Hazards Earth Syst. Sci.* 11, 333–341.doi:10.5194/nhess-11-333-2011

Bowman, D. D., Ouillon, G., Sammis, C. G., Sornette, A., and Sornette, D. (1998). An Observational Test of the Critical Earthquake Concept. *J. Geophys. Res.* 103 (24), 359372–359424. doi:10.1029/98jb00792

Boyarchuk, K. A., Karelin, A. V., and Nadolski, A. V. (2010). Statistical Analysis of the Chemical Potential Correction Value of the Water Vapor in Atmosphere on the Distance from Earthquake Epicenter. *Issues electro Mech.* 116, 39–46.

Cervone, G., Maekawa, S., Singh, R. P., Hayakawa, M., Kafatos, M., and Shvets, A. (2006). Surface Latent Heat Flux and Nighttime LF Anomalies Prior to the Mw=8.3 Tokachi-Oki Earthquake. *Nat. Hazards Earth Syst. Sci.* 6, 109–114. doi:10.5194/nhess-6-109-2006

Chen, S., Liu, M., Xing, L., Xu, W., Wang, W., Zhu, Y., et al. (2016). Gravity Increase before the 2015 Mw 7.8 Nepal Earthquake. *Geophys. Res. Lett.* 43. doi:10.1002/2015GL06659510.1002/2015gl066595

Contadakis, M. E. (2011). The European VLF/LF Radio Network to Search for Earthquake Precursors: Setting up and Natural/man-Made Disturbances. *Nat. Hazards Earth Syst. Sci.* 11, 333–341. doi:10.5194/nhess-11-333-2011

Davidenko, D. V., and Pulinets, S. A. (2019). Deterministic Variability of the Ionosphere on the Eve of Strong (M ≥ 6) Earthquakes in the Regions of Greece and Italy According to Long-Term Measurements Data. *Geomagn. Aeron.* 59 (4), 493–508. doi:10.1134/s001679321904008x

De Santis, A., Cianchini, G., Qamili, E., Frepoli, A., De Santis, A., Balasis, G., et al. (2010). Potential Earthquake Precursory Pattern from Space: The 2015 Nepal Event as Seen by Magnetic Swarm Satellites, *Earth Planet. Sci. Lett.*, The 2009 L'Aquila (Central Italy) Seismic Sequence as a Chaotic Process, Tectonophysics, 496 44–52, 461, 19–126.

De Santis, A., Cianchini, G., Marchetti, D., Piscini, A., Sabbagh, D., Perrone, L., et al. (2020). A Multiparametric Approach to Study the Preparation Phase of the 2019 M7.1 Ridgecrest (California, United States) Earthquake. *Front. Earth Sci.*, 8 doi:10.3389/feart.2020.540398

Deb, A., Gazi, M., and Barman, C. (2016). Anomalous Soil Radon Fluctuations - Signal of Earthquakes in Nepal and Eastern India Regions. *J. Earth Syst. Sci.* No. 8, 125. December, 1657–1665. doi:10.1007/s12040-016-0757-z

Dobrovolsky, I. P., Zubkov, S. I., Myachkin, V. I., and Miachkin, V. I. (1979). Estimation of the Size of Earthquake Preparation Zones. *Pageoph* 117, 1025–1044. doi:10.1007/bf00876083

Fu, C.-C., Lee, L.-C., Yang, T. F., Lin, C.-H., Chen, C.-H., Walia, V., et al. (2019). Gamma Ray and Radon Anomalies in Northern Taiwan as a Possible

Preearthquake Indicator Around the Plate Boundary, *Geofluids* ID 4734513, 2019, 1–14. doi:10.1155/2019/4734513

Fu, C.-C., Wang, P.-K., Lee, L.-C., Lin, C.-H., Chang, W.-Y., Giuliani, G., et al. (2015). Temporal Variation of Gamma Rays as a Possible Precursor of Earthquake in the Longitudinal Valley of Eastern Taiwan. *J. Asian Earth Sci.* 114, 362–372. doi:10.1016/j.jseaes.2015.04.035

Giuliani, G., Attanasio, A., and Fioravanti, G. (2013). Gamma Detectors for Continuous Monitoring of Radon. *J. Int. Environ. Appl. Sci.* 8 (4), 541–550.

Gruber, A., and Krueger, A. F. (1984). The Status of the NOAA Outgoing Longwave Radiation Data Set. *Bull. Amer. Meteorol. Soc.* 65, 958–962. doi:10.1175/1520-0477(1984)065<0958:tsotno>2.0.co;2

Harris, G. (2015). *Everest Climbers Are Killed as Nepal Quake Sets off Avalanche*. New York: NY Times.

Hayakawa, M. (2013). *Earthquake Prediction Studies: Seismo Electromagnetics*. Tokyo, Japan: TERRAPUB, 168.

Hayakawa, M. (2015). *Earthquake Prediction with Radio Techniques*. Singapore: Wiley, 294.

Hayakawa, M., Kasahara, Y., Nakamura, T., Muto, F., Horie, T., Maekawa, S., et al. (2010). A Statistical Study on the Correlation between Lower Ionospheric Perturbations as Seen by Subionospheric VLF/LF Propagation and Earthquakes. *J. Geophys. Res.* 115, a–n. doi:10.1029/2009JA015143

Hõrrak, U. (2001). "Contribution of Air Ion Mobility Classes to Air Conductivity,"*Dissertationes Geophysicales Universitatis Tartuensis*. in *Air Ion Mobility Spectrum at a Rural Area* (Tartu, Estonia: Tartu University), 15, 81.

Karastathis, V. K., Eleftheriou, G., Tselentis, A., Tsinganos, K., Kafatos, M., Ouzounov, D., et al. (2019). Real-time Monitoring of Soil Radon Concentration at Seismically Active Areas in Greece in -18, 27th IUGG Assembly (Montreal Canada.

Klimenko, M. V., Klimenko, V. V., Zakharenkova, I. E., Pulinets, S. A., Zhao, B., and Tsidilina, M. N. (2011). Formation Mechanism of Great Positive TEC Disturbances Prior to Wenchuan Earthquake on May 12, 2008. *Adv. Space Res.* 48, 488–499. doi:10.1016/j.asr.2011.03.040

Kolvankar, V., More, S., and Thakur, N. (2010). Earth Tides and Earthquakes. *New Concepts Glob. Tectonics Newsl.* 57, 54–84.

Kon, S., Nishihashi, M., and Hattori, K. (2010). Ionospheric Anomalies Possibly Associated with M>=6.0 Earthquakes in the Japan Area during 1998-2010: Case Studies and Statistical Study. *J. Asian Earth Sci.* 41 (4-5), 410–420. doi:10.1016/j.jseases.2010.10.005

Kuo, C. L., Lee, L. C., and Huba, J. D. (2014). An Improved Coupling Model for the Lithosphere-Atmosphere-Ionosphere System. *J. Geophys. Res. Space Phys.* 119, 3189–3205. doi:10.1002/2013ja019392

Li, W., Guo, J., Yue, J., Yang, Y., Li, Z., and Lu, D. (2016). Contrastive Research of Ionospheric Precursor Anomalies between Calbuco Volcanic Eruption on April 23 and Nepal Earthquake on April 25, 2015. *Adv. Space Res.* 57 (10), 2141–2153. doi:10.1016/j.asr.2016.02.014

Liu, J. Y., Chuo, Y. J., Shan, S. J., Tsai, Y. B., Chen, Y. I., Pulinets, S. A., et al. (2004). Pre-earthquake Ionospheric Anomalies Registered by Continuous GPS TEC Measurements. *Ann. Geophys.* 22, 1585–1593. doi:10.5194/angeo-22-1585-2004

Maekawa, S., Horie, T., Yamauchi, T., Sawaya, T., Ishikawa, M., Hayakawa, M., et al. (2006). A Statistical Study on the Effect of Earthquakes on the Ionosphere, Based on the Subionospheric LF Propagation Data in Japan. *Ann. Geophys.* 24, 2219–2225. doi:10.5194/angeo-24-2219-2006

Marchitelli, V., Harabaglia, P., TroiseDe Natale, C. G., and De Natale, G. (2020). On the Correlation between Solar Activity and Large Earthquakes Worldwide. *Sci. Rep.* 10, 11495. doi:10.1038/s41598-020-67860-3

Maurya, A. K., Venkatesham, K., Tiwari, P., Vijaykumar, K., Singh, R., Singh, A. K., et al. (20162016). The 25 April 2015 Nepal Earthquake: Investigation of Precursor in VLF Subionospheric Signal. J. *Geophys. Res. Space Phys.* 121. doi:10.1002/2016JA022721

Mehta, A., and Susskind, J. (1999). Outgoing Longwave Radiation from the TOVS Pathfinder Path A Data Set. *J. Geophys. Res.* 104, , 1999 NO. D10, 12193–12212. doi:10.1029/1999jd900059

Němec, F., Santolík, O., Parrot, M., and Berthelier, J. J. (2008). Spacecraft Observations of Electromagnetic Perturbations Connected with Seismic Activity. *Geophys. Res. Lett.* 35, L05109. doi:10.1029/2007GL032517

Ohring, G., and Gruber, A. (1982). Satellite Radiation Observations and Climate Theory. *Adv. Geophys.* 25, 237–304.

Oikonomou, C., Haralambous, H., and Muslim, B. (2016). Investigation of Ionospheric TEC Precursors Related to the M7.8 Nepal and M8.3 Chile Earthquakes in 2015 Based on Spectral and Statistical Analysis. *Nat. Hazards* 83, 97–116. doi:10.1007/s11069-016-2409-7

Ouzounov, D., Bryant, N., Logan, T., Pulinets, S., and Taylor, P. (2006). Satellite thermal IR Phenomena Associated with Some of the Major Earthquakes in 1999-2003. *Phys. Chem. Earth, Parts A/B/C* 31, 154–163. doi:10.1016/j.pce.2006.02.036

Ouzounov, D., Liu, D., Chunli, K., Cervone, G., Kafatos, M., and Taylor, P. (2007). Outgoing Long Wave Radiation Variability from IR Satellite Data Prior to Major Earthquakes. *Tectonophysics* 431, 211–220. doi:10.1016/j.tecto.2006.05.042

Ouzounov, D., Pulinets, S., and Davidenko, D. (2015). Revealing Pre- Earthquake Signatures in Atmosphere and Ionosphere Associated with 2015 M7.8 and M7.3 Events in NepalPreliminary Results. Available at: https://arxiv.org/abs/1508.01805.

Ouzounov, D., Pulinets, S., Hattori, K., and Taylor Ed's, P. (2018a). *Pre-Earthquake Processes: A Multi-Disciplinary Approach to Earthquake Prediction Studies*. American Geophysical UnionJohn Wiley & Sons, Inc., 385. Available at: https://agupubs.onlinelibrary.wiley.com/doi/book/10.1002/9781119156949.

Ouzounov, D., Pulinets, S., Kafatos, M. C., Taylor, P., Ouzounov, D., Pulinets, S., et al. (2018b). "Thermal Radiation Anomalies Associated with Major Earthquakes," in *The Book "Pre-earthquake Processes: A Multidisciplinary Approach to Earthquake Prediction Studies", Geophysical Monograph 234. Multiparameter Assessment of Pre-Earthquake Atmospheric Signals; in the Book "Pre-earthquake Processes: A Multidisciplinary Approach to Earthquake Prediction Studies", Geophysical Monograph 234.* Editors D. Ouzounov, S. Pulinets, K. Hattori, and P. Taylor (AGU & WileyAGU & Wiley), 259339–274357. doi:10.1002/9781119156949.ch15

Ouzounov, D., Pulinets, S., Romanov, A., Romanov, A., Jr., Tsybulya, K., Davidenko, D., et al. (2011c). Atmosphere-ionosphere Response to the M9 Tohoku Earthquake Revealed by Multi-Instrument Space-Borne and Ground Observations: Preliminary Results. *Earthq Sci.* 24, 557–564. doi:10.1007/s11589-011-0817-z

Parrot, M. (2009).Anomalous Seismic Phenomena: View from Space, in *The Book: Electromagnetic Phenomena Associated with Earthquakes* (Ed. by M. Hayakawa), Transworld Research Network, 205–233.

Prakash, R., Singh, R. K., and Srivastava, H. N. (2015). Outgoing Long Wave Radiation (OLR) from Kalpana Satellite Prior to Nepal Earthquake of April 25, 2015 IJRET: *Int. J. Res. Eng. Tech. eISSN* 2319-1163, 2321–7308

Pulinets, O. D. S., Hattori, K. M., and Kafatos, P. Taylor. (2011b). "Atmospheric Signals Associated with Major Earthquakes. A Multi-Sensor Approach," in *The Book Frontier of Earthquake Short-Term Prediction Study*. Editor M. Hayakawa (Springer- Nature: Japan), 510–531.

Pulinets, S., Ouzounov, D., Karelin, A., and Davidenko, D. (2018). "Lithosphere–Atmosphere–Ionosphere–Magnetosphere Coupling—A Concept for Pre-Earthquake Signals Generation," in *The Book "Pre-earthquake Processes: A Multidisciplinary Approach to Earthquake Prediction Studies", Geophysical Monograph 234.* Editors D. Ouzounov, S. Pulinets, K. Hattori, and P. Taylor (Bristol, UK: AGU & Wiley), 79–99.

Pulinets, S. A., and Boyarchuk, K. A. (2004). *Ionospheric Precursors of Earthquakes*. Berlin, Heidelberg, New York: Springer, 315.

Pulinets, S. A., Kotsarenko, A. N., Ciraolo, L., and Pulinets, I. A. (2007). Special Case of Ionospheric Day-To-Day Variability Associated with Earthquake Preparation. *Adv. Space Res.* 39, 970–977. doi:10.1016/j.asr.2006.04.032

Pulinets, S. A., Ouzounov, D., Karelin, A. V., Boyarchuk, K. A., and Pokhmelnykh, L. A. (2006). The Physical Nature of Thermal Anomalies Observed before Strong Earthquakes. *Phys. Chem. Earth, Parts A/B/C* 31, 143–153. doi:10.1016/j.pce.2006.02.042

Pulinets, S., and Davidenko, D. (2014). Ionospheric Precursors of Earthquakes and Global Electric Circuit. *Adv. Space Res.* 53 (5), 709–723. doi:10.1016/j.asr.2013.12.035

Pulinets, S., Ouzounov, D., Davidenko, D., and Budnikov, P. (2020). Principles of Organizing Earthquake Forecasting Based on Multiparameter Sensor-WEB Monitoring Data. *E3s Web Conf.* 196, 03004. doi:10.1051/e3sconf/202019603004

Pulinets, S., and Ouzounov, D. (2011). Lithosphere–atmosphere–ionosphere Coupling (LAIC) Model–A Unified Concept for Earthquake Precursors

Validation. *J. Asian Earth Sci.* 41 (4), 371–3822. doi:10.1016/j.jseaes.2010.03.005

Pulinets, S., and Ouzounov, D. (2018). *The Possibility of Earthquake Forecasting: Learning from Nature*. Bristol, UK: Institute of Physics Books, IOP Publishing, 168pp.

Pulinets, S. (2011). The Synergy of Earthquake Precursors. *Earthq Sci.* 24, 535–548. doi:10.1007/s11589-011-0815-1

Pulinets, S., Tsidilina, M., Ouzounov, D., and Davidenko, D. (2021). From Hector Mine M7.1 to Ridgecrest M7.1 Earthquake. A Look from a 20-Year Perspective. *Atmosphere* 12, 262. doi:10.3390/atmos12020262

Qi, Y., Wu, L., Ding, Y., and Mao, W. (2020). Microwave Brightness Temperature Anomalies Associated with the 2015 Mw 7.8 Gorkha and Mw 7.3 Dolakha Earthquakes in Nepal. *IEEE Trans. Geosci. Remote Sensing* 2020 (99), 1–11. doi:10.1109/TGRS.2020.3036079

Rozhnoi, A., Solovieva, M., Levin, B., Hayakawa, M., and Fedun, V. (2014). Meteorological Effects in the Lower Ionosphere as Based on VLF/LF Signal Observations. *Nat. Hazards Earth Syst. Sci.* 14, 2671–2679. doi:10.5194/nhess-14-2671-2014

Rozhnoi, A., Solovieva, M., Molchanov, O., Schwingenschuh, K., Boudjada, M., Biagi, P. F., et al. (2009). Anomalies in VLF Radio Signals Prior the Abruzzo Earthquake (M=6.3) on 6 April 2009. *Nat. Hazards Earth Syst. Sci.* 9, 1727–1732. doi:10.5194/nhess-9-1727-2009

Rozhnoi, A., Solovieva, M., Parrot, M., Hayakawa, M., Biagi, P.-F., Schwingenschuh, K., et al. (2015). VLF/LF Signal Studies of the Ionospheric Response to strong Seismic Activity in the Far Eastern Region Combining the DEMETER and Ground-Based Observations. *Phys. Chem. Earth, Parts A/B/C* 85-86, 141–149. doi:10.1016/j.pce.2015.02.005

Rozhnoi, A., Solovieva, M. S., and Hayakawa, M. (2013). "VLF/LF Signals Method for Searching of Electromagnetic Earthquake Precursors Earthquake Prediction Studies," in *Book Seismo Electromagnetics, TERRAPUB* (Tokyo: Masashi Hayakawa), 31–48.

Rozhnoi, A., Solovieva, M. S., Molchanov, O. A., and Hayakawa, M. (2004). Middle Latitude LF (40 kHz) Phase Variations Associated with Earthquakes for Quiet and Disturbed Geomagnetic Conditions. *Phys. Chem. Earth, Parts A/B/C* 29, 589–598. doi:10.1016/j.pce.2003.08.061

Scholz, C. H., Sykes, L. R., and Aggarwal, Y. P. (1973). Earthquake Prediction: A Physical Basis. *Science* 181, 4102803–4102810. doi:10.1126/science.181.4102.803

Shah, M., and Jin, S. (2016), Pre-seismic thermal Anomalies of the 2015 Mw = 7:8 Gorkha (Nepal) Earthquake from MODIS Surface Temperature. *Progress in Electromagnetic Research Symposium*. Shanghai, China: PIERS), 4755–4758. doi:10.1109/PIERS.2016.7735743

Sornette, D., and Sammis, C. G. (1995). Complex Critical Exponents from Renormalization Group Theory of Earthquakes: Implications for Earthquake Predictions. *J. Phys. France* 5, 607–619. doi:10.1051/jp1:1995154

Tramutoli, V., Aliano, C., Corrado, R., Filizzola, C., Genzano, N., Lisi, M., et al. (2013). On the Possible Origin of Thermal Infrared Radiation (TIR) Anomalies in Earthquake-Prone Areas Observed Using Robust Satellite Techniques (RST). *Chem. Geology.* 339, 157–168. doi:10.1016/j.chemgeo.2012.10.042

Tramutoli, V., Cuomo, V., Filizzola, C., Pergola, N., and Pietrapertosa, C. (2005). Assessing the Potential of thermal Infrared Satellite Surveys for Monitoring Seismically Active Areas: The Case of Kocaeli (İzmit) Earthquake, August 17, 1999. *Remote Sensing Environ.* 96, 409–426. doi:10.1016/j.rse.2005.04.006

Tronin, A. A., Hayakawa, M., and Molchanov, O. A. (2002). Thermal IR Satellite Data Application for Earthquake Research in Japan and China. *J. Geodynamics* 33, 519–534. doi:10.1016/s0264-3707(02)00013-3

Wu, H.-C., and Tikhonov, I. N. (2014). Jet Streams Anomalies as Possible Short-Term Precursors of Earthquakes with M>6.0. *Res. Geophys.* 4, 4939. doi:10.4081/rg.2014.4939

Xiong, P., Shen, X. H., Bi, Y. X., Kang, C. L., Chen, L. Z., Jing, F., et al. (2010). Study of Outgoing Longwave Radiation Anomalies Associated with Haiti Earthquake. *Nat. Hazards Earth Syst. Sci.* 10, 2169–2178. doi:10.5194/nhess-10-2169-2010

Yasuoka, Y., Igarashi, G., Ishikawa, T., Tokonami, S., and Shinogi, M. (2006). Evidence of Precursor Phenomena in the Kobe Earthquake Obtained from Atmospheric Radon Concentration. *Appl. Geochem.* 21, 1064–1072. doi:10.1016/j.apgeochem.2006.02.019072

Yasuoka, Y., Kawada, Y., Nagahama, H., Omori, Y., Ishikawa, T., Tokonami, S., et al. (2009). Preseismic Changes in Atmospheric Radon Concentration and Crustal Strain. *Phys. Chem. Earth, Parts A/B/C* 34, 431–434. doi:10.1016/j.pce.2008.06.005

Zhou, Y., Yang, J., Zhu, F., Su, F., HuZhai, L. W., and Zhai, W. (2017). Ionospheric Disturbances Associated with the 2015 M7.8 Nepal earthquake7.8 Nepal Earthquake. *Geodesy and Geodynamics* 8 (4), 221–228. doi:10.1016/j.geog.2017.04.004

Zolotov, O. V. (2015). *Earthquake Effects in Variations of the Total Electron Content*. Murmansk, Russia: Murmansk Arctic State University, 146.

Zoran, M., Savastru, R., Savastru, D., Chitaru, C., Baschir, L., and Tautan, M. (2012). Monitoring of Radon Anomalies in South-Eastern Part of Romania for Earthquake Surveillance. *J. Radioanal. Nucl. Chem.* 293, 769–781. doi:10.1007/s10967-012-1780-4

Conflict of Interest: The authors declare that the research was conducted in the absence of any commercial or financial relationships that could be construed as a potential conflict of interest.

frontiers in Earth Science

ORIGINAL RESEARCH
published: 20 December 2021
doi: 10.3389/feart.2021.659296

Flood Susceptibility Modeling in a Subtropical Humid Low-Relief Alluvial Plain Environment: Application of Novel Ensemble Machine Learning Approach

Manish Pandey[1,2]*, *Aman Arora*[1,3,4]*, *Alireza Arabameri*[5], *Romulus Costache*[6,7], *Naveen Kumar*[8], *Varun Narayan Mishra*[9], *Hoang Nguyen*[10,11], *Jagriti Mishra*[12,13], *Masood Ahsan Siddiqui*[4], *Yogesh Ray*[14], *Sangeeta Soni*[15] and *UK Shukla*[16]

[1]University Center for Research and Development (UCRD), Chandigarh University, Mohali, India, [2]Department of Civil Engineering, University Institute of Engineering, Chandigarh University, Mohali, India, [3]Bihar Mausam Seva Kendra, Planning and Development Department, Government of Bihar, Patna, India, [4]Department of Geography, Faculty of Natural Sciences, Jamia Millia Islamia, New Delhi, India, [5]Department of Geomorphology, Tarbiat Modares University, Tehran, Iran, [6]Department of Civil Engineering, Transilvania University of Brasov, Brasov, Romania, [7]Danube Delta National Institute for Research and Development, Tulcea, Romania, [8]Physical Research Laboratory, Ahmedabad, India, [9]Centre for Climate Change and Water Research, Suresh Gyan Vihar University, Jaipur, India, [10]Department of Surface Mining, Mining Faculty, Hanoi University of Mining and Geology, Hanoi, Vietnam, [11]Innovations for Sustainable and Responsible Mining (ISRM) Group, Hanoi University of Mining and Geology, Hanoi, Vietnam, [12]Civil Engineering Research Institute for Cold Region, Sapporo, Japan, [13]Institute of Engineering and Technology, GLA University, Mathura, India, [14]National Centre for Polar and Ocean Research, Ministry of Earth Sciences, Government of India, Goa, India, [15]School of Computer and Systems Sciences, Jaipur National University, Jaipur, India, [16]Center for Advanced Study in Geology, Institute of Science, Banaras Hindu University, Varanasi, India

Edited by:
Dimitar Ouzounov,
Chapman University, United States

Reviewed by:
Nguyen Thi Thuy Linh,
Thuyloi University, Vietnam
Saeid Janizadeh,
Tarbiat Modares University, Iran

***Correspondence:**
Manish Pandey
manish07sep@gmail.com
Aman Arora
aman.jmi01@gmail.com

Specialty section:
This article was submitted to Environmental Informatics and Remote Sensing,
a section of the journal Frontiers in Earth Science

Received: *01 February 2021*
Accepted: *28 October 2021*
Published: *20 December 2021*

Citation:
Pandey M, Arora A, Arabameri A, Costache R, Kumar N, Mishra VN, Nguyen H, Mishra J, Siddiqui MA, Ray Y, Soni S and Shukla UK (2021) Flood Susceptibility Modeling in a Subtropical Humid Low-Relief Alluvial Plain Environment: Application of Novel Ensemble Machine Learning Approach.
Front. Earth Sci. 9:659296.
doi: 10.3389/feart.2021.659296

This study has developed a new ensemble model and tested another ensemble model for flood susceptibility mapping in the Middle Ganga Plain (MGP). The results of these two models have been quantitatively compared for performance analysis in zoning flood susceptible areas of low altitudinal range, humid subtropical fluvial floodplain environment of the Middle Ganga Plain (MGP). This part of the MGP, which is in the central Ganga River Basin (GRB), is experiencing worse floods in the changing climatic scenario causing an increased level of loss of life and property. The MGP experiencing monsoonal subtropical humid climate, active tectonics induced ground subsidence, increasing population, and shifting landuse/landcover trends and pattern, is the best natural laboratory to test all the susceptibility prediction genre of models to achieve the choice of best performing model with the constant number of input parameters for this type of topoclimatic environmental setting. This will help in achieving the goal of model universality, i.e., finding out the best performing susceptibility prediction model for this type of topoclimatic setting with the similar number and type of input variables. Based on the highly accurate flood inventory and using 12 flood predictors (FPs) (selected using field experience of the study area and literature survey), two machine learning (ML) ensemble models developed by bagging frequency ratio (FR) and evidential belief function (EBF) with classification and regression tree (CART), CART-FR and CART-EBF, were applied for flood susceptibility zonation mapping. Flood and non-flood points randomly generated using flood inventory have been apportioned in 70:30 ratio for training and validation of the ensembles. Based on the evaluation performance using threshold-independent evaluation statistic, area under receiver operating characteristic (AUROC) curve, 14 threshold-dependent evaluation metrices, and seed cell area index (SCAI) meant for assessing different aspects of ensembles, the study suggests that CART-EBF (AUC_{SR} = 0.843; AUC_{PR} = 0.819) was a better performant than CART-FR (AUC_{SR} = 0.828; AUC_{PR} = 0.802). The variability in performances of these novel-advanced ensembles and their comparison with results of other published models espouse the need of testing these as well as other genres of susceptibility models in other topoclimatic environments also. Results of this study are important for natural hazard managers and can be used to compute the damages through risk analysis.

Keywords: CART, FR, EBF, ensembles, Middle Ganga Plain, Ganga Foreland Basin

1 INTRODUCTION

Floods in the changing climatic and anthropogenic scenario over the Holocene period have been impacting the living conditions of humans (Macklin and Lewin, 2003). Owing to the recurring floods and their devastating worldwide societal implications, the United Nations Sustainable Development Goals (UNSDGs) incorporate flood risk management and mitigation as one of its principal aims (UNSDG, 2013). Depending upon the geological, hydrological, climatic, and societal factors, floods have been variously classified (Sikorska et al., 2015). However, the widely accepted definition of flood encompasses the views of hydrologists, hazard managers, and sociologists, i.e., floods occur when the rise of water levels, caused by meteorological, hydrological, geomorphic, anthropological, and societal factors, can result in inundated areas which otherwise remain dry thereby causing loss of life, agriculture (including livestock), and property (Hubbart and Jones, 2009). The state of Bihar in India faces annual flooding incurring a loss of life, property, and agriculture (livestock included), in the tune of approximately ₹146,301.71 million (CWC, 2018). Previous studies have suggested that the Ganga River Basin (GRB) in the Himalayan Foreland Basin (HFB) is currently under active tectonic regime (Kumar, 2020). It is experiencing subsidence due to subsurface structural activities accentuating floods occurring due to various reasons (Shukla et al., 2012; Gupta et al., 2014). Apart from tectonically induced ground subsidence, landuse/landcover (LULC) induced (Kumar et al., 2018), climate change-induced (Arora et al., 2021a), river embankment breach induced (Bhatt et al., 2010), etc., factors cause frequent flooding in the GRB. Advancement in remote sensing technology has proved to be helpful in monitoring and prediction of the flooding (Jiménez-Jiménez et al., 2020). Many aspects of floods are quantifiable using continuously growing remote sensing satellite technology and their output products (Plaza et al., 2009).

The recent developments in remote sensing satellite technologies and sensors (Toth and Jóźków, 2016; Zhang X. et al., 2019; Han et al., 2019; Weiss et al., 2020; Yang et al., 2021), rise in number of available platforms for the satellite data access (Boerner, 2007; Rizzato et al., 2020), and improvements in other low altitude geospatial technologies like lightweight unmanned aerial vehicles (UAVs) (Rizzato et al., 2020) have aided to ease the monitoring and analysis of natural hazards and disasters (Gillespie et al., 2007) at various spatial and temporal scales. Since monitoring floods in urban settings is difficult due to narrow open space among the concrete jungles, use of UAVs immensely helps to monitor and quantify the flooded and flood-induced damages (Yalcin, 2018). Challenges, advantages, and disadvantages of using UAVs for such purposes in urban settings are discussed in detailed fashion in the literature (Feng et al., 2015). Freely available remote sensing products such as optical, radar, and hyperspectral datasets are more popular in studies quantifying different aspects of natural hazards (Lin and Yan, 2016; Yao et al., 2019). These remote sensing datasets are used to monitoring of current flood events (Ban et al., 2017) and to compute different set of variables that are entered as input in flood prediction models (Arora et al., 2021a).

In recent years, modeling development has attracted the attention of many researchers in various scientific disciplines (Cheng and Han, 2016; He et al., 2018; Chen et al., 2021). Multi-criteria decision-making (MCDM) (Opricovic and Tzeng, 2004; Abdullahi et al., 2015; De Brito and Evers, 2016; Turskis et al., 2019) and artificial intelligence (Suman et al., 2016; Guikema, 2020; Sun et al., 2020; Tan et al., 2021) models are very popular among researchers. There are a wide variety of flood inundation prediction models, e.g., statistical models including bivariate and multivariate (Tehrany et al., 2014), machine learning models, multi-criteria decision-making (MCDM) (Nachappa et al., 2020), and an ensemble of two or more models (Arabameri et al., 2020c). Guerriero et al. (2018) have discussed a more exhaustive discussion of existing methods on the flood inundation models prediction with their pros and cons. Also, new models are being devised and tested regularly (Razavi Termeh et al., 2018). However, different flood susceptibility models perform with different levels of accuracy and sensitivity (Bui et al., 2018) giving rise to inconsistency in model performances in different environmental settings. Currently, there appears to be a challenging task to find a model with a high level of predictability in diverse topographic and climatic settings. This task requires rigorous testing of various flood susceptibility prediction index (FSPI) models in different topoclimatic settings like low-relief floodplain environment with humid subtropical monsoon climate (Hong et al., 2018b) and mountainous high-relief rugged terrain with the semiarid climatic regime (Ahmadlou et al., 2018).

As pointed out in the previous paragraph, different types of susceptibility models accrue differences in accuracy and sensitivity in a similar or same topoclimatic setting. Furthermore, new models

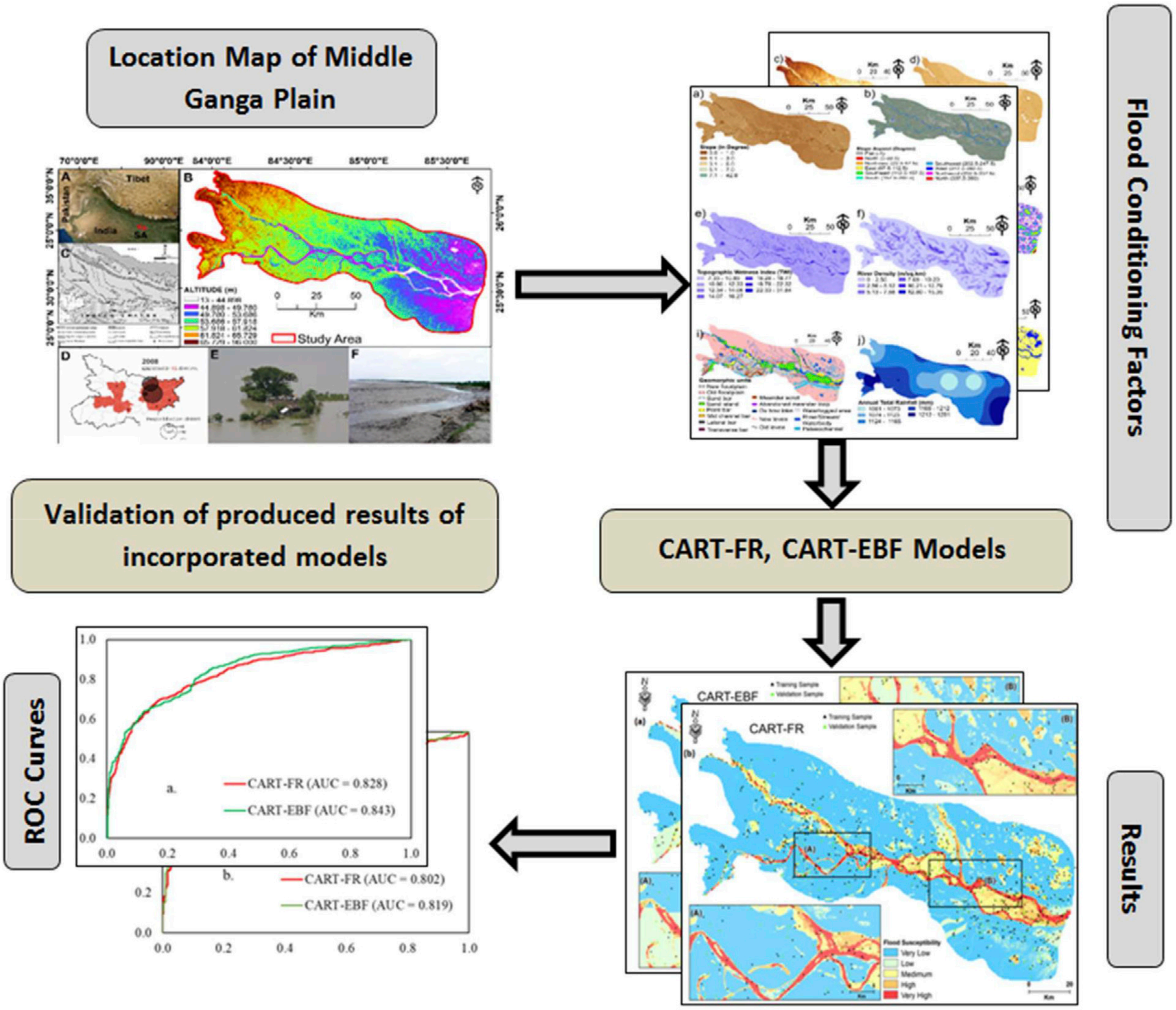

GRAPHICAL ABSTRACT

are constantly being developed and tested to achieve a better level of accuracy and sensitivity and to overcome disadvantages arising out of different factors discussed by researchers (Reichenbach et al., 2018). Additionally, the need to develop new models and test the previously developed ones in different settings is clearly visible in the hazard modeling community in the present decade (Panahi et al., 2021). To further this current practice among the hazard modeling community, we, in this study, present two new ensemble models and test their performance for a typical topoclimatic setting. We test the performance of one recently developed novel-advanced ensemble model viz. CART-FR and one new ensemble model (CART-EBF) developed for the first time by us to predict flood occurrences and delineate flood susceptibility zones in a region of the Middle Ganga Plain environment. We apply 12 widely used flood predictors namely geomorphology, altitude, slope, aspect, plan curvature, topographic wetness index (TWI), drainage density, distance to the river, distance from the road, soil type, annual rainfall, and landuse/landcover (LULC). This study also attempts to assess the contribution significance and efficiency of different flood predictors by using information gain (IG) method, through analysis of weightage rankings assigned by various ensemble models. This flood predictor ranking may assist flood hazard managers during the policy formulation and mitigation measures implementation.

2 MATERIALS AND METHODS

2.1 Study Area

The part of the Middle Ganga Plain (MGP) investigated for flood susceptibility prediction, covering an area of ~10,138.5 km^2, in this study is located in between the Upper and the Lower Ganga Plains (**Figure 1**). It lies between latitude 25°14′48.00″N–26°14′24.60″N and longitude 83°51′46.19″E–85°45′3.25″E. About 55.4% of the GRB (Singh et al., 2007) is covered with a thick layer of alluvium brought and deposited by a dense network of streams. There are a number of tectonic structures, both in the deep basement and at the

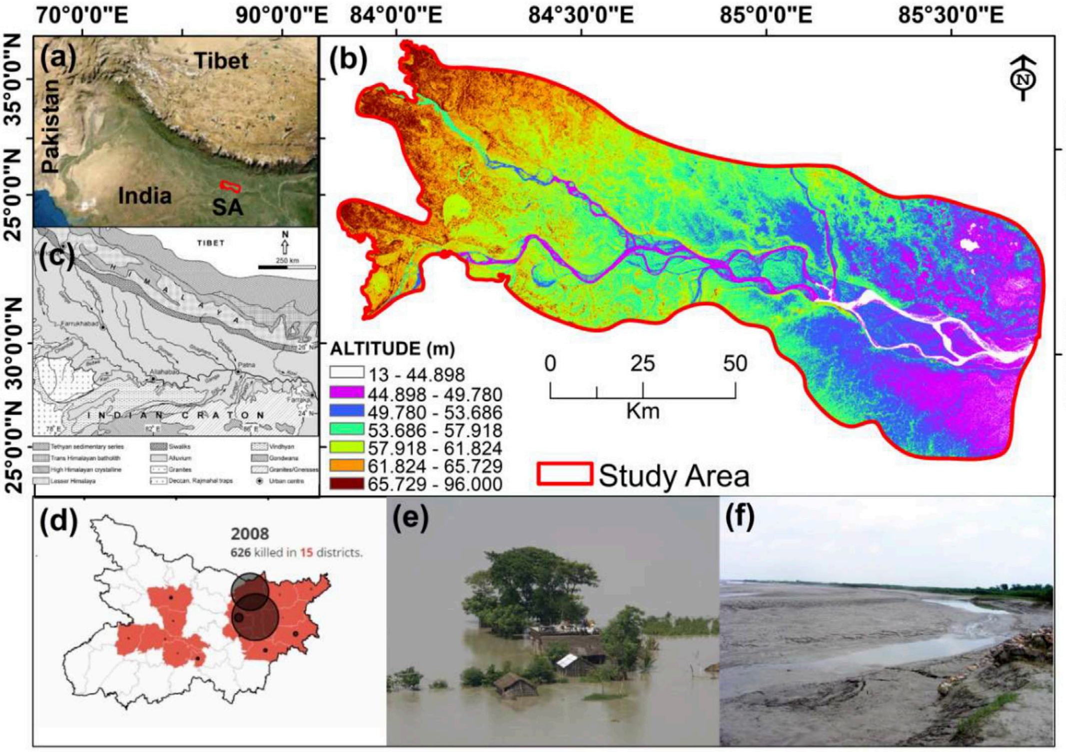

FIGURE 1 | Location of the study area. **(A)**: Location of the studied area marked on the map of India. It also shows Tibet and Pakistan in the northeastern and northwestern sides respectively. **(B)**: Elevation of the study area classified using Natural Break (NB) method with input from SRTM 30m digital elevation model. **(C)**: broad beological profile of the study area and its surroundings. This section also shows major drainages of the Ganga River Basin of which our study area is a part. **(D)** Loss of lives due to 2008 Bihar floods in 15 districts is shown here. **(E,F)** are photographs of the flood situation in the study area. **(E,F)**: field photographs captured in the study area caused by 2008-Bihar flood.

surface which produce surface geomorphic markers revealing continuous active tectonic activity in MGP (Singh, 1996). The Ganga plain is also undergoing subsidence as a result of tectonics as well as excess groundwater depletion (Sahu et al., 2010). The study area is drained by several tributaries including Gomti River, Ghaghara River, Gandaki river, and Kosi river (these tributaries join the Ganga from the left bank); and Yamuna River, Son River, and Punpun river (these join the right bank of the Ganga). This densely populated area has been on the constant radar of national disaster management agencies for very long.

GRB experiences a humid subtropical climate featuring four seasons—the winter season (January–March), summers (April–May), monsoon (June–September), and post-monsoon (OctoberDecember) (Dimri, 2019). According to the Indian Meteorological Department (IMD), the average annual mean, maximum, and minimum temperature experienced in GRB in 35 years (1969–2004) are 24.82°C, 31.22°C, and 18.44°C, respectively.

The MGP records average annual rainfall on the order of 100–120 cm, three-quarters of which is downpoured within 4 months long monsoon season (Trivedi et al., 2019). The influence of western disturbances (WDs) on Indian monsoonal rainfall is well-documented in the form of sporadic rains and hailstorms during the southward migration of intertropical convergence in winter months (Dimri and Chevuturi, 2016). The seasonal variability in the Ganga River discharge has led hydrologists to term river discharge of Indian River Network systems associated with monsoon systems such as monsoonal discharge, post-monsoonal discharge, summer or winter monsoon discharge (Gupta, 1984). The monsoon season river discharge in the Ganga River increases by 50–100 times due to heavy rainfall downpour.

2.2 Data and Methodology

Data preparation is the first step in scientific works (Feng et al., 2020). **Table 1** provides the datasets used for preparing the flood predictors derived from Shuttle Radar Topography Mission (SRTM) digital elevation model (DEM) (30 m resolution), and other data sources, and flood inventory computed from Landsat-5 thematic mapper (TM) satellite imagery. The flood occurrence susceptibility modeling flow diagram shown in **Figure 2** suggests that this research work has been accomplished in the follwing six steps: 1) obtain least cloudy Landsat 5 TM images of the study area from National Aeronautical Space Agency's (NASA's) earth explorer portal (https://earthexplorer.usgs.gov/) and generate the flood polygon for the "2008 Bihar Flood" event using normalized difference water index (NDWI) thresholding. The input datasets used in this study have been discussed in detail in **Section 2** and its subsections in the study by Arora et al. (2021b), 2) create the flood inventory and the flood predictors, 3) generate flood and

TABLE 1 | Satellite and DEM data characteristic details used in the study.

SN	Image scene ID	CC	Event time	Acquisition date	Processing level	Spatial reference
1	LT05_L1TP_141042_20080528_20161031_01_T1	SCC 0% LCC 0%	Preflood	28-05-2008	L1TP	Projection: UTM
2	LT05_L1TP_141042_20081019_20161029_01_T1	SCC 1% LCC 1%	Post Flood	19-10-2008	L1TP	Datum & Spheroid: WGS84
3	LT05_L1TP_141042_20080901_20161029_01_T1	SCC 9% LCC 9%	During Flood	01-09-2008	L1TP	—
4	SRTM v4 DEM	—	—	11–22 Feb 2000	—	Zone: 44N

CC, cloud cover; SCC, scene cloud cover; LCC, land cloud cover.

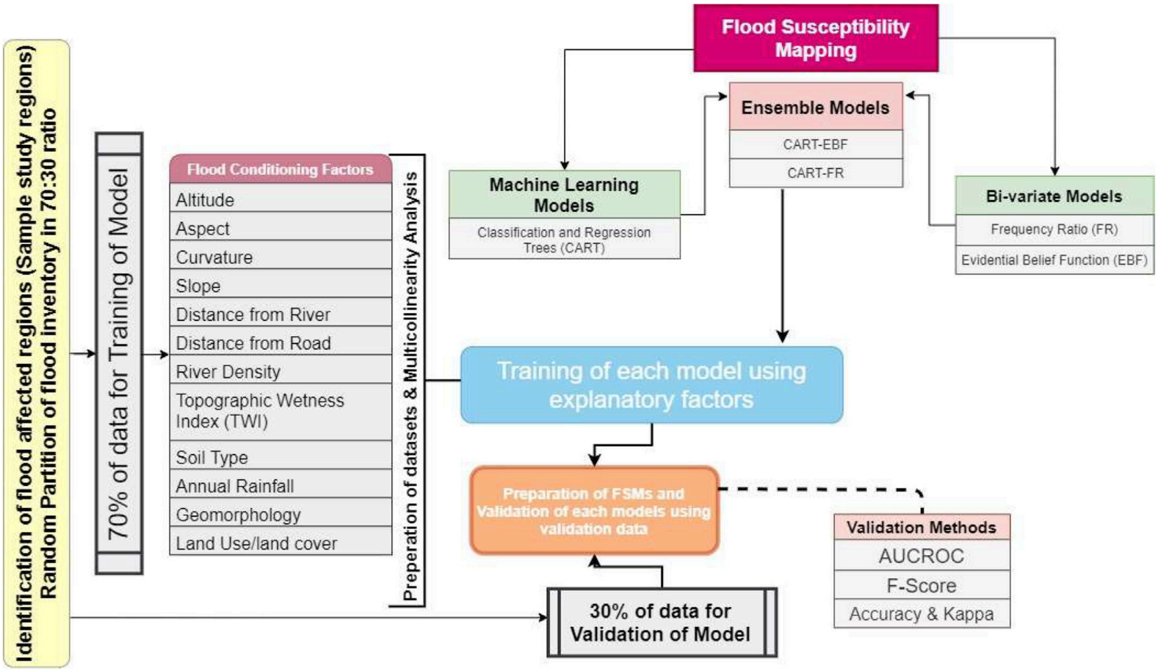

FIGURE 2 | Flow diagram showing step-by-step methodology employed in this study.

non-flood points for model training and validation, 4) test the conditioning factors of flood and non-flood points for multicollinearity, and also, apply the feature selection methods on all the flood predictors for a proper understanding of the suitability and contribution potential of all the factors involved. Here, we have applied information gain, 5) calculate the weightage of all the flood predictors using bivariate frequency ratio and evidential belief function models; also, devise the ensemble models with MLP, and CART machine learning models; and 6) perform model evaluations using various statistical parameters (discussed in the respective sections).

2.2.1 Flood Inventorying

As suggested by Arora et al. (2021b), this step involves the computation of NDWI from the selected satellite scenes. The details of NDWI computation method, based on Gao (1996), are presented in Arora et al. (2021b). Flood pixels are separated from non-flooded pixels by applying a threshold ≥0.20 to the NDWI raster.

2.2.2 Flood Predictors

We have selected 12 flood predictors (**Table 2**) based on an extensive literature survey and our knowledge of the geomorphic, hydrologic, and climatic conditions of the study area. The slope angle is defined as the rate of change of elevation with Euclidean distance. Slope is one of the factors that determine and influence soil type, moisture content, and vegetation and, therefore, affects the surface runoff (Yang et al., 2020) and infiltration rates (Nassif and Wilson, 1975; Liu and Singh, 2004). Thus, the slope has both indirect and direct effects on flood inundation (Al-Rawas and Valeo, 2010). We computed the slope degree using ArcGIS 10.3 and DEM data and classified the slope range of 0–42.80° into five categories using the natural break method (**Figure 3A**).

Slope direction is one of the variables that bear a relationship with the availability of soil moisture, geomorphic stability,

TABLE 2 | Multicollinearity test results of all the conditioning factors; information gain (IG) attribute evaluation method for selection of flood conditioning factors using 300 flood and 300 non-flood points in Weka Software.

Multicollinearity analysis			**Information gain analysis**		
Conditioning factor	**VIF**	**TOL**	**Weight**	**Rank**	**Conditioning factor**
TWI	1.96	0.51	0.3195	1	Geomorphology
Distance from river	1.39	0.72	0.1549	2	Soil
River density	1.39	0.72	0.0618	3	LULC
Altitude	1.77	0.56	0.0332	4	Distance to road
Aspect	1.28	0.78	0.031	5	Altitude
Curvature	1.05	0.95	0.0277	6	TWI
Rainfall	1.05	0.95	0.0256	7	Aspect
Distance from road	1.12	0.89	0.0256	8	Slope
Slope	1.53	0.65	0.0246	9	Stream density
Soil	1.15	0.87	0.0123	10	Distance to River
Geomorphology	1.34	0.75	0.0000023	11	Curvature
LULC	1.42	0.70	0.0000014	12	Rainfall

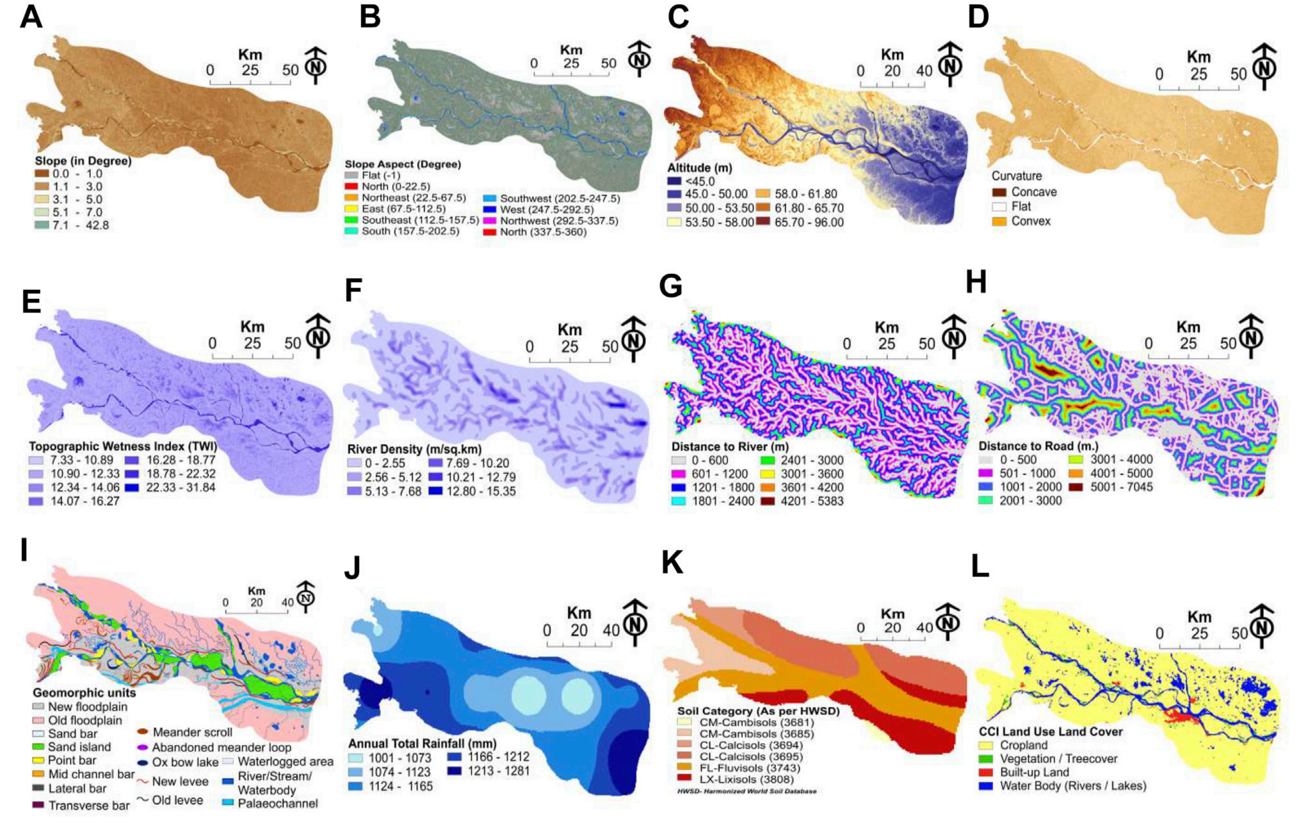

FIGURE 3 | Flood conditioning factors used for modeling of flood susceptibility. From **(A–L)** the maps indicate Altitude, Slope; Aspect; TWI; River Density; Distance to Road; Annual Rainfall (mm); Soils; Curvature, Distance to River; LULC; and Geomorphology.

exposure to radiation at the surface, wind (dry or wet), and rainfall intensity. Hence, it has an established relationship with flooding (Siahkamari et al., 2018). We used 3-D Analyst of SRTM DEM in ArcGIS 10.3 to calculate slope direction and categorized it into ten classes (**Figure 3B**).

Altitude affects the flood level in two ways: 1) elevation from the channel bed level decides how far from the rivers will inundation occur and 2) height from sea level controls atmospheric phenomena and hence type and magnitude of precipitation. In this study, SRTM v.4 30 m digital elevation model (DEM) derived low altitude range (13–96 m) surface of the area is classified into seven categories using the natural break method (**Figure 3C**).

Plan curvature or planform curvature is the directionality parallel to the maximum slope and decides the flow direction (Kimerling et al., 2016). We have used SRTM DEM to compute and reclassify three categories of planform curvature namely negative, zero, and positive indicating concave, flat, and convex surfaces, respectively (**Figure 3D**).

TWI is a quantitative measure indicating topographic control on hydrological processes. It is computed using the formula: TWI $= \ln\left(\frac{A_s}{\beta}\right)$ where A_s denotes the specific catchment area (m^2/m), and β equals slope angle in degrees. TWI values determine the surface saturation condition which is one of the governing factors in surface runoff and hence becomes one of the determinants of potential flooding in a watershed. Here, we categorized the TWI map of the study into six classes (**Figure 3E**).

River density also known as drainage density (D_d) represents the stream channel length per unit area. It is calculated using the formula suggested by Horton (1932): $D_d = \frac{L_T}{A}$, where L_T is the total stream length serving an area, and A is the contributing area. Thus, D_d bears a directly proportional relationship with potential flood prediction. The higher the drainage density (D_d), the higher is the probability of flooding in a watershed. We have reclassified the D_d range of 0–15.35 into six categories using the natural break method in ArcGIS 10.3 (**Figure 3F**). The drainage density is also established to be an indirect indicative of active tectonic activities (Han et al., 2003). Since the area is tectonically active, this parameter has been included to incorporate the effects of active tectonic activities to the flood potential.

Euclidean distance from the river channel is an important factor determining the extent of the inundated area by a flood (Khosravi et al., 2018). The areas far away from the river channel in a watershed are less probable to flooding than the ones nearer to the channel. Relationship of flood susceptibility to the distance to the river channel is subjective as the relationship varies from place to place depending on various factors (Choubin et al., 2019). We calculated the Euclidean distance to river channels in the Spatial Analyst Toolbox of the ArcGIS 10.3 and later interpolated and reclassified it into 10 categories to produce the map of "distance to the river" (**Figure 3G**).

Distance from the road is one of the important independent variables used in flood susceptibility modeling. The road networks in modern-day urban agglomerations increase impervious surfaces which contribute to changing the surface hydrological properties. Road network data used in this study have been obtained from Open Street Map Portal which is a collaborative mapping project (CMP). The data quality and its usability are described in Fan et al. (2014). After producing the map using interpolation, the data have been reclassified into seven categories (**Figure 3H**).

Geomorphology is closely connected to flood susceptibility (Mokarram and Sathyamoorthy, 2016). Floods sculpture landforms by the processes of erosion and deposition. Sometimes, extreme flood events destroy the landforms formed by different geomorphic agents. Thus, the interrelationship between floods and landforms of different scales (spatial and temporal) is established since the dawn of geomorphology as a discipline. In this study, geomorphological units were extracted from Google Earth Pro© through onscreen digitization method at 1:500/1,000 scale. Seventeen microscale geomorphic units have been identified through the classification of the study area (**Figure 3I**). Fine-scale geomorphology being another proxy that connotes the effects of active tectonic activities and seismological perturbances in the surface has also been taken as one of the exploratory variables of flood susceptibility, but it has previously been ignored in flood susceptibility modeling community. Some of the geomorphic markers mapped in this area which represent effects of active tectonic activity include 1) asymmetrical meander belts (Leeder and Alexander, 1987), 2) abrupt scarp faces, 3) highly sinuous mountain fronts (Taloor et al., 2019), 4) unpaired terraces (Joshi et al., 2016), 5) unilateral migration (Latrubesse, 2015), 6) shifted fan lobes and terraces (Jolley et al., 1990), etc.

Climate change affects hydrological processes (Tian et al., 2020; He, 2021). Rainfall variations have an impact on flash flooding (Mahtab et al., 2018). Prolonged rainfall events or a set of short-interval events of different intensities and magnitudes often prompt floods. In this study, we have used the global CFSR annual rainfall dataset to extract rainfall conditions in the study area (Trivedi et al., 2019). The dataset is provided on a 1000 m spatial resolution which has been resampled to 30 m resolution data by using the nearest neighbor (NN) method (**Figure 3J**). The data range of 1,001–1,081 mm is reclassified into six classes using the natural break method.

Different characteristics of soil affect various hydrologic properties of the surface (Zhang et al., 2019b). Soil types with high permeability and high infiltration ratio show less susceptibility to flooding and vice versa (Krogh and Greve, 2006; FAO and ISRIC, 2012). Soil map produced by FAO and ITPS (2015) used in this study is resampled at 30 m resolution and classified into six categories (**Figure 3K**).

LULC can alter and control factors such as moisture retention capacity of the surface, infiltration rate, surface runoff, heat albedo and hence bears a well-known relationship with flood possibility in an area. For example, if an area has been converted to built-up land from forested land, the probability of flooding increases owing to the increased imperviousness caused by altered surface cover type (Rogger et al., 2017). The LULC data produced by climate change initiative (CCI) program of the European Space Agency (ESA) have been used in this study. The subset of LULC data obtained from ESA archived 300 m spatial resolution, annual worldwide dataset generated for the period 1992–2015 (Li et al., 2018), has been reprocessed using nearest neighbor resampling procedure at 30 m resolution (**Figure 3L**). The manual provided by the agency gives a full description of the dataset which readers can access to gain better knowledge (ESA, 2017).

2.2.3 Multicollinearity Assessment Through the Variance Inflation and Tolerance Analysis

Multicollinearity analysis (Alin, 2010) (also known as collinearity) is the foremost important step in the regression analyses. The concept of multicollinearity refers to the property of predictor variables not showing dependency on one another which Dormann et al. (2013) phrase as "non-independence of the predictor variables." The noncollinear relationship among flood predictors (or independent variables/predictor variables) is warranted to get unbiased model results. Collinearity among the predictor variables is determined through "variance of inflation

(VIF)" and "tolerance (TOL)" for a case $X = \{X_1, X_2, X_3, \ldots\ldots, X_N\}$ with the formula for which mathematical expressions are given as:

$$\mathrm{TOL} = 1 - R_j^2, \tag{1}$$

$$\mathrm{VIF} = \frac{1}{\mathrm{TOL}}, \tag{2}$$

where R_j^2 = coefficient of determination of an explanatory variable's regression on all the other explanatory variables. For the above case X, jth explanatory variable Xj's regression on all the other explanatory variables like $X_1, X_2, X_3, \ldots\ldots X_N$ yields the input variable R_j^2 needed for computation of VIF and TOL. The value of VIF>10 and TOL <0.1 is indicative of severe multicollinearity among the explanatory variables. VIF was calculated by "exploratory regression" which is an embedded tool in Spatial Statistics Toolbox of ArcGIS 10.3. The VIF and TOL values are presented in **Table 2**.

2.2.4 Feature Selection Method for Flood Predictors

For determination of the significance of controlling factors and ranking flood predictors as per their contribution in the prediction of flood phenomena, the information gain (IG) method (**Section 2.2.4.1**) was applied using the Weka software v3.9.4, developed by the University of Waikato, Hamilton, New Zealand.

2.2.4.1 Information Gain

IG is one of the most widely used methods of feature selection in various machine learning (ML) applications including landslide modeling (Đurić et al., 2019) and flood modeling (Costache and Tien Bui, 2019). This method is found to be one of the fastest and simplest methods used for ranking the features (Hall and Holmes, 2003).

The concept of entropy is one of the main tenets of the "information theory" and serves as the basis of IG:

$$\begin{aligned}\mathrm{IG}(t) = -\sum\nolimits_{i=1}^{|C|} P(C_i)\log P(C_i) + P(t)\sum\nolimits_{i=1}^{|C|} P(C_i|t)\log P(C_i|t)\\ + P\left(\bar{t}\right) \times \sum\nolimits_{i=1}^{|C|} P\left(C_i\middle|\bar{t}\right)\log P\left(C_i\middle|\bar{t}\right),\end{aligned} \tag{3}$$

where C_i= the ith category; $P(C_i)$= the probability of ith category; $P(t)$ and $P(\bar{t})$ represent the probabilities of occurrence and no-occurrence of phenomena "t", respectively. The entropy value of C_i, for discrete variables, can be defined as:

$$H(C) = -\sum_{i=1}^{k} P(C_i)\log_2(P(C_i)) \tag{4}$$

This equation assumes that C_i picks its values from $\{C_1, C_2, C_3, \ldots\ldots, C_k\}$ and $P(C_i)$ is the probability such that $C = C_i$

The decision of flood predictor selection using the IG based on entropy values of variables computed from D training dataset comprising n number of flood predictors can be expressed as follows (Chapi et al., 2017):

$$\mathrm{IG}(D,\ F) = \frac{\mathrm{Entropy}\ (D) - \mathrm{Entropy}\ (D, F)}{\mathrm{SplitEntropy}\ (D, F)}, \tag{5}$$

$$\mathrm{Entropy}\ (D) = -\sum\nolimits_{i=1}^{2} \frac{(Y_i, F)}{|D|}\log_2\frac{n(Y_i, F)}{|D|}, \tag{6}$$

$$\mathrm{Entropy}\,(D, F) = -\sum\nolimits_{j=1}^{m} \frac{D_j}{|D|}\mathrm{Entropy}\,(D), \tag{7}$$

$$\mathrm{SplitEntropy}\,(D, F) = -\sum\nolimits_{j=1}^{m} \frac{|D_j|}{|D|}\log_2\frac{|D_j|}{|D|}. \tag{8}$$

3 MODELS EMPLOYED FOR FLOOD SUSCEPTIBILITY PREDICTION INDEX MAPPING

For the present work, two base bivariate statistical models, viz. FR and EBF, have been used to compute weightage for each of the twelve flood predictors. Subsequently, those flood predictors' weight values have been used to train the ensemble advanced ML models namely CART, FR, and EBF models. In the subsequent subsections, the brief functionality of each of the individual models is described, and later, how the two bivariate model-based weights are used for ensembling the other three machine learning models is presented.

3.1 Models Applied for Data Preparation

3.1.1 Evidential Belief Function

This algorithm is based on Dempster-Shafer's theory of evidence (Dempster, 1967; Smith and Shafer, 1976). Four important functions form the EBF: 1) belief function (Bel), 2) plausibility function (PLs), 3) disbelief function (Dis), 4) uncertainty function (Unc).

$$m\text{: } 2^{\Theta} = \left\{\theta, T_P, \overline{T_P,\ \Theta}\right\} \quad \text{where} \quad \Theta = \left\{T_{P,}\ \overline{T_P}\right\}, \tag{10}$$

where T_P represents spring generated class pixels, $\overline{T_P}$ represents class pixels not influenced by spring, and θ is an empty set.

The above equation yields the Bel (belief function) calculated with the help of the following equation (Park, 2011):

$$\begin{aligned}\left[\lambda(T_P)_{A_{ij}}\right] = \left[\frac{N\left(S \cap A_{ij}\right)}{N(S)}\right] / \left[\left\{N\left(A_{ij} - N\left(S \cap A_{ij}\right)\right)\right\} / [N(P)\right.\\ \left. - N(S)]\right],\end{aligned} \tag{11}$$

$$\text{Belief function (Bel)} = \left(\frac{\left[\lambda(T_P)_{A_{ij}}\right]}{\sum\left[\lambda(T_P)_{A_{ij}}\right]}\right) \tag{12}$$

where $N(S \cap A_{ij})$ = density of flood pixels occurring in A_{ij}; $N(S)$ = total density of whole flood occurring in the study area; $N(A_{ij})$ = the density of pixels in A_{ij}; $N(P)$ = the density of pixels in the whole study area P.

The disbelief function (Dis) can be derived as:

$$\begin{aligned}\left[\lambda(\bar{T}_P)_{A_{ij}}\right] = \left[\frac{N(S) - N\left(S \cap A_{ij}\right)}{N(S)}\right] \Big/ \left[\left(N(P) - N(S) - N\left(A_{ij}\right)\right.\right.\\ \left.\left. + N\left(S \cap A_{ij}\right)/N(P) - N(S)\right)\right],\end{aligned} \tag{13}$$

$$\text{Disbelief (Dis)} = \left(\left[\lambda(\bar{T}_P)_{A_{ij}}\right]\right) \Big/ \sum\left[\lambda\left(\bar{T}_P\right)_{A_{ij}}\right] \tag{14}$$

And the following equations are used to compute uncertainty (Unc) and plausibility (PLs):

$$\text{Uncertainty (Unc)} = [(1 - (\text{Belief}) - (\text{Disbelief}))] \tag{15}$$

$$\text{Plausibility (Pls)} = [1 - (\text{Disbelief})] \tag{16}$$

3.1.2 Frequency Ratio

Frequency ratio is a frequently used bivariate statistical model. It represents the probability of event occurrence; in our case, the event is the flood pixel (Arabameri et al., 2019b).

The frequency ratio (FR) computation uses the following mathematical expression:

$$FR = \frac{\dfrac{N_{pix}(SX_i)}{\sum_{i=1}^{m} SX_i} \quad \text{(flood occurance ratio)}}{\dfrac{N_{pix}(X_j)}{\sum_{j=1}^{n} N_{pix}(X_j)} \quad \text{(area ratio)}}, \tag{17}$$

where $N_{pix}(SX_i)$ = the number of pixels with flood events within class i of factor variable X; $N_{pix}(X_j)$ = the number of pixels within the factor variable X_j; m = the number of classes in the parameter variable Xi; and n = the number of factors in the study area (Regmi et al., 2014).

3.1.3 Classification and Regression Tree

CART is a powerful data mining machine learning nonparametric algorithm proposed by Breiman et al. (1984). As the name suggests, it can perform both the classification and regression of number, binary, and categorical type of variables (Haughton and Oulabi, 1993). After performing the classification of variables in either number, binary, or categorical format, the average response values are computed using the mathematical expression:

$$I(\text{Split}) = \left\lfloor 0.25 \left\{ q(1-q)^u \sum\nolimits_k \left|PL(k) - PR(k)\right| \right. \right\rfloor^2, \tag{18}$$

where k = index of the target classes; PL(k) and PR(k) = distribution of the probability of the target classes associated with the left and right child nodes, respectively; u= penalty trolled by the user when unequal sized child nodes are generated.

The resulting outcome of the CART model comes in a very complex form of a decision tree which needs pruning to extract only relevant and most important info out of it.

3.2 Ensemble Models Applied for Flood Susceptibility Prediction Index Computation

Due to the limitations of stand-alone models (Hapuarachchi and Wang, 2008; Hapuarachchi et al., 2011) and the advantages of ensemble models (Fernández et al., 2018; Zounemat-Kermani et al., 2020), in recent years, the use of ensemble models has expanded among researchers (Fernández et al., 2018; Zounemat-Kermani et al., 2020; Costache et al., 2021). Two ensemble models are used to derive the Flood Susceptibility Prediction Index and corresponding zonation maps. These ensembles are generated through the combination of CART and bivariate statistics models—FR and EBF. The factor class/category coefficients derived with the help of FR and EBF models are used as input in the CART.

3.3 Database Establishment

For the present research work, a database consisting of 12 flood predictors for a total number of 300 flood points was prepared using ArcGIS. Since the flood-prone area identification was performed following a binary classification of pixels, it was necessary to create another data sample, having the same number of points (300), consisting of non-flood locations (Ali et al., 2020). To ensure the objectivity of the results, the non-flood locations were randomly distributed across the entire study area.

3.4 Feature Selection With IG

The involvement of multiple predictors to estimate the susceptibility to a specific natural hazard can lead to issues related to the prediction (Costache, 2019). To overcome this shortcoming and to eliminate the noisy data from the workflow, the predictive ability of the 12 flood predictors was tested using information gain (IG). To determine the flood predictors' significance, all the three models were applied using Weka 3.9 software.

3.5 EBF and FR Coefficient Normalization

EBF and FR coefficients were used to code the predictor class/category. These two types of coefficients were calculated using the procedure described in **Sections 3.1.2, 3.1.3**. Furthermore, to bring the EBF and FR values to the same range of values, the normalization procedure was applied using **Equation 23** proposed by Costache et al. (2020):

$$y = \frac{(x - \min(d)) \times (\max(n) - \min(n))}{\text{maz}(d) - \min(d)} + \min(n), \tag{23}$$

where y = standardized value of x, x = variable's current value, d = range limit of the variable values, and n = standardized range limit.

3.6 Preparation of the Training and Validating Datasets

After obtaining the normalized EBF- and FR-derived weightage database, we need to set up the training and validation samples using this newly generated dataset. Previous studies (Arabameri et al., 2019a; Bui et al., 2019a) suggest that the training sample is established to represent 70% of the total dataset, while the other 30% is apportioned for validating the dataset. Thus, we used 210 flood and 210 non-flood pixels as the training dataset, while 90 flood and 90 non-flood locations were used in the validation process. The Subset Features tool from ArcGIS was used to randomly split the dataset.

3.7 Setting the Configuration for Hybrid Ensemble Models

3.7.1 CART-EBF and CART-FR Ensembles

The two CART-based ensembles were trained with the help of Salford Predictive Modeler v8.2 (Costache et al., 2020). The trial process was used to optimize the CART ensembles' parameters (minimum cases of parent nodes and terminal nodes) whose values were established in accordance with the highest AUC. Finally, the weights of the flood predictors for CART-EBF and CART-FR ensembles were also determined.

3.8 Model Performance Evaluation and Comparison

Performance evaluation is the most important step in scientific works (Zhang et al., 2019a). Because no single or a set of universally valid model evaluation measurement matrices related guidelines could be found such as AUROC, TSS, RMSE (Zhou et al., 2018; Alam et al., 2020), and others, we have chosen two types of matrices to evaluate the performance of models used in this study: 1) threshold-independent and 2) threshold-dependent. Under the first category, area under the receiver operating characteristic (AUROC) curve has been used. In the case of the threshold-dependent performance evaluation matrix, we have used true skill statistics (TSS) and others (see **Table 6**). It should be noted that many of the threshold-dependent matrices (West et al., 2016) listed in **Table 6** are derived from AUROC curve (the abbreviations used in this section are given in **Table 6** and its appended note given just below the table).

The AUROC graph plot is a biaxial plot with "sensitivity" (*y*-axis parameter) versus "1-specificity" (*x*-axis parameter) (Jiménez-Valverde, 2012). The AUROC value ranges from 0.5 (inaccurate) to 1 (highly accurate).

The matrices plotted on the two axes of the ROC curve, sensitivity (also called true positive rate), and specificity (or true negative rate) are expressed in mathematical form as:

$$\mathrm{TPR} = \text{ Sensitivity} = \frac{\mathrm{FP}}{\mathrm{FP} + \mathrm{TN}}, \tag{26}$$

$$\mathrm{FPR} = 1 - \text{Specificity} = \frac{\mathrm{TP}}{\mathrm{TP} + \mathrm{FN}}, \tag{27}$$

where FP= number of false-positive cases, TN= number of true-negative cases, TP = number of true-positive cases, and FN = number of false-negative cases. The TPR, also termed as sensitivity, is the representative of the probability of a test predicting true events to be true. And the FPR, which is also known by the names "1-specificity," indicates the probability of a test predicting a non-event to be a true event. The AUROC value range of 0.5–1.00 has different implications in terms of the accuracy of model performance.

The specificity and sensitivity values using different cutoff thresholds for both models CART-EBF & CART-FR are provided in **Table 4**.

The threshold-dependent statistic metric used in this work, the "true skill statistics (TSS)" (Flueck, 1987), is one of the popularly used skill score measures for categorical datasets in forecast-related studies. This matrix's discovery traces back to its first proposal by Peirce (1884) and is also widely called by the name "HanssenKuipers" discriminant (Wilks, 1995)/or Kuipers' performance index/or the true skill statistic (Allouche et al., 2006). Cohen's Kappa is dependent on the prevalence of sample points affecting the sensitivity and specificity of the model performance, and the TSS overcomes this disadvantage (Allouche et al., 2006). Besides, the accuracy, F-score, Cohen's kappa (Cohen, 1960), Matthew's correlation coefficient (MCC), TPR (sensitivity), TNR (specificity), FPR (fall out), informedness (bookmaker informedness; BMI), etc. (see **Table 6** and the appended notes for details of the list of matrices and their expansions and calculation formulas) are also dependent on independent variables that control AUROC, such as TP, TN, FP, and FN have also been calculated for the performance evaluation of the models. All the performance evaluators (statistic matrices) listed in **Table 6** are used for assessing different facets of model performances viz. accuracy, precision, robustness, sensitivity, consistency, the goodness of fit between observed and estimated values of natural phenomena, most of which are derived from the 2X2 contingency confusion matrix generated from binary classification scheme. There is a long list of classifier performance evaluation matrices. However, their suitability for a particular type of modeling exercise has not been put forward by the ML community yet (Seliya et al., 2009). Seliya et al. (2009) studied twenty-two of such evaluators with their meanings, what their higher or lower values imply as well as the relationship among them.

The Kappa statistic assesses the agreement between two distinguished sets of classification while catering to the randomness in the classification (Baattrup-Pedersen et al., 2012). The Kappa statistics can be calculated using the following equation:

$$\mathrm{K} = \frac{\mathrm{P_{obs}} - \mathrm{P_{exp}}}{1 - \mathrm{P_{exp}}}, \tag{28}$$

where $\mathrm{P_{obs}}$ = observed agreements = (TP + TN), and it is representative of the correctly classified inundated and non-inundated pixels; $\mathrm{P_{exp}}$ = expected agreements = [{(TP + FN) x (TP + FP)} + {(FP + TN) x (FN + TN)}]; it equates to the proportion of inundated and non-inundated pixels which were expected to show agreement, on the basis of chance (Hoehler, 2000).

The value of k-index varies between 0 and 1; the value moving towards 0 indicates less agreement, whereas those moving towards higher values, i.e., towards 1 indicate the model's prediction accuracy heading towards or near to perfection. Cohen (1960) presented fivefold classification of k-index such that: $K \leq 0$ (no agreement); 0.01–0.20 (slight agreement); 0.21–0.40 (fair agreement); 0.41–0.60 (moderate agreement); 0.61–0.80 (substantial agreement), and 0.81–1.00 near to perfect agreement.

We have also employed the seed cell area index (SCAI), and frequency ratio plots (FRP) for classification accuracy assessment of the models as the second round of validating the modeled

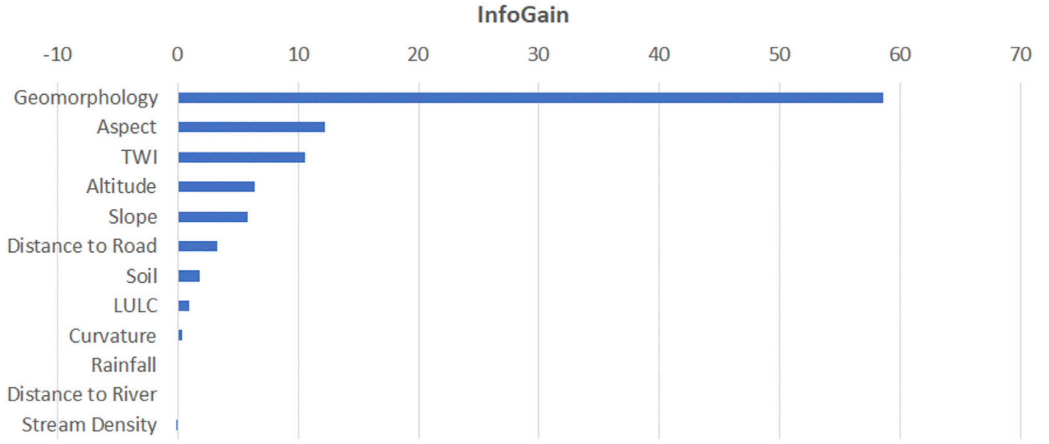

FIGURE 4 | Importance of flood predictors derived through the use of IG arranged in order of their contribution to flood occurrence prediction.

classification results. The SCAI index computation takes into account the mathematical expression equating the ratio of each classified class and the susceptible seed cell percent values (Süzen and Doyuran, 2004):

$$\mathrm{SCAI}\,(\%) = \frac{\dfrac{\mathrm{N_{pix}}\left(\mathrm{X_j}\right)}{\sum_{j=1}^{n}\mathrm{N_{pix}}\left(\mathrm{X_j}\right)}\ (\text{area ratio})\ \times 100}{\dfrac{\mathrm{N_{pix}}\,(\mathrm{SX_i})}{\sum_{i=1}^{m}\mathrm{SX_i}}\ (\text{flood susceptible occurance ratio}) \times 100}, \tag{29}$$

where$\mathrm{N_{pix}}\,(\mathrm{SX_i})$ = number of flood pixels within class i of flood predictor X; $\mathrm{N_{pix}}\,(\mathrm{X_j})$ = number of pixels within the flood predictor variable $\mathrm{X_j}$; m = number of classes in the parameter Xi and n = number of total factors selected for the study area. In our study, there is an inverse relationship between SCAI and the accuracy of prediction of susceptible classes (Arabameri et al., 2020b). In other words, low SCAI value for "high" and "very high" FSPI sensitivity classes and high SCAI value for "low" and "very low" FSPI sensitivity classes validate that the classification results of FSPI zones are correctly demarcated in the resultant flood susceptibility maps (Dragićević et al., 2015). The FRP method of classification validation behaves inverse to the SCAI values methods (Aghdam et al., 2017). Therefore, these two additional second rounds of validation will add an extra level of confidence in the results of the modeled susceptibility prediction index.

4 RESULTS

4.1 Selecting the Flood Predictors

We selected a list of flood predictors based on an extensive literature survey and familiarity with the topographic, hydrologic, climatic, and anthropic settings of the study area. Afterward, we selected the most significant and least redundant features or flood predictors by applying three statistical measures meant for checking multicollinearity, retrieving weights, and ranking of the variable features. We also analyzed interdependence among the flood predictors by applying the test of multicollinearity; furthermore, the application of IG (**Figure 4**) test methods has helped in ranking the flood predictors in order of their contribution to the flood occurrence probability.

4.1.1 Multicollinearity and IG Analyses of Feature Selection

Interdependency of flood predictors has been assessed by applying multicollinearity analysis. This analysis shows that all the flood predictors listed in **Table 2** have variance inflation factor (VIF) and tolerance (TOL) > 10 and <0.1, respectively, which do not show sign of collinearity and hence can be included in the models applied for flood susceptibility zonation exercise.

The IG method applied to retrieve weightage and ranking shown in **Figure 4** helps to assign rank to the flood predictors and is given in **Table 2**. The calculated IG ranks and weightages have ascertained the significance of the role of predictors in flood occurrence prediction. Geomorphology has been found to be the first ranker signifying its most important contribution in the flood susceptibility prediction process. IG method suggests that the first four most important flood predictors (descending order) are non-DEM-derived factors viz. geomorphology, soil, LULC, and "distance-to-road." And the least significant predictors (increasing order of significance) are rainfall, curvature, "distance-to-river," and stream density. As per IG, almost all the DEM-derived topography-related parameters, except curvature, are middle-level performants in their significance to flood contribution.

4.1.2 EBF and FR Coefficients

The FR and EBF model results for each class of every flood predictor have provided base weight values for training and validating data points for CART model ensembles. At first, we classified all the flood predictors' values using the methods listed in **Table 3**. Subsequently, the EBF and FR weights corresponding to the original class values for each of the flood predictors at the

TABLE 3 | FR and EBF values of factor class/categories (FR values taken from Arora et al., 2019b).

Factors	Class	Class percentage (%)	Flood locations percentage (%)	FR	EBF
Altitude	0–45.0	2.34	7.71	3.29	0.39
	45.1–49.9	14.42	30.43	2.11	0.25
	50.0–53.5	19.92	24.43	1.23	0.15
	53.6–57.9	25.36	23.29	0.92	0.11
	58.0–61.8	19.61	11.29	0.58	0.07
	61.9–65.7	12.98	2.71	0.21	0.03
	65.8–96.0	5.38	0.14	0.03	0.01
Aspect	Flat	27.83	42.86	1.54	0.17
	North	9.34	8.71	0.93	0.10
	Northeast	9.13	7.57	0.83	0.09
	East	8.34	7.43	0.89	0.10
	Southeast	9.45	7.43	0.79	0.09
	South	9.43	7.00	0.74	0.08
	Southwest	9.09	6.71	0.74	0.08
	West	8.16	6.00	0.74	0.08
	Northwest	9.21	6.29	0.68	0.08
Curvature	Concave	14.10	13.86	0.98	0.33
	Flat	46.23	51.14	1.11	0.37
	Convex	39.66	35.00	0.88	0.30
Distance from river (m)	0–600	38.93	56.71	1.46	0.40
	600–1,200	28.46	27.86	0.98	0.27
	1,201–1800	19.22	12.00	0.62	0.17
	1801–2,400	9.22	2.86	0.31	0.08
	2,401–3,000	2.86	0.43	0.15	0.04
	3,001–3,600	0.90	0.14	0.16	0.04
	3,601–4,200	0.31	0.00	0.00	0.00
	4,201–5,383	0.09	0.00	0.00	0.00
Geomorphology	New Floodplain	23.45	27.57	1.18	0.07
	Old Floodplain	49.12	21.14	0.43	0.03
	Palaeochannel	3.07	1.29	0.42	0.02
	Point bar	2.95	10.43	3.53	0.21
	River/Stream/Waterbody	8.22	3.71	0.45	0.03
	Sand Island	6.88	2.86	0.42	0.02
	Waterlogged Area	3.70	18.29	4.95	0.29
	Levee	2.61	14.71	5.65	0.33
Landuse	Cropland	86.27	61.46	0.71	0.12
	Vegetation	1.36	2.58	1.90	0.31
	Settlement	1.57	0.29	0.18	0.03
	Water	10.80	35.67	3.30	0.54
Rainfall (mm/year)	1,001–1,073	7.09	8.71	1.23	0.22
	1,074–1,123	21.88	25.71	1.18	0.22
	1,124–1,165	37.08	31.29	0.84	0.15
	1,166–1,212	25.09	22.57	0.90	0.16
	1,213–1,281	8.86	11.71	1.32	0.24
River density (km/km2)	0–2.55	66.69	49.29	0.74	0.08
	2.56–5.12	25.10	36.43	1.45	0.16
	5.13–7.68	6.08	11.00	1.81	0.20
	7.69–10.20	1.55	2.00	1.29	0.15
	10.21–12.79	0.44	1.14	2.62	0.29
	12.80–15.35	0.15	0.14	0.98	0.11
Road to distance (m)	0–500	43.80	26.14	0.60	0.07
	501–1,000	14.68	15.29	1.04	0.12
	1,001–2000	21.81	29.29	1.34	0.16
	2001–3,000	10.51	13.86	1.32	0.16
	3,001–4,000	5.52	11.14	2.02	0.25
	4,001–5,000	2.80	3.71	1.33	0.16
	5,001–7,045	0.88	0.57	0.65	0.08
Slope angle (°)	0.0–1.0	29.39	37.14	1.26	0.18
	1.1–3.0	58.46	50.29	0.86	0.12
	3.1–5.0	9.95	8.57	0.86	0.12
	5.1–7.0	1.85	3.14	1.70	0.24
	7.1–42.8	0.35	0.86	2.46	0.34
Soil	1	1.23	0.57	0.46	0.11

(Continued on following page)

TABLE 3 | (*Continued*) FR and EBF values of factor class/categories (FR values taken from Arora et al., 2019b).

Factors	Class	Class percentage (%)	Flood locations percentage (%)	FR	EBF
	2	11.25	4.71	0.42	0.10
	3	5.38	0.86	0.16	0.04
	4	27.57	15.86	0.58	0.13
	5	34.28	61.00	1.78	0.44
	6	20.29	17.00	0.84	0.19
TWI	7.33–10.89	33.94	27.00	0.80	0.06
	10.90–12.33	28.14	22.86	0.81	0.07
	12.34–14.06	19.39	20.14	1.04	0.08
	14.07–16.27	9.81	11.14	1.14	0.09
	16.28–18.77	4.57	6.29	1.37	0.11
	18.78–22.32	3.74	10.71	2.87	0.23
	22.33–31.84	0.42	1.86	4.41	0.35

subclass level were computed using methods discussed in **Sections 4.1.1, 4.1.2**, respectively. The elevation class ranges "0–45.0" and "65.8–96.0" show maximum (FR = 3.29; EBF = 0.39) and minimum (FR = 0.03; EBF = 0.01) weights for both FR and EBF, respectively. The slope aspect classes that provide maximum (FR = 1.54; EBF = 0.17) and minimum (FR = 0.68; EBF = 0.08) FR and EBF weights are flat (−10–00) and northwest (292.50–337.50). Out of the three curvature classes, class range assigned as flat gives the maximum FR (1.11) and EBF (0.37) weights whereas "convex" class renders the minimum weight for both FR (0.88) and EBF (0.30) models. The flood predictor "distance from river" class ranges which produced maximum (FR = 1.46; EBF = 0.40) and minimum (FR = 0; EBF = 0) weights by FR and EBF models are "0–600" and "3,601–4,200" as well as "4,201–5,383." The FR and EBF models have assigned maximum (FR = 5.65; EBF = 0.33) and minimum (FR = 4.95; EBF = 0.29) weights to levee and waterlogged areas, two geomorphological classes, respectively. It can be noted that the maximum (FR = 3.30; EBF = 0.54) and minimum (FR = 0.18; EBF = 0.03) FR and EBF weight, respectively, have been assigned to "water" and "settlement" classes. The FR maximum and minimum weights for "rainfall" classes are 1.32 and 0.84, and as per EBF for the same "rainfall" classes, the value ranges from 0.24 to 0.15, respectively. As per FR and EBF, the maximum (2.62) and minimum (0.74) weights for river density have fallen in the same classes as 0.29 (max) and 0.08 (min), respectively. In the case of "distance to road" flood predictor classes "3,001–4,000" and "0–500," maximum and minimum weights computed using FR are 2.02 (max) and 0.60 (min); and that by EBF are 0.25 (max) and 0.07 (min), respectively. The maximum (FR = 2.46; EBF = 0.34) and minimum (FR = 0.86; EBF = 0.12) FR and EBF weights delivered to account for the "slope angle" classes viz. "7.1–42.8" and "1.1–3.0" and "3.1–5.0", respectively. Fifth soil class (FL-Fluvisol-3743) and third soil class (CL-Calcisol-3694) were recognized as maximum (1.78) and minimum (0.16), respectively, by FR; and that by EBF model, weightage values are 0.44 as maximum and 0.04 as a minimum. TWI class (22.33–31.84) has been the one with maximum weight value for both FR as well as EBF (FR = 4.41; EBF = 0.35); and the TWI class "7.33–10.89" is representative of minimum (FR = 0.80; EBF = 0.06) weight as per FR and EBF both. Classwise weights of each class of every flood predictor for FR and WBF are tabulated in **Table 3**.

4.1.3 Flood Susceptibility Prediction Index Zonation Results

All the hybrid models were trained and validated using normalized flood predictor values for each class representing the controls of flood susceptibility in the MGP (see **Section 3.6**). After estimating the FR- and EBF-based flood predictor weights of the entire 600 flood and non-flood points, the trial-and-error method using backward and forward propagation was applied to obtain the CART ensemble weights for those points. Four categories of results were obtained by the use of EBF- and FR-based ensembles: 1) the ensembles have arranged the flood predictors in the sequence of their significance (ascending order of weight assigned to the flood predictors); 2) by using these weights for each subclass of every flood predictor, the flood susceptibility prediction index (FSPI) of the entire study area was obtained and classified into "very low," "low," "medium," "high," and "very high" flood susceptible zones using natural break (NB) method (**Figures 5A,B**); 3) corresponding to each class of FSPI, the entire study area was delineated into 5 zonation units (with the percentage of area appendages to each class) (the areal share of each FSPI zone using four different segmentation methods is presented in **Figures 6A–C**); and 4) the accuracy, sensitivity, precision, robustness, etc. of all the models indicating how well the models performed in this low-relief, subhumid monsoon-dominated topoclimatic setting have been computed. For both of the ensembles, these different levels of results are presented in the subsections below. Since the natural break (NB) method is most widely used and quantile (QNTL) accrued the highest areal percentage shares in the "high" and "very high" classes, FSPI % shares were separately computed for all the methods using these two methods and are presented in **Figures 7A,B**.

4.1.3.1 CART-EBF and CART-FR

Following the training procedure keeping in mind different cut-off thresholds corresponding to specificity and sensitivity values of both the models (**Table 4**), the minimum cases of parent nodes for the CART-EBF ensemble were established at 24, while

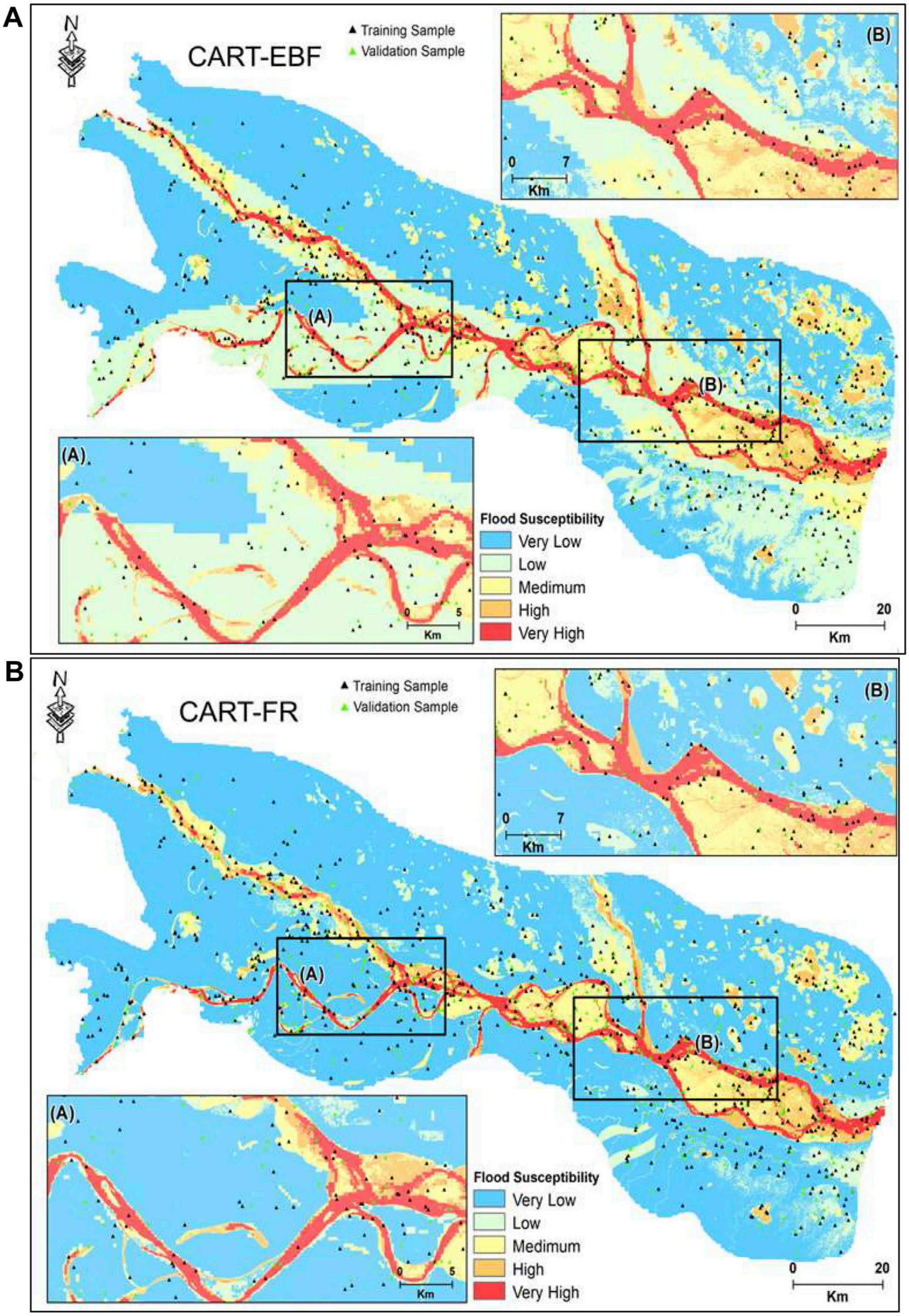

FIGURE 5 | Flood susceptibility map using six ensemble models computed using methods discussed in **Section 5.1**; **(A, B)** show FSPI classified results according to CART-EBF and CART-FR results. Boxed areas A and B are zoomed windows in each of the model output maps to show detailed FSPI conditions nearby confluence zones.

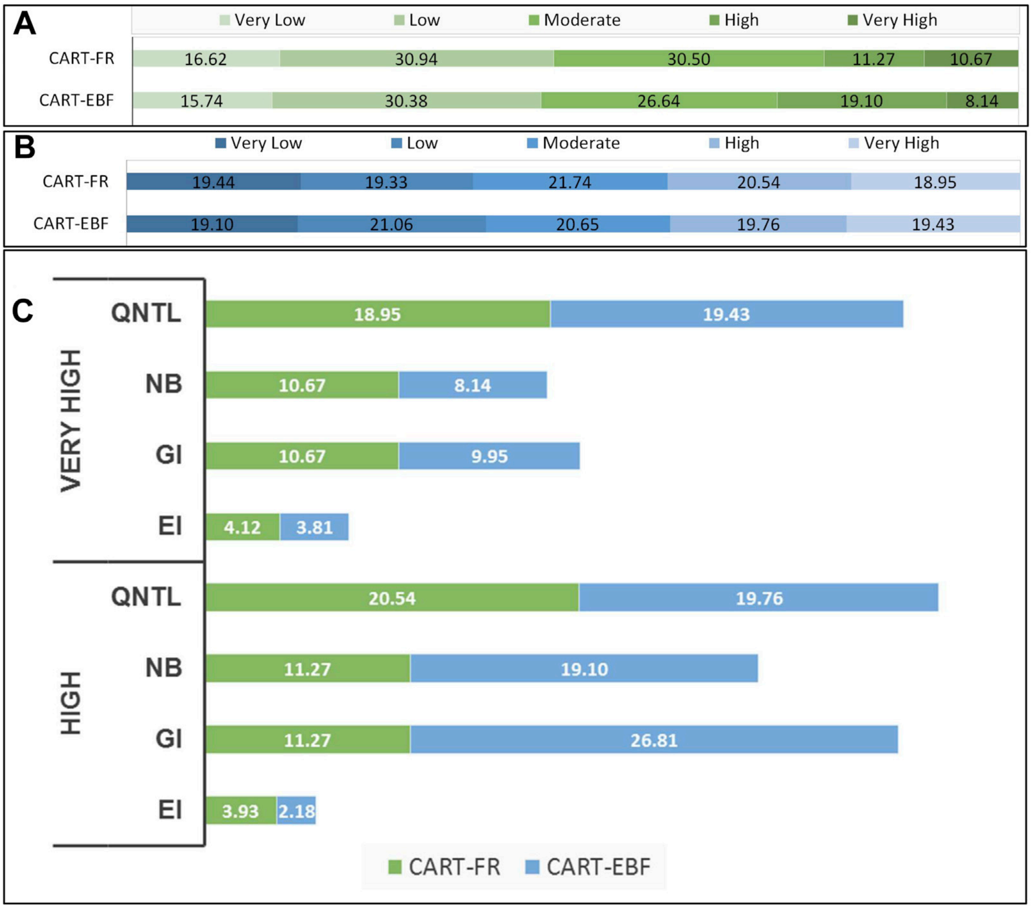

FIGURE 6 | FSPI histogram classification of both models' outputs. In parts **(A)** and **(B)**, Percentage share of areal coverage in "very low," "low," "medium," "high," and "very high" categories as classified by Natural Break (NB) and Quantile (QNTL) methods, respectively, is visualized, whereas, in part **(C)**, areal coverage (%) by using four methods (EI-Equal Interval; GI-Geometric Interval; NB-Natural break; and QNTL-quantile) for only "high" and "very high" classes is demonstrated.

the minimum cases of terminal nodes were kept equal to 10. Instead, in terms of the CART-FR model, the optimal minimum cases of parent nodes resulted to be 27, while the optimal minimum cases of terminal nodes were 12. Based on these details, the models, in the next step, have computed the weights for each of the flood predictors which are arrayed in **Table 5**. According to this **Table 5**, the CART-EBF and CART-FR have, computationally, annexed the "land use" (0.115) and the "geomorphology" (0.125) as highest weight scorers, respectively, followed by soil (0.114), geomorphology (0.111), altitude (0.073), TWI (0.021), aspect (0.020), river density (0.019), distance from river (0.015), road distance (0.015), rainfall (0.01), curvature (0.002), and slope angle (0.001) as per CART-EBF, and altitude (0.121), land use (0.054), soil (0.046), rainfall (0.039), distance from river (0.024), TWI (0.014), aspect (0.008), river density (0.007), curvature (0.005), road distance (0.004), and slope angle (0.002) according to CART-FR.

By applying these flood predictors' weights, the FSPI values were computed in raster calculator embedded in Spatial Analyst of ArcMap version 10.3 and categorized into 5 classes for carrying out flood zonation using four classification methods QNTL, NB, GI, and EI. The highest percentage share of flood pixels in the "very high" class category has been noted by QNTL (19.43%), and the second, third, and fourth rankers stood out to be GI (9.94%), NB (8.14%), and EI (3.81%) for CART-EBF. And for CART-FR, the first rank has been registered by QNTL (19.64%), followed by the lower rank holders in descending order as GI (5.11%), NB (3.92%), and EI (0.89%) respectively.

4.2 Model Performance Validation Through AUROC and Other Statistical Measures

In **Table 6**, model performance evaluation statistic matrices belonging to two categories of evaluators viz. cutoff-dependent, cutoff-independent, most of which are derived from confusion matrix related parameters, such as TP, TN, FP, and FN, are presented. These are used to assess different aspects of model performances, such as model accuracy or efficiency, precision, robustness, randomness driven performance, etc. Rahmati et al. (2019) reviewed 21 threshold-dependent model performance evaluation indices to judge

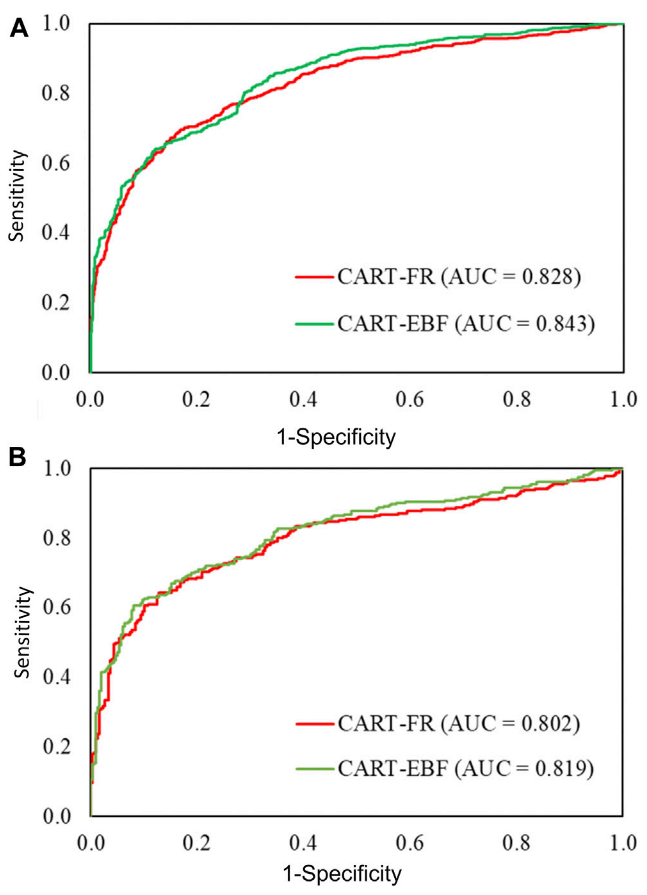

FIGURE 7 | Area under receiver operating characteristics (AUROC) curve for the model was constructed in a single graph in order to compare the model's performance. Validation of the models was performed using 30% of the randomly generated flood points specifically segregated from the points kept for the purpose of validation using AUROC statistical method. Panel **(A)** is computed using training dataset (represents model success rate) and Panel **(B)** with validation datasets (shows model prediction rate).

different aspects of the functioning of susceptibility models used in the field of natural hazard studies. We have used only 14 of those evaluators (given in **Table 6**) to refrain from making model evaluation sections of the paper lengthy. As suggested by Rahmati et al. (2019), the threshold-independent and threshold-dependent evaluators used in this work are discussed in the following **Sections 4.2.1**, **4.2.2**, respectively.

4.2.1 Threshold-independent Matrices

Area under receiver operating characteristic (AUROC) curve, success rate curve (SRC: ROC computed using training dataset), and prediction rate curve (PRC: ROC computed using validation dataset) for all the modeled results are given in **Figures 7A,B** and **Table 4**. For the training dataset, CART-EBF (84.3%) has performed better than CART-FR (82.8%), whereas AUROC concept applied to the dataset used for validation of models results in a higher prediction rate for CART-EBF (81.9%) and slightly lower for CART-FR (80.2%).

TABLE 4 | Specificity and sensitivity values using different cut-off thresholds.

Model	Cut-off threshold	Specificity	Sensitivity	Sum
CART-EBF	0.01	35.2	98.4	133.6
	0.1	56.1	96.4	152.5
	0.2	63.8	94.8	158.6
	0.3	75.3	90.1	165.4
	0.4	84.9	88.3	173.2
	0.5	86.5	86.4	172.9
	0.6	90.6	85.8	176.4
	0.7	92.1	81.2	173.3
	0.8	93.5	77.9	171.4
	0.9	96.2	67	163.2
	0.99	98.8	56.5	155.3
CART-FR	0.01	44.6	97.1	141.7
	0.1	58.9	96.5	155.4
	0.2	71.8	94.5	166.3
	0.3	77.5	92.7	170.2
	0.4	82.8	91.3	174.1
	0.5	90.3	90.2	180.5
	0.6	92	82.7	174.7
	0.7	96.7	79.5	176.2
	0.8	97.2	75.2	172.4
	0.9	98.5	68.9	167.4
	0.99	98.9	55	153.9

TABLE 5 | Weights of conditioning factors within the applied models.

Factors	CART-EBF	CART-FR
Altitude	0.073	0.121
Aspect	0.020	0.008
Curvature	0.002	0.005
Distance from river	0.015	0.024
Geomorphology	0.111	0.125
Land use	0.115	0.054
Rainfall	0.010	0.039
River density	0.019	0.007
Road distance	0.015	0.004
Slope angle	0.001	0.002
Soil	0.114	0.046
TWI	0.021	0.014

4.2.2 Threshold-dependent Matrices

All 14 threshold-dependent evaluation matrices are presented in **Table 4**. The detailed definition, formulae, and their interpretation are given by Frattini et al. (2010) and Rahmati et al. (2019). In terms of the overall accuracy of ensembles (for both training and validation datasets), the CART-EBF (Acc_{SR} = 81.40%; $Acc_{PR=}$79.60%) outsmarts the CART-FR (Acc_{SR} = 75.9%; $Acc_{PR=}$74.0%). In this study, both ensembles have exhibited sensitivity (TPR: true positive rate or the ability of models to correctly predict positives or flood points) in the range of 78.5–82.4% for the training dataset and 76.0–80.9% for validation dataset. The models' ability to correctly predict the negatives, i.e., non-flood points, is adjudged by the specificity or true negative rate (TNR) was found to be 0.738 for CART-FR for training dataset and for validation phases, and the TNR value is 0.723. The PPV (positive predictive value), also called as confidence or precision of predictive capacity of models, and its

TABLE 6 | Minimum and maximum FSPI values for all the flood susceptibility classes as per CART- EBF and CART-RF models.

	FSPI_ CART- EBF	
Class	Minimum	Maximum
Very low	0.000	0.235
Low	0.235	0.408
Medium	0.408	0.573
High	0.573	0.757
Very high	0.757	1.000
	FSPI_ CART- FR	
Class	Minimum	Maximum
Very low	0.000	0.153
Low	0.153	0.282
Medium	0.282	0.459
High	0.459	0.667
Very high	0.667	1.000

complementary metric FDR [false discovery rate, which deals with conceptualization of Type I error. See Frattini et al. (2010) for the definition of Type I and II errors] are used here to see how precisely the ensembles used here can predict flood pixels and non-flood pixels, respectively. The higher values of PPV and lower value of FDR are indicative of the high precision of prediction capability of ensembles. CART-FR with PPV: 0.714; FDR: 0.286 (for training data) and PPV: 0.783; FDR: 0.298 (for validation dataset) has been found to perform a little imprecisely than CART-EBF (**Table 6**). It should be noted that the lower the value of FNR, the better the model performance. Though accuracy and F1-score have been widely used to assess model performances, they sometimes lead to misleading implications. The F1-score does not take into account all the four primary matrices of the confusion matrix and that is where MCC (Mathew's Correlation Coefficient) plays a decisive role as it overcomes this shortcoming by incorporating all the four matrices (Chicco and Jurman, 2020). A look at the F1-Score and MCC values of the ensembles in **Table 6** reveals that when adjudged based on overall accuracy as well as F1 and MCC, the same sequence of performance levels emerges for both models. The k-index or kappa index, one of the most widely used statistic for model performance accuracy assessment, suffers from a lacuna involving its overdependence on prevalence or pervasiveness of samples (Allouche et al., 2006). Hence, to overcome this issue, an alternative measure, true skill statistic (TSS) has been computed and is presented in **Table 6**. According to k-index and TSS as well, when considered concomitantly, the CART-EBF model is the better accurately performing model during the training and validation phases than the CART-FR. **Table 6** lists the "informedness" or "bookmaker informedness; BMI," statistic referred to be the "only unbiased indicator" of model accuracy which helps with an informed selection of models.

4.2.3 SCAI- and FRP-Based Performance Evaluation

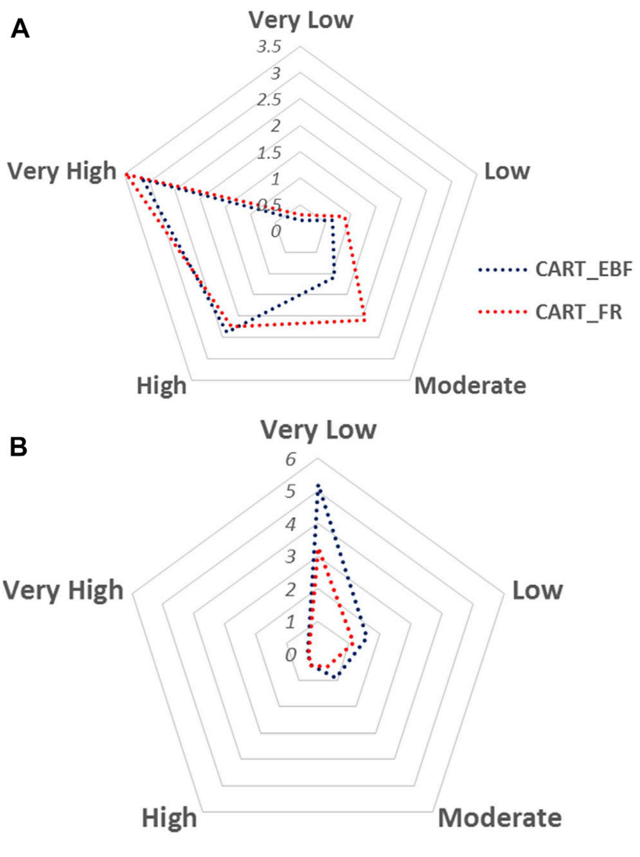

FIGURE 8 | Ensemble model result validation using: **(A)** Frequency Ratio Plot (FRP); and **(B)** Seed Cell Area Index (SCAI) methods.

The second round of validation matrices, SCAI-, and FRP-based performance of both ensembles' accuracy was performed to gain an extra level of confidence in model results. The computation of SCAI & FRP at the classwise level was performed as per methods discussed in **Sections 3.8**, **4.1.2**, respectively. In this study, as visible in **Figure 8B**, CART-EBF (SCAI = 5.209 for "very low" class) performs more accurately than CART-FR (SCAI = 83.263 for "very low" class). The FRP-based performance in **Figure 8A** shows that the FR values of the lower class of both ensembles are lower, just opposite to the behavior of SCAI, and that of "high" and "very high" susceptibility classes are higher. This pattern of FPR classwise values conforms to the result implications provided by SCAI values; and that have presented a better confidence level about the models' performance accuracy for both models.

4.3 Flood Pixel Distribution Vis-à-Vis FSPI Classes

Figures 6A–C and **Table 7** represent the final zonation of flood susceptible areas modeled by both the ensembles (classified using the natural break method). It shows areas highly susceptible (covering "high" and "very high" classes collectively) to flood menace and the safer zones. The FSPI values in the "high" and "very high" classes were used to compute the distribution of areas falling under these two classes (**Figure 6**). Since the QNTL has been found to delineate the highest percentage of areas under "very high"

TABLE 7 | Statistical metrices used for model performance evaluation (Note: All the abbreviations used in this table are expanded and defined below this table itself).

Measures	Training		Validation	
	CART-FR	CART-EBF	CART-FR	CART-EBF
TP	347	388	146	161
TN	391	403	162	170
FP	139	98	62	47
FN	95	83	46	38
ACC	0.759	0.814	0.74	0.796
TPR	0.785	0.824	0.76	0.809
TNR	0.738	0.804	0.723	0.783
PPV	0.714	0.798	0.702	0.774
FDR	0.286	0.202	0.298	0.226
NPV	0.805	0.829	0.779	0.817
FPR	0.262	0.196	0.277	0.217
FNR	0.215	0.176	0.24	0.191
k-index	0.519	0.628	0.481	0.591
TSS	0.523	0.628	0.483	0.592
F1	0.748	0.811	0.73	0.791
MCC	0.521	0.628	0.482	0.592
BMI	0.523	0.628	0.484	0.592
TS	0.597	0.682	0.575	0.654
AUROC	0.828	0.843	0.802	0.819

Abbreviation	Expansion/meaning	Formulae
TP	True positive/correctly predicting a label (model predicts “yes,” and it’s “yes”)	—
TN	True negative/correctly predicting the other label (model predicts “no,” and it’s “no”)	—
FP	False positive/falsely predicting a label (model predicts “yes,” but it’s “no”)	—
FN	False negative/missing and incoming label (model predicts “no,” but it’s “yes”)	—
TPR	True positive rate/sensitivity	—
TNR	True negative rate/or specificity (SPC)	—
PPV	Positive predictive value/or precision	$PPV = TP/(TP + FP)$
NPV	Negative predictive value	$NPV = TN/(TN + FN)$
FPR	False positive rate/or fall-out	$FPR = FP/(FP + TN)$
FDR	False discovery rate	$FDR = FP/(FP + TP)$
FNR	False negative rate/or miss rate	$FNR = FN/(FN + TP)$
ACC	Accuracy	ACC=(TP + TN)/((TP + TN + FN + FP))
F1	F1 Score	$F - Score\ (F_\beta) = (1 + \beta^2)\ (Precision \times Sensitivity)/(\beta^2)$ $(Precision + Sensitivity)$; β = default parameter, commonly taken to be between 0.5 and 2, but here in this study, it is taken to be 1
MCC	Matthew’s correlation coefficient	$MCC = (TP^*TN - FP^*FN)/\sqrt[2]{\{(TP + FP)^*(TP + FN)^*(TN + FP)^*(TN + FN)\}}$
TSS	True skill statistic Allouche et al. (2006)	$TSS = TPR + TNR - 1$
k-index	Kappa statistic or kappa coefficient	Formulae of Kappa index is given in main body text
AUROC	Area under receiver operating characteristic curve/ it assesses the model’s capability to predict correctly	$AUROC = (\sum TP + \sum TN)/(P + N)$; P = number of flood pixels; N = number of non-flood pixels
BMI	Bookmaker Informedness or simply Informedness or BM	$BMI = TPR + NPR - 1$
TS	Threat score/used to measure the ability to correct or observe events; it penalizes FNs, FPs	$TS = TP/(TP + FN + FP)$

The abbreviations used in the above table are here to avoid any inconvenience for readers to have a quick lookout on the table values.

class, as discussed in **Section 4.1.3**, and in most of the published results, the final zonal classifications are performed by using NB, and the QNTL-based areal shares (in %) corresponding to the NB-based areal shares of “high” and “very high” classes are also shown and discussed here in this section using **Figures 6A,B**. The CART-EBF covers 27.24% areal coverage (as per NB classification method), whereas, as per the QNTL methods, CART-EBF encompasses 49.49% area under high and very high classes [see **Table 7** (for FSPI) and **Supplementary Table S1A** for % areal coverage by each class]. The lower areal percentage coverage was produced by CART-FR (21.94% as per NB) and 29.49% as per QNTL.

5 DISCUSSION

5.1 Flood Predictor Significance

Predictor selection for the natural hazard susceptibility prediction aiming at determining the significance levels of contributing factors/control factors is done at three stages (Janizadeh et al., 2019). 1) First, multicollinearity analysis (VIF and TOL) is performed before training the models. This helps to root out all the interdependent control factors. 2) Then, orderly levels of contribution of control factors in computation of natural hazard susceptibility prediction indices (NHSPIs) are analyzed using the factor selection techniques such as IG, relief-F, RF. Control factors with weights higher than zero only are included in the model training and validation processes. 3) Finally, by application of all the models, weights are retrieved to all the conditioning factors. The second-stage results using IG were useful for winnowing out the flood predictors with zero weightage values to be included in the analysis even when their multicollinearity results of the first stage allowed them to be included for further step of the model training. The output from the third stage of the control factor is helpful at the policy formulation level in hazard management. The exact knowledge of the area-specific flood-predicting control factors will help hazard-related policy formulators to allocate funds that manage those respective flood predictors on a priority basis as compared to others. There are numerous techniques used for assessing the significance of contributing factors at aforesaid second and third stages. The type and number of conditioning factors (for floods) depend upon several variables including type topographic and climatic settings (Benson, 1963; Merz et al., 2014) as well as the type of flood, e.g., flash flood, precipitation-induced riverine flood, coastal storm flood, tsunami induced flooding (Pignatelli et al., 2009), or glacial lake outburst flood (GLOF) (Aggarwal et al., 2017)/landslide lake outburst flood (LLOF) (Srivastava et al., 2017). The quality of topographic data (Cook and Merwade, 2009) can also affect the predictor significance. High-resolution LiDAR-derived DEMs (Laks et al., 2017) and their derivatives behave differently than those which are derived using freely available DEMs, such as SRTM 30 m, ASTER 30 m, AW3D 30 m. For fluvial or riverine floods in mountainous areas, terrain parameters perform better when derived from ALOS World 3D 30 m (AW3D 30 m) (Boulton and Stokes, 2018), but the situation gets reversed for flat floodplain environmental setting like MGP (Tanaka et al., 2019). Since there is no specific guideline set for choosing the predictor significance assessment method and several previous studies use the medium resolution DEM dataset for deriving topography-based predictors (Santos et al., 2019), SRTM 30 m version 4 DEM-derived topographic variables were computed (see **Section 2**), and their significance was analyzed using IG. The results of this analysis show that detailed geomorphological mapping derived geomorphic units have played a very important role in flood susceptibility prediction using IG method. The second rank assigned to "distance to river" by this method appears to be true as the "2008 Bihar" flood, which is the source of flood inventory in this work, was a riverine flood due to overbank flooding caused by levee breach in the upstream Kosi megafan area leading to the sudden supply of water discharged for the lower reaches (UNDP Emergency Analyst, 2008). There was a time lag of around 10 days between the excessive rainfall in upper catchments, Kosi levee breach, and 2008 Bihar flooding (for which we have created our flood inventory), that's why "rainfall" has scored least significance as a flood predictor. The reason for geomorphology bearing the first place on the significance score scale is that in the fluvial environments, most of the geomorphic forms evolve through processes governed by rivers' hydrological, hydraulic, erosive, depositional, etc., characteristics. In a study conducted in the mountainous catchment of the northeast region, Lao Cai, of Vietnam, the DEM-derived predictor "slope angle" has received the highest predictive value whereas another DEM-derived parameter "curvature" was reported to be the least predictive factor (Bui et al., 2019a). The same study highlights that four other predictors, out of 12 used in that study, which have scored high significance scores, were DEM-derived parameters. In this study, four DEM-derived parameters: aspect, TWI, altitude, and slope have scored significant weights as per IG, equivalent to second, third, fourth, and fifth ranks, respectively. Irrespective of their apparent image of being dominant control factors of floods, rainfall could not stand among first five contributing factors in this study which conforms to the findings by other studies conducted in different parts of the globe (Tien Bui et al., 2020). Khosravi et al. (2019) conducted a study in a hilly moderate relief topographic setting (altitude range: 29–1,410 m) located in China and found that rainfall doesn't have significant predictive significance. In their study, altitude scored the highest predictive significance followed by distance from river, NDVI, soil, slope, lithology, LULC, STI, rainfall, SPI, and curvature. There are variations in the significance scores of DEM-derived contributing factors such as slope, aspect, curvature, stream power index (SPI), terrain surface texture (TST), topographic position index (TPI), etc. and that may be because of a number of factors related to DEM resolution, algorithms used (IG, relief-F, RF, SWARA, etc.), type of topographic setting (plain or mountainous), number of factors used in the modeling exercise, etc. We could not find a study that has sorted out this issue of variability in the significance scores of conditioning factors due to the variability in data quality, use of different techniques/algorithms, number of conditioning factors, to name a few among others. Hence, there is a need for future research on this theme.

5.2 Nature of Flood, Predictor Selection, Topoclimatic Setting

The literature is replete with studies conducted with the aims of applying a new model for susceptibility prediction of different types of natural phenomena like floods (Ngo et al., 2018). Looking at the number and type of conditioning factors used by these studies, it appears that there is no clear guideline as to how many conditioning factors and which conditioning factors should be applied for, say, floods susceptibility, or landslide susceptibility, or ground subsistence susceptibility, or groundwater potential mapping exercises that can accrue to most optimal model performance. One common practice seen in the flood susceptibility modeling studies is that most of the researchers use "geology" or lithology as one of the control factors for flash floods, riverine floods, and storm surge related floods irrespective of whether they occur in mountainous regions, floodplain zones of low-relief settings, high mountain plateau provinces (Ngo et al., 2018), or coastal zones (Dodangeh et al., 2020), and in all these studies, the significance level of "lithology" stood out to (Di et al., 2019) be at sixth or later ranks. But there has been no study which employed detailed microlevel "geomorphology" as a control factor in low-relief topographic zone's riverine flooding events. Selection of geomorphology as a proxy for flood susceptibility has been essentially chosen here because the area is affected by active tectonic perturbances, and continuous and fast groundwater depletion is causing ground subsidence. And geomorphology directly reveals those effects. Vegetation in different types of topographic and climatic settings shows the variance in their type (Kumar, 2016), and hence, vegetation diversity in different terrain types will alter the characteristics of NDVI and its threshold (Davenport and Nicholson, 1993). Keeping these associations between vegetation diversity changes and topoclimatic environmental variability, application of NDVI threshold may change its significance score, and hence, model performance too can follow suit.

5.3 Comparative Assessment of Ensemble Models' Performance Vis-à-Vis Topoclimatic Setting

The EBF- and FR-based two ensembles with CART used in this work have yielded accuracy levels, as adjudged in terms of the threshold-independent statistics like AUROC, in the range of widely acceptable limits as per the classification scheme of AUROC values followed by Fressard et al. (2014). Both the ensemble models' AUROC has been found to be within the range of 0.828–0.8432 (for training dataset) and 0.802–0.819 (for validation dataset). The higher AUROC, for both the training and validation datasets (also known as success rate or SR and prediction rate or PR of the model), has been scored by CART-EBF (SR = 0.843; PR = 0.819) and slightly lower by CART-FR (SR = 0.828; PR = 0.802) (**Figures 7A,B**). It is worth noting that this study has been performed in a low altitude (altitude range: <45.0–96.0 m AMSL) humid monsoonal climatic region undergoing constant active tectonic perturbances (Valdiya, 1976; Brown and Nicholls, 2015) and hence frequent and more severe flooding in the low-lying subsiding areas. In such a topographic environment, the use of moderate spatial resolution digital elevation data lends more levels of uncertainty errors which further propagate in other derivatives computed using this data (Oksanen and Sarjakoski, 2005). In such topographic settings, augmentation of topographic data quality has the potential to enhance the accuracy of DEM-derived input parameters (Sanders, 2007) and hence the models' performances (van Westen et al., 2008). By applying the LR-, MLP-, and CART-based ensemble with a different bivariate model viz. statistical index (SI) for an area located in the mountainous and hilly part of Romania (altitudinal range: 242–1,463 m AMSL, characterized by temperate continental climate), Costache et al. (2020) have achieved both success rate and prediction rate accuracies of 0.94 (MLP-SI), 0.939 (CART-SI), 0.925 (LR-SI) and 0.927 (MLP-SI), 0.922 (CART-SI), 0.901 (LR-SI), respectively. There are 10 flood control factors selected by Costache et al. (2020), for flash flood occurrence prediction in his study area, and four out of them viz. L-S factor, hydrological soil group (HSG), stream power index (SPI), and topographic position index (TPI) are different from our study. In another study, Costache and Tien Bui (2019) investigated flash flood susceptibility prediction in different parts of Romania in similar topoclimatic setting for flash flood susceptibility prediction but with 14 flood predictors, five of which are different from ours, and achieved almost same levels of accuracy of success and prediction rates, as their previous study discussed just above in this section, but better than ours, ranging from MLP-FR (0.94), CART-FR (0.937) and MLP-FR (0.981), CART-FR (0.929), respectively. MLP-EBF trained and validated with 10 flash flood conditioning factors in hilly and mountainous catchment dominated by temperate climate has accrued 0.912 AUROC success rate accuracy and 0.806 prediction rate accuracy in identifying torrential valleys vulnerable to flash floods (Costache et al., 2019). In almost similar (similar to ours) flat terrain setting and climate, Hong et al. (2018a) have conducted a study wherein the altitude range was between <40–720 m AMSL in the southeastern part of China to investigate the fuzzy weight of evidence (fuzzy-WofE)-based ensembles with logistic regression (LR), random forest (RF), and support vector machine (SVM) using 11 conditioning factors, three of which differed from ours, but their reported success rate accuracy and prediction rate accuracy levels were in the range of 0.9519 (fWofE-LR)–0.9882 (fWofE-SVM) and 0.9652 (fWofE-LR)–0.9865 (fWofE-SVM), respectively. This study reveals that SVM- and fuzzy-WofE-based ensemble has the capability to perform much better, accuracy-wise, in like MGP topoclimatic setting, with freely available moderate quality DEM-like ASTER 30 m.

Other reasons that affect model performance levels include quality of flood inventory generated using different methodologies, like some use NDWI (Jain et al., 2005), mNDWI (Mohammadi et al., 2017) with different threshold values, or some other methods using various sensors of satellite datasets such as optical Landsat 7 ETM+ and Landsat 8 OLI imageries (Kumar, 2016), or radar data (Ward et al., 2014), and water surface DEM and bare-earth LiDAR DEM differencing (Guerriero et al., 2018). Variations in the number of flood and non-flood points meant for training and validation of models, resolution of DEM to derive topography-based flood predictors, and other related parameters also affect the flood inventory accuracy and hence alter the model performance. Regarding DEM data quality, Podhorányi et al. (2013) who have used LiDAR derived DEM data, have asserted that the DEM data quality has an inverse relationship with the level of uncertainties involved, i.e. better the data quality, lesser is the level of uncertainty in DEM derived parameters. And hence, for better performance of susceptibility models, higher quality DEM is warranted. On the other hand, Chen et al. (2020) have used freely available different DEMs in the spatial resolution range of 30–90 m (all derived by resampling of 30 m ASTER DEM), and they reported that DEM spatial resolution does not necessarily affect the susceptibility model results. It should be noted that the difference between Chen's results and that of Podhorányi's maybe because Chen has derived all the seven variants of DEMs from the same ASTER 30 m data whereas the latter created their DEM from point clouds collected using LiDAR which has proven excellent in several aspects over freely available moderate resolution DEMs (Goulden et al., 2014). Different statistic matrices presented here in this work indicate different aspects of model performances like how good the prediction accuracy is or how sensitive the model behaves and what is the overall performance of the individual ensembles or how badly the model fails to predict flood or non-flood pixels, and other such aspects.

6 CONCLUSION AND RECOMMENDATIONS FOR FUTURE RESEARCH

To achieve the goal of flood susceptible area zonation of MGP based on FSPI produced by applying different ensembles of models, this study is the next in the series of models' testing after Arora et al. (2021b). This study, based on AUROC, has shown that the CART-based ensembles with bivariates EBF and FR perform reasonably well with both success and prediction. When it comes to utilizing moderate resolution-based conditioning factors, by using as less as 12 conditioning factors only, the decision of selecting ensembles for flood zonation mapping, which is an essential requirement for achieving sustainable development goals (SDGs) set by United Nations related to flooding, it is recommended that CART-EBF should be given priority over CART-FR. Different threshold-dependent statistic indices connote different aspects of model performances (detailed in references cited in **Section 3.8**), and based on user's requirements, the researchers and agencies are recommended to make their choices. Another point that emerges out of the models' output used herein is that both the models have their performance accuracies in the range of "good" as per the traditional AUROC classification scheme.

Detailed microscale geomorphic mapping is based on "geomorphology" as playing the best contributor in the susceptibility prediction mapping. The rank of geomorphology as number one in tectonically active areas and in fluvial floodplain areas affected by regular riverine flooding appears to be because this factor incorporates effects of active tectonic activity and ground subsidence related to excessive and fast groundwater depletion. Looking at its significance, it is advised that the government of concerned areas having similar topoclimatic setting first gets the areas geomorphologically mapped by using high-resolution satellite to be used as input in the flood susceptible zonation exercises. The research by Arora et al. (2021a) also vindicates this observation.

Some of the limitations faced in this work are: 1) instead of ground truth points collected using GPS in the field, we have used Google Earth Pro® for validation of non-flood points; 2) moderate resolution DEM used for computation of input flood predictions. Use of DEMs prepared using point cloud obtained with unmanned aerial vehicles (UAVs) or pulsed laser light-based LiDAR DEMs, or terrestrial laser scanning (TLS) device-based DEMs would have affected the model performance accuracy that affects the susceptibility zone percentage shares. The testing of all kinds of models, both standalone and ensembles, of all family of models, for instance, machine learning, statistical, multicriteria decision-making models highlighting their advantages and disadvantages as well as new model development is recommended to have a better understanding of optimality in the behavior of models. Since in the forthcoming future, the age is going to be of machines, space-based monitoring, and quantification of all natural and man-made phenomena with the best possible accuracy and precision will be the prime information that will be needed. In the coming future, the missions like surface water and oceans topography (SWOT) (Morrow et al., 2019) will be the need of the time to monitor all the phenomena including floods from space, and instantaneous susceptibility prediction zonation of areas will be instantly planned to be done in such missions at the control rooms of such missions. Model universalization by the selection of the best model through rigorous testing and validation of the available models of different genres performing with higher accuracy in a particular type of topoclimatic environmental setting will help guide such future missions.

DATA AVAILABILITY STATEMENT

The original contributions presented in the study are included in the article/**Supplementary Material**, and further inquiries can be directed to the corresponding authors.

AUTHOR CONTRIBUTIONS

AArora and MP: Conceptualization, database preparation, and model output presentation in map and graph chart form and manuscript writing; AA and RC: Modeling and analysis; NK, VNM, HN, JM, MAS, YR, SS, and UKS: Manuscript writing, enhancement, guidance during write up, and manuscript revision during first and second rounds of review.

ACKNOWLEDGMENTS

The authors are grateful to the department of geography, JMI for allowing the GIS lab for carrying out the part of analyses. The lab facility at the Department of Civil Engineering, Chandigarh University, Punjab, is acknowledged for they have allowed some part of the work to be carried out therein. Any use of trade, firm, or product name is for descriptive purposes only and does not imply endorsement by the authors.

REFERENCES

Abdullahi, S., Pradhan, B., and Jebur, M. N. (2015). GIS-based Sustainable City Compactness Assessment Using Integration of MCDM, Bayes Theorem and RADAR Technology. *Geocarto Int.* 30, 365–387. doi:10.1080/10106049.2014.911967

Aggarwal, S., Rai, S. C., Thakur, P. K., and Emmer, A. (2017). Inventory and Recently Increasing GLOF Susceptibility of Glacial Lakes in Sikkim, Eastern Himalaya. *Geomorphology* 295, 39–54. doi:10.1016/j.geomorph.2017.06.014

Aghdam, I. N., Pradhan, B., and Panahi, M. (2017). Landslide Susceptibility Assessment Using a Novel Hybrid Model of Statistical Bivariate Methods (FR and WOE) and Adaptive Neuro-Fuzzy Inference System (ANFIS) at Southern Zagros Mountains in Iran. *Environ. Earth Sci.* 76, 237. doi:10.1007/s12665-017-6558-0

Ahmadlou, M., Karimi, M., Alizadeh, S., Shirzadi, A., Parvinnejhad, D., Shahabi, H., et al. (2018). Flood Susceptibility Assessment Using Integration of Adaptive Network-Based Fuzzy Inference System (ANFIS) and Biogeography-Based Optimization (BBO) and BAT Algorithms (BA). *Geocarto Int.* 34, 1252–1272. doi:10.1080/10106049.2018.1474276

Al-Rawas, G. A., and Valeo, C. (2010). Relationship between Wadi Drainage Characteristics and Peak-Flood Flows in Arid Northern Oman. *Hydrological Sci. J.* 55, 377–393. doi:10.1080/02626661003718318

Alam, M. M., Zhu, Z., Eren Tokgoz, B., Zhang, J., and Hwang, S. (2020). Automatic Assessment and Prediction of the Resilience of Utility Poles Using Unmanned Aerial Vehicles and Computer Vision Techniques. *Int. J. Disaster Risk Sci.* 11, 119–132. doi:10.1007/s13753-020-00254-1

Ali, S. A., Parvin, F., Pham, Q. B., Vojtek, M., Vojteková, J., Costache, R., et al. (2020). GIS-based Comparative Assessment of Flood Susceptibility Mapping Using Hybrid Multi-Criteria Decision-Making Approach, Naïve Bayes Tree, Bivariate Statistics and Logistic Regression: A Case of Topľa basin, Slovakia. *Ecol. Indicators* 117, 106620. doi:10.1016/j.ecolind.2020.106620

Alin, A. (2010). Multicollinearity. *Wires Comp. Stat.* 2, 370–374. doi:10.1002/wics.84

Allouche, O., Tsoar, A., and Kadmon, R. (2006). Assessing the Accuracy of Species Distribution Models: Prevalence, Kappa and the True Skill Statistic (TSS). *J. Appl. Ecol.* 43, 1223–1232. doi:10.1111/j.1365-2664.2006.01214.x

Arabameri, A., Rezaei, K., Cerdà, A., Conoscenti, C., and Kalantari, Z. (2019a). A Comparison of Statistical Methods and Multi-Criteria Decision Making to Map Flood hazard Susceptibility in Northern Iran. *Sci. Total Environ.* 660, 443–458. doi:10.1016/j.scitotenv.2019.01.021

Arabameri, A., Saha, S., Chen, W., Roy, J., Pradhan, B., and Bui, D. T. (2020b). Flash Flood Susceptibility Modelling Using Functional Tree and Hybrid Ensemble Techniques. *J. Hydrol.* 587, 125007. doi:10.1016/j.jhydrol.2020.125007

Arabameri, A., Saha, S., Roy, J., Tiefenbacher, J. P., Cerda, A., Biggs, T., et al. (2020c). A Novel Ensemble Computational Intelligence Approach for the Spatial Prediction of Land Subsidence Susceptibility. *Sci. Total Environ.* 726, 138595. doi:10.1016/j.scitotenv.2020.138595

Arabameri, A., Yamani, M., Pradhan, B., Melesse, A., Shirani, K., and Tien Bui, D. (2019b). Novel Ensembles of COPRAS Multi-Criteria Decision-Making with Logistic Regression, Boosted Regression Tree, and Random forest for Spatial Prediction of Gully Erosion Susceptibility. *Sci. Total Environ.* 688, 903–916. doi:10.1016/j.scitotenv.2019.06.205

Arora, A., Arabameri, A., Pandey, M., Siddiqui, M. A., Shukla, U. K., Bui, D. T., et al. (2021a). Optimization of State-Of-The-Art Fuzzy-Metaheuristic ANFIS-Based Machine Learning Models for Flood Susceptibility Prediction Mapping in the Middle Ganga Plain, India. *Sci. Total Environ.* 750, 141565. doi:10.1016/j.scitotenv.2020.141565

Arora, A., Pandey, M., Siddiqui, M. A., Hong, H., and Mishra, V. N. (2021b). Spatial Flood Susceptibility Prediction in Middle Ganga Plain: Comparison of Frequency Ratio and Shannon's Entropy Models. *Geocarto Int.* 36, 2085–2116. doi:10.1080/10106049.2019.1687594

Baattrup-Pedersen, A., Andersen, H. E., Larsen, S. E., Nygaard, B., and Ejrnæs, R. (2012). Predictive Modelling of Protected Habitats in Riparian Areas from Catchment Characteristics. *Ecol. Indicators* 18, 227–235. doi:10.1016/j.ecolind.2011.11.012

Ban, H.-J., Kwon, Y.-J., Shin, H., Ryu, H.-S., and Hong, S. (2017). Flood Monitoring Using Satellite-Based RGB Composite Imagery and Refractive Index Retrieval in Visible and Near-Infrared Bands. *Remote Sensing* 9, 313. doi:10.3390/rs9040313

Benson, M. A. (1963). *Factors Influencing the Occurrence of Floods in a Humid Region of Diverse Terrain*. Geological Survey: US Department of the Interior. doi:10.3133/wsp1580B

Bhatt, C. M., Srinivasa Rao, G., Manjushree, P., and Bhanumurthy, V. (2010). Space Based Disaster Management of 2008 Kosi Floods, North Bihar, India. *J. Indian Soc. Remote Sens* 38, 99–108. doi:10.1007/s12524-010-0015-9

Boerner, W.-M. (2007). "Recent Advancements of Radar Remote Sensing; Air- and Space-Borne Multimodal SAR Remote Sensing in Forestry & Agriculture, Geology, Geophysics (Volcanology and Tectonology): Advances in P0L-SAR, IN-SAR, POLinSAR and POL-DIFF-IN-SAR Sensing and Imaging with Applications to Environmental and Geodynamic Stress-Change Monitoring," in *2007 Asia-Pacific Microwave Conference* (IEEE), 1–4. doi:10.1109/APMC.2007.4555164

Boulton, S. J., and Stokes, M. (2018). Which DEM Is Best for Analyzing Fluvial Landscape Development in Mountainous Terrains? *Geomorphology* 310, 168–187. doi:10.1016/j.geomorph.2018.03.002

Breiman, L., Friedman, J. H., Olshen, R. A., and Stone, C. J. (1984). *Classification and Regression Trees*. Oxfordshire, England: Routledge. doi:10.1201/9781315139470

Brown, S., and Nicholls, R. J. (2015). Subsidence and Human Influences in Mega Deltas: The Case of the Ganges-Brahmaputra-Meghna. *Sci. Total Environ.* 527-528, 362–374. doi:10.1016/j.scitotenv.2015.04.124

Bui, D. T., Panahi, M., Shahabi, H., Singh, V. P., Shirzadi, A., Chapi, K., et al. (2018). Novel Hybrid Evolutionary Algorithms for Spatial Prediction of Floods. *Sci. Rep.* 8, 15364. doi:10.1038/s41598-018-33755-7

Bui, D. T., Tsangaratos, P., Ngo, P.-T. T., Pham, T. D., and Pham, B. T. (2019a). Flash Flood Susceptibility Modeling Using an Optimized Fuzzy Rule Based Feature Selection Technique and Tree Based Ensemble Methods. *Sci. Total Environ.* 668, 1038–1054. doi:10.1016/j.scitotenv.2019.02.422

Chapi, K., Singh, V. P., Shirzadi, A., Shahabi, H., Bui, D. T., Pham, B. T., et al. (2017). A Novel Hybrid Artificial Intelligence Approach for Flood Susceptibility Assessment. *Environ. Model. Softw.* 95, 229–245. doi:10.1016/j.envsoft.2017.06.012

Chen, S., Zhan, R., Wang, W., and Zhang, J. (2021). Learning Slimming SAR Ship Object Detector through Network Pruning and Knowledge Distillation. *IEEE J. Sel. Top. Appl. Earth Observations Remote Sensing* 14, 1267–1282. doi:10.1109/JSTARS.2020.3041783

Chen, Z., Ye, F., Fu, W., Ke, Y., and Hong, H. (2020). The Influence of DEM Spatial Resolution on Landslide Susceptibility Mapping in the Baxie River basin, NW China. *Nat. Hazards* 101, 853–877. doi:10.1007/s11069-020-03899-9

Cheng, G., and Han, J. (2016). A Survey on Object Detection in Optical Remote Sensing Images. *ISPRS J. Photogrammetry Remote Sensing* 117, 11–28. doi:10.1016/j.isprsjprs.2016.03.014

Chicco, D., and Jurman, G. (2020). The Advantages of the Matthews Correlation Coefficient (MCC) over F1 Score and Accuracy in Binary Classification Evaluation. *BMC Genomics* 21, 6. doi:10.1186/s12864-019-6413-7

Choubin, B., Moradi, E., Golshan, M., Adamowski, J., Sajedi-Hosseini, F., and Mosavi, A. (2019). An Ensemble Prediction of Flood Susceptibility Using Multivariate Discriminant Analysis, Classification and Regression Trees, and Support Vector Machines. *Sci. Total Environ.* 651, 2087–2096. doi:10.1016/j.scitotenv.2018.10.064

SUPPLEMENTARY MATERIAL

The Supplementary Material for this article can be found online at: https://www.frontiersin.org/articles/10.3389/feart.2021.659296/full#supplementary-material

Cohen, J. (1960). A Coefficient of Agreement for Nominal Scales. *Educ. Psychol. Meas.* 20, 37–46. doi:10.1177/001316446002000104

Cook, A., and Merwade, V. (2009). Effect of Topographic Data, Geometric Configuration and Modeling Approach on Flood Inundation Mapping. *J. Hydrol.* 377, 131–142. doi:10.1016/j.jhydrol.2009.08.015

Costache, R. (2019). Flash-Flood Potential Assessment in the Upper and Middle Sector of Prahova River Catchment (Romania). A Comparative Approach between Four Hybrid Models. *Sci. Total Environ.* 659, 1115–1134. doi:10.1016/j.scitotenv.2018.12.397

Costache, R., Hong, H., and Pham, Q. B. (2020). Comparative Assessment of the Flash-Flood Potential within Small Mountain Catchments Using Bivariate Statistics and Their Novel Hybrid Integration with Machine Learning Models. *Sci. Total Environ.* 711, 134514. doi:10.1016/j.scitotenv.2019.134514

Costache, R., Pham, Q. B., Arabameri, A., Diaconu, D. C., Costache, I., Crăciun, A., et al. (2021). Flash-flood Propagation Susceptibility Estimation Using Weights of Evidence and Their Novel Ensembles with Multicriteria Decision Making and Machine Learning. *Geocarto Int.* 1, 1–32. doi:10.1080/10106049.2021.2001580

Costache, R., Pham, Q. B., Sharifi, E., Linh, N. T. T., Abba, S. I., Vojtek, M., et al. (2019). Flash-Flood Susceptibility Assessment Using Multi-Criteria Decision Making and Machine Learning Supported by Remote Sensing and GIS Techniques. *Remote Sensing* 12, 106. doi:10.3390/rs12010106

Costache, R., and Tien Bui, D. (2019). Spatial Prediction of Flood Potential Using New Ensembles of Bivariate Statistics and Artificial Intelligence: A Case Study at the Putna River Catchment of Romania. *Sci. Total Environ.* 691, 1098–1118. doi:10.1016/j.scitotenv.2019.07.197

CWC (2018). Flood Damage Statistics (Statewise and for the Country as a Whole) for the Period 1953 to 2016; Central Water Commission (CWC), Flood Forecast Monitoring Directorate, Government of India. Available at: http://www.indiaenvironmentportal.org.in/content/456110/flood-damage-statistics-statewise-and-for-the-country-as-a-whole-for-the-period-1953-to-2016/.

Davenport, M. L., and Nicholson, S. E. (1993). On the Relation between Rainfall and the Normalized Difference Vegetation Index for Diverse Vegetation Types in East Africa. *Int. J. Remote Sensing* 14, 2369–2389. doi:10.1080/01431169308954042

De Brito, M. M., and Evers, M. (2016). Multi-criteria Decision-Making for Flood Risk Management: A Survey of the Current State of the Art. *Nat. Hazards Earth Syst. Sci.* 16, 1019–1033. doi:10.5194/nhess-16-1019-2016

Dempster, A. P. (1967). Upper and Lower Probabilities Induced by a Multivalued Mapping. *Ann. Math. Statist.* 38, 325–339. doi:10.1214/aoms/1177698950

Di, B., Zhang, H., Liu, Y., Li, J., Chen, N., Stamatopoulos, C. A., et al. (2019). Assessing Susceptibility of Debris Flow in Southwest China Using Gradient Boosting Machine. *Sci. Rep.* 9, 12532. doi:10.1038/s41598-019-48986-5

Dimri, A. P., and Chevuturi, A. (2016). "Western Disturbances - Structure," in *Western Disturbances - an Indian Meteorological Perspective* (Cham: Springer International Publishing), 1–26. doi:10.1007/978-3-319-26737-1_1

Dimri, A. P. (2019). Comparison of Regional and Seasonal Changes and Trends in Daily Surface Temperature Extremes over India and its Subregions. *Theor. Appl. Climatol* 136, 265–286. doi:10.1007/s00704-018-2486-5

Dodangeh, E., Choubin, B., Eigdir, A. N., Nabipour, N., Panahi, M., Shamshirband, S., et al. (2020). Integrated Machine Learning Methods with Resampling Algorithms for Flood Susceptibility Prediction. *Sci. Total Environ.* 705, 135983. doi:10.1016/j.scitotenv.2019.135983

Dormann, C. F., Elith, J., Bacher, S., Buchmann, C., Carl, G., Carré, G., et al. (2013). Collinearity: a Review of Methods to deal with it and a Simulation Study Evaluating Their Performance. *Ecography* 36, 27–46. doi:10.1111/j.1600-0587.2012.07348.x

Dragićević, S., Lai, T., and Balram, S. (2015). GIS-based Multicriteria Evaluation with Multiscale Analysis to Characterize Urban Landslide Susceptibility in Data-Scarce Environments. *Habitat Int.* 45, 114–125. doi:10.1016/j.habitatint.2014.06.031

Đurić, U., Marjanović, M., Radić, Z., and Abolmasov, B. (2019). Machine Learning Based Landslide Assessment of the Belgrade Metropolitan Area: Pixel Resolution Effects and a Cross-Scaling Concept. *Eng. Geology.* 256, 23–38. doi:10.1016/j.enggeo.2019.05.007

ESA (2017). Land Cover CCI Product User Guide Version 2.0. Available at: http://maps.elie.ucl.ac.be/CCI/viewer/download/ESACCI-LC-Ph2-PUGv2_2.0.pdf.

Fan, H., Zipf, A., Fu, Q., and Neis, P. (2014). Quality Assessment for Building Footprints Data on OpenStreetMap. *Int. J. Geographical Inf. Sci.* 28, 700–719. doi:10.1080/13658816.2013.867495

FAO and ITPS (2015). *Main Report: Status of the World's Soil Resources; Food and Agriculture Organization of the United Nations and Intergovernmental Technical Panel on Soils.* Rome: Italy.

FAO, I., and ISRIC, I. (2012). *JRC: Harmonized World Soil Database*. Version 1.2. Rome, Italy IIASA, Laxenburg, Austria: FAO.

Feng, Q., Liu, J., and Gong, J. (2015). Urban Flood Mapping Based on Unmanned Aerial Vehicle Remote Sensing and Random Forest Classifier-A Case of Yuyao, China. *Water* 7, 1437–1455. doi:10.3390/w7041437

Feng, Z. K., Niu, W. J., Tang, Z. Y., Jiang, Z. Q., Xu, Y., Liu, Y., et al. (2020). Monthly Runoff Time Series Prediction by Variational Mode Decomposition and Support Vector Machine Based on Quantum-Behaved Particle Swarm Optimization. *J. Hydrol.* 583, 1. doi:10.1016/j.jhydrol.2020.124627

Fernández, A., García, S., Galar, M., Prati, R. C., Krawczyk, B., and Herrera, F. (2018). "Ensemble Learning," in *Learning from Imbalanced Data Sets* (Cham: Springer International Publishing), 147–196. doi:10.1007/978-3-319-98074-4_7

Flueck, J. A. (1987). "A Study of Some Measures of Forecast Verification," in *Preprints, 10th Conf. On Probability and Statistics in Atmospheric Sciences, Edmonton, AB, Canada, Amer. Meteor. Soc* (IEEE), 69–73.

Frattini, P., Crosta, G., and Carrara, A. (2010). Techniques for Evaluating the Performance of Landslide Susceptibility Models. *Eng. Geology.* 111, 62–72. doi:10.1016/j.enggeo.2009.12.004

Fressard, M., Thiery, Y., and Maquaire, O. (2014). Which Data for Quantitative Landslide Susceptibility Mapping at Operational Scale? Case Study of the Pays d'Auge Plateau Hillslopes (Normandy, France). *Nat. Hazards Earth Syst. Sci.* 14, 569–588. doi:10.5194/nhess-14-569-2014

Gao, B.-c. (1996). NDWI-A Normalized Difference Water index for Remote Sensing of Vegetation Liquid Water from Space. *Remote Sensing Environ.* 58, 257–266. doi:10.1016/S0034-4257(96)00067-3

Gillespie, T. W., Chu, J., Frankenberg, E., and Thomas, D. (2007). Assessment and Prediction of Natural Hazards from Satellite Imagery. *Prog. Phys. Geogr. Earth Environ.* 31, 459–470. doi:10.1177/0309133307083296

Goulden, T., Hopkinson, C., Jamieson, R., and Sterling, S. (2014). Sensitivity of Watershed Attributes to Spatial Resolution and Interpolation Method of LiDAR DEMs in Three Distinct Landscapes. *Water Resour. Res.* 50, 1908–1927. doi:10.1002/2013WR013846

Gudiyangada Nachappa, T., Tavakkoli Piralilou, S., Gholamnia, K., Ghorbanzadeh, O., Rahmati, O., and Blaschke, T. (2020). Flood Susceptibility Mapping with Machine Learning, Multi-Criteria Decision Analysis and Ensemble Using Dempster Shafer Theory. *J. Hydrol.* 590, 125275. doi:10.1016/j.jhydrol.2020.125275

Guerriero, L., Focareta, M., Fusco, G., Rabuano, R., Guadagno, F. M., and Revellino, P. (2018). Flood hazard of Major River Segments, Benevento Province, Southern Italy. *J. Maps* 14, 597–606. doi:10.1080/17445647.2018.1526718

Guikema, S. (2020). Artificial Intelligence for Natural Hazards Risk Analysis: Potential, Challenges, and Research Needs. *Risk Anal.* 40, 1117–1123. doi:10.1111/risa.13476

Gupta, N., Kleinhans, M. G., Addink, E. A., Atkinson, P. M., and Carling, P. A. (2014). One-dimensional Modeling of a Recent Ganga Avulsion: Assessing the Potential Effect of Tectonic Subsidence on a Large River. *Geomorphology* 213, 24–37. doi:10.1016/j.geomorph.2013.12.038

Gupta, S. P. Das. (1984). *The Ganga Basin. Part II*. New Delhi, India: Central Board for Prevention and Control of Water Pollution.

Hall, M. A., and Holmes, G. (2003). Benchmarking Attribute Selection Techniques for Discrete Class Data Mining. *IEEE Trans. Knowl. Data Eng.* 15, 1437–1447. doi:10.1109/TKDE.2003.1245283

Han, Y., Zhao, Y., Zhang, Y., Wang, J., Yang, S., Hong, Z., et al. (2019). A Cooperative Framework Based on Active and Semi-supervised Learning for Sea Ice Classification Using EO-1 Hyperion Data. *Trans. Jpn. Soc. Aero. S Sci.* 62, 318–330. doi:10.2322/tjsass.62.318

Han, Z., Wu, L., Ran, Y., and Ye, Y. (2003). The Concealed Active Tectonics and Their Characteristics as Revealed by Drainage Density in the North China plain (NCP). *J. Asian Earth Sci.* 21, 989–998. doi:10.1016/S1367-9120(02)00175-X

Hapuarachchi, H. A. P., Wang, Q. J., and Pagano, T. C. (2011). A Review of Advances in Flash Flood Forecasting. *Hydrol. Process.* 25 (18), 2771–2784. doi:10.1002/hyp.8040

Hapuarachchi, H. A. P., Wang, Q. J., and Pagano, T. C. (2011). A Review of Advances in Flash Flood Forecasting. *Hydrol. Process.* 25, 2771–2784. doi:10.1002/hyp.8040

Haughton, D., and Oulabi, S. (1993). Direct Marketing Modeling with CART and CHAID. *J. Direct Mark.* 7, 16–26. doi:10.1002/dir.4000070305

He, G., Xing, S., Xia, Z., Huang, Q., and Fan, J. (2018). Panchromatic and Multi-Spectral Image Fusion for New Satellites Based on Multi-Channel Deep Model. *Machine Vis. Appl.* 29, 933–946. doi:10.1007/s00138-018-0964-5

He, Z. (2021). Sensitivities of Hydrological Processes to Climate Changes in a Central Asian Glacierized Basin. *Front. Water* 3, 1. doi:10.3389/frwa.2021.683146

Hoehler, F. K. (2000). Bias and Prevalence Effects on Kappa Viewed in Terms of Sensitivity and Specificity. *J. Clin. Epidemiol.* 53, 499–503. doi:10.1016/S0895-4356(99)00174-2

Hong, H., Panahi, M., Shirzadi, A., Ma, T., Liu, J., Zhu, A.-X., et al. (2018a). Flood Susceptibility Assessment in Hengfeng Area Coupling Adaptive Neuro-Fuzzy Inference System with Genetic Algorithm and Differential Evolution. *Sci. Total Environ.* 621, 1124–1141. doi:10.1016/j.scitotenv.2017.10.114

Hong, H., Tsangaratos, P., Ilia, I., Liu, J., Zhu, A.-X., and Chen, W. (2018b). Application of Fuzzy Weight of Evidence and Data Mining Techniques in Construction of Flood Susceptibility Map of Poyang County, China. *Sci. Total Environ.* 625, 575–588. doi:10.1016/j.scitotenv.2017.12.256

Horton, R. E. (1932). Drainage-basin Characteristics. *Trans. AGU* 13, 350. doi:10.1029/TR013i001p00350

Hubbart, J. A., and Jones, J. R. (2009). "Floods," in *Encyclopedia of Inland Waters* (Elsevier), 88–91. doi:10.1016/B978-012370626-3.00229-5

Jain, S. K., Singh, R. D., Jain, M. K., and Lohani, A. K. (2005). Delineation of Flood-Prone Areas Using Remote Sensing Techniques. *Water Resour. Manage.* 19, 333–347. doi:10.1007/s11269-005-3281-5

Janizadeh, S., Avand, M., Jaafari, A., Phong, T. V., Bayat, M., Ahmadisharaf, E., et al. (2019). Prediction Success of Machine Learning Methods for Flash Flood Susceptibility Mapping in the Tafresh Watershed, Iran. *Sustainability* 11, 5426. doi:10.3390/su11195426

Jiménez-Jiménez, S. I., Ojeda-Bustamante, W., Ontiveros-Capurata, R. E., and Marcial-Pablo, M. d. J. (2020). Rapid Urban Flood Damage Assessment Using High Resolution Remote Sensing Data and an Object-Based Approach. *Geomatics, Nat. Hazards Risk* 11, 906–927. doi:10.1080/19475705.2020.1760360

Jiménez-Valverde, A. (2012). Insights into the Area under the Receiver Operating Characteristic Curve (AUC) as a Discrimination Measure in Species Distribution Modelling. *Glob. Ecol. Biogeogr.* 21, 498–507. doi:10.1111/j.1466-8238.2011.00683.x

Jolley, E. J., Turner, P., Williams, G. D., Hartley, A. J., and Flint, S. (1990). Sedimentological Response of an Alluvial System to Neogene Thrust Tectonics, Atacama Desert, Northern Chile. *J. Geol. Soc.* 147, 769–784. doi:10.1144/gsjgs.147.5.0769

Joshi, L. M., Pant, P. D., Kotlia, B. S., Kothyari, G. C., Luirei, K., and Singh, A. K. (2016). Structural Overview and Morphotectonic Evolution of a Strike-Slip Fault in the Zone of North Almora Thrust, Central Kumaun Himalaya, India. *J. Geol. Res.* 2016, 1–16. doi:10.1155/2016/6980943

Khosravi, K., Pham, B. T., Chapi, K., Shirzadi, A., Shahabi, H., Revhaug, I., et al. (2018). A Comparative Assessment of Decision Trees Algorithms for Flash Flood Susceptibility Modeling at Haraz Watershed, Northern Iran. *Sci. Total Environ.* 627, 744–755. doi:10.1016/j.scitotenv.2018.01.266

Khosravi, K., Shahabi, H., Pham, B. T., Adamowski, J., Shirzadi, A., Pradhan, B., et al. (2019). A Comparative Assessment of Flood Susceptibility Modeling Using Multi-Criteria Decision-Making Analysis and Machine Learning Methods. *J. Hydrol.* 573, 311–323. doi:10.1016/j.jhydrol.2019.03.073

Kimerling, A. J., Muehrcke, P., Muehrcke, J. O., and Muehrcke, P. M. (2016). *Map Use: reading, Analysis, Interpretation*. CA: Esri Press Redlands.

Krogh, L., and Greve, M. H. (2006). Evaluation of World Reference Base for Soil Resources and FAO Soil Map of the World Using Nationwide Grid Soil Data from Denmark. *Soil Use Manag.* 15, 157–166. doi:10.1111/j.1475-2743.1999.tb00082.x

Kumar, R. (2016). Flood hazard Assessment of 2014 Floods in Sonawari Sub-district of Bandipore District (Jammu&Kashmir): An Application of Geoinformatics. *Remote Sensing Appl. Soc. Environ.* 4, 188–203. doi:10.1016/j.rsase.2016.10.002

Kumar, R. (2020). Late Cenozoic Himalayan Foreland basin: Sedimentologic Attributes. *Episodes* 43, 417–428. doi:10.18814/epiiugs/2020/020026

Kumar, R., Singh, R., Gautam, H., and Pandey, M. K. (2018). Flood hazard Assessment of August 20, 2016 Floods in Satna District, Madhya Pradesh, India. *Remote Sensing Appl. Soc. Environ.* 11, 104–118. doi:10.1016/j.rsase.2018.06.001

Laks, I., Sojka, M., Walczak, Z., and Wróżyński, R. (2017). Possibilities of Using Low Quality Digital Elevation Models of Floodplains in Hydraulic Numerical Models. *Water* 9, 283. doi:10.3390/w9040283

Latrubesse, E. M. (2015). Large Rivers, Megafans and Other Quaternary Avulsive Fluvial Systems: A Potential "who's Who" in the Geological Record. *Earth-Science Rev.* 146, 1–30. doi:10.1016/j.earscirev.2015.03.004

Leeder, M. R., and Alexander, J. (1987). The Origin and Tectonic Significance of Asymmetrical Meander-Belts. *Sedimentology* 34, 217–226. doi:10.1111/j.1365-3091.1987.tb00772.x

Li, W., MacBean, N., Ciais, P., Defourny, P., Lamarche, C., Bontemps, S., et al. (2018). Gross and Net Land Cover Changes in the Main Plant Functional Types Derived from the Annual ESA CCI Land Cover Maps (1992-2015). *Earth Syst. Sci. Data* 10, 219–234. doi:10.5194/essd-10-219-2018

Lin, Z., and Yan, L. (2016). A Support Vector Machine Classifier Based on a New Kernel Function Model for Hyperspectral Data. *GIScience & Remote Sensing* 53, 85–101. doi:10.1080/15481603.2015.1114199

Liu, Q. Q., and Singh, V. P. (2004). Effect of Microtopography, Slope Length and Gradient, and Vegetative Cover on Overland Flow through Simulation. *J. Hydrol. Eng.* 9, 375–382. doi:10.1061/(ASCE)1084-0699(2004)9:5(375)

Macklin, M. G., and Lewin, J. (2003). River Sediments, Great Floods and Centennial-Scale Holocene Climate Change. *J. Quat. Sci.* 18, 101–105. doi:10.1002/jqs.751

Mahtab, M. H., Ohara, M., and Rasmy, M. (2018). The Impact of Rainfall Variations on Flash Flooding in Haor Areas in Bangladesh. *Water Conserv. Manag.* 2, 06–10. doi:10.26480/wcm.02.2018.06.10

Merz, B., Aerts, J., Arnbjerg-Nielsen, K., Baldi, M., Becker, A., Bichet, A., et al. (2014). Floods and Climate: Emerging Perspectives for Flood Risk Assessment and Management. *Nat. Hazards Earth Syst. Sci.* 14, 1921–1942. doi:10.5194/nhess-14-1921-2014

Mohammadi, A., Costelloe, J. F., and Ryu, D. (2017). Application of Time Series of Remotely Sensed Normalized Difference Water, Vegetation and Moisture Indices in Characterizing Flood Dynamics of Large-Scale Arid Zone Floodplains. *Remote Sensing Environ.* 190, 70–82. doi:10.1016/j.rse.2016.12.003

Mokarram, M., and Sathyamoorthy, D. (2016). Relationship between Landform Classification and Vegetation (Case Study: Southwest of Fars Province, Iran). *Open Geosci.* 8, 1. doi:10.1515/geo-2016-0027

Morrow, R., Fu, L.-L., Ardhuin, F., Benkiran, M., Chapron, B., Cosme, E., et al. (2019). Global Observations of Fine-Scale Ocean Surface Topography with the Surface Water and Ocean Topography (SWOT) Mission. *Front. Mar. Sci.* 6, 1. doi:10.3389/fmars.2019.00232

Nassif, S. H., and Wilson, E. M. (1975). The Influence of Slope and Rain Intensity on Runoff and Infiltration/L'influence de l'inclinaison de terrain et de l'intensité de pluie sur l'écoulement et l'infiltration. *Hydrological Sci. Bull.* 20, 539–553. doi:10.1080/02626667509491586

Ngo, P.-T., Hoang, N.-D., Pradhan, B., Nguyen, Q., Tran, X., Nguyen, Q., et al. (2018). A Novel Hybrid Swarm Optimized Multilayer Neural Network for Spatial Prediction of Flash Floods in Tropical Areas Using Sentinel-1 SAR Imagery and Geospatial Data. *Sensors* 18, 3704. doi:10.3390/s18113704

Oksanen, J., and Sarjakoski, T. (2005). Error Propagation of DEM-Based Surface Derivatives. *Comput. Geosciences* 31, 1015–1027. doi:10.1016/j.cageo.2005.02.014

Opricovic, S., and Tzeng, G.-H. (2004). Compromise Solution by MCDM Methods: A Comparative Analysis of VIKOR and TOPSIS. *Eur. J. Oper. Res.* 156, 445–455. doi:10.1016/S0377-2217(03)00020-1

Panahi, M., Jaafari, A., Shirzadi, A., Shahabi, H., Rahmati, O., Omidvar, E., et al. (2021). Deep Learning Neural Networks for Spatially Explicit Prediction of Flash Flood Probability. *Geosci. Front.* 12, 101076. doi:10.1016/j.gsf.2020.09.007

Park, N.-W. (2011). Application of Dempster-Shafer Theory of Evidence to GIS-Based Landslide Susceptibility Analysis. *Environ. Earth Sciearth Sci.* 62, 367–376. doi:10.1007/s12665-010-0531-5

Peirce, C. S. (1884). The Numerical Measure of the success of Predictions. *Science* ns-4, 453–454. doi:10.1126/science.ns-4.93.453-a10.1126/science.ns-4.93.453.b

Pignatelli, C., Sansò, P., and Mastronuzzi, G. (2009). Evaluation of Tsunami Flooding Using Geomorphologic Evidence. *Mar. Geology.* 260, 6–18. doi:10.1016/j.margeo.2009.01.002

Plaza, A., Benediktsson, J. A., Boardman, J. W., Brazile, J., Bruzzone, L., Camps-Valls, G., et al. (2009). Recent Advances in Techniques for Hyperspectral Image Processing. *Remote Sensing Environ.* 113, S110–S122. doi:10.1016/j.rse.2007.07.028

Podhorányi, M., Unucka, J., Bobál', P., and Říhová, V. (2013). Effects of LIDAR DEM Resolution in Hydrodynamic Modelling: Model Sensitivity for Cross-Sections. *Int. J. Digital Earth* 6, 3–27. doi:10.1080/17538947.2011.596578

Rahmati, O., Kornejady, A., Samadi, M., Deo, R. C., Conoscenti, C., Lombardo, L., et al. (2019). PMT: New Analytical Framework for Automated Evaluation of Geo-Environmental Modelling Approaches. *Sci. Total Environ.* 664, 296–311. doi:10.1016/j.scitotenv.2019.02.017

Razavi Termeh, S. V., Kornejady, A., Pourghasemi, H. R., and Keesstra, S. (2018). Flood Susceptibility Mapping Using Novel Ensembles of Adaptive Neuro Fuzzy Inference System and Metaheuristic Algorithms. *Sci. Total Environ.* 615, 438–451. doi:10.1016/j.scitotenv.2017.09.262

Regmi, A. D., Devkota, K. C., Yoshida, K., Pradhan, B., Pourghasemi, H. R., Kumamoto, T., et al. (2014). Application of Frequency Ratio, Statistical index, and Weights-Of-Evidence Models and Their Comparison in Landslide Susceptibility Mapping in Central Nepal Himalaya. *Arab. J. Geosci.* 7, 725–742. doi:10.1007/s12517-012-0807-z

Reichenbach, P., Rossi, M., Malamud, B. D., Mihir, M., and Guzzetti, F. (2018). A Review of Statistically-Based Landslide Susceptibility Models. *Earth-Science Rev.* 180, 60–91. doi:10.1016/j.earscirev.2018.03.001

Rizzato, S., Leo, A., Monteduro, A. G., Chiriacò, M. S., Primiceri, E., Sirsi, F., et al. (2020). Advances in the Development of Innovative Sensor Platforms for Field Analysis. *Micromachines* 11, 491. doi:10.3390/mi11050491

Rogger, M., Agnoletti, M., Alaoui, A., Bathurst, J. C., Bodner, G., Borga, M., et al. (2017). Land Use Change Impacts on Floods at the Catchment Scale: Challenges and Opportunities for Future Research. *Water Resour. Res.* 53, 5209–5219. doi:10.1002/2017WR020723

Suzen, M. L. t., and Doyuran, V. (2004). A Comparison of the GIS Based Landslide Susceptibility Assessment Methods: Multivariate versus Bivariate. *Environ. Geology.* 45, 665–679. doi:10.1007/s00254-003-0917-8

Sahu, S., Raju, N. J., and Saha, D. (2010). Active Tectonics and Geomorphology in the Sone-Ganga Alluvial Tract in Mid-ganga Basin, India. *Quat. Int.* 227, 116–126. doi:10.1016/j.quaint.2010.05.023

Sanders, B. F. (2007). Evaluation of On-Line DEMs for Flood Inundation Modeling. *Adv. Water Resour.* 30, 1831–1843. doi:10.1016/j.advwatres.2007.02.005

Santos, P. P., Reis, E., Pereira, S., and Santos, M. (2019). A Flood Susceptibility Model at the National Scale Based on Multicriteria Analysis. *Sci. Total Environ.* 667, 325–337. doi:10.1016/j.scitotenv.2019.02.328

Seliya, N., Khoshgoftaar, T. M., and Van Hulse, J. (2009). "A Study on the Relationships of Classifier Performance Metrics," in *2009 21st IEEE International Conference on Tools with Artificial Intelligence* (IEEE), 59–66. doi:10.1109/ICTAI.2009.25

Shukla, U. K., Srivastava, P., and Singh, I. B. (2012). Migration of the Ganga River and Development of Cliffs in the Varanasi Region, India during the Late Quaternary: Role of Active Tectonics. *Geomorphology* 171-172, 101–113. doi:10.1016/j.geomorph.2012.05.009

Siahkamari, S., Haghizadeh, A., Zeinivand, H., Tahmasebipour, N., and Rahmati, O. (2018). Spatial Prediction of Flood-Susceptible Areas Using Frequency Ratio and Maximum Entropy Models. *Geocarto Int.* 33, 927–941. doi:10.1080/10106049.2017.1316780

Sikorska, A. E., Viviroli, D., and Seibert, J. (2015). Flood-type Classification in Mountainous Catchments Using Crisp and Fuzzy Decision Trees. *Water Resour. Res.* 51, 7959–7976. doi:10.1002/2015WR017326

Singh, I. B. (1996). Geological Evolution of Ganga Plain - an Overview. *J. Palaeontol. Soc. India* 41, 99–137.

Singh, M., Singh, I. B., and Müller, G. (2007). Sediment Characteristics and Transportation Dynamics of the Ganga River. *Geomorphology* 86, 144–175. doi:10.1016/j.geomorph.2006.08.011

Smith, A. F. M., and Shafer, G. (1976). A Mathematical Theory of Evidence. *Biometrics* 32, 703. doi:10.2307/2529769

Srivastava, P., Kumar, A., Chaudhary, S., Meena, N., Sundriyal, Y. P., Rawat, S., et al. (2017). Paleofloods Records in Himalaya. *Geomorphology* 284, 17–30. doi:10.1016/j.geomorph.2016.12.011

Suman, S., Khan, S. Z., Das, S. K., and Chand, S. K. (2016). Slope Stability Analysis Using Artificial Intelligence Techniques. *Nat. Hazards* 84, 727–748. doi:10.1007/s11069-016-2454-2

Sun, W., Bocchini, P., and Davison, B. D. (2020). Applications of Artificial Intelligence for Disaster Management. *Nat. Hazards* 103, 2631–2689. doi:10.1007/s11069-020-04124-3

Taloor, A. K., Kotlia, B. S., Jasrotia, A. S., Kumar, A., Alam, A., Ali, S., et al. (2019). Tectono-climatic Influence on Landscape Changes in the Glaciated Durung Drung basin, Zanskar Himalaya, India: A Geospatial Approach. *Quat. Int.* 507, 262–273. doi:10.1016/j.quaint.2018.09.030

Tan, L., Guo, J., Mohanarajah, S., and Zhou, K. (2021). Can We Detect Trends in Natural Disaster Management with Artificial Intelligence? A Review of Modeling Practices. *Nat. Hazards* 107, 2389–2417. doi:10.1007/s11069-020-04429-3

Tanaka, K., Fujihara, Y., Hoshikawa, K., and Fujii, H. (2019). Development of a Flood Water Level Estimation Method Using Satellite Images and a Digital Elevation Model for the Mekong Floodplain. *Hydrological Sci. J.* 64, 241–253. doi:10.1080/02626667.2019.1578463

Tehrany, M. S., Lee, M.-J., Pradhan, B., Jebur, M. N., and Lee, S. (2014). Flood Susceptibility Mapping Using Integrated Bivariate and Multivariate Statistical Models. *Environ. Earth Sci.* 72, 4001–4015. doi:10.1007/s12665-014-3289-3

Tian, P., Lu, H., Feng, W., Guan, Y., and Xue, Y. (2020). Large Decrease in Streamflow and Sediment Load of Qinghai-Tibetan Plateau Driven by Future Climate Change: A Case Study in Lhasa River Basin. *CATENA* 187, 104340. doi:10.1016/j.catena.2019.104340

Tien Bui, D., Hoang, N.-D., Martínez-Álvarez, F., Ngo, P.-T. T., Hoa, P. V., Pham, T. D., et al. (2020). A Novel Deep Learning Neural Network Approach for Predicting Flash Flood Susceptibility: A Case Study at a High Frequency Tropical Storm Area. *Sci. Total Environ.* 701, 134413. doi:10.1016/j.scitotenv.2019.134413

Toth, C., and Jóźków, G. (2016). Remote Sensing Platforms and Sensors: A Survey. *ISPRS J. Photogrammetry Remote Sensing* 115, 22–36. doi:10.1016/j.isprsjprs.2015.10.004

Trivedi, A., Saxena, A., Chauhan, M. S., Sharma, A., Farooqui, A., Nautiyal, C. M., et al. (2019). Vegetation, Climate and Culture in Central Ganga plain, India: A Multi-Proxy Record for Last Glacial Maximum. *Quat. Int.* 507, 134–147. doi:10.1016/j.quaint.2019.02.019

Turskis, Z., Antuchevičienė, J., Keršulienė, V., and Gaidukas, G. (2019). Hybrid Group MCDM Model to Select the Most Effective Alternative of the Second Runway of the Airport. *Symmetry* 11, 792. doi:10.3390/sym11060792

UNDP Emergency Analyst (2008). *Situation Report: Bihar Flood 2008*. Patna: EHA.

UNSDG (2013). Open Working Group Proposal for Sustainable Development Goals. *United Nations Sustain. Dev. Goals* 1, 1–35.

Valdiya, K. S. (1976). Himalayan Transverse Faults and Folds and Their Parallelism with Subsurface Structures of North Indian plains. *Tectonophysics* 32, 353–386. doi:10.1016/0040-1951(76)90069-X

van Westen, C. J., Kuriakose, S. L., and Kuriakose, S. L. (2008). Spatial Data for Landslide Susceptibility, hazard, and Vulnerability Assessment: An Overview. *Eng. Geology.* 102, 112–131. doi:10.1016/j.enggeo.2008.03.010

Ward, D. P., Petty, A., Setterfield, S. A., Douglas, M. M., Ferdinands, K., Hamilton, S. K., et al. (2014). Floodplain Inundation and Vegetation Dynamics in the Alligator Rivers Region (Kakadu) of Northern Australia Assessed Using Optical and Radar Remote Sensing. *Remote Sensing Environ.* 147, 43–55. doi:10.1016/j.rse.2014.02.009

Weiss, M., Jacob, F., and Duveiller, G. (2020). Remote Sensing for Agricultural Applications: A Meta-Review. *Remote Sensing Environ.* 236, 111402. doi:10.1016/j.rse.2019.111402

West, A. M., Kumar, S., Brown, C. S., Stohlgren, T. J., and Bromberg, J. (2016). Field Validation of an Invasive Species Maxent Model. *Ecol. Inform.* 36, 126–134. doi:10.1016/j.ecoinf.2016.11.001

Wilks, D. S. (1995). "Chapter 7 Forecast Verification," in *Part of Volume: Statistical Methods in the Atmospheric Sciences*. Editor D. S. Wilks (Springer), 233–283. doi:10.1016/S0074-6142(06)80043-4

Yalcin, E. (2018). Two-dimensional Hydrodynamic Modelling for Urban Flood Risk Assessment Using Unmanned Aerial Vehicle Imagery: A Case Study of Kirsehir, Turkey. *J. Flood Risk Manag.* 12, e12499. doi:10.1111/jfr3.12499

Yang, J., El-Kassaby, Y. A., and Guan, W. (2020). The Effect of Slope Aspect on Vegetation Attributes in a Mountainous Dry valley, Southwest China. *Sci. Rep.* 10, 16465. doi:10.1038/s41598-020-73496-0

Yang, Q., Liu, C., and Liang, J. (2021). Unsupervised Automatic Classification of All-Sky Auroral Images Using Deep Clustering Technology. *Earth Sci. Inform.* 14, 1327–1337. doi:10.1007/s12145-021-00634-1

Yao, H., Qin, R., and Chen, X. (2019). Unmanned Aerial Vehicle for Remote Sensing Applications-A Review. *Remote Sensing* 11, 1443. doi:10.3390/rs11121443

Zhang, L., Huettmann, F., Liu, S., Sun, P., Yu, Z., Zhang, X., et al. (2019a). Classification and Regression with Random Forests as a Standard Method for Presence-Only Data SDMs: A Future Conservation Example Using China Tree Species. *Ecol. Inform.* 52, 46–56. doi:10.1016/j.ecoinf.2019.05.003

Zhang, L., Juenger, T. E., Lowry, D. B., and Behrman, K. D. (2019b). Climatic Impact, Future Biomass Production, and Local Adaptation of Four Switchgrass Cultivars. *GCB Bioenergy* 11, 956–970. doi:10.1111/gcbb.12609

Zhang, X., Han, X., Li, C., Tang, X., Zhou, H., and Jiao, L. (2019c). Aerial Image Road Extraction Based on an Improved Generative Adversarial Network. *Remote Sensing* 11, 930. doi:10.3390/rs11080930

Zhou, C., Yin, K., Cao, Y., Ahmed, B., Li, Y., Catani, F., et al. (2018). Landslide Susceptibility Modeling Applying Machine Learning Methods: A Case Study from Longju in the Three Gorges Reservoir Area, China. *Comput. Geosciences* 112, 23–37. doi:10.1016/j.cageo.2017.11.019

Zounemat-Kermani, M., Stephan, D., Barjenbruch, M., and Hinkelmann, R. (2020). Ensemble Data Mining Modeling in Corrosion of concrete Sewer: A Comparative Study of Network-Based (MLPNN & RBFNN) and Tree-Based (RF, CHAID, & CART) Models. *Adv. Eng. Inform.* 43, 101030. doi:10.1016/j.aei.2019.101030

Conflict of Interest: The authors declare that the research was conducted in the absence of any commercial or financial relationships that could be construed as a potential conflict of interest.

The reviewer NL declared a past co-authorship with the authors AA, AA, RC to the handling Editor.

Advantages of publishing in Frontiers

OPEN ACCESS

Articles are free to read
for greatest visibility
and readership

FAST PUBLICATION

Around 90 days
from submission
to decision

HIGH QUALITY PEER-REVIEW

Rigorous, collaborative,
and constructive
peer-review

TRANSPARENT PEER-REVIEW

Editors and reviewers
acknowledged by name
on published articles

Frontiers
Avenue du Tribunal-Fédéral 34
1005 Lausanne | Switzerland

Visit us: www.frontiersin.org
Contact us: frontiersin.org/about/contact

REPRODUCIBILITY OF RESEARCH

Support open data
and methods to enhance
research reproducibility

DIGITAL PUBLISHING

Articles designed
for optimal readership
across devices

FOLLOW US

@frontiersin

IMPACT METRICS

Advanced article metrics
track visibility across
digital media

EXTENSIVE PROMOTION

Marketing
and promotion
of impactful research

LOOP RESEARCH NETWORK

Our network
increases your
article's readership